MOLECULAR WATER OXIDATION CATALYSTS BASED ON COPPER AND NICKEL COMPLEXES

Pablo Garrido Barros

UNIVERSITAT ROVIRA i VIRGILI

Molecular Water Oxidation Catalysts Based on Copper and Nickel Complexes

PABLO GARRIDO BARROS

DOCTORAL THESIS
2018

UNIVERSITAT ROVIRA I VIRGILI
MOLECULAR WATER OXIDATION CATALYSTS BASED ON COPPER AND NICKEL COMPLEXES
Pablo Garrido Barros

UNIVERSITAT ROVIRA I VIRGILI
MOLECULAR WATER OXIDATION CATALYSTS BASED ON COPPER AND NICKEL COMPLEXES
Pablo Garrido Barros

Pablo Garrido Barros

Molecular Water Oxidation Catalysts Based on Copper and Nickel Complexes

DOCTORAL THESIS

Supervised by

Prof. Antoni Llobet

Institute of Chemical Research of Catalonia

Tarragona

2018

UNIVERSITAT ROVIRA I VIRGILI
MOLECULAR WATER OXIDATION CATALYSTS BASED ON COPPER AND NICKEL COMPLEXES
Pablo Garrido Barros

ICIQ - Institut Català d'Investigació Química

Avgda, Països Catalans 16,

43007 Tarragona (Spain)

Prof. Antoni Llobet, Group Leader at the Institute of Chemical Research of Catalonia,

I STATE that the present study, entitled "Molecular Water Oxidation Catalysts Based on Copper and Nickel Complexes" presented by Pablo Garrido Barros for the award of the degree of Doctor, has been carried out under my supervision in my group at the Institute of Chemical Research of Catalonia and that it fulfills all the requirements to be eligible for the International Doctor Distinction.

Tarragona, July 26th, 2018

Doctoral Thesis Supervisor

Prof. Antoni Llobet

Acknowledgments

In this section, I would like to aknowledge all the people that contributed to make this work possible.

Siempre he dicho que mi trabajo consiste en imitar a las plantas y la forma en que hacen la fotosíntesis. Y una de las primeras cosas que entendí es que ellas, por sí solas, no pueden fabricar su propio alimento, sino que necesitan del agua y del sol para hacerlo. De la misma forma, yo no hubiese sido capaz de realizar esta tesis doctoral sin la ayuda y el apoyo de numerosas personas a las que me gustaría agradecer.

En primer lugar, quiero empezar por agradecer a mi supervisor Antoni Llobet. Hace seis años me dio la oportunidad de empezar a trabajar con él durante una beca de verano y ahora, tras un año de máster y cuatro de doctorado, no podría estar más contento por ello. No solo le agradezco por acogerme, si no por haber sido un referente y un guía durante todo este tiempo y por haberme transmitido su pasión por lo que hacemos. Su apoyo y confianza en mi trabajo han sido fundamentales para mi crecimiento personal y profesional y para aprender a construir mi camino hacia el futuro. Esta etapa siempre será una experiencia inolvidable.

Hacer el doctorado en el ICIQ no ha sido un deporte individual, si no que he podido contar con un magnifico equipo con el que me alegro de haber compartido este partido. Y aunque los jugadores han ido cambiando a lo largo del tiempo, todos han hecho su aportanción indispensable: Laia, Lorenzo, Isidoro, Sam, Serena, CJ, Abi, Asmaul, Laura, Natalii, Primavera, Marta, Navid, Jan, Dooshaye, Jordi and Jana. Especialmente me gustaría agradecer a Fernando, Carolina y Mª José, con quienes he tenido la suerte de compartir todo mi viaje aquí. Y por supuesto a Roc, al que veo como un hermano mayor. Su amor por la

planificación y sus consejos han sido fundamentales a la hora de definir mi trayectoria.

I would also like to aknowledge Professor Victor Batista from Yale University and Professor Jonas Peters from Caltech. They accepted me as visiting student during my PhD and treated me as part of their own lab team. I had the great opportunity of working in their groups and learning from them and that has become a priceless experience in my life. They made me feel like at home besides the huge distance between Spain and USA. I also want to thank all the people I met during those two research stays, with an especial mention to Joaquín, Zoila and Matt. They took care of me just in the hardest moments when I felt lonely. Thanks for being my "American" family.

Mi estancia en Tarragona no hubiese sido lo mismo sin mi grupo de amigos: Funes, Elena, Lea, Sergi, Vane, Marcos, Adi, Bruna, Víctor y Fernando. Ellos me han dado una vida llena de alegría, fiestas y risas al margen del trabajo. Especialmente el "Chache" y el "Chenpion" a quienes me ha tocado aguantarlos tanto como compañeros de trabajo como de amigos. Pero sin ellos el ocio y el trabajo no hubiesen sido ni la mitad de divertidos. Es una suerte contar con compañeros y amigos como vosotros, porque imagino que aguantarme tanto tiempo a mi tampoco es fácil.

También he de destacar por separado a mi gran amigo Funes. Desde que recibí un álbum de fotos lleno de recuerdos de la Summer Fellow, tuve claro que pasaríamos esta aventura juntos. Además de un buen amigo, ha sido una fuente de conocimiento e inspiración tanto en el trabajo como en la cocina y el mejor compañero (que no pareja) de salsa y LOL que se puede tener. Esas tardes de cocina, marea, cervezas y fiesta han sido mi gasolina para poder continuar en la carrera.

Aunque durante este tiempo de doctorado no hayan podido estar físicamente conmigo, toda mi familia y especialmente Mayte, Javi, Tamara y Paula, siempre han estado presentes con su apoyo desde Granada.

Quizás es un buen momento para mirar hacia atrás y buscar los responsables de la persona en que me he convertido hoy. A mi madre, Rosa, mi padre, Manuel y mi hermana, María, no hay suficientes palabras para agradeceros la confianza que siempre habéis tenido en mí y el apoyo incondicional que me habéis dado, no solo durante el doctorado, sino con cualquier proyecto u objetivo que me hubiese marcado en la vida. Me habéis enseñado de lo que soy capaz y gracias a vosotros siempre he luchado y lucharé cada batalla que se me presente. Gracias por hacerme ser quien soy hoy.

Para terminar, quería citar las palabras que el padre del premio nobel de física Richard Feyman (uno de mis ídolos) le solía decir de pequeño: "Everything goes because the sun is shining" que en español vendría a significar: "Todo funciona porque el sol brilla". Y por eso mi último agradecimiento es para ti, Marta. Por aguantarme todo este tiempo, por ayudarme a ser mejor, por pasar conmigo todos los buenos y malos momentos y por ser mi compañera tanto de las aventuras pasadas como de las que aún nos quedan por vivir. Porque tú eres el sol que hace que todo mi mundo funcione.

The work performed in the present doctoral thesis has been possible thanks to the Institute of Chemical Research of Catalonia (ICIQ) and the funding of: MINECO, AGAUR and FEDER (CTQ2016-80058-R, CTQ2015-73028-EXP, SEV 2013-0319, ENE2016-82025-REDT (FOTOFUEL), CTQ2016-81923-REDC (INTECAT), 2014 SGR-915, 2017 SGR-1631) and "La Caixa" foundation for the PhD grant.

List of publications

1- "Redox Non-Innocent Ligand Controls Water Oxidation Over-potential in a New Family of Mononuclear Cu-Based Efficient Catalysts" Garrido-Barros, P.; Funes-Ardoiz, I.; Drouet, S.; Benet-Buchholz, J.; Maseras, F.; Llobet, A. J. Am. Chem. Soc. 2015, 137, 6758-6761.

2- "Single Electron Transfer Steps in Water Oxidation Catalysis. Redefining the Mechanistic Scenario" Funes-Ardoiz, I.; Gar-rido-Barros, P.; Llobet, A.; Maseras, F. ACS Catal. 2017, 7, 1712-1719.

3- "How to make an efficient and robust molecular catalyst for water oxidation" P Garrido-Barros, C Gimbert-Suriñach, R Matheu, X Sala, A Llobet. Chem. Soc. Rev. 2017, 46, 6088-6098.

4- "Electronic pi-Delocalization Boosts Catalytic Water Oxida-tion by Cu (II) Molecular Catalysts Heterogenized on Gra-phene Sheets" Pablo Garrido-Barros, Carolina Gimbert-Suriñach, Dooshaye Moonshiram, Antonio Picón, Pere Monge, Victor S Batista, Antoni Llobet. J. Am. Chem. Soc. 2017, 139, 12907-12910

5- "Light driven styrene epoxidation and hydrogen generation us-ing H 2 O as an oxygen source in a photoelectrosynthesis cell" Pau Farràs, C Di Giovanni, JN Clifford, P Garrido-Barros, E Palomares, A Llobet, Green Chem., 2016, 18, 255-260

6- "Ru–bis(pyridine)pyrazolate (bpp)-Based Water-Oxidation Catalysts Anchored on TiO2: The Importance of the Nature and Position of the Anchoring Group" Laia Francàs, Craig Richmond, Pablo Garrido-Barros, Nora Planas, Stephan Roe-ser, Jordi Benet-Buchholz, Lluís Escriche, Xavier Sala, Antoni Llobet Chem. Eur. J. 2016, 22, 5261-5268

7- "Elucidating light-induced charge accumulation in an artificial analogue of methane monooxygenase enzymes using time-resolved X-ray absorption spectroscopy" Dooshaye Moon-shiram, Antonio Picón, Alvaro Vazquez-Mayagoitia, Xiaoyi Zhang, Ming-Feng Tu, Pablo Garrido-Barros, Jean-Pierre Mahy, Frédéric Avenier, Ally Aukauloo, Chem. Commun. 2017, 53, 2725-2728

8- "Elucidating the Nature of the Excited State of a Heteroleptic Copper Photosensitizer by using Time-Resolved X-ray Ab-sorption Spectroscopy" Dooshaye Moonshiram, Pablo Gar-rido-Barros, Carolina Gimbert-Suriñach, Antonio Picón, Cunming Liu, Xiaoyi Zhang, Michael Karnahl, Antoni Llobet Chem. Eur. J. 2018, 24, 6464-6472

9- Garrido-Barros, P.; Funes-Ardoiz, I.; Farrás, P.; Gimbert-Suriñach, C.; Maseras, F.; Llobet, A. In "Water as an oxygen source for oxidation reactions in Catalytic Oxidations in Or-ganic Synthesis". Muniz, K. Ed.; Georg Thieme Verlag KG, Stuttgart, New York, 2017.

Abstract

Chapter 1. General introduction

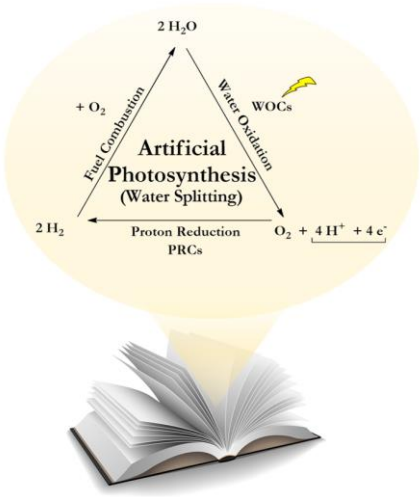

This chapter deals with the general description of the background and the remaining challenges in the field of molecular water oxidation catalysis (mol-WOC). Firstly, an introduction about the current energetic scheme based on fossil fuels gives rise to the exposure of the motivations for new strategies based on artificial photsynthesis as potential solution. As part of this strategy, the analysis of the water oxidation reaction together with the historical development of molecular catalysts leads to stablish the main key factors that determine the progress in the field. Finally, the advances in transferring the catalytic activity from homogeneous molecular catalysts to heterogeneous molecular anodes is presented as one of the final steps in the design of practical photochemical cells for artificial photosynthesis.

Chapter 2. Objectives

Chapter 3. Redox non-innocent ligands in copper-catalyzed water oxidation

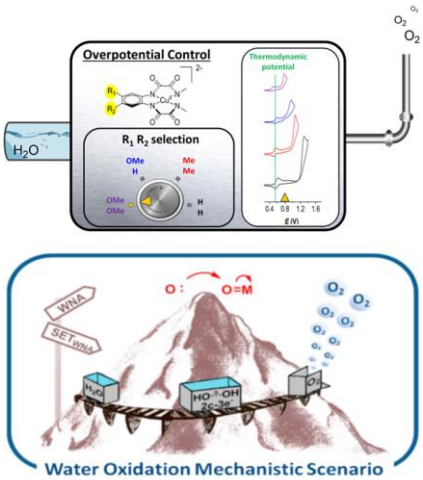

Chapter 3 explores the use of redox non-innocent ligands for molecular water oxidation catalysis using the copper complex $[Cu^{II}(mox)]^{2-}$. The influence of the ligand oxidation on the catalytic mechanism allows an excellent control on the overpotential, that can be lowered to a record value of 170 mV. Moreover, the computational study of the O-O bond formation step in three different copper catalysts reveals an unprecedented mechanism based on single electron transfers.

Chapter 4. From ligand-based to metal-based electron transfer in water oxidation catalysis

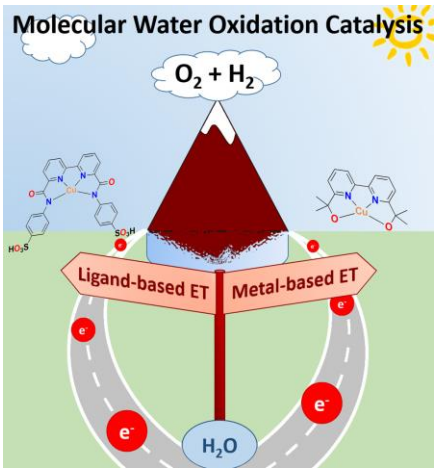

New copper complexes are developed for water oxidation catalysis bearing different scafolds. The first two complexes contains redox non-innocent ligands that can accumulate two oxidative equivalents so that the metal center act as an spectator in the electron transfer processes. A third complex has been synthetized bearing a redox innocent ligand. Those systems allow to explore the opportunities and limitations of using redox non-inocent ligands in water oxidation catalysis.

Chapter 5. From molecules to solid state: Copper-Based Molecular Anodes

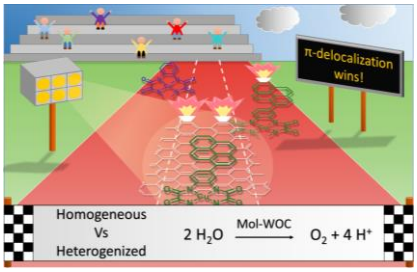

The copper complex $[Cu^{II}\text{-mox}]^{2-}$ has been modified to include a pyrene functionality resulting in an improvement of the catalytic features compared to the unmodified homologue. Moreover, both complexes have been used to build molecular anodes by anchoring on graphene-based electrodes through π-π stacking. The extended π-interations exerted by the graphene enhance the catalytic performance of both catalysts, reaching one the highest kinetic constants in copper WOC.

Chapter 6. An extension to Nickel

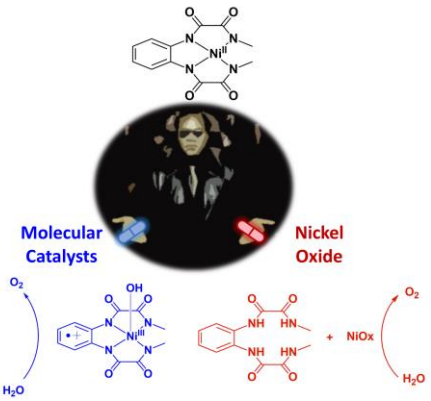

Motivated by the lack of information in nickel-based mol-WOC, the previous strategies using copper complexes are applied to the development of nickel catalysts. The complex $[Ni^{II}\text{-mox}]^{2-}$ is synthetized and its catlytic performance toward water oxidation is evaluated. This system allows to study the factors determining the low stability of molecular nickel complexes in aqueous solutions under oxidative conditions and thus, their opportunities as molecular catalysts or precursor of active nickel oxides

Chapter 8. General conclusions

Chapter 9. Annexes

Table of Contents

Chapter 1

General Introduction

This chapter deals with the general description of the background and the remaining challenges in the field of molecular water oxidation catalysis (mol-WOC). Firstly, an introduction about the current energetic scheme based on fossil fuels gives rise to the exposure of the motivations for new strategies based on artificial photsynthesis as potential solution. As part of this strategy, the analysis of the water oxidation reaction together with the historical development of molecular catalysts leads to stablish the main key factors that determine the progress in the field. Finally, the advances in transferring the catalytic activity from homogeneous molecular catalysts to heterogeneous molecular anodes is presented as one of the final steps in the design of practical photochemical cells for artificial photosynthesis.

General Introduction

1.1 The energy scheme: Causes and Consequences

Only in the year 2015, the world total energy consumption was around 575 quadrillion British thermal units (BTU), what is 14,489.70 millions of tonnes of oil equivalent (Mtoe), according to the last data released by the U.S. Energy Information Administration (U.S. EIA).[1] By itself, this amount of energy is just a large number without much meaning unless we contextualize it. In a social context, taking into account the world population in the same year, around 7.4 billion of people, it involves that each single person consumed the energy equivalent to 2 tons of oil fuel in one year and this value begins to take on meaning. Moreover, considering the social inequalities, this is a low value compared with the personal consumption of an inhabitant from an OECD (Organisation for Economic Co-operation and Development) country for instance. In a temporal context, when we look at the past, a clear trend reveals a continuous growth in the consumption levels (Figure 1), with a 65% of increase from 1990 to 2015. If we now look to the future, similar trend is projected for at least the next 20 years, involving 30% more consumption by 2040. Although the rise is getting slower, the future is characterized by a growing of 3.4% per year in the global economy and an expansion from 7.4 billions of people to more than 9 in 2040 determining the necessary increase in energy consumption. Asian countries like India and China will position as the main energy consumers with the largest share in the global energy use of around 11%.

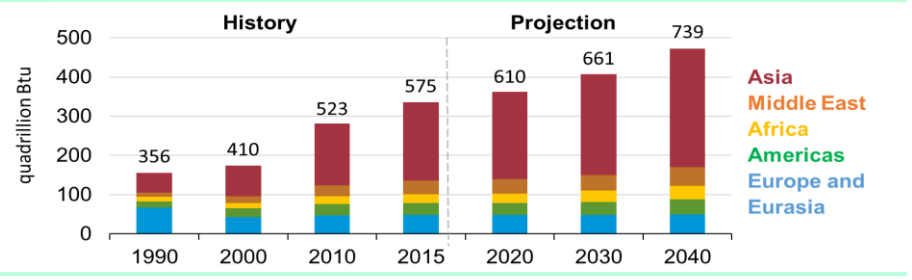

Figure 1. World total energy consumption and expectations for the time range 1990-2040. Source: *EIA, International Energy Outlook 2018*.

Another important factor that helps us to understand the consumption data is the resource of energy we employ to satisfy our growing needs. According to the U.S. EIA, in 2015 the 83% of the final consumed energy was provided by fossil fuels including oil, natural gas and coal (Figure 2). This situation is not new, as the energy mix has been long dominated by fossil fuels despite the slow decrease in its use in favor of the renewable sources.

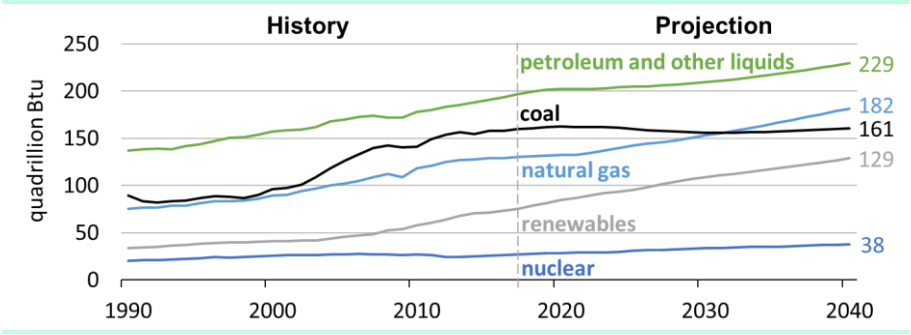

Figure 2. World energy consumption and expectations by energy spource for the time range 1990-2040. Source: *EIA, International Energy Outlook 2018*.

All previous data define a current energy scheme with a high, continuously growing demand that is mainly supplied by fossil fuels. In the search for the causes responsible for this situation, three main factors can be pointed out:

- Historical population growth. As recorded by United Nations,[2] population has increased from less than 1 billion around 200 years ago to 7.4 in 2015, involving a subsequent increase in the energy needs.
- Improvement of the life standards mainly in the most developed countries. The energy consumption per capita has inevitably raised to meet the increasingly demanding needs, besides an irresponsible energy use unconcerned about the consequences.

General Introduction

- Since the industrial revolution, fossil fuels have been the key gear that has guided the human development. These energetic products are the basis of our society and have become essential for several important sectors such as industry and transportation. The alternatives sources of energy including renewables or the nuclear energy have encountered significant barriers in their development like low efficiencies, intermittent production, storage problems or exploitation risks. Therefore, they have not been competitive opponent to fossil fuels.

However, despite the widespread use of this energy scheme all over the world, it is far from being an ideal energy model as it involves three non-negligible consequences:

- Depletion of fossil fuels reserves: Oil, coal and natural gas have been generated and accumulated in the Earth crust during million of years so that their current fast exploitation makes them a non-renewable source of energy. Estimations from the Global Resource Observatory (Anglia Ruskin University) reveal that few places in the world have fossil fuels reserves for more than 100 years.[3]
- Unequal reserves distribution:[4] Most of the international conflicts we are living nowadays hide some geopolitical reasons in order to dominate the production and distribution channel of fossil fuels. They constitute a large part of a state's economy and are currently contributing to deepen the difference between developed and underdeveloped countries.
- Pollution derived from its use: Perhaps this is the most important and concerning consequence for the current society. The use of fossil fuels to obtain energy generate large amount of CO_2 emissions that are responsible for the global warming the Earth is experiencing.[5] There is a clear correlation between the CO_2 levels

and the superficial temperature[6] (Figure 3) and, despite the slow mechanisms that our planet uses to regulate it, living beings cannot adapt to the fast and drastic warming.

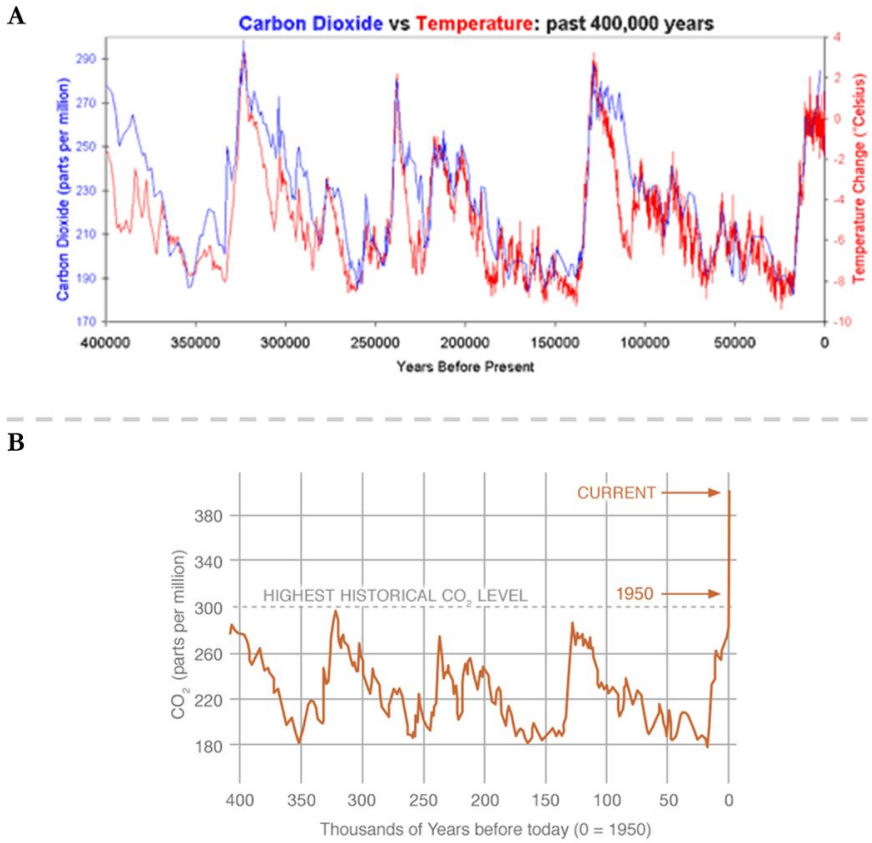

Figure 3. (A) Vostok ice core records for carbon dioxide concentration and temperature change until 1999.[6] (B) Global mean carbon dioxide concentration. Source: *National Oceanic and Atmospheric Administration, U.S. Department of Commerce.*

Since 1992 with the creation of the United Nations Framework Convention on Climate Change (UNFCCC), governments of different countries around the world started to concern about the global warming and its harmful consequences and proposed several actions as measures to reduce them. One of the first treaty was known as the Kyoto Protocol created in 1997 to reduce greenhouse gas emissions in the state parties.[7]

Specifically, the aim was reducing the emissions around 5.2% by 2012 and they made available several tools to help countries meeting the objectives. Since 1995 the Conferences of the Parties (COP) is the yearly conference in charge of assessing the progress and solving the problems regarding the compliance with the protocol. Although only 9 countries of the 36 parties failed with the objective, the total amount of CO_2 due to the non-participating countries resulted in the global failure.

More recently, in 2016, a new agreement known as the Paris agreement was signed by 195 countries in order to reduce the temperature increase below 2ºC regarding preindustrial levels.[8] This new agreement, which starts after the Kyoto protocol finishes in 2020, assumes that meeting the objective would considerably reduce the effects of the climate change. However, comply with all the pledges provided in the agreement will only reduce the energy-related emissions so that the rise in the temperature will be 2.7ºC by 2100. The lower use of coal and oil in favour of natural gas and renewables energies is not enough to ensure a sustainable future. Although those measures would have an important impact on electricity generation, nowadays there is not a simple alternative to oil fuels in transportation and petrochemicals production, so its demand is expected to continue growing. A deeper change in the current production and life models is required and that would likely involve a necessary carbon neutral economy.

1.2 Artificial Photosynthesis: Toward Solar Fuels

Sun is the most promising source of energy for human being due to several features:

- It is a renewable source of energy in the time scale of human life.
- It is carbon neutral.

- The Earth's surface receives in one hour an amount of energy in form of radiation enough to supply one year of global energy demand.[9]

These reasons have led scientists to focus on the development of technologies that can take advantage of that energy source. In the history of humankind, sunlight has been long used as source of heat by using the derived thermal energy. Light can interact with the matter at a vibrational level and that produces an increase in the temperature that can be used for several applications like warming, cooking or even for obtaining mechanical energy that would be eventually transformed into electricity. This is the basis for the development of the so-called thermal solar energy. On the other hand, light can also interact with semiconductors so that it promotes an electron flow and thus the direct conversion of solar into electrical energy, known as photovoltaic (PV) solar energy. This technology, which is performed in the photovoltaic cells, has been studied for years and nowadays it provides around the 5% of the total energy consumption with growth expectations.[2,10]

However, both the thermal and photovoltaic solar energies present a major drawback: their energy production model does not contemplate the storage of the solar energy into fuels. The final form of energy that those technologies produce is either heat, mechanical energy or electricity. Instead, as aforementioned, around the 83% of the final consumed energy is provided by fuels.[2,10] Those data reflect that the main consuming sectors, *i.e.* industry and transportation, follow an operation scheme based on the combustion of fuels to obtain the required energy. Therefore, it is imperative to explore the ways of harvesting the solar energy into chemical bonds and producing what would be called solar fuels.

Importantly, this idea has been already implemented by nature in the process known as natural photosynthesis.[11,12] Through this process, the photosynthetic organisms (green plants and algae) use water and carbon

General Introduction

dioxide as raw material and sunlight as energy input to synthetize carbohydrates, whose chemical bonds store the absorbed solar energy. Those carbohydrates will be later consumed as fuels to obtain again the energy for performing the life functions and releasing carbon dioxide to the environment. The reactions involved in the storage of solar energy are summarized in Scheme 1 and, from a redox point of view, they can be divided into the two half-reactions: water oxidation and CO_2 reduction (Calvin Cycle).

Scheme 1. Representation of the natural photosynthesis and artificial photosynthesis processes.

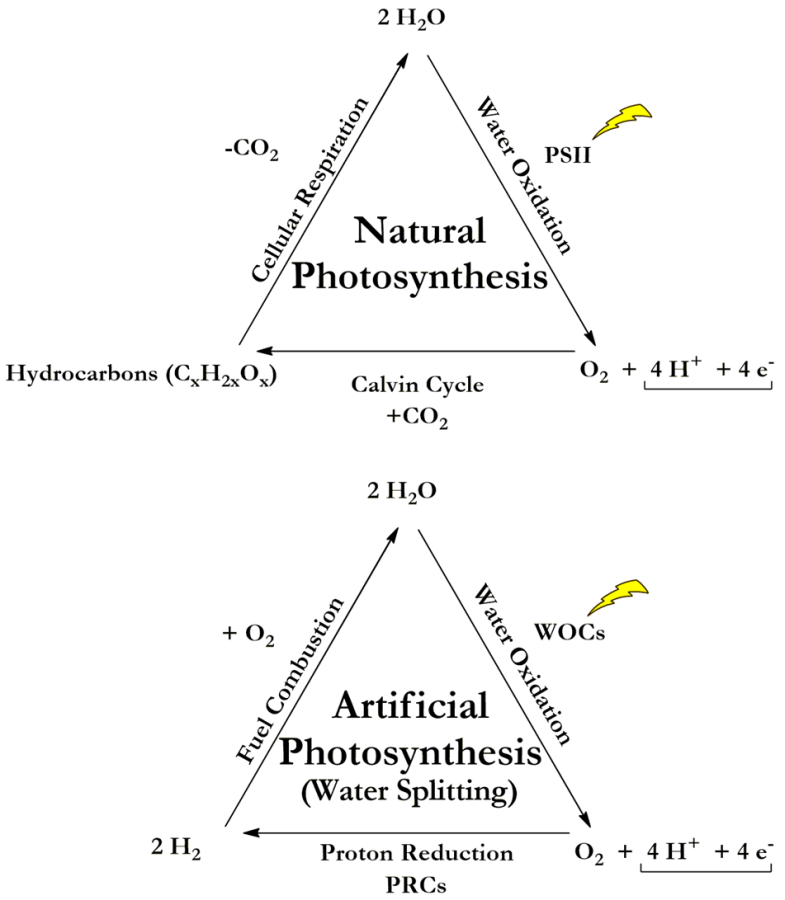

Following a similar scheme, artificial photosynthesis has emerged as a promising technology to harvest the solar energy into fuels.[13,14] This process generally involves the oxidation of water to molecular oxygen releasing protons and electrons and the further reduction of those protons to molecular hydrogen, reason why this process is also known as water splitting. Alternatively, other schemes can be propose by changing the nature of the molecules that are oxidized and reduced. For example, for synthetic purposes, organic compounds can be oxidized using water to other chemicals with commercial interest, what is also termed as "organic-substrate-assisted water splitting" (OSA-WS).[15] In the same way, protons and electrons can be used for other reduction reactions coupled to water oxidation such as carbon dioxide to carbohydrates, nitrogen to ammonia or any other reductions of organic compounds. Those reduced products can be also employed as fuel like the hydrogen or for other industrial processes as starting materials.

1.2.1 Technical aspects

From a technical point of view, the reactions involved in the artificial photosynthesis have generally three requirements:

- An input of energy as they are thermodynamically demanding. In order to have an efficient way to store energy that input would be fully provided by the sunlight.
- A strategy to overcome the kinetic barriers and make the reactions efficient from a practical time-scale perspective.
- Separation of the different products obtained from the overall process, as they would be used with different purposes.

Since water only interact with light at a vibrational level, the first requirement can be accomplish with the use of a light absorber, which should be able to uptake the sunlight and transfer it to the rest of the system. Normally, specific transition metal complexes and semiconductor are

employed for this purpose as the light produces the excitation of their valence electrons and eventually they are transferred to promote the necessary transformations.[13] Regarding the second requirement, many molecules and materials have been proposed to catalyze both reactions with different mechanisms that in general lower the activation barriers for each redox half-reaction.[16,17] Currently, this is an highly active field of research in chemistry and the recent advances exceed the rate at which those reactions take place in the natural system. Finally, in order to separate the product of the reactions, a scheme based on two compartments separated by a semipermeable membrane is frequently used so that each half reaction is performed in a different compartment and then products are obtained separately.

Keeping in mind the previous technical requirements, different designs can be proposed to integrate all the components necessary for the artificial photosynthesis. Particularly, those designs can be gathered in three groups: PV/electrolyzer, Integrated Photoelectrochemical Cell (PEC) or mixed colloid devices.[18]

PV/electrolyzer, as indicated by its name, incorporates a photovoltaic cell that acts as the light absorber and transfer the produced electricity to an electrochemical cell, where the catalysts for both reactions are located and connected respectively to an anode and a cathode. Using the incoming electrical power, those catalysts carry out the water splitting process immersed in an electrolyte solution. Despite that the technology for this design is already developed, its cost is generally high due to the expensive PV production. On the other hand, mixed colloid systems are based on simple and low cost technologies but the concept of their operation has to be still proven. The operating basis consists of using particles including the three component: light absorber, oxidation catalyst and reduction catalyst. Those particles would remain in suspension in an electrolyte solution and operate independently of other particles yielding both products in the same compartment. Finally, the integrated PEC systems are

based on an intermediate scheme. They propose the use of a photoanode incorporating the light absorber and the oxidation catalyst, coupled to a photocathode containing also a light absorber and the reduction catalysts. Both photoelectrodes would be wired through electrical connection and separated by a membrane into two compartments.

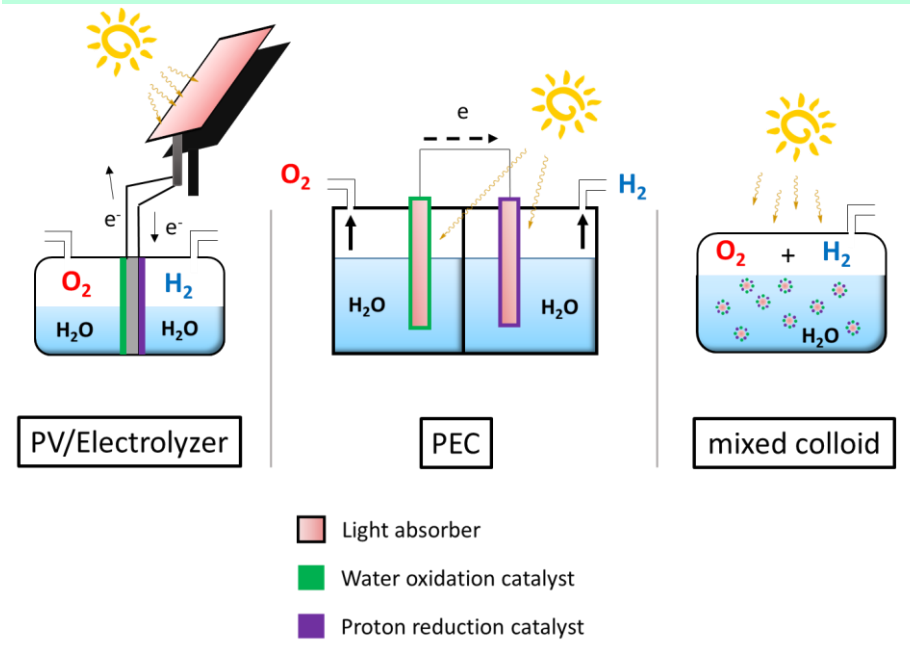

Figure 4. Schematic representation of the three general designs for an artificial photosynthetic cell.

An important aspect of the photosynthetic system, independently of the design, is the need to be efficient, stable and operate at an industrial level.[19] Moreover, all the components of the system have to meet those constraints at the same time that they operate in compatible conditions with each other. Therefore, beside the individual performance of each component, the compatibility and combined features are essential for a practical device.

General Introduction

According to the previous description, artificial photosynthesis technology presents three main advantages compared to other renewables strategies:

- The use of sunlight as the only energy input, taking into account that this resource is renewable, highly abundant and well distributed over the Earth.
- Artificial photosynthesis for fuel production uses only water as main raw materials, which is also the only product from the combustion of molecular hydrogen. In the case of using CO_2 also as starting material to produce fuels, the combustion of those fuels would release the same amount of CO_2 as initially consumed. Therefore, this process constitutes a closed cycle for the energy generation without emissions of net amount of CO_2 or other waste products.
- Finally, the technology for the use of carbohydrates as fuels is already developed and implanted in the industry and transportation. Moreover, in the case of producing hydrogen as fuel, many private enterprises and public organism are currently working on implementing hydrogen-based energetic scheme.[20] No further deep development is needed for the implementation of artificial photosynthesis as energy production process.

Meanwhile, other renewables resources such as wind or hydraulic power are currently not able to cover the whole energy supply. Besides the high initial investment and the instability of the production, they are very inefficient and the produced electric energy (they mainly convert primary energy into electricity instead of fuels) is currently difficult to store. As to nuclear fission energy, the problems associated with the waste storage and operation safety has slowed its development despite the high efficiency. In contrast, nuclear fusion energy is much safer in terms of waste treatment but it needs many technological requirements that involve high

complexity and large investments. Moreover, the energy storage problem remains since no fuel is produced in the process. Finally, biomass has been lately considered as a potential option for energy production because it does not produce net CO_2 emissions. However, the raw material cost, the large cultivation area needed (responsible for the 87% of the deforestation in Malaysia) and the easy degradation of the biodiesel fuel hinders a significant develop of this approach.

1.2.2 Current accomplishments and challenges

Research in the field of artificial photosynthesis started more than 40 years ago and partial objectives have been already accomplished.[18] It is thus important to analyze the current situation in order to perform further rational research driven by the remaining needs and challenges. Those advances are summarized in the following list:

- Separators: Semipermeable separators for the anodic and cathodic compartment have been commercialized for years. They can operate in both acidic and alkaline media and are mainly based on perfluorinated sulfonic acid polymers[21] or asbestos separators[22] respectively. Those materials could be readily adapted for their use in the integrated PEC, although further research in this area would be always welcome in terms of decreasing cost.
- Catalysts: high activity rates have been reached using mainly materials comprising noble metal and noble metal oxides.[23] For proton reduction in acidic media, Pt features one of the highest activity and stability, whereas Ru and Ir oxides are employed for the water oxidation. Some progress has been also achieved trying to move on non-noble metals for proton reduction such as MoS_2. In alkaline media, Ni based oxides dominate the water oxidation field while Ni-Mo composites have been extensively used for the proton reduction reaction.

- Light absorbers: three metal oxides have been deeply studied as light absorbers in tandem water splitting system, being Fe_2O_3,[24] WO_3[25] and $BiVO_4$.[26] All of them have band gaps in the visible range and can be successfully coupled to water oxidation catalyst resulting in high photocurrents under operation. Regarding other material than oxides, only Silicon[27,28] and Indium phosphide[29] have shown promising results for solar-driven water-splitting.

Beside all those advances, more effort is needed to address the remaining challenges in the field. One of the major requirements is related with the development of new water oxidation catalysts that operates under milder pH and overpotential conditions. Previous advances show that alkaline media are used for high activity during water oxidation,[17] although those conditions enhance the corrosion of the system components, which is accelerated under anodic potentials. Moreover, the coupling proton reduction reaction is favored at low pH values though, imposing the need to work at acidic-neutral conditions. In addition, catalysts based on non-noble metal are also required to reduce the cost of the water oxidation reaction. The highest activities in acidic media have been reached with Ru and Ir oxides but those metals are expensive for practical applications partially due to their relative low abundance. A third important requirement would be the transparent character of the catalysts or supporting electrode, as otherwise they would lower the efficiency of the light absorbers.

In this context, molecules such as first row transition metal (TM) complexes are potential candidates to be used as catalysts for water oxidation. Those abundant metals are in general harmless and inexpensive and there is a wide range of techniques for synthesis and characterization of molecular species. Therefore, they offer an ideal platform to study both the operating reaction mechanisms and the factors that affect the kinetic.

Moreover, this knowledge can ultimately be translated into a rational design of more active and robust catalysts by fine-tuning of their electrical and structural features.

1.3 Molecular Water Oxidation Catalysis

1.3.1 General aspects

Water oxidation catalysis (WOC) to molecular dioxygen (Eq 1) is not only an essential reaction in biology, due to its implications in the natural photosynthesis, but also a key step in the development of new sustainable energy schemes based on artificial photosynthesis.[13,14]

$$2\,H_2O \rightarrow O_2 + 4\,H^+ + 4\,e^-, E^0 = 1.23\ vs\ NHE \qquad (1)$$

As already mentioned, this oxidation reaction is thermodynamically demanding with a standard redox potential of E°=1.23 V vs at pH=0 (Figure 5A). Moreover, from a mechanistic point of view, it involves the transfer of four electron, the cleavage of four O-H bonds and the eventual formation of a double O-O bond.[30] This multiple bond breaking and formation lead to a complex mechanistic scenario that is reflected in the high kinetic barrier of this reaction. Therefore, there is an extra amount of energy that we need to supply to the system to overcome that kinetic barrier and this is known as overpotential (η). The development of an efficient catalytic system lies in the capacity to generate stable catalysts working at acidic-neutral pH values and at low overpotentials, close to the thermodynamic redox potential for the water oxidation.

General Introduction

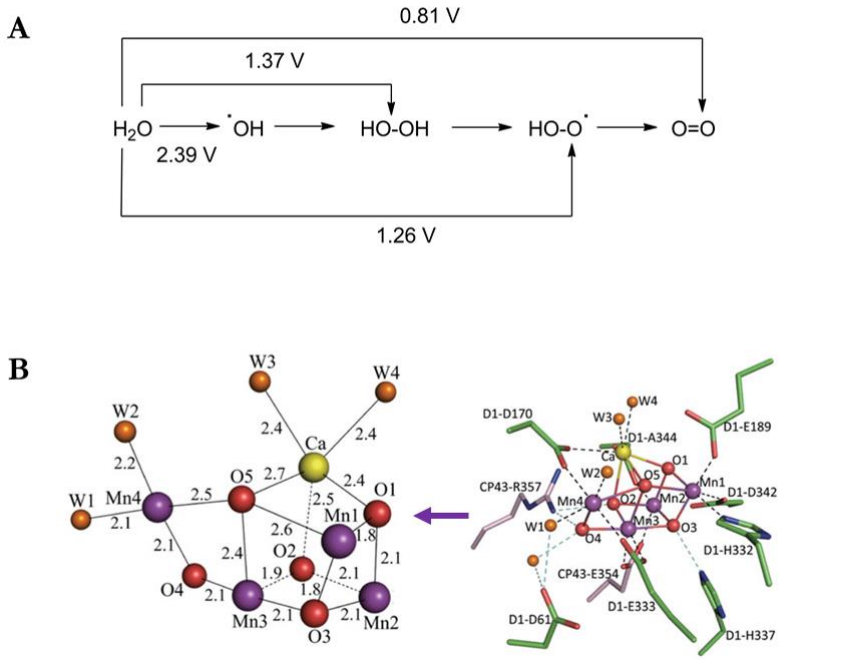

Figure 5. (A) Latimer diagram of water at pH 7. All redox potential values are reported vs NHE. (B) X-Ray structure of the Oxygen Evolving Complex (OEC) cluser with (right) and without (left) the surrounding aminoacid residues. Figure taken from reference 32.

As aforementioned, nature has accomplished this goal using the so-called Oxygen Evolving Center (OEC) composed by a manganese cluster with the formula Mn_4O_5Ca.[12,31] This cluster has been identified inside the Photosystem II as the water oxidation catalyst with an overpotential of 0.43 V and a turnover frequency (TOF) between 100 s^{-1} and 400 s^{-1}. Thanks to the current great atomic resolution of the X-Ray analysis for the OEC (up to 1.95 Å) we currently know its structure, that is shown in Figure 5B.[32,33] This cluster includes three Mn atoms and one Ca atom linked by oxo bridges resulting in a cubane-like structure. There is a fourth dangling Mn atom bonded to the cubane by another oxo bridge. The Ca and the dangling Mn atoms are also bonded to water molecules that are thought to have an important role in the overall mechanism. Finally, some aminoacid residues are also coordinated to the metal centers of the cubane leading

to a complex tridimensional structure. Thanks to the efforts made by researchers using X-ray Diffraction, X-Ray Absorption, electrochemical and computational studies, the mechanism of this catalyst has been partially revealed.[31,32,33,34,35,36] The Mn_4O_5Ca is known to be oxidized until four oxidative equivalents are accumulated and releasing 4 protons in the process. Then the O-O bond formation takes place following a mechanism that is still under investigation.

This natural cluster has been a source of inspiration in the design of catalytic system for water oxidation due to its high efficiency and fast reaction rates.[13,36] Specifically, in the case of molecular water oxidation catalysis (Mol-WOC) based on transition metal complexes, the design is based on the coordinative interaction metal-aqua groups, in a similar way as Mn and Ca atoms are bonded to aqua groups in the natural cluster. Control on the electronic and geometrical structure of the complexes by ligand design would determine their general features and particularly the catalytic performance toward water oxidation. Therefore, ligand design in catalysis has been an extensively studied field in chemistry in order to guide a rational discovery of more active and stable catalysts.[37]

1.3.2. The "Ru school": mechanistic lessons in molecular WOC

Although water oxidation by an artificial catalysts was first developed in 1902 by Cohen and Glazer using oxides materials ,[38] molecular catalysts appeared far later in 1982 due to the previous required development of coordination chemistry. It started with the report by Meyer group of a polypyridyl Ru-aqua complex *cis,cis*-$[[Ru(bpy)_2(H_2O)]_2(\mu\text{-}O)]^{4+}$, **1** (Scheme 2), so-called blue dimer, that resulted in the first family of catalysts, based on a polypyridyl architecture.[39] This complex was the first molecularly well-characterized water oxidation catalyst and contributed to stablish the basis of catalysis for complexes based on metal-aqua interactions. Complex **1** was a model to study the two fundamental steps in the catalytic water oxidation by molecular complexes: accumulation of oxidative

General Introduction

charges and O-O bond formation. Since then, most of the molecular catalysts developed in the last 30 years have been based on Ru complexes and they have been the major contribution to the current mechanistic knowledge in molecular WOC.

Scheme 2. (A) Structural representation of the catalyst **1** and the proposed mechanism for the catalytic water oxidation based on the experimental evidences (bpy ligands are omitted for simplicity). (B) Structural representation of catalysts **2** and **3**.

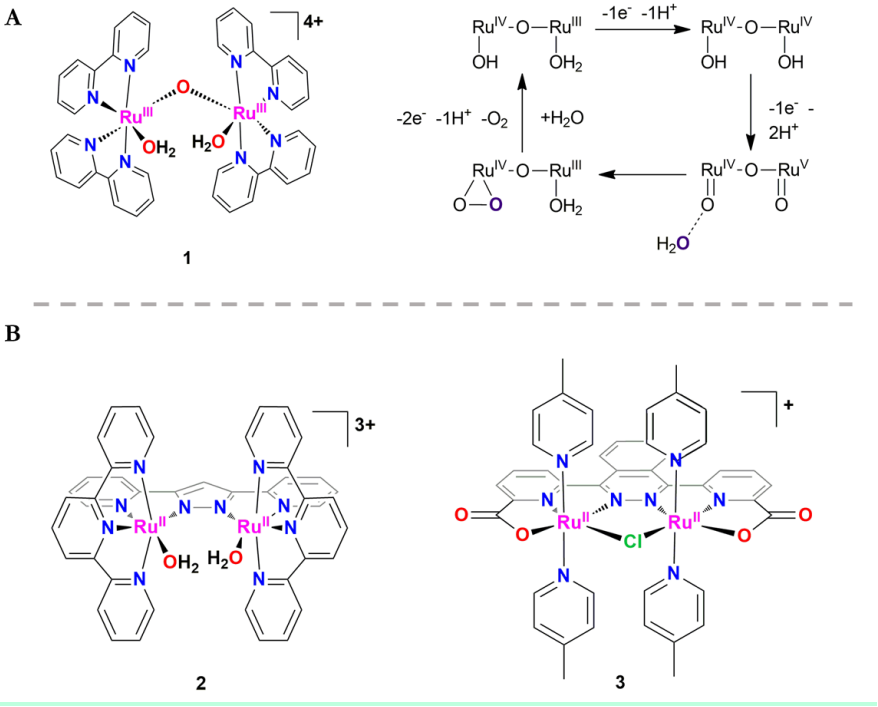

Thanks to the dimer structure of **1**, having two Ru(II) centers connected by an oxo bridge, and the high electron-donating character of the pyridine groups the blue dimer was able to accumulate four oxidative equivalents (two oxidations in each metal center), such as the Mn cluster in the PSII, leading to highly oxidized Ru(IV)-O-Ru(IV) complex. One of the keys for reaching such high oxidation states is based on the **Proton Coupled Electron Transfer (PCET)**, consisting in the concerted release of one electron and one proton, which was discovered by Meyer group (Scheme

3).[40,41,42] This process helps the oxidation to take place at lower potentials due to two reasons:

- The simultaneous loss of a proton and an electron avoids the formation of more energetic intermediates in the oxidation process since the total charge in the complex remains equal.
- The proton loss generates a coordinating oxygen group with more electron-donor character that stabilizes high oxidation states in the metal.

Scheme 3. Scheme of the proton and electron transfer processes using the aquo-complex c-[Ru(bpy)(py)(H_2O)]$^{2+}$ as model at pH 7. Blue arrows ar associated to proton transfers, green arrows represent electron transfers and orange arrows are proton coupled electron transfers. The latter are the lowest energy pathways connecting the different oxidation states.

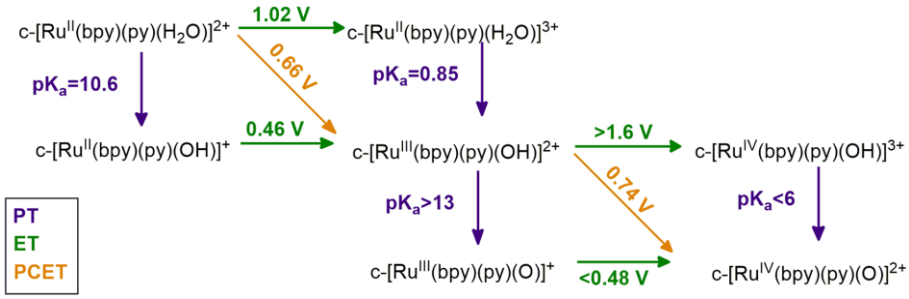

In the case of the blue dimer, it ends up forming two Ru(IV)=O groups where the oxygen atom is highly activated with a positive partial charge due to the acidic character of the Ru(IV) center. Then, this activated species enables the **O-O bond formation** required for the eventual release of molecular oxygen. For this step, two alternative mechanisms have been envisioned depending on the involvement of either an external water molecule or another M=O unit[43] and are summarized in Scheme 4:

General Introduction

- **Water Nucleophilic Attack (WNA)**: As indicated by its name, an external water (or hydroxo) molecule performs a nucleophilic attack to the M=O unit resulting in the formation of the hydroperoxo species M-O-O-H. This pathway takes place when the character of the M=O unit is close to a polarized double bond with a partial positive charge in the oxygen.
- **Interaction of two M=O units (I2M)**: This second alternative involves the coupling of two activated M=O unites to form the species M-O-O-M. In contrast with the previous WNA, this pathway is more likely to happen when the oxygen has a radical character formally generating the isoelectric species M-O·.

Scheme 4. The two alternative accepted mechanisms for the O-O bond formation, WNA and I2M, using the complex **2** as a model. The apical ligands are not drawn for clarity. Red oxygen atoms correspond to ^{18}O initially labelled catalyst whereas blue oxygen atoms refer to the initially non-labelled solvent $H_2{}^{16}O$.[37]

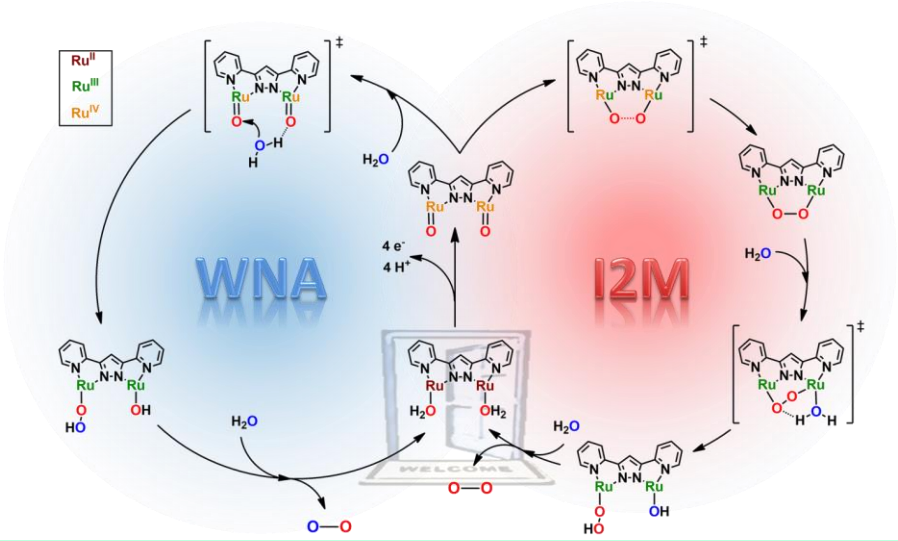

In the case of complex **1**, a deep characterization based on UV-vis, EPR, rRAMAN, X-Ray and isotopic labelling experiments reveals that a WNA takes place after two consecutive PCET, instead of the speculated I2M mechanism due to the dimer structure.[30,44,45,46,47,48,49] Despite the thorough mechanistic study carried out using complex **1**, its poor performance as a

WOC was far from practical applications, with an observed turnover number (TON) and turnover frequency (TOF) values of 13.2 and 0.004 s^{-1} respectively. This complex was sensitive to several reaction pathways leading to decomposition: Ligand oxidation, μ-oxo bridge cleavage and water induced anation.[30,50,51]

Following the previously discussed mechanistic aspects, the development of water oxidation catalysts based on complexes took off using as functional model the polypyridyl Ru-aqua scaffold. No significant advance was achieved in terms of catalytic activity until 2004, when Llobet *et al.* reported on the synthesis and performance of a new dinuclear complex named cis,cis-$[[Ru(trpy)(H_2O)]_2(\mu\text{-bpp})]^{3+}$, **2**.[52] This catalyst, based on the aromatic bridge bis(2-pyridyl)-3,5-pyrazolate (bpp^-), features enhanced TON values of 512 and a faster kinetic constant of 0.014 s^{-1}. The change of the μ-oxo bridge by the bpp^- scaffold was essential to confer extra stability to the complex under oxidative potentials. Moreover, the proximity of the two Ru-O moieties exerted by the ligand scaffold allowed the I2M mechanism operates for the O-O bond formation. That finding was essential for the development of new complexes based on polyaromatic organic architectures bridging two Ru centers.[53,54,55] In particular, Sun and coworkers reported on a ligand bridge bearing carboxylate groups, **3**, that was able to increase the TOF up to 1.2 s^{-2}.[56] However, not all the bridge architectures were found to be favored as the exceeding proximity of the Ru-O groups can promote the repulsion and prevent the catalytic activity.[57]

One further step towards the design of more efficient catalysts was achieved when Thummel *et al.* reported on the activity of the first mononuclear Ru based catalyst **4**, represented in Chart 1.[58] Up to then, two metal centers were thought to be necessary for the accumulation of four oxidative charges before the O-O bond formation in a similar way as it happens in the natural OEC. However, the activity of the mononuclear

General Introduction

complex **4** was later the inspiration for the development of more mononuclear Ru-based catalysts that were in general simpler and easier to prepare. The mechanism of mononuclear Ru complexes was tested by Meyer et al. using the catalyst $[Ru(trpy)(bpy)(H_2O)]^{2+}$.[59,60] The operation mode was based in three previous PCET steps that led to the formation of Ru^{V}=O species, which were sensitive to the WNA by a water molecule from the solution. The resulting hydroperoxo intermediate Ru^{III}-OOH undergoes one more oxidation step with the release of one proton and the eventual generation of molecular oxygen. That way, the required four oxidation steps can take place nonconsecutively with the O-O bond formation step in between, avoiding the formation of too high oxidation states in the metal center.

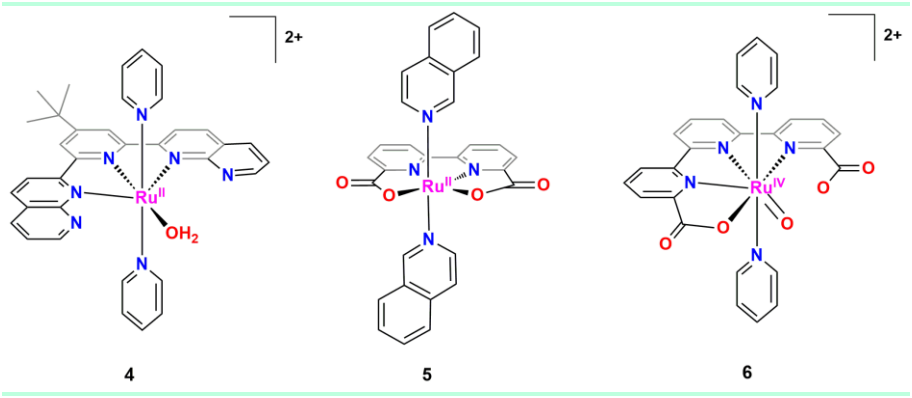

Chart 1. Structural representation of catalysts **4**, **5** and **6**.

A step further was achieved by Sun, Llobet and coworkers when they reported on a new family of **seven-coordinated**, mononuclear, Ru-based catalysts bearing the (6,6'-dicarbonixilate-2,2'-dipyridyl) ligand (bda^{2-}).[61,62,63] One of the developed complexes, **5**, was able to oxidized water with a TOF of 303 s^{-1}, which was comparable to the natural OEC. The TON was also unprecedented with a total value of 55,000. Both parameters were approaching to the required ones for a practical application.

Mechanistic studies based on UV-vis, isotopic labelling, catalytic experiments and electrochemical measurements revealed that complex **5** operates through an I2M pathway for the O-O bond formation.

One of the most recent advances was achieved in 2015 by Llobet *et al.* when they reported on the complex $[Ru^{IV}(OH)(tda\text{-}\kappa\text{-}N^3O)(py)_2]^+$, **6**, with tda^{2-} being [2,2':6',2"-terpyridine]-6,6"-dicarboxylate.[64] This complex was formed upon controlled potential electrolysis (CPE) at pH 11 from the analogous complex $[Ru^{II}(tda)(py)_2]^+$by insertion of a water molecule leading to a seven coordinated complex. The advantage of this new catalyst lies on the dangling carboxylate group that acts as an intramolecular proton acceptor group helping in the deprotonation of the water molecules during the water oxidation catalysis. Using similar ligand scaffold as the bda^{2-}, the presence of the intramolecular proton acceptor group enhances the kinetic constant for the catalytic water oxidation up to 8,000 s^{-1} at pH 7, becoming the fastest molecular catalyst ever reported.

1.3.3 First row TM complexes: new generation of catalysts

The discovery of molecular catalysts based on first row TM complexes appeared later than in the case of Ru catalysts. Generally, metals such as Ni, Fe, Co, Cu, and Mn are more abundant and harmless from an environmental point of view so that they are attracting candidates for water oxidation catalysis. In the recent years, a fast development of such catalysts is taking place and promising results have been obtained.

Manganese Catalysts

Manganese is an attractive metal due to its involvement in the natural OEC from the PSII.[12] Moreover, its high abundance and low cost make it the ideal candidate to explore water oxidation catalysis based on molecular complexes. In fact, this was the first transition metal from the first row to be implemented in a molecular catalyst by Naruta and co-workers

in 1994. They synthetized dinuclear Mn complexes, **7**, that showed catalytic activity in MeCN:water solutions containing nBu_4NOH affording a TON value of 9.2.[65,66] This initial report reveals the requirement of having two Mn centers close to perform water oxidation since the mononuclear counterpart did not show any catalytic activity. Five years later in 1999, the groups of Crabtree and Brudvig reported on the use of a new Mn dimer based on two μ-oxo bridges connecting both metal centers, **8**.[67,68,69] This catalyst was able to promote chemical water oxidation using sodium hypochlorite as sacrificial electron acceptor (SEA), so it inspired a family of catalysts based on modified ligand architectures.[70,71,72,73,74] Initially, TON of 4 was achieved in 6 h with a TOF value of 0.0033 s^{-1} showing a modest activity toward water oxidation that was assigned to the low stability of the μ-oxo bridges, as already mentioned for the blue dimer. Moreover, it was also demonstrated that the 25% of the evolved oxygen came from the ClO^- group of the SEA and this catalyst eventually degrades to catalytically active MnO_4^-.[75] Mechanistic proposals were based on UV-vis and electron paramagnetic resonance (EPR) and pointed to the formation of a Mn^V=O as the active species for the O-O bond formation, that would take place through a WNA pathway.[67,76,77,78]

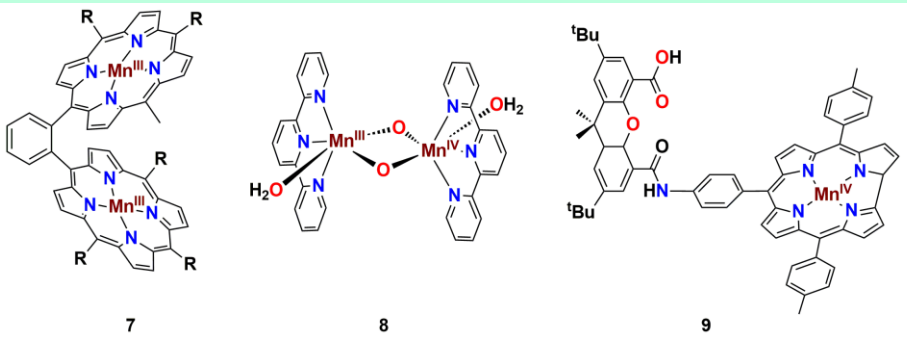

Chart 2. Structural representation of Mn catalysts **7**, **8** and **9**.

The development of more dimer Mn complexes continued, with increasing TON values when using two electron oxidants such as H_2O_2, Oxone or NaClO. Åkermark and co-workers developed a new dimer complex

based on imidazole, carboxylate and phenol groups that was able to work with one-electron oxidants such as $[Ru(bpy)_3]^{3+}$ thanks to the lower over-potential toward water oxidation.[79] Few mononuclear, highly-oxidized Mn=O complexes have also been reported to catalyze the water oxidation using different ligand scaffolds such as modified salens,[80] corroles (like complex **9**)[81] and polypyridines,[82] that in general are electron-rich ligands to favor the formation of high-valent $Mn^{IV/V}$=O species. Beside those advances, the catalysis based on Mn has shown to be modest and often doubts arise about the real active species and the source of the evolved oxygen.

Iron Catalysts

Iron is also an abundant and inexpensive transition metal that has attracted the attention of researchers. It is involved in a number of molecules with important roles in natural processes and its coordination chemistry has been extensively studied. However, the examples of iron-based catalysts for water oxidation are very limited. The first example of molecular catalyst based on iron was reported by Collins et al. in 2010 and consisted of tetraamido macrocyclic ligands (TAMLs) with four negative charges that were able to stabilize the high oxidation states of iron centers, **10**.[83] This type of complexes had already been used for oxidation reactions using H_2O_2 and O_2 and showed high oxidizing power for the degradation of organic dyes due to the formation of Fe^{IV}=O species.[84,85,86,87,88] They were first studied in chemical water oxidation with Ce^{IV} as SEA and showed modest activities with TON values slightly over 16 and TOF values of 1.3 s^{-1}. Moreover, they found an interesting dependence of the substituent of the phenyl ring with the catalytic performance ranging from no activity to the highest values just mentioned. That was first assigned to the acid stability of the ligand that was increased with electron withdrawing groups and later it was found also a positive influence in lowering the kinetic barrier for the O-O bond formation. A first order dependence

with the catalyst concentration reveals a single metal mechanism supporting the WNA as pathway to form the O-O bond. However, the stability of those complexes was poor in comparison to other reported Ru and Ir catalysts. Further study of these complexes for electrochemical water oxidation showed the poor reversibility of the redox features corresponding to the one-electron Fe^{III}/Fe^{IV} oxidation, what suggests low stability under electrochemical conditions and the possible involvement of iron oxide nanoparticles as real catalyst.[89]

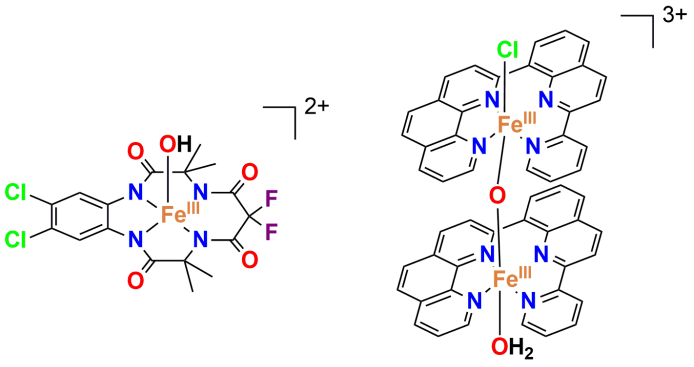

10 **11**

Chart 3. Structural representation of Fe catalysts **10** and **11**.

Soon later, in 2011, Lloret-Fillol *et al.* described the catalytic activity of a family of iron complexes based on tetra- and penta- dentate nitrogen-containing ligand motifs that were commercially available.[90] Those complexes were claimed to catalyze the water oxidation using Ce^{IV} as SEA and only those with free coordinating position in a *cis-* configuration showed activity in contrast with the complexes bearing *trans-* free positions. Two years later, Llobet and Fukuzumi groups reported on similar Nonheme iron complexes as water oxidation catalysts revealing that iron oxide nanoparticles were involved during catalysis.[91] Those finding sowed the doubt about the real catalytic activity of that family of complexes and further experimental evidences are needed to rule out the degradation of

the easily oxidizable ligands and the eventual presence of active iron oxides.

In contrast with Ru and Mn, development dinuclear iron catalysts is mainly limited to the example of Thummel and co-workers that recently reported on the iron dimer **11**.[92] That complex featured a μ-oxo bridge and was found to be more active than the mononuclear counterpart, revealing the importance of the electronic coupling between both iron centers. A mechanism based on the formation of a Fe^{III}-O-Fe^{V}=O species and the subsequent nucleophilic attack of a water molecule to that species was proposed, affording around 1,000 TONs and a TOF value of around 2.2 s^{-1} when Ce^{IV} was used as SEA.

Cobalt Catalysts

Cobalt has been extensively involved in the development of heterogeneous water oxidation catalysts based on cobalt oxide and showed high activity and stability.[93] Moreover, molecular cubanes[94,95,96,97] mimicking the OEC as well as polyoxometallates (POMs) based on Co[98,99,100,101,102] have been also evaluated as catalysts. However, the field of molecular Co complexes for water oxidation has been less investigated and only few examples are known. The initial reports by Berlinguette[103] and Nocera,[104] based on a Py5 (Py5= 2,6-bis(1,1-bis(2-pyridyl)ethyl)pyridine)]) and a β-octafluoro hangman corrole respectively, **12** and **13**, were the first examples of complexes showing catalytic activity. The key feature of those architectures consists in the ability of the ligands to stabilize high valent Co^{IV} species, which were also the active centers of the Cobalt oxides catalysts. Despite that, the performance of those complexes was poor when compared to the highly active Ru or Ir catalysts. More effort was put on the development of Co catalysts using other ligand scaffolds such as porphyrins,[105,106] salens,[107] TAMLs[108] and polypyridyl[109,110] backbones, based on the previous results, but all of them resulted in moderate activities. What is more, a recent reinvestigation of a cobalt salen complex showed

that it was just acting as precatalyst for the formation of active Co oxides, and that arises doubts again about the real catalytic species when using molecular cobalt complexes.[111] The common feature of generating stable Co^{IV}=O species was pursued in all the cases in order to promote the O-O bond formation, that was mainly proposed to take place through a WNA pathway.

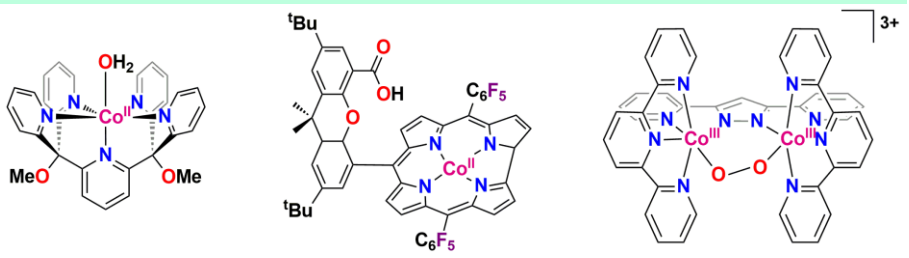

12 13 14

Chart 4. Structural representation of Co catalysts **12**, **13** and **14**.

As in the case of iron, the development of dinuclear catalysts is an unexplored field. Llobet and co-workers reported on the synthesis and catalytic activity of a cobalt dinuclear complex based on the already known bpp⁻ ligand, **14**.[112] Although the activity was also modest, they were able to characterize several intermediates and find a WNA mechanism based on labelling experiments, resonance Raman, electron paramagnetic resonance and X-ray absorption spectroscopies.[113] On the other hand, the second developed complex based on a dimer structure bearing the tpa ligand (tpa meaning tris(2-pyridylmethyl)amine) and a peroxo bridge[114] was eventually demonstrate to act as a precatalysts of highly active Cobalt oxide.[115]

Nickel Catalysts

In general, molecular Ni-based water oxidation catalysis is a relatively unkown field and only few examples have been reported, although the lack of evidencies for homogeneous molecular catalysis often makes difficult to obtain meaningful conclusions.

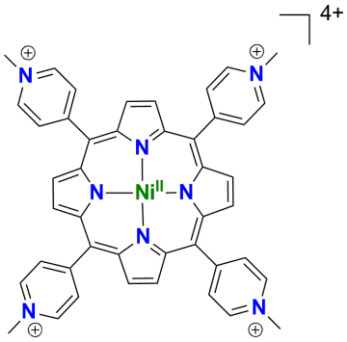

15

Chart 5. Structural representation of Ni catalysts **15**.

One of the first examples of molecular catalysts was based on a Ni porphyrin **15**, which shows activity from pH 2 to 8 when tested electrochemically.[116] Linear dependence of the catalytic current with the catalyst concentration supported a unimolecular mechanism that was proposed to go through the generation of high valent Ni^{IV} species based on experimental evidences. However, moderate performance was achieved with a TOF value of 0.67 s^{-1}. Several complexes have been developed based on the cyclam macrocyclic ligand (1,4,8,11-tetraazacyclotetradecane) and modified analogous and tested as electrocatalytic water oxidation catalysts.[117,118,119] They all showed irreversible waves related with the one-electron oxidation Ni^{II}/Ni^{III} and increasing catalytic current intensities upon CPE when analyzing the oxygen evolved, both indicating the possible presence of Ni oxides as real catalyst. This was previously showed by Spiccia and coworkers[120] and later demonstrated by M. M. Najafpour *et al.*, who showed the presence of Ni oxide nanoparticles on the surface of the electrode.[121]

Copper catalysts

As in the case of iron, copper coordination chemistry has been extensively developed due to its implication in natural biological systems.[122] For instance, a number of complexes have been reported for O_2 activation

showing a rich chemistry with interesting redox features. However, the development of Cu-based water oxidation catalysts has been less extense, although more examples are known in comparison with Ni or Fe. The main drawback of Cu against other first row TM is the lower redox flexibility toward high oxidation states, as Cu^{IV} complexes are unstable. Moreover, Cu^{III} does not generally have enough redox potential to oxidized water.

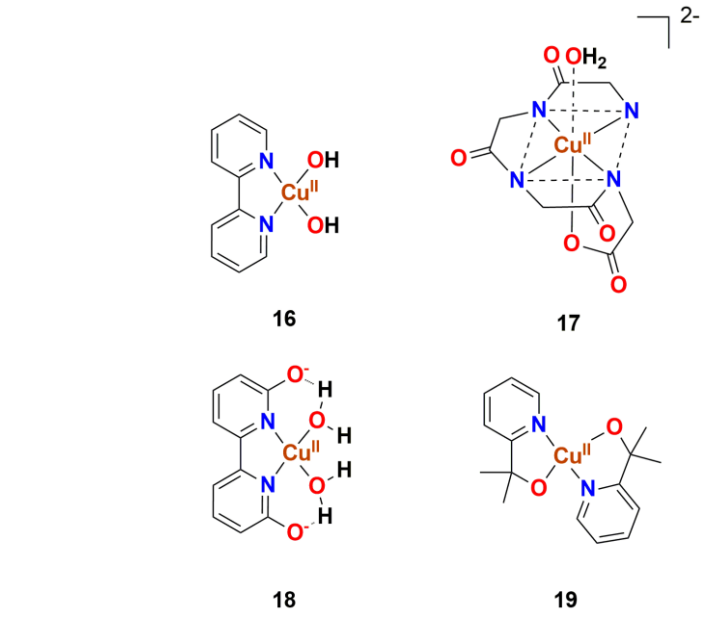

Chart 6. Structural representation of Cu catalysts **16**, **17**, **18** and **19**.

Mayer *et al.* developed the first example of molecular catalyst capable of electrochemically oxidizing water to dioxygen in 2012.[123] It consisted of the $[Cu^{II}(bpy)(OH)_2]$ complex, **16**, which was able to oxidize water in alkaline solutions (11.8-13.3) at high oxidation potentials (overpotential of around 750 mV). Despite the simplicity of this system and the high TOF value of 100 s^{-1}, the harsh conditions (high pH and overpotential) were an important obstacle for practical applications. Moreover, the mechanistic cycle remain unknown and information about the relevant oxidation states or O-O bond formation pathways were missing. Meyer and co-

workers followed the development of catalysts by introducing the copper complex **17** bearing the triglycylglycine ligand.[124] Although this scaffold is unusual among water oxidation catalysts, the Cu complex showed catalytic activity at pH 11 with an overpotential of around 520 mV and a TOF of 33 s^{-1}. The tetraanionic character of the ligand could be the reason for the stabilization of high oxidation states in the metal center active towards O-O bond formation. However, once again, a lack of experimental evidences about the mechanism made difficult to obtain conclusions, although a cycle based on Cu^{IV}=O species was proposed with a single-site pathway for the oxygen evolution suggesting WNA.

Lin et al. introduced the tool of using redox active ligands by designing the 6,6'-dihydroxo bipyridine ligand and the corresponding copper complex **18**.[125] This complex was analogous to the first reported **16** but it features a lower overpotential for electrocatalytic water oxidation of around 510 mV due to the involvement of the ligand into the electron transfers. That way, high valent Cu^{IV} complexes that are difficult to stabilize were avoided. Regarding the O-O bond formation mechanism, the lack of experimental or computational work resulted in a complete ignorance about the possible pathways. The group of Papish has also worked with the same ligand framework and has studied the influence of ligand-copper stoichiometry into the catalytic activity.[126]

Copper complexes bearing ami-polypyridine ligands have been also tried in basic pH values leading to good rates of catalysis (13.1-18.7 s^{-1}) and intermediate overpotentials (440-570 mV).[127] One of the most recent results was reported by Crabtree and Brudvig groups showing the catalytic activity of the $[(pyalk)_2Cu]$ complex (pyalk = 2-pyridyl-2-propanoate), **19**.[128] They demonstrated the homogeneous performance under basic conditions (pH>10.4) with an intermediate overpotential of 520-580 mV and modest TOF value of 0.7 s^{-1}. This catalyst bears a redox inactive ligand that is claimed not to participate in the electron transfer during water

oxidation and confers high robustness to the catalyst, which is able to work for 12 h giving rise to TON value of 30.

Although more examples are known in the Cu-based water oxidation field, they lack evidences about their stability and role as real catalysts. Regarding the discussed molecular catalysts, in general, they offer few mechanistic information and that makes hard to perform a rational design. Those catalysts share few features so that no common factors can be proposed as essential for the development of more active and stable catalysts. One of the main challenges still remaining is to design ligand frameworks that resist against acid demetallation when working at acidic-neutral pH values and operate at low overpotentials.

1.3.4 Lessons from first row TM catalysts

The general conclusion that one can make is that the field of first row TM complexes as water oxidation catalysts is immature, although a fast development is taking place. Unfortunately, there is still an important lack of mechanistic information and the methodologies to assess the catalytic performance are too diverse to compare among different catalysts. Oxygen evolution has been tested using SEA as well as electrochemical methods and therefore comparison between TOF and TON values is complicated.

Regarding stability, first row TMs usually form complexes with more labile character than Ru complexes and then, they are easily degraded under harsh conditions such as extreme pH values or high anodic potentials. Therefore, developing complexes that can withstand the high oxidation state required during water oxidation remained a challenge during many years. First row TM complexes are widely considered to degrade through two general pathways represented in Scheme 5:

- The first one results from the high potential required to generate the high oxidation states of those metal centers, which are the

responsible for the O-O bond formation. At those potentials, many organic functionalities are also sensitive to oxidation so that their incorporation in a ligand scaffold can compromise the integrity of the complex and drive to oxidative degradation. Depending on the degree of ligand oxidation, this deactivation pathway can result in modified molecular species or go all the way to the formation of metal oxide (Figure 1A).

- The second one is related to the metal-ligand bond lability that facilitates the competition of solvent water molecules for the coordination positions in the metal center, releasing solvated ions available to form oxides. This aspect is even more important when the coordinating groups in the ligand are sensitive to protonation since this largely decreases the coordination bond strength and thus restricts the pH range of stability (Figure 1A).

Scheme 5. General deactivation reactions in molecular water oxidation catalysis by 1st row transition metals complexes.

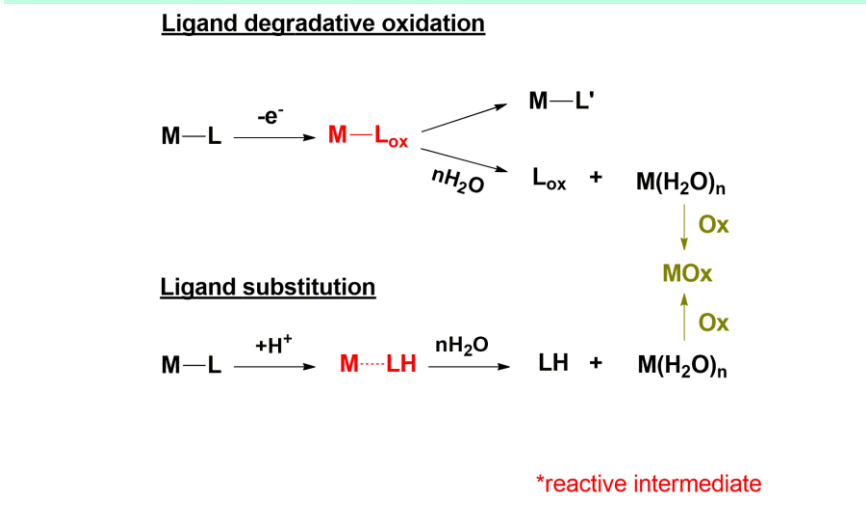

Solvated metal ions released from those processes are normally blamed for the subsequent formation of metal oxides upon oxidation conditions. Generally, those metal oxides feature high activity and sometimes act as the only real catalysts. In fact, degradation of molecular species is not

necessarily an undesirable side reaction since the resulting metal oxides can feature improved catalytic performance as compared with the same materials prepared by traditional deposition methods.[120]

All those stability problems have prevent researchers from extensively studying the performance of first row TM complexes as catalysts and the factors that determine their activity towards water oxidation. The fast generation of those catalysts has been driven by relatively random design criteria and thus has resulted in a lack of rationalization of the catalytic performance. Different ligand scaffolds, overall charges, nature of the coordinating groups and metal centers have drawn a confusing panorama for the first row TM catalysts. Moreover, most of the mechanistic proposals are based in the Ru chemistry despite the evident differences in redox properties. Beside this, the absence of accurate proofs to discard the presence of metal oxide as real catalysts make even more difficult to obtain relevant conclusions. Therefore, deeper understanding of the catalytic and degradation mechanisms is essential to establish the real catalytic species and thus to obtain meaningful information for the design of more stable and active molecular catalyst based on inexpensive first row TM.

1.4 Molecular photoanodes:

From a practical point of view, implementation of catalysts into photoelectrochemical cells would benefit from working in a heterogeneous way, *i.e.* using an active anode containing both the light absorber and the catalysts in contact so that the electron transfer is optimized. Molecular catalysts are usually assessed in homogeneous phase for simplicity reasons, but an important objective would be anchoring those molecules to anodes and photoanodes resulting in hybrid catalysts. Those so-prepared catalysts would benefit from both molecular and material features: the molecular catalysts could be optimized by rational design of the ligand and then implemented as robust heterogeneous electrodes into the cell

upon anchorage. The interest on those materials has open a new field of research that aim to successfully transfer the catalytic features of molecular catalysts to the solid state, which sometimes can be a real challenge.

1.4.1 Molecular photoanode architecture

Five components are fundamental to build a molecular photoanode:

- Molecular catalysts. As discussed before, many molecular catalysts have been developed so that the best performing ones could be tested for implementation on the anodes.
- Anchoring group. The molecular structure should have some functionality able to interact with the electrode support and keep the molecule attached in a robust way. Moreover, it has to be conductive and allow the electron transfer between the electrode and the catalyst.
- Anchorage support. This component would be a conductive solid material that interact chemically or physically with the anchoring group of the molecular catalyst and the electrode.
- Light absorber. In order to capture the light and promote the electron transfer required in the redox reactions, the light absorber should be in contact with the electrode and close enough to the catalysts for the chemical interaction.
- Supporting electrode. In order to connect electrically the two half-reactions taking place in a photoelectrochemical cell, the electrode should be in contact with the light absorber and the catalysts through the anchorage support to receive or release the electrons involved in the catalytic process.

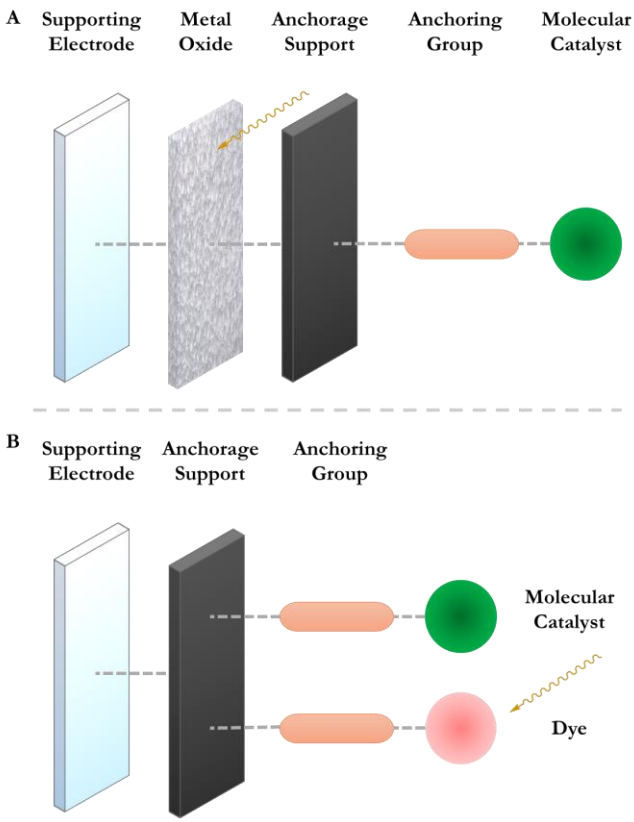

Figure 6. Schematic drawing of the alternative building of photoanodes for water oxidation.

Sometimes, the same material can perform the role of the light absorber and the anchorage support. That happens with semiconductors such as WO_3[25] or $BiVO_4$[26] since they are light absorber that can be deposited on electrodes and interact with the molecules through the metal centers from their chemical structure. Instead, those semiconductor can also bear supporting material to anchor catalysts through different strategies than metal-oxide bonding. On the other hand, anchoring of a molecular light absorber (dye) would be also needed if the support material is not a semiconductor that transfers the solar energy. Therefore, these two options result in the two general architectures used in the field, which are represented in **Figure 6** based on semiconductor or dyes absorbers.

1.4.1 Anchoring strategies

In order to build molecular photoanodes, the molecular catalysts (and the light absorber when molecular dyes are used instead of metal oxides) require specific functional groups that interact with the anchorage support. Those anchoring groups should be hydrolytically and oxidatively stable at the working pH and potentials in order to avoid the loss of catalyst under operation. The nature of the functionality connecting the molecular catalyst and the support can be diverse depending on the type of support used. There are two main groups of supports: metal oxides and carbon materials.[129,130]

Metal oxides

Regarding anchoring to metal oxides, the most common and widely used anchoring groups have traditionally been the carboxylic, phosphonic and sulfonic acids. The synthesis of ligands containing those groups normally involve the use of a commercial precursor that contain either the acidic or the ester form. If the ester forms are used, a further step involving the hydrolysis of the ester is needed and can be performed in basic or acid conditions depending on the molecule stability.[130] Once the acid form is obtained, those groups anchor to the metal oxide by bonding with the metal atoms in the surface of the support. By FT-IR measurements and computational simulations, the surface binding has been studied and it is often proposed a bidentate mode where two oxygens are covalently bridging to different metal centers.[131,132,133,134] The main disadvantage of those groups is the relatively poor stability in aqueous solution as hydrolytic release of the molecules occurs at neutral to acid pH values.[133] Moreover, the buffer anions can compete for the binding place in the oxide surfaces decreasing even more the stability. Regarding electron transfer,[130] carboxylic acids have better electron injection dynamics than the others so that is favored to anchor dye molecules but not recommended for catalyst since recombination processes might interfere in the catalytic reaction.

General Introduction

Phosphonic acids on the other hand, have moderate electron injection efficiencies so that they can accumulate the charge separation needed to oxidize the catalysts and eventually the water molecules.

Scheme 6. Binding modes of the most popular anchoring groups for metal oxides supports.

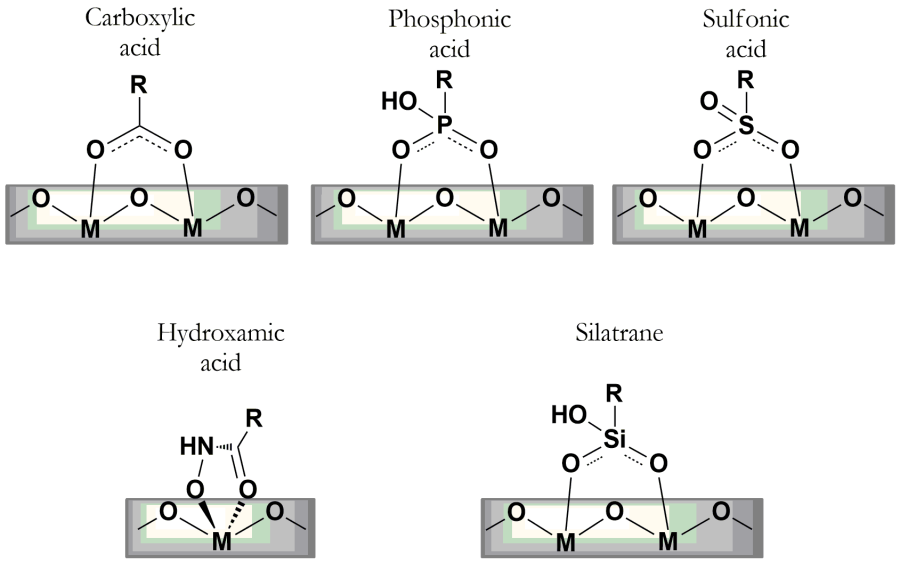

Hydroxamic acid have been also used as anchoring groups, although less extensively than previous alternatives. Usually, they are not commercially available so a synthetic work based on multistep process is required starting from carboxylic acids or esters.[130,135,136] Hydroxamic acid has several possibilities for the binding modes among which the monochelating mode is the more experimentally evidenced, based on the chelating interaction of two oxygen atoms with a metal center in the oxide surface. The advantage of this group is the high stability in aqueous solution from basic to acidic media.[137,138] The electron injection is similarly efficient as in the case of carboxylic groups, so not favored for catalysts binding.[130]

Finally, more recently, sylatranes have been employed as anghoring groups for metal oxide surfaces. The synthesis of these groups involves assembling pentacoordinate, hypervalent caged silicon compounds but

once introduced, their high stability prevent that group from rest of reactions that might be required to obtain the final complex.[130] Sylatranes bind the surface of the metal oxide by forming Si-O-M bonds, more likely in a bidentate form.[139] As in the case of the hydroxamic acid, the stability of these groups is high both from acid to basic solutions.[140] Sylatranes have low recombination kinetics thanks to a lower electronic coupling so they are recommended to bind catalysts.[130]

Carbon Materials

Carbon electrodes are cheap materials with good electronic conductivities that have been widely used in electrochemistry as working electrodes. Depending on the way the carbon is organized in the electrode, there are different types: from glassy carbon electrodes to nanostructured carbon materials. Moreover, multiwalled carbon nanotubes, graphene and other high-surface carbon materials are used to increase the surface where catalysts can bind. The anchorage on all of those surfaces is similar and can be based on three different main strategies.[129]

Scheme 7. Strategies for anchoring of molecules on the surface of carbonous electrodes.

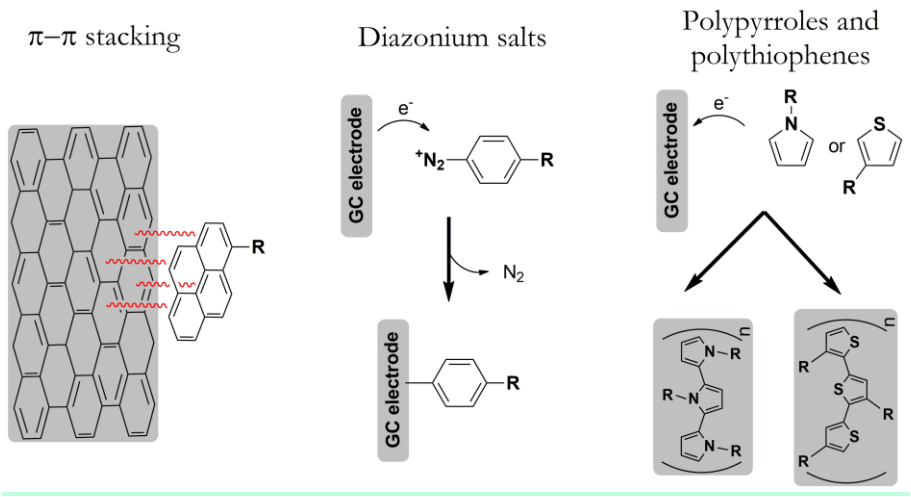

One of the easiest ways to anchor molecules to carbon surfaces is through π-π stacking forces. Groups such as pyrene can be attached to the catalyst molecule by carbon-carbon or other type of bonds and they can eventually interact with the carbon surface leading to a strong binding. That binding does not require chemical reactions so just by mixing the pyrene modified molecule and the carbon support the interaction is achieved after certain time. The simplicity of this method makes it one of the most promising. However, structural hindrance should be carefully avoided for the correct pi-pi interaction.

A second method involves the covalent bond between the carbon surface and the molecule by the use of diazonium salts. Those groups can react by electroreduction releasing N2 and forming organic radicals that couple to the electrode surface. This bond is highly stable from a chemical point of view. The third and last method would be based on the use of N-substituted pyrroles or C-substituted tiophenes, which upon anodic potential they can polymerized on the surface of the electrode.

1.4.2 Main achievements in molecular anodes

This section will only focus on molecular anodes, *i.e.* the anchorage of molecular catalysts to support materials and electrodes. Implementation of light absorbers to those molecular anodes to build molecular photoanodes will not be described. Ruthenium molecular catalysts have been long used to anchor on the surface of the electrodes by most of the previously described methods. One of the first examples involved the use of carboxylic and phosphonic acids, developed by Llobet and Meyer groups for dinuclear and mononuclear complexes respectively, **20**, **21** and **22**.[141,142,143] They synthetized the modified ligands bearing the acid groups and initially deposited the complexes on TiO_2 and ITO surfaces, that work as the working electrodes and anchorage support. The electrochemistry of the anchored catalysts was evaluated resulting in a successful transfer of the catalytic features to the solid state except for the case of

complex **20**. In that last case, the position of the anchoring group determine a surface binding that provoked the blocking of the active sites of the catalyst by interaction between the Ru metal centers and the oxo groups of the surface. That revealed the importance of the anchoring architecture in order to retain the catalytic activity. In the other two cases, the coverage achieved by Llobet strategy was higher (0.5 nmol/cm^2) than the case of Meyer for the mononuclear catalysts (0.1 nmol/cm^2), although both of them showed similar TOF values (0.3 and 0.36 s^{-1}), which was a significant improvement respect to the TOF in homogeneous phase (0.07 and 0.15 s^{-1} respectively).

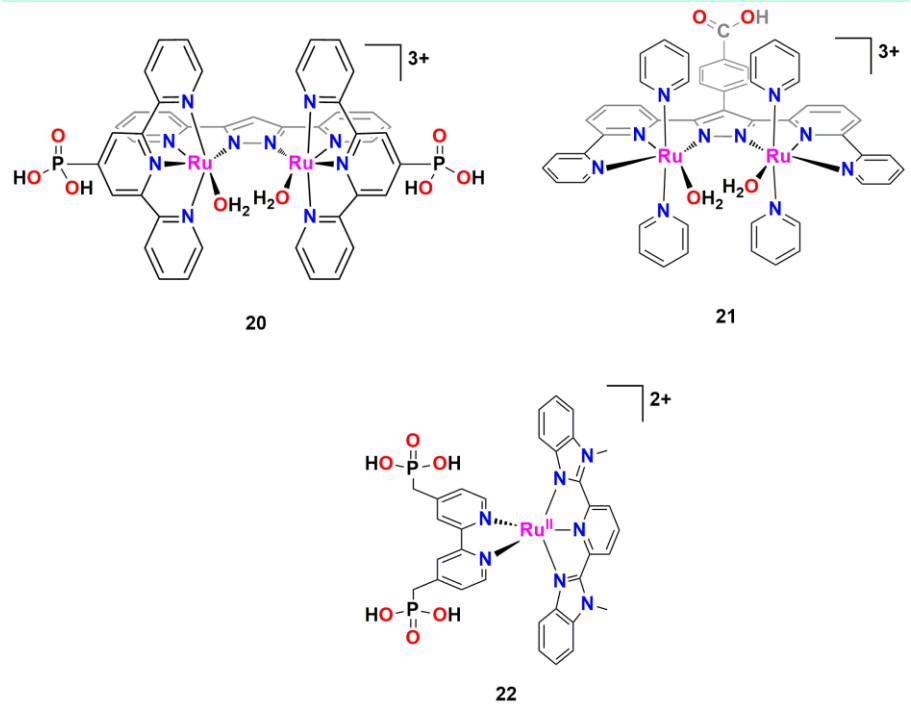

Chart 7. Structural representation of Ru catalysts **20**, **21** and **22**.

On the other hand, Sun et al. were using the pi-pi stacking strategy to attach mononuclear ruthenium catalysts based on the bda ligand to MWCNT as anchorage support, **23**.[144] The hybrid material containing the catalyst and the support was deposited on the surface of ITO electrodes

for performing electrochemical water oxidation. Same group also explored the use of diazonium salts[145] as method to attach the catalysts to similar carbon electrodes. The pyrrole group for electropolymerization was explored by Llobet *et al.* using the Hbpp as bridging ligand and modified terpyridines including pyrroles functionalities for anchorage to glassy carbon electrodes as support.[146] In the case of the catalyst attached with pyrene functionalities to MWCNT the coverage was higher than previous examples (1.8 nmol/cm^2) although the TOF value decreased from 30 s^{-1} in the homogeneous phase to 0.3 s^{-1} once anchored. However, different methods and conditions to measure the TOF were employed.

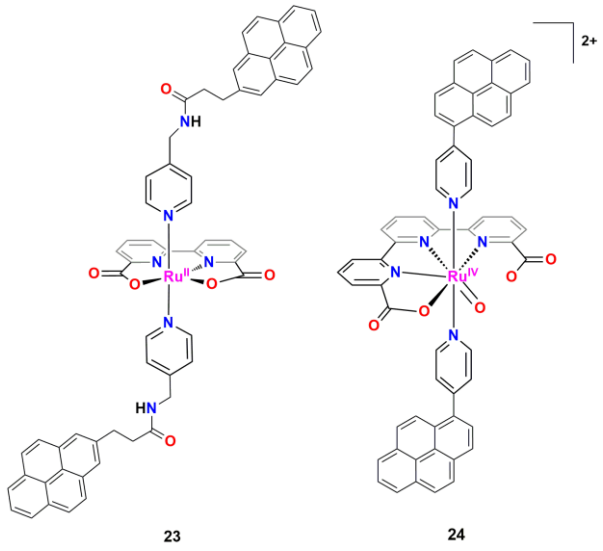

23 24

Chart 8. Structural representation of Ru catalysts **23** and **24**.

Finally, Llobet *et al.* employed the strategy based on pyrene functionalities to anchor the mononuclear Ruthenium catalysts based on the tda ligand, **24**, which has shown the highest intrinsic activity from the literature.[147] They were able to transfer the catalytic activity to glassy carbon electrodes and Silicon based photoanodes. Importantly, the kinetic of the catalytic process was not influenced by the anchoring process as they obtained similar TOF values being the most active molecular anode to the date, with around 1,000,000 TONs.

1.5 References

1 *Annual Energy Outlook 2018 with projections to 2050*, U.S. Energy Information Administration, 2018.

2 *World Population 2017*, United Nations, Department of Economic and Social Affairs, 2017.

3 *Global Resource Observatory Database*, Global Resource Observatory, Anglia Ruskin University, 2018.

4 Mcglade, C.; Ekins, P. *Nature*, **2014**, *517*, 187–190.

5 *Energy and Climate Change*, International Energy Agency, 2015.

6 Petit, J. R.; Jouzel, J.; Raynaud, D.; Barkov, N. I.; Barnola, J.-M.; Basile, I.; Bender, M.; Chappellaz, J.; Davis, M.; Delaygue, G.; Delmotte, M.; Kotlyakov, V. M.; Legrand, M.; Lipenkov, V. Y.; Lorius, C.; Pépin, L.; Ritz, C.; Saltzman, E.; Stievenard, M. *Nature*, **1999**, *3999*, 429-436.

7 *Kyoto Protocol to the United Nations Framework Convention On Climate Change,* United Nations Framework Convention on Climate Change (UNFCCC), 1998.

8 *Adoption of the Paris Agreement. Proposal by the President*, Paris Climate Change Conference – November 2015, COP 21, Paris, France, 2015.

9 *Energy...beyond oil*; Armstron, F. B., Katherine, Ed.; Oxford University Press: UK, 2007

10 *Key world energy statistics 2017*, International Energy Agency, 2017.

11 Nelson, N.; Ben-She, A. *Nat. Rev. Mol. Cell. Biol.* **2004**, *5*, 971-982

12 McEvoy, J. P.; Brudvig, G. W. *Chem. Rev.* **2006**, *106*, 4455-4483.

13 Berardi, S.; Drouet, S.; Francas, L.; Gimbert-Surinach, C.; Guttentag, M.; Richmond, C.; Stoll, T.; Llobet, A. *Chem. Soc. Rev.* **2014**, *43*, 7501−7519.

14 Grätzel, M. *Acc. Chem. Res.* **1981**, 14, 376– 384

15 Garrido-Barros, P., Funes-Ardoiz, I., Farràs, P., Gimbert-SuriÇach, C., Maseras, F., Llobet, A. Science of Synthesis: Catalytic Oxidation in Organic Synthesis, Georg Thieme Verlag KG Stuttgart, New York, **2017**, 63.

16 Kärkaäs, M. D.; Verho, O.; Johnston, E. V.; Åkermark, B. *Chem. Rev.* **2014**, *114*, 11863-12001

17 McCrory, C. C. L.; Jung, S.; Peters, J. C.; Jaramillo, T. F. *J. Am. Chem. Soc.*, **2013**, *135*, 16977-16987.

18 Mckone, J. R.; Lewis, N. S.,; Gray, H. B. *Chem. Mat.* **2014**, *26*, 407-414.

19 Vesborg, P. C. K.; Jaramillo, T. F. *RSC Adv.* **2012**, 2, 7933-7940.

20 Dirección General de Investigación, C. E., Ed. Bruselas, 2003

21 Mauritz, K. A.; Moore, R. B. *Chem. Rev.* **2004**, *104*, 4535-4586.

22 Ursúa, A.; Gandia, L.; Sanchis, P. *Proc. IEEE* **2012**, *100*, 410-426.

23 McCrory, C. C. K.; Jung, S.; Ferrer, I. M.; Chatman, S. M.; Peters, J. C.; Jaramillo, T. F. *J. Am. Chem. Soc.* **2015**, *137*, 4347-4357.

24 Hamann, T. *Dalton Trans.* **2012**, *41*, 7830-7834.

25 Liu, X.; Wang, F.; Wang, Q. *Phys. Chem. Chem. Phys.* **2012**, *14*, 7894-7911.

26 Seabold, J. A.; Choi, K.-S. *J. Am. Chem. Soc.* **2012**, *134*, 2186-2192.

27 Dominey, R. N.; Lewis, N. S.; Bruce, J. A.; Bookbinder, D. C.; Wrighton, M. S. *J. Am. Chem. Soc.* **1982**, *104*, 467-482.

28 Walter, M.; Warren, E.; McKone, J.; Boettcher, S.; Qixi, M.; Santori, L.; Lewis, N. *Chem. Rev.* **2010**, *110*, 6446-6473.

29 Aharon-Shalom, E.; Heller, A. *J. Electrochem. Soc.* **1982**, *129*, 2865-2866.

30 Liu, F.; Concepcion, J. J.; Jurss, J. W.; Cardolaccia, T.; Templeton, J. L.; Meyer, T. J. *Inorg. Chem.* **2008**, *47*, 1727-1752.

31 Rappaport, F.; Guergova-Kuras, M.; Nixon, P. J.; Diner, B. A.; Lavergne, J. *Biochemistry* **2002**, *41*, 8518-8527.

32 Umena, Y.; Kawakami, K.; Shen, J.-R.; Kamiya, N. *Nature* **2011**, *473*, 55-60

33 Suga, M.; Akita, F.; Hirata, K.; Ueno, G.; Murakami, H.; Nakajima, Y.; Shimizu, T.; Yamashita, K.; Yamamoto, M.; Ago, H.; Shen, J.-R. *Nature* **2015**, *517*, 99-103

34 Cox, N.; Pantazis, D. A.; Neese, F.; Lubitz, W. *Acc. Chem. Res.* **2013**, *46*, 1588-1596

35 Glöckner, C.; Kern, J.; Broser, M.; Zouni, A.; Yachandra, V.; Yano, J. *J. Biol. Chem.* **2013**, *288*, 22607-22620

36 Dismukes, G. C.; Brimblecombe, R.; Felton, G. A. N.; Pryadun, R. S.; Sheats, J. E.; Spiccia, L.; Swiegers, G. F. *Acc. Chem. Res.* **2009**, *42*, 1935-1943

37 Garrido-Barros, P.; Gimbert-Suriñach, C.; Matheu, R.; Sala, X.; Llobet, A. *Chem. Soc. Rev.* **2017**, *46*, 6099-6098.

38 Coehn, A.; Gläser, M. *Zeits. Anorg. Chem.* **1902***, 33,* 9-24.

39 Gersten, S. W.; Samuels, G. J.; Meyer, T. J. *J. Am. Chem. Soc.* **1982**, 104, 4029–4030.

40 Moyer, B. A.; Meyer, T. J. *J. Am. Chem. Soc.* **1978**, *100*, 3601-3603.

41 Nagle, J. K.; Bernstein, J. S.; Young, R. C.; Meyer, T. J. *Inorg. Chem.* **1981**, *20*, 1760-1764.

42 Weinberg, D. R.; Gagliardi, C. J.; Hull, J. F.; Murphy, C. F.; Kent, C. A.; Westlake, B.; Paul, A.; Ess, D. H.; McCafferty, D. G; Meyer, T. J. *Chem. Rev.* **2012**, *112*, 4016-4093.

43 Sala, X.; Maji, S.; Bofill, R.; Garcia-Anton, J.; Escriche, L.; Llobet, A. *Acc. Chem. Res.* **2014**, *47*, 504-516

44 Concepcion, J. J.; Jurss, J. W.; Brennaman, M. K.; Hoertz, P. G.; Patrocinio, A. O. T.; Murakami Iha, N. Y.; Templeton, J. L.; Meyer, T. J. *Acc. Chem. Res.* **2009**, *42*, 1954-1965.

45 Alperovich, I.; Smolentsev, G.; Moonshiram, D.; Jurss, J. W.; Concepcion, J. J.; Meyer, T. J.; Soldatov, A.; Pushkar, Y. *J. Am. Chem. Soc.* **2011**, *133*, 15786-15794.

46 Jurss, J. W.; Concepcion, J. J.; Butler, J. M.; Omberg, K. M.; Baraldo, L. M.; Thompson, D. G.; Lebeau, E. L.; Hornstein, B.; Schoonover, J. R.; Jude, H.; Thompson, J. D.; Dattelbaum, D. M.; Rocha, R. C.; Templeton, J. L.; Meyer, T. J. *Inorg. Chem.* **2012**, *51*, 1345-1358.

47 Moonshiram, D.; Jurss, J. W.; Concepcion, J. J.; Zakharova, T.; Alperovich, I.; Meyer, T. J.; Pushkar, Y. *J. Am. Chem. Soc.* **2012**, *134*, 4625-4636.

48 Hurst, J. K.; Cape, J. L.; Clark, A. E.; Das, S.; Qin, C. *Inorg. Chem.* **2008**, *47*, 1753-1764.

49 Hurst, J. K.; Roemeling, M. D.; Lymar, S. V. *J. Phys. Chem. B* **2015**, *119*, 7749-7760.

50 Hurst, J. K. *Coordination Chemistry Reviews* **2005**, *249*, 313-328.

51 Binstead, R. A.; Chronister, C. W.; Ni, J.; Hartshorn, C. M.; Meyer, T. J. *J. Am. Chem. Soc.* **2000**, *122*, 8464.

52 Sens, C.; Romero, I.; Rodriguez, M.; Llobet, A.; Parella, T.; Benet-Buchholz, J. *J. Am. Chem. Soc.* **2004**, *126*, 7798-7799.

53 Deng, Z.; Tseng, H.-W.; Zong, R.; Wang, D.; Thummel, R. *Inorg. Chem.* **2008**, *47*, 1835-1848.

54 Wada, T.; Tsuge, K.; Tanaka, K. *Inorg. Chem.* **2000**, *40*, 329-337.

55 Neudeck, S.; Maji, S.; López, I.; Meyer, S.; Meyer, F.; Llobet, A. *J. Am. Chem. Soc.* **2014**, *136*, 24-27.

56 Xu, Y.; Fischer, A.; Duan, L.; Tong, L.; Åkermark, B.; Sun, L. *Angew. Chem. Int. Ed.* **2010**, *49*, 8934-8937.

57 Betley, T. A.; Wu, Q.; Van Voorhis, T.; Nocera, D. G. *Inorg. Chem.* **2008**, *47*, 1849-1861.

58 Zong, R.; Thummel, R. P. *J. Am. Chem. Soc.* **2005**, *127*, 12802-12803.

59 Concepcion, J. J.; Jurss, J. W.; Templeton, J. L.; Meyer, T. J. *J. Am. Chem. Soc.* **2008**, *130*, 16462-16463.

60 Chen, Z.; Concepcion, J. J.; Luo, H.; Hull, J. F.; Paul, A.; Meyer, T. J. *J. Am. Chem. Soc.* **2010**, *132*, 17670-17673.

61 Duan, L.; Bozoglian, F.; Mandal, S.; Stewart, B.; Privalov, T.; Llobet, A.; Sun, L. *Nat. Chem.* **2012**, *4*, 418-423.

62 Duan, L.; Fischer, A.; Xu, Y.; Sun, L. *J. Am. Chem. Soc.* **2009**, *131*, 10397-10399.

63 Wang, L.; Duan, L.; Wang, Y.; Ahlquist, M. S. G.; Sun, L. *Chem. Commun.* **2014**, *50*, 12947-12950.

64 Matheu, R.; Ertem, M. Z.; Benet-Buchholz, J.; Coronado, E.; Batista, V. S.; Sala, X.; Llobet, A. *J. Am. Chem. Soc.* **2015**, *137*, 10786-10795.

65 Naruta, Y.; Sasayama, M.-A.; Sasaki, T. *Angew. Chem., Int. Ed.* **1994**, *33*, 1839–1841.

66 Shimazaki, Y.; Nagano, T.; Takesue, H.; Ye, B.-H.; Tani, F.; Naruta, Y. *Angew. Chem., Int. Ed.* **2004**, *43*, 98–100.

67 Limburg, J.; Vrettos, J. S.; Liable-Sands, L. M.; Rheingold, A. L.; Crabtree, R. H.; Brudvig, G. W. *Science* **1999**, *283*, 1524–1527.

68 Limburg, J.; Vrettos, J. S.; Chen, H.; de Paula, J. C.; Crabtree R. H.; Brudvig, G. W. *J. Am. Chem. Soc.* **2001**, *123*, 423–430.

69 Cady, C. W.; Shinopoulos, K. E.; Crabtree, R. H.; Brudvig, G. W. *Dalton Trans.* **2010**, *39*, 3985–3989.

70 Limburg, J.; Brudvig, G. W.; Crabtree, R. H. *J. Am. Chem. Soc.* **1997**, *119*, 2761–2762.

71 Chen, H.; Tagore, R.; Das, S.; Incarvito, C.; Faller, J. W.; Crabtree, R. H.; Brudvig, G. W. *Inorg. Chem.* **2005**, *44*, 7661–7670.

72 Najafpour, M. M.; McKee, V. *Catal. Commun.* **2010**, *11*, 1032–1035.

73 Yamazaki, H.; Igarashi, S.; Nagata, T.; Yagi, M. *Inorg.*

Chem. **2012**, *51*, 1530–1539.

74 Yamazaki, H.; Ueno, T.; Aiso, K.; Hirahara, M.; Aoki, T.; Nagata, T.; Igarashi, S.; Yagi, M. *Polyhedron* **2013**, *52*, 455–460.

75 Najafpour, M. M.; Moghaddam, A. N.; Dau. H.; Zaharieva, I. *J. Am. Chem. Soc.* **2014**, *136*, 7245–7248.

76 Hatakeyama, M.; Nakata, H.; Wakabayashi, M.; Yokojima, S.; Nakamura, S. *J. Phys. Chem. A* **2012**, *116*, 7089–7097.

77 Rivalta, I.; Yang, K. R.; Brudvig, G. W.; Batista, V. S.; *ACS Catal.* **2015**, *5*, 2384–2390.

78 Khan, S.; Yang, K. R.; Ertem, M. Z.; Batista, V. S.; Brudvig, G. W. *ACS Catal.* **2015**, *5*, 7104–7113.

79 Karlsson, E. A.; Lee, B.-L.; Åkermark, T.; Johnston, E. V.; Kärkäs, M. D.; Sun, J.; Hansson, Ö.; Bäckvall, J.-E.; Åkermark, B.; *Angew. Chem., Int. Ed.* **2011**, *50*, 11715– 11718.

80 Ashmawy, F. M.; McAuliffe, C. A.; Parish, R. V.; Tames, J. *J. Chem. Soc., Dalton Trans.* **1985**, 7, 1391–1397.

81 Gao, Y.; Liu, J.; Wang, M.; Na, Y.; Åkermark, B.; Sun, L. *Tetrahedron* **2007**, *63*, 1987–1994.

82 Lee, W.-T.; Muñoz III, S. B.; Dickie, D. A.; Smith, J. M. *Angew. Chem., Int. Ed.* **2014**, *53*, 9856–9859.

83 Ellis, W. C.; McDaniel, N. D.; Bernhard, S.; Collins, T. J. *J. Am. Chem. Soc.* **2010**, *132*, 10990–10991.

84 Ryabov, A. D.; Collins, T. J. *Adv. Inorg. Chem.* **2009**, *61*, 471–521.

85 Ghosh, A.; de Oliveira, F. T.; Yano, T.; Nishioka, T.; Beach, E. S.; Kinoshita, I.; Münck, E.; Ryabov, A. D.; Horwitz C. P.; Collins, T. J. *J. Am. Chem. Soc.* **2005**, *127*, 2505–2513.

86 Tang, L. L.; Gunderson, W. A.; Weitz, A. C.; Hendrich, M. P.; Ryabov, A. D.; Collins, T. J. *J. Am. Chem. Soc.* **2015**, *137*, 9704–9715.

87 Chanda, A.; Shan, X.; Chakrabarti, M.; Ellis, W. C.; Popescu, D. L.; de Oliveira, F. T.; Wang, D.; Que Jr., L.; Collins, T. J.; Münck, E.; Bominaar, E. L. *Inorg. Chem.* **2008**, *47*, 3669–3678.

88 de Oliveira, F. T.; Chanda, A.; Banerjee, D.; Shan, X.; Mondal, S.; Que Jr., L.; Bominaar, E. L.; Münck, E.; Collins, T. J. *Science* **2007**, *315*, 835–838.

89 Pattanayak, S.; Chowdhury, D. R.; Garai, B.; Singh, K. K.; Paul, A.; Dhar, B. B.; Gupta, S. S. *Chem. - Eur. J.* **2017***, 23,* 3414−3424.

90 Lloret-Fillol, J.; Codolà, Z.; Garcia-Bosch, I.; Gómez, L.; Pla, J. J.; Costas, M. *Nat. Chem.* **2011**, *3*, 807–813.

91 Hong, D.; Mandal, S.; Yamada, Y.; Lee, Y.-M.; Nam, W.; Llobet, A.; Fukuzumi, S. *Inorg. Chem.* **2013**, *52*, 9522-9531.

92 Wickramasinghe, L. D.; Zhou, R.; Zong, R.; Vo, P.; Gagnon, K. J.; Thummel, R. P. *J. Am. Chem. Soc.* **2015**, *137*, 13260–13263.

93 Kanan, M. W.; Nocera, D. G. *Science*, **2008**, *321*, 1072-1075.

94 Beattie, J. K.; Hambley, T. W.; Klepetko, J. A.; Masters, A. F.; Turner, P. *Polyhedron* **1998**, *17*, 1343–1354.

95 Chakrabarty, R.; Bora, S. J.; Das, B. K. *Inorg. Chem.* **2007**, *46*, 9450–9462.

96 Dimitrou, K.; Folting, K.; Streib, W. E.; Christou, G. *J. Am. Chem. Soc.* **1993**, *115*, 6432–6433.

97 Dimitrou, K.; Brown, A. D.; Concolino, T. E.; Rheingold, A. L.; Christou, G. *Chem. Commun.* **2001**, *0*, 1284–1285.

98 Yin, Q.; Tan, J. M.; Besson, C.; Geletii, Y. V.; Musaev, D. G.; Kuznetsov, A. E.; Luo, Z.; Hardcastle, K. I.; Hill, C. L. *Science*, **2010**, *328*, 342–345.

99 Huang, Z.; Luo, Z. ; Geletii, Y. V.; Vickers, J. W.; Yin, Q.; Wu, D.; Hou, Y.; Ding, Y.; Song, J.; Musaev, D. G.; Hill C. L.; Lian, T. *J. Am. Chem. Soc.* **2011**, *133*, 2068–2071.

100 Lv, H.; Geletii, Y. V.; Zhao, C.; Vickers, J. W.; Zhu, G.; Luo, Z.; Song, J.; Lian, T.; Musaev, D. G.; Hill, C. L. *Chem. Soc. Rev.* **2012**, *41*, 7572–7589.

101 Wang, S.-S.; Yang, G.-Y. *Chem. Rev.* **2015**, *115*, 4893–4962.

102 Han, X.-B.; Li, Y.-G.; Zhang, Z.-M.; Tan, H.-Q.; Lu, Y.; Wang, E.-B. *J. Am. Chem. Soc.* **2015**, *137*, 5486–5493.

103 Wasylenko, D. J.; Ganesamoorthy, C.; Borau-Garcia, J.; Berlinguette, C. P. *Chem. Commun.* **2011**, *47*, 4249–4251.

104 Dogutan, D. K.; McGuire R.; Nocera, D. G. *J. Am. Chem. Soc.* **2011**, *133*, 9178–9180.

105 Nakazono, T.; Parent, A. R.; Sakai, K. *Chem. Commun.* **2013**, *49*, 6325–6327.

106 Wang, D.; Groves, J. T. *Proc. Natl. Acad. Sci. U. S. A.* **2013**, *110*, 15579–15584.

107 Pizzolato, E.; Natali, M.; Posocco, B.; Montellano López, A.; Bazzan, I.; Di Valentin, M.; Galloni, P.; Conte, V.; Bonchio, M.; Scandola, F.; Sartorel, A.; *Chem. Commun.* **2013**, *49*, 9941–9943.

108 Du, H.-Y.; Chen, S.-C.; Su, X.-J.; Jiao, L.; Zhang, M.-T. *J. Am. Chem. Soc.* **2018,** *140*, 1557-1565

109 Leung, C.-F.; Ng, S.-M.; Ko, C.-C.; Man, W.-L.; Wu, J.; Chen, L.; Lau, T.-C. *Energy Environ. Sci.* **2012**, *5*, 7903–7907.

110 Wang, H.; Lu, Y.; Mijangos, E.; Thapper, A. *Chin. J. Chem.* **2014**, *32*, 467–473.

111 Najafpour, M. M.; Feizi, H. *Catal. Sci. Technol.* **2018**, *8*, 1840-1848.

112 Rigsby, M. L.; Mandal, S.; Nam, W.; Spencer, L. C.; Llobet, A.; Stahl, S. S. *Chem. Sci.* **2012**, *3*, 3058–3062.

113 Gimbert-Suriñach, C.; Moonshiram, D.; Francàs, L; Planas, N.; Bernales, V.; Bozoglian, F.; Gdua, A.; Mognon, L.; López, I.; Hoque, M. A.; Gagliardi, L.; Cramer, C. J.; Llobet, A. *J. Am. Chem. Soc.* **2016**, *138*, 15291-15294.

114 Wang, H.-Y.; Mijangos, E.; Ott, S.; Thapper, A. *Angew. Chem., Int. Ed.* **2014**, *53*, 14499–14502.

115 Wang, J.-W.; Sahoo, P.; Lu, T.-B. *ACS Catal.* **2016**, *6*, 5062-5068.

116 Han, Y.; Wu, Y.; Lai, W.; Cao, R. *Inorg. Chem.* **2015**, *54*, 5604-5613.

117 Wang, J.-W.; Hou, C.; Huang, H.-H.; Liu, W.-J.; Ke, Z.-F.; Lu, T.-B. *Catal. Sci. Technol.* **2017**, *7*, 5585-5593.

118 Luo, G.-Y.; Huang, H.-H.; Wang, J.-W.; Lu, T.-B. *ChemSusChem* **2016**, *9*, 485-491.

119 Zhang, M.; Zhang, M.-T.; Hou, C.; Ke, Z.-F.; Lu, T.-B. *Angew. Chem. Int. Ed.* **2014**, *53*, 13042-13048.

120 Singh, A.; Chang, S. L. Y.; Hocking, R. K.; Bach, U.; Spiccia, L. *Catal. Sci. Technol.* **2013**, *3*, 1725-1732.

121 Najafpour, M. M.; Feizi, H. *Dalton Trans.* **2018**, *47*, 6519-6527

122 Solomon, E. I.; Heppner, D. E.; Johnston, E. M.; Ginsbach, J. W.; Cirera, J.; Qayyum, M.; Kieber-Emmons, M. T.; Kjaergaard, C. H.; Hadt, R. G.; Tian, L. *Chem. Rev.* **2014**, *114*, 3659-3853.

123 Barnett, S. M.; Goldberg, K. I.; Mayer, J. M. *Nat. Chem.* **2012**, *4*, 498−502.

124 Zhang, M.-T.; Chen, Z.; Kang, P.; Meyer, T. J. *J. Am. Chem. Soc.* **2013**, *135*, 2048−2051.

125 Zhang, T.; Wang, C.; Liu, S.; Wang, J.-L.; Lin, W. *J. Am. Chem. Soc.* **2014**, *136*, 273−281.

126 Gerlach, D. L.; Bhagan, S.; Cruce, A. A.; Burks, D. B.; Nieto, I.; Truong, H. T.; Kelley, S. P.; Herbst-Gervasoni, C. J.; Jernigan, K. L.; Bowman, M. K.; Pan, S.; Zeller, M.; Papish, E. T. *Inorg. Chem.* **2014**, *53*, 12689−12698.

127 Shen, J.; Wang, M.; Zhang, P.; Jiang, J.; Sun, L. *Chem.Commun.* **2017**, *53*, 4374-4377.

128 Fisher, K. J.; Materna, K. L.; Mercado, B. Q.; Crabtree, R. H.; Brudvig, G. W. *ACS Catal.* **2017**, *7*, 3384-3387.

129 Bullock, R. M.; Das, A. K.; Appel, A. M. *Chem. - Eur. J.* **2017***, 23,* 7626−7641.

130 Materna, K. L.; Crabtree, R. H.; Brudvig, G. W. *Chem. Soc. Rev.* **2017**, *46*, 6099-6110.

131 Ernstorfer, R.; Gundlach, L.; Felber, S.; Storck, W.; Eichberger, R.; Willig, F. *J. Phys. Chem. B* **2006**, *110*, 25383–25391.

132 Brennan, B. J.; Llansola Portoles, M. J.; Liddell, P. A.; Moore, T. A.; Moore, A. L.; Gust, D. *Phys. Chem. Chem. Phys.* **2013**, *15*, 16605–16614.

133 Bae, E.; Choi, W.; Park, J.; Shin, H. S.; Kim, S. B.; Lee, J. S. *J. Phys. Chem. B* **2004**, *108*, 14093–14101.

134 Guerrero, G.; Mutin, P. H.; Vioux, A. *Chem. Mater.* **2001**, *13*, 4367–4373.

135 Brennan, B. J.; Koenigsmann, C.; Materna, K. L.; Kim, P. M.; Koepf, M.; Crabtree, R. H.; Schmuttenmaer, C. A.; Brudvig, G. W. *J. Phys. Chem. C*, **2016**, *120*, 12495–12502.

136 Brennan, B. J.; Chen, J.; Rudshteyn, B.; Chaudhuri, S.; Mercado, B. Q.; Batista, V. S.; Crabtree, R. H.; Brudvig, G. W. *Chem. Commun.* **2016**, *52*, 2972–2975.

137 McNamara, W. R.; Milot, R. L.; Song, H.-E.; Snoeberger III, R. C.; Batista, V. S.; Schmuttenmaer, C. A.; Brudvig, G. W.; Crabtree, R. H. *Energy Environ. Sci.* **2010**, *3*, 917–923.

138 McNamara, W. R.; Snoeberger III, R. C.; Li, G.; Richter, C.; Allen, L. J.; Milot, R. L.; Schmuttenmaer, C. A.; Crabtree, R. H.; Brudvig, G. W.; Batista, V. S. *Energy Environ. Sci.* **2009**, *2*, 1173–1175.

139 Materna, K. L.; Rudshteyn, B.; Brennan, B. J.; Kane, M. H.; Bloomfield, A. J.; Huang, D. L.; Shopov, D. Y.; Batista, V. S.; Crabtree, R.H.; Brudvig, G. W. *ACS Catal.* **2016**, *6*, 5371–5377.

140 Materna, K. L.; Brennan, B. J.; Brudvig, G. W. *Dalton Trans.* **2015**, *44*, 20312–20315.

141 Francas, L.; Richmond, C.; Garrido-Barros, P.; Planas, N.; Roeser, S.; Benet-Buchholz, J.; Escriche, L.; Sala, X.; Llobet, A. *Chem. Eur. J.* **2016**, *22*, 5261-5268.

142 Chen, Z.; Concepcion, J. J.; Jurss, J. W.; Meyer, T. J. *J. Am. Chem. Soc.* **2009**, *131*, 15580-15581.

143 Odrobina, J.; Scholz, J.; Pannwitz, A.; Francàs, L.; Dechert, S.; Llobet, A.; Jooss, C.; Meyer, F. *ACS Catal.* **2017**, *7*, 2116-2125

144 Li, F.; Zhang, B.; Li, X.; Jiang, Y.; Chen, L.; Li, Y.; Sun, L. *Angew. Chem. Int. Ed.* **2011**, *50*, 12276- 12279.

145 Tong, L.; Gothelid, M.; Sun, L. *Chem. Commun.* **2012**, *48*, 10025-10027

146 Mola, J.; Mas-Marza, E.; Sala, X.; Romero, I.; Rodríguez, M.; Viñas, C.; Parella, T.; Llobet, A. *Angew. Chem. Int. Ed.* **2008**, *47*, 5830-5832.

147 Creus, J.; Matheu, R.; Peñafiel, I.; Moonshiram, D.; Blondeau, P.; Benet-Buchholz, J.; García-Antón, J.; Sala, X.; Godard, C.; Llobet, A. *Angew. Chem. Int. Ed.* **2016**, *55*, 15382-15386.

Chapter 2

Objectives

The past four decades of research in molecular water oxidation have led to important advances as disussed in the General Introduction. However, many challenges still remain in order to achieve the required progress for practical aplications. In this chapter, the main objectives of the present thesis are described regarding those challenges.

Objectives

II

Over the last decades, the field of molecular water oxidation has been dominated by the development of Ru complexes that act as efficient catalysts. The detailed study of some of those catalytic systems has allowed researchers to reveal the main factors involved in the high activity and stability and has eventually allowed to perform a rational design of improved catalysts. Only in the last 15 years, the TOF of the reported systems has increased exponentially exceeding the value corresponding to the Mn cluster in the natural oxygen evolving complex. Thanks to those advances, a further step towards the building of artificial photosynthetic devices has been achieved by anchoring some of the most active catalysts to photoanodes that are able to perform solar driven water oxidation.

Despite all the previous progress in Ru chemistry, using cheaper and more abundant transition metals remains as a challenge for the design of inexpensive and efficient practical devices. As already mentioned in the General Introduction, there has been a sudden and random production of molecular catalysts based on first row transition metals during the last 10 years. However, the lack of detailed studies about the real active species and the mechanistic pathways, together with the modest activities reached, has prevented researchers from following a rational design of more robust and active catalysts, which is essential for the progress in the field. For this reason, the general objective of the present PhD Thesis is the design and thorough analysis of molecular catalysts based on first row transition metals in order to identify the factors that determine the activity and stability under catalytic conditions. This would allow us to make an iterative cycle based on the rational redesign of new catalysts with improved performance (Scheme 1). The best performing catalyst resulting from that rational design will be employed for studying its implementation in molecular anodes as the following step toward practical devices.

Scheme 1. Iterative process for the rational design of improved molecular catalysts.

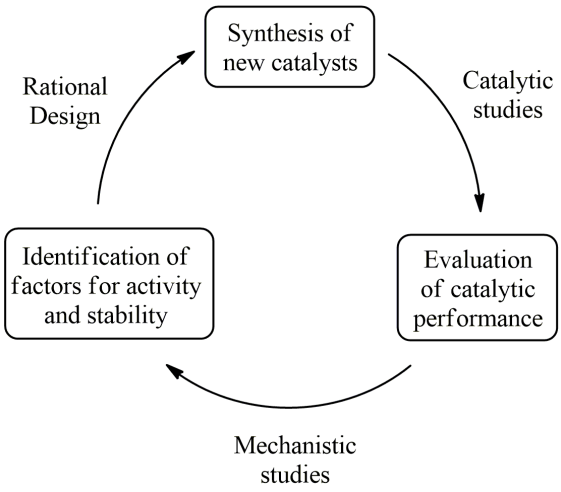

The general objective discussed above can be divided into different partial specific objectives:

- **Objective 1**: Synthesis and characterization of copper complexes based on the tetraamide ligand N^1,$N^{1\prime\prime}$-(1,2-phenylene)bis(N^2-methyloxalamide) H_4mox (Chart 1), that is able to stabilize high oxidation states of the metal center thanks to the strong electron-donation exerted by the four negatively charged amide groups. Moreover, this ligand scaffold has a redox non-innocent character as the phenyl ring can oxidize to form a radical species. Final evaluation of their capability to catalyze the water oxidation will be performed with special interest in identifying the role of the ligand oxidation into the catalytic cycle.

Objectives

Chart 1. Schematic representation of the ligands used in this work.

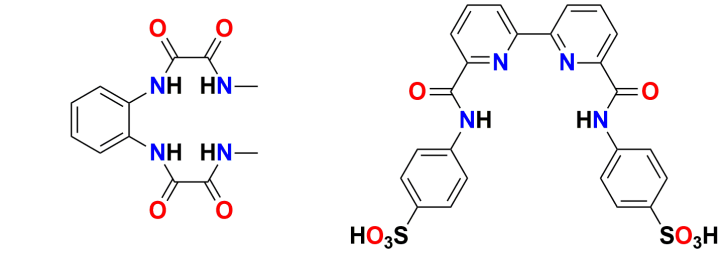

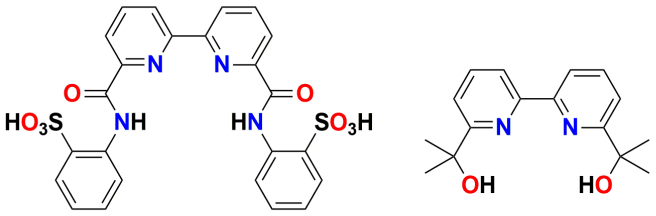

- **Objective 2**: Computational study of the O-O bond formation mechanistic pathways open to Cu-based water oxidation catalysis. For that aim, several catalysts with different features will be used as models in order to find common factors in their mechanisms and compare them with Ru-based catalysis.
- **Objective 3**: Design and synthesis of Cu-based molecular catalysts bearing the redox non-innocent ligands 4,4'-(([2,2'-bipyridine]-6,6'-dicarbonyl)bis(azanediyl)) dibenzenesulfonic acid (*p*-H_4BDAM) and 2,2'-(([2,2'-bipyridine]-6,6'-dicarbonyl)bis(azanediyl))dibenzenesulfonic acid (*o*-H_4BDAM) (Chart 1), that can accumulate several oxidative equivalents forming diradical species. This strategy allows exploring the catalytic process where all the electron transfer steps are ligand-based, avoiding the high energy-demanding oxidation of the metal center. This work will be compared with the copper complex based on the redox innocent ligand 6,6'-diisopropanol-2,2'-bipyridine

(H_2bpk), where only the metal center is in principle expected to mediate in the electron transfers upon oxidation.

- **Objective 4**: Employing the best performing molecular catalyst based on copper complexes to prepare molecular anodes for water oxidation catalysis based on inexpensive carbon materials. For that aim, pyrene functionalities will be incorporated in the ligand backbone in order to promote π-π interactions with graphene-based electrodes.
- **Objective 5**: Due to the lack of information regarding molecular Ni-based water oxidation catalysis, a final objective will be to extend the previous knowledge developed for copper complexes to the preparation and evaluation of molecular Ni complexes as water oxidation catalysts.

Chapter 3

Redox non-innocent ligands in copper-catalyzed water oxidation

Chapter 3 explores the use of redox non-innocent ligands for molecular water oxidation catalysis using the copper complex $[Cu^{II}(mox)]^{2-}$. The influence of the ligand oxidation on the catalytic mechanism allows an excellent control on the overpotential, that can be lowered to a record value of 170 mV. Moreover, the computational study of the O-O bond formation step in three different copper catalysts reveals an unprecedented mechanism based on single electron transfers.

III

Paper A: Redox Non-innocent Ligand Controls Water Oxidation Overpotential in a New Family of Mononuclear Cu-Based Efficient Catalysts

Garrido-Barros, P.; Funes-Ardoiz, I.; Drouet, S.; Benet-Buchholz, J.; Maseras, F.; Llobet, A. *J. Am. Chem. Soc.* **2015**, *137*, 6758-6761.

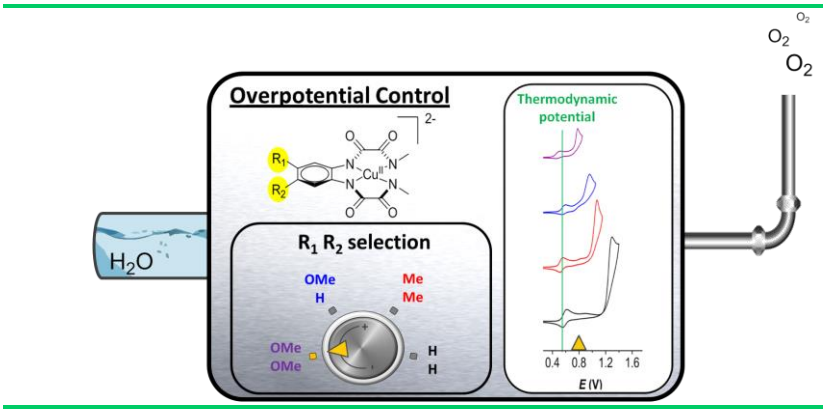

Abstract

A new family of tetra-anionic tetradentate amidate ligands, N_1,N_1' -(1,2-phenylene)bis(N_2-methyloxalamide) (H_4L1), and its derivatives containing electron-donating groups at the aromatic ring have been prepared and characterized, together with their corresponding anionic Cu(II) complexes, $[(LY)Cu]^{2-}$. At pH 11.5, the latter undergoes a reversible metal-based III/II oxidation process at 0.56 V and a ligand-based pHdependent electron-transfer process at 1.25 V, associated with a large electrocatalytic water oxidation wave (overpotential of 700 mV). Foot-of-the-wave analysis gives a catalytic rate constant of 3.6 s^{-1} at pH 11.5 and 12 s^{-1} at pH 12.5. As the electron-donating capacity at the aromatic ring increases, the overpotential is drastically reduced down to a record low of 170 mV. In addition, DFT calculations allow us to propose a complete catalytic cycle

that uncovers an unprecedented pathway in which crucial O − O bond formation occurs in a two-step, one-electron process where the peroxo intermediate generated has no formal M − O bond but is strongly hydrogen bonded to the auxiliary ligand.

Contributions:

Pablo Garrido Barros synthetized and characterized all the compounds, carried out the electrochemical and spectroscopic analysis, collaborated in the computational calculations and prepared the manuscript.

A.1. Introduction

Molecular water oxidation catalysis by transition metal complexes[1] is a highly active field of research at present due to its implications in new energy conversion schemes based on splitting water with sunlight.[2] In addition, water oxidation is also of interest in biology because it is the reaction that takes place at the oxygen-evolving complex of photosystem II in green plants and algae.[3] The very high thermodynamic potential needed for water oxidation (1.23 V vs NHE at pH 0.0) implies necessarily the use of transition metal complexes containing oxidatively rugged ligands, in order to come up with long-lasting systems that can have potential commercial applications.[2c,4] In addition, these complexes need to work in water as a solvent, imposing an additional requirement for the auxiliary ligands to be substitutionally inert at the pH of action; otherwise, they end up generating the corresponding aqua/hydroxo complexes and the free ligand. This is especially critical for first-row transition metal complexes, as has been previously shown in the literature,[5] because there will only be a limited pH range where the integrity of the complex is maintained. Furthermore, ligand liberation from the metal complex is an additional driving force toward the formation of metal oxides and/or mixed oxo-hydroxides that will be highly dependent on working pH. On the other hand, an interesting feature of water oxidation catalyst (WOC)

design is the use of redox noninnocent ligands that can help with the difficult task of managing the multiple protons and multiple electrons transfers needed to carry out the water oxidation reaction.[6] This feature would be particularly useful if the ligand-based redox processes are tied to the rate-determining step (rds) of the catalytic process and not linked to unwanted radical-based reactions leading to fast decomposition.[7]

A.2. Results and discussion

In order to explore the options for water oxidation catalysis based on oxidatively rugged but redox-active ligands, we have prepared a family of four Cu(II) complexes containing the tetradentate amidate acyclic ligands H_4LY (Y = 1−4) with different substituent groups at the aromatic ring (see Figure 1). The H_4LY (Y = 2−4) ligands are new compounds that have been prepared following related procedures already described for the unsubstituted ligand H_4L1.[8]

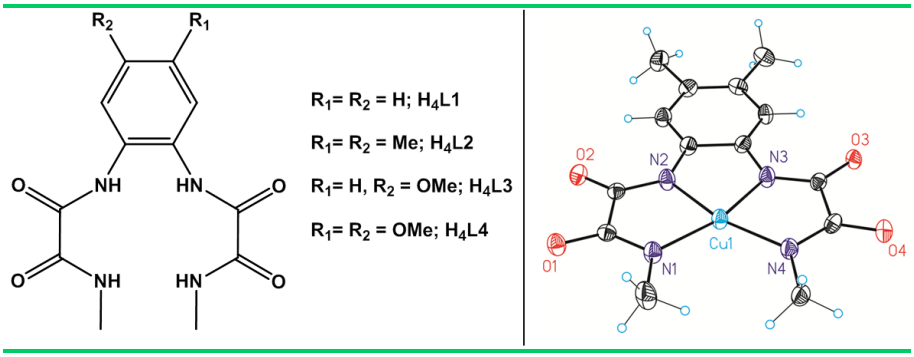

Figure 1. (Left) Ligand structures and (right) ORTEP figure of $[(L2)Cu]^{2-}$ complex.

The new copper complexes reported here, $[(LY)Cu](NMe_4)_2$ (Y = 2 − 4), have been characterized by the usual spectroscopic techniques and by monocrystal X-ray diffraction analysis. An ORTEP view of the cationic part of complex $[(L2)Cu](NMe_4)_2$ is depicted in Figure 1, while those for

the other methoxy derivatives are presented in the Supporting Information (SI). It is interesting to observe here that the d^9 Cu(II) ion is four-coordinate with a basically square planar geometry, manifesting the existence of π-delocalization over the phenyl and amidate moieties of the ligand and ensuring strong ligand bonding to the metal center.

The redox properties of the anionic complexes $[(LY)Cu]^{2-}$ (Y = 1−4) were investigated by cyclic voltammetry (CV) and amperometric techniques using a mercury sulfate reference electrode saturated with K_2SO_4 (MSE) unless explicitly indicated. All redox potentials in the present work are reported versus NHE by adding 0.65 V to the measured potential. Figure 2 shows the CV experiments carried out for $[(L1)Cu]^{2-}$ in the pH range 11.5−12.5.

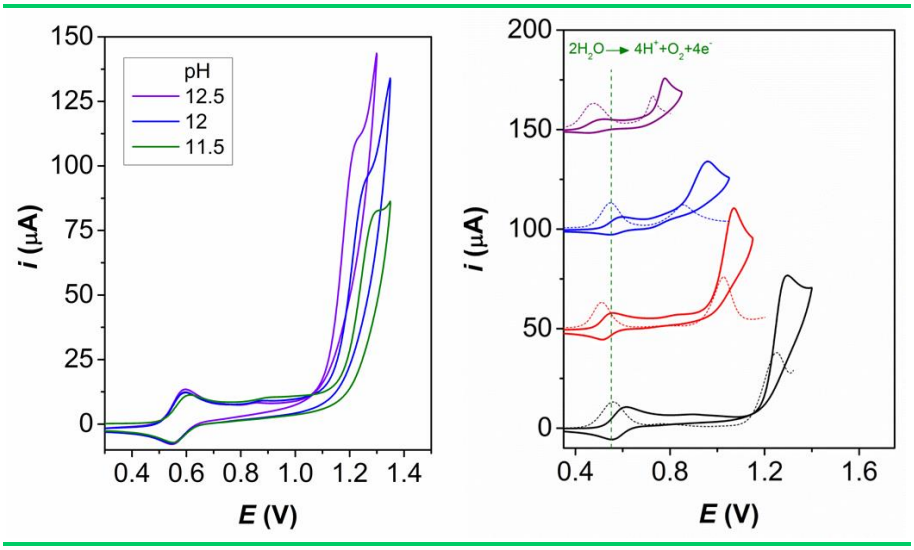

Figure 2. (Left) CV experiments with 1 mM $[(L1)Cu]^{2-}$ in phosphate buffer (0.1 M of ionic strength) at different pH values. (Right) CV and DPV for complexes $[(LY)Cu]^{2-}$ (Y = 1−4). The green vertical dashed line indicates the thermodynamic E° for the $4e^-$ oxidation of water to dioxygen at pH 11.5. CVs are run at a scan rate of 100 mV/s.

A first pH-independent, chemically reversible, and electrochemically quasi-reversible wave at $E_{1/2}$ = 0.56 V vs NHE (ΔE = 71 mV), eq 1, is associated with the formation of a d^8 Cu(III)

$[(L1)Cu^{III}]^{-}$ (**B**) + $1e^{-} \rightarrow [(L1)Cu^{II}]^{2-}$ (**A**) $\quad E_{1/2} = 0.56$ V (1)

square planar ion with very low reorganizational energy, as inferred from the very small differences in their respective geometries, and with a relatively low potential due the tetraanionic nature of the L1 ligand (the **A** and **B** labels indicated here are also used in Figure 3). A second pH-dependent wave (approximately 59 mV/pH unit) observed at more anodic potentials, eq 2, is associated with a ligand-based aryl oxidation,

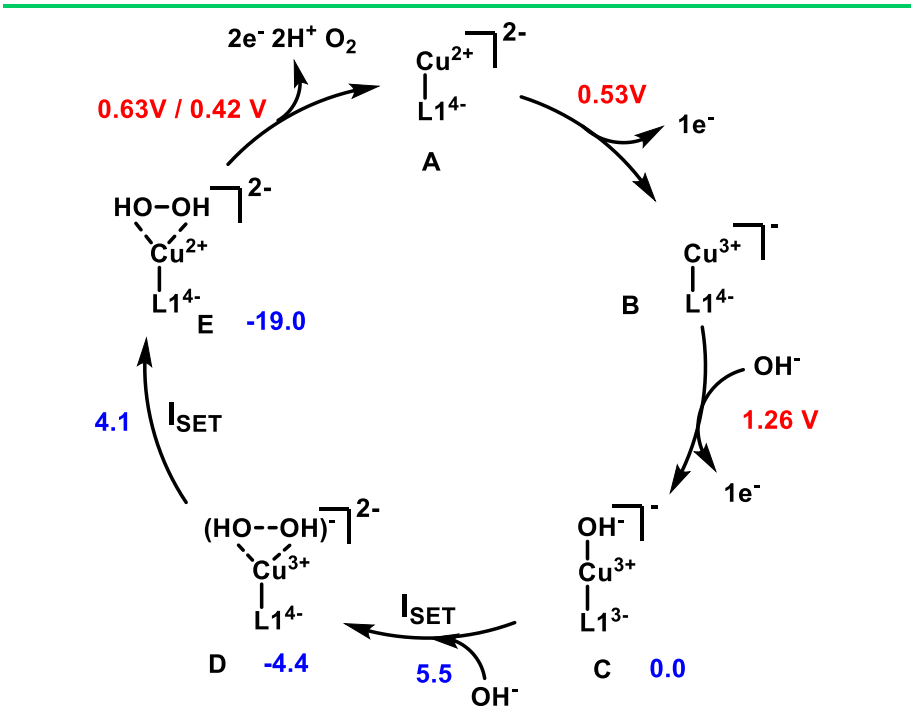

Figure 3. Calculated catalytic cycle. Free energy changes for steps at the electrode are indicated explicitly in volts (red) and for steps in solution are indicated in kcal/mol (blue).

$[(L1\cdot)Cu^{III}(OH)]^{-}$(**C**) + 1e- $\rightarrow [(L1)Cu^{III}]^{-}$(**B**) + OH^{-} $E_{1/2}$=1.25 V (2)

forming formally a phenyl radical cation, together with the coordination of a hydroxido ligand. This ligand-based oxidation had been previously proposed on electrochemical grounds for related complexes[9] and is further supported by the strong inductive effects exerted by the phenyl

substituents, as will be shown further below and also supported by DFT calculations (vide infra). In the presence of water, this wave is associated with a large electrocatalytic anodic current due the catalytic oxidation of water to dioxygen. In order to obtain kinetic information about the catalytic process, a foot-of-the-wave analysis (FOWA) was carried out to calculate the apparent rate constant, k_{obs}. We followed the methodology described in the literature,[10] assuming that the rds is the last electron-transfer step coupled to a chemical reaction. The largest slope at the very beginning of the catalytic process gives an impressive value of k_{obs}= 3.56 s^{-1} that is basically independent of the scan rate and thus in agreement with the model proposed. These kinetic values compare well with the ones reported in the literature for related complexes (see Table 1, below). However, since different methods are used for this type of calculation, the comparisons should be done with caution.

To confirm the stability of the WOCs, spectroelectrochemical experiments were performed using an OTTLE cell, scanning from 0.4 to 1.25 V and back to the original 0.4 V at a very low scan rate of 2 mV/s that allows for complete transformations during the redox events. Under these conditions, the initial complex is fully recovered, as ascertained by both UV−vis spectroscopy and charge integration under the III/II wave (see SI for details). Bulk electrolysis experiments for complex $[(L1)Cu]^{2-}$ (E_{app} = 1.3 V at pH 11.5 with a 2.5 cm^2 ITO working electrode) show a current density of 0.11 mA/cm^2 that slowly decays to 0.06 mA/cm^2. Simultaneous measurement of the oxygen gas generated by a Clark electrode confirms the generation of dioxygen with a Faradaic efficiency close to 100%. The decrease of current intensity over time is a consequence of lower activity of the catalyst as the pH decreases, as has been shown by FOWA. Furthermore, both CV and UV−vis spectroscopy (see SI) show that the initial species are totally retained, and, in addition, restoring the initial pH by adding base restores the initial activity. Similarly, sequential base addition during bulk electrolysis experiments maintains the catalyst

activity over long periods of time (1 h) without apparent losses (see SI). Further, no copper oxide adsorption at the ITO electrode surface could be detected under the present conditions, as confirmed by CV, UV−vis, and EDX analysis, evidencing the molecular nature of the electrocatalytic water oxidation.

The nature of the species generated in the catalytic cycle was also investigated by DFT calculations (B3LYP-D3 calculations with implicit SMD solvation, see SI for computational details), which nicely complement the results obtained experimentally. A complete catalytic cycle is presented in Figure 3, including the energies involved in the different steps. At oxidation state II, the catalyst remains in its resting state and is activated by two consecutive one-electron transfers, as shown by CV techniques and described in eqs 1 and 2. The computed oxidation potentials, 0.53 and 1.26 V, are in good agreement with the experimental values of 0.56 and 1.25 V, respectively. Calculations confirmed the radical cationic ligand nature of species **C**, as the attempts to obtain a Cu(IV) species always reverted to the Cu(III) complex with internal electron transfer from the ligand (Figure S27).

Species **C**, [(L1$^{\bullet}$)Cu(III)(OH)], reacts with an additional OH^- from the media to ultimately produce intermediate **E** (see Figure 3) with a peroxo unit, [(L1)Cu(II)(HO−OH)], as usually assumed in this type of chemistry following a concerted two-electron step.[5b,11] However, it follows an unusual path that deserves some comment.

In the usual water nucleophilic attack (WNA) pathway, the OH^- would directly attack the O and form the O−O bond in a single step through a moderate energy transition state. Our attempts to locate such a transition state failed, revealing instead the more complex picture indicated in Figure 4.

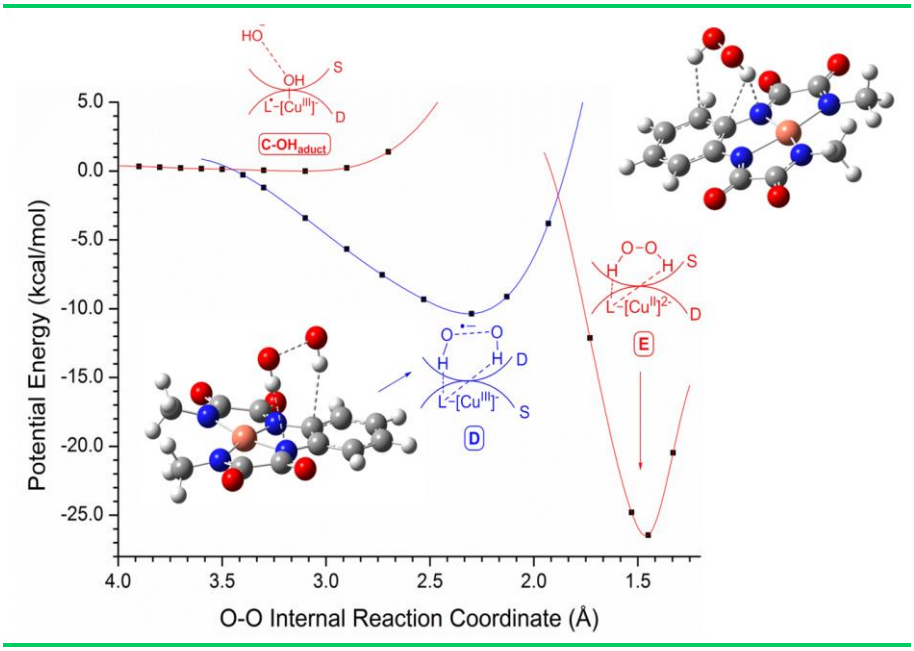

Figure 4. Potential energy relaxed scan for the O−O bond formation. The energy barrier for the second I_{SET} is estimated from changes of potential energy in the coordinate scan.

There is no direct connection between species **C** and **E** (the two curves in red) through a two-electron transfer. Instead, they are connected through an additional electronic state, shown in blue in the figure. This electronic state, which we have labeled as species **D**, results from **C** by transfer of one electron from the incoming OH^- to the [(L1$^{\bullet}$)Cu(III)] moiety (initially in a doublet state) to form a $(HO{-}{-}{-}OH)^{\bullet-}$ radical anion fragment with a partial O−O bond (doublet state, with an O---O distance of 2.3 Å) and hydrogen bonded to the [(L1)Cu(III)] complex (H-bonding distances between 2.5 and 2.9 Å, see SI). **D** then evolves to **E** through a second electron transfer, converting the HO−OH unit to a singlet state and the [(L1)Cu(II)] unit to a doublet. In species **E**, the HO−OH fragment is again strongly hydrogen bonded to the [(L1)Cu(II)] moiety (see SI). We propose to label this type of mechanism as single-electron transfer water nucleophilic attack (SET-WNA), differing from the traditional

WNA, where the two electrons are transferred in a single step. Of course, this SET-WNA mechanism would be impossible in the absence of a transition metal able to undergo a fast single electron transfer toward the HO−OH moiety formation. The generation of hydroxyl radical species would otherwise be prohibitively high. Thus, in this new SET-WNA mechanism, the O−O bond formation step can be considered to involve two consecutive intramolecular single electron transfer (I_{SET}) steps. Another interesting particularity of our SET-WNA mechanism proposed here is the absence of a direct Cu−O bond in species **D** and **E**; instead, the $(HO{---}OH)^{\bullet-}$ and $(HO{-}OH)^{2-}$ moieties are bonded to the $[(L1)Cu]^{2-}$ metal complex via hydrogen bonding, as has been already indicated above. Precedent for intramolecular ligand-based hydrogen bonding has been reported recently for related Fe complexes.[12] In our case, the SET-WNA mechanism has the important consequence of allowing the O−O bond formation with a very low barrier of 5.5 kcal/mol, thus practically instantaneously after species **C** is formed by oxidation at the electrode in the presence of a basic solution. The evolution from **E** to dioxygen release and recovery of catalyst **A** follows a more conventional pathway, which is discussed in detail in the SI, although it is worth mentioning that the [(L1)Cu(II)-(HOOH)] complex **E** is first oxidized to the corresponding [(L1)Cu(III)(HOOH)] species by a metal-based electron transfer at 0.63 V. Then, a proton-coupled electron transfer happens at a potential of 0.42 V, resulting in the formation of a $[(L1)Cu(III)(HOO^{\bullet})]$ complex which evolves dioxygen and a free proton. These values indicate that those two processes experimentally occur in a single step involving two electrons and one proton.

As evidenced by CV and confirmed by DFT, the rds involves the generation of the radical cation species **C** and its reaction with OH^-. It is thus reasonable that electronic perturbation of the aromatic ring should strongly influence both thermodynamics and kinetics of the water oxidation reaction catalyzed by this type of complexes. For this purpose, we

have prepared a family of copper complexes containing electron-donating groups such as Me and OMe in the aromatic ring, as indicated in Figure 1. The CV depicted in Figure 2 clearly shows how the onset of the catalytic wave is shifted to the cathodic region as a function of the strength of the electron-donating group. In particular, it is impressive to see that, for complex $[(L4)Cu]^{2-}$, the overpotential at which water oxidation occurs is 530 mV lower than for $[(L1)Cu]^{2-}$ and is situated at only 170 mV above the thermodynamic value. This is the first example in the literature where a rational ligand variation allows us to exert such a degree of control over the electrocatalytic water oxidation overpotential, driving it to a record low for first row transition metal complexes.[13]

A set of electrochemical parameters and kinetic data is presented in Table 1, together with related data for other Cu complexes described previously in the literature.[8b,14] It is interesting to observe that, for $[(L1)Cu]^{2-}$and $[(L2)Cu]^{2-}$ (entries 1 and 2, Table 1), the rate constants are 3.56 and 3.58 s^{-1}, respectively, whereas for $[(L3)Cu]^{2-}$ and $[(L4)Cu]^{2-}$ (entries 3 and 4, Table 1), the rate constants decrease by 1 order of magnitude, suggesting an important involvement of the electron-transfer process at the rds and a significant stabilization of the radical cation active species. On the other hand, increasing the pH from 11.5 to 12.5 increases the rate constant up to 11.96 s^{-1}. It is also important to realize here that, as the strength of the electron-donating group increases, the oxidative ruggedness of the radical cation species decreases, manifesting the existence of a decomposition pathway coupled to the water oxidation catalysis for complexes $[(L3)Cu]^{2-}$ and $[(L4)Cu]^{2-}$. We are focusing at present on ligand design to improve oxidative stability. Nevertheless, $[(L1)Cu]^{2-}$ is the most oxidatively rugged Cu-based WOC reported to date, as judged electrochemically by the charge under the III/II redox wave before and after the electrocatalytic wave (see SI). The fastest Cu-based WOC complex reported, $[(bpy)Cu(OH)_2]$, works under an overpotential of 750 mV at pH 12.5 (see entry

Table 1. Kinetic and Electrochemical Data of Complexes $[(LY)Cu]^{2-}$ (Y = 1−4) and Related Cu Complexes Described in the Literature That Have Been Reported To Act as Water Oxidation Catalysts.

Ent.[a]	Catalyst[b]	pH	η, mV[c]	k_{obs},s^{-1}[d]
1[tw]	$[(L1)Cu]^{2-}$	11.5	700	3.56[e]
2[tw]	$[(L2)Cu]^{2-}$	11.5	400	3.58
3[tw]	$[(L3)Cu]^{2-}$	11.5	270	0.43
4[tw]	$[(L4)Cu]^{2-}$	11.5	170	0.16
5[14c]	$[(Py_3P)Cu(OH)]^{-}$	8.0	~500	20
6[14g]	$[(dhbp)Cu(OH_2)_2]$	12.4	~540	0.4
7[14a]	$[(bpy)Cu(OH)_2]$	12.5	750	100
8[14d]	$[Cu_2(BPMAN)(\mu\text{-}OH)]^{3+}$	7.0	~1050	0.6

[a]tw = this work. [b]Py_3P = N,N-bis(2-(2-pyridyl)ethyl)pyridine-2,6- dicarboxamidate; dhbp = 6,6'-dihydroxy-2,2'-bpy; bpy = 2,2'-bpy; bpman = 2,7-[bis(2-pyridylmethyl)aminomethyl]-1,8-naphthyridine. [c]Measured by DPV for entries 1−4 and 8 and from the initial foot of the electrocatalytic wave or the half-peak potential for CVs for the rest. [d]Measured by FOWA in complexes $[(LY)Cu]^{2-}$ and other methodologies for the other complexes. [e]k_{obs} = 11.96 s^{-1} at pH 12.5.

8, Table 1), whereas the complex $[(Py_3P)Cu(OH)]^{-}$ (entry 5, Table 1) has been reported to work at pH 8.0 with a rate constant of 20 s^{-1} and an overpotential of approximately 500 mV. Finally, a dinuclear complex, $[Cu_2(BPMAN)(\mu\text{-}OH)]^{3+}$ (entry 8, Table 1), has been reported that works at pH 7, is relatively slow, 0.6 s^{-1}, and works under an overpotential of 1050 mV. Clearly, more molecular Cu-based WOCs are needed in order to understand the factors that allow us to rationally build fast complexes with oxidatively rugged ligands that work ideally at pH 7 and with low overpotentials.

A.3. Conclusions

In conclusion, we have prepared a family of Cu complexes that are capable of oxidizing water to dioxygen and whose rate determining step involves the redox activity of the ligand. Further fine-tuning of the ligand backbone allows reducing the overpotential for water oxidation in this

family of complexes by more than 500 mV, all the way to a record low overpotential of 170 mV. In addition, DFT analysis puts forward an unprecedented pathway where the O−O bond formation occurs in a two-step, one-electron processes and where the peroxo intermediate generated has no formal M−O bond, in sharp contrast with the previous mechanism described in the literature.[11] The interplay between electrons being removed from the metal and/or the ligands opens up new avenues for molecular water oxidation catalyst design. We are at present focusing our attention on developing further families of molecular water oxidation catalysts based on redox noninnocent and oxidatively rugged ligands.

A.4. Acknowledgments

We thank MINECO (CTQ2014-57761-R, CTQ-2013-49075- R, SEV-2013-0319, CTQ2014-52974-REDC), the ICIQ Foundation, and the EU COST actions CM1202 and CM1205. I.F.-A. also thanks the Severo Ochoa pre-doctoral training fellowship (Ref: SVP-2014-068662). P.G.-B. thanks "La Caixa" Foundation for a Ph.D. grant.

A.5. References

1 Berardi, S.; Drouet, S.; Francas, L.; Gimbert-Surinach, C.; Guttentag, M.; Richmond, C.; Stoll, T.; Llobet, A.*Chem. Soc. Rev.* **2014**, *43*, 7501-7519

2 a) Melis, A. *Energy Environ. Sci.* **2012**, *5*, 5531-5539. b) Alstrum-Acevedo, J. H.; Brennaman, M. K.; Meyer, T. J. *Inorg. Chem.* **2005**, *44*, 6802-6827. c) Nocera, D. G. *Acc. Chem. Res.* **2012**, *45*, 767-776.

3 Cox, N.; Pantazis, D. A.; Neese, F.; Lubitz, W. *Acc. Chem. Res.* 2013, *46*, 1588-1596.

4 a) Zhou, J.; Xi, W.; Hurst, J. K. *Inorg. Chem.* **1990**, *29*, 160-167. b) Radaram, B.; Ivie, J. A.; Singh, W. M.; Grudzien, R. M.; Reibenspies, J. H.; Webster, C. E.; Zhao, X. *Inorg. Chem.* **2011**, *50*, 10564-15071. c) Hong, D.; Mandal, S.; Yamada, Y.; Lee, Y.-M.; Nam, W.; Llobet, A.; Fukuzumi, S. *Inorg. Chem.* **2013**, *52*, 9522-9531.

5 a) Wang, D.; Ghirlanda, G.; Allen, J. P. *J. Am. Chem. Soc.* **2014**, *136*, 10198-10201. b) Karlsson, E. A.; Lee, B.-L.; Åkermark, T.; Johnston, E. V.; Kärkäs, M. D.; Sun, J.; Hansson, Ö.; Bäckvall, J.-E.; Åkermark, B. *Angew. Chem., Int. Ed.* **2011**, *50*, 11715-11718. c) Crabtree, R. H. *Chem. Rev.* **2015**, *115*, 127-150.

6 a) Muckerman, J. T.; Polyansky, D. E.; Wada, T.; Tanaka, K.; Fujita, E. *Inorg. Chem.* **2008**, *47*, 1787-1802. b) Boyer, J. L.; Rochford, J.; Tsai, M.-K.; Muckerman, J. T.; Fujita, E. *Coord. Chem. Rev.* **2010**, *254*, 309-330.

7 a) Chirik, P. J.; Wieghardt, K. *Science* **2010**, *327*, 794-795. b) Choudhuri, M. M. R.; Kaim, W.; Sarkar, B.; Crutchley, R. J. *Inorg. Chem.* **2013**, *52*, 11060-11066.

8 a) Ruiz, R.; Surville-Barland, C.; Aukauloo, A.; Anxolabehere-Mallart, E.; Journaux, Y.; Cano, J.; Carmen Munoz, M. J. Chem. Soc., *Dalton Trans.* **1997**, 745-751. b) Fu, L.-Z.; Fang, T.; Zhou, L.-L.; Zhan, S.-Z. *RSC Adv.* **2014**, *4*, 53674-53680.

9 Ottenwaelder, X.; Aukauloo, A.; Journaux, Y.; Carrasco, R.; Cano, J.; Cervera, B.; Castro, I.; Curreli, S.; Munoz, M. C.; Rosello, A. L.; Soto, B.; Ruiz-Garcia, R. *Dalton Trans.* **2005**, 2516-2526.

10 Costentin, C.; Drouet, S.; Robert, M.; Savéant, J.-M. *J. Am. Chem. Soc.* **2012**, *134*, 11235-11242.

11 Sala, X.; Maji, S.; Bofill, R.; García-Antón, J.; Escriche, L.; Llobet, A. *Acc. Chem. Res.* **2014**, *47*, 504-516.

12 Bichler, B.; Glatz, M.; Stoger, B.; Mereiter, K.; Veiros, L. F.; Kirchner, K. *Dalton Trans.* **2014**, *43*, 14517-14519

13 a) Ellis, W. C.; McDaniel, N. D.; Bernhard, S.; Collins, T. J. *J. Am. Chem. Soc.* 2010, *132*, 10990-10991. b) Liao, R.-Z; Li, X.-C.; Siegbahn, P. E. M.Eur. J. *Inorg. Chem.* **2014**, 728-741.

14 a) Barnett, S. M.; Goldberg, K. I.; Mayer, J. M. *Nat. Chem.* **2012**, *4*, 498-502. b) Zhang, M.-T.; Chen, Z.; Kang, P.; Meyer, T. J. *J. Am. Chem. Soc.* 2013, *135*, 2048-2051. c) Coggins, M. K.; Zhang, M.-T.; Chen, Z.; Song, N.; Meyer, T. J. *Angew. Chem., Int. Ed.* **2014**, *53*, 12226-12230. d) Su, X.-J.; Gao, M.; Jiao, L.; Liao, R.-Z.; Siegbahn, P. E. M.; Cheng, J.-P.; Zhang, M.-T. *Angew. Chem., Int. Ed.* **2015**, *54*, 4909-4914. e) Pap, J. S.; Szyrwiel, L.; Sranko, D.; Kerner, Z.; Setner, B.; Szewczuk, Z.; Malinka, W. *Chem. Commun.* **2015**, *51*, 6322-6324. f) Gerlach, D. L.; Bhagan, S.; Cruce, A. A.; Burks, D. B.; Nieto, I.; Truong, H. T.; Kelley, S. P.; Herbst-Gervasoni, C. J.; Jernigan, K. L.; Bowman, M. K.; Pan, S.; Zeller, M.; Papish, E. T. *Inorg. Chem.* **2014**, *53*, 12689-12698. g) Zhang, T.; Wang, C.; Liu, S.; Wang, J.-L.; Lin, W. *J. Am. Chem. Soc.* **2014**, *136*, 273-281.

A.6. Supporting Information

Experimental Section

Materials

The chemicals used in this work have been purchased to Sigma Aldrich Chemical Co. No further purification has been done. The used solvents were HPLC grade. High purity deionized water was obtained by passing distilled water through a nanopore Milli-Q water purification system. Aqueous basic buffer solutions at several pH values were prepared using specific concentrations of dibasic and tribasic phosphate salts such that the final ionic strength was 0.1 M.

Elemental Analysis and Mass Spectrometry

Elemental Analysis of the samples was carried out in a Thermo Finnigan elemental analyzer Flash 1112 model.

Nominal mass analyses were performed in Electrospray mode with a LCT Premier mass spectrometer (TOF analyser, Micromass-Waters) in methanol by direct injection.

Spectroscopic Techniques

NMR spectroscopy was carried out in a 400 MHz Bruker Advance II spectrometer and a Bruker Advance 500 MHz. All the measurements were done at room temperature in deuterated DMSO using residual protons as internal references.

UV-vis spectra were obtained using a Cary 50 (Varian) UV-vis spectrophotometer with 1 cm and 2 mm quartz cuvettes in basic solution (pH 11.5, phosphate buffer 0.1 M of ionic strength) with a complex concentration of 1 mM.

Electrochemistry

Cyclic voltammetry, linear sweep voltammetry and differential pulse voltammetry experiment were carried out on an IJ-Cambria CHI-660 potentiostat. Solutions of the complexes were placed in one-compartment three-electrode cells. Glassy Carbon (GC) or BDD (Boron Doped Diamond) disk electrodes (3 mm of diameter in both cases) were used as working electrodes, Mercury/Mercurous sulfate (K_2SO_4 sat) as reference electrode (unless explicity mentioned) and Pt wire as counter electrode. Working electrode pretreatment before each measurement consisted in polishing with 0.05 μm alumina paste, rinsing after with water and acetone and blow-dried finally. All redox potentials in the present work are reported versus NHE by adding 0.65 V to the measured potential.

CVs and LSVs were collected at 100 mV·s-1except other specification. DPV were obtained with the following parameters: amplitude= 50 mV, step height=4 mV, pulse width= 0.05 s, pulse period= 0.5 s and sampling width= 0.0167 s. $E_{1/2}$ values for the redox processes studied in this work are estimated according to the potential at the I_{max} in DPV measurements. Both kind of measurement were done applying IR compensation.

When acetonitrile was used as organic solvent, tetrabutylammonium hexafluorophosphate ($[NBu_4]PF_6$) was added in a concentration of 0.1M to act as supporting electrolyte.

O2 evolution experiment

Controlled Potential Electrolysis (CPE) experiments were performed at different potentials to catalyze the water oxidation by the reported catalysts using a two-compartment cell closed with septum. As working electrode large surface glassy carbon (spongy shape), BDD and ITO (rectangular shape with 2.5 cm^2 surface) electrodes were used together with a silver/silver chloride (KCl sat) as reference electrode. These ones were

placed in one of the compartment that was filled with a 2 mM basic solution of the catalyst (pH 11.5, phosphate buffer 0.1 M of ionic strength). In the other compartment, containing only the buffer solution, a mesh platinum counter electrode was used.

The oxygen evolution was monitored with an OXNP type Clark electrode in gas phase (from Unisense Company). The CPE was carried out using an IJ-Cambria CHI-660 potentiostat and was started as soon as the Oxygen sensor signal was stable under air atmosphere. During the experiment, solutions both compartments were vigorously stirred. Calibration of the oxygen sensor was performed after each experiment by adding known amount of pure oxygen into the cell using a Hamilton syringe. The results of the water oxidation catalysis with copper complexes were compared with blank experiment in the same conditions but in the absence of catalyst. The Faraday efficiency was determined according to the total charge passed during the CPE and the total amount of generated oxygen by taking into account that water oxidation is a 4 oxidations process.

ITO electrodes were purchased from Delta Technologies, Limited. Specs: Corning® alkaline earth boro-aluminosilicate glass, 50x75x1.1 mm, indium tin oxide coated one surface, Rs= 4-10 ohms, cut edges. They were cut to the appropriate size, pretreated by sonication in isopropanol and acetone (15 min with each one) and blow-dried. After each CPE experiment, the working electrodes were rinsed with water and placed in fresh buffer solution to perform CV measurements. That way, we are able to observe the formation of electroactive species when comparing these results with the CVs of these electrodes previous to the CPE experiment.

Spectroelectrochemistry

Spectroelectrochemical study was carried out in an optically transparent thin-layer electrochemical (OTTLE) cell (OMNI-CELL SPECAC, by Prof. Frantisek Hartl's group, University of Reading). This cell contains

two Pt grid electrodes (working and counter) and a silver wire pseudo reference electrode (-0.2 V respect to NHE). This cell is filled with less than 0.3 ml of a 4 mM catalyst solution in phosphate buffer at pH 11.5 (0.1 M of ionic strength) avoiding gas bubbles formation within the thin layer. The optical path length is about 0.2 mm.

The OTTLE cell was placed in a Cary 50 (Varian) UV-vis spectrophotometer and the electrodes were connected to an IJ-Cambria CHI-660 potentiostat. Then, a cyclic voltammetry was performed at 2 $mV \cdot s^{-1}$ in order to allow enough time for the redox processes to take paced in all the solution volume and UV-vis spectra were recorded continuously to monitor the changes in the electronic structure.

Synthesis of H_4LY

The four ligands used in this work were prepared with a procedure similar the previously reported one[1,2]: 0.6 mmol of the corresponding o-phenylenediamine precursor (o-phenylenediamine for L1; 4,5-dimethyl-1,2-phenylenediamine for L2; 4-methoxy-o-phenylenediamine dihydrochloride for L3; 4,5-dimethoxy-o-phenylenediamine dihydrochloride for L4) were dissolved in 3 ml of THF and 0.136 ml of ethyl chlorooxoacetate (1.2 mmol) were added dropwise. This mixture was refluxed during 1 h and the appearing solid waste was removed by filtration. Then, the resulting solution was evaporated until we got an oil product and distilled water was added slowly that led to the formation of a powdery solid consisting of the diethyl ester precursor. It was filtered, rinsed with water and dried to further solubilize it (0.46 mmol) in 2.3 ml of methanol. Afterward, 0.12 ml of a 40% wt. solution of methylamine in water was added and the mixture was heated to 70 ºC for 1 h. The appearing solid consist of the corresponding ligand H_4LY, and was filtered, washed with methanol and ether and dried under vacuum.

H_4L1

Yield: 145.25 mg, 0.522 mmol, 87%. ^{1}H-NMR (DMSO-d6): δ [ppm]= 10.46 (H-NPh, s, 2H), 8.96 (H-NMe, q, J= 4.8 Hz, 2H), 7.60 (H-2, dd, J= 6, 3.6 Hz , 2H), 7.28 (H-1, dd, J= 6, 3.6 Hz, 2H) and 2.73 (H-6, d, J= 4.8 Hz, 6 H). All the NMR assignments are keyed in the Scheme S1 shown below.

H_4L2

Yield: 156.16 mg, 0.510mmol, 85%. Elemental Analysis calc.(%) for $C_{14}H_{18}N_4O_4$: C 54.89, H 5.92, N 18.29, found (%): C 55.00, H 6.09, N 17.80. ESI-MS (MeOH) m/z (negative mode): 305.1 [H_4L2-H]-,327.1 [H_4L2-2H+Na]-. ^{1}H-NMR (DMSO-d6): δ [ppm]= 10.31 (H-NPh, s, 2 H), 8.91 (H-NMe, q, J= 4.5 Hz, 2 H), 7.34 (H-2, s, 2 H), 2.73 (H-6, d, J= 5 Hz, 6 H) and 2.20 (H-7, s, 6 H). ^{13}C-NMR (DMSO-d6): δ [ppm]= 160.59 (C-5, 2C), 158.98 (C-4, 2 C), 134.72 (C-1, 2 C), 127.85 (C-3, 2 C), 126.50 (C-2, 2 C), 26.52 (C-6, 2 C) and 19.53 (C-7, 2 C).

H_4L3

Yield: 125.45 mg, 0.407 mmol,68%. Elemental Analysis calc.(%) for $C_{13}H_{16}N_4O_5$: C 50.65, H 5.23, N 18.17, found (%): C 50.72, H 5.40, N 17.84. ESI-MS (MeOH) m/z (negative mode): 307.1 [H_4L3-H]-, 329.1 [H_4L3-2H+Na]-. ^{1}H-NMR (DMSO-d6) :δ [ppm]= 10.39 (H-NPh, s, 1 H), 10.34 (H-N'Ph, s, 1 H), 8.98 (H-N'Me, q, J= 4.5 Hz, 1 H), 8.91 (H-NMe, q, J= 4.5 Hz, 1 H), 7.42 (H-2, d, J= 8.5 Hz, 1 H), 7.27 (H-1', d, J= 3 Hz, 1 H), 6.86 (H-2',dd, J= 9, 3 Hz, 1 H), 3.75(H-7, s, 3 H), 2.73 (H-6, d, J= 4.5 Hz, 3 H) and 2.72 (H-6', d, J= 4.5 Hz, 3 H). ^{13}C-NMR (DMSO-d6): δ [ppm]= 160.60 (C-5, 1 C), 160.45 (C-5', 1 C), 159.28 (C-4, 1 C), 158.87 (C-4', 1 C), 157.66 (C-1, 1 C), 131.84 (C-3, 1 C), 127.37 (C-2, 1 C), 122.71 (C-3', 1 C), 111.76 (C-2', 1 C), 110.47 (C-1', 1 C), 55.86 (C-7, 1 C), 26.55 (C-6, 1 C) and 26.49 (C-6', 1 C)

H_4L4

Yield: 130.20 mg, 0.385mmol, 64%. Elemental Analysis calc.(%) for $C_{14}H_{18}N_4O_6$: C 49.70, H 5.36, N 16.56, found (%): C 50.00, H 5.45, N 16.24. ESI-MS (MeOH) m/z (negative mode): 337.2 [H_4L3-H]-,359.1 [H_4L4-2H+Na]-. ^{1}H-NMR (DMSO-d6): δ [ppm]= 10.31 (H-NPh, s, 2 H), 8.93 (H-NMe, q, J= 4.5 Hz, 2 H), 7.19 (H-2, s, J=, 2 H), 3.73 (H-7, s, 6 H) and 2.73 (H-6, d, J= 4 Hz, 6 H). ^{13}C-NMR (DMSO-d6): δ [ppm]= 160.60 (C-5, 2 C), 158.93 (C-4, 2 C),146.93 (C-1, 2 C), 123.20 (C-3, 2 C), 109.48 (C-2, 2 C), 56.21 (C-7, 2 C), and 26.52 (C-6, 2 C).

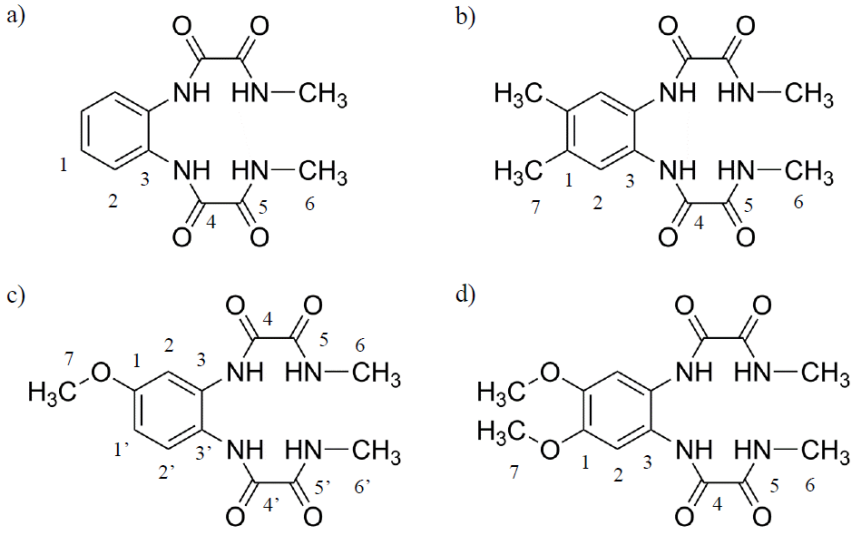

Scheme S1. Representation of the four ligand used in this work: (a) L1, (b) L2, (c) L3 and (d) L4. Numbers represent magnetically non-equivalent carbon atoms.

III

Synthesis of [(LY)Cu](NMe$_4$)$_2$

The copper complexes here analyzed have been synthesized according to the same reference aforementioned[1,2] : 0.4 mmol of the corresponding ligand was suspended in methanol (8 mL) and the mixture was sonicated for 15 min. Afterward, 0.84 ml of a tetramethylammonium hydroxide (25% wt. methanolic solution, 2 mmol) were added and all the reacting volume was heated at 70 ºC with vigorous stirring. After about 30 min all the ligand was completely dissolved and copper(II) perchlorate hexahydrate was added dropwise in a methanolic solution (0.4 mmol in 4 mL). The appearing precipitate (tetramethylammonium perchlorate) was filtered of and the solution was concentrated down to about 1 ml. Then, by adding 1 ml of acetonitrile the remaining waste precipitates again. After removing it by filtration, the copper complex ([(LY)Cu](NMe$_4$)$_2$) was precipitated using equal volume of ether and acetone. This product was filtered, washed with acetone and ether, and dried under vacuum.

[(L1)Cu](NMe$_4$)$_2$

Yield: 188.49 mg, 0.388 mmol, 97%. Elemental Analysis calc. (%) for $C_{20}H_{34}CuN_6O_4 \cdot 2.5H_2O$: C 45.23, H 7.40, N 15.82, found (%): C 45.69, H 7.79, N 15.33. ESI-MS (MeOH) m/z (negative mode): 338.0 [(L1)Cu+H]$^-$, 323.0 [(L1)Cu-Me+H]$^-$, 360.0 [(L1)Cu+Na]$^-$, 406.0 [(L1)Cu+2·H$_2$O+MeOH+H]$^-$.

[(L2)Cu](NMe$_4$)$_2$

Yield: 178.91 mg, 0.348 mmol, 87%. Elemental Analysis calc.(%) for $C_{22}H_{38}CuN_6O_4 \cdot 0.5H_2O$: C 50.51, H 7.51, N 16.06, found (%): C 50.80, H 7.85, N 15.93. ESI-MS (MeOH)m/z (negative mode): 366.0 [(L2)Cu+H]$^-$, 351.0 [(L2)Cu-Me+H]$^-$, 388.0 [(L2)Cu+Na]$^-$, 434.0 [(L2)Cu+2·H$_2$O+MeOH+H]$^-$, 420.0 [(L2)Cu+Na+MeOH]$^-$.

[(L3)Cu](NMe4)2

Yield: 165.16 mg, 0.320 mmol, 80%. Elemental Analysis calc.(%) for$bC_{21}H_{36}CuN_6O_5 \cdot 2.5\ H_2O \cdot 1MeOH$: C 44.55, H 7.65, N 14.17, found (%): C 44.29, H 7.93, N 13.93. ESI-MS (MeOH)m/z (negative mode): 368.0 $[(L3)Cu+H]^-$, 353.0 $[(L3)Cu-Me+H]^-$, 390.0 $[(L3)Cu+Na]^-$, 422.0 $[(L3)Cu+Na+MeOH]^-$.

[(L4)Cu](NMe4)2

Yield: 170.39 mg, 0.312mmol, 78%. Elemental Analysis calc.(%) for $C_{22}H_{38}CuN_6O_6 \cdot 2\ H_2O \cdot 4MeOH$: C 43.96, H 8.23, N 11.83, found (%): C 44.16, H 8.70, N 11.44. ESI-MS (MeOH) m/z (negative mode): 398.0 $[(L4)Cu+H]^-$, 383.0 $[(L4)Cu-Me+H]^-$, 466.0 $[(L2)Cu+2 \cdot H_2O+MeOH+H]^-$.

Spectroscopic Characterization

NMR Spectroscopy

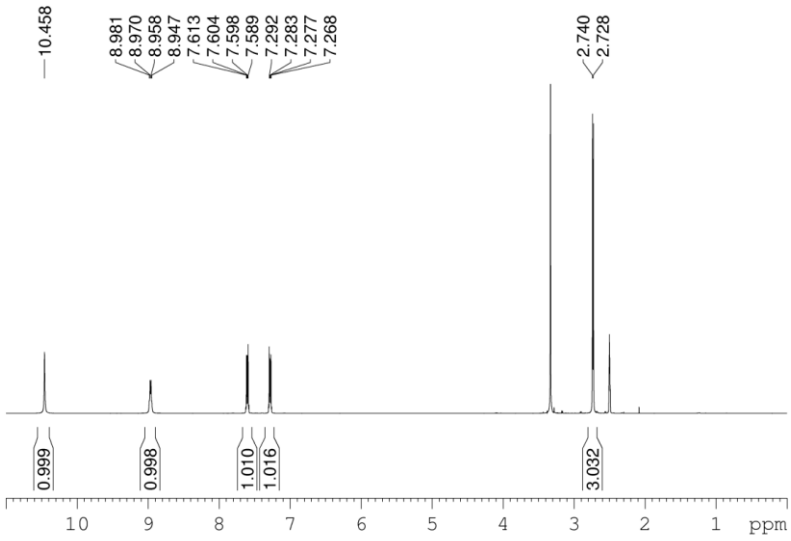

Figure S1. ^{1}H-NMR spectrum of the ligand H_4L1 in d_6-DMSO (400 MHz).

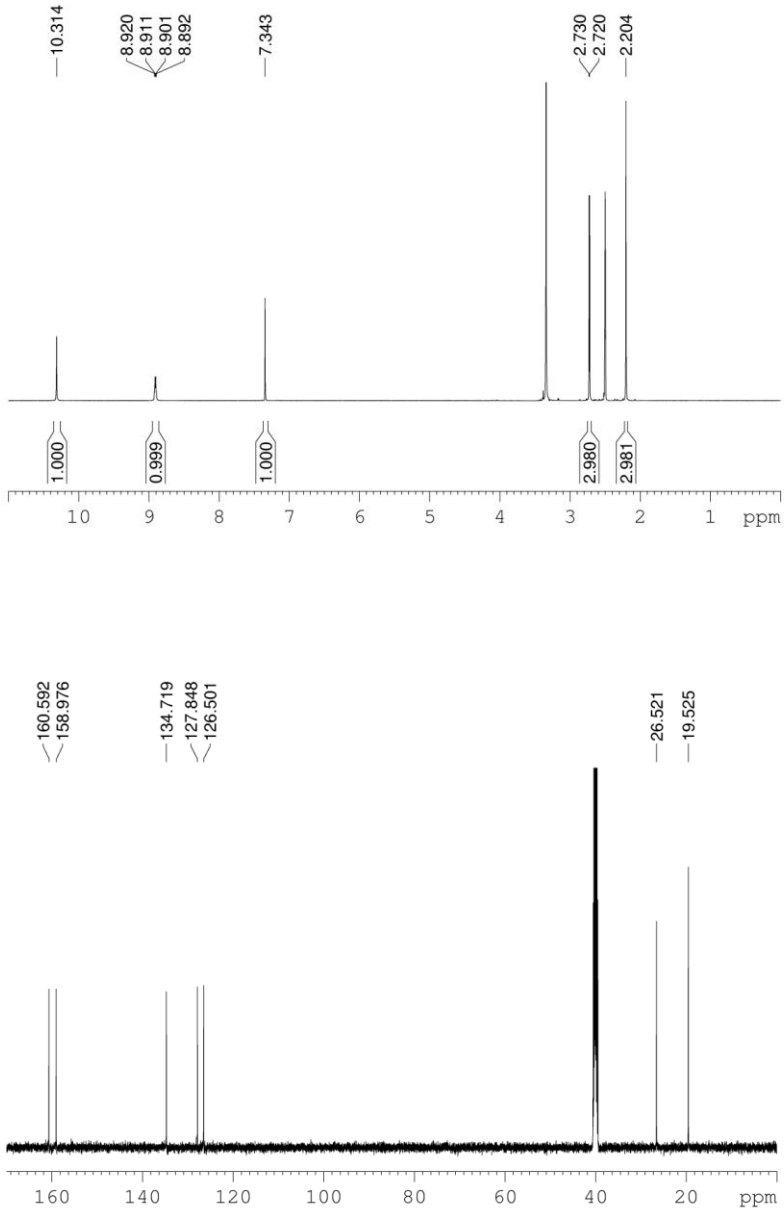

Figure S2. ^{1}H-NMR (500 MHz) (top) and ^{13}C-NMR (500 MHz) (bottom) spectra of the ligand H_4L2 in d_6-DMSO.

III

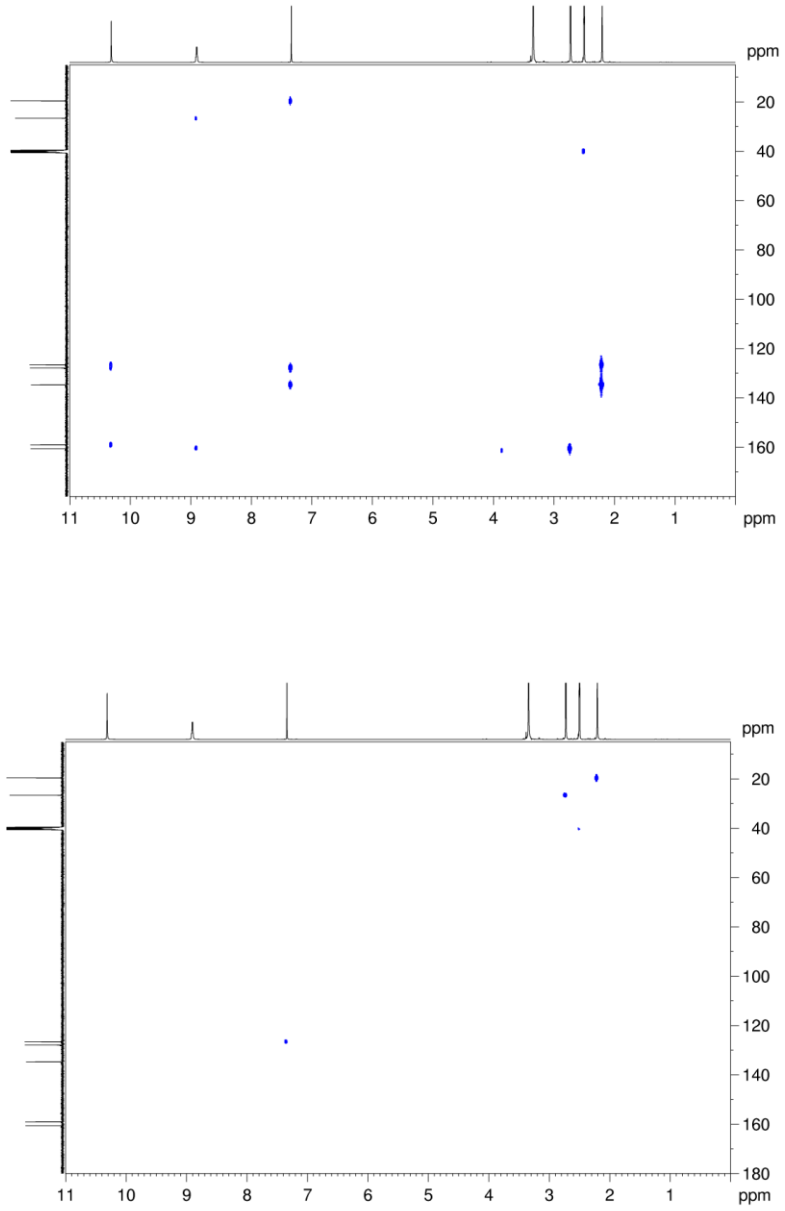

Figure S3. ^{1}H-^{13}C HMBC (500 MHz) (top) and HMQC (500 MHz) (bottom) spectra of the ligand H_4L2 in d_6-DMSO.

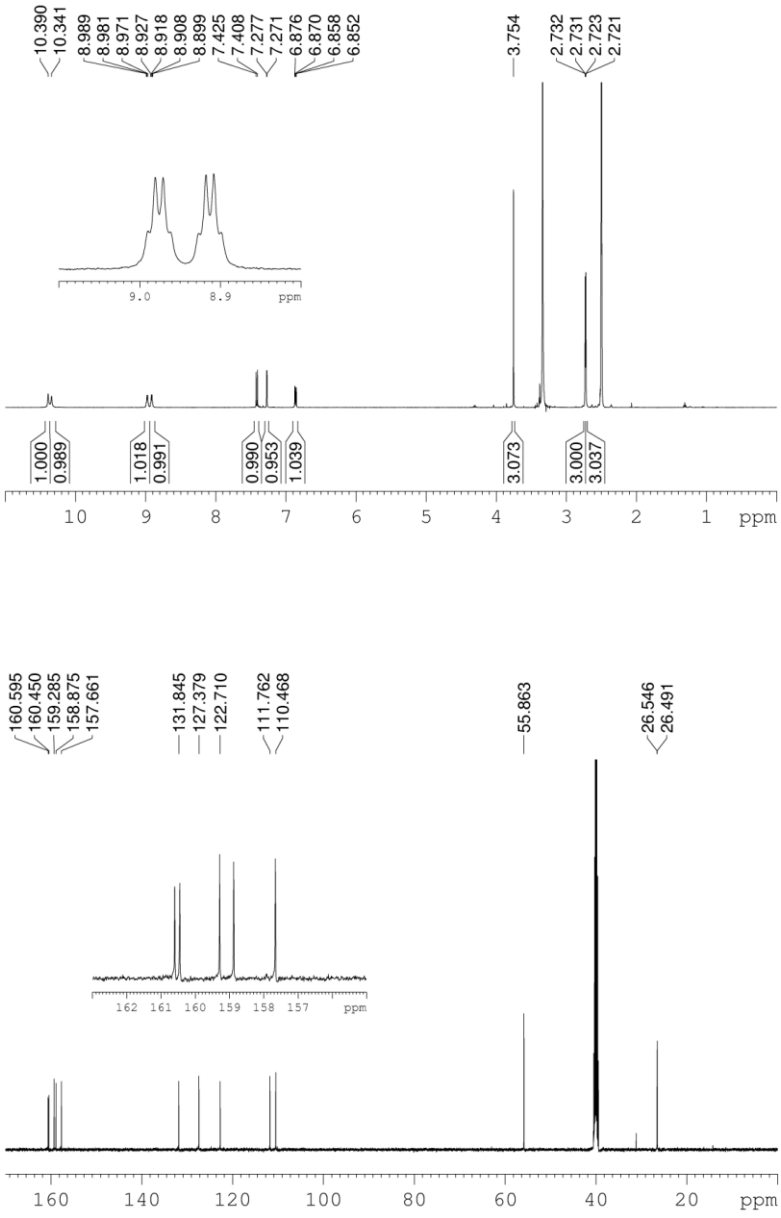

Figure S4. ^{1}H-NMR (500 MHz) (top) and ^{13}C-NMR (500 MHz) (bottom) spectra of the ligand H_4L3 in d_6-DMSO.

III

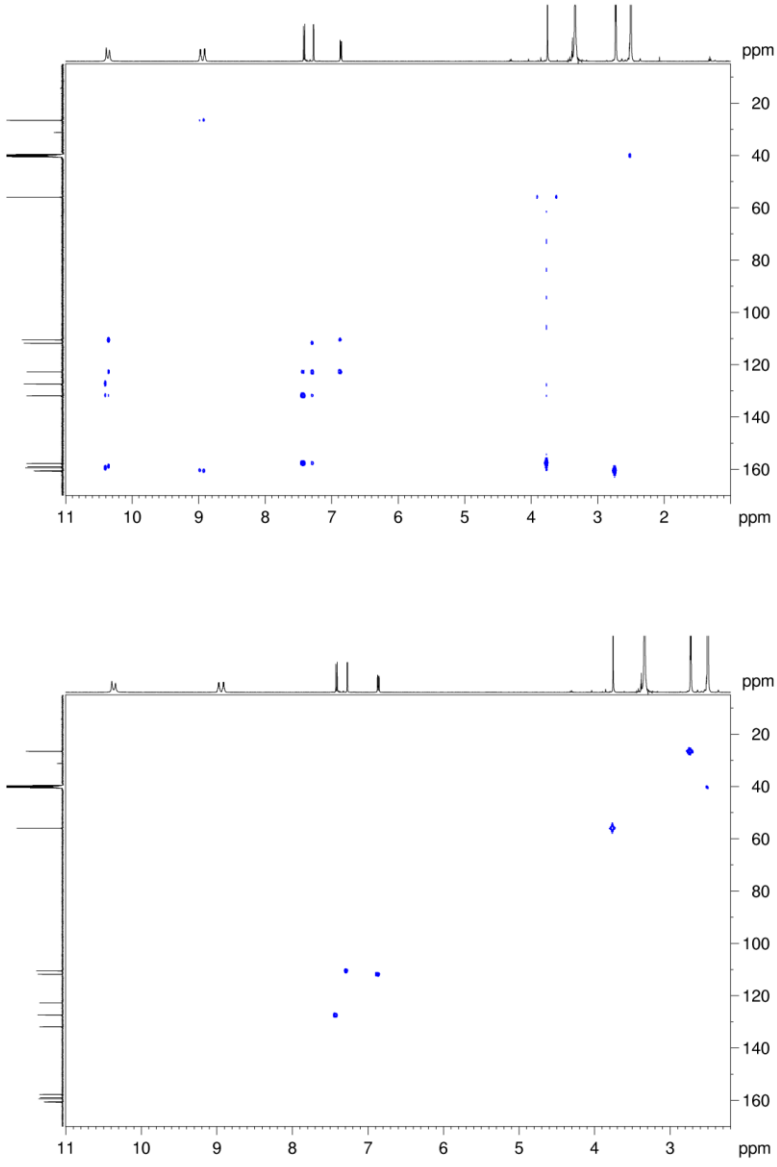

Figure S5. ^{1}H-^{13}C HMBC (500 MHz) (top) and HMQC (500 MHz) (bottom) spectra of the ligand H_4L3 in d_6-DMSO.

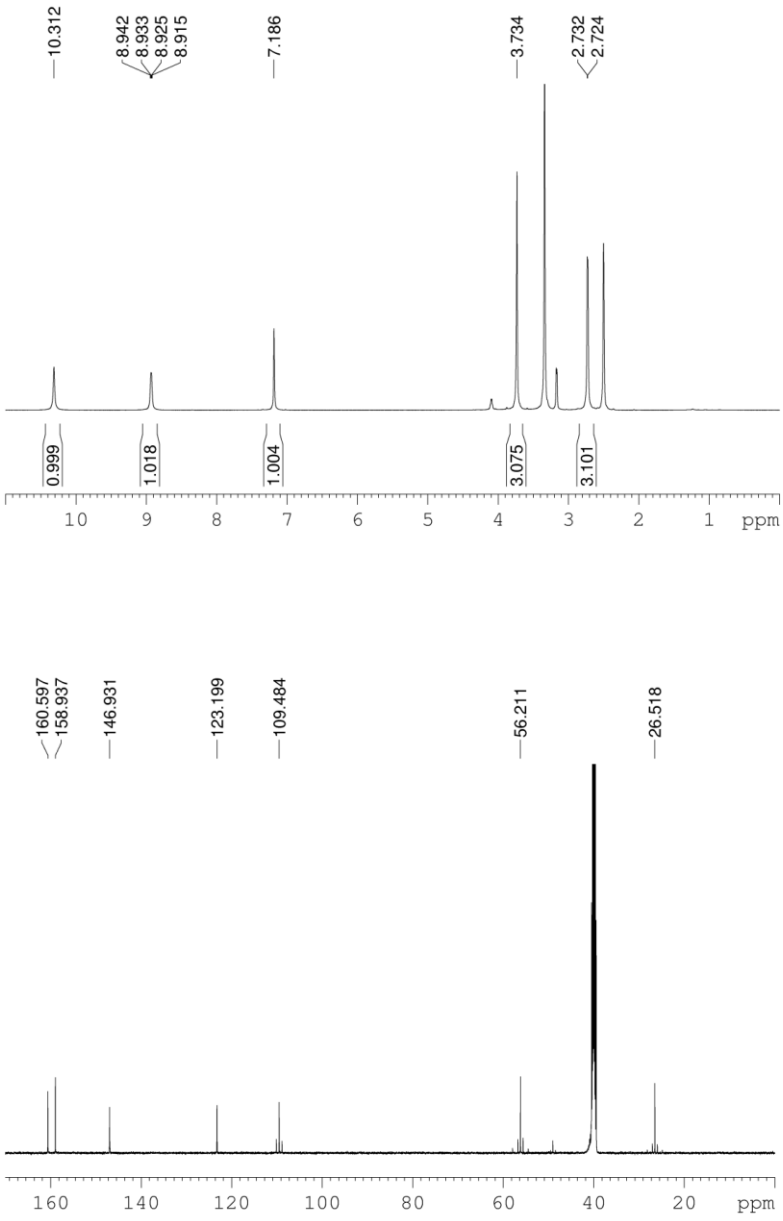

Figure S6. ^{1}H-NMR (500 MHz) (top) and ^{13}C-NMR (500 MHz) (bottom) spectra of the ligand H_4L4 in d_6-DMSO.

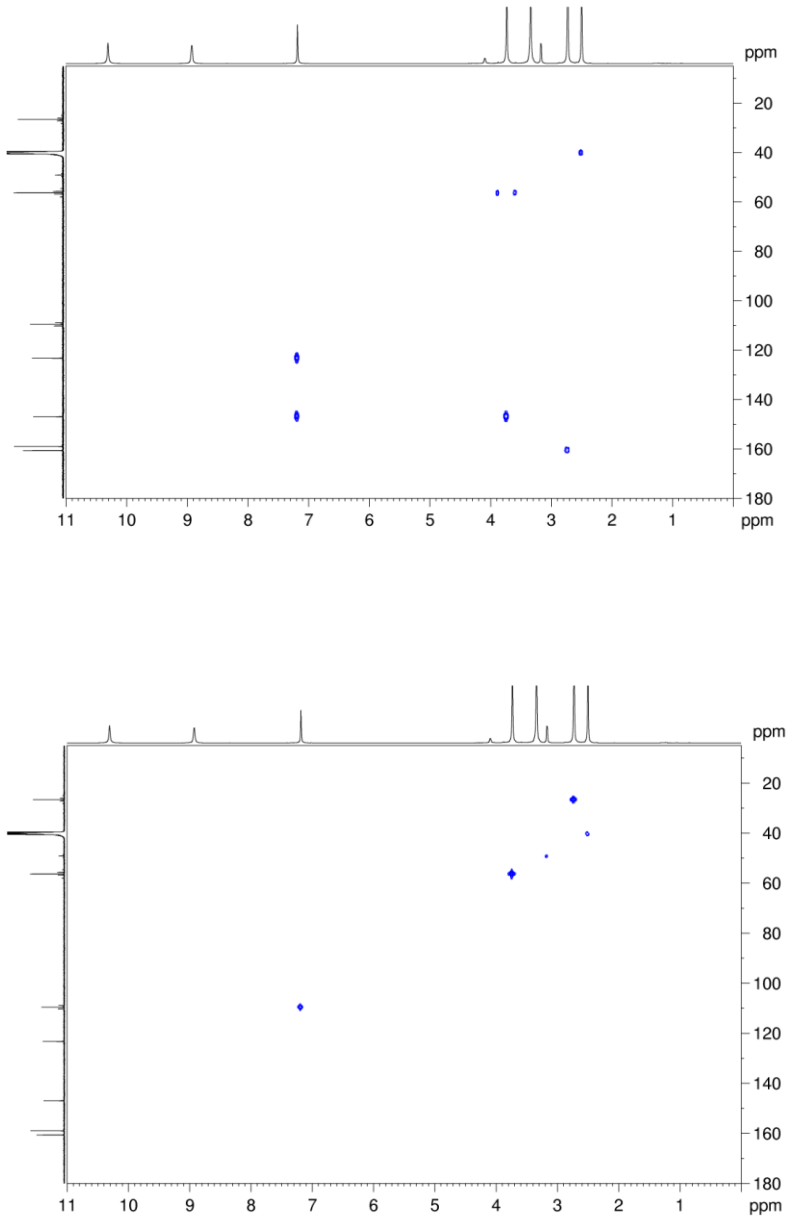

Figure S7. ^{1}H-^{13}C HMBC (500 MHz) (top) and HMQC (500 MHz) (bottom) spectra of the ligand H_4L4 in d_6-DMSO.

UV-vis Spectroscopy

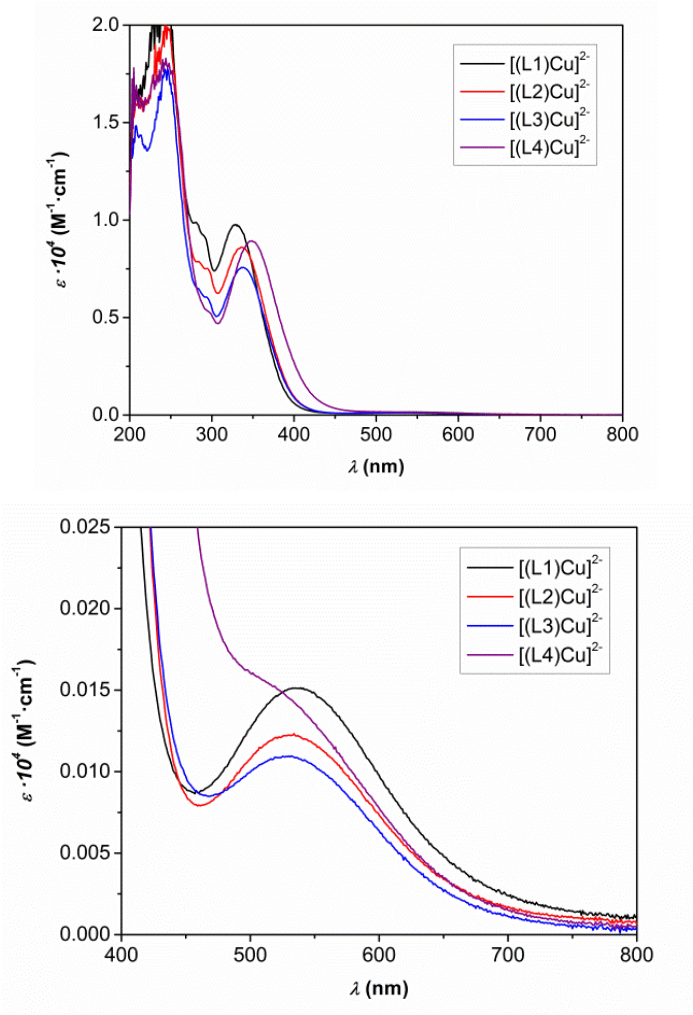

Figure S8. (Left) UV-vis spectra of the four copper complexes recorded in 1mM [cat] basic solution (pH 11.5, phosphate buffer with 0.1 M of ionic strength). (Right) UV-vis spectra enlargement of the visible region for the four copper complexes.

III

X-Ray Crystallography

X-ray Crystal Structure Determination. Crystals of [(L2)Cu](NMe$_4$)$_2$, [(L3)Cu](NMe$_4$)$_2$ and [(L4)Cu](NMe$_4$)$_2$ were obtained by slow diffusion of ether/acetone (1:1) in methanolic solution of the complexes. The measured crystals were prepared under inert conditions immersed in perfluoropolyether as protecting oil for manipulation.

Data collection: Crystal structure determinations for [(L2)Cu](NMe$_4$)$_2$ and [(L4)Cu](NMe$_4$)$_2$ were carried out using a Apex DUO diffractometer equipped with a Kappa 4-axis goniometer, an APEX II 4K CCD area detector, a Microfocus Source E025 IuS using MoKα radiation, Quazar MX multilayer Optics as monochromator and an Oxford Cryosystems low temperature device Cryostream 700 plus (T = -173 ˚C). Crystal structure determination for [(L3)Cu](NMe$_4$)$_2$ was carried out using a Rigakudiffractometer equipped with a Pilatus 200K area detector, a Rigaku MicroMax-007HF microfocus rotating anode with MoKα radiation, Confocal Max Flux optics and an Oxford Cryosystems low temperature device Cryostream 700 plus (T = -173 ˚C). Full-sphere data collection was used with $\omega$and φscans. *Programs used:* Data collection APEX-2[3], data reduction Bruker Saint[4] V/.60A and absorption correction SADABS[5] for L2 and L4 and data collection, data reduction and absorption correction for L3 with CrystalClear[6].

Structure Solution and Refinement: Crystal structure solution was achieved using direct methods as implemented in SHELXTL[7] and visualized using the program XP. Missing atoms were subsequently located from difference Fourier synthesis and added to the atom list. Least-squares refinement on F^2 using all measured intensities was carried out using the program SHELXTL. All non hydrogen atoms were refined including anisotropic displacement parameters.

Comments to the structures: $[(L2)Cu](NMe_4)_2$: The asymmetric unit contains one molecule of the metal complex, two $N(CH_3)_4$cations and two water molecules. This compound crystallized as a two domain crystal (ratio 50:50). The collected data were processed with TWINABS taking in account overlapping reflections (TWINABS to be cited).[8] $[(L3)Cu](NMe_4)_2$. The asymmetric unit contains one molecule of the metal complex, two $N(CH_3)_4$ cations and two water molecules. The main molecule is disordered inverted in two orientations (ratio 65:35). $[(L4)Cu](NMe_4)_2$. The asymmetric unit contains a half molecule of the metal complex, two half $N(CH_3)_4$ cations and highly disordered acetone molecules. The metal complex molecule is disordered in two positions around a mirror plane (ratio 0.5:0.5). Also the half $N(CH_3)_4$ cations are partially disorder around a mirror plane. In order to avoid the highly disordered acetone molecules, which could not be properly refined, the program SQUEEZE was applied to remove them from the electron density (SQUEEZE to be cited).[9]

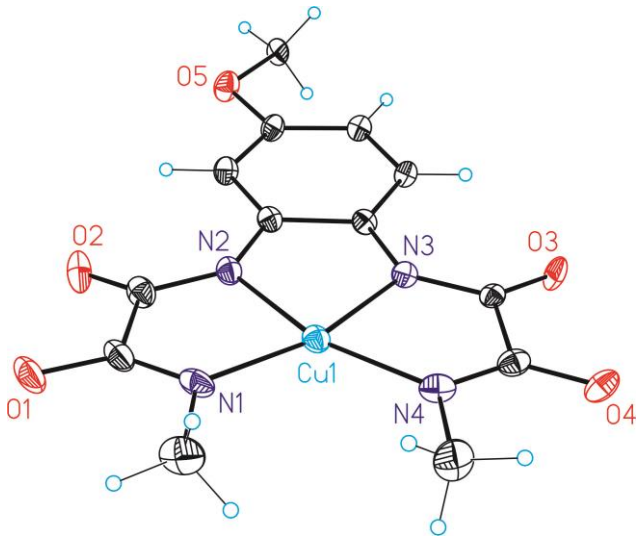

Figure S9. ORTEP drawing (thermal ellipsoids 50 %) of $[(L3)Cu](NMe_4)_2$.

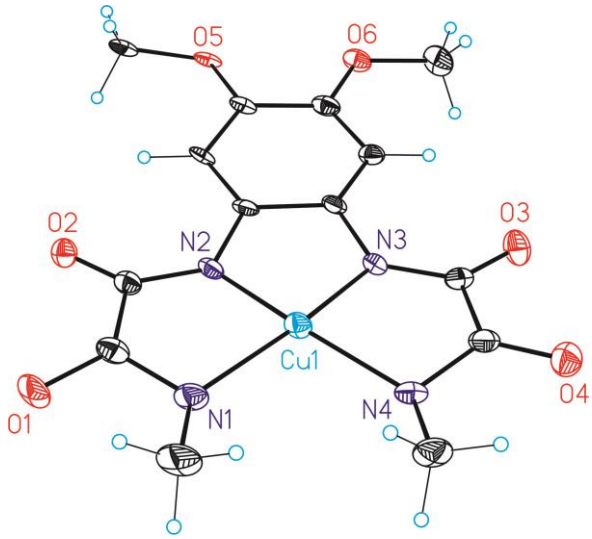

Figure S10. ORTEP drawing (thermal ellipsoids 50 %) of [(L4)Cu](NMe$_4$)$_2$.

Table S1: Crystal data for compounds [(L2)Cu](NMe$_4$)$_2$, [(L3)Cu](NMe$_4$)$_2$ and [(L4)Cu](NMe$_4$)$_2$.

Compound	[(L2)Cu](NMe$_4$)$_2$	[(L3)Cu](NMe$_4$)$_2$	[(L4)Cu](NMe$_4$)$_2$
Formula	$C_{23}H_{46}Cu_1N_6O_7$	$C_{21}H_{40}Cu_1N_6O_7$	$C_{22}H_{38}Cu_1N_6O_6$
Solvents	2 x H_2O	2 x H_2O	Disordered acetone
Formula weight	582.20	552.13	546.12
Crystal size (mm^3)	0.12 x 0.12 x 0.04	0.20 x 0.20 x 0.20	0.30 x 0.10 x 0.02
Crystal color	pink	colorless	orange
Temp (K)	100	100	100
Crystal system	monoclinic	orthorhombic	monoclinic
Space group	$P2_1/c$	*P*bca	$P2_1/m$

A (Å)	22.068(2)	11.9851(19)	13.082(3)
B (Å)	8.1388(7)	16.023(3)	6.8151(16)
C (Å)	15.9847(15)	26.249(4)	19.224(4)
α (deg)	90	90	90
β (deg)	100.7913(17)	90	93.616(7)
γ (deg)	90	90	90
V (Å^3)	2820.2(4)	5040.7(13)	1710.5(6)
Z	4	8	2
ρ (g/cm^3)	1.371	1.455	1.060 (SQUEEZE)
μ (mm^{-1})	0.825	0.919	0.675
θ_{max} (°)	26.44	27.47	26.96
Reflec. measured	51822	25139	15004
Unique reflections	5144 [R_{int}= 0.0607]	4552 [R_{int}= 0.0322]	2734 [R_{int}= 0.0905]
Absorpt. correct.	TWINABS	SADABS	SADABS
Trans. min/max	0.745/0.968	0.645/0.838	0.759/0.987
Parameters/Restrains	381/47	534/435	285/392
R1/wR2 [I>2σ(I)]	0.0556/0.1367	0.0701/0.1342	0.0635/0.1532
R1/wR2 [all data]	0.0650/0.1414	0.0932/0.1421	0.0987/0.1660
Goodness-of-fit (F^2)	1.134	1.321	1.027
Peak/hole (e/Å^3)	1.335/□ 0.703	0.464/□□□ 498	0.861/□ 0.993

Electrochemistry

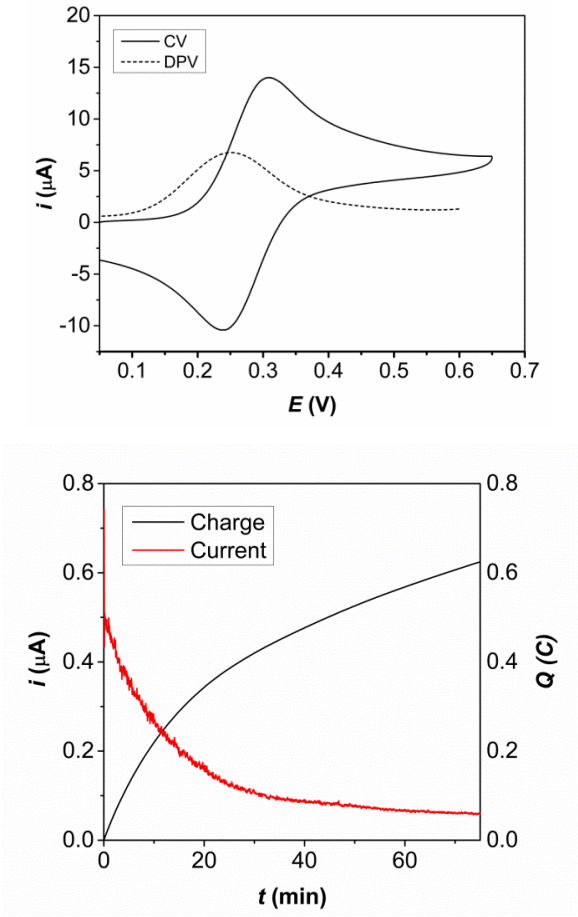

Figure S11. (Left) CV and DPV of 1mM $[(L1)Cu]^{2-}$ in acetonitrile solution containing 0.1 M of tetrabutylammonium hexafluorophosphate. GC working electrode and 100 mV/s of scan rate. (Right) Controlled Potential Electrolysis (CPE) at 0.85 V in 1mM $[(L1)Cu]^{2-}$ aqueous solutions at pH 11.5 containing phosphate buffer with 0.1 M ionic strength. Large surface Pt mesh working electrode was used.

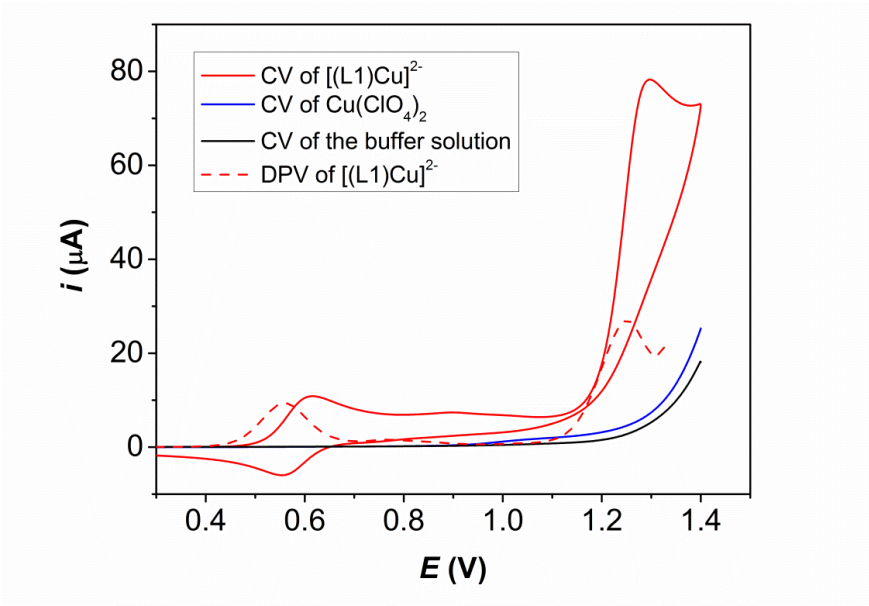

Figure S12. CVs of 1mM $[(L1)Cu]^{2-}$(red) and 1mM $[Cu(ClO_4)_2]$ (blue) in phosphate buffer at pH 11.5 (0.1 M of ionic strength). The black line corresponds to a blank CV. The red dashed line is the DPV of the $[(L1)Cu]^{2-}$ complex. GC working electrode and 100 mV/s of scan rate.

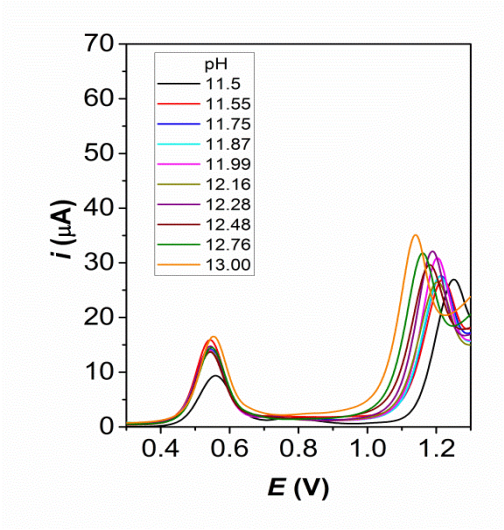

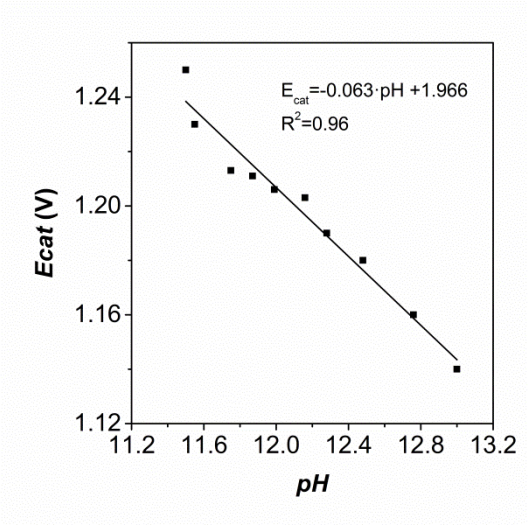

Figure S12. (Left) DPVs of 1mM $[(L1)Cu]^{2-}$ in phosphate buffer at different pH values (0.1 M of ionic strength). (Right) pH dependence of the E_{cat} value from the DPV experiments.

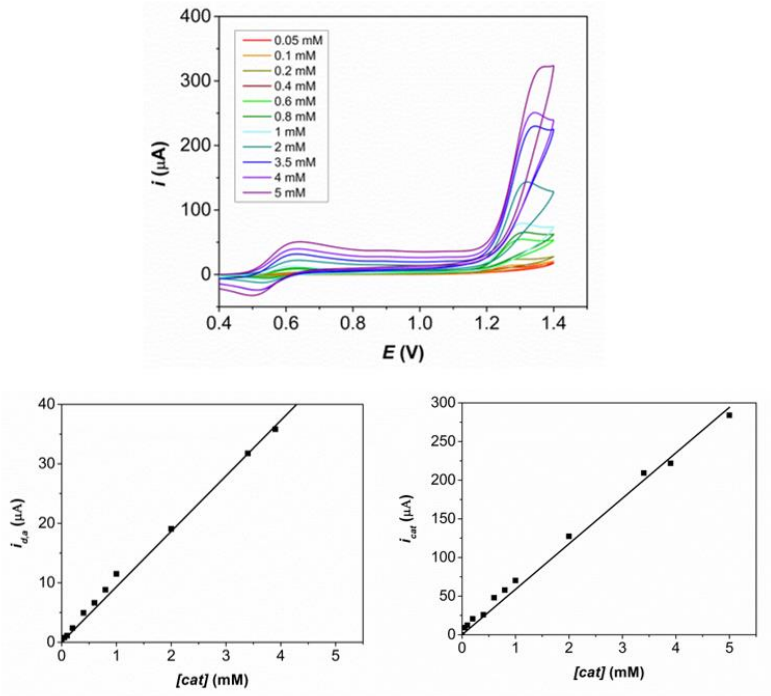

Figure S13. (Top) CVs of aqueous solution at pH 11.5 (phosphate buffer with 0.1 M of ionic strength) containing different concentrations of the complex $[(L1)Cu]^{2-}$. GC working electrode and 100 mV/s of scan rate. (Bottom, left) Anodic peak intensity corresponding to the reversible oxidation Cu^{II}/Cu^{III} (at 0.62 V) is represented versus the concentration of the catalyst. (Bottom, right) Catalytic peak current (maximum intensity of the catalytic wave) is represented versus the concentration of the catalyst.

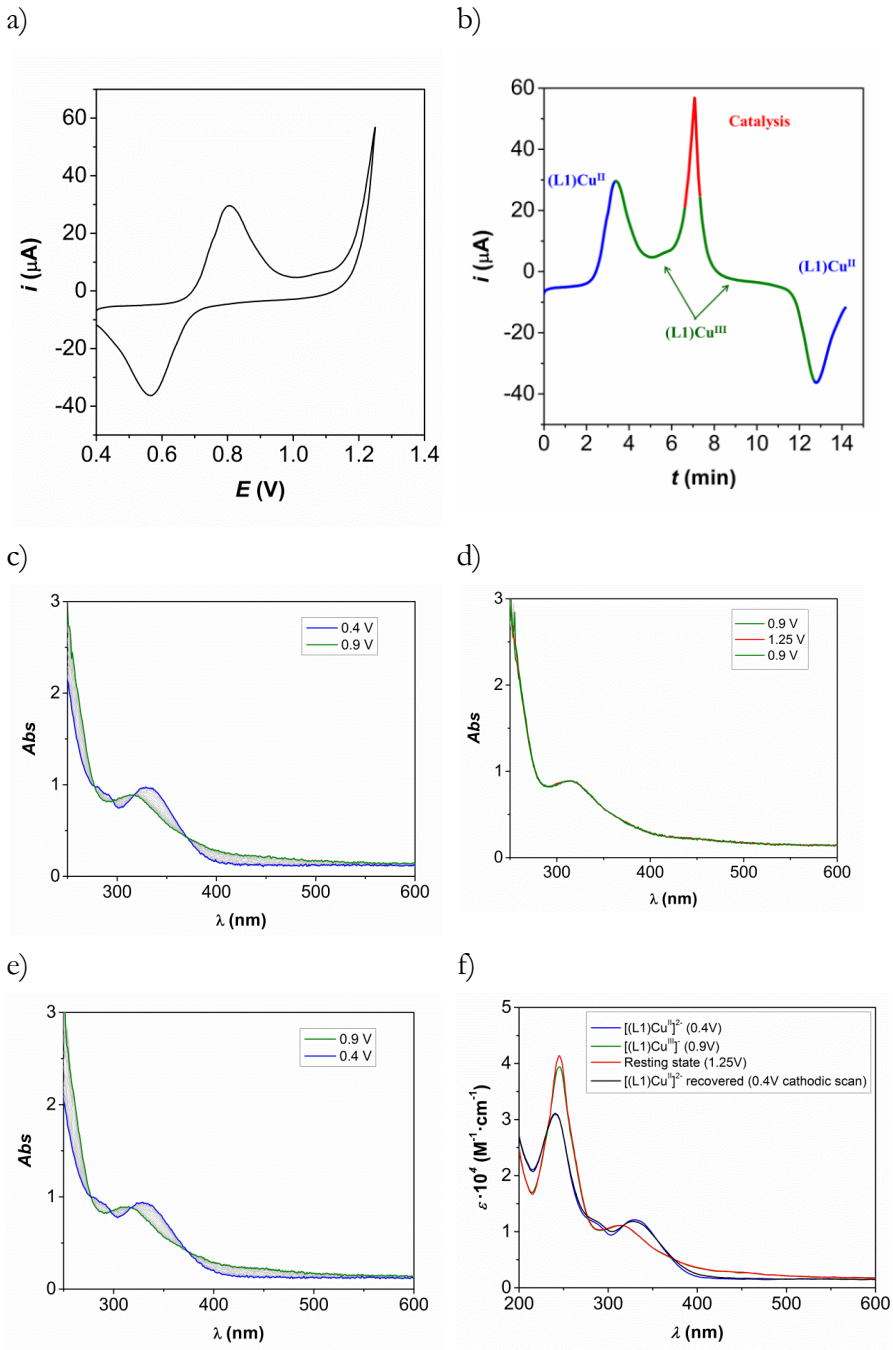

Figure S14. (a) CV performed during the spectroelectrochemistry experiment in an OTTLE type spectroelectrochemical cell at 2 mV/s with Pt mesh working

and counter electrode and a silver wire pseudo reference electrode (-0.2 V respect to NHE). (b) Same CV as in a) represented as *i* vs *t* by transforming potential values into time with the scan rate.

Below they are shown the UV-vis spectra for the $[(L1)Cu]^{2-}$ species recorded at different potentials while performing the CV: (c) 0.4-0.9V (0-5min) (d) 0.9-1.25-0.9V (5-10min) and (e) 0.9-0.4V (10-14min). They were recorded every 10 s. (e) Representative UV-vis spectra for some of the species of the $[(L1)Cu]^{2-}$ catalyst involved in the catalytic cycle.

Moreover, the ratio of ε at 330 nm in the spectra of before and after catalysis is 1.185/1.205=0.9834, basically 100% recovery.

Kinetic analysis by FOWA and TON calculation

Under catalytic conditions the equation below is operative, [10,11,12]

$$\frac{i_{cat}}{i_d} = \frac{n \cdot 2.24 \cdot \sqrt{\frac{R \cdot T}{F \cdot V} \cdot k_{obs}}}{1 + \exp\left[\frac{F}{R \cdot T}(E^0_{cat} - E)\right]}$$

where E^0_{cat} is the standard potential for the catalysis-initiating redox couple (1.25 V calculated from DPV), i_{cat} is the current intensity in the presence of substrate, i_d is the current intensity in the absence of substrate (here we approximate this current to the current associated with the Cu^{III}/Cu^{II} couple), n is the number of electrons involved in the catalytic cycle (4 e^- in water oxidation), F is the faraday constant, v is the scan rate, k_{obs} is defined as "$k_{cat} \cdot C^o_A$" where C^o_A is the concentration of substrate (55.56 M for water), and R is 8.314 $J \cdot mol^{-1}K^{-1}$. Background corrected CVs of catalyst $[(L1)Cu^{II}]^{2-}$ at different scan rates (5 – 100 $mV \cdot s^{-1}$) are shown in Figure 3. Now, k_{obs} can be extracted from the plot of i_{cat}/i_d *vs.* $1/(1+\exp[(F/RT)(E^o_{cat}-E)])$.

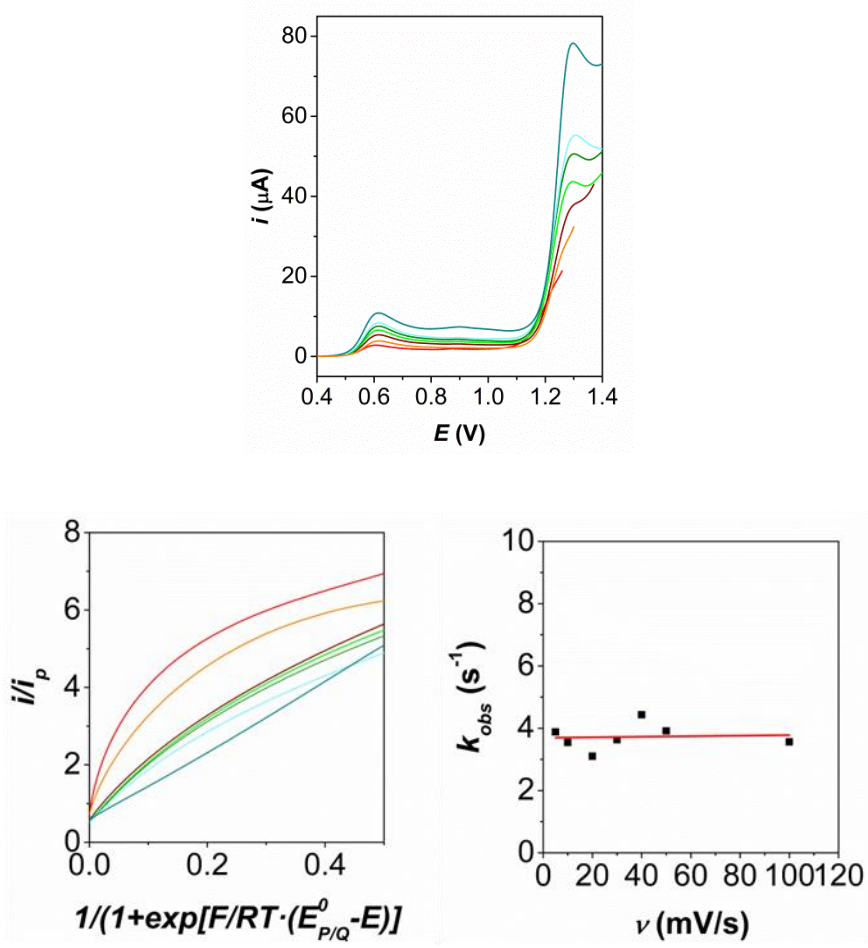

Figure S15. (Top) Background corrected Linear Sweep Voltammetries at pH = 11.5 in similar conditions as in Figure 2 at several scan rates of 5 (red) , 10 (orange), 20 (brown), 30 (green), 40 (dark green), 50 (cyan) and 100 mV/s (turquoise) respectively. (Bottom left) Foot of the wave analysis (FOWA) plotting i_{cat}/i_d *vs.* $1/(1+\exp[(F/RT)(E^o_{cat}-E)])$ at each scan rate (same color code). (Bottom right) Plot of the different k_{cat} values extracted from FOWA at each scan rate. The red line represents the average k_{cat} value.

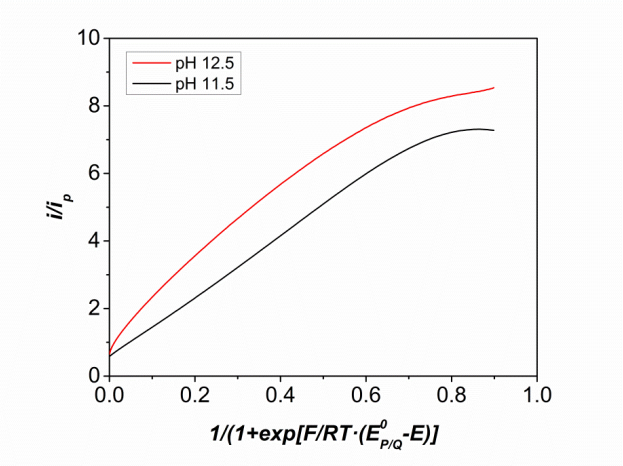

Figure S16. Foot-of-the-wave analyses for the $[(L1)Cu]^{2-}$ complex at pH 11.5 and 12.5. Data were obtained from background corrected CV responses in phosphate solutions (1mM [cat], 0.1M ionic strength) at 100 mV/s using GC as working electrode.

In order to calculate the turnover number of the oxygen evolution experiment, we started taking into account the amount of catalyst in the bulk solution (0.012 mmol) and the amount of oxygen generated over 5000 s (0.006 mmol) yielding a TON of 0.5 approximately. However, this calculation underestimate the real TON value since only the catalyst surrounding the electrode is involved in the water oxidation. Savéant and co-workers[13] developed a methodology taking into account this fact in electrocatalytic process. In addition, Lin and co-workers adapted this formula to the water oxidation reaction:[14]

$$TON = \frac{k_{obs}t}{1 + \exp\left[\frac{F}{R \cdot T}(E^0_{cat} - E)\right]}$$

Furthermore, Lin considered the different behavior of ITO and glassy carbon electrode, using the difference in density current for transferring the k_{obs} from one electrode to the other. In our case, the ITO is 8 times slower than the glassy carbon electrode which leads to a k_{obs} of 0.445 s^{-1} in ITO (3.56 in glassy carbon electrode). The calculated TON considering the catalytic amount around the electrode is 1947.

Bulk electrolysis and O2 evolution

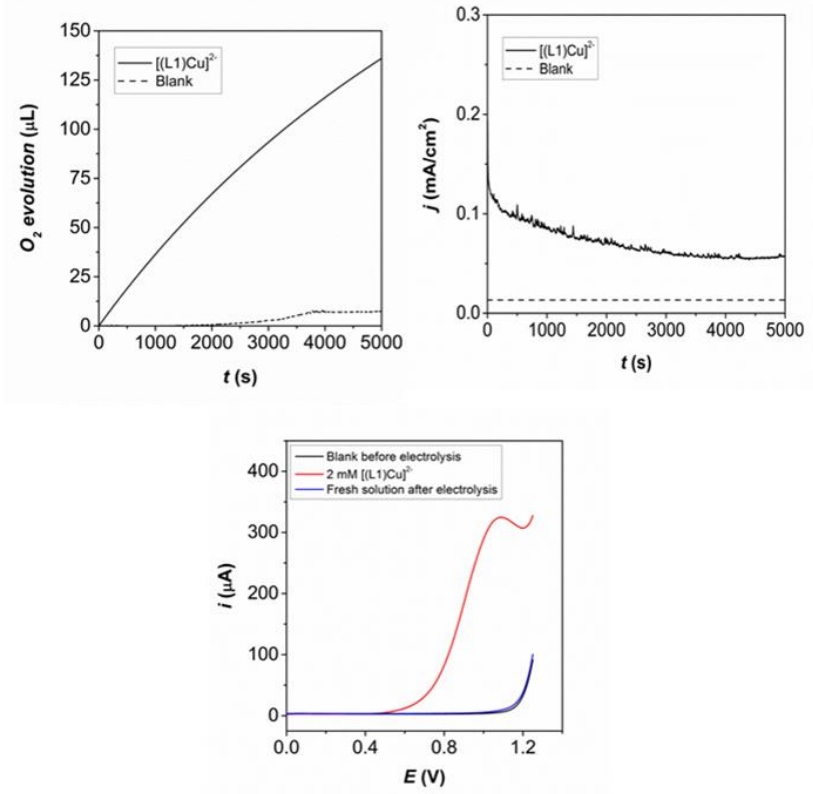

Figure S17. (Top, left) Clark electrode measurement during CPE at 1.3 V in phosphate buffer solution at pH 11.5 (0.1 M of ionic strength) with (solid line) and without (dash line) 2 mM of $[(L1)Cu]^{2-}$. ITO working electrode (2.5 cm^2), AgCl reference electrode and Pt mesh counter electrode (Top, right) Current obtained during the CPE experiments at 1.3 V. The Faraday efficiency is 99.8%. (Bottom) Linear Sweep Voltammetry of buffer solution at pH 11.5 with (red) and without (black) 2 mM of $[(L1)Cu]^{2-}$, using ITO working electrode, AgCl reference electrode (reported E values were obtained by adding 0.2 V to the experimental ones), Pt wire counter electrode and 100 mV/s of scan rate. The blue line is the CV of the ITO after the CPE experiment in fresh buffer solution and shows no deposition of electroactive species.

Redox non-innocent ligands in copper-catalyzed water oxidation

Bulk electrolysis with added base

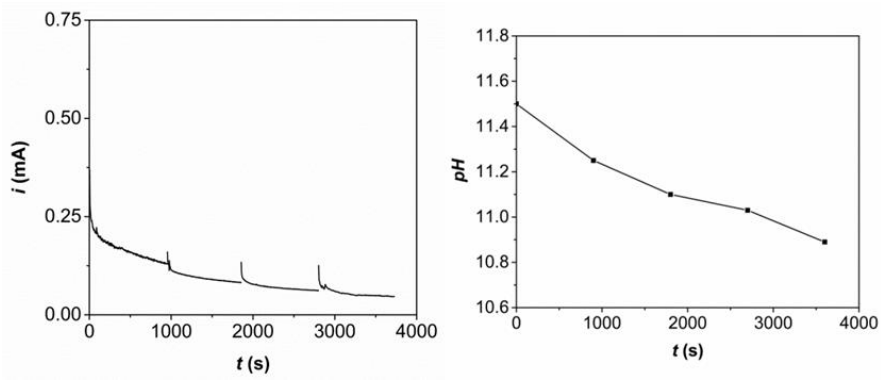

Figure S18. (Left) Controlled Potential Electrolysis at 1.3 V in 2mM $[(L1)Cu]^{2-}$ aqueous solution at pH 11.5 containing phosphate buffer with 0.1 M ionic strength. ITO working electrode, Ag/AgCl reference electrode and Pt mesh counter electrode were used. Every 15 min, the CPE was stopped, the pH was measured and a new CPE was set at 1.3 V for 15 min more. The process was repeated 4 times. (Right) pH values obtained from the CPE at 1.3 V.

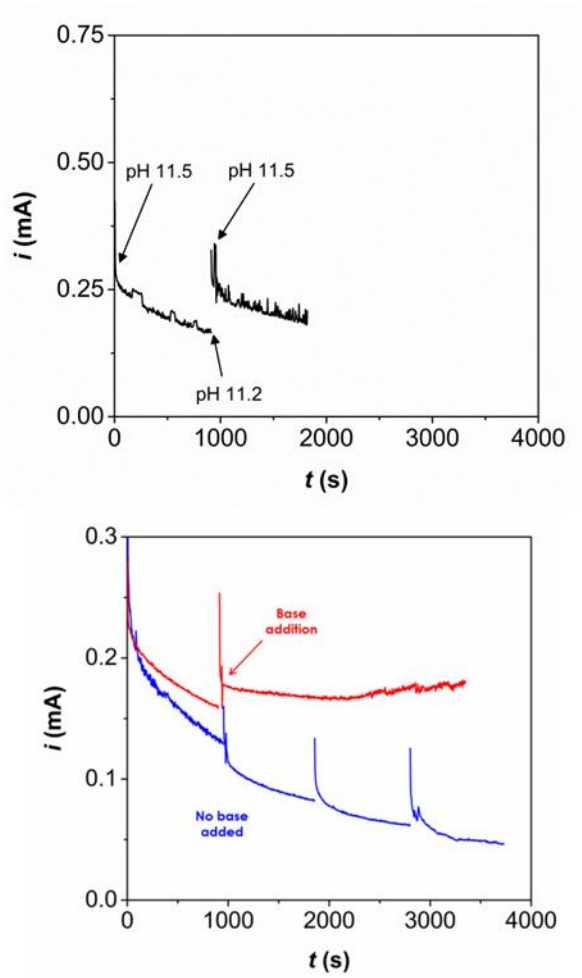

Figure S19. (Left) Controlled Potential Electrolysis at 1.3 V in the same conditions as the experiment in Figure . After the first 15 minutes, the CPE was stopped and the pH was readjusted to 11.5. The initial current values were recovered in the following 15 minutes of CPE. (Right) The same experiment as before was repeated but after 15 min of CPE, basic solution containing 1M of NMe_4OH was added so that the activity of the catalyst was maintained constant for around 1 hour. It was represented together with the first CPE experiment when no base was added (blue line).

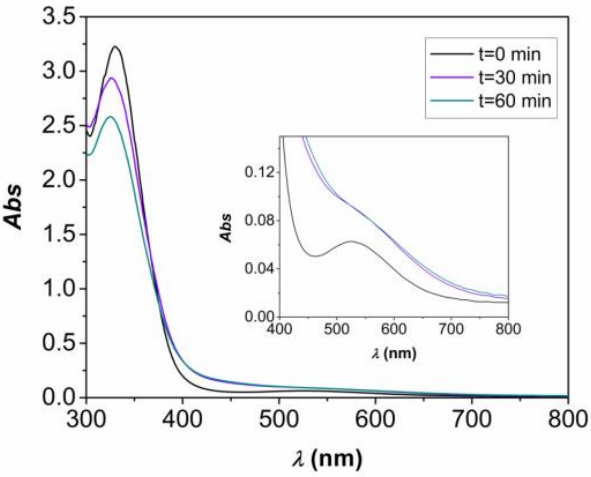

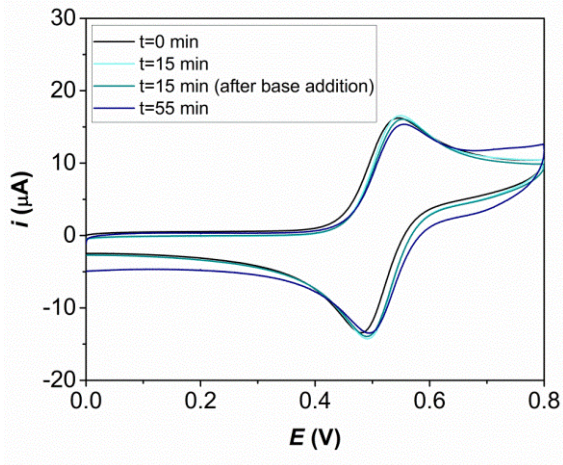

Figure S20. (Left) UV-vis spectra of the 2mM $[(L1)Cu]^{2-}$ basic solutions recorded at different times of the CPE experiment at 1.3 V shown in figure S16. (Right) CVs of the 2mM $[(L1)Cu]^{2-}$ basic solutions recorded at different times of the CPE experiment at 1.3 V with addition of base shown in figure S17 right. GC disk working electrode, mercury/mercurous sulfate reference electrode, Pt wire counter electrode and 100 mV/s of scan rate.

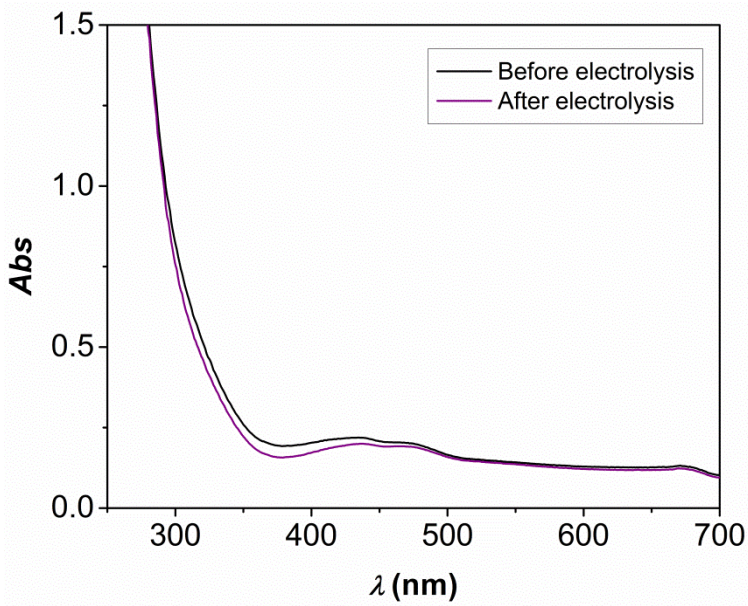

Figure S21. UV-vis spectra of the ITO electrode before (top) and after (bottom) the CPE experiment at 1.3 V in 2mM $[(L1)Cu]^{2-}$ aqueous solutions at pH 11.5 containing phosphate buffer with 0.1 M ionic strength.

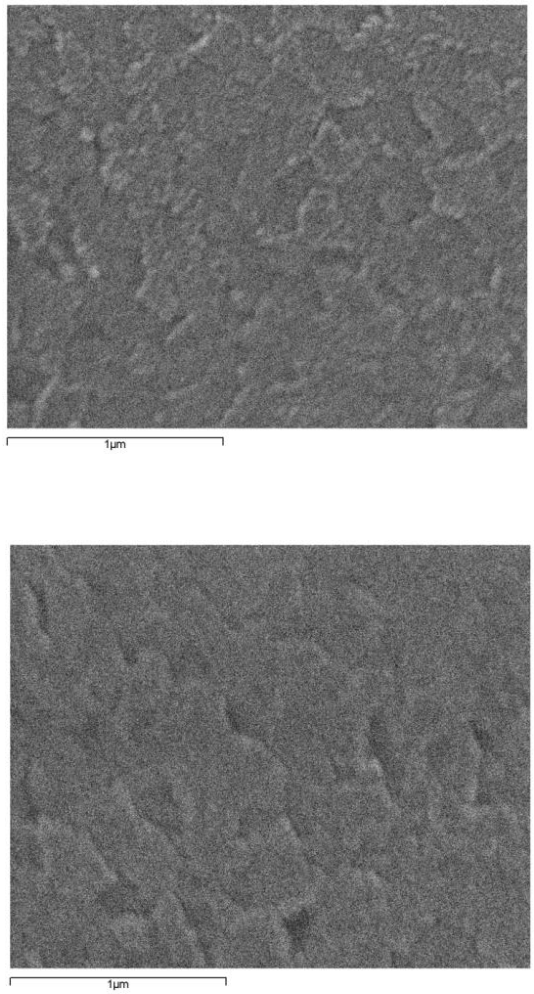

Figure S22. SEM images of the ITO electrode before (left) and after (right) the CPE experiment at 1.3 V in 2mM $[(L1)Cu]^{2-}$ aqueous solutions at pH 11.5 containing phosphate buffer with 0.1 M ionic strength.

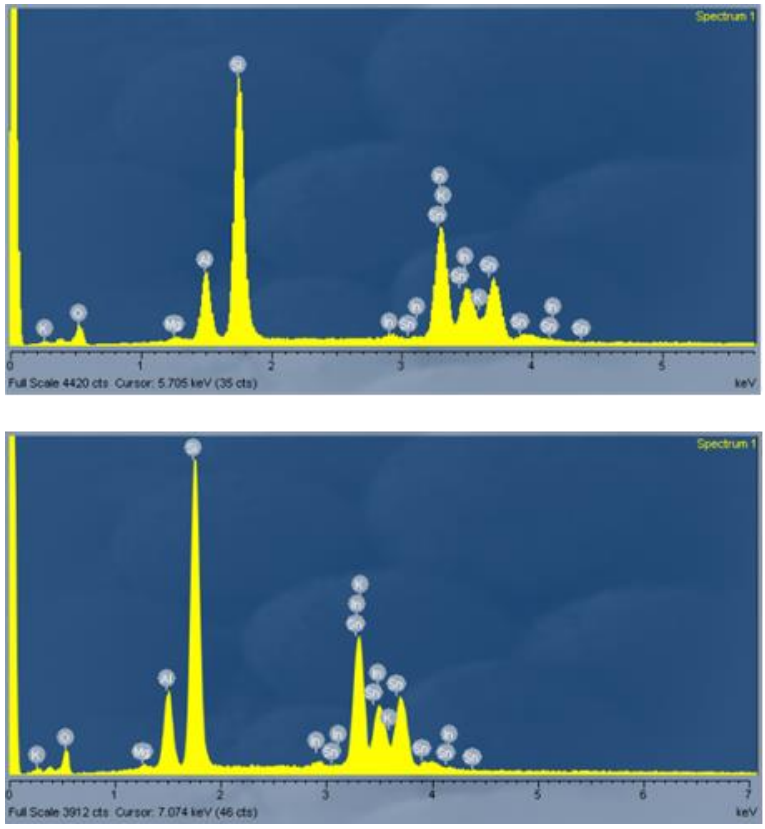

Figure S23. EDX spectra of the ITO electrode Before/After before (left) and after (right) the CPE experiment at 1.3 V in 2mM $[(L1)Cu]^{2-}$ aqueous solutions at pH 11.5 containing phosphate buffer with 0.1 M ionic strength. There is no appreciable changes in the composition of the electrode.

Table S2: Chemical composition of the ITO electrodes obtained from EDX spectra.

Electrode	O %	Mg %	Al %	Si %	K %	In %	Sn %	Total %
Before CPE	32.81	0.74	9.38	37.42	3.11	12.4	4.14	100
After CPE	34.56	0.61	8.89	36.79	2.72	12.28	4.15	100

Electrochemistry and O2 evolution with substituted catalysts

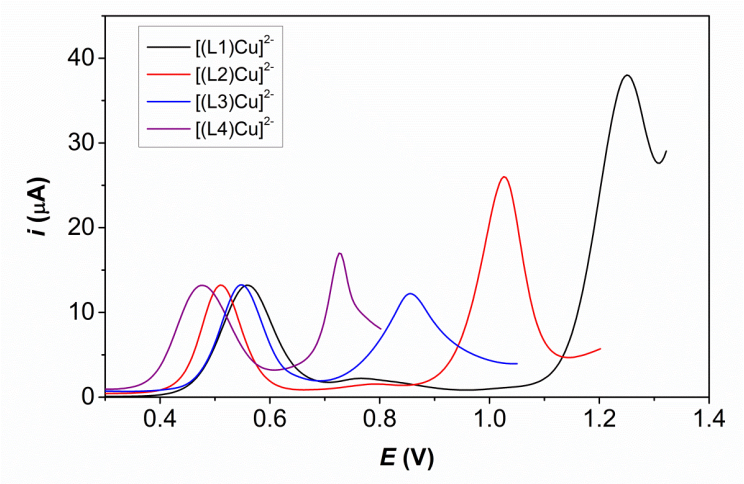

Figure S24. DPV of basic solutions containing 1mM of the four different catalysts in phosphate buffer at pH 11.5 (0.1 M of ionic strength), GC working electrode.

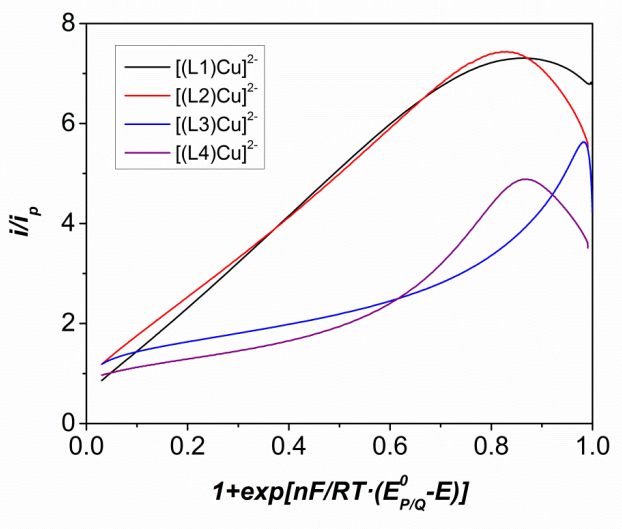

Figure S25. Foot-of-the-wave analyses for the four complexes. Data were obtained from background corrected CV responses of each catalyst in phosphate solutions (1mM [cat], pH 11.5, 0.1M ionic strength) at 100 mV/s using GC as working electrode.

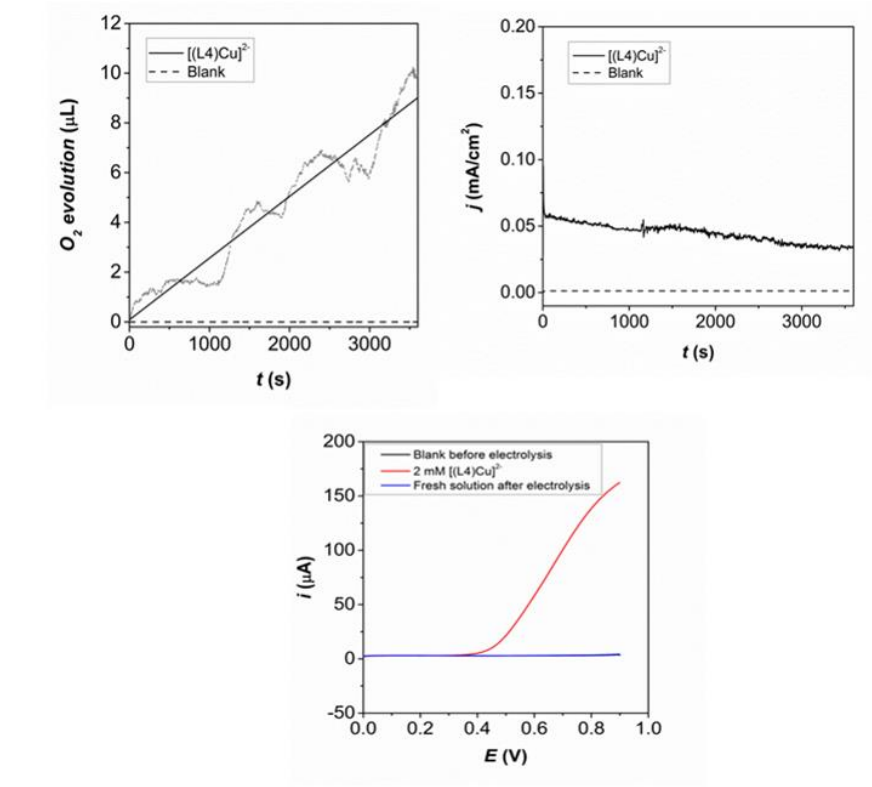

Figure S26. (Top, left) Clark electrode measurement during CPE at 0.9 V in phosphate buffer solution at pH 11.5 (0.1 M of ionic strength) with (solid line) and without (dash line) 2 mM of $[(L4)Cu]^{2-}$. ITO working electrode (2.5 cm^2), AgCl reference electrode and Pt mesh counter electrode. (Top, right) Current obtained during the CPE experiments at 0.9 V. The Faraday efficiency is 46.95 %. (Bottom) Linear Sweep Voltammetry of buffer solution at pH 11.5 with (red) and without (black) 2 mM of $[(L1)Cu]^{2-}$, using ITO working electrode, AgCl reference electrode (reported E values were obtained by adding 0.2 V to the experimental ones), Pt wire counter electrode and 100 mV/s of scan rate. The blue line is the CV of the ITO after the CPE experiment in fresh buffer solution and shows no deposition of electroactive species.

Comparative data on Cu-based water oxidation catalysts

Table S3. Kinetic and electrochemical data of complexes $[(LY)Cu]^{2-}$ (Y = 1-4) and related Cu complexes described in the literature that have been reported to act as WOCS.

Entry[a]	Catalyst[b]	pH	$E^{o}_{III/II}$, V (ΔE, mV)	E^{o}_{cat}, V[d]	η, (mV)[e]	k_{obs}, s^{-1}[,f]	TON[i] (s^{-1})
1[tw]	$[(L1)Cu]^{2-}$	11.5	0.56 (71)	1.25	600	3.56[g]	1947
2[tw]	$[(L2)Cu]^{2-}$	11.5	0.51 (74)	1.03	400	3.58	-
3[tw]	$[(L3)Cu]^{2-}$	11.5	0.55 (69)	0.85	270	0.43	-
4[tw]	$[(L4)Cu]^{2-}$	11.5	0.48 (67)	0.73	170	0.16	-
5[15]	$[(6,6'\text{-dhbp})_2Cu(OH_2)]$	12.6	0.97 [c]		477	0.36	-
6[16]	$[(Py_3P)Cu(OH)]^{-}$	8.0	1.29 [c]		~500	20[h]	-
7[17]	$[(6,6'\text{-dhbp})Cu(OH_2)_2]$	12.4	1.0 [c]		~540	0.4	400
8[18]	$[(H_{-2}2GH)Cu(OH_2)]$	11.0	~0.65 (80)		~620	53	-
9[19]	$[(opba)Cu]^{2-}$	10.8	~0.89[c]		636	1.13	-
10[20]	$[(TGG)Cu(OH_2)]^{2-}$	11.0	0.58 (70)		~650	33	-
11[21]	$[(bpy)Cu(OH)_2]$	12.5	1.4[c]		750	100	-
12[22]	$[Cu_2(BPMAN)(\mu\text{-}OH)]^{3+}$	7.0	> 1.87[c]	1.87	~1050	0.6	-

(a) tw stands for this work. (b) bpy is 2,2'-bpy; dhbp is 6,6'-dihydroxy-2,2'-bpy; TGG is triglycylglycine; Py_3P is N,N-bis(2-(2-pyridyl)ethyl)pyridine-2,6-dicarboxamidate; bpman is 2,7-[bis(2-pyridylmethyl)aminomethyl]-1,8-naphthyridine; opba is o-phenylenebis(oxamato); $H_{-2}2GH$ is H-Gly-Dap(H-Gly)-His-NH2. (c) The III/II redox couple is proposed to appear under the catalytic wave. (d) Measured by DPV. (e) Measured by DPV for entries 1-4 and 12 and from the initial foot of the electrocatalytic wave or the half-peak potential for CVs for the rest. (f) Measured by FOWA in complexes [Cu(LY)] and other methodologies for the other complexes. (g) k_{obs} = 11.96 at pH = 12.5. (h) In a 0.1 M $[HPO_4^{2-}]$. (i) TON values calculated with Foot-of-the-wave analysis developed by Savéant and co-workers.[23]

Computational Study

Computational Details

All calculations were carried out with the Gaussian09 program package[24] using the DFT method. The selected functional was B3LYP with empirical dispersion correction of Grimme (B3LYP-D3).[25,26] The selected basis set was 6-31+G(d) for C, N, O and H,[27] and LANL2TZ(f) for Cu.[28,29] Solvation was introduced implicitly through the SMD model,[30] with water as the solvent. All geometry optimizations were computed in solution without symmetry restrictions. We confirmed the nature of all computed stationary points as minima or transition states through vibrational frequency calculations. Free energy corrections were calculated at 298.15 K and 105 Pa pressure, including zero point energy corrections (ZPE). In addition, a correction term of 1.9 kcal/mol (at 298 K) was added when necessary to account for the standard state concentration of 1 M. Unless otherwise mentioned, all reported energy values are free energies in solution.

In the transformation from free energies to electrochemical magnitudes we took from the chemical Literature the values of 4.28 V for the absolute potential of the standard hydrogen electrode[31] and-11.72 eV for the free energy of the proton in aqueous solution at pH=1.[32]The value for the free energy of the proton was translated to the experimental pH value of 11.5 by adding a correction term of -0.059*pH, following the same procedure as other authors.[33]

The functional for the DFT calculations was selected by calibration with respect to the experimental value for the oxidation of Cu(II) to Cu(III) catalyst (0.56 V). Different functionals were analyzed, and the results are summarized in Table S1. The agreement is very good with experiment (discrepancy smaller than 1 kcal/mol) for B3LYP-D3, M06 and M06-D3. Agreement is moderate with wB97xD (discrepancy of 5.5 kcal/mol), and bad with M06L, M062X and B97D (errors larger than 10 kcal/mol). It is

clear that the percentage of HF exchange in the functional affects considerably the energy difference. In this case, the common hybrid methods (around 20% of HF exchange) have the best performance. We selected B3LYP-D3 for convenience.

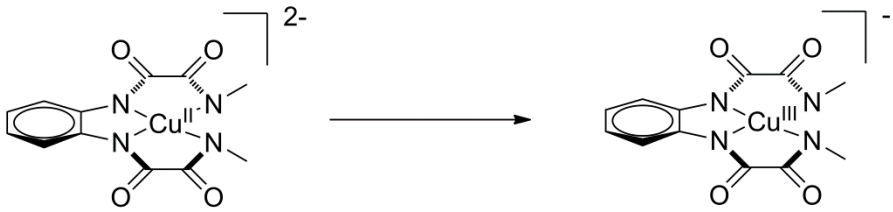

Scheme S2. Oxidation reaction from $[(L1)Cu^{II}]^{2-}$ to $[(L1)Cu^{III}]^{-}$ used for the method comparison.

Table S4. Computed E^0 values for the indicated oxidation process (V), and comparison with the experimental value (kcal/mol)

Method	E^0 (V)	G_{comput} - G_{exper} (kcal/mol)
B3LYP-D3	0.53	-0.7
M06	0.58	0.5
M06-D3	0.57	0.2
M06L	-0.05	-14.1
M062X	1.66	25.4
B97D	-0.05	-14.1
wB97xD	0.80	5.5

Spin Distribution in Compound C

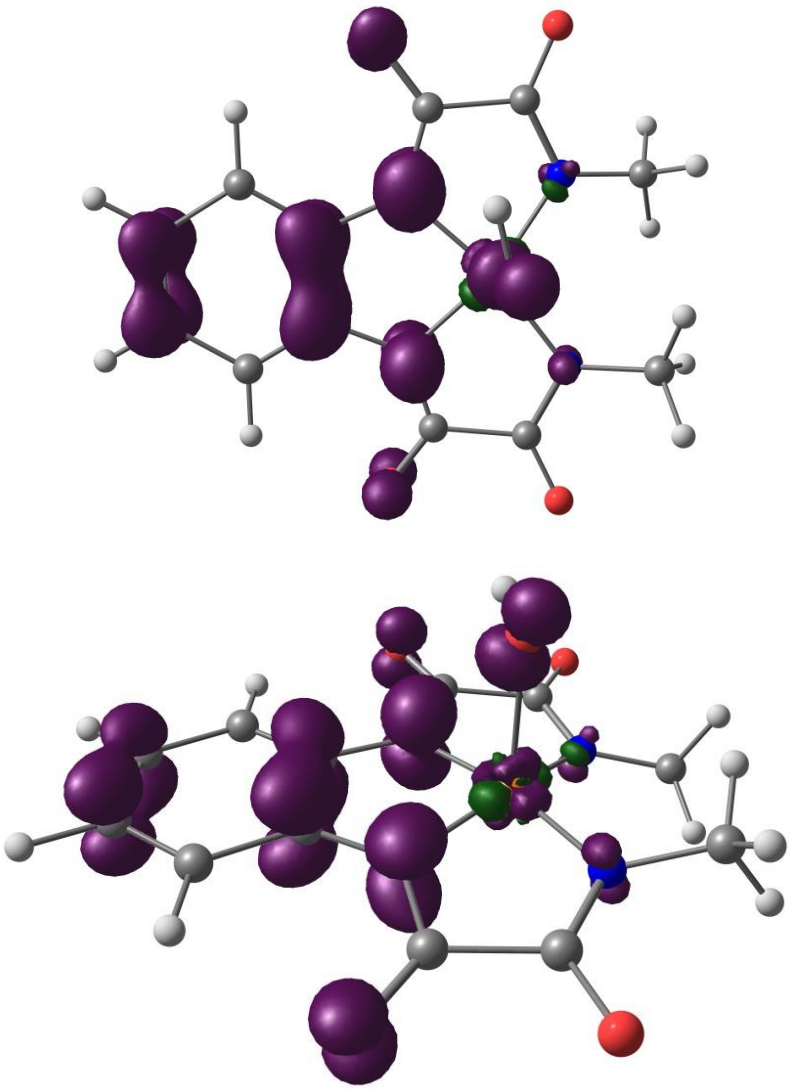

Figure S27. Two different views of spin density distribution in compound C.

H-bond found in species D and E

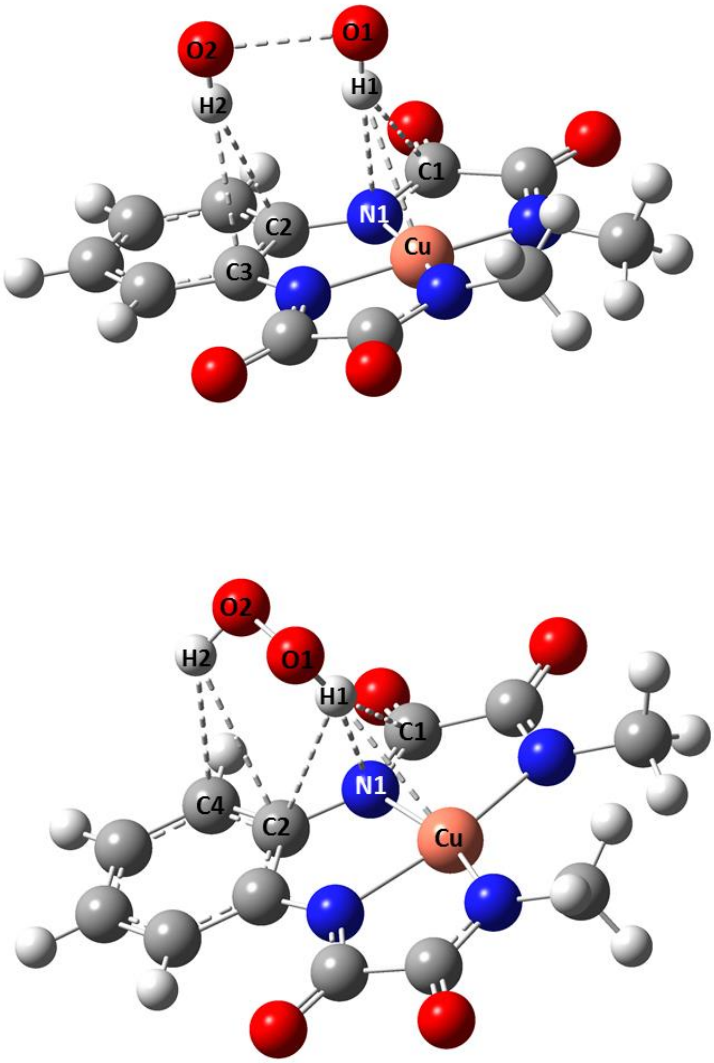

Figure S28. Structure of the species D and E with the identified hydrogen bond.

Table S5. Geometrical parameters of the identified hydrogen bonds represented in Figure S26.

Species	Atoms involved	d_{O-H}	$d_{H-C/N/Cu}$	$d_{C/N/Cu-O}$	$\hat{a}_{O-H-C/N/Cu}$
D	O1-H1-C1	0.973	2.870	3.689	142.45
	O1-H1-N1	0.973	2.483	3.445	169.70
	O1-H1-Cu	0.973	2.633	3.470	144.30
	O2-H2-C2	0.975	2.803	3.742	161.85
	O2-H2-C3	0.975	2.646	3.580	160.63
E	O1-H1-C1	0.986	2.631	3.508	148.27
	O1-H1-C2	0.986	2.579	3.260	126.15
	O1-H1-N1	0.986	2.052	2.987	157.61
	O1-H1-Cu	0.986	2.633	3.500	146.42
	O2-H2-C2	0.979	2.885	3.393	113.24
	O2-H2-C4	0.979	2.783	3.501	130.71

Conversion from E to A

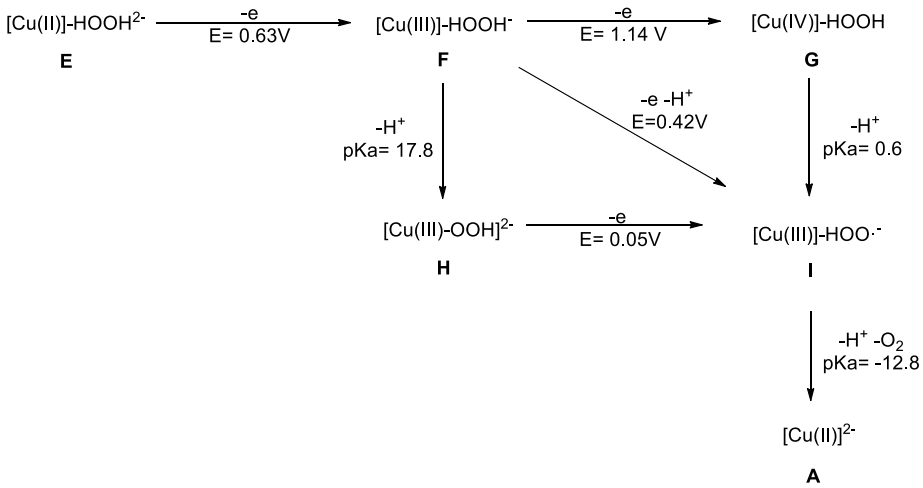

Scheme S3. Calculated water oxidation mechanism after the O-O bond formation, corresponding to the oxidation of H_2O_2 to O_2 and catalyst recovery.

Once the hydrogen peroxide is formed, the subsequent oxidations occur easily. The first one is a one electron oxidation of the metal center (E to F, 0.63 V) forming the Cu(III) intermediate. After that, the most favored pathway is the proton coupled-electron transfer with a potential of only 0.42 V (F to I). It is important to notice that again an oxygen centered radical is formed (I). This species is deprotonated in the last step, which leads to release of dioxygen and recovery of the catalyst complex A.

Overpotential-Ligand: QSAR model

Here is analyzed the relationship between the overpotential of the different catalysts and the electronic structure of their corresponding ligands in order to rationalize the observed behavior.

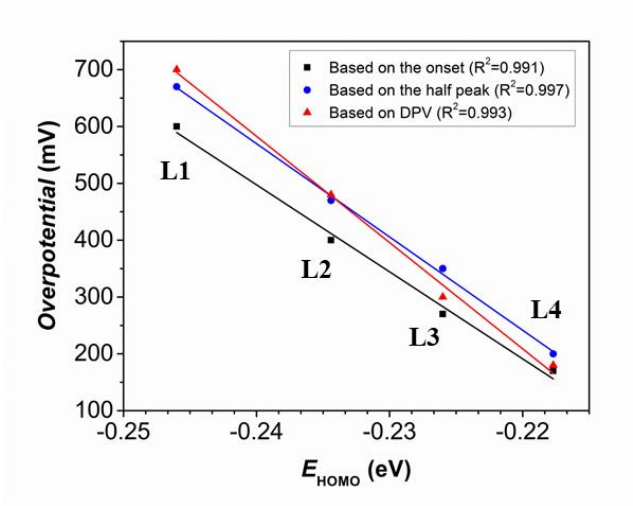

Figure S29. Plot of the relationship between the HOMO energy of each ligand with the observed overpotential for the corresponding complex. Overpotential values have been obtained from CVs and DPVs measurements and the energies of the HOMO have been calculated by optimizing the structure of free ligand molecules with the same computational methods as used before for the copper complexes. The results indicate that the more electron-donating substituents of the aromatic ring increase the overall energy of the HOMO and thus, they are favoring the electron release from the ligand to give the oxidized molecule. This stabilizes the resulting radical in the copper complex and leads to a decrease in the overpotential of the water. It provides us a relevant tool to control the water oxidation catalysis.

References

1 Stumpf, H. O.; Pei, Y.; Kahn, O.; Sletten, J.; Renard, J. P. *J. Am. Chem. Soc.***1993**, *115*, 6738.

2 Ruiz, R.; Surville-Barland, C.; Aukauloo, A.; Anxolabehere-Mallart, E.; Journaux, Y.; Cano, J.; Munoz, M. C. *J. Chem. Soc., Dalton Trans.***1997**, 745.

3 Data collection with APEX II version v2013.4-1.Bruker (2007).Bruker AXS Inc., Madison, Wisconsin, USA.

4 Data reduction with Bruker SAINT version V8.30c. Bruker (2007). Bruker AXS Inc., Madison, Wisconsin, USA.

5 SADABS: V2012/1 Bruker (2001). Bruker AXS Inc., Madison, Wisconsin, USA.Blessing, ActaCryst. (1995) A51 33-38.

6 Data collection with CrystalClear-SM Expert 2.1 b29.Rigaku 2013.

7 Sheldrick, G.M. *ActaCryst.* **2008** A64, 112-122. SHELXTL version V6.14.

8TWINABS Version 2008/4 Bruker AXS.Blessing, ActaCryst. (1995) A51 33-38.

9 SQUEEZE implemented in Platon. Platon: Spek, A.L. J. Appl. Cryst. 2003, 36, 7-13; SQUEEZE: P. Van der Sluis& A.L. Spek, ActaCryst. 1990, A46, 194-201.

10 Costentin, C.; Savéant, J.-M. *ChemElectroChem***2014**, *1*, 1226.

11 Rountree, E. S.; McCarthy, B. D.; Eisenhart, T. T.; Dempsey, J. L. *Inorg. Chem.***2014**, *53*, 9983.

12 Sander, A. C.; Maji, S.; Francàs, L.; Böhnisch, T.; Dechert, S.; Llobet, A.; Meyer, F. *ChemSusChem***2015**, n/a.

13 Costentin, C.; Drouet, S.; Robert, M.; Savéant, J.-M. *J. Am. Chem. Soc.* **2012**, *134*, 11235.

14 Zhang, T.; Wang, C.; Liu, S.; Wang, J.-L.; Lin, W. *J. Am. Chem. Soc.* **2014**, *136*, 273.

15 Gerlach, D. L.; Bhagan, S.; Cruce, A. A.; Burks, D. B.; Nieto, I.; Truong, H. T.; Kelley, S. P.; Herbst-Gervasoni, C. J.; Jernigan, K. L.; Bowman, M. K.; Pan, S.; Zeller, M.; Papish, E. T. *Inorg. Chem.* **2014**, *53*, 12689.

16 Coggins, M. K.; Zhang, M.-T.; Chen, Z.; Song, N.; Meyer, T. J. *Angew. Chem. Int. Ed.* **2014**, *53*, 12226

17 Zhang, T.; Wang, C.; Liu, S.; Wang, J.-L.; Lin, W. *J. Am. Chem. Soc.* **2014**, *136*, 273.

18 Pap, J. S.; Szyrwiel, L.; Sranko, D.; Kerner, Z.; Setner, B.; Szewczuk, Z.; Malinka, W. *Chem. Commun.* **2015**, *51*, 6322.

19 Fu, L.-Z.; Fang, T.; Zhou, L.-L.; Zhan, S.-Z. *RSC Advances* **2014**, *4*, 53674.

20 Zhang, M.-T.; Chen, Z.; Kang, P.; Meyer, T. J. *J. Am. Chem. Soc.* **2013**, *135*, 2048.

21 Barnett, S. M.; Goldberg, K. I.; Mayer, J. M. *Nat Chem***2012**, *4*, 498.

22 Su, X.-J.; Gao, M.; Jiao, L.; Liao, R.-Z.; Siegbahn, P. E. M.; Cheng, J.-P.; Zhang, M.-T. *Angew. Chem. Int. Ed.* **2015**, *54*, 4909.

23 Costentin, C.; Drouet, S.; Robert, M.; Savéant, J.-M. *J. Am. Chem. Soc.* **2012**, *134*, 11235.

24 Gaussian 09, Revision **A.1**, M. J. Frisch, G. W. Trucks, H. B. Schlegel, G. E. Scuseria, M. A. Robb, J. R.

Cheeseman, G. Scalmani, V. Barone, B. Mennucci, G. A. Petersson, H. Nakatsuji, M. Caricato, X. Li, H. P.

Hratchian, A. F. Izmaylov, J. Bloino, G. Zheng, J. L. Sonnenberg, M. Hada, M. Ehara, K. Toyota, R. Fukuda, J.

Hasegawa, M. Ishida, T. Nakajima, Y. Honda, O. Kitao, H. Nakai, T. Vreven, J. A. Montgomery, Jr., J. E.

Peralta, F. Ogliaro, M. Bearpark, J. J. Heyd, E. Brothers, K. N. Kudin, V. N. Staroverov, R. Kobayashi, J.

Normand, K. Raghavachari, A. Rendell, J. C. Burant, S. S. Iyengar, J. Tomasi, M. Cossi, N. Rega, J. M. Millam,

M. Klene, J. E. Knox, J. B. Cross, V. Bakken, C. Adamo, J. Jaramillo, R. Gomperts, R. E. Stratmann, O. Yazyev,

A. J. Austin, R. Cammi, C. Pomelli, J. W. Ochterski, R. L. Martin, K. Morokuma, V. G. Zakrzewski, G. A. Voth,

P. Salvador, J. J. Dannenberg, S. Dapprich, A. D. Daniels, Ö. Farkas, J. B. Foresman, J. V. Ortiz, J. Cioslowski,

and D. J. Fox, Gaussian, Inc., Wallingford CT, **2009**.

25 A.D. Becke, *J. Chem. Phys.***1993**, *98*, 5648.

26 S. Grimme, J. Antony, S. Ehrlich, H. Krieg, *J. Chem. Phys.***2010**, *132*, 154104.

27 a) W.J. Hehre, R. Ditchfield, J.A. Pople, J. Chem. Phys. **1972**, 56, 2257. b) P.C. Hariharan, J.A. Pople, *Theoret. ChimicaActa***1973**, *28*, 213. c) M.M. Francl, W.J. Petro, W.J. Hehre, J.S. Binkley, M.S. Gordon, D.J. DeFrees and J.A. Pople, *J. Chem. Phys.***1982**, *77*, 3654.

28 a) P. J. Hay, W. R. Wadt, *J. Chem. Phys.***1985**, *82*, 270. b) P. J. Hay, W. R. Wadt, *J. Chem. Phys.***1985**, *82*, 284. c) P. J. Hay, W. R. Wadt, *J. Chem. Phys.***1985**, *82*, 299.

29 Taken from EMSL Basis set Library: a) D. Felier*, J. Comp. Chem.***1996**, *17*, 1571. b) K.L. Schuchardt, B.T. Didier, T. Elsethagen, L. Sun, V. Gurumoorthi, J. Chase, J. Li, T.L. Windus, *J. Chem. Inf. Model.*, **2007**, *47*, 1045.

30 S. A. V. Marenich, C. J. Cramer, D. G. Truhlar, *J. Phys. Chem. B*, **2009**, *113,* 6378.

31 a) A. Lewis, J. A. Bumpus, D. G. Truhlar, C. J. Cramer *J. Chem. Ed.***2004**, *81*, 596. b) A. Lewis, J. A. Bumpus, D. G. Truhlar, C. J. Cramer *J. Chem. Ed.***2007**, *84*, 934 [Erratum].

32 A. V. Marenich, A. Majunmdar, M. Lenz, C. J. Cramer, D. G. Truhlar, *Angew. Chem. Int. Ed.***2012**, *51*, 12810.

33 S.G. Winikoff, C.J. Cramer, *Catal. Sci. Technol.***2014**, *4*, 2484.

Paper B: Single Electron Transfer Steps in Water Oxidation Catalysis. Redefining the Mechanistic Scenario

Funes-Ardoiz, I.; Garrido-Barros, P.; Llobet, A.; Maseras, F. *ACS Catal.*. **2017**, *7*, 1712-1719.

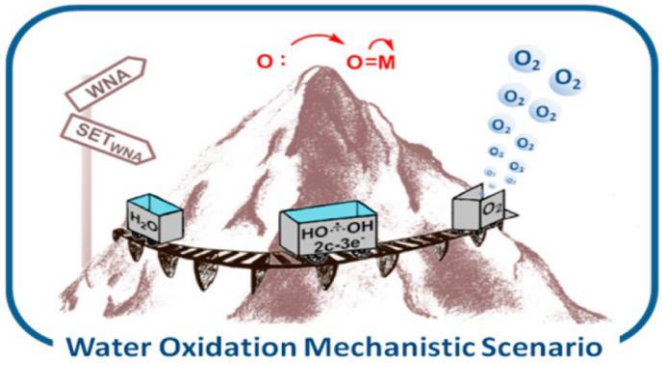

Abstract

The systematic computational study of the mechanism for water oxidation in four different complexes confirms the existence of an alternative mechanism for the O−O bond formation step to those previously reported: the single electron transfer−water nucleophilic attack (SET-WNA). The calculated mechanism relies on two SET steps and features the existence of an intermediate with a $(HO\cdots OH)^-$ moiety in the vicinity of the metal center. It is operative in at least three representative copper based complexes and is the only option that explains the experimentally observed efficiency in two of them. The proposal of this reaction pathway redefines the mechanistic scenario and, importantly, generates a promising avenue for designing more efficient water oxidation catalysts based on first row transition metals.

Contribution

Pablo Garrido Barros performed the research on the [(L3)CuII(OH)$_2$] and [RuII(L3)(L4)(H$_2$O)]$^{2+}$ systems and. Together with the rest of authors, analyzed the results and collaborated in the writing of the text.

B.1. Introduction

Water splitting driven by sunlight to produce molecular oxygen and hydrogen is regarded as one of the most promising approaches for the generation of clean fuels in a sustainable manner.[1,2] Hydrogen generated in this manner is generally labeled as solar-hydrogen[3] and is regarded as a way of storing solar energy into chemical bonds, in a similar manner as done by photosystem II of green plants and algae.[4]

From an electrochemical perspective, the water splitting reaction consists of two half reactions: water oxidation to molecular oxygen and proton reduction to hydrogen. Particularly the water oxidation to dioxygen has been traditionally regarded as the bottleneck for the design of practical devices that can carry out water splitting with sunlight.[5,6,7,8] The water oxidation to dioxygen reaction, besides being energy demanding (E° = 1.23 V vs NHE at pH = 0), is also molecularly complex since it requires the breaking of four H−O bonds and the releasing of 4 electrons and 4 protons together with the formation of an O−O bond. This complex mechanistic scenario generally translates into very high overpotentials needed for the reaction to proceed.[9]

One of the potential strategies to overcome high activation energies consists in the involvement of transition metals as catalysts. Indeed, a number of Ru[10,11,12,13,14,15,16,17] and Ir[18,19,20,21,22] complexes have been recently described as efficient catalysts for this reaction. Furthermore, the understanding of the different mechanisms involved in these catalytic processes as well as the potential deactivation pathways has been crucial for the development of the field. However, better catalysts, more robust

and efficient, are needed to be able to incorporate them in devices that can carry out water splitting with sunlight.

In order to progress in this front, it is essential to gain a deeper understanding of the reaction mechanisms that can operate in water oxidation catalysis. From this perspective, it is imperative to spectroscopically characterize reaction intermediates as well as their reactivity. In this respect, the theoretical methodologies become an extremely valuable tool to complement experimental work, especially in systems with such a complexity as the water oxidation reaction catalyzed by transition metals.

Mechanistic and theoretical studies have been carried out mainly with Ru complexes and have led to proposal of two main pathways for the O−O bond formation step depending on whether an external water molecule is involved or not. Thus, a water nucleophilic attack (WNA) and interaction of two M-O species (I2M) have been extensively discussed by our group and others.[23,24]

Transition metals in their high oxidation states containing the M-O group can be described using two resonant forms depending on whether the oxidation occurs solely at the metal center or at the oxygen, as depicted on the left-hand side of Figure 1. All over the present paper we will use formal oxidation states, since this allows easy tracking of electron trafficking, although it is obvious that the real species will be a mixing of both resonant forms.

Redox non-innocent ligands in copper-catalyzed water oxidation

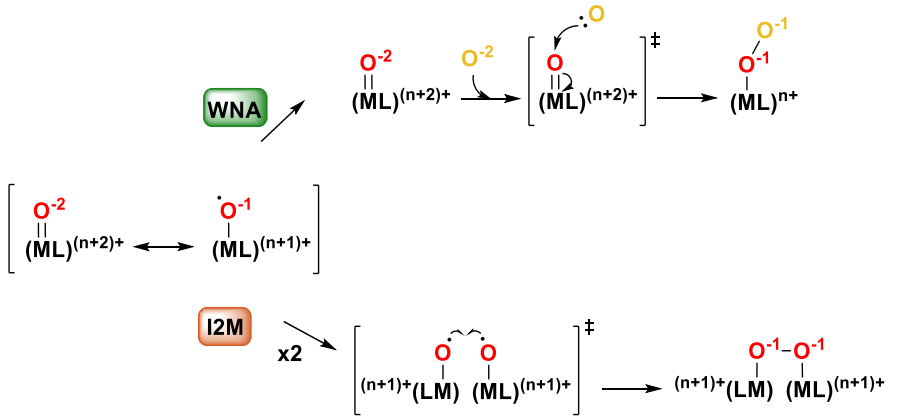

III

Figure 1. Schematic view of water nucleophilic attack (WNA) and interaction of two M-O species (I2M) mechanisms. Formal oxidation states for the metal and oxygen atoms are indicated as superscripts.

A WNA mechanism (Figure 1) is found when the auxiliary ligands favor the stabilization of the oxo form shown in Figure 1 top, and an I2M mechanism is found when the favored species resemble those of the oxyl radical form depicted in the lower part of Figure 1. The WNA involves a concerted two-electron process from the incoming water molecule to the metal center of the M-oxo group, resulting in the formation of a peroxide intermediate and the reduction of the metal center by two units. On the other hand, the I2M mechanism involves a radical coupling where the oxidation state of the metal center remains unchanged.

Recently several first row transition metal complexes have been reported as catalysts for the water oxidation reaction.[25,26,27,28,29,30,31,32,33,34,35,36,37,38,39,40] While these catalysts are of interest because of their high abundance and low toxicity, their performance is much poorer than those of their Ru or Ir analogues, and in addition, their mechanistic pathways are in most cases basically unknown. [28,29,30,41,42,43]

We have very recently reported, a new complex based on Cu, containing the amidate ligand OPBAN (o-phenylenebis-(oxamidate)) that can carry out the water oxidation reaction in a very efficient manner.[31] Surprisingly,

from a mechanistic perspective, it does not follow the WNA or I2M schemes just described but rather a step by step one electron process that we have termed SET-WNA. Computational homogeneous catalysis has been, until now, dominated by two-electron transfers,[44] but there is an increasing recognition of the presence of single electron transfer (SET) steps in first-row homogeneous catalysis.[45,46]

Therefore, it seems necessary and reasonable to raise these approaches to water oxidation catalysis using first row transition metals with the final aim of proposing a reasonable and complete mechanistic scenario. We will reexamine here the part of the mechanism leading to formation of the peroxide from water, as the subsequent oxidation of peroxide to di-oxygen seems straightforward.[31] It is particularly important to place the SET-WNA mechanism in the general context of WO, as its electronic requirements will lead to different paradigms for catalyst optimization. The present work thus aims at the description of a complete and integrated view of all the potential pathways leading to low energy O−O bond formation by transition metal catalysts. We report here the DFT study of three different copper based catalysts as well as a ruthenium based system (Scheme 1), and evaluate the feasibility of the SET-WNA mechanism for each of them. The computational results are, in all cases, compared with available experimental data, and they allow us to map the different accessible O−O bond formation pathways that, in turn, reveal the most important features for WO catalyst design.

B.2. Results and discussion

B.2.1 SET-WNA mechanism in copper systems: [(OPBAN)CuII]$^{2-}$, [(6,6'bobp)CuII(OH$_2$)$_2$], [(bpy)CuII(OH)$_2$].

We first proposed the existence of a single electron transfer−water nucleophilic attack (SET-WNA) mechanism in a joint experimental and computational communication on [(OPBAN)Cu^{II}]$^{2-}$ (OPBAN = o-phenylenebis(oxamidate)) complex, hereafter [(L1)Cu^{II}]$^{2-}$, **1a**.[31] We will

briefly recall and extend the results on this system here, and compare them with those on other copper complexes that have been shown experimentally to efficiently catalyze water oxidation. The new complexes studied are [(6,6'bobp)$Cu^{II}(OH_2)_2$] (where 6,6'-bobp = [2,2'-bipyridine]-6,6'-bis(olate)), hereafter [(L2)$Cu^{II}(OH_2)_2$], **2a**,[30] and [(bpy)$Cu^{II}(OH)_2$] (bpy = 2,2'-bipyridine), hereafter [(L3)$Cu^{II}(OH)_2$], **3a**.[28]

The key intermediates in the computed oxidation sequence for the three complexes are shown in eqs 1−3, respectively (the full set of accessible species is reported in the Supporting Information, Supplementary Figures 1 and 2). The active species is formed by two consecutive one electron oxidations that can be metal or ligand based. The highest potentials correspond to system **3**, where the L3 ligand is not oxidized, since its redox potential is too high, and thus the second electron is removed directly from the Cu−O moiety, forming an oxyl group, **3c**. In the other two systems, the ancillaryligands acts as redox non-innocent. For **2**, the first step involves the removal of an electron from the ligand whereas this happens in the second step for complex **1**. All these potentials are in good agreement with the reported experimental ones[28,30,31] and eqs 1−3 explain the observed pH dependence.

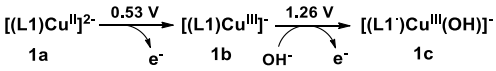

(1)

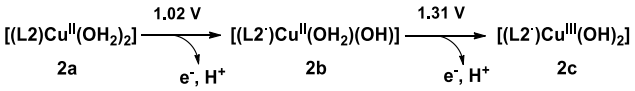

(2)

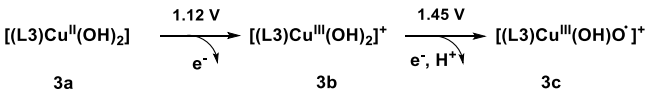

(3)

The setup for the reaction between species **1c**, **2c**, and **3c**, with a hydroxyl/oxyl group bound to the metal and an external hydroxyl group, is typical of the WNA mechanism, but we did not find this mechanism to be preferred in any of the three cases. For the **1c**/**2c** complexes, we could not locate a transition state connecting them directly to the resulting intermediates **1e**/**2e** (see Figure 2), where both oxygen atoms have a formal oxidation state of −1. The reason for this impossibility is apparent in the potential energy scans in the top part of Figure 2.

Intermediates **1c**/**2c** and **1e**/**2e** are at the bottom of two wells in red in the potential energy scan, and the energy of both curves increases sharply before they meet. Instead, the connection between the two intermediates takes place through an additional intermediate **1d**/**2d**, depicted in blue. This intermediate has a complex electronic structure, as the unpaired electron is shared by both oxygen atoms, forming a $2c-3e^-$ bond[47] with a length around 2.30 Å. This bond has a formal order of 0.5 and a formal oxidation state of −1.5 in each oxygenatom (Figure S3). The interaction is certainly in the limits of what can be called a bond, and because of this, it is marked with dashed lines in the Figures and Schemes. Intermediates **1d** and **2d** lie in the bottom of rather shallow wells in the potential energy surface and are unlikely to be characterized experimentally, which makes calculations very helpful for this particular problem. In fact, intermediate **1d** will be in equilibrium with a species resulting from dissociation of the $(HO\cdots OH)^-$ moiety, which we have computed as being 4.3 kcal/mol more stable in free energy. We have not introduced it in the diagram for the sake of simplicity, as the two fragments have to get together for the reaction to continue. As this species is kinetically important, the barrier for the step from **1d** to **TS 1d-e** will increase by 4.3 kcal/mol, still clearly affordable at room temperature. Such a dissociation problem is absent in system **2**.

Redox non-innocent ligands in copper-catalyzed water oxidation

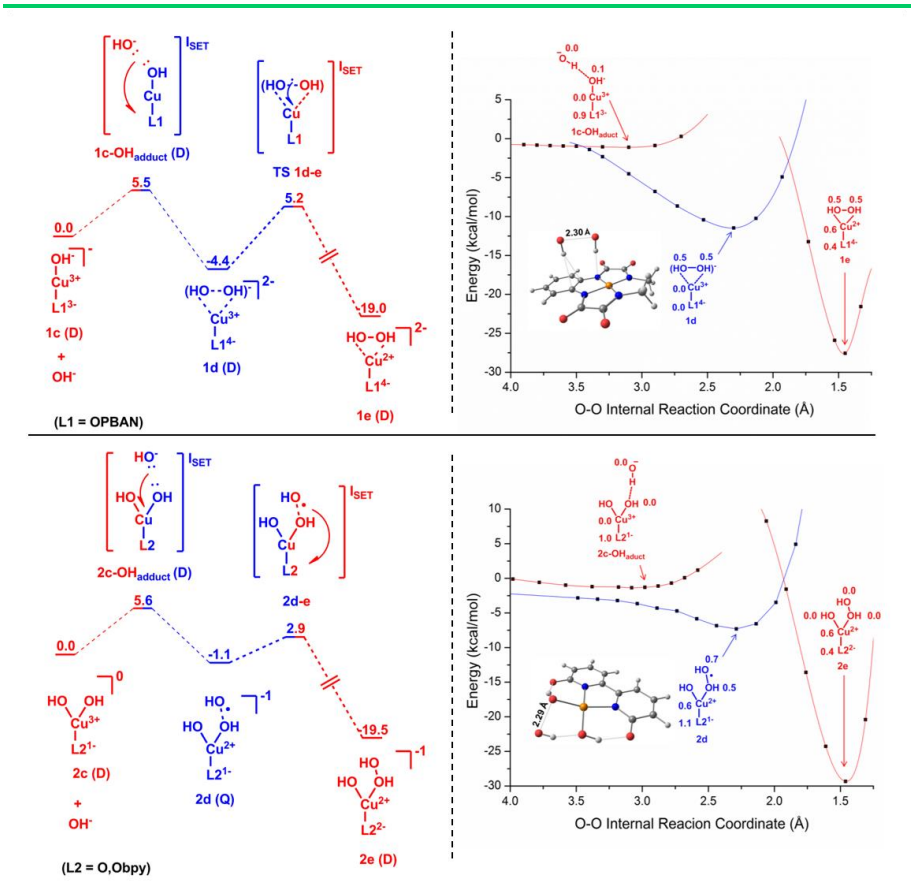

Figure 2. (a) Free energy profiles of $[(L1)Cu^{II}]^{2-}$ (top) and $[(L2)Cu^{II}(OH_2)_2]$ (bottom), where L1 = o-phenylenebis(oxamidate) and L2 = [2,2'-bipyridine]-6,6'-bis(olate). Energies in kcal/mol. (b) Potential energy relaxed scan for both complexes of the O−O reaction coordinate. The drawings at the top are updated versions of those previously reported by us.[31] The color code is based on the electronic nature of the oxygen centers: red when they are closed shell; blue when they involve unpaired electrons.

Intermediate **1d**/**2d** connects **1c**/**2c** to **1e**/**2e** through single electron transfer steps. The connection between **1c** and **1d** takes place through outer-sphere transfer, as the O−O distance is above 3.5 Å. We could not find a transition state in the potential energy surface for this step (even looking in a two dimension potential energy surface) because the system is very sensitive to the electron transfer and goes directly to compound **1d** (Figure 3a) once the external OH is reorganized from hydrogen bond

to O−O interaction. From the potential energy scan, the barrier is expected to be very low in the potential energy surface, further complicating the location of the transition state. We could estimate a free energy barrier of 5.5/5.6 kcal/mol as the difference between a long-range adduct and the separate reactants. It is worth noticing that we did not find a crossing between the curves corresponding to **2c** and **2d** in the potential energy surface, but this has no significant effect on the reactivity, as the free energy of the separate reactants associated with **2c** and the free energy of intermediate **2d** are almost equal, suggesting an easy crossing between surfaces. In addition, the relaxed scan was carried out in one dimension and probably the crossing would be related with the torsion of the Cu−O--OH bond but it is not relevant for the reactivity. For the connection between **1d** and **1e**, we could locate the transition state **TS 1d-e**, which was not reported in our previous communication.

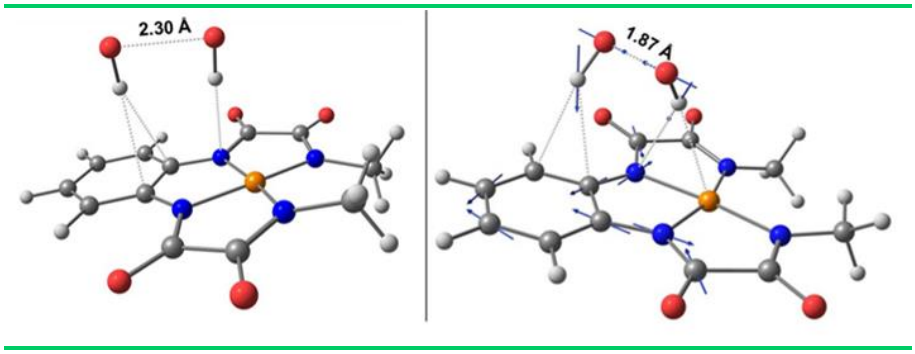

Figure 3. (a) Optimized structure for **1d**. (b) Optimized structure for **TS 1d-e**. Arrows indicate the displacement vectors of the normal mode associated with the imaginary frequency. Distances are in Å.

TS 1d-e (Figure 3b) contains an unpaired electron on the ligand (spin 1.0) and an additional open-shell between the copper (spin 0.6) and oxygen (spin −0.3 each) centers. This transition state has an energy 9.6 kcal/mol above intermediate **1d**, which increases to 13.9 kcal/mol if we take into account the off-cycle dissociation of **1d**. This constitutes the highest barrier in the process, which is thus obviously affordable at room

temperature. The origin of the barrier is the changes in the catalyst structure associated with the uptake of one electron, as the Cu−N distances increase from values between 1.88 and 1.91 Å in **1d** (a Cu(III) complex) to values between 1.98 and 2.10 Å in **1e** (a Cu(II) complex). Although the HO···OH moiety is not attached covalently to the metal center (only by hydrogen bonds), the transition vectors show clearly the involvement of the catalyst in the transition state. In addition, we analyzed the influence of explicit water molecules in this transition state, but there is no effect in our system (section 7 in the SI), probably due to the absence of proton release in the transition state.

The connection between **2d** (quartet) and **2e** (doublet) should take place through a minimum energy crossing point (MECP), which we could not locate for technical reasons (see computational details in the SI), but we could estimate for it a low relative energy of 2.9 kcal/mol from the relaxed potential energy scan. The origin of this transition state, and therefore the existence of the intermediate **2d** and the crossing point between **2d** and **2e**, is the reorganization energy in the metal complex due to the different oxidation states of the ligand in both species. For example, the Cu−N bond distances change from 2.09 to 2.10 Å in **2d** to 2.02−2.03 Å in **2e**. The existence of states with different multiplicities can be, in fact, related to the concept of multistate reactivity.[46] In spite of the minor differences between systems **1** and **2**, it is clear from Figure 2 that they share the same mechanism. We notice here that the possible intramolecular O−O bond formation process between the two hydroxyl ligands in **2c** was found to have a prohibitively high barrier (Figure S4). These mechanisms agree with the first order kinetic demonstrated for both catalysts.

A slightly different scenario is obtained for complex **3c**, where the ligand oxidation is very high in energy and thus the ligand is not oxidized, unlike the intermediates **1c** and **2c**. In contrast, the intermediate **3c** is oxidized at the Cu−O bond, producing a radical character on the oxygen atom. In this case, we could characterize an intramolecular WNA mechanism for

O−O formation, similar to the reported one by Zhang and coworkers in a dimeric copper system.[48] The reductive coupling between the hydroxyl and the oxyl center can take place through a transition state **TS 3c-d'** that is 7.0 kcal/mol above **3c** (Figure S5). In this transition state, the O−O bond formation occurs simultaneously with the reduction of Cu(III) to Cu(II). However, the SET-WNA pathway involving an external hydroxyl group gives a lower barrier (Figure S6). Indeed, there is a 2c-3e$^-$ O---O intermediate similar to those reported above, which evolves through a low energy path (Figure S6) toward the product. The highest point in this path is 3.6 kcal/mol above **3c**, thus significantly below the 7.0 kcal/mol reported above for the **TS 3c-d'** in the intramolecular WNA path.

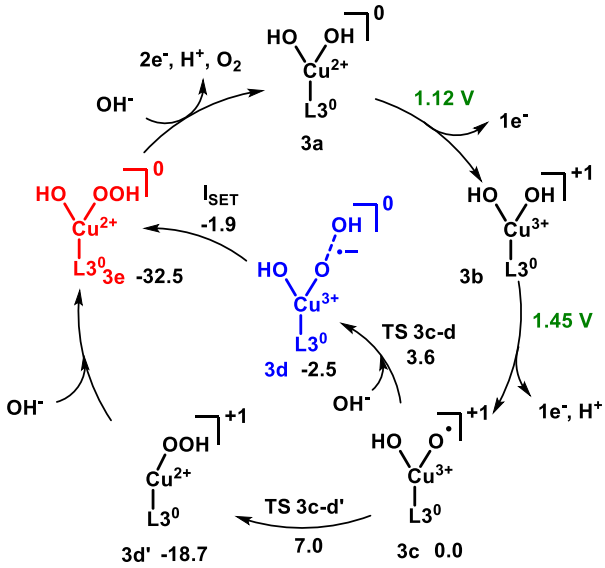

Figure 4. Catalytic cycle for the [(L3)Cu^{II}(OH)$_2$] complex where both the intramolecular WNA and intermolecular SET-WNA pathways are represented. Free energy changes for steps at the electrode are indicated explicitly in volts (green) and for steps in solution are indicated in kcal/mol with respect to **3c** (black).

The two catalytic pathways just described for the [(L3)-Cu^{II}(OH)$_2$] complex are summarized in Figure 4. It is worth mentioning here that the low barrier obtained for the SET-WNA mechanism in conjunction with the high potential needed to reach the active species in this **3c** system is fully

consistent with the reported turnover frequency of 100 s^{-1}, which is the highest described to date for Cu catalysts. More significantly, it confirms the prevalence of this type of mechanism for Cu-based water oxidation catalysts, even when the ligand is not involved in the redox process.

The computed barriers for the three systems reported above are in all cases below 15 kcal/mol, which suggests very fast reactions at room temperature. The observed reaction rates are not so fast in the experimental reports because of the low stability of the catalysts and the need for an oxidation reaction at the electrode for its generation, not considered in this work. The kinetic relevance of this oxidation at the electrode is, in fact, strongly suggested by the correlation between the applied overpotential and the overall turnover frequency.[31]

B.2.2 Extension to Ru systems? The case of [(L3)(damp)RuII(H_2O)]$^{2+}$.

We finally explored how the SET-WNA mechanism could perform in cases where the conventional WNA mechanisms are well established. We chose the [(L3)(damp)$Ru^{II}(H_2O)]^{2+}$ (damp = 2,6-bis((dimethylamino)-methyl)pyridine) system, hereafter [(L3)(L4)$Ru^{II}(H_2O)]^{2+}$, that has been studied both experimentally and computationally.[14] In eq 4 we present the oxidation sequence that has been reported for this system. The active species **4d** can be viewed also as having a formal Ru(IV) state, as there is a partial oxyl character (0.4 e^- in the oxygen and 0.6 in the Ru). A conventional WNA transition state has been computationally

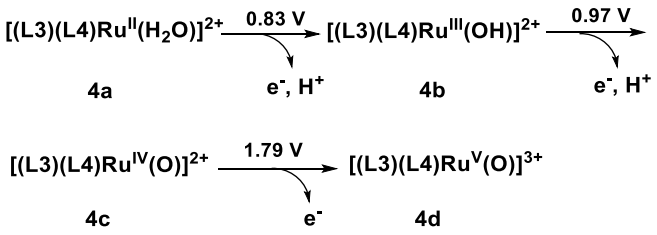

(4)

reported for the interaction of this complex with an external water molecule with a relative free energy of 20.7 kcal/mol. In this transition state, a lone electron pair of water attacks the oxygen center on ruthenium, and leads to a hydroperoxyl intermediate, $[(L3)(L4)Ru^{III}(OOH)]^{2+}$, releasing the proton to the water cluster in the transition state, that further evolves to generate dioxygen after one electron oxidation.

An eventual SET-WNA mechanism from **4d** should go through an intermediate where an electron is transferred from the external water to the complex. We found this process to be not feasible, and the results are summarized in Figure 5.

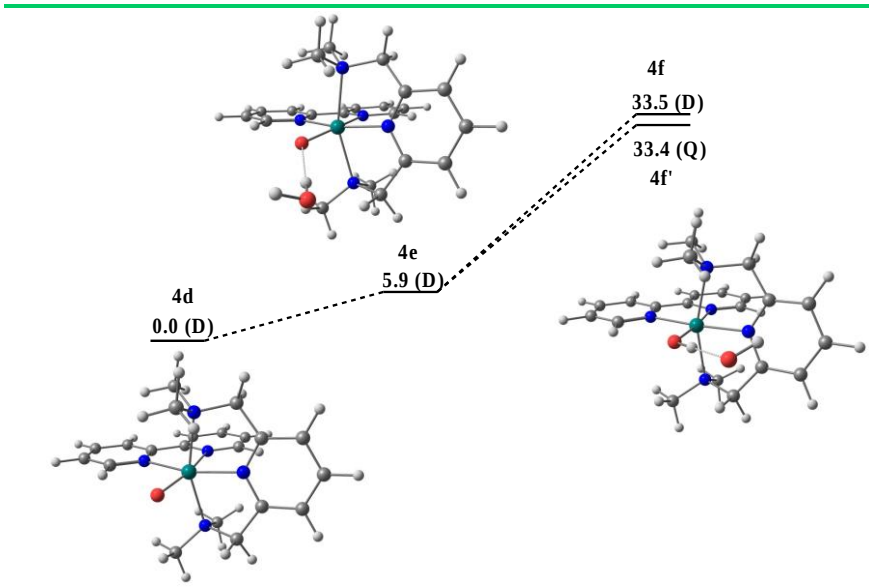

Figure 5. Free energy profile for the generation of $Ru^{IV}-OH---HO^{\bullet}$ intermediate in $[(L3)(L4)Ru^{II}(H_2O)]^{2+}$.

An adduct between the complex and the external water can be found, but the intermediate with the $2c-3e^-$ bond between the two oxygen atoms is not formed. We tried to force this type of species with transfer of a H• radical from water to the catalyst (in a way analogous to the R-H activation chemistry previously reported by Neese and co-workers).[46] We could reach in this way the Ru(IV) complex shown in Figure 4 (species **4f**). This

complex, either in the doublet or quadruplet state, has an energy more than 10 kcal/mol above the competing WNA transition state, most likely because the oxygen centered •OH radical is not sufficiently stabilized by the Ru−OH moiety. These results clearly indicate that the SET-WNA mechanism is not operative in the Ru WOC chemistry.

B.3. Overview of the new mechanistic scenario

The results reported above make a strong case that SET-WNA has to be added to the list of mechanisms available for water oxidation. We make an effort in this section to put together all available mechanisms in a single view, summarized in Figure 6. The overall process consists of the abstraction of at least two electrons, by either chemical or electrochemical methods from a metal complex, and the absorption by this complex of two electrons from two oxygen centers (each in formal oxidation state −2) to make a peroxide bond (each oxygen atom in formal oxidation state −1).

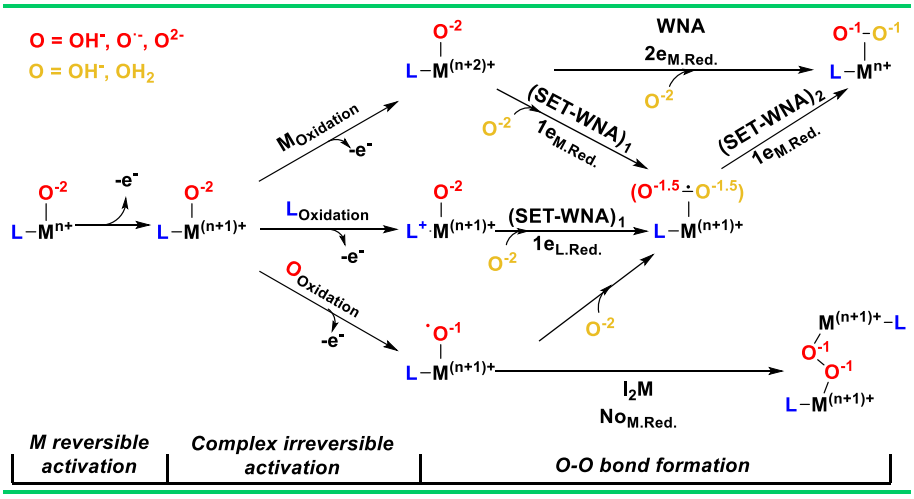

Figure 6. Overview of the water oxidation mechanisms. The oxygen initially attached to the metal is marked in red; the incoming oxygen is marked in yellow.

The left part of Figure 6 deals with the electron abstraction from the complex. The reaction usually starts with the oxidation of the metal center in

a reversible way. This step is shared by the four systems analyzed in this work, with the peculiarity that for the Ru the two electrons are mainly abstracted from the metal center. The next step involves the removal of an additional electron that can occur at three different sites within the complex: the metal center, the ancillary ligand, or the oxygen ligand itself. In Ru complexes with neutral ligands such as $[(L3)(L4)Ru^{II}(H_2O)]^{2+}$, described above, the electron is mainly abstracted from the metal center. In the $[(L3)Cu^{II}(OH)_2]$ system, the second electron is removed from the oxygen ligand, since the IV/III metal based redox potential for copper is very high. This produces the corresponding Cu(III)- oxyl species, that is very active. Finally, the combination of a metal difficult to oxidize and a redox-active ligand leads to an intermediate situation with a ligand-centered radical, as happens in $[(L1)Cu^{II}]^{2-}$ and $[(L2)Cu^{II}(OH_2)_2]$.

After the oxidation is completed, the system is ready for the O−O bond formation step. Again, three different mechanisms are available, water nucleophilic attack (WNA), single-electron transfer water nucleophilic attack (SET-WNA), and interaction of two M-O units (I2M). The WNA mechanism is formally the simplest, as it proceeds in one step through a single transition state. A lone pair in the external oxygen attacks the metal bound oxo center, which in turn transfers two electrons to the metal. As a result, the metal oxidation state is diminished by two units, and a single O−O bond is formed. The WNA mechanism thus requires a metal center in a high oxidation state, which can remove enough charge from the oxygen center to make it suitable for nucleophilic attack. This is most easily accomplished with second- or third-row transition metal centers, as is the case for the $[(L3)(L4)Ru^{II}(H_2O)]^{2+}$ discussed above. A second well-recognized mechanism is the I2M, which requires relatively accessible oxyl species that are able to couple. Each oxygen atom is already oxidized to oxidation state −1 by the external oxidant, and thus, formally no metal reduction takes place. This mechanism requires stable oxyl radical complexes with low charges, as the two complexes need to come together.

The additional mechanism we are proposing, SET-WNA, shares similarities with the two previously described but has some specific features. In SET-WNA, the external oxygen does not transfer two electrons in a single step to the complex, but makes two single one electron transfers. The most significant difference between the SET-WNA mechanism and the WNA and I2M just described is the formation of a $(HO\cdots OH)^-$ fragment, where there are two electrons in the σ O−O orbital and one in the σ* O−O, thus with a bond order of 0.5. We have shown in the examples above that it is operative for the three copper complexes studied. The SET-WNA mechanism completes the general scheme by connecting the two conventional mechanisms, as it may proceed in principle either from the $M^{(n+2)+}$ oxo systems typical of WNA or from the $M^{(n+1)+}$ oxyl systems typical of I2M. More significantly, SET-WNA depends critically on the stability of the $M^{(n+1)+}$ $(HO\cdots OH)^-$ intermediate, defining thus a new paradigm for catalyst optimization. The SET-WNA fits well with the characteristics of first row transition metals, and has been shown to operate with fast catalysts where the overpotential is easily controlled. The introduction of this new mechanism will help experimental and computational chemists to design new efficient WOCs based on first row transition metals as well as explore and characterize their low energy pathways.

B.4. Computatoinal details

All calculations were performed using the DFT approach with the B3LYP-D3 functional[49,50] using Gaussian09 as program package.[51] The selected basis set was 6-31+G(d) for C, N, O, and H,[52,53] and LANL2TZ(f) for Cu.[54,55] Solvation was introduced implicitly with water as the solvent. A pH of 11.5, corresponding to those of experimental system 1, was used when necessary. The explicit introduction of a water molecule was evaluated (Figure S7) and found to be not necessary. All geometry optimizations were carried out in solution without symmetry restrictions. Free energy corrections were calculated at 298.15 K and 105 Pa pressure,

including zero point energy corrections (ZPE). In addition, a correction term of 1.9 kcal/mol (at 298 K) was added when necessary to account for the standard state concentration of 1 M. We used this standard state to compare the effectiveness of the different catalyst regardless of the experimental conditions. Unless otherwise mentioned, all reported energy values are free energies in solution. We checked the stability with respect to excitations of the electronic state of intermediates **1d**, **2d**, **3d**, and **TS 1d-e**, and all of them were found to be stable.[56] The B3LYP-D3 computational method was benchmarked in a previous work and found to provide satisfactory results for this type of systems.[31] Full computational details, including those of benchmarking, are provided in the Supporting Information. A data set collection of computational results is available in the ioChem-BD repository[57] and can be accessed via https://doi.org/10.19061/iochem-bd-1-26.

B.5. Acknowledgments

We thank MINECO and FEDER (Grants CTQ2014-57761-R, CTQ-2016-80058-R, Severo Ochoa Excellence Accreditation 2014-2018 SEV-2013-0319, CTQ-2014-52974-REDC) and CERCA Programme/Generalitat de Catalunya for financial support. I.F.-A. thanks the Severo Ochoa predoctoral training fellowship (ref: SVP-2014-0686662). P.G.-B. thanks "La Caixa" foundation for a Ph.D. grant.

B.6. References

1 Melis, A. *Energy Environ. Sci.* **2012**, *5*, 5531–5539.

2 Gust, D.; Moore, T. A.; Moore, A. L. *Acc. Chem. Res.* **2009**, *42*, 1890–1898.

3 Nowotny, J.; Sorrell, C. C.; Sheppard, L. R.; Bak, T. *Int. J. Hydrogen Energy* **2005**, *30*, 521–544.

4 Cox, N.; Pantazis, D. A.; Neese, F.; Lubitz, W. *Acc. Chem. Res.* **2013**, *46*, 1588–1596.

5 Sun, L.; Hammarstrom, L.; Akermark, B.; Styring, S. *Chem. Soc. Rev.* **2001**, *30*, 36–49.

6 Alstrum-Acevedo, J. H.; Brennaman, M. K.; Meyer, T. J. *Inorg. Chem.* **2005**, *44*, 6802–6827.

7 Nocera, D. G. *Acc. Chem. Res.* **2012**, *45*, 767–776.

8 Youngblood, W. J.; Lee, S.-H. A.; Kobayashi, Y.; Hernandez-Pagan, E. A.; Hoertz, P. G.; Moore, T. A.; Moore, A. L.; Gust, D.; Mallouk, T. E. *J. Am. Chem. Soc.* **2009**, *131*, 926–927.

9 Dau, H.; Limberg, C.; Reier, T.; Risch, M.; Roggan, S.; Strasser, P. *ChemCatChem* **2010**, *2*, 724–761.

10 Sala, X.; Romero, I.; Rodríguez, M.; Escriche, L.; Llobet, A. *Angew. Chem., Int. Ed.* **2009**, *48*, 2842–2852.

11 Romain, S.; Vigara, L.; Llobet, A. *Acc. Chem. Res.* **2009**, *42*, 1944–1953.

12 Duan, L.; Bozoglian, F.; Mandal, S.; Stewart, B.; Privalov, T.; Llobet, A.; Sun, L. *Nat. Chem.* **2012**, *4*, 418–423.

13 Neudeck, S.; Maji, S.; López, I.; Meyer, S.; Meyer, F.; Llobet, A. *J. Am. Chem. Soc.* **2014**, 136, 24–27.

14 Vigara, L.; Ertem, M. Z.; Planas, N.; Bozoglian, F.; Leidel, N.; Dau, H.; Haumann, M.; Gagliardi, L.; Cramer, C. J.; Llobet, A. *Chem. Sci.* **2012**, *3*, 2576–2586.

15 Concepcion, J. J.; Jurss, J. W.; Brennaman, M. K.; Hoertz, P. G.; Patrocinio, A. O. T.; Murakami Iha, N. Y.; Templeton, J. L.; Meyer, T. J. *Acc. Chem. Res.* **2009**, *42*, 1954–1965.

16 Zong, R.; Thummel, R. P. *J. Am. Chem. Soc.* **2005**, *127*, 12802–12803.

17 Schulze, M.; Kunz, V.; Frischmann, P. D.; Würthner, F. *Nat. Chem.* **2016**, *8*, 576–583.

18 Hull, J. F.; Balcells, D.; Blakemore, J. D.; Incarvito, C. D.; Eisenstein, O.; Brudvig, G. W.; Crabtree, R. H. *J. Am. Chem. Soc.* **2009**, *131*, 8730–8731.

19 Lalrempuia, R.; McDaniel, N. D.; Müller-Bunz, H.; Bernhard, S.; Albrecht, M. *Angew. Chem., Int. Ed.* **2010**, *49*, 9765–9768.

20 Thomsen, J. M.; Sheehan, S. W.; Hashmi, S. M.; Campos, J.; Hintermair, U.; Crabtree, R. H.; Brudvig, G. W. *J. Am. Chem. Soc.* **2014**, *136*, 13826–13834.

21 Woods, J. A.; Bernhard, S.; Albrecht, M. In *Molecular Water Oxidation Catalysis*; Llobet, A., Ed.; John Wiley & Sons, Ltd: New York, **2014**; p 113.

22 McDaniel, N. D.; Coughlin, F. J.; Tinker, L. L.; Bernhard, S. *J. Am. Chem. Soc.* **2008**, *130*, 210–217.

23 Sala, X.; Maji, S.; Bofill, R.; García-Antón, J.; Escriche, L.; Llobet, A. *Acc. Chem. Res.* **2014**, *47*, 504–516.

24 Concepcion, J. J.; Tsai, M.-K.; Muckerman, J. T.; Meyer, T. J. *J. Am. Chem. Soc.* **2010**, *132*, 1545–1557

25 Yin, Q.; Tan, J. M.; Besson, C.; Geletii, Y. V.; Musaev, D. G.; Kuznetsov, A. E.; Luo, Z.; Hardcastle, K. I.; Hill, C. L. *Science* **2010**, *328*, 342–345.

26 Ellis, W. C.; McDaniel, N. D.; Bernhard, S.; Collins, T. J. *J. Am. Chem. Soc.* **2010**, *132*, 10990–10991.

27 Wasylenko, D. J.; Ganesamoorthy, C.; Borau-Garcia, J.; Berlinguette, C. P. *Chem. Commun.* 2011, *47*, 4249–4251.

28 Barnett, S. M.; Goldberg, K. I.; Mayer, J. M. *Nat. Chem.* **2012**, *4*, 498–502.

29 Zhang, M.-T.; Chen, Z.; Kang, P.; Meyer, T. J. *J. Am. Chem. Soc.* **2013**, *135*, 2048–2051.

30 Zhang, T.; Wang, C.; Liu, S.; Wang, J.-L.; Lin, W. *J. Am. Chem. Soc.* **2014**, *136*, 273–281.

31 Garrido-Barros, P.; Funes-Ardoiz, I.; Drouet, S.; Benet-Buchholz, J.; Maseras, F.; Llobet, A. *J. Am. Chem. Soc.* **2015**, *137*, 6758–6761.

32 Han, Y.; Wu, Y.; Lai, W.; Cao, R. *Inorg. Chem.* **2015**, *54*, 5604–5613.

33 Dogutan, D. K.; McGuire, R.; Nocera, D. G. *J. Am. Chem. Soc.* **2011**, *133*, 9178–9180.

34 Gerlach, D. L.; Bhagan, S.; Cruce, A. A.; Burks, D. B.; Nieto, I.; Truong, H. T.; Kelley, S. P.; Herbst-Gervasoni, C. J.; Jernigan, K. L.; Bowman, M. K.; Pan, S.; Zeller, M.; Papish, E. T. *Inorg. Chem.* **2014**, *53*, 12689–12698.

35 Pap, J. S.; Szyrwiel, L.; Sranko, D.; Kerner, Z.; Setner, B.; Szewczuk, Z.; Malinka, W. *Chem. Commun.* **2015**, *51*, 6322–6324 .

36 Rigsby, M. L.; Mandal, S.; Nam, W.; Spencer, L. C.; Llobet, A.; Stahl, S. S. *Chem. Sci.* **2012**, *3,* 3058–3062.

37 Karlsson, E. A.; Lee, B.-L.; Åkermark, T.; Johnston, E. V.; Kärkäs, M. D.; Sun, J.; Hansson, Ö.; Bäckvall, J.-E.; Åkermark, B. *Angew. Chem., Int. Ed.* **2011**, *50*, 11715–11718.

38 Young, K. J.; Takase, M. K.; Brudvig, G. W. *Inorg. Chem.* **2013**, *52*, 7615–7622.

39 Gao, Y.; Liu, J.; Wang, M.; Na, Y.; Åkermark, B.; Sun, L. *Tetrahedron* **2007**, *63*, 1987–1994.

40 Leung, C.-F.; Ng, S.-M.; Ko, C.-C.; Man, W.-L.; Wu, J.; Chen, L.; Lau, T.-C. *Energy Environ. Sci.* **2012**, *5*, 7903–7907.

41 Liao, R.-Z.; Li, X.-C.; Siegbahn, P. E. M.; Eur. J. *Inorg. Chem.* **2014**, 728–741.

42 Panda, C.; Debgupta, J.; Díaz Díaz, D.; Singh, K. K.; Sen Gupta, S.; Dhar, B. B. *J. Am. Chem. Soc.* **2014**, *136*, 12273–12282.

43 Ertem, M. Z.; Gagliardi, L.; Cramer, C. J. *Chem. Sci.* **2012**, *3*, 1293–1299.

44 García-Melchor, M.; Braga, A. A. C.; Lledós, A.; Ujaque, G.; Maseras, F. *Acc. Chem. Res.* **2013**, *46*, 2626–2634.

45 Shaik, S.; Kumar, D.; de Visser, S. P.; Altun, A.; Thiel, W. *Chem. Rev.* **2005**, *105*, 2279–2328.

46 Ye, S.; Geng, C.-Y.; Shaik, S.; Neese, F. *Phys. Chem. Chem. Phys.* **2013**, *15*, 8017–8030.

47 Harcourt, R. D. *J. Am. Chem. Soc.* **1980**, *102*, 5195–5201.

48 Su, X. -J.; Gao, M.; Jiao, L.; Liao, R. -Z.; Siegbahn, P. E. M.; Cheng, J. -P.; Zhang, M. -T. *Angew. Chem., Int. Ed.* **2015**, *54*, 4909–4914.

49 Becke, A. D. *J. Chem. Phys.* **1993**, *98*, 5648–5652.

50 Grimme, S.; Antony, J.; Ehrlich, S.; Krieg, H. *J. Chem. Phys.* **2010**, *132*, 154104.

51 Frisch, M. J.; Trucks, G. W.; Schlegel, H. B.; Scuseria, G. E.; Robb, M. A.; Cheeseman, J. R.; Scalmani, G.; Barone, V.; Mennucci, B.; Petersson, G. A.; Nakatsuji, H.; Caricato, M.; Li, X.; Hratchian, H. P.; Izmaylov, A. F.; Bloino, J.; Zheng, G.; Sonnenberg, J. L.; Hada, M.; Ehara, M.; Toyota, K.; Fukuda, R.; Hasegawa, J.; Ishida, M.; Nakajima, T.; Honda, Y.; Kitao, O.; Nakai, H.; Vreven, T.; Montgomery, J. A., Jr.; Peralta, J. E.; Ogliaro, F.; Bearpark, M.; Heyd, J. J.; Brothers, E.; Kudin, K. N.; Staroverov, V. N.; Kobayashi, R.; Normand, J.; Raghavachari, K.; Rendell, A.; Burant, J. C.; Iyengar, S. S.; Tomasi, J.; Cossi, M.; Rega, N.; Millam, J. M.; Klene, M.; Knox, J. E.; Cross, J. B.; Bakken, V.; Adamo, C.; Jaramillo, J.; Gomperts, R.; Stratmann, R. E.; Yazyev, O.; Austin, A. J.; Cammi, R.; Pomelli, C.; Ochterski, J. W.; Martin, R. L.; Morokuma, K.; Zakrzewski, V. G.; Voth, G. A.; Salvador, P.; Dannenberg, J. J.; Dapprich, S.; Daniels, A. D.; Farkas, Ö.; Foresman, J. B.; Ortiz, J. V.; Cioslowski, J.; Fox, D. J.Gaussian 09, Revision D.01; Gaussian, Inc.: Wallingford, CT, **2009**.

52 Francl, M. M.; Petro, W. J.; Hehre, W. J.; Binkley, J. S.; Gordon, M. S.; DeFrees, D. J.; Pople, J. A. *J. Chem. Phys.* **1982**, *77*, 3654–3665.

53 Clark, T.; Chandrasekhar, J.; Schleyer, P. V. R. *J. Comput. Chem.* **1983**, 4*,* 294–301.

54 Ehlers, A. W.; Böhme, M.; Dapprich, S.; Gobbi, A.; Höllwarth, A.; Jonas, V.; Köhler, K. F.; Stegmann, R.; Veldkamp, A.; Frenking, G. *Chem. Phys. Lett.* **1993**, *208*, 111–114.

55 Roy, L. E.; Hay, P. J.; Martin, R. L. *J. Chem. Theory Comput.* **2008**, *4*, 1029–1031.

56 Bauernschmitt, R.; Ahlrichs, R. J. Chem. Phys. 1996, 104, 9047–9052.

57 Alvarez-Moreno, M.; de Graaf, C.; Lopez, N.; Maseras, F.; Poblet, J. M.; Bo, C. *J. Chem. Inf. Model.* **2015**, *55*, 95–103.

B.7. Supporting information

Activation of $[(L2)Cu(OH_2)_2]$ Catalyst

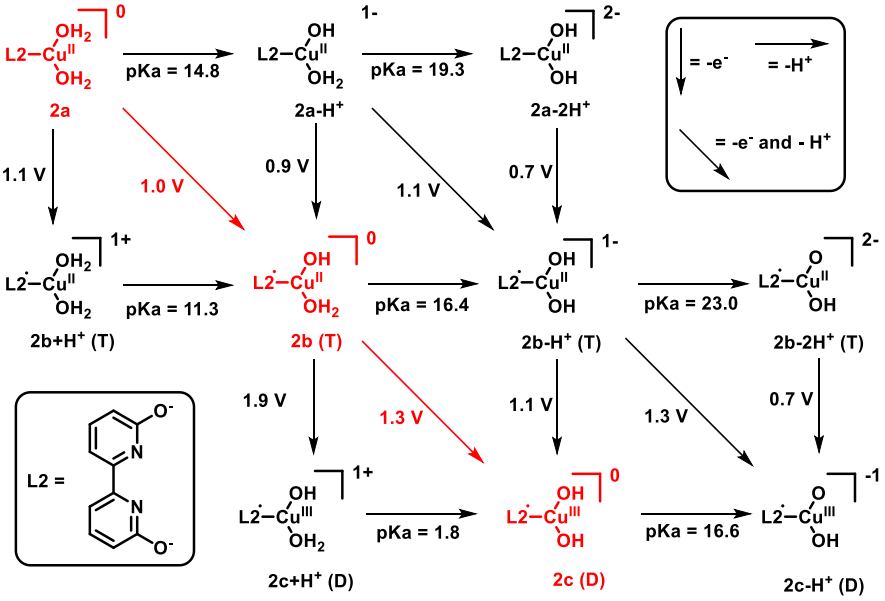

Figure S1. Possible pathways for $[(L2)Cu(OH_2)_2]$ catalyst activation. The PCET processes are calculated at 12.4 pH.

The activation of the Cu(II) complex takes place in two consecutive PCET processes, one at 1.0 V and the other at 1.3 V. In all the second row (after the first oxidation), the triplet state is always more stable than the singlet. The triplet is more stable due to the high delocalization of the unpaired electron inside the ligand. This explains small differences between our calculations and the previously reported ones. The key point from the previous calculations is in any case reproduced by our calculations: the species resulting after the second oxidation step has an unpaired electron in the ligand.

Activation of [(L3)Cu(OH)$_2$] Catalyst

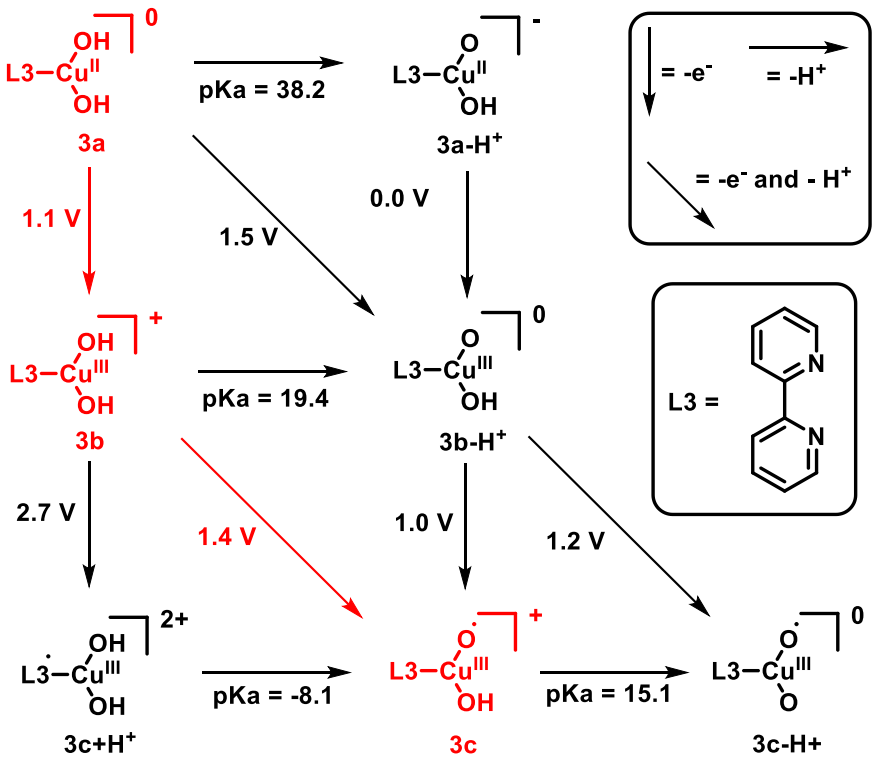

Figure S2. Possible pathways for [(L3)Cu^{II}(OH)$_2$] catalyst activation. The PCET processes are calculated at 12.5 pH.

The activation of the Cu(II) complex starts with the oxidation of the initial species **3a** at 1.1V. Afterwards, the PCET is the most favorable process at 1.4 V. We confirmed with our methodology the same active species than previously reported.

Comparison of spin distributions in key intermediates for systems $[(L1)Cu^{II}]^{2-}$ and $[(L2)Cu^{II}(OH_2)_2]$

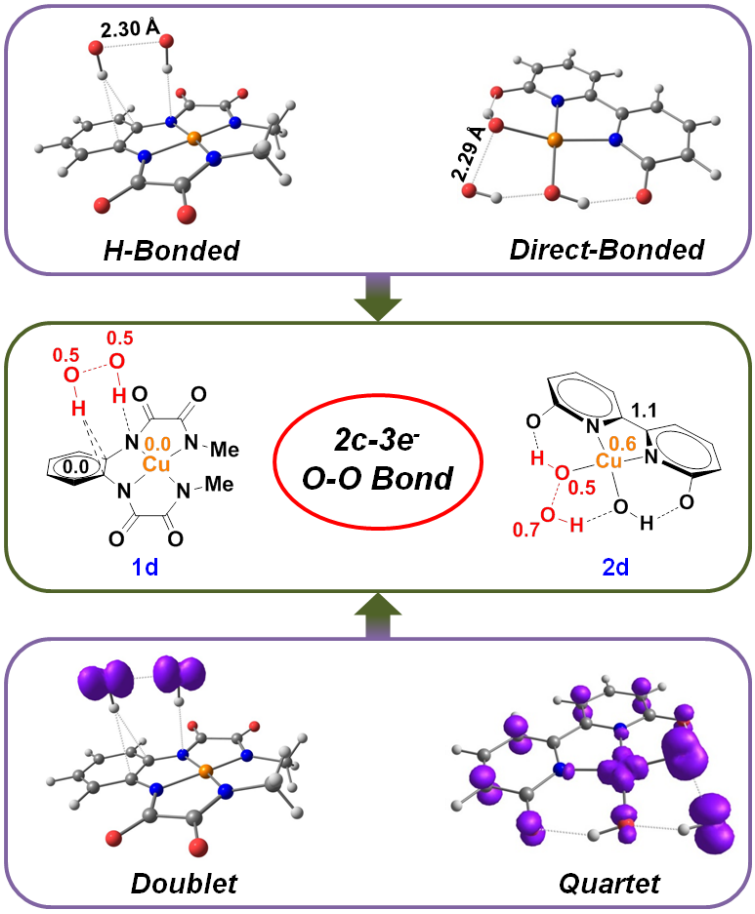

Figure S3. Comparison of the 2c-3e- species for $[(L1)Cu^{II}]^{2-}$ (left) and $[(L2)Cu^{II}(OH_2)_2]$ (right). The upper figures represent the molecular structure, the middle figures display the atom Mulliken spin densities and the bottom figures show the spin density distribution.

Intramolecular Relaxed Scan of 2c

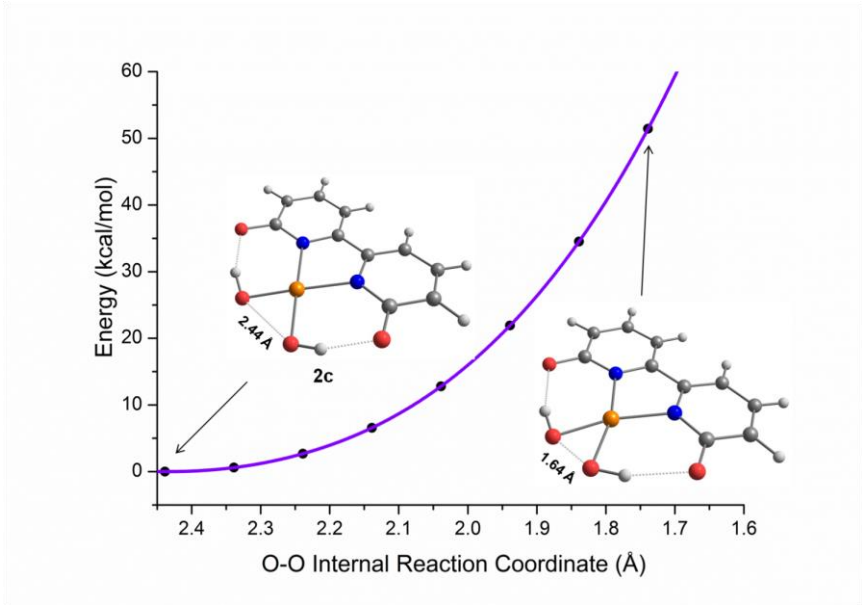

Figure S4. Potential energy relaxed scan of the intramolecular HO---OH coupling in **2c** intermediate. Energies relative to species X in kcal/mol.

The intramolecular coupling is not possible in the intermediate **2c**. The barrier increases above 50 kcal/mol, which is far higher than the SET-WNA calculated process.

Intramolecular Relaxed Scan of 3c

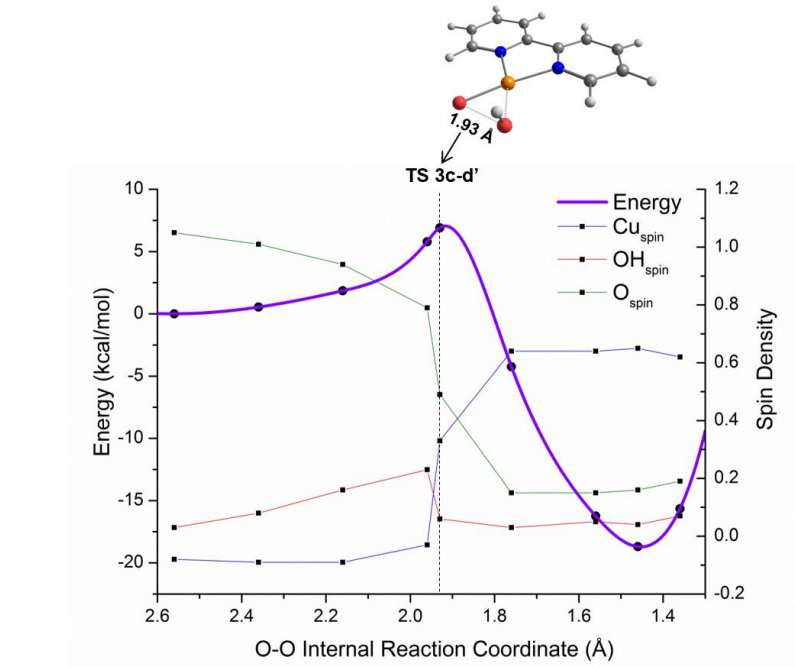

Figure S5. Potential energy relaxed scan of the intramolecular HO---O· coupling in intermediate **3c**. Energies relative to species **3c** in kcal/mol. Spin densities of all displayed species are shown in green (O), red (OH) and blue (Cu).

The intramolecular coupling mechanism was found from intermediate **2c** but the barrier is higher than the SET-WNA process (7.0 vs 3.6 kcal/mol). The transition state is clearly concerted with an electron transferring from the oxyl moiety to the copper metal center. The main difference to the $[(L2)Cu(OH_2)_2]$ species is that the O moiety is actually oxidized at the intermediate 3c instead of the ligand. This fact makes one oxygen (the OH) nucleophilic and the other (O) electrophilic, allowing the "nucleophilic" attack of the OH moiety to the formal O with one electron released from the O to the copper during the transition state.

SET-WNA profile and scan in process in [(L3)Cu^{II}(OH)$_2$]

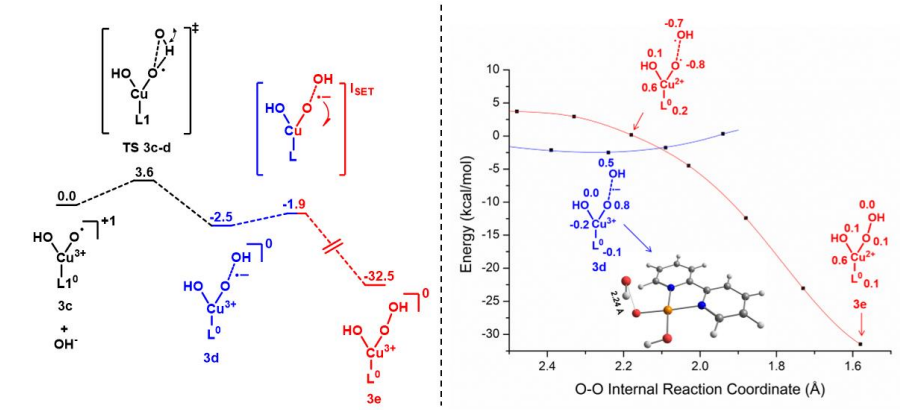

Figure S6. (Left) Free energy profiles of [(L3)Cu^{II}(OH)$_2$] where L3 = 2,2'-bipyridine. ISET energy obtained from the potential energy scan. Energies in kcal/mol. (Right) Potential energy relaxed scan of both complexes of the O-O reaction coordinate.

Influence of added water molecules in catalysis by $[(L1)Cu^{II}]^{2-}$

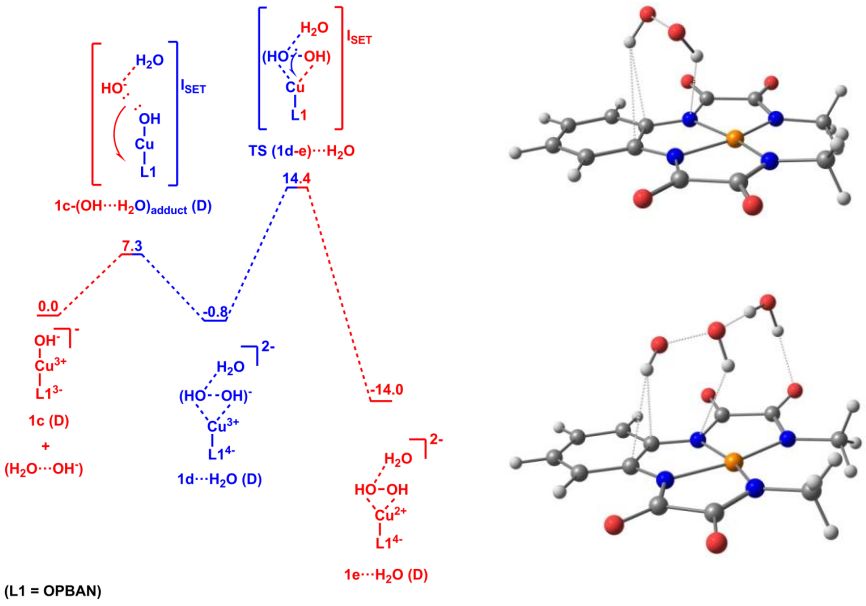

Figure S7. (Left) Free energy profile of the optimization of a water molecule with the frozen optimized structure of the $[(L1)Cu^{II}]^{2-}$ catalyst. Energies in kcal/mol. (Right) Optimized structure for **TS (1d-e)** (top) and **TS (1d-e)···H_2O** (bottom).

We repeated the calculation of all species involved in the O-O formation process with $[(L1)Cu^{II}]^{2-}$ with the addition of an explicit water solvent molecules. In most cases, the procedure consisted of freezing the fragment reported in the main text and letting the water molecule to optimize. In all cases, the water molecule ended forming a hydrogen bond with a hydroxo group. More significantly, as can be seen by comparing Fig. 2 and Fig. S3, in all cases the free energy of the system was higher than that of the separated fragments complex plus water. The enthalpic binding between the two fragments is too small to overcome the entropic tendency of the fragments to separate. This result was further confirmed by a full geometry optimization of the transition state with an extra water molecule, also shown in Fig. S3. The free energy was in this case 1.8

kcal/mol above that of the system with the separated water, thus confirming that the addition of an extra solvent molecule in the first coordination sphere does not affect our calculations.

Full Computational Details

All calculations were carried out with the Gaussian09 program package[1] using the DFT method. The selected functional was B3LYP with empirical dispersion correction proposed by Grimme (B3LYP-D3).[2,3] The selected basis set was 6-31+G(d) for C, N, O and H,[4] and LANL2TZ(f) for Cu.[5,6] Solvation was introduced implicitly through the SMD model,[7] with water as the solvent. All geometry optimizations were computed in solution without symmetry restrictions. We confirmed the nature of all computed stationary points as minima or transition states through vibrational frequency calculations. Free energy corrections were calculated at 298.15 K and 105 Pa pressure, including zero point energy corrections (ZPE). In addition, a correction term of 1.9 kcal/mol (at 298 K) was added when necessary to account for the standard state concentration of 1 M. Unless otherwise mentioned, all reported energy values are free energies in solution.

In the cases where the transition states cannot be found (or do not exist) we estimate the reaction energy barriers from potential energy relaxes scan, applying entropic corrections from the minima to compute an estimated free energy change.

In the transformation from free energies to electrochemical magnitudes we took from the chemical Literature the values of 4.28 V for the absolute potential of the standard hydrogen electrode[8] and-11.72 eV for the free energy of the proton in aqueous solution at pH=1.[9] The value for the free energy of the proton was translated to the experimental pH value by adding a correction term of -0.059*pH, following the same procedure as other authors.[10] The experimental pH was 11.5 for catalyst **1**, 12.4 for catalyst **2** and 12.5 for catalyst **3**.

Finally, for the calculations with explicit water molecules included (section S8), the general procedure was to freeze the catalyst with the OH groups (**1c**, **1d**, **TS (1d-e)** and **1e**) and to optimize a water molecule around the catalyst. The validity of this simplified treatment was confirmed through a full optimization of the transition state **TS (1d-e)···H_2O** without any restrictions, which provided nearly identical results.

The functional for the DFT calculations was B3LYP-D3 based on the calibration carried out in a previous work on related systems,[11] where its performance was compared with that of M06, M06-D3, M06L, M06-2X, ωB97xD and B97D.

References

1 Gaussian 09, Revision D.1, M. J. Frisch, G. W. Trucks, H. B. Schlegel, G. E. Scuseria, M. A. Robb, J. R. Cheeseman, G. Scalmani, V. Barone, B. Mennucci, G. A. Petersson, H. Nakatsuji, M. Caricato, X. Li, H. P. Hratchian, A. F. Izmaylov, J. Bloino, G. Zheng, J. L. Sonnenberg, M. Hada, M. Ehara, K. Toyota, R. Fukuda, J. Hasegawa, M. Ishida, T. Nakajima, Y. Honda, O. Kitao, H. Nakai, T. Vreven, J. A. Montgomery, Jr., J. E. Peralta, F. Ogliaro, M. Bearpark, J. J. Heyd, E. Brothers, K. N. Kudin, V. N. Staroverov, R. Kobayashi, J. Normand, K. Raghavachari, A. Rendell, J. C. Burant, S. S. Iyengar, J. Tomasi, M. Cossi, N. Rega, J. M. Millam, M. Klene, J. E. Knox, J. B. Cross, V. Bakken, C. Adamo, J. Jaramillo, R. Gomperts, R. E. Stratmann, O. Yazyev, A. J. Austin, R. Cammi, C. Pomelli, J. W. Ochterski, R. L. Martin, K. Morokuma, V. G. Zakrzewski, G. A. Voth, P. Salvador, J. J. Dannenberg, S. Dapprich, A. D. Daniels, Ö. Farkas, J. B. Foresman, J. V. Ortiz, J. Cioslowski, and D. J. Fox, Gaussian, Inc., Wallingford CT, **2009**.

2 A.D. Becke, *J. Chem. Phys.***1993**, *98*, 5648.

3 S. Grimme, J. Antony, S. Ehrlich, H. Krieg, *J. Chem. Phys.***2010**, *132*, 154104.

4 a) W.J. Hehre, R. Ditchfield, J.A. Pople, J. Chem. Phys. **1972**, 56, 2257. b) P.C. Hariharan, J.A. Pople, *Theoret. ChimicaActa***1973**, *28*, 213. c) M.M. Francl, W.J. Petro, W.J. Hehre, J.S. Binkley, M.S. Gordon, D.J. DeFrees and J.A. Pople, *J. Chem. Phys.***1982**, *77*, 3654.

5 a) P. J. Hay, W. R. Wadt, *J. Chem. Phys.***1985**, *82*, 270. b) P. J. Hay, W. R. Wadt, *J. Chem. Phys.***1985**, *82*, 284. c) P. J. Hay, W. R. Wadt, *J. Chem. Phys.***1985**, *82*, 299.

6Taken from EMSL Basis set Library: a) D. Felier, *J. Comp. Chem.***1996**, *17*, 1571. b) K.L. Schuchardt, B.T. Didier, T. Elsethagen, L. Sun, V. Gurumoorthi, J. Chase, J. Li, T.L. Windus, *J. Chem. Inf. Model.*, **2007**, *47*, 1045.

7 S. A. V. Marenich, C. J. Cramer, D. G. Truhlar, *J. Phys. Chem. B*, **2009**, *113,* 6378.

8a) A. Lewis, J. A. Bumpus, D. G. Truhlar, C. J. Cramer *J. Chem. Ed.***2004**, *81*, 596. b) A. Lewis, J. A. Bumpus, D. G. Truhlar, C. J. Cramer *J. Chem. Ed.***2007**, *84*, 934 [Erratum].

9 A. V. Marenich, A. Majunmdar, M. Lenz, C. J. Cramer, D. G. Truhlar, *Angew. Chem. Int. Ed.***2012**, *51*, 12810.

10S.G. Winikoff, C.J. Cramer, *Catal. Sci. Technol.***2014**, *4*, 2484.

11 P. Garrido-Barros, I. Funes-Ardoiz, S. Drouet, J. Benet-Buchholz, F. Maseras, A. Llobet, *J. Am. Chem. Soc.* **2015**, *137*, 6748-6761.

Chapter 4

From ligand-based to metal-based electron transfer in water oxidation catalysis

New copper complexes are developed for water oxidation catalysis bearing different scafolds. The first two complexes contains redox non-innocent ligands that can accumulate two oxidative equivalents so that the metal center act as an spectator in the electron transfer processes. A third complex has been synthetized bearing a redox innocent ligand. Those systems allow to explore the opportunities and limitations of using redox non-inocent ligands.

From ligand-based to metal-based electron transfer in water oxidation catalysis

Paper C: Ligand based water oxidation catalysis

Gil-Sepulcre, M.; Garrido-Barros, P.; Funes-Ardoiz, I.; Maseras, F.; Llobet, A. **2018**, *manuscript in preparation*

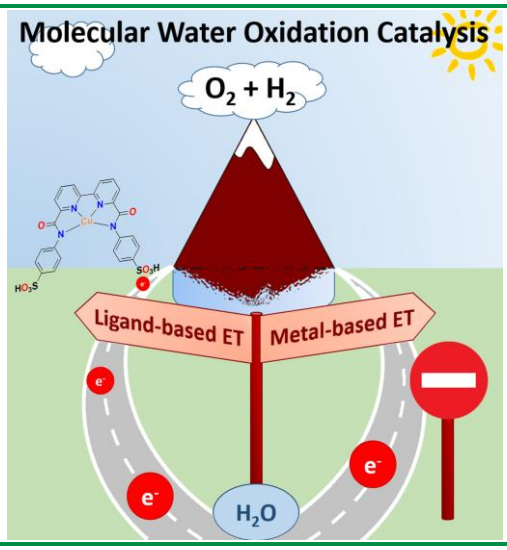

IV

Abstract

Two new tetradentate ligands, 4,4'-(([2,2'-bipyridine]-6,6'-dicarbonyl)bis(azanediyl)) dibenzenesulfonic acid (*p*-L) and its homologue containing the sulfonate group at ortho position with respect to the amidate scaffold (*o*-L), have been synthesized. These new ligands have been used for the preparation of the complexes of general formula $[(L)Cu^{II}]^{2-}$ (L = *p*-L (**1**$^{2-}$); L = *o*-L (**2**$^{2-}$)), which have been fully characterized by X-ray diffraction and electrochemical techniques. At pH 11.4 only complex **1**$^{2-}$ exhibits a raise in the current associated with water oxidation (WO) at an overpotential of 835 mV confirmed by O_2-detection experiments during 1 hour of bulk electrolysis at 1.6 V vs. NHE. Electrochemical and computational studies reveal the important redox non-innocent character of the ligand, whose oxidation is directly involved in the water oxidation mechanism. In contrast, the oxidation state of the metal center remains unchanged during catalysis.

Chapter 4

Contributions:

Pablo Garrido Barros performed the computational calculations and, together with Marcos Gil-Sepulcre, carried out the preparation and characterization of the compounds, the electrochemical and spectroscopic analysis, and the preparation of the manuscript.

C.1. Introduction

Molecular water oxidation (WO) driven by transition metal complexes[1,2,3] is a promising and active field at present for its implication in the obtaining of solar fuels from water and sunlight.[4] In particular, molecular complexes offers an accessible platform to study the mechanistic aspect of the catalytic reaction and the factors that determine its kinetic. That information is an indispensable tool for the design of more active catalysts.[5]

Moreover, the possibility to anchor those complexes on the surface of electrodes bases the strategy of generating molecular hybrid material for fast and stable catalysis.[6,7,8,9,10,11] However, developing an efficient and robust water splitting device using cheap and abundant non-noble metal catalysts is still a great challenge for the scientific community. Several first-row transition metal complexes such as iron,[12] cobalt,[13] manganese[14] and copper[15,16,17,18,19,20,21] have been developed and tested towards WO, becoming a promising alternative to the extensively studied ruthenium[22,23] and iridium[24] catalysts. In particular, molecular copper-based complexes are relative new actors in this field and have become attractive candidates for WO catalysis during the last years due to their earth-abundance, relative easy synthesis and the available exhaustive studies on their coordination chemistry.

Elizarova first[25] and Mayer and co-workers later reported on Cu(II) complexes bearing a simple 2,2'-bipyridine ligand, which were capable of

oxidizing water into dioxygen.[15] Since this first works, the bipyridine moiety has been modified by introducing hydroxyl pendant groups.[18] These groups confer the redox-active character of the ligand so that they are able to lower the overpotentials, facilitating the proton coupled electron transfer (PCET) process and stabilizing the key intermediates. The potential of redox-active ligands for water oxidation catalysis was further explored by our group. We recently reported on a family of new Cu(II) complexes that are capable to drastically downshift the overpotential to a value as low as 170 mV.[20] The key for this unprecedented overpotential is the presence of four amidate groups, which decrease the potential of the Cu(III)/Cu(II) couple, together with the non-innocent nature of the ligand that allows a fine control on the overpotential by changing the substituents in the aromatic ring.

One of the key factor using redox active ligands is precisely the opportunity to avoid the high oxidation states of the metal centers, which are normally energetic intermediates reactive toward the formation of stable and active metal oxides.[26] Moreover, a number of biological reaction involving natural copper complexes proceed with the formation of radical intermediates in the organic moieties as they usually lead to fast reaction kinetics.[27] Therefore, studying the electron transfer processes in radical copper complexes is essential for understanding how they work and favoring the desired catalytic reactions.

Herein, we present the synthesis and full characterization of a new family of Cu(II) complexes [(*p*-L)Cu](Na)$_2$ (**1**$^{2-}$) and [(*o*-L)Cu](Na)$_2$ (**2**$^{2-}$) containing two new tetra-anionic ligands 4,4'-(([2,2'-bipyridine]-6,6'-dicarbonyl)bis(azanediyl)) dibenzenesulfonic acid (*p*-L) and 2,2'-(([2,2'-bipyridine]-6,6'-dicarbonyl)bis(azanediyl)) dibenzenesulfonic acid (*o*-L), which differ in the position of the sulfonate group with respect to the amide moiety (Scheme 1). We evaluate their behavior as redox active ligands and their role in the water oxidation catalysis.

Scheme 1. Schematic drawing of the ligands described in this work.

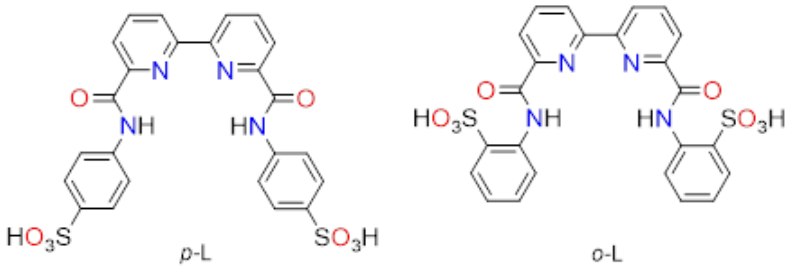

C.2. Results and Discussion

C.2.1. Synthesis and characterization of complexes $\mathbf{1}^{2-}$ *and* $\mathbf{2}^{2-}$.

The new ligands 4,4'-(([2,2'-bipyridine]-6,6'-dicarbonyl)bis(azanediyl)) dibenzenesulfonic acid (*p*-L) and 2,2'-(([2,2'-bipyridine]-6,6' dicarbonyl)bis(azanediyl)) dibenzenesulfonic acid (*o*-L) were synthetized via the reaction of the corresponding sulfanilic acid with [2,2'-bipyridine]-6,6'-dicarboxylic acid after its previous conversion into the corresponding acyl chloride with $SOCl_2$. Both were obtained as white powders in high yield (85 % and 82 % for *p*-L and *o*-L respectively); a detailed description of their synthetic pathways is provided in the Electronic Supplementary Information together with a full characterization by ^{1}H-NMR, ^{13}C-NMR and ESI-MS (Figures S1-11 and S14-15). It is interesting to note the 2 ppm downfield shift of the amide proton observed in the ^{1}H-NMR spectrum of *o*-L (vs *p*-L) due to the proximity of the sulfonate groups. Suitable crystals for X-ray diffraction analysis were also obtained for *o*-L by slow diffusion of EtOH in an aqueous solution of the ligand (Figure S19 and Table S1).

Synthesis of $\mathbf{1}^{2-}$ and $\mathbf{2}^{2-}$ involved the use of NaOH(aq.) in MeOH as a base to deprotonate the amidate groups of the corresponding ligand, which then react with $Cu(ClO_4)_2$ to form the copper complex. The purification was carried out via evaporation of MeOH and crystallization by slow diffusion of acetone into the remaining aqueous solution, yielding $\mathbf{1}^{2-}$ and $\mathbf{2}^{2-}$

as green and blue crystals respectively. We obtained a moderate yield around 30%, which could be related with the partial conversion of the Cu^{2+} precursor into copper hydroxide in basic media.[28] Both complexes were characterized by X-ray diffraction (Figure 1), UV-Vis spectroscopy, mass spectrometry and elemental analysis (Figures S16-18).

The X-Ray structure of complex $\mathbf{1}^{2-}$ (Figure 1, left, and Table S3) confirmed the presence of a Cu(II) metal center with a distorted square planar geometry bonded to the four N donor atoms. There is also a contact or slightly elongated bond with an oxygen atom in the apical position at a distance of 2.31 Å, probably coming from one water molecule. All Cu–N_{bpy} distances are 1.95 Å and close to 2.00 Å for the Cu–N_{amide} bonds, thus manifesting a strong coordination to the metal center. On the other hand, the rigidity of the *p*-L scaffold is made patent when observing the N_{amide}–Cu–N_{amide} (119.69º) and N_{bpy}–Cu–N_{bpy} (78.27º) angles, which are far from the ideal square planar geometry (90º). Complex $\mathbf{2}^{2-}$ (Figure 1, right, and Table S2) also displays a distorted square planar geometry, showing similar Cu – N bond distances (1.95-2.00 Å) and N_{amide}–Cu–N_{amide} (120.78º) and N_{bpy}–Cu–N_{bpy} (78.49º) angles to those in $\mathbf{1}^{2-}$. However, some significant differences arise between $\mathbf{1}^{2-}$ and $\mathbf{2}^{2-}$. First, the apical position of $\mathbf{2}^{2-}$ is occupied by an oxygen atom from the sulfonate moiety (instead of the water molecule observed in $\mathbf{1}^{2-}$), which is in contact with a Cu–O distance of 2.61 Å. Then, weak π-π stacking interactions at 3.77 Å between both phenyl groups take place for complex $\mathbf{2}^{2-}$.

It is also interesting to note that the disposition of the sulfonate moieties in *para* with respect to the amide moieties facilitates the formation of an interesting polymeric-type 2D framework connected through the sulfonate groups (Figure S20).

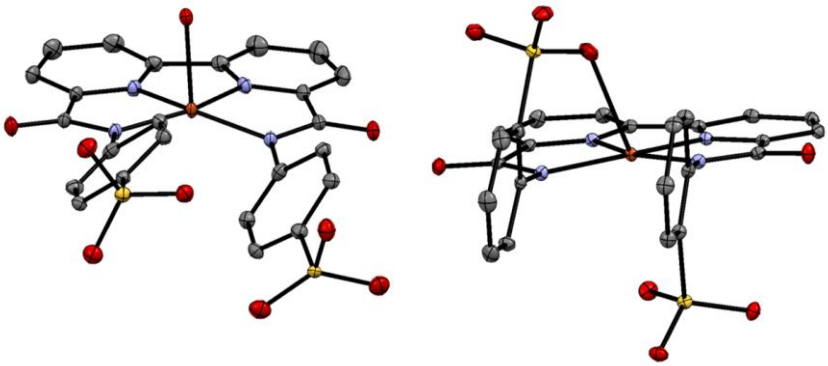

Figure 1. ORTEP representation of $\mathbf{1a}^{2-}$ (left) and $\mathbf{2a}^{2-}$ (right) at 50% probability level. The solvent molecules, sodium and hydrogen atoms have been omitted for clarity. Colour code: C, grey; N, blue; O, red; S, yellow; Cu, orange.

C.2.2. Electrochemical behavior DMF

The redox properties of both ligands were first investigated in DMF by electrochemical techniques. All the potentials presented in this work are referenced vs. NHE by adding 0.648 V to the measured potential (see Experimental Section for further details). As observed in the cyclic voltammetry (CV) measurements of the free ligands (Figure S21), they exhibit an irreversible wave at $E_{p,a}^{L}$ = 1.29 V for *p*-L and $E_{p,a}^{L'}$ = 1.24 V for *o*-L, thus suggesting their non-innocent redox character. Then, we studied the electrochemical behavior of the copper complexes $\mathbf{1}^{2-}$ and $\mathbf{2}^{2-}$ that is presented in Figure 2. The initial anodic scan for $\mathbf{1}^{2-}$ shows two irreversible electron transfer processes at $E_{p,a}^{1}$ = 1.21 V and $E_{p,a}^{2}$ = 1.42 V. In the case of $\mathbf{2}^{2-}$, these waves appear at $E_{p,a}^{1'}$ = 1.00 V and $E_{p,a}^{2'}$ = 1.19 V, thus showing a smaller shift (195 mV) between them compared to $\mathbf{1}^{2-}$ (210 mV). The presence of two anodic peaks has also been confirmed by DPV (Figure S22).

From ligand-based to metal-based electron transfer in water oxidation catalysis

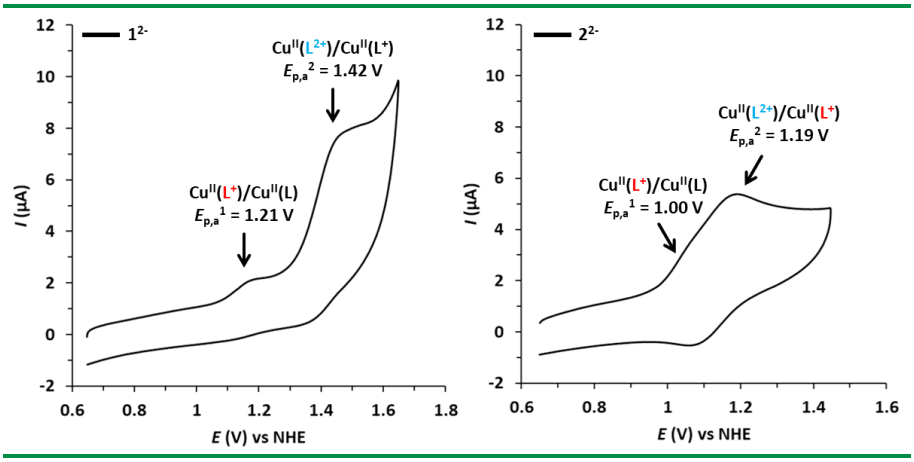

Figure 2. Cyclic Voltammograms of $\mathbf{1}^{2-}$ (left) and $\mathbf{2}^{2-}$ (right) in DMF containing 0.1 M of TBAPF. Conditions: scan rate of 100 mV/s and [Complex] = 1 mM.

IV

Since Zn is a redox non-active metal, the homologues $[(p\text{-L})Zn^{II}]^{2-}$ and $[(o\text{-L})Zn^{II}]^{2-}$ were synthetized in order to study the nature of the electron transfers. Two irreversible oxidation waves, $E_{p,a}{}^{1} = 1.01$ V and $E_{p,a}{}^{2} = 1.20$ V for $[(p\text{-L})Zn^{II}]^{2-}$ and $E_{p,a}{}^{1'} = 0.87$ V and $E_{p,a}{}^{2'} = 1.02$ V for $[(o\text{-L})Zn^{II}]^{2-}$ were observed in the CV experiments of these complexes (Figure S26), revealing the capability of the ligands to undergo two oxidation processes once bonded to a metal center. Those oxidation waves are also shifted roughly 150-200 mV respect to the corresponding Cu(II) complexes, as was expected due to the more electron deficient character of the Cu(II) metal center.

Therefore, the redox processes observed both for $\mathbf{1}^{2-}$ and $\mathbf{2}^{2-}$ in organic media (DMF) were associated with two consecutive ligand-based oxidations. The difference in the $E_{p,a}$ values (230 mV) between complexes $\mathbf{1}^{2-}$ and $\mathbf{2}^{2-}$ suggests that the ligand oxidation may occur in the phenyl moieties, in contrast with the similar values in the potentials which would be expected if the oxidation was centered in the similar bipyridyl rings. Moreover, formation of radical cations in phenyl moieties during water oxidation catalysis has been previously reported in the literature[20,11] while bipyridyl rings appears to be more redox innocent.[15,21]

In case of $\mathbf{1}^{2-}$, the first and second oxidation waves are irreversible in a scan rate window of 25-500 mV/s (Figure S23). On the other hand, the waves of $\mathbf{2}^{2-}$ turned reversible at higher scan rates. This is also consistent, with the higher stability of the trans arrangements of the sulfonate groups in $\mathbf{2}^{2-}$.

A higher increase in the current of the second oxidation wave of $\mathbf{1}^{2-}$ with respect to $\mathbf{2}^{2-}$ can be also appreciated. This behavior is probably related with a higher reactivity of complex $\mathbf{1}^{2-}$ respect to $\mathbf{2}^{2-}$, which after the formation of the diradical species [(p-L^{2+})Cu^{II}] is more reactive toward oxidative processes, provoking an increase in the current and the irreversible character.

In the exploration of cathodic potentials, CVs of complex $\mathbf{1}^{2-}$ and $\mathbf{2}^{2-}$ showed the presence of one irreversible reduction wave at an $E_{p,c}$ value around -0.4 V for both cases (Figure S24). Those reduction processes can be assigned to the reduction of Cu(II) to Cu(I). The observed irreversible character of the Cu(II)/Cu(I) wave is highly consistent with the oxidation wave appearing around E = 0.34 V in the corresponding anodic scan, which is related with the oxidation of solvated Cu(I) resulting from complex degradation. This is further confirmed by the CV of $Cu(ClO_4)_2$ shown in Figure S25 that features a reversible wave at around 0.34 V due to the Cu(II)/Cu(I) redox couple from free copper ions in solution. One plausible explanation for the demetallation process could be the preferred tetrahedral geometry of Cu(I) complexes. Therefore, the reduction of the square planar Cu(II) complexes brings the need of Cu(I) to adopt a tetrahedral disposition, which is not allowed by the highly rigid planar ligand, provoking eventually the breakage of the Cu-N bonds and subsequent release of Cu(I) ions.

C.2.3. Electrochemical Water Oxidation Catalysis

In order to test the electrocatalytic activity of complexes $\mathbf{1}^{2-}$ and $\mathbf{2}^{2-}$ toward water oxidation, their electrochemical behavior was analyzed in aqueous solutions at different pH values (Figures S27-29). The initial CVs performed at pH 7 and 9 show a wide oxidative wave centered at 1.37 V for $\mathbf{1}^{2-}$ and 1.27 V for $\mathbf{2}^{2-}$, both assigned to ligand-based oxidations according with previous measurements in DMF. Similarly, the non-reversible character of those waves can be again explained by the formation of highly reactive radical species in aqueous media, which in the absence of catalytic activity, may be followed by reactions leading to degradation of the complex.

Those experiments also showed the pH independent character of the electron-transfer processes (Figure S30). This behavior indicates that there is no proton coupled electron transfer derived from the sulfonate groups or possible coordinated water molecules in the apical position of complex $\mathbf{1}^{2-}$ in the working pH range (7-11.4). This observation nicely agrees with the DFT calculations as discussed in following section, which show the low pKa value for the sulfonate groups and the disfavored coordination of solvent molecules in the apical position.

Interestingly, at the more basic pH, there is an apparent increase in the current of the ligand-based oxidation in complex $\mathbf{1}^{2-}$ suggesting that a possible electrocatytic process might be taking place. However, the increase in the background current from glassy carbon oxidation at high potential and pH partially overlaps with previous electrocatalytic process. In the case of complex $\mathbf{2}^{2-}$, the increase in the current seems to be only associated to the increased signal of the background.

We repeated the experiments performed at pH 11.4 using the more oxidative robust Boron Doped Diamond (BDD) electrode with the aim of avoiding the residual current derived from the glassy carbon electrode

mentioned above. As expected, $\mathbf{1}^{2-}$ displays a steep rise in the current starting at around 1.30 V clearly differentiated from the background signal of the electrode in buffer solution, which is tentatively assigned to electrocatalytic water oxidation (Figure 3). In contrast, the apparent absence of electrocatalytic current above the blank in the experiments performed with $\mathbf{2}^{2-}$ strongly suggests its inactivity towards water oxidation. Instead, a wide oxidation peak is observed with a relative irreversible character that we relate to the one or two electron oxidation of the ligand followed by its partial degradation.

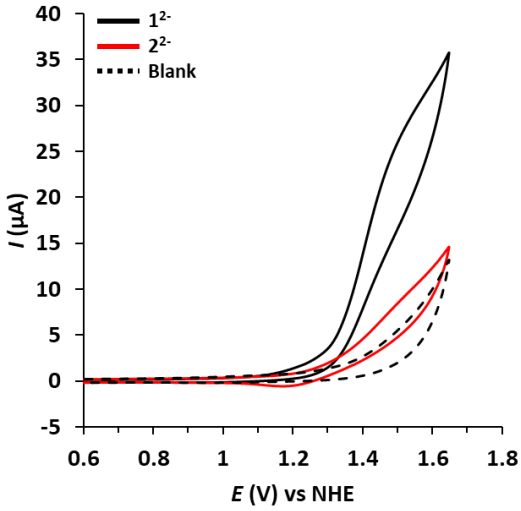

Figure 3. Cyclic Voltammograms of $\mathbf{1}^{2-}$ (black line) and $\mathbf{2}^{2-}$ (red line) in 0.1 M phosphate buffer pH 11.4. Black dashed line corresponds to a blank with no catalyst. Conditions: scan rate of 100 mV/s, [Complex] = 1 mM. BDD disk as working electrode.

The ligand-based nature of the previous oxidations was again confirmed by DPV measurements of the free ligand (Figure S33) and by the electrochemical behavior of the corresponding Zn^{II} complexes in aqueous solution at pH 11.4. Both $[(p\text{-L})Zn^{II}]^{2-}$ and $[(o\text{-L})Zn^{II}]^{2-}$ feature two electron transfers at similar redox potentials as the ones observed in DMF,

which are also shifted by 200 mV from the waves corresponding to the copper complexes (Figure S31).

However, despite the capacity of the ligand to accommodate two oxidative charges once coordinated to Zn^{II}, the complexes do not show any electrocatalytic wave. Therefore, the Cu center displays essential role in the coordination of OH^- necessary for its oxidation to dioxigen, although only the ligand is involved in the electron transfer processes. Previous results confirmed that for complex $\mathbf{1}^{2-}$ at pH 11.4 the electrocatalytic activity appears as a consecuence of two consecutive oxidations both centered in the aryl groups of the ligand backbone. Interestingly, complex $\mathbf{2}^{2-}$ is also able to accommodate two oxidative charges in the ligand framework but no electrocatalytic activity appears despite its similar redox behavior to complex $\mathbf{1}^{2-}$.

The kinetic of water oxidation reaction was studied following "foot of the wave analysis" (FOWA),[14] which allows the calculation of the apparent rate constant k_{obs} (Figure S34). The calculated value of k_{obs} = 10.53 s^{-1} is comparable to other reported copper-based complexes containing redox non-innocent ligands.[18,20]

Following previous observations of electrocatalytic activity we assess the evolution of oxygen by $\mathbf{1}^{2-}$ and $\mathbf{2}^{2-}$ using controlled potential electrolysis (CPE) at 1.6 V vs. NHE. For these experiments we used a large surface area boron-doped diamond plate working electrode (~1.5 cm^2) with 1 mM catalyst buffer solutions and a Clark-type electrode to detect and monitor the oxygen evolved at three different pH values (7, 9 and 11.4). In strong agreement with the previous electrochemical measurements, no oxygen evolution above background was observed below pH 11.4 when using either $\mathbf{1}^{2-}$ or $\mathbf{2}^{2-}$ (Figures S35 and S36). In contrast, in the case of $\mathbf{1}^{2-}$, a steady formation of dioxygen was detected immediately after starting the experiment at pH 11.4 (Figure 4, left). No significant induction time was observed in the catalytic curve, supporting the homogeneity of $\mathbf{1}^{2-}$.

Thus, $\mathbf{1}^{2-}$ is active towards water oxidation producing 0.017mmol of O_2 over 100 min. On the contrary, no oxygen evolved compared to the blank with $\mathbf{2}^{2-}$ as catalyst under the same conditions (Figure 4, right), confirming that $\mathbf{2}^{2-}$ is not active towards water oxidation. This is in good agreement with the absence of current above the blank in the CV experiments performed at pH 11.4.

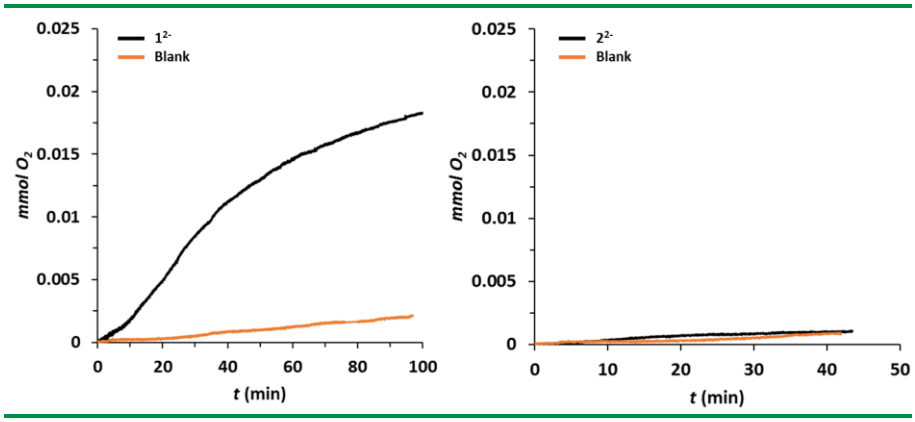

Figure 4. Oxygen evolution measurements given in mmol O2 vs. time (min) for complexes $\mathbf{1}^{2-}$ (left) and $\mathbf{2}^{2-}$ (right) at 1.5 mM concentration using a Clark probe electrode during a CPE at 1.6 V vs. NHE in 0.1 M phosphate buffer pH 11.4. Blank data in the absence of complex is shown in orange.

To evaluate the homogeneity of $\mathbf{1}^{2-}$, BDD electrodes used for the oxygen detection were immersed in a new catalyst-free buffer solution and CVs were registered (Figure S37 and S38). In comparison with the blank experiments, no catalytic response derived from the formation of active heterogeneous copper oxide materials on the surface of the electrodes was observed. Several CV cycles were performed on a 1 mM solution in 0.1 M phosphate buffer at pH 11.4 (Figure 5. left) and we observed a decrease in the current of the electrocatalytic wave, probably due to a deactivation process promoted by the high reactivity of the diradical species. The electrode was again immersed in a new catalyst-free buffer solution and CVs were registered (Figure 5, right). We did not observe any appearing catalytic activity as compared with the previous behavior. Glassy carbon electrode subjected to catalytic water oxidation electrolysis

during 30 minutes at 1.6 V vs. NHE with 1.5 mM solutions of complex $\mathbf{1}^{2-}$ was also analyzed by scanning electron microscopy (SEM) and energy dispersive X-ray spectroscopy (EDX), showing again no evidence of nanoparticles, film formation or copper-based heterogeneous materials over the surface (Figures S39-41). These results support the homogeneity of the catalytic active species. In addition, the possibility of a electrocatalytic response due to the presence of free Cu^{2+} was also discarded by comparing the CV of $Cu(ClO_4)_2$ in phosphate buffer at pH 11.4 with complex $\mathbf{1}^{2-}$ (Figure S32). This test revealed an onset potential similar to the blank for $Cu(ClO_4)_2$ and approximately 300 mV shifted towards higher potentials with respect to the electrocatalytic wave of $\mathbf{1}^{2-}$.

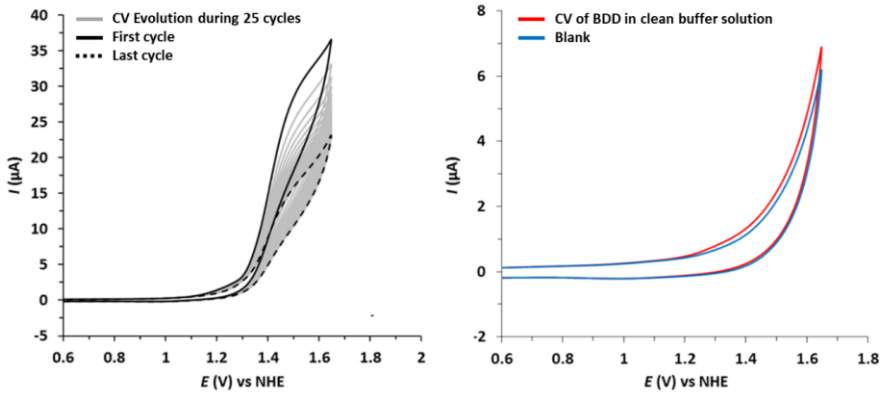

Figure 5. Left, Evolution of CV profile of $\mathbf{1}^{2-}$ in 0.1 M phosphate buffer (pH 11.4) after 25 cycles. Right, CV measurement with a BDD electrode that has performed the previous 25 cycles of the complex (red line) or of a blank solution (blue line) immersed in a freshly-prepared catalyst-free 0.1 M phosphate buffer pH 11, showing no catalytic response due to the presence of heterogeneous materials deposited onto the surface of the electrode. Conditions: scan rate of 100 mV/s, [Complex] = 1 mM. BDD as working electrode.

C.2.4. Computational study

We further investigate the mechanism of water oxidation catalyzed by $\mathbf{1}^{2-}$ by DFT calculations using the B3LYP-D3 functional and the implicit

SMD solvation method (See Computational Details). The main mechanisms computed for the O-O bond formation step are summarized in the catalytic cycle of Figure 6. We firstly explored the starting point of the catalytic cycle and according to the calculated pKa values (-7.9 and -0.2 for each sulfonate group), complex $\mathbf{1}^{2-}$ is deprotonated in the working pH range. Moreover, all the attempts to coordinate a water molecule in the apical position reverted to the formation of hydrogen bond between the unbounded water and the nitrogen from one amide group. Finally, even the coordination of hydroxo groups is thermodynamically disfavored by 3.6 kJ/mol. Those results are in agreement with the absence of proton coupled electron transfers for this complex $\mathbf{1}^{2-}$.

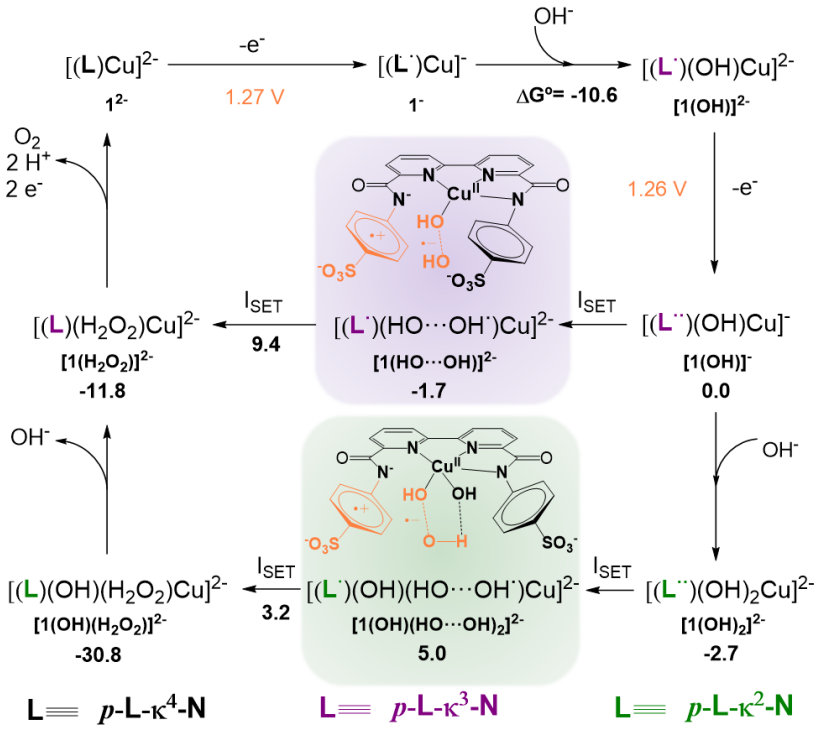

Figure 6. Catalytic cycle for catalyst $\mathbf{1}^{2-}$ representing the SET-WNA mechanism from the two substituted intermediates **[1(OH)]**$^{-}$ and **[1(OH)$_2$]**$^{2-}$. Free energy changes are indicated as black number in kcal·mol^{-1} and calculated redox potential as orange number in volts.

Upon one electron removal, the most stable oxidized species consist of a triplet Cu(II) complex with a radical cation mainly centered on one of the phenyl-amidate moiety as shown in Figure 6 and S44, **1**$^{-}$. The calculated oxidation potential is 1.27 V, which is in good agreement with the experimental value (1.37 V). Interestingly, this ligand oxidation causes a decrease on the strength of the Cu-$N_{amidate}$ bond since now part of the electron density of the amidate is used to stabilize the phenyl radical cation. As a consequence, the Cu-N_{amide} distance increases from 2.05 Å to 2.14 Å. This bond weakening then favors the substitution of the coordinated amide by a hydroxo molecule (ΔG^{o}= -10.6 kcal/mol) generating [(*p*-L$^{\cdot}$-κ-N^{3})Cu^{II}(OH)]$^{2-}$, **[1(OH)]$^{2-}$**.

The calculated oxidation potential for **[1(OH)]$^{2-}$** is 1.26 V, giving rise to the formation of a second radical by releasing one electron from the still coordinated phenyl-amidate group and forming [(*p*-L$^{\cdot\cdot}$-κ-N^{3})Cu^{II}(OH)]$^{-}$, **[1(OH)]$^{-}$**. The proximity between the oxidation potentials (1.27 V and 1.26 V) hinder the observation of both processes independently in agreement with what is found experimentally. The doubly oxidized quartet species **[1(OH)]$^{-}$** features again an increased Cu-N_{amide} distance, from 2.07 Å to 2.21 Å., that again favors hydroxo substitution by 2.7 kcal/mol to generate [(*p*-L$^{\cdot\cdot}$-κ-N^{2})Cu^{II}(OH)$_2$]$^{2-}$, **[1(OH)$_2$]$^{2-}$**, with a highly distorted tetrahedral geometry (Figure 7).

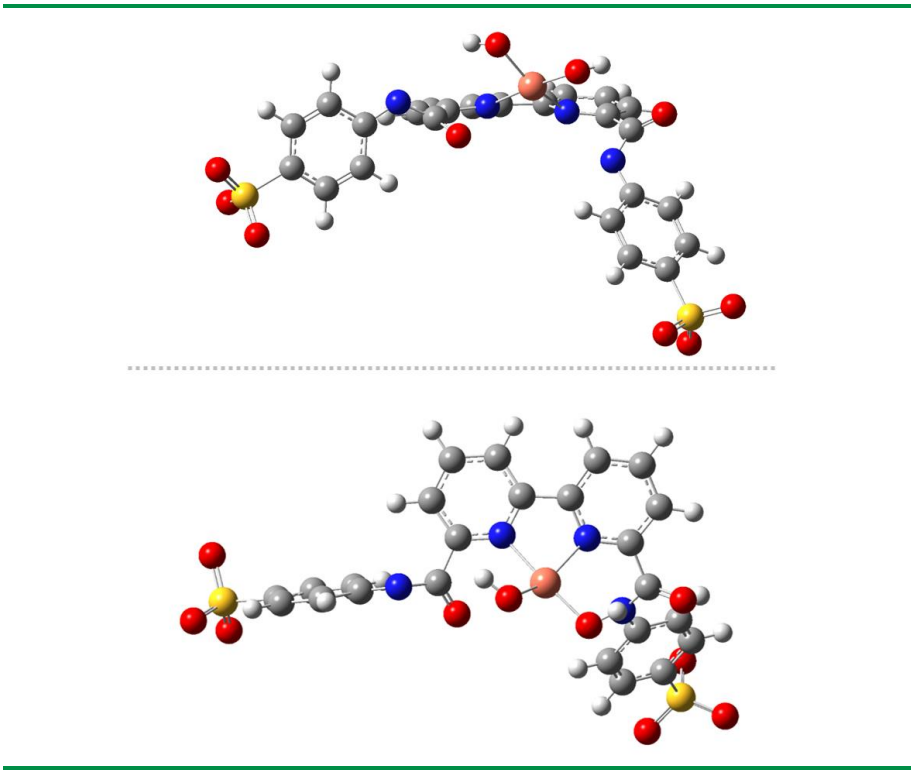

Figure 7. Two different views of DFT optimized structures for the species $[1(OH)_2]^{2-}$.

We have considered both doubly oxidized substituted species, $[1(OH)]^-$ and $[1(OH)_2]^{2-}$, as possible intermediates for the O-O bond formation due to their similar energy. Both structures are quartets, presenting an unpaired electron on the copper center and the other two unpaired electrons in each phenyl-amidate moieties. The calculated pKa for the coordinated hydroxo groups are 13.7 for $[1(OH)]^-$ and 21.6 for $[1(OH)_2]^{2-}$, indicating that they remain protonated.

Starting with $[1(OH)]^-$, the presence of an external OH^- molecule even at long distances of around 4 Å promotes a single electron transfer from the latter to reduce one of the phenyl-amidate groups, suggesting that the previously reported Single Electron Transfer-Water Nucleophilic Attack (SET-WNA) mechanism is again operative in these type of copper WOCs.[29] This highly favored electron transfer prevents us from finding

the adduct between **[1(OH)]**$^{-}$ and the external OH^{-}, as well as the associated transition state, that might be a reorganization process with low energy barrier. The new electronic structure evolves to an intermediate **[1(HO···OH)]**$^{-2}$ where both oxygen atoms form a two centres-three electrons bond (2c-3e-) with a formal order of 0.5 and a bond distance of 2.23 A (Figure S45 and S46) while one of the sulfonate groups is reduced.

Upon subsequent approximation of the two oxygen centers, there is a second single electron transfer to reduce the second phenyl-amidate moiety forming the hydroperoxo species **[1(HO-OH)]**$^{-2}$ in the doublet state, where the two oxygen atoms are connected by a bond with an order 1. The quartet species **[1(HO···OH)]**$^{-2}$ and the doublet **[1(HO-OH)]**$^{-2}$ are connected by a minimum energy crossing point (MECP) but we were not able to compute for technical reasons (see Electronic Supplementary Information). Instead, the barrier for this second electron transfer can be estimated from the potential energy scan to be 9.4 kcal·mol^{-1}.

This new example of SET-WNA mechanism, where the reaction proceeds via two consecutive single electron transfers, resembles to the previously reported catalyst [(6,6'-bobp)$Cu^{II}(OH_2)_2$].[29] The only difference using catalyst **1**$^{2-}$ is the spectator role of the copper center from an electronic point of view, since its oxidation state remains unchanged while both SET steps involve the reduction of the ligand. However, the copper is essential in coordinating the hydroxo group to promote the O-O bond formation in the equatorial position. Attempts to characterize a traditional Water Nucleophilic Attack (WNA) involving a concerted two-electron transfer failed as its energy becomes unaffordable.

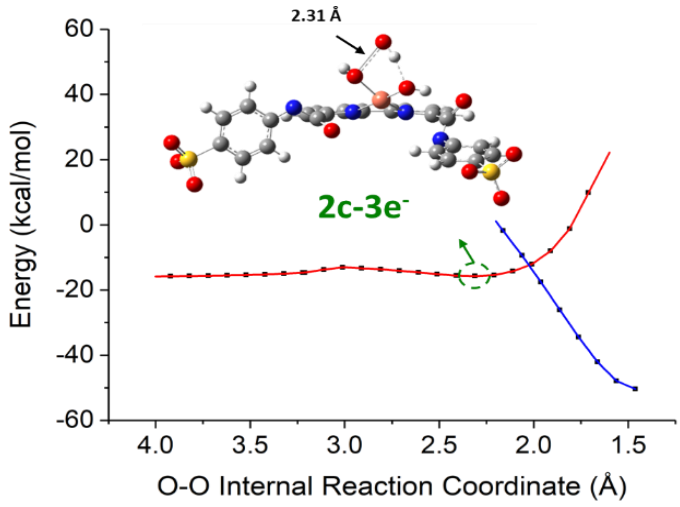

Figure 8. Potential energy relaxed scan for catalyst $\mathbf{1}^{2-}$ of the O-O reaction coordinate. Red color represents the quartet state while blue color indicates the doublet state. The inset drawing and the optimized structure to the right represents the 2c-3e$^-$ intermediate.

Regarding now the doubly oxidized species $\mathbf{[1(OH)_2]^{2-}}$, two pathways for the O-O bond formation are available as it can follow a similar SET-WNA mechanism with an external OH- or promoting an intramolecular oxygen coupling between both bonded hydroxo groups. The first option is depicted in Figure 6 and involves a similar profile as using $\mathbf{[1(OH)]^{2-}}$, with the formation of the (2c-3e-) intermediate featuring a O-O bond distance of 2.32 Å and an bond order of 0.5. Once again, the proximity of an external OH- molecule promotes the easy first single electron transfer and prevent us from finding the adduct species and the corresponding crossing point between both electronic states. We observed a little hill in the first scan at a O-O distance of 3.00 Å that is related with a reorganization of the hydrogen bonds in the system involving a negligible barrier (Figure 8). Regarding the second electron transfer occurring through a MECP, the estimated energy from the potential energy scan depicted in Figure 8 is in this case 3.2 kcal·mol^{-1} which involves a lower barrier for the formation of the O-O bond than for $\mathbf{[1(OH)]^-}$, although the 2c-3e

intermediate **[1(OH)(HO···OH)]$^{3-}$** is less stable than **[1(HO···OH)]$^{2-}$**. Therefore, both substituted intermediates **[1(OH)]$^{-}$** and **[1(OH)2]$^{2-}$** could be responsible for the catalytic activity of catalyst **1^{2-}**. The plausible intramolecular pathway in **[1(OH)$_2$]$^{2-}$** was discarded due to the high potential energy (more than 30 kcal·mol^{-1}) to bring both oxygens near to each other so that they can form the O-O bond, as depicted in the relaxed scan of the intramolecular reaction in Figure S47.

This new example of SET-WNA mechanism highlight the relevance of single electron transfers in water oxidation catalyzed by first row transition metals complexes, in contrast to the well stablish WNA involving a concerted two electron transfer. It is important to note that the equatorial position is preferred for supporting the species involved in the O-O bond formation when available, as shown with **1^{2-}**. In this case, the oxidation of the coordinating amides and their relative flexibility enable the introduction of coordinating OH^{-} in the equatorial plane against the less favored coordination in the apical position.

C.3. Conclusions

New tetradentate bipyridine-based ligands containing strong electron-donating amidate groups have been synthetized and successful coordinated, forming their corresponding copper complexes. These complexes have been tested concerning their capacity of oxidizing water at basic pH. While **1^{2-}** operates under basic conditions with an overpotential of 835 mV, **2^{2-}** resulted to be inactive. One of the most interesenting finding is the strong redox character of the ligands that in the case of complex **1^{2-}**, is the only responsible for the electron transfer processes during water oxidation catalysis. The ability to oxidize twice thanks to the two phenylamidate groups makes possible the oxidation of two hydroxides all the way to release oxygen. To our best knowledge, this is the first copper complex example where the metal centers remain as a mere spectator

from the redox point of view, although it is essential for the coordination of hydroxides molecule enabling the O-O bond formation.

Finally, the lack of reactivity of $\mathbf{2}^{2-}$ can be rationalized due to the ortho configuration of the sulfonate groups in the phenyl moieties, which blocks the imperative approximation of OH^- molecules during WO catalysis. The ability of copper to coordinate oxo groups from the ligand architecture hinder the coordination of water or hydroxo molecules, which are necessary to promote the O-O bond formation.

C.4. Acknowledgments

We thank MINECO and FEDER (Grants CTQ2014-57761-R, CTQ-2016-80058-R, Severo Ochoa Excellence Accreditation 2014-2018 SEV-2013-0319, CTQ-2014-52974-REDC) and CERCA Programme/Generalitat de Catalunya for financial support. I.F.-A. thanks the Severo Ochoa predoctoral training fellowship (ref: SVP-2014-0686662). P.G.-B. thanks "La Caixa" foundation for a Ph.D. grant.

C.5. References

1 Berardi, S.; Drouet, S.; Francas, L.; Gibert-Surinach, C.; Guttentag, M.; Richmond, C.; Stoll, T.; A. Llobet, *Chem. Soc. Rev.*, **2014**, *43*, 7501

2 J. D. Blakemore, R. H. Crabtree and G. W. Brudvig, *Chem. Rev.* 2015, **115**, 12974.

3 M. D. Kärkäs, O. Verho, E. V. Johnston, B. Åkermark, *Chem. Rev.*, 2014, **114**, 11863.

4 N. S. Lewis, *Science,* 2016, **351**, 19201.

5 Garrido-Barros, P.; Gimbert-Suriñach, C.; Matheu, R.; Sala, X.; Llobet, A. *Chem. Soc. Rev.* **2017**, *46* (20).

6 Materna, K. L.; Crabtree, R. H.; Brudvig, G. W. *Chem. Soc. Rev.* **2017**, *46*, 6099-6110.

7 Materna, K. L.; Rudshteyn, B.; Brennan, B. J.; Kane, M. H.; Bloomfield, A. J.; Huang, D. L.; Shopov, D. Y.; Batista, V. S.; Crabtree, R.H.; Brudvig, G. W. *ACS Catal.* **2016**, *6*, 5371–5377.

8 Odrobina, J.; Scholz, J.; Pannwitz, A.; Francàs, L.; Dechert, S.; Llobet, A.; Jooss, C.; Meyer, F. *ACS Catal.* **2017**, *7*, 2116-2125.

9 Li, F.; Zhang, B.; Li, X.; Jiang, Y.; Chen, L.; Li, Y.; Sun, L. *Angew. Chem. Int. Ed.* **2011**, *50*, 12276- 12279

10 Creus, J.; Matheu, R.; Peñafiel, I.; Moonshiram, D.; Blondeau, P.; Benet-Buchholz, J.; García-Antón, J.; Sala, X.; Godard, C.; Llobet, A. *Angew. Chem. Int. Ed.* **2016**, *55*, 15382-15386.

11 Garrido-Barros, P.; Gimbert-Suriñach, C.; Moonshiram, D.; Picón, A.; Monge, P.; Batista, V. S.; Llobet, A. *J. Am. Chem. Soc.* **2017**, *139*, 12907-12910.

12 W. C. Ellis, N. D. McDaniel and T. J. Collins, *J. Am. Chem. Soc.*, 2010, **132**, 10990.

13 D. J. Wasylenko, C. Ganesamoorthy, J. Borau-Garcia and C. P. Berlinguette, *Chem. Commun*., 2011, **47**, 4249;

14 Y. Naruta, M. Sasayama and T. Sasaki, *Angew. Chem. Int. Ed. Engl.*, 1994, **33**, 1839.

15 Barnett, S. M.; Goldberg, K. I.; Mayer, J. M. *Nat. Chem.* **2012**, *4*, 498−502.

16 M.-T. Zhang, Z. Chen, P. Kang and T. Meyer, *J. Am. Chem. Soc.* 2013, **135**, 2048.

17 J. S. Pap, L. Szyrwiel, D. Srankó, Z. Kerner, B. Setner, Z. Szewczuk and W. Malinka, *Chem. Commun.*, 2015, **51**, 6322.

18 Zhang, T.; Wang, C.; Liu, S.; Wang, J.-L.; Lin, W. *J. Am. Chem. Soc.* **2014**, *136*, 273−281.

19 Gerlach, D. L.; Bhagan, S.; Cruce, A. A.; Burks, D. B.; Nieto, I.; Truong, H. T.; Kelley, S. P.; Herbst-Gervasoni, C. J.; Jernigan, K. L.; Bowman, M. K.; Pan, S.; Zeller, M.; Papish, E. T. *Inorg. Chem.* **2014**, *53*, 12689−12698.

20 P. Garrido-Barros, I. Funes-Ardoiz, S. Drouet, J. Benet-Buchholz, F. Maseras and A. Llobet, *J. Am. Chem. Soc.*, 2015, **137**, 6758.

21 Fisher, K. J.; Materna, K. L.; Mercado, B. Q.; Crabtree, R. H.; Brudvig, G. W. *ACS Catal.* **2017**, *7*, 3384-3387.

22 L. Duan, F. Bozoglian, S. Mandal, B. Stewart, T. Privalov, A. Llobet and L. Sun, *Nature Chemistry*, 2012, **4**, 418;

23 R. Matheu, M. Z. Ertem, J. Benet-Buchholz, E. Coronado, V. S. Batista, X. Sala and A. Llobet, *J. Am. Chem. Soc.*, 2015, **137**, 10786.

24 G. M. Rodriguez, G. Gatto, C. Zuccaccia and A. Macchioni, *ChemSusChem*, 2017, **10**, 4503.

25 Elizarova, G.L., Matvienko, L.G., Lozhkina, N.V. Zamarev, K. I. React. Kinet. Catal. Lett. **1981**, *16,* 191-194.

26 McCrory, C. C. L.; Jung, S.; Peters, J. C.; Jaramillo, T. F. *J. Am. Chem. Soc.*, **2013**, *135*, 16977-16987.

27 Solomon, E. I.; Heppner, D. E.; Johnston, E. M.; Ginsbach, J. W.; Cirera, J.; Qayyum, M.; Kieber-Emmons, M. T.; Kjaergaard, C. H.; Hadt, R. G.; Tian, L. *Chem. Rev.* **2014**, *114*, 3659-3853.

28 B. Beverskog, I. Puigdomenech, *J. Electrochem. Soc.*, 1997, **144**, 3476.

29 Funes-Ardoiz, I.; Garrido-Barros, P.; Llobet, A.; Maseras, F. *ACS Catal.* **2017**, *7*, 1712-1719.

C.6. Supporting Information

Experimental Section

Materials

All general reagents and chemicals were used as purchased from Sigma-Aldrich, Fluka and Merck chemical companies without further purification unless otherwise stated. The ligand precursor ([2,2'-bipyridine]-6,6'-dicarboxylic acid) was prepared according to the experimental procedure reported in the literature.[1] Air and moisture sensitive reactions were carried out under N_2 or Ar in oven-dried (120°C) glassware. Evaporation of solvents *in vacuo* was done with a *Büchi Rotevapor R-200* at 40°C.

Instrumentation and measurements

NMR spectra were measured on a *Bruker AV-500* and *Bruker 300 MHz* spectrometers. All NMR experiments were performed at room temperature in corresponding deuterated solvents and using internal protons as reference.

UV-Vis spectra were measured on a *Cary 50 UV-vis* spectrometer by *Varian Inc.*

Electrospray ionization mass spectra (ESI-MS) were performed on an *Agilent Technologies 6130-Quadrupole LC/MS* connected to an *Agilent Technologies HPLC-1200 series*. Samples were dissolved in MeOH or H_2O and injected directly with an auto-sampler.

Electrochemical measurements

Differential pulse voltammetry (DPV) and cyclic voltammetry (CV) were measured on a CHI660D potentiostat using a three-electrode cell. Glassy carbon (GC) or boron-doped diamond (BDD) (d = 3 mm) working electrodes were employed while a Pt rod/mesh was used as counter electrode and a Hg/$HgSO_4$ (K_2SO_4 sat.) or Ag/AgCl (KCl sat.) electrode was used

as a reference electrode. Working electrodes were polished with 1 and 0.05 micron alumina paste, washed with distilled water and acetone and sonicated in acetone for 5 minutes before each measurement. DMF employed for electrochemical measurements was prepared containing the necessary amount of n-Bu_4NPF_6 ($TBAPF_6$) as supporting electrolyte to yield a 0.1 M ionic strength. CVs were typically recorded at different scan rates from 25 to 1000 mV/s. DPVs were recorded with the following parameters: amplitude= 50 mV, step height=4 mV, pulse width= 0.05 s. All redox potentials in the present work are reported versus NHE by adding 0.648 V to the measured potential.

O_2 evolution experiments

Controlled Potential Electrolysis (CPE) experiments were performed at different potentials and different pH values to catalyze the water oxidation reaction by the complexes by using a two-compartment cell closed with a septum. As working electrode large surface BDD electrodes (rectangular shape with 1.5 cm^2 surface) were used together with a silver/silver chloride (KCl sat.) as a reference electrode. These ones were placed in one of the compartments that was filled with a 1 mM solution of the complex (phosphate buffer pH 7, borate buffer pH 9 or phosphate buffer pH 11.4, of 0.1 M ionic strength). In the other compartment, containing only the buffer solution, a mesh platinum counter electrode was used.

The oxygen evolution was monitored with an OXNP type Clark electrode in gas phase (from Unisense Company). The CPE was carried out using an IJ-Cambria CHI-660 potentiostat and was started as soon as the oxygen sensor signal was stable under air atmosphere. During the experiment, solutions of both compartments were vigorously stirred. Calibration of the oxygen sensor was performed after each experiment by adding known amounts of pure oxygen into the cell using a Hamilton syringe. The results of the water oxidation catalysis with the complexes

were compared with blank experiments under the same conditions but in the absence of the complex. The Faradaic efficiency was determined according to the total charge passed during the CPE and the total amount of generated oxygen by taking into account that water oxidation is a 4 e^- oxidation process.

Synthesis of *p*-L and *o*-L

The general procedure for the synthesis of ligands *p*-L and *o*-L was adapted from the literature[2] as follows: 500 mg (2.05 mmol) of [2,2'-bipyridine]-6,6'-dicarboxylic acid were suspended in 20 mL of $SOCl_2$ and the mixture was refluxed at 85 ºC under a nitrogen atmosphere during 6 hours. After complete dissolution of the reactant, $SOCl_2$ was completely removed under vacuum, yielding a white powder corresponding to the corresponding acyl chloride derivative. The white solid was re-suspended in 40 mL of dry DCM and the temperature was decreased until 0 ºC using an ice bath. Then, a catalytic amount of NEt_3 was added dropwise and stirred for 10 minutes. Finally, a previously prepared solution of the corresponding sulfonated phenylamine (705.6 mg, 4.1 mmol) in 40 mL of dry DCM were added dropwise to the reaction volume and the mixture was vigorous stirred for 72 h at room temperature. The appearing solid consisted in the corresponding ligand (*p*-L or *o*-L), which was filtered and washed with DCM and Et_2O, yielding the desired product without further purification.

p-L

Yield: 931 mg, 1.68 mmol, 82%. ^{1}H-NMR (DMSO-d_6): δ [ppm] = 10.70 (H_4, s, 2H), 9.24 (H_1, dd, J= 7.3, 1.6 Hz, 2H), 8.30 ($H_{2\text{-}3}$, m, 4H), 7.90 (H_5, d, J= 8.7 Hz, 2H), 7.65 (H_6, d, J= 8.7 Hz, 2H). ^{13}C-NMR (DMSO-d_6): 162,9 (C_6), 153.9 (C_5), 150.0 (C_1), 144.7 (C_{10}), 139.8 (C_4), 138.6 (C_7), 126.5 (C_9), 125.3 (C_2), 123.7 (C_3), 120.4 (C_8). ESI-MS (MeOH) m/z negative mode: 553.0 [*p*-L -H^+]$^-$, 276.1 [*p*-L -2H^+]$^{2-}$. Elemental analysis (% found):

C, 54.60; H, 6.71; N, 10.58. Calcd for $C_{24}H_{14}N_4O_8S_2 \cdot 3\ Et_3N \cdot 2\ H_2O$: C, 54.53; H, 6.61; N, 10.60.

o-L

Yield: 965 mg, 1.74 mmol, 85%. 1H-NMR (DMSO-d_6): δ [ppm] = 12.55 (H_4, s, 2H), 9.51 (H_1, dd, J= 7.3, 1.7 Hz, 2H), 8.67 (H_5, dd, J= 8.2, 1.1 Hz, 2H), 8.26 ($H_{2\text{-}3}$, m, 4H), 7.82 (H_8, dd, J= 7.7, 1.7 Hz, 2H), 7.43 (H_6, t, J= 1.2 Hz, 2H), 7.14 (H_7, td, J= 7.5, 1.2 Hz, 2H). ^{13}C-NMR (DMSO-d_6): 162,4 (C_6), 153.9 (C_5), 149.6 (C_1), 139.9 (C_4), 136.8 (C_{12}), 135.3 (C_7), 130.1 (C_9), 127.6 (C_8), 125.4 (C_2), 123.2 ($C_{1\text{-}2}$), 120.2 ($C_{3\text{-}7}$). ESI-MS (MeOH) m/z negative mode: 553.0 [*p*-L -H^+]$^-$, 276.1 [*p*-L -$2H^+$]$^{2-}$. Elemental analysis (% found): C, 55.35; H, 5.95; N, 10.65. Calcd for $C_{24}H_{14}N_4O_8S_2 \cdot 3\ Et_3N$: C, 55.44; H, 5.37; N, 10.77.

IV

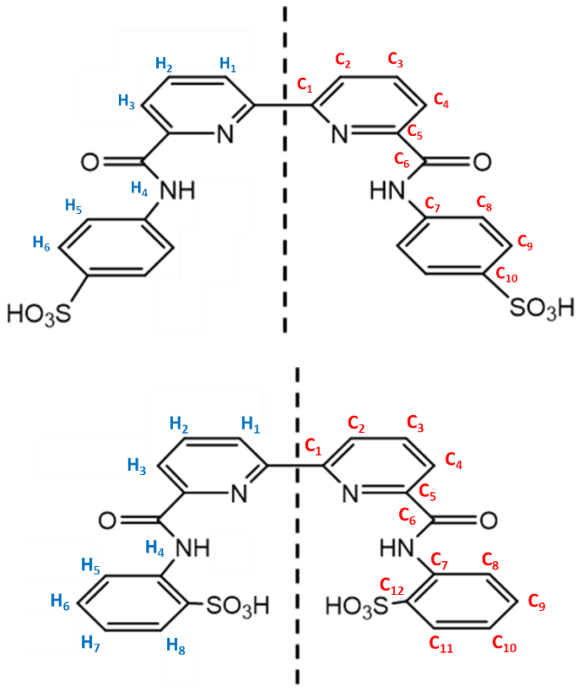

Figure S1: Schematic drawing of the two ligands synthetized in this work: p-L (left) and o-L (right) and their 1H-NMR and 13C-NMR assignments.

Synthesis of complexes 1^{2-} and 2^{2-}

The general procedure for the synthesis of the copper complexes was adapted from a previous work published.[3] 50 mg (0.09 mmol) of the corresponding ligand were suspended in 4 mL of MeOH and stired during 15 minutes. Afterwards, 3.6 mL (4 eq.) of 0.1 M $NaOH_{aq.}$ were added to the reaction mixture and vigorously stirred during 30 minutes at room temperature. After complete dissolution of the ligand, 33.3 mg (0.09 mmol) of copper perchlorate hexahydrate dissolved in 4 mL of MeOH were added dropwise to the mixture, which was allowed to react overnight (16 h) at room temperature. Then, the reaction mixture was filtrated through celite and MeOH was evaporated under vacuum, and the remaining solution was diffused with acetone, yielding the corresponding complexes.

Complex 1^{2-}

Yield: 19 mg, 0.03 mmol, 32% ESI-MS (MeOH) m/z negative mode: 636.0 $[M\text{-}Na^+]^-$, 614.0 $[M\text{-}Na^+ + H^+]^-$. Elemental analysis (% found): C, 40.18; H, 2.52; N, 7.74. Calcd for $C_{24}H_{14}CuN_4Na_2O_8S_2 \cdot 3\ H_2O$: C, 40.37; H, 2.82; N, 7.85.

Complex 2^{2-}

Yield: 15 mg, 0.02 mmol, 25%. ESI-MS (MeOH) m/z negative mode: 636.0 $[M\text{-}Na^+]^-$, 614.0 $[M\text{-}Na^+ + H^+]^-$. Elemental analysis (% found): C, 36.89; H, 2.98; N, 7.01. Calcd for $C_{24}H_{14}CuN_4Na_2O_8S_2 \cdot 0.5\ NaOCl_4 \cdot 3\ H_2O$: C, 37.18; H, 2.60; N, 7.26.

Synthesis of complexes $[(p\text{-}L)Zn]^{2-}$ and $[(o\text{-}L)Zn]^{2-}$

The general procedure for the synthesis of the zinc complexes was similar to the synthesis of the copper complexes. To a suspension of the corresponding ligand 200 mg (0.36 mmol) in 16 mL of MeOH, 14.4 mL (4 eq.) of 0.1 M $NaOH_{aq.}$ were added to the reaction mixture and vigorously

stirred during 30 minutes at room temperature. After complete dissolution of the ligand, 131 mg (0.36 mmol) of zinc trifluoromethanesulfonate dissolved in 4 mL of MeOH were added dropwise to the mixture, which was allowed to react overnight (16 h) at room temperature. Afterwards, a white precipitate appeared, which was filtrated and washed with H_2O (2 x 2 mL) and dried over vacuum yielding the corresponding complexes as white solids.

[(p-L)Zn]$^{2-}$

Yield: 193 mg, 0.29 mmol, 81%. ^{1}H-NMR (D_2O-d_2): δ [ppm] = 8.04 (H_{1-2}, m, 4H), 7.67 (H_3, dd, J= 7.5, 1.3 Hz, 2H), 7.20 (H_4, d, = 8.5 Hz, 4H), 6.36 (H_5, d, J= 8.5 Hz, 4H). Elemental analysis (% found): C, 39.77; H, 3.44; N, 7.56. Calcd for $C_{24}H_{14}CuN_4Na_2O_8S_2Zn \cdot 4\ H_2O$: C, 39.28; H, 3.02; N, 7.63.

IV

[(o-L)Zn]$^{2-}$

Yield: 169 mg, 0.26 mmol, 71%. ^{1}H-NMR (D_2O-d_2): δ [ppm] = 8.60 (H_1, d, J= 7.9 Hz 4H), 7.93 (H_4, d, J= 8.1 Hz, 2H), 7.83 (H_2, d, J= 7.8 Hz, 2H), 7.56 (H_{3-7}, m, 4H), 7.21 (H_5, t, J= 7.8 Hz,2H), 6.96 (H_6, t, J= 7.7 Hz,2H). Elemental analysis (% found): C, 42.60; H, 3.02; N, 8.14. Calcd for $C_{24}H_{14}N_4Na_2O_8S_2Zn \cdot 1.2\ H_2O$: C, 42.06; H, 2.4; N, 8.18.

Spectroscopic Characterization

NMR Spectroscopy

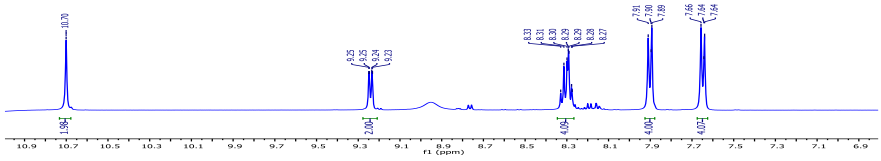

Figure S2. ^{1}H-NMR spectrum of the ligand *p*-L (DMSO-d_6, 500 MHz, 25 °C).

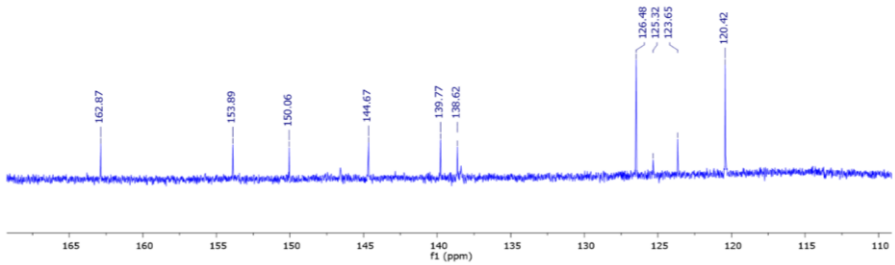

Figure S3. ^{13}C-NMR spectrum of the ligand *p*-L (DMSO-d_6, 500 MHz, 25 °C).

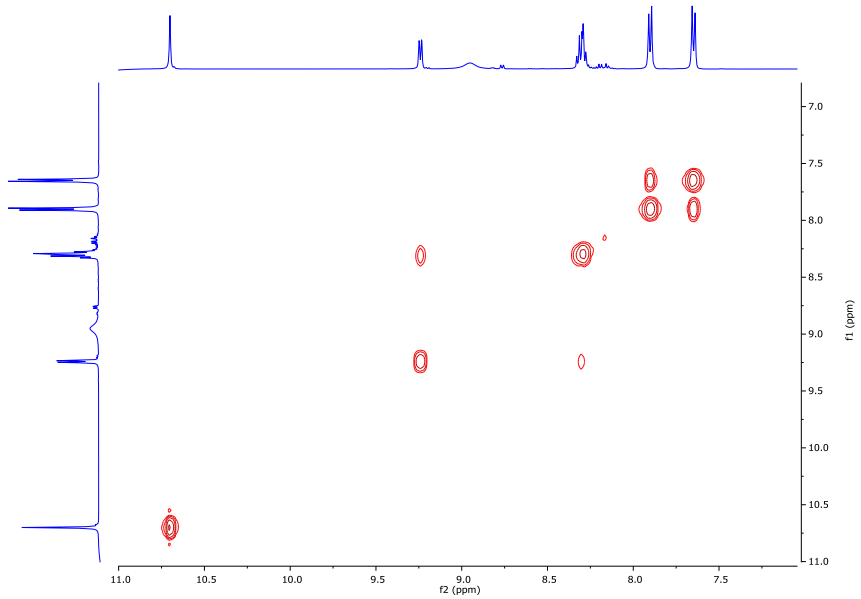

IV

Figure S4. COSY spectrum of the ligand *p*-L (DMSO-d_6, 500 MHz, 25 °C).

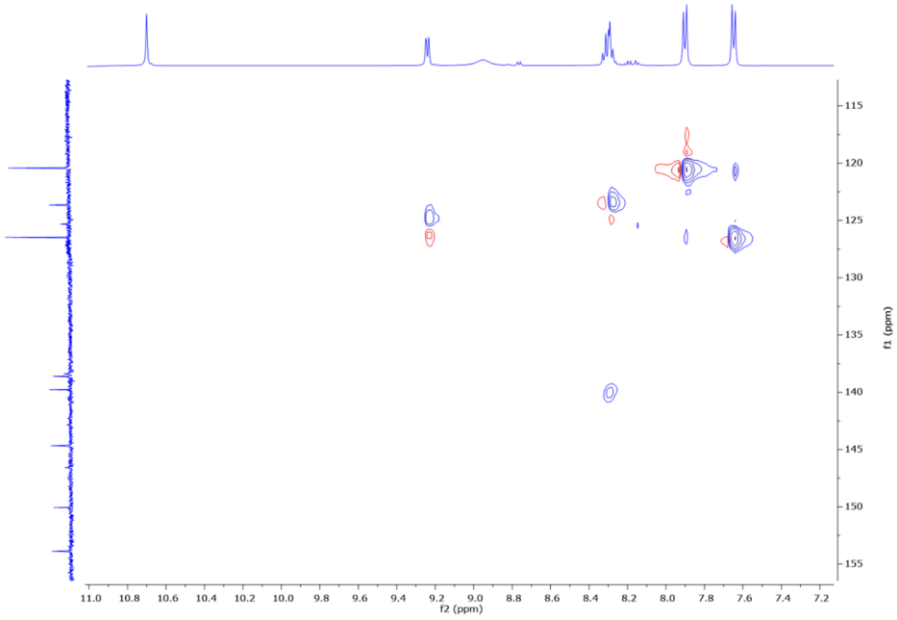

Figure S5. HSQC spectrum of the ligand *p*-L (DMSO-d_6, 500 MHz, 25 °C).

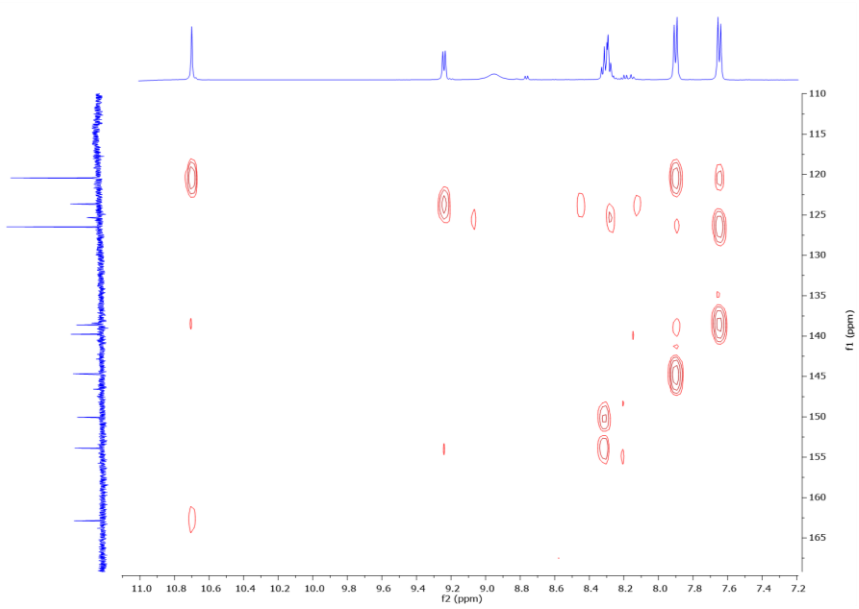

Figure S6. HMBC spectrum of the ligand *p*-L (DMSO-d_6, 500 MHz, 25 °C).

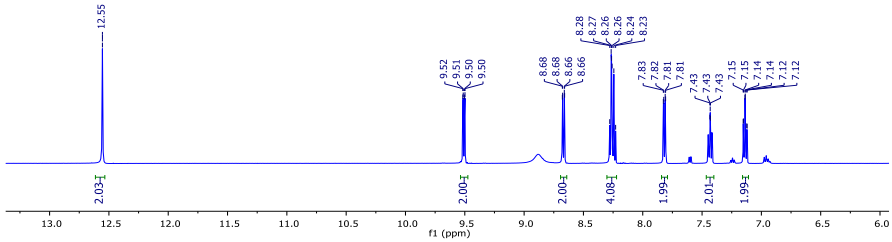

Figure S7. ^{1}H-NMR spectrum of the ligand *o*-L (DMSO-d_6, 300 MHz, 25 °C).

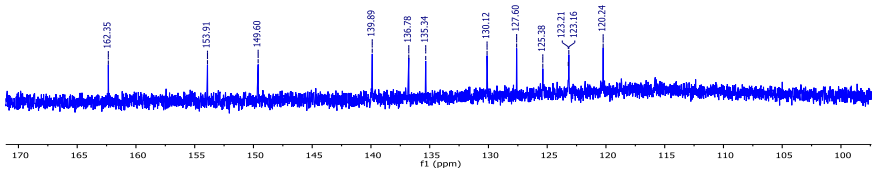

Figure S8. ^{13}C-NMR spectrum of the ligand *o*-L (DMSO-d$_6$, 500 MHz, 25 °C).

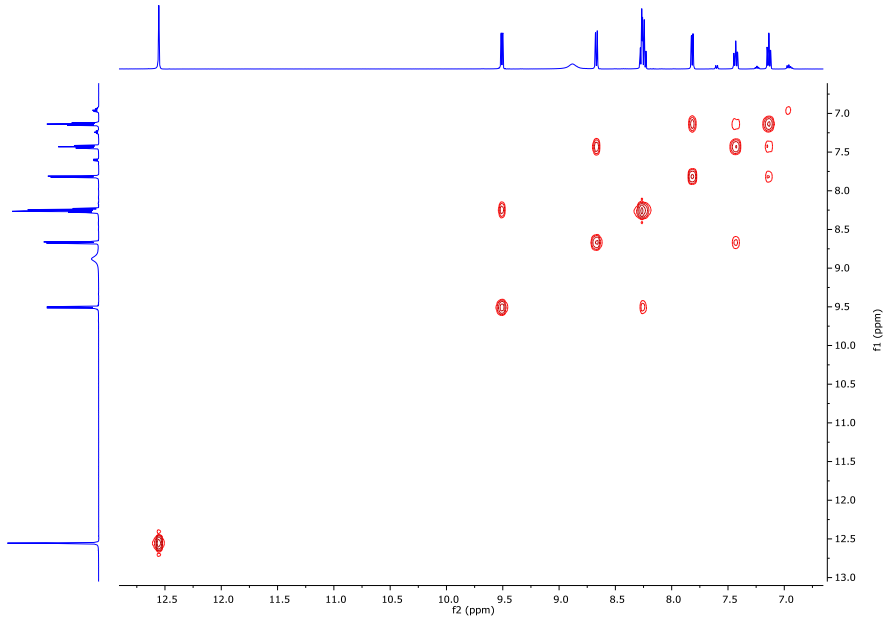

Figure S9. COSY spectrum of the ligand *o*-L (DMSO-d$_6$, 500 MHz, 25 °C).

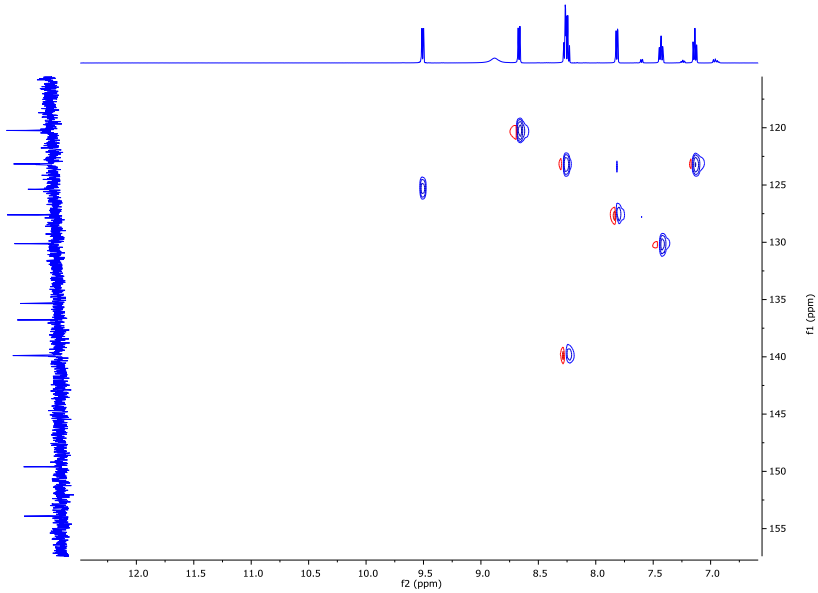

Figure S10. HSQC spectrum of the ligand *o*-L (DMSO-d_6, 500 MHz, 25 °C).

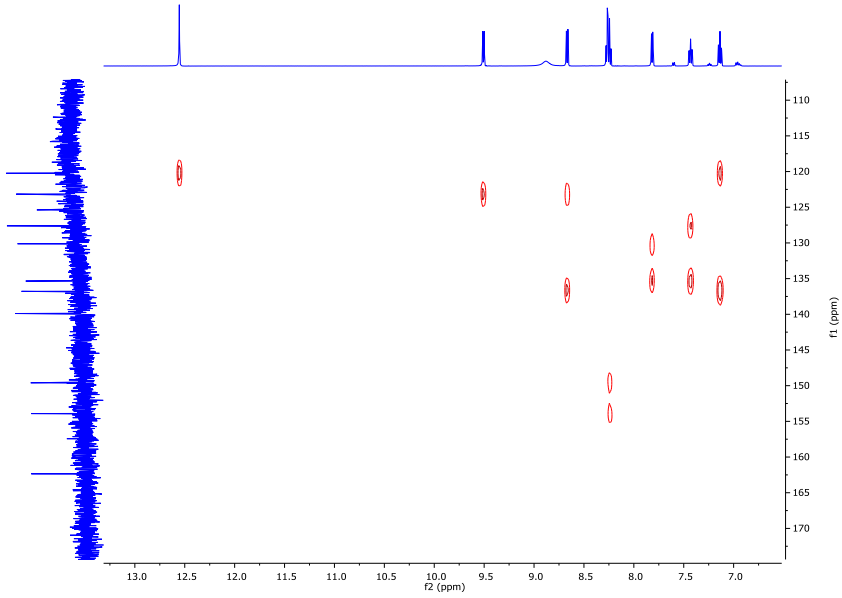

Figure S11. HMBC spectrum of the ligand *o*-L (DMSO-d_6, 500 MHz, 25 °C).

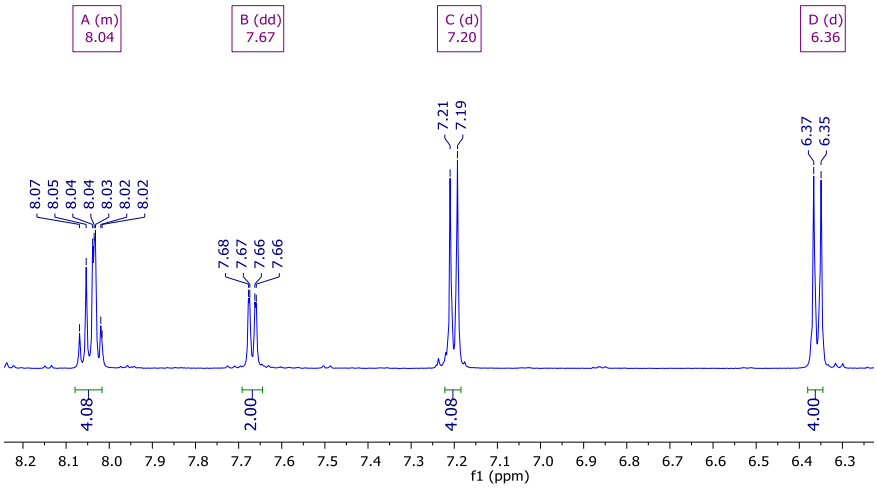

Figure S12. ^{1}H-NMR spectrum of the complex **[(*p*-L)Zn]$^{2-}$** (D_2O-d_6, 500 MHz, 25 °C).

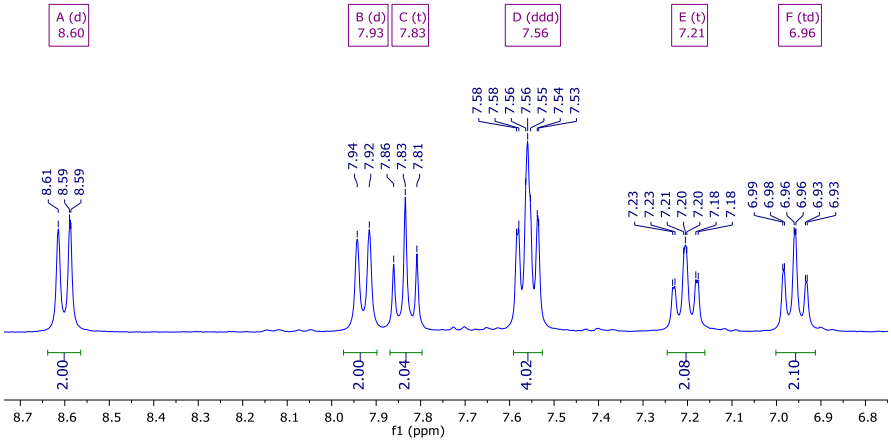

Figure S13. ^{1}H-NMR spectrum of the ligand **[(*o*-L)Zn]$^{2-}$** (D_2O-d_6, 500 MHz, 25 °C).

Mass-spectrometry

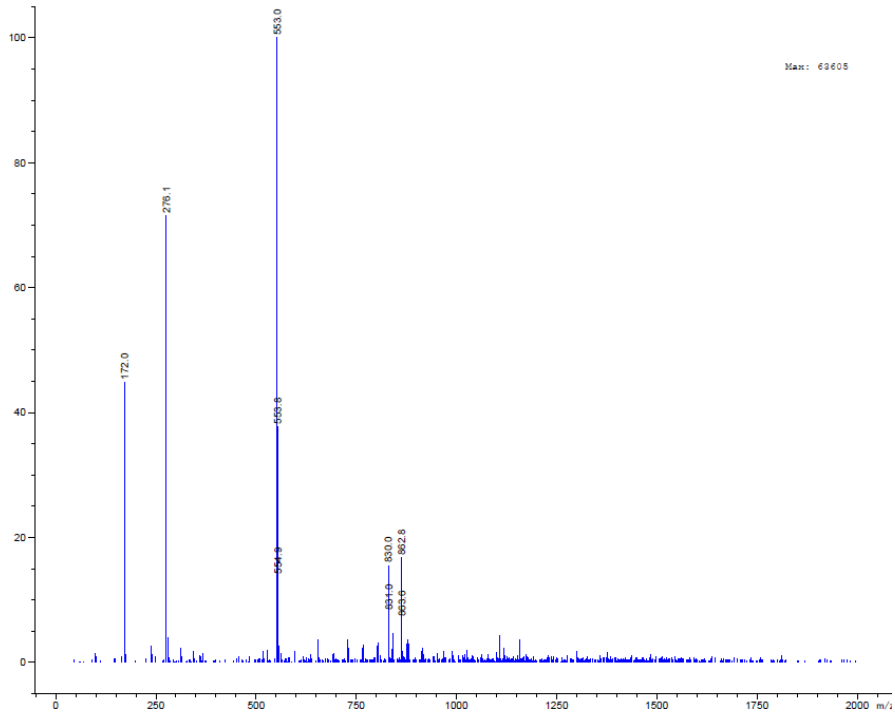

Figure S14. (-)-ESI-MS spectrum for the ligand *p*-L. m/z = 553.0 $[M\text{-}H^{+}]^{-}$; m/z = 276.1 $[M\text{-}2H^{+}]^{2-}$.

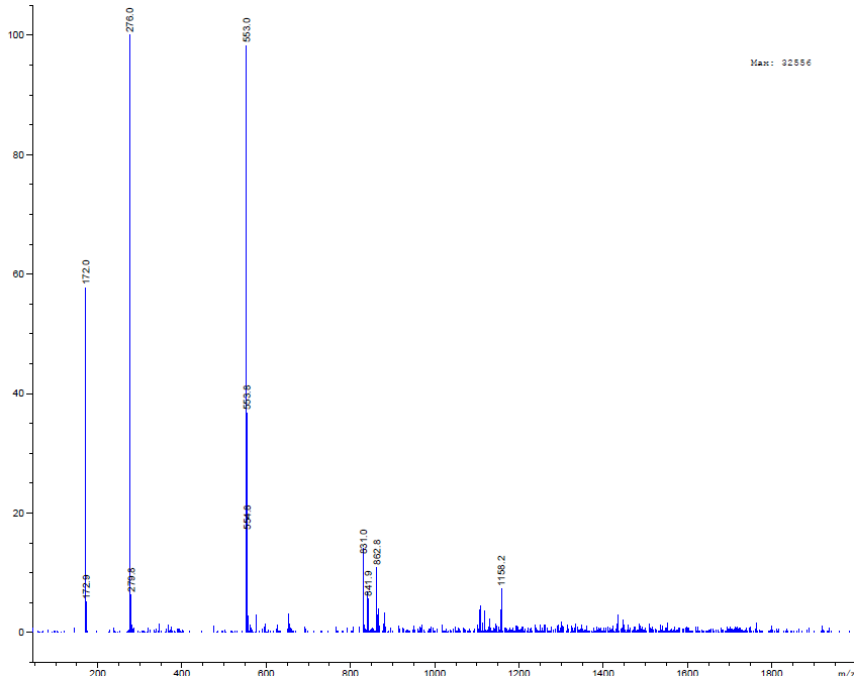

Figure S15. (-)-ESI-MS spectrum for the ligand *o*-L. m/z = 553.0 $[M\text{-}H^+]^-$; m/z = 276.1 $[M\text{-}2H^+]^{2-}$.

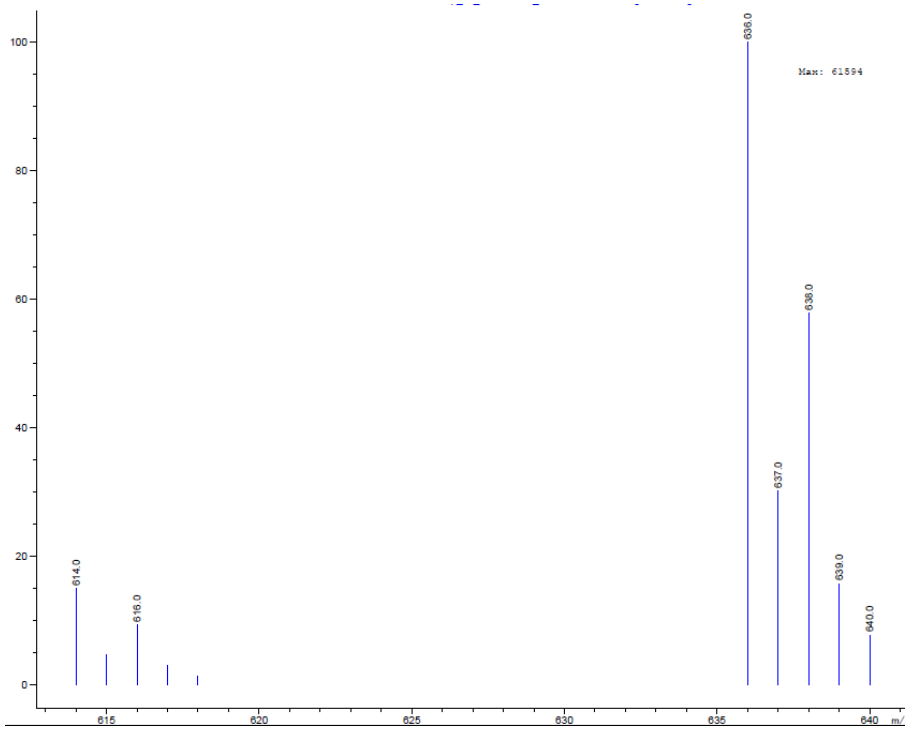

Figure S16. (-)-ESI-MS for $\mathbf{1}^{2-}$. m/z = 636.0 $[M\text{-}Na^+]^-$; m/z = 614.0 $[M\text{-}Na^+ + H^+]$.

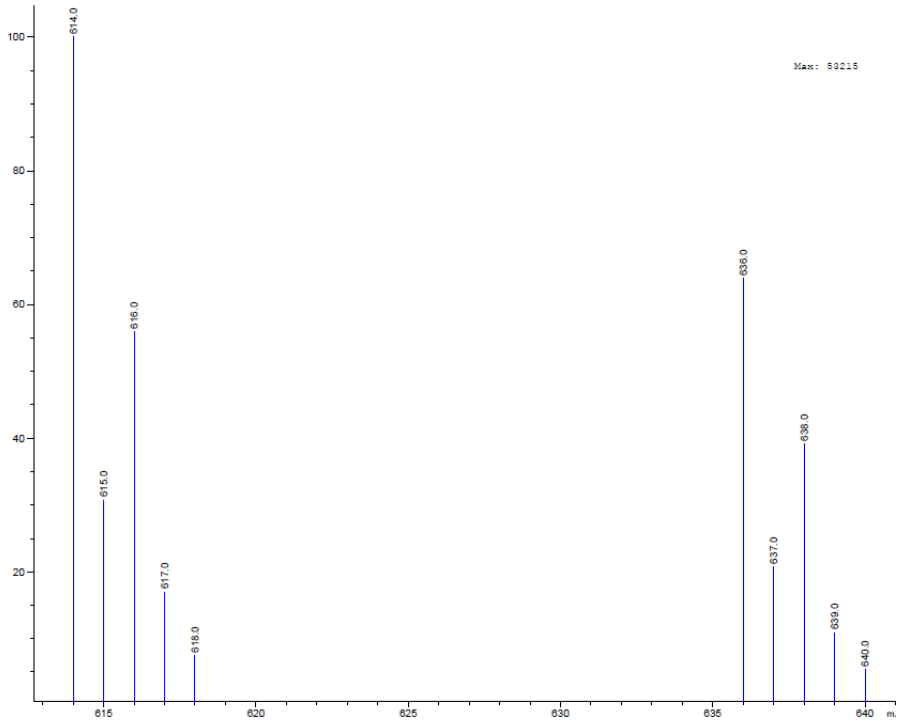

Figure S17. (-)-ESI-MS for $\mathbf{2}^{2-}$. m/z = 636.0 $[M\text{-}Na^{+}]^{-}$; m/z = 614.0 $[M\text{-}Na^{+}+H^{+}]$.

UV-Vis spectroscopy

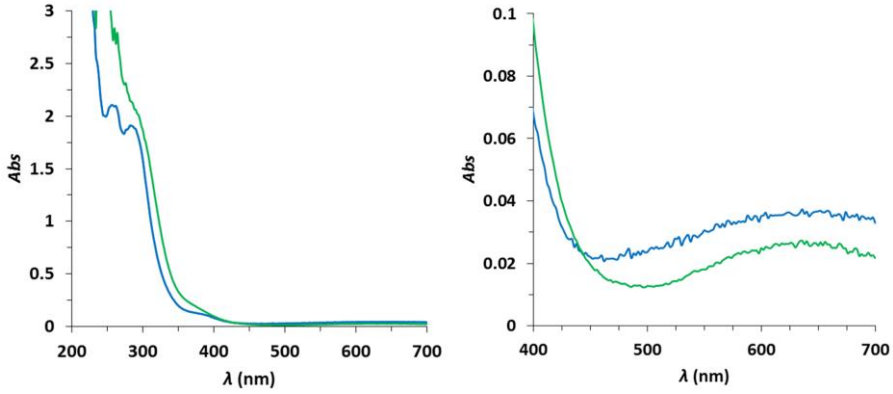

Figure S18. (Left) UV-vis spectra of $\mathbf{1}^{2-}$ (green line) and $\mathbf{2}^{2-}$ (blue line). **(Right)** UV-vis spectra enlargement of the visible region for both copper complexes. Conditions: [**Complex**] = 0.1 mM in 0.1 M phosphate buffer (pH 11.4).

X-Ray Crystallography

Crystal preparation: Crystals of $\mathbf{1}^{2-}$, $\mathbf{2}^{2-}$and *p*-L were grown in water (by slow diffusion of acetone for $\mathbf{1}^{2-}$ and $\mathbf{2}^{2-}$, and EtOH for *o*-L). The crystals were selected using a Zeiss stereomicroscope using polarized light and prepared under inert conditions immersed in perfluoropolyether as protecting oil for manipulation.

Data collection: Crystal structure determinations for samples $\mathbf{1}^{2-}$, $\mathbf{2}^{2-}$and *o*-L were carried out using a Apex DUO Kappa 4-axis goniometer equipped with an APPEX 2 4K CCD area detector, a Microfocus Source E025 IuS using MoKα radiation, Quazar MX multilayer Optics as monochromator and an Oxford Cryosystems low temperature device Cryostream 700 plus (T = -173 ˚C). Full-sphere data collection was used with ω and φ scans. *Programs used:* Bruker Device: Data collection APEX-2[4], data reduction Bruker Saint[5] V/.60A and absorption correction SADABS[6].

Structure Solution and Refinement: Crystal structure solution was achieved using the computer program SHELXT[7]. Visualization was performed with the program SHELXle[8]. Missing atoms were subsequently located from difference Fourier synthesis and added to the atom list. Least-squares refinement on F^2 using all measured intensities was carried out using the program SHELXL 2015[9]. All non-hydrogen atoms were refined including anisotropic displacement parameters. **Comments to the structures:** Sample *o*-L: The asymmetric unit contains half a molecules of the organic salt. The main molecule shows *Ci*-symmetry. $\mathbf{2}^{2-}$: The asymmetric unit contains one molecule of the copper metal complex, two sodium cations and eight molecules of water. $\mathbf{1}^{2-}$: The asymmetric unit contains one molecule of the metal complex, two sodium cations and 6.75 water molecules which are highly disordered (18 positions) The sulfoxide groups and the sodium cations are disorder in three orientations with an approximated ratio of 33:33:33. One of the disordered sodium cations is

additionally split in two positions (33:33:22:11). In the CIF-file a B-Alert related to D-H without acceptor is commented in relation to the water molecules: In this highly disordered structure there were 18 positions for 6.75 disordered water molecules and it was not possible to assign correctly all the corresponding hydrogen atom positions.

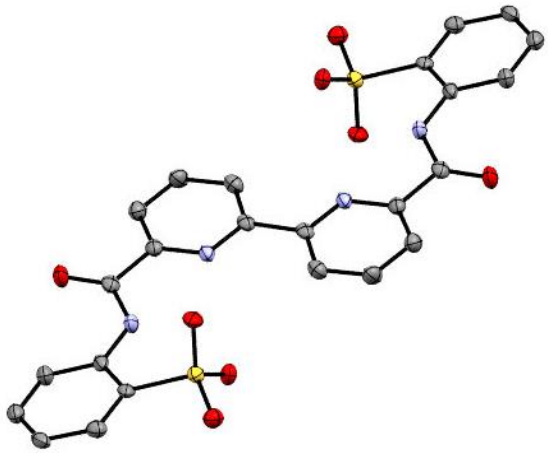

Figure S19. ORTEP representation of *o*-L at 50% probability level. The counter ions, solvent molecules and hydrogen atoms have been omitted for clarity. Colour code: C, grey; N, blue; O, red; S, yellow.

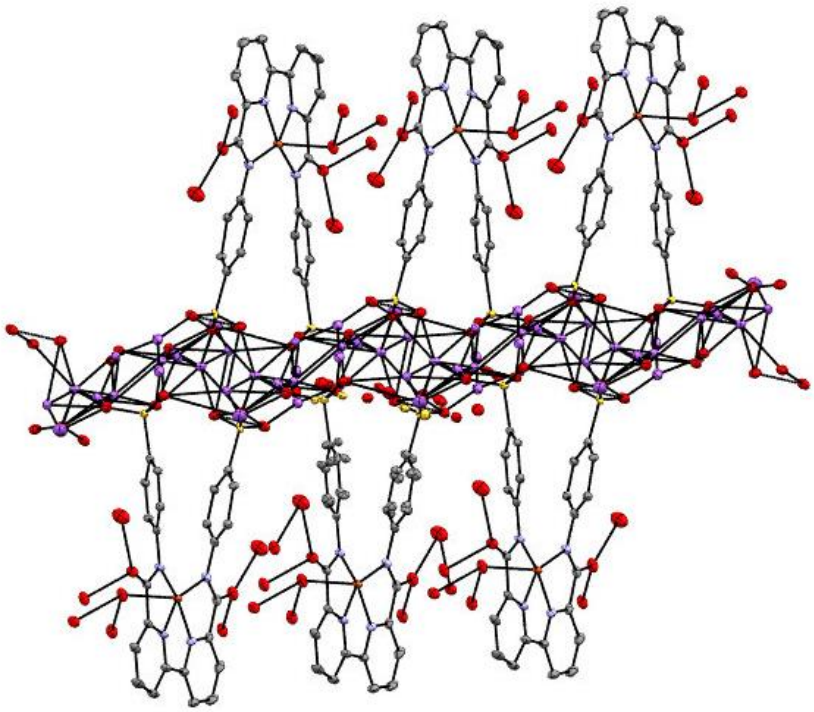

Figure S20. X-Ray structure representation of 2D polymeric framework of $\mathbf{1}^{2-}$. Colour code: C, grey; N, blue; O, red; S, yellow; Na, Purple; Cu, Orange.

Table S1. Crystal data and structure refinement for *o*-L.

Identification code *o*-L

Empirical formula C36 H48 N6 O8 S2

Formula weight 756.92

Temperature 100(2) K

Wavelength 0.71073 Å

Crystal system Monoclinic

Space group P2(1)/c

Unit cell dimensions a = 14.4650(14)Å α= 90°.

b = 8.5135(9)Å β = 109.155(3)°.

c = 15.7483(14)Å γ = 90°.

Volume 1832.0(3) Å3

Z 2

Density (calculated) 1.372 Mg/m3

Absorption coefficient 0.206 mm-1

F(000) 804

Crystal size 0.30 x 0.05 x 0.05 mm3

Theta range for data collection 2.654 to 25.391°.

Index ranges -16<=h<=17,-6<=k<=10,-18<=l<=15

Reflections collected 13699

Independent reflections 3343[R(int) = 0.0878]

Completeness to theta =25.391° 98.9%

Absorption correction Multi-scan

Max. and min. transmission 0.990 and 0.541

Refinement method Full-matrix least-squares on F2

Data / restraints / parameters 3343/ 0/ 238

Goodness-of-fit on F2 0.999

Final R indices [I>2sigma(I)] R1 = 0.0493, wR2 = 0.1071

R indices (all data) R1 = 0.0942, wR2 = 0.1269

Largest diff. peak and hole 0.314 and -0.474 e.Å-3

Table S2. Crystal data and structure refinement for $\mathbf{2}^{2-}$.

Identification code $\mathbf{2}^{2-}$

Empirical formula C24 H30 Cu N4 Na2 O16 S2

Formula weight 804.16

Temperature 100(2) K

Wavelength 0.71073 Å

Crystal system Monoclinic

Space group P2(1)/c

Unit cell dimensions a = 7.5982(3)Å α = 90°.

b = 17.2572(6)Å β= 98.6877(10)°.

c = 24.3433(9)Å γ = 90°.

Volume 3155.4(2) Å3

Z 4

Density (calculated) 1.693 Mg/m3

Absorption coefficient 0.934 mm-1

F(000) 1652

Crystal size 0.40 x 0.10 x 0.05 mm3

Theta range for data collection 2.063 to 34.993°.

Index ranges -12<=h<=10,-24<=k<=27,-38<=l<=38

Reflections collected 38704

Independent reflections 13011[R(int) = 0.0346]

Completeness to theta =34.993° 93.6%

Absorption correction Multi-scan

Max. and min. transmission 0.955 and 0.798

Refinement method Full-matrix least-squares on F2

Data / restraints / parameters 13011/ 0/ 506

Goodness-of-fit on F2 1.073

Final R indices [I>2sigma(I)] R1 = 0.0423, wR2 = 0.0932

R indices (all data) R1 = 0.0556, wR2 = 0.0978

Largest diff. peak and hole 1.087 and -0.796 e.Å-3

Table S3. Crystal data and structure refinement for $\mathbf{1}^{2-}$.

Identification code $\mathbf{1}^{2-}$

Empirical formula C24 H27.50 Cu N4 Na2 O14.75 S2

Formula weight 781.64

Temperature 100(2) K

Wavelength 0.71073 Å

Crystal system Triclinic

Space group P-1

Unit cell dimensions a = 7.1558(3)Å α = 70.5590(10)°

b = 12.3988(5)Å β = 89.3240(10)°

c = 18.4833(7)Å γ = 80.6830(10)°

Volume 1524.44(11) Å3

Z 2

Density (calculated) 1.703 Mg/m3

Absorption coefficient 0.961 mm-1

F(000) 801

Crystal size 0.50 x 0.50 x 0.03 mm3

Theta range for data collection 1.762 to 33.916°.

Index ranges -11<=h<=11,-19<=k<=17,-28<=l<=28

Reflections collected 34506

Independent reflections 11681[R(int) = 0.0302]

Completeness to theta =33.916° 94.6%

Absorption correction Multi-scan

Max. and min. transmission 0.972 and 0.863

Refinement method Full-matrix least-squares on F2

Data / restraints / parameters 11681/ 1914/ 965

Goodness-of-fit on F2 1.120

Final R indices [I>2sigma(I)] R1 = 0.0452, wR2 = 0.1120

R indices (all data) R1 = 0.0544, wR2 = 0.1165

Largest diff. peak and hole 0.936 and -0.564 e.Å-3

Electrochemistry in Organic Solvents (DMF)

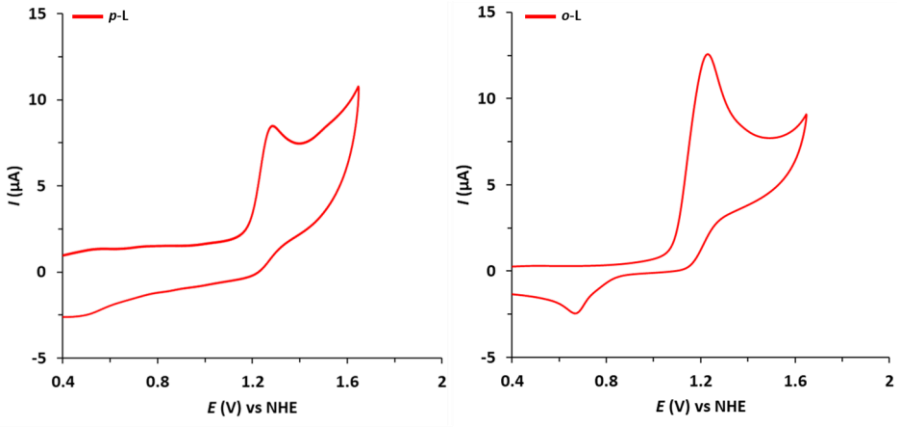

Figure S21. (**Left**) Cyclic Voltammograms of *p*-L (left) and *o*-L (right) in DMF containing 0.1 M of TBAPF. Conditions: scan rate of 100 mV/s and [ligand] = 1 mM. Conditions: 1 mM of ligand or complex in DMF containing 0.1 M of TBAPF. GC disk as working electrode.

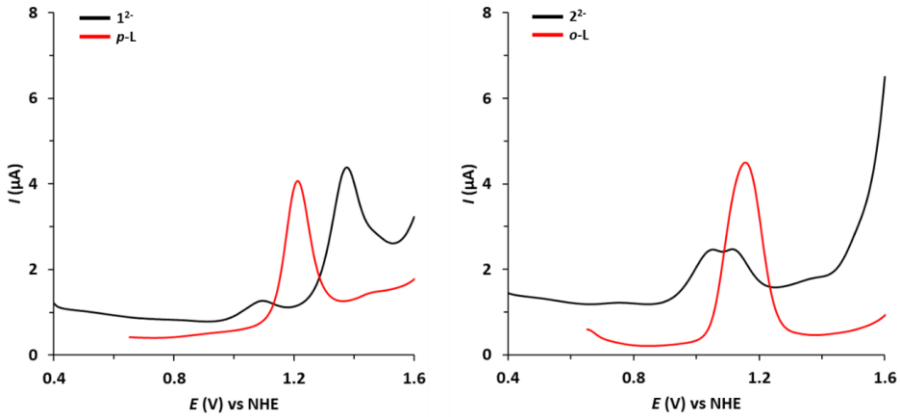

Figure S22. (**Left**) DPV experiments of **1²⁻** (black line) and *p*-L (red line). (**Right**) DPV experiments of **2²⁻** (black line) and *o*-L (red line). Conditions: 1 mM of ligand or complex in DMF containing 0.1 M of TBAPF. GC disk as working electrode.

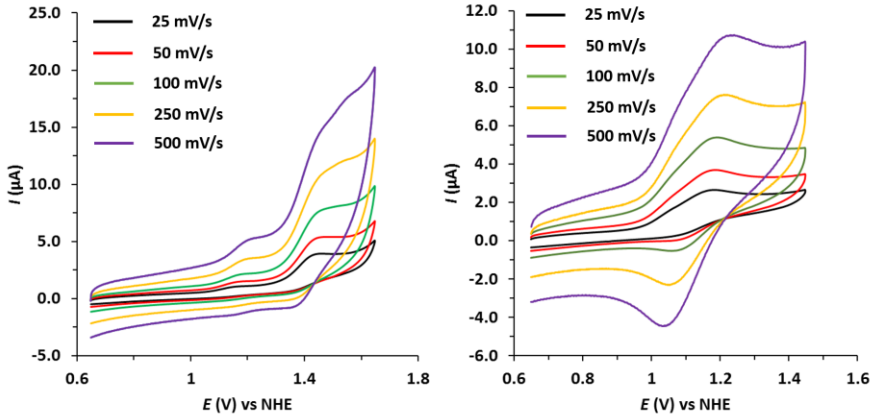

Figure S23. Cyclic Voltammograms of $\mathbf{1}^{2-}$ (left) and $\mathbf{2}^{2-}$ (right) at different scan rates (25-500 mV/s). Conditions: 1 mM of complex in DMF containing 0.1 M of $TBAPF_6$. GC disk as working electrode.

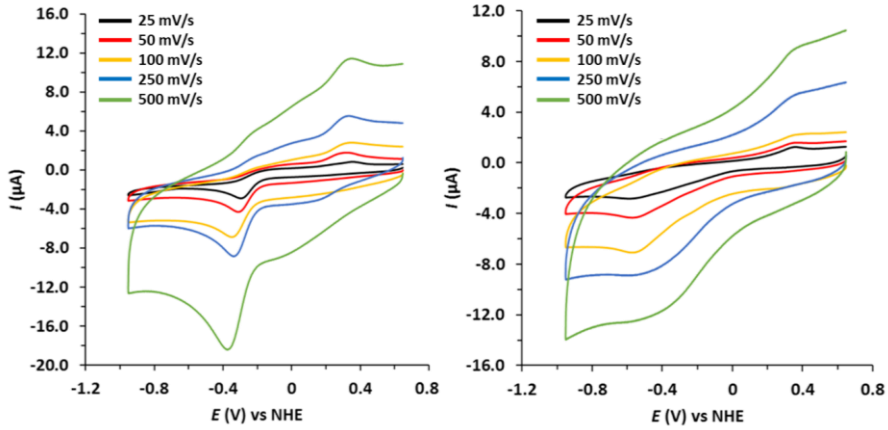

Figure S24. Cyclic Voltammograms of $\mathbf{1}^{2-}$ (left) and $\mathbf{2}^{2-}$ (right) at different scan rates (25-500 mV/s). Conditions: 1 mM of complex in DMF containing 0.1 M of $TBAPF_6$. GC disk as working electrode.

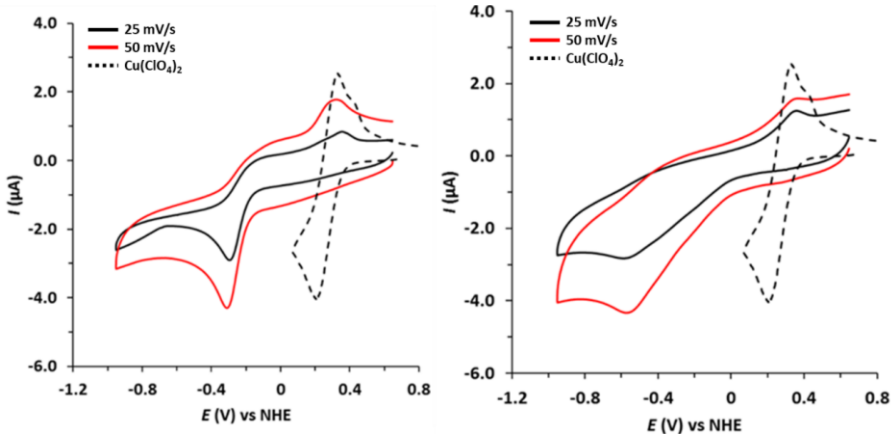

Figure S25. Cyclic Voltammograms of $\mathbf{1}^{2-}$ (left) and $\mathbf{2}^{2-}$ (right) at low scan rates (25-50 mV/s). Dashed black line corresponds to a blank solution containing 1 mM of $Cu(ClO_4)_2$ salt at 100 mV/s scan rate. Conditions: 1 mM of complex in DMF containing 0.1 M of TBAPF. GC disk as working electrode.

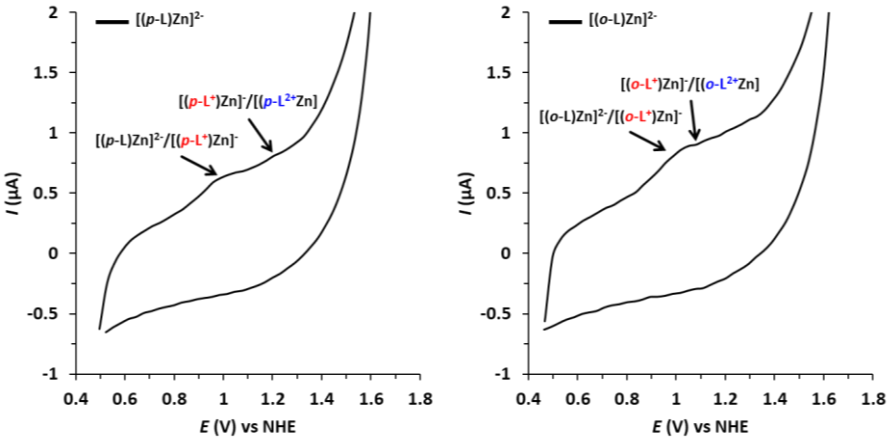

Figure S26. Cyclic Voltammograms of **[(*p*-L)Zn]$^{2-}$** (left) and **[(*o*-L)Zn]$^{2-}$** (right) in DMF containing 0.1 M of TBAPF. Conditions: scan rate of 100 mV/s and [Complex] = 8 mM.

From ligand-based to metal-based electron transfer in water oxidation catalysis

Electrochemical behaviour in water

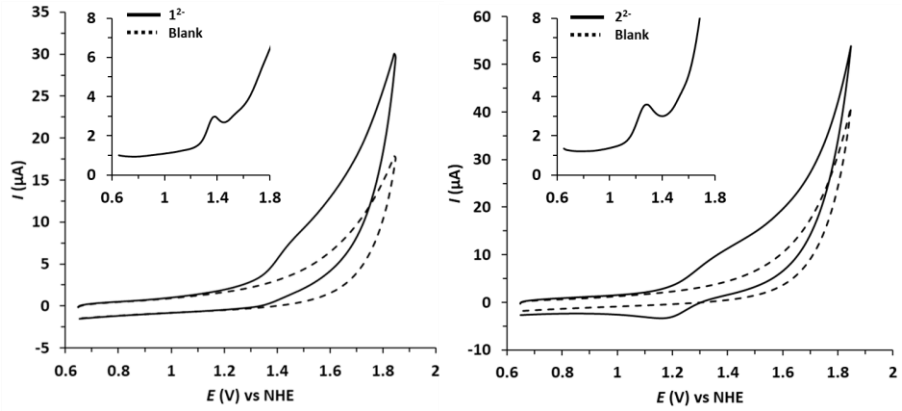

Figure S27. Cyclic Voltammograms of $\mathbf{1}^{2-}$ (left) and $\mathbf{2}^{2-}$ (right) in 0.1 M phosphate buffer pH 7.0. *Inset* Differential Pulse Voltammograms for $\mathbf{1}^{2-}$ and $\mathbf{2}^{2-}$. Dashed black line corresponds to a blank with no catalyst. Conditions: scan rate of 100 mV/s, [**Complex**] = 1 mM. GC as working electrode.

IV

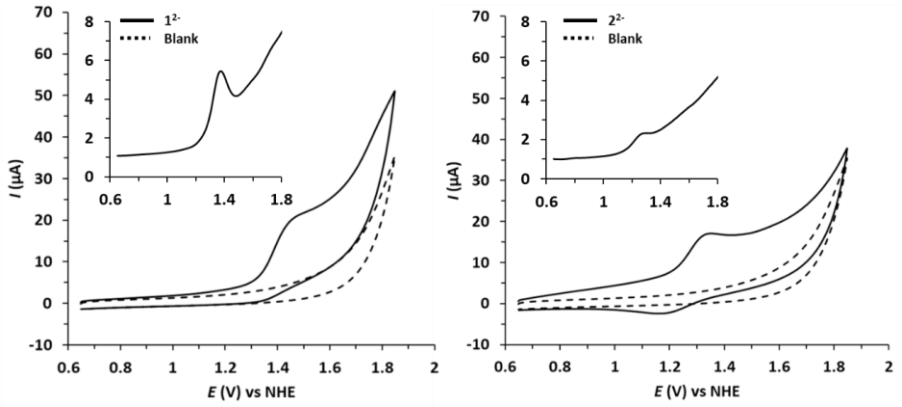

Figure S28. Cyclic Voltammograms of $\mathbf{1}^{2-}$ (left) and $\mathbf{2}^{2-}$ (right) in 0.1 M phosphate buffer pH 9.0. *Inset* Differential Pulse Voltammograms for $\mathbf{1}^{2-}$ and $\mathbf{2}^{2-}$. Dashed black line corresponds to a blank with no catalyst. Conditions: scan rate of 100 mV/s, [**Complex**] = 1 mM. GC disk as working electrode.

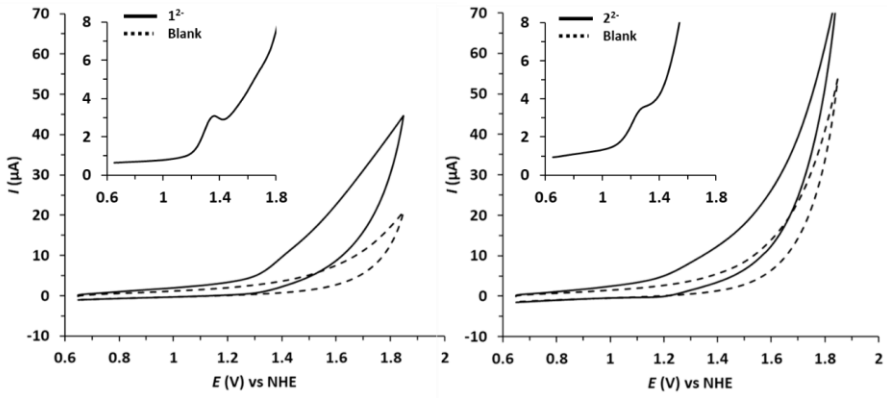

Figure S29. Cyclic Voltammograms of $\mathbf{1}^{2-}$ (left) and $\mathbf{2}^{2-}$ (right) in 0.1 M phosphate buffer pH 11.4. *Inset* Differential Pulse Voltammograms for $\mathbf{1}^{2-}$ and $\mathbf{2}^{2-}$. Dashed black line corresponds to a blank with no catalyst. Conditions: scan rate of 100 mV/s, [**Complex**] = 1 mM. GC as working electrode.

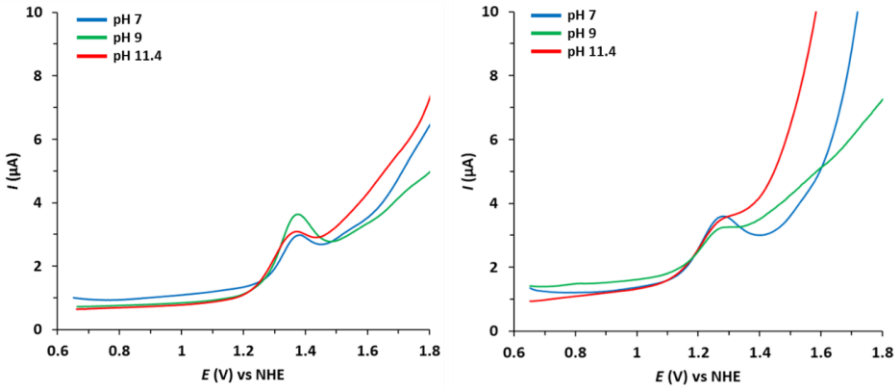

Figure S30. DPV experiments of $\mathbf{1}^{2-}$ (left) and $\mathbf{2}^{2-}$ (right), 1 mM concentration in phosphate buffers (pH 7.0, 9.0 and 11.4). GC as working electrode.

From ligand-based to metal-based electron transfer in water oxidation catalysis

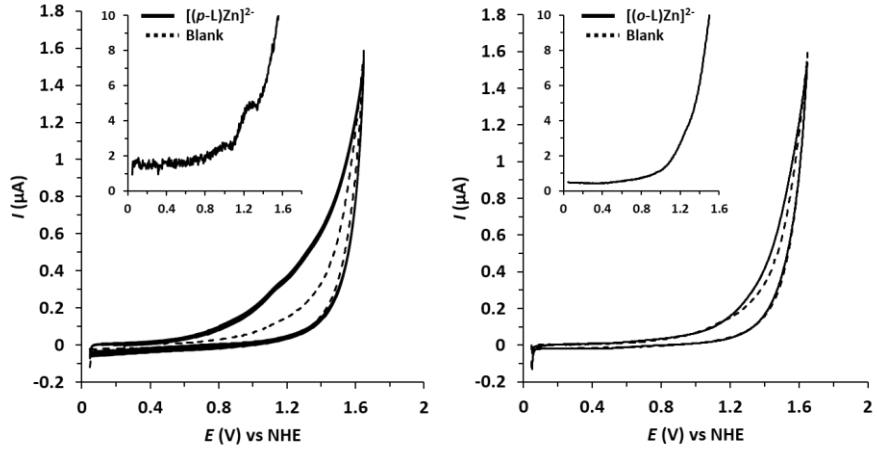

Figure S31. Cyclic Voltammograms of **[(*p*-L)Zn]$^{2-}$** (left) and **[(*o*-L)Zn]$^{2-}$** (right) in 0.1 M phosphate buffer pH 11.4. *Inset* Differential Pulse Voltammograms for **[(*p*-L)Zn]$^{2-}$** and **[(*o*-L)Zn]$^{2-}$**. Dashed black line corresponds to a blank with no catalyst. Conditions: scan rate of 100 mV/s, [**Complex**] = 8 mM. GC as working electrode.

IV

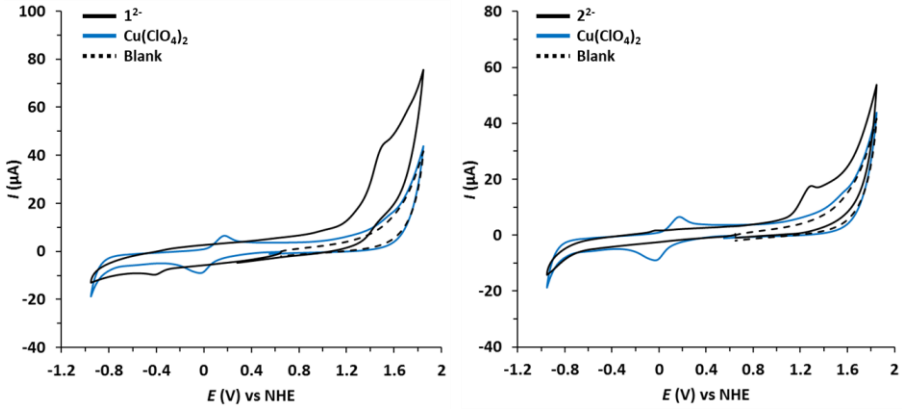

Figure S32. Cyclic Voltammograms of **1^{2-}** (left) and **2^{2-}** (right) in 0.1 M phosphate buffer pH 11.4, showing the electrocatalytic response of the complex (solid black line), $Cu(ClO_4)_2$ (solid blue line) and the blank (dashed line). Conditions: scan rate of 100 mV/s, [**Complex**] = 1 mM. BDD disk as working electrode.

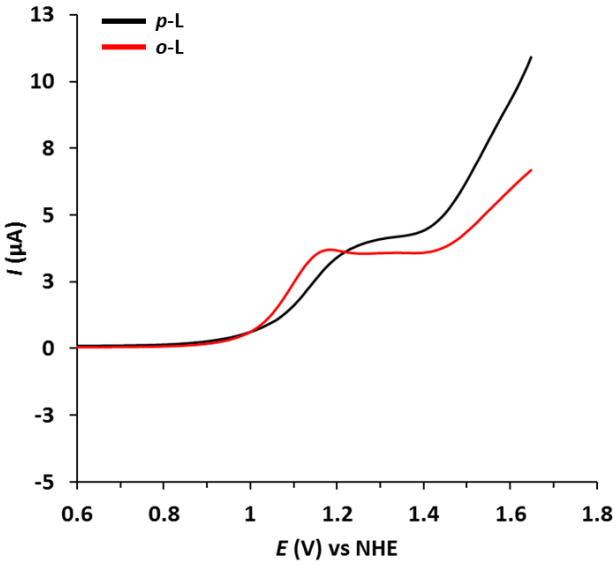

Figure S33. DPV experiments of *p*-L (black line) and *o*-L (red line) in 0.1 M phosphate buffer pH 11.4. [**Ligand**] = ~1 mM. BDD disk as working electrode.

From ligand-based to metal-based electron transfer in water oxidation catalysis

Determination of the kinetic constant. Foot of the Wave Analysis (FOWA).

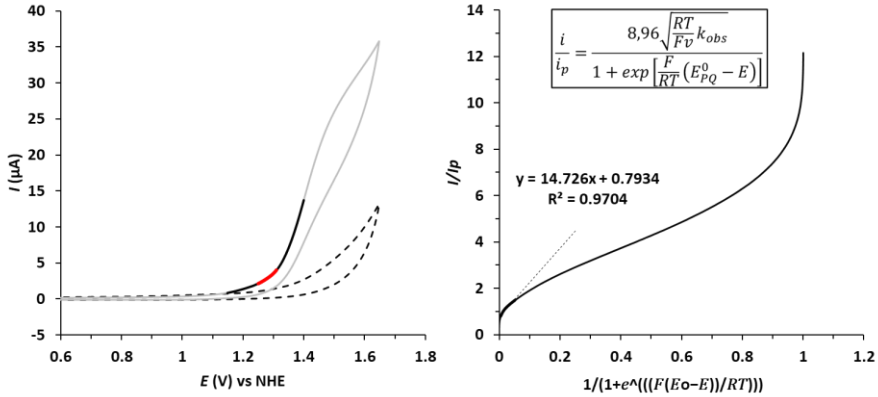

Figure S34. (Left) CVs of 1 mM solution of $\mathbf{1}^{2-}$ in 0.1 M phosphate buffer (pH 11.4) at 100 mV/s scan rate (grey line) and the blank (dashed line). Solid red line corresponds to the experimental data used for FOWA analysis and Solid black line shows the region used for the determination of k_{obs}. (Right) FOWA of $\mathbf{1}^{2-}$ by plotting i/i_p^0 vs. $1/\{1+\exp[(F/RT)(E^0_{PQ}-E)]\}$. *Inset* FOWA equation operative under catalytic conditions, where E^0_{PQ} corresponds to the standard potential for the catalytic wave (observed at 1.35 V according to the DPV shown in Figure S30), i is the current in the presence of substrate, i_p^0 corresponds to the peak current of one-electron redox process of the catalyst (This value was extracted from the Cu^{II}/Cu^{I} couple observed at -0.4 V according to the CV shown in Figure S32), F is the faradaic constant (96485 C mol^{-1}) and R is 8.314 J mol^{-1} K^{-1}.[10]

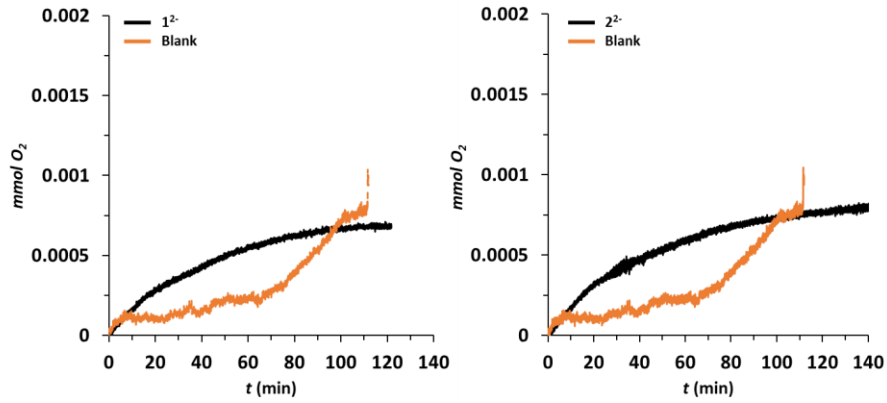

Figure S35. Oxygen evolution measurements given in mmol O_2 vs. time (min) for complexes $\mathbf{1}^{2-}$ (left) and $\mathbf{2}^{2-}$ (right) at 1.5 mM concentration using a Clark probe electrode during a CPE at 1.6 V vs. NHE in 0.1 M phosphate buffer pH 7. Blank data in the absence of complex is shown in orange.

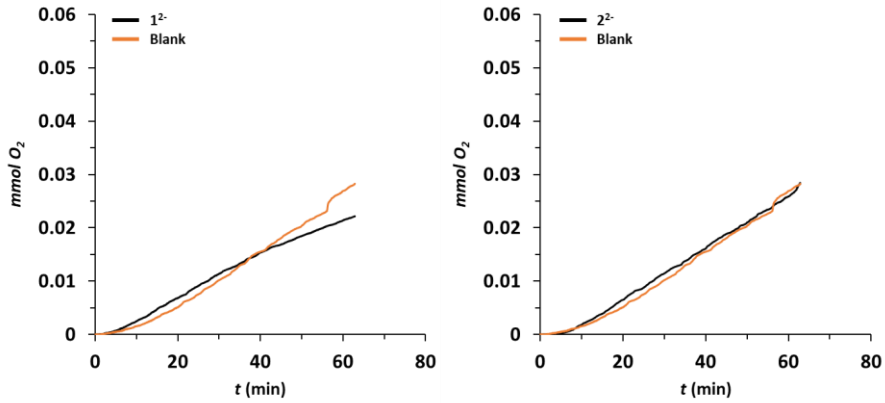

Figure S36. Oxygen evolution measurements given in mmol O_2 vs. time (min) for complexes $\mathbf{1}^{2-}$ (left) and $\mathbf{2}^{2-}$ (right) at 1.5 mM concentration using a Clark probe electrode during a CPE at 1.6 V vs. NHE in 0.1 M borate buffer pH 9. Blank data in the absence of complex is shown in orange.

From ligand-based to metal-based electron transfer in water oxidation catalysis

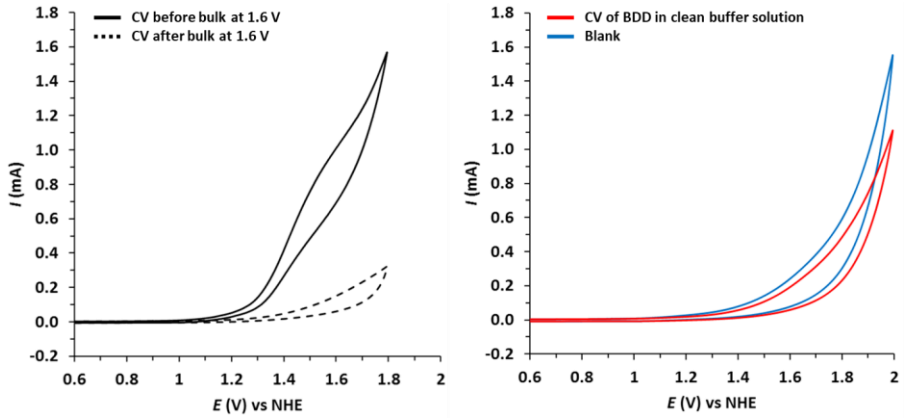

Figure S37. (Left) CV measurements for $\mathbf{1}^{2-}$ before (black solid line) and after (black dashed line) a CPE at 1.6 V during 95 min in 0.1 M phosphate buffer pH 11.4. **(Right)** Comparison of CVs of a blank solution after a CPE at 1.6 V during 95 min and the mechanically polished BDD electrode under a blank solution, showing no catalytic response due to the presence of heterogeneous materials deposited onto the surface of the electrode. Conditions: scan rate of 100 mV/s. BDD plate as working electrode, Pt mesh counter electrode and Ag/AgCl as reference electrode.

IV

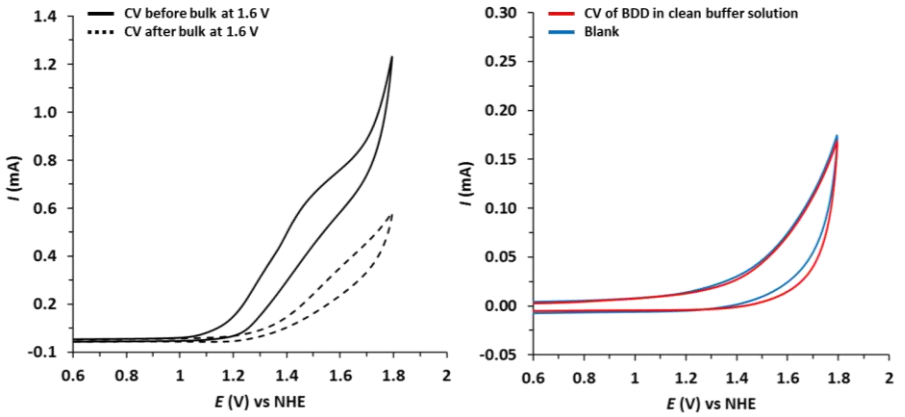

Figure S38. (Left) CV measurements of $\mathbf{2}^{2-}$ before (black solid line) and after (black dashed line) a CPE at 1.6 V during 45 min in 0.1 M phosphate buffer pH 11.4. **(Right)** Comparison of CVs of a blank solution after a CPE at 1.6 V during 95 min and of the mechanically polished BDD electrode under a blank solution, showing no catalytic response due to the presence of heterogeneous materials deposited onto the surface of the electrode. Conditions: scan rate of 100 mV/s. BDD plate as working electrode, Pt mesh counter electrode and AgCl as reference electrode.

Scanning Electron Microscopy

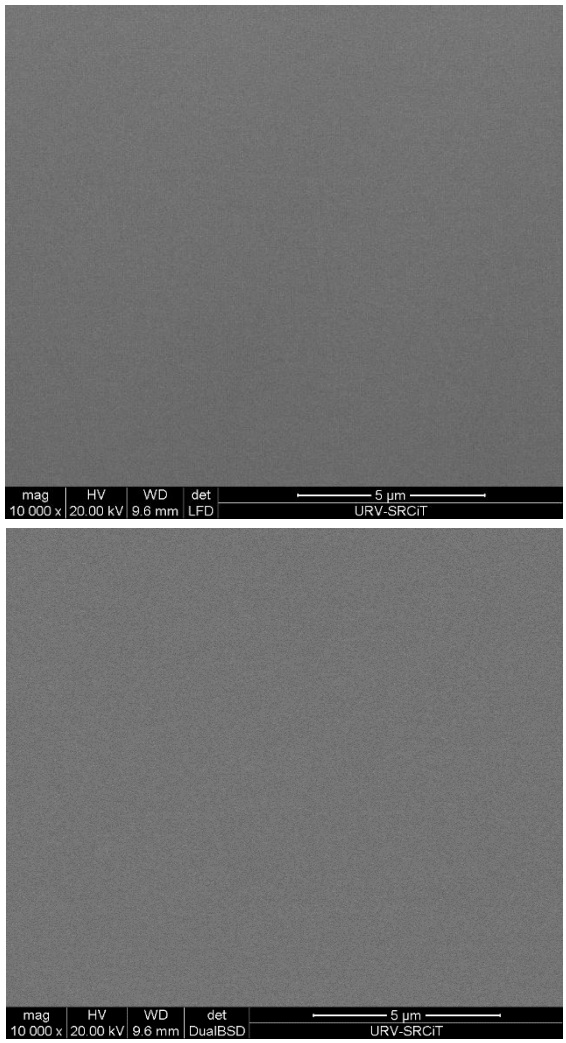

Figure S39. SEM micrographs (left) and corresponding back-scattered electron micrographs (right) of a glassy carbon electrode after a 20 minute electrolysis of $\mathbf{1}^{2-}$ (1.5 mM) in phosphate buffer pH 11.4 at 1.6 V vs. NHE. There is no appreciable presence of copper oxide nanoparticles or deposited materials on the electrode.

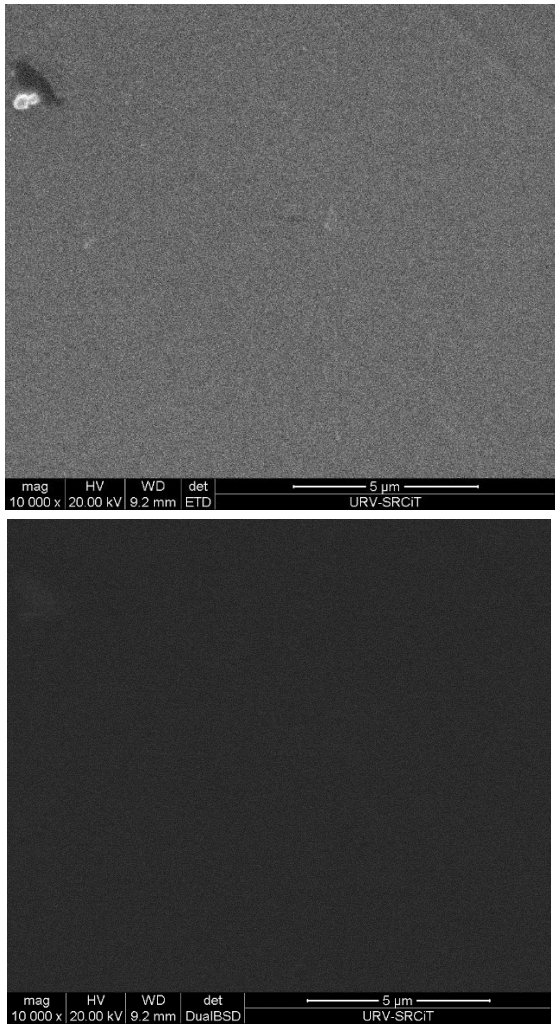

Figure S40. SEM micrographs (left) and corresponding back-scattered electron micrographs (right) of glassy carbon electrode after a 20 minute electrolysis of $\mathbf{2}^{2-}$ (1.5 mM) in phosphate buffer pH 11.4 at 1.6 V vs. NHE. There is no appreciable presence of copper oxide nanoparticles or deposited materials on the electrode.

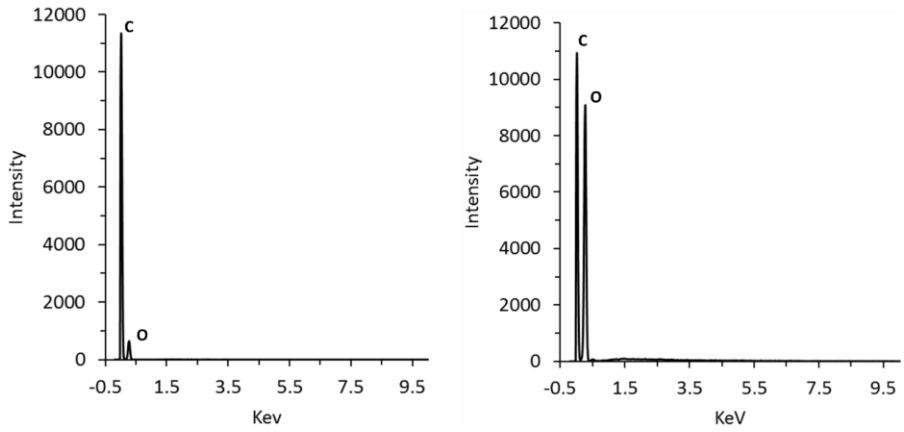

Figure S41. EDX spectra of the glassy carbon electrode after a 20 minute electrolysis of $\mathbf{1}^{2-}$(left) and $\mathbf{2}^{2-}$ (right) in phosphate buffer pH 11.4 at 1.6 V vs. NHE. There is no appreciable presence of copper on the surface of the electrode.

Computational studies

Computational Details

We perform all the calculations with the Gaussian09 program package[11] using the DFT methodology. We employed B3LYP functional including empirical dispersion correction proposed by Grimme (B3LYP-D3).[12,13] We split the basis set into 6-31+G(d) for C, N, S, O and H,[14] and LANL2TZ(f) for Cu.[15,16] Implicit solvation was introduced through the SMD model,[17] with water as the solvent. All geometry optimizations were computed in solution without symmetry restrictions. We confirmed the nature of all computed stationary points as minima or transition states through vibrational frequency calculations. Free energy corrections were calculated at 298.15 K and 105 Pa pressure, including zero point energy corrections (ZPE). In addition, a correction term of 1.9 kcal/mol (at 298 K) was added when necessary to account for the standard state concentration of 1 M, except for water whose considered concentration was 55.6 M and the correction term 4.3 kcal/mol. Unless otherwise mentioned, all reported energy values are free energies in solution.

We estimate the reaction energy barriers from potential energy relaxes scan when the transition states cannot be found (or do not exist), applying entropic corrections from the minima to compute an estimated free energy change.

In the transformation from free energies to electrochemical magnitudes we took from the literature the values of 4.28 V for the absolute potential of the standard hydrogen electrode[18] and-11.72 eV for the free energy of the proton in aqueous solution at pH=1.[19] The value for the free energy of the proton was translated to the experimental pH value by adding a correction term of -0.059*pH, following the same procedure as other authors.[20]

The functional for the DFT calculations was B3LYP-D3 based on the calibration carried out in a previous work on related systems,[3,22] where its performance was compared with that of M06, M06-D3, M06L, M06-2X, ωB97xD and B97D. In order to validate this DFT methodology, we compared the calculated optimized structures with the X-Ray ones. The following table summarize all the main metrics of the coordination environment for the copper metal center:

Table S4. Comparison of the main metrics for the X-Ray structure and the DFT optimized structure of complexes $\mathbf{1}^{2-}$ and $\mathbf{2}^{2-}$.

Complex	Metric	X-Ray (Solid)	DFT Optimized (Water)
1^{2-}	$Cu\text{-}N_{bpy}$	1.95 Å, 1.95 Å	2.00 Å, 2.00 Å
	$Cu\text{-}N_{amide}$	2.00 Å, 2.00 Å	2.04 Å, 2.05 Å
	$N_{bpy}\text{-}Cu\text{-}N_{bpy}$	78.27°	77.55°
	$N_{amide}\text{-}Cu\text{-}N_{amide}$	119.69°	123.15°
2^{2-}	$Cu\text{-}N_{bpy}$	1.95 Å, 1.95 Å	1.99 Å, 1.99 Å
	$Cu\text{-}N_{amide}$	2.00 Å, 2.00 Å	2.02 Å, 2.03 Å
	$N_{bpy}\text{-}Cu\text{-}N_{bpy}$	78.49°	78.02°
	$N_{amide}\text{-}Cu\text{-}N_{amide}$	120.78°	123.01°

Moreover, we also validate our methodology with respect to the experimental value for the redox potential of the Cu(III)/Cu(II) redox couple for both catalysts in water solutions:

From ligand-based to metal-based electron transfer in water oxidation catalysis

Table S5. Comparison of the experimental and calculated redox potential for the Cu(III)/Cu(II) couples in complexes $\mathbf{1}^{2-}$ and $\mathbf{2}^{2-}$.

Complex	$E_{1/2}^{o}$ (exp)	$E_{1/2}^{o}$ (calc)
1^{2-}	1.37 V	1.27 V
2^{2-}	1.27 V	1.14 V

Speciation for complex 1^{2-} in water

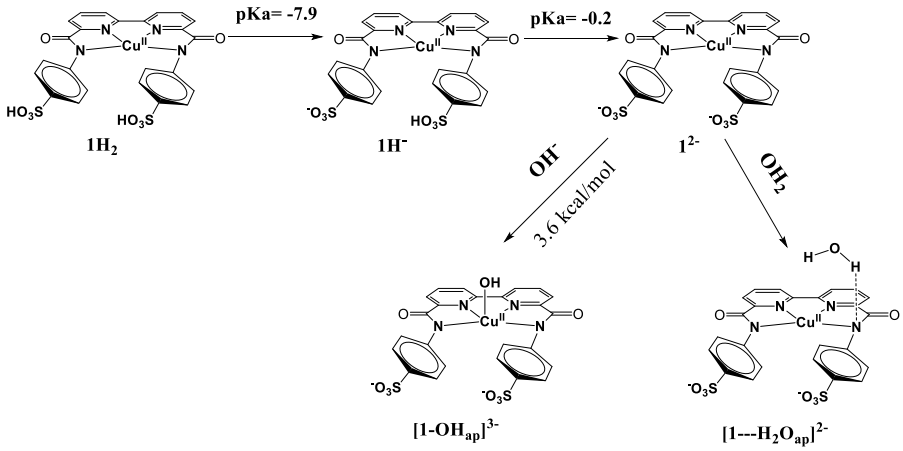

Figure S42. Deprotonation processes in complex $\mathbf{1}^{2-}$ and apical coordination of hydroxo or water molecules. The corresponding pK_a values or the free energy changes for each process are indicated above the arrows.

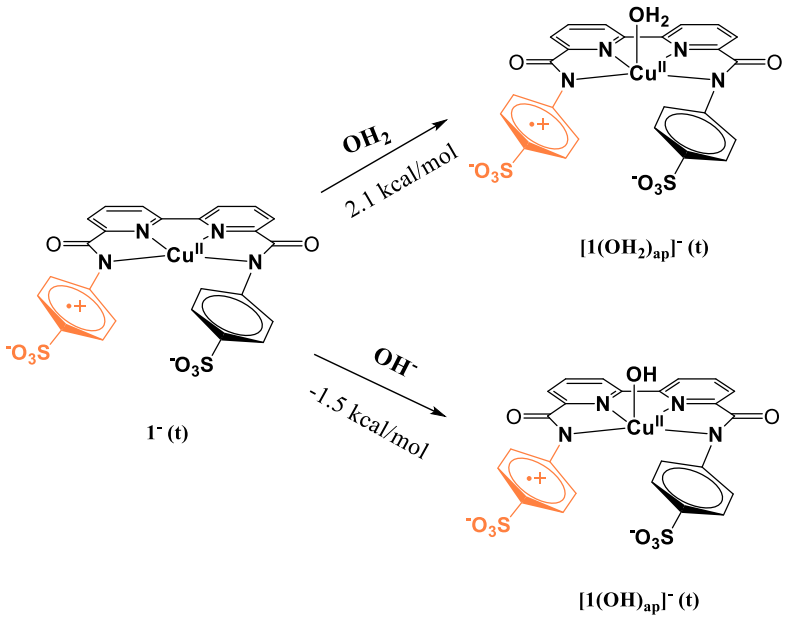

Figure S43. Apical coordination of hydroxo or water molecules in the one electron oxidized complex $\mathbf{1}^{-}$. The corresponding values of the free energy changes for each process are indicated above the arrows.

From ligand-based to metal-based electron transfer in water oxidation catalysis

Electrochemical activation for complex 1^{2-}

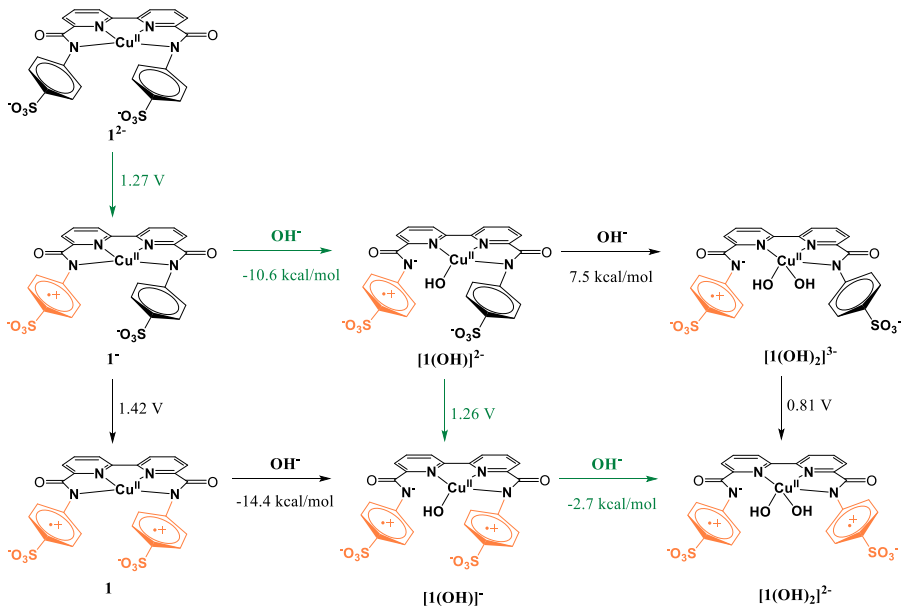

Figure S44. Possible pathways for the oxidation ox catalyst $\mathbf{1^{2-}}$ to generate an active species for the O-O bond formation step.

Potential energy relaxed scan for [1(OH)]⁻

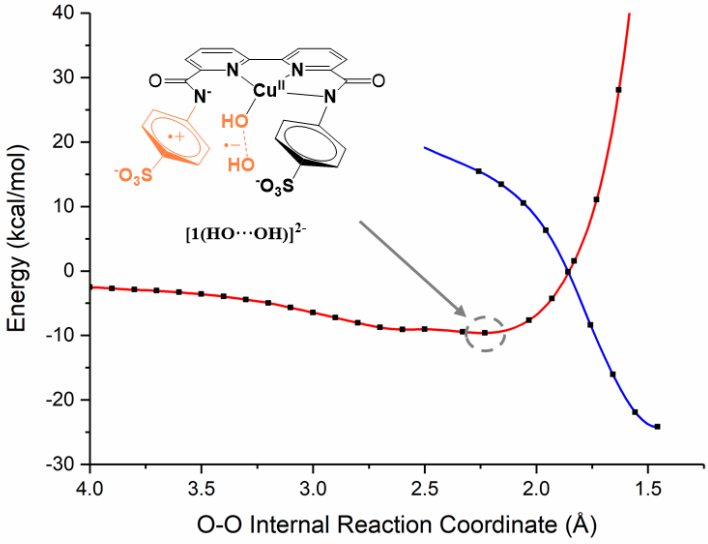

Figure S45. Potential energy relaxed scan for catalyst $\mathbf{1}^{2-}$ of the O-O reaction coordinate. Red colour represents the quartet state while blue colour indicates the doublet state.

From ligand-based to metal-based electron transfer in water oxidation catalysis

Structure and spin density distribution of 2c-3e intermediates

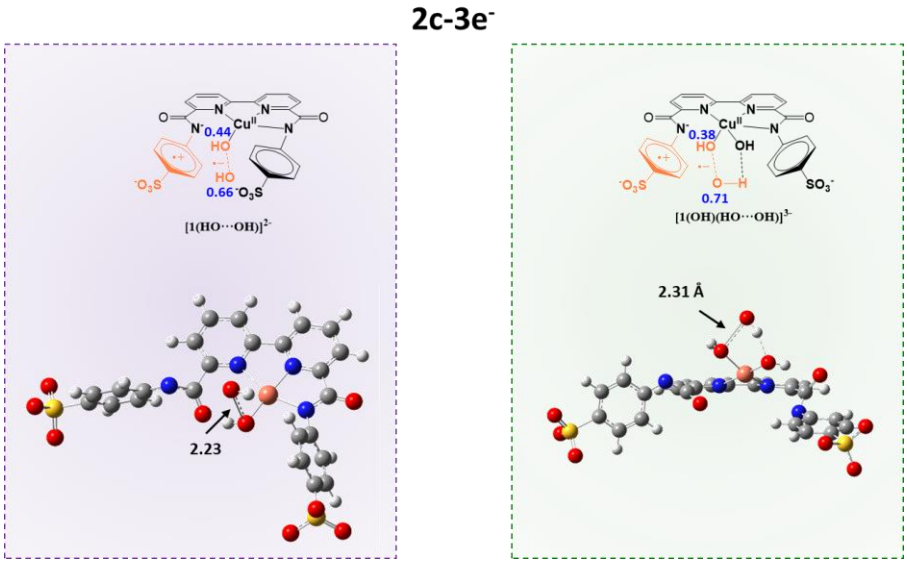

Figure S46. Schematic drawing with the spin distribution of each oxygen atom in blue (top) and optimized structure (bottom) of the 2c-3e intermediates for **[1(OH)]**$^{-}$ (left) and **[1(OH)$_2$]**$^{2-}$ (right) catalysts.

Intramolecular relaxed scan for [1(OH)$_2$]$^{2-}$

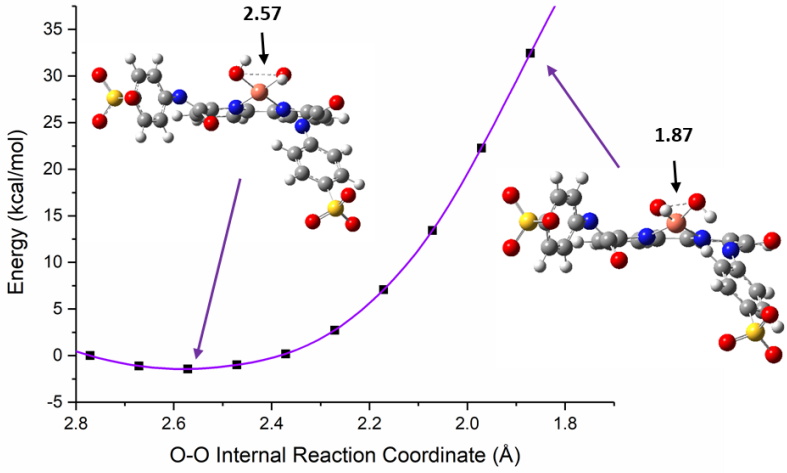

Figure S47. Potential energy relaxed scan of the intramolecular HO---OH coupling using catalyst **[1(OH)$_2$]$^{2-}$**.

References

1 G. Bozoklu, C. Marchal, C. Gateau, J. Pécaut, D. Imbert and M. Mazzanti, *Chem. Eur. J.*, 2010, **16**, 6159-6163.

2 J. Shao, Y.-H. Qiao, H. Lin and H.-K. Lin, *J. Lumin.*, 2008, **128**, 1985-1988.

3 P. Garrido-Barros, I. Funes-Ardoiz, S. Drouet, J. Benet-Buchholz, F. Maseras and A. Llobet, *J. Am. Chem. Soc.*, 2015, **137**, 6758-6761.

4 Data collection with APEX II version v2013.4-1. Bruker (2007). Bruker AXS Inc., Madison, Wisconsin, USA.

5 Data reduction with Bruker SAINT version V8.30c. Bruker (2007). Bruker AXS Inc., Madison, Wisconsin, USA.

6 SADABS: V2012/1 Bruker (2001). Bruker AXS Inc., Madison, Wisconsin, USA. R. H. Blessing, *Acta Cryst.*, 1995, ***A51***, 33-38.

7 SHELXT; V2014/4 (Sheldrick 2014), G. M. Sheldrick, *Acta Cryst.*, 2015, **A71**, 3-8.

8 SHELXle; C.B. Huebschle, G.M. Sheldrick and B. Dittrich, *J. Appl. Cryst.*, 2011, **44**, 1281-1284.

9 SHELXL; SHELXL-2014/7 (Sheldrick 2014). G.M. Sheldrick, *Acta Cryst.*, 2015, **C71**, 3-8.

10 R. Matheu, S. Neudeck, F Meyer, X. Sala and A. Llobet *ChemSusChem*, 2016, **9**, 3361-3369.

11 Gaussian 09, Revision **D.01**, M. J. Frisch, G. W. Trucks, H. B. Schlegel, G. E. Scuseria, M. A. Robb, J. R. Cheeseman, G. Scalmani, V. Barone, B. Mennucci, G. A. Petersson, H. Nakatsuji, M. Caricato, X. Li, H. P. Hratchian, A. F. Izmaylov, J. Bloino, G. Zheng, J. L. Sonnenberg, M. Hada, M. Ehara, K. Toyota, R. Fukuda, J. Hasegawa, M. Ishida, T. Nakajima, Y. Honda, O. Kitao, H. Nakai, T. Vreven, J. A. Montgomery, Jr., J. E. Peralta, F. Ogliaro, M. Bearpark, J. J. Heyd, E. Brothers, K. N. Kudin, V. N. Staroverov, R. Kobayashi, J. Normand, K. Raghavachari, A. Rendell, J. C. Burant, S. S. Iyengar, J. Tomasi, M. Cossi, N. Rega, J. M. Millam, M. Klene, J. E. Knox, J. B. Cross, V. Bakken, C. Adamo, J. Jaramillo, R. Gomperts, R. E. Stratmann, O. Yazyev, A. J. Austin, R. Cammi, C. Pomelli, J. W. Ochterski, R. L. Martin, K. Morokuma, V. G. Zakrzewski, G. A. Voth, P. Salvador, J. J. Dannenberg, S. Dapprich, A. D. Daniels, Ö. Farkas, J. B. Foresman, J. V. Ortiz, J. Cioslowski, and D. J. Fox, Gaussian, Inc., Wallingford CT, 2009.

12 A.D. Becke, *J. Chem. Phys.*, 1993, **98**, 5648-5652.

13 S. Grimme, J. Antony, S. Ehrlich and H. Krieg, *J. Chem. Phys.*, 2010, **132**, 154104.

14 a) W.J. Hehre, R. Ditchfield, J.A. Pople, *J. Chem. Phys.*, 1972, **56**, 2257. b) P.C. Hariharan, J.A. Pople, *Theor. Chim. Acta.*, 1973, **28**, 213-222. c) M.M. Francl, W.J. Petro, W.J. Hehre, J.S. Binkley, M.S. Gordon, D.J. DeFrees and J.A. Pople, *J. Chem. Phys.*, 1982, **77**, 3654-3665.

15 a) P. J. Hay and W. R. Wadt, *J. Chem. Phys.*, 1985, **82**, 270-283. b) P. J. Hay and W. R. Wadt, *J. Chem. Phys.*, 1985, **82**, 284-298. c) P. J. Hay and W. R. Wadt, *J. Chem. Phys.*, 1985, **82**, 299-310.

16 Taken from EMSL Basis set Library: a) D. Felier, *J. Comp. Chem.,* 1996, **17**, 1571-1586. b) K.L. Schuchardt, B.T. Didier, T. Elsethagen, L. Sun, V. Gurumoorthi, J. Chase, J. Li and T.L. Windus, *J. Chem. Inf. Model.,* 2007, **47**, 1045-1052.

17 S. A. V. Marenich, C. J. Cramer and D. G. Truhlar, *J. Phys. Chem. B.*, 2009, **113**, 6378-6396.

18 a) A. Lewis, J. A. Bumpus, D. G. Truhlar and C. J. Cramer, *J. Chem. Ed.*, 2004, **81**, 596-603. b) A. Lewis, J. A. Bumpus, D. G. Truhlar and C. J. Cramer, *J. Chem. Ed.*, 2007, **84**, 934 [Erratum].

19 A. V. Marenich, A. Majunmdar, M. Lenz, C. J. Cramer and D. G. Truhlar, *Angew. Chem. Int. Ed.,* 2012, **51**, 12810-12814.

20 S.G. Winikoff and C.J. Cramer, *Catal. Sci. Technol.*, 2014, **4**, 2484-2489.

21 I. Funes-Ardoiz, P. Garrido-Barros, A. Llobet and F. Maseras, *ACS Cat.*, 2017, **7**, 1712-1719.

Paper D: Transition from redox innocent to redox non-innocent ligand enables catalytic water oxidation

Garrido-Barros, P.; Gil-Sepulcre, M.; Bozoglian, F.; Holub, J.; Zamudio, J.; Llobet, A. **2018**, *manuscript in preparation*

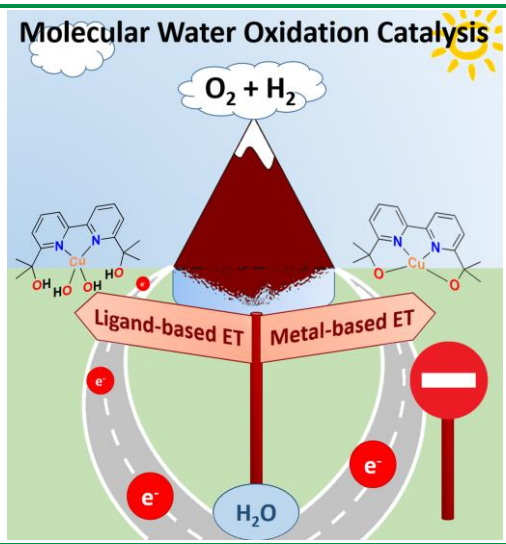

Abstract

The present work covers the study of the copper complex [(bpk)Cu] (bpk is 6,6'-diisopropanoate-2,2'-bipyridine) as a water oxidation catalyst. This Cu(II) complex bear a redox innocent ligand and shows high stability upon oxidation to Cu(III) species in the pH range from 7 to 12. Unfortunately, the lack of more easily-accessed oxidation states prevent the complex from catalyzing the water oxidation. However, at pH between 13 and 14, the complex undergoes a partial ligand decoordination with concominant coordination of hydroxo molecules. The remaining dangling alkoxo groups get protonated forming alcohols and this groups are susceptible to be oxidized at affordable potentials around 1-1.2 V conferring the ligand a redox non-innocent character. The formed hydroxo species have been spectroscopically and electrochemically characterized

featuring catalytic activity toward water oxidation. The catalytic mechanism has been computationally studied revealing the essential role of the ligand oxidation in the electron transfers that enable the O-O bond formation.

Contributions:

Pablo Garrido Barros performed the computational calculations and, together with Marcos Gil-Sepulcre carried out the preparation and characterization of the compounds, the electrochemical and spectroscopic analysis, and the preparation of the manuscript.

D.1. Introduction

Water splitting to generate hydrogen and oxygen from water and sunlight is a potential strategy for renewable energy production.[1,2,3] The hydrogen produced in this way stores the solar energy into chemical bonds and can be further used as a clean fuel. From a redox point of view, water splitting can be separated into the two half-reactions: water oxidation and proton reduction. One of the current challenge regarding water splitting is the development of water oxidation catalysts to overcome the kinetic restrictions of this reaction. Most of the initial work in this field involved the use of Ru and Ir molecular complexes that were able to catalyze the oxidation of water to molecular oxygen. [4,5] However, this 2nd and 3rd row transition metals are generally more expensive and less abundant than the 1st row transition metals. This is the reason for the recent take off of molecular catalysts based on Fe, Cu, Ni, and Co complexes.[6,7,8]

Particularly, copper has been focused of extensive study and a number of molecular complexes have been reported as homogeneous catalysts. [9,10,11,12,13,14,15] First examples of copper catalysts involved the use of redox innocent and redox non-innocent bidentate ligands based on a bypyridine scaffold forming square planar complexes with hydroxo groups coordinated in the equatorial position.[9,12] In those complexes, two consecutive

oxidation steps take place before the O-O bond formation but, interestingly, they do not lead to Cu(IV) species in any case. Instead, Cu(III) species with a radical located either in an coordinating OH^- group or in the bipyridine ligand were formed, depending on the redox innocent or redox non-innocent character of the ligand respectively. Both complexes were also found to form the O-O bond with a similar mechanism based on single electron transfer, so called Single Electron Transfer-Water Nucleophilic Attack (SET-WNA).[16]

Shortly after, the copper complex $[(mox)Cu^{II}]^{2-}$ was reported with a tetraanionic redox-non innocent ligand *N*[1],*N*[1]'-(1,2-phenylene)bis(*N*[2]-methyloxalamide) H_4mox, which was also oxidized to form an active Cu(III) radical species $[(mox\cdot)Cu^{III}]$.[14] The tetradentate ligand saturates all the equatorial positions so that the chemistry related with the O-O bond formation takes place in the apical position where an OH^- is weakly coordinated thanks to the electron deficient character of the doubly oxidized species forming $[(mox\cdot)(OH)Cu^{III}]^-$. A SET-WNA mechanism was again found to be operative besides the significant differences with previous bipyridine systems. More recently, a Cu complex has been reported where two bidentate pyalk ligand saturate again the four equatorial positions of the Cu metal center.[15] Due to the redox-innocent character of the ligand and the absence of OH^- coordination, this complex cannot accumulate two oxidative equivalents to form an electron deficient species that can coordinate a hydroxide molecule in the apical position and promote the O-O bond formation, such as in the case of $[(mox)Cu^{II}]^{2-}$. Instead, once the complex is oxidized to a Cu(III) species, a hydroxide molecule binds the metal center in a equatorial position with a concomitant decoordination of a pyridine group thanks to the flexibility of the coordination environment.[17] Then the coordinated OH^- group is also oxidized through a proton coupled electron transfer (PCET) to form the active species $[(pyalk)_2(O\cdot)Cu^{III}]$ which promotes the O-O bond formation by a WNA mechanism.

The results with previous catalysts show that Cu(IV) species are never reached before the O-O bond formation. Instead, to access the higher oxidation states needed to promote the O-O bond formation, either the ligand or a coordinated OH^- have to assume the role of oxidizing to form active species. Therefore, a redox non-innocent ligand or coordination of hydroxide molecules are essential features that a copper-based water oxidation catalyst requires. This is in agreement with recent results by Batista where they study the complex **[(bpk)Cu^{II}]** (bpk is 6,6'-diisopropanoate-2,2'-bipyridine).[17] This complex lacks of redox non-innocent ligand and its rigid coordination environment prevent OH^- molecules to coordinate the metal center. Moreover, only the one-electron oxidized Cu(III) species is easily accessed but it is not electron deficient enough to coordinate OH^- molecules in the apical position. Then, it was found to be inactive at basic pH toward water oxidation catalysis. Therefore, using **[(bpk)Cu^{II}]** as model of inactive complex, we have studied the factors that determine the presence or absence of catalytic activity in this complex as well as the possible catalytic mechanism.

D.2. Results and discussion

D.2.1. Synthesis, characterization and electrochemical behavior of [(bpk)CuII]

The synthesis of the ligand 6,6'-diisopropanol-2,2'-bipyridine (H_2bpk) and its copper complex **[(H_2bpk)Cu^{II}]$^{2+}$** are summarized in Figure S2. 6,6'-Dimethyl-2,2'-bipyridine was oxidized to the corresponding dicarboxylic acid using potassium dichromate[18] and subsequent esterification in acid media using methanol afforded the precursor dimethyl [2,2'-bipyridine]-6,6'-dicarboxylate.[19] Final product was obtained via Grignard reaction using MeMgBr, with an overall yield of around 20%. Complexation using $Cu(OTf)_2$ in acetonitrile afforded the copper complex **[(H_2bpk)Cu^{II}]$^{2+}$**, that was crystallized from diethyl ether diffusion into an acetonitrile solution resulting in long blue crystal needles. Both, the

ligand and its corresponding complex were fully characterized by NMR, IR, UV-vis, EA and ESI-MS (Figures S4-13).

The X-Ray structure of **[(H$_2$bpk)Cu^{II}]$^{2+}$** revealed a distorted square planar geometry where the two alcohol groups are placed slightly below the plane formed by the copper and the bipyridine moiety (Figure 1 and Table S1). Distances for Cu-N bonds are 1.918 and 1.915 Å whereas they significantly increase to 1.985 and 1.976 Å in the case of Cu-O bonds. Moreover, the N-Cu-N and O-Cu-O angles are 81.69° and 116.71° respectively, reflecting the distortion from the ideal 90° in a square planar geometry. All those metrics, in contrast with structure of the chemically similar **[(Hpyalk)$_2$(Cl$^-$)Cu^{II}]$^+$** and **[(pyalk)$_2$Cu^{II}]** complexes,[15] reveal the relatively high rigidity of this copper complex supported by the tetradentate ligand H$_2$bpk. In the apical position, one of the triflate anion shows in a long contact with the metal center at a distance of 2.336 Å, although this position is expected to remain uncoordinated in solution.

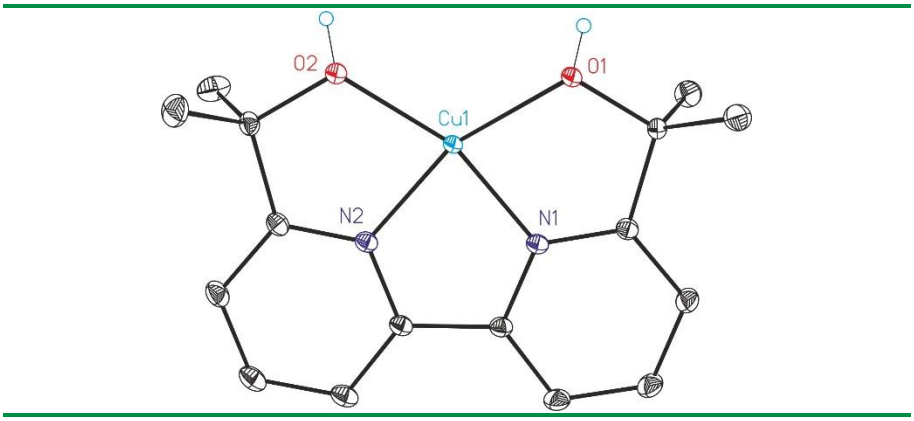

Figure 1. (A) ORTEP view of **[(H$_2$bpk)Cu]$^{2+}$** at 50% probability level. The counter ions, solvent molecules and hydrogen atoms have been omitted for clarity. Colour code: C, grey; N, blue; O, red; H, white; Cu, light blue.

The UV-vis spectra of complex **[(H$_2$bpk)Cu^{II}]$^{2+}$** in acetonitrile solutions features an absorption band at λ = 650 nm that might be related with a

MLCT process (Figure S13). At lower wavelengths, there are two prominent bands at 314 and 302 nm, with a small shoulder at 293 nm, that we associate to π-π^* transitions in the ligand.

Regarding aqueous media, **[(H$_2$bpk)Cu^{II}]$^{2+}$** is soluble in phosphate buffer solution at pH higher than 6, featuring a similar 650 nm band in the UV-vis spectrum, which indicate that the coordination environment is the same in acetonitrile than in water (Figure 2, left). Regarding the bands in the UV region, some differences can be observed depending on the pH of the solution. At pH 7, the UV-vis spectrum shows one main band at 290 and two shoulders at 302 and 314 nm. When we increase the pH up to 8 the band at 293 nm starts to decrease whereas the band at 314 nm increases its intensity. This change is more pronounced when we increase the pH up to 10, where the band at 293 nm remains as a low intensity shoulder. In all the cases, the band placed at 650 nm experienced a small increase in the intensity although does not shift the energy. Upon higher increase up to 12 we observe the same trend, with only two prominent bands at 302 and 314 nm, and the smaller band at 650 which remain unchanged. We associate these changes in the UV-vis spectra to the different protonation states of the ligand. As the pH decreases to 7, both alkoxo groups get protonated resulting in an unstable complex that eventually demetallates at lower pH values by ligand substitution releasing copper ions and free ligand as a white solid. The protonated complexes feature the three main bands at 293 and 302 and 650 nm, with a shoulder at 313 nm. At higher pH values, those groups consecutively deprotonate yielding finally the soluble uncharged complex **[(bpk)Cu^{II}]**, whose spectrum features the main bands at 302, 313, and 650 nm and a shoulder at 293 nm.

From ligand-based to metal-based electron transfer in water oxidation catalysis

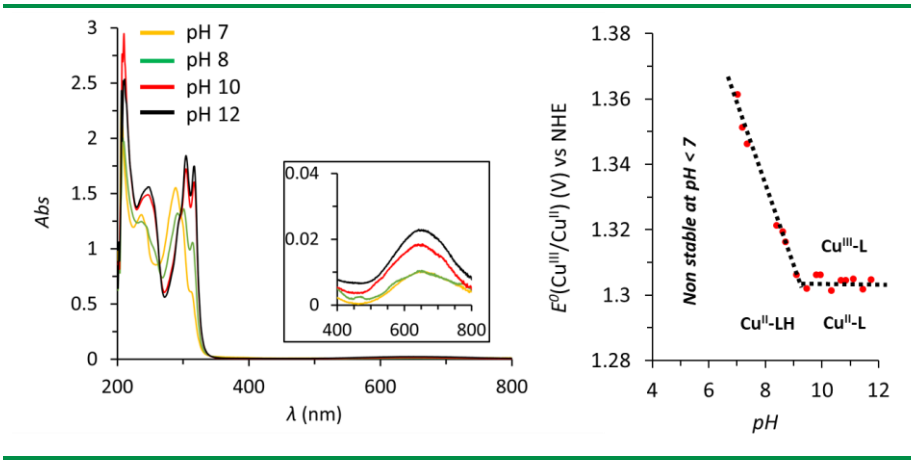

Figure 2. (Left) UV-Vis spectra of complex **[(H$_2$bpk)Cu]$^{2+}$** in a 0.1 M phosphate aqueous solution at different pH values. The inset shows a zoom of the 400-800 nm region with the bands corresponding to the MLCT. (B) Pourbaix diagram obtained by measuring the E^0 for the Cu(III)/Cu(II) redox couple from the previous CV experiments (Figure S15).

IV

We further explore the complex's speciation and its electrochemical behavior by cyclic voltammetry (CV) and differential pulse voltammetry (DPV). In pH 7 solutions, this complex shows a reversible wave at $E_{1/2}$=1.36 V with a peak to peak separation higher than 60 mV ($E_{p,a}$=1.41 V and $E_{p,c}$=1.31 V) corresponding to one-electron transfer process (Figure S14). This wave is assigned to the redox couple Cu^{III}/Cu^{II}, in agreement with the complex bearing similar reported ligand pyalk.[15] When scanning through cathodic potentials, the complex presents a wide quasi-reversible wave at around $E_{1/2}$=-0.03 V together with the appearance of a new oxidative peak in the subsequent anodic scan at around 0.36 V. The first quasi-reversible wave is related to the redox couple Cu^{II}/Cu^{I} that would involve a high reorganizational energy due to the change from square planar Cu^{II} to tetrahedral Cu^{I} geometry. This would explain the high peak to peak separation and the quasi-reversible character of this wave. On the other hand, the appearing oxidative wave at 0.36 V is related to free Cu^{+} ions as compared with a CV of $Cu(ClO_4)_2$ in the same buffer solution (Figure S18). The reason for the release of metal ions from the complex lies in the attempt to adopt a tetrahedral geometry

upon reduction typical for d^{10} Cu^{I} complexes that is frustrated by the high rigidity of the ligand.

Upon pH increase, the redox wave associated to Cu^{III}/Cu^{II} undergoes a shift toward lower potential in the pH range from 7 to 9 indicating the presence of a proton coupled electron transfer (PCET) that facilitates the oxidation to Cu^{III} (Figure 2, left). In those pH values, the coordinated ligand is mono-protonated but oxidation to the more electron deficient Cu^{III} causes an increase in the acidity of the coordinating alcohol and then eases the proton release turning back to the coordinated alkoxo form. From pH 9, since the ligand is deprotonated, the wave for the Cu^{III}/Cu^{II} redox couple stays unchanged at around 1.23 V with a full reversible character that demonstrate the high stability of the Cu^{II} and Cu^{III} complexes. We have not found any indication of electrocatalytic processes using **[(bpk)Cu^{II}]** under those reported conditions and possible water oxidation catalysis at higher potential values would lie behind the background current of the electrode. All these processes are summarized in the Pourbaix diagram of Figure 2, showing a PCET event with a slope of 40 mV per pH unit (similar to complex [$(pyalk)_2Cu$]) and pKa values for the alkoxo groups of around 7 and 9.5.

D.2.2. Ligand opening and formation of Cu-hydroxo species

Following the initial absence of electrocatalytic water oxidation by **[(bpk)Cu^{II}]**, we further analyzed its electrochemical behavior at extreme pH values between 13 and 14. As shown in Figure 3, the aforementioned reversible wave for the Cu^{III}/Cu^{II} redox couple turns into irreversible waves at similar potential values indicating that electrocatalytic water oxidation might be taking place. At pH 13 the irreversible wave is larger than at pH 14, where the electrocatalytic current is only slightly higher than the background signal as was already reported by Batista and coworkers.[17] That result indicates the presence of two processes at different pH values, one generating a very active species and a second one yielding less active

or inactive species. In order to explore the reason for the appearance of catalytic activity at those higher pH values, we analyzed the species involved in solution by spectroscopic techniques.

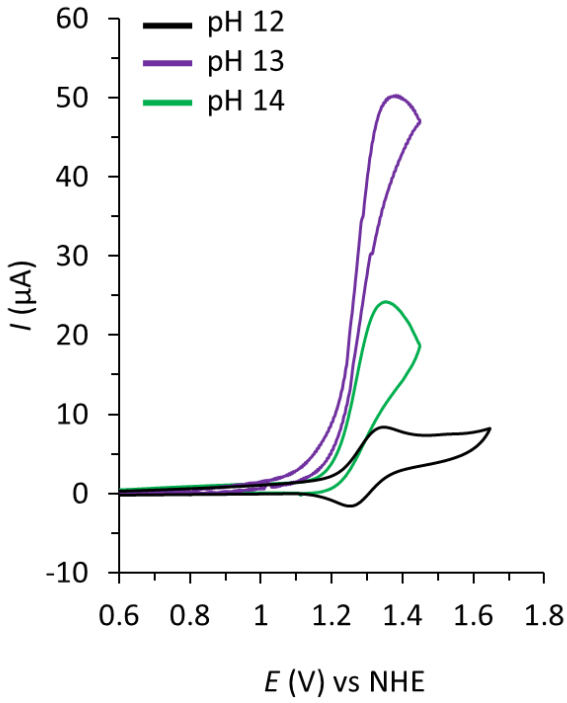

Figure 3. CVs of a 0.1 M phosphate aqueous solution containing 1 mM of the complex **[(bpk)Cu^{II}]** at different basic pH values. A GC disk was used as working electrode and the scan rate was set to 100 mV·s-1.

We first performed a spectrophotometric acid-base titration examining the UV-vis spectra of **[(bpk)Cu^{II}]** upon basification of the solution from pH 12 to pH 14 by successive addition of *conc.* NaOH (10 M) solution (Figure 4). As already discussed, the complex features two main bands at 315 and 304 nm with a small shoulder at 290 nm at pH 12 corresponding to the fully deprotonated ligand. This features however changed from pH 13.0 to 13.6 so that the two main bands decrease the intensity while the shoulder increases resulting in a spectrum that strongly reminds to the monoprotonated **[(Hbpk)Cu^{II}]$^{+}$** complex (Figure 2, left). As the pH increased to 14, those changes followed similar trend and become more

evident with a faster decrease of the bands at 315 and 304 nm in contrast to the relative increase of the band at 290 nm. The final spectrum has similar features as the one obtained at pH 6 for the protonated complex **[(H2bpk)Cu^{II}]$^{2+}$**. Plot of the maximum absorbance at 304 nm allows us to distinguish between those two regions of pH with different slopes where the monoprotonated and deprotonated species are formed respectively. Due to the high concentration of OH^-, we assign those two processes to the coordination of a hydroxo group coming from the media with the subsequent decoordination of one alkoxo group. The uncoordinated alkoxo group has now higher pKa than coordinated to the electron deficient metal center so that it protonates, as will be further supported by DFT (Figure S5 and S36). In the less alkaline region from 13 to 13.6, only one hydroxo group is introduced producing the complex **[(Hbpk)(OH)Cu^{II}]** whereas at higher pH both alkoxo groups are substituted giving rise to the complex **[(H$_2$bpk)(OH)$_2$Cu^{II}]**. Those two new species are the responsible for the appearance of catalytic activity.

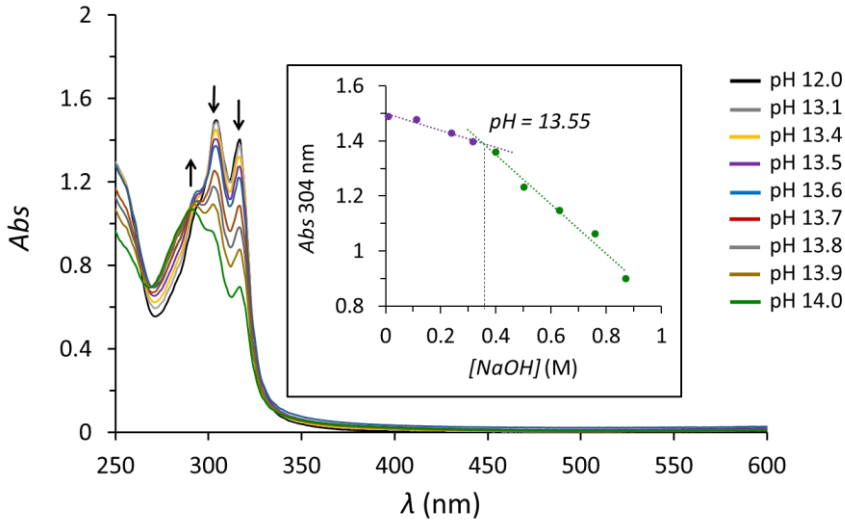

Figure 4. UV-Vis spectra of 1mM aqueous solution of **[(H$_2$bpk)Cu]$^{2+}$** in 0.1 M phosphate buffer at different pH values. The pH was adjusted by addition of a conc. NaOH (40 %). The inset shows the evolution of the absorption at 304 nm with the pH value of the solution.

From ligand-based to metal-based electron transfer in water oxidation catalysis

Scheme 1. (A) Mechanistic pathways for the formation of the Cu-hydroxo species that are active toward catalytic water oxidation.

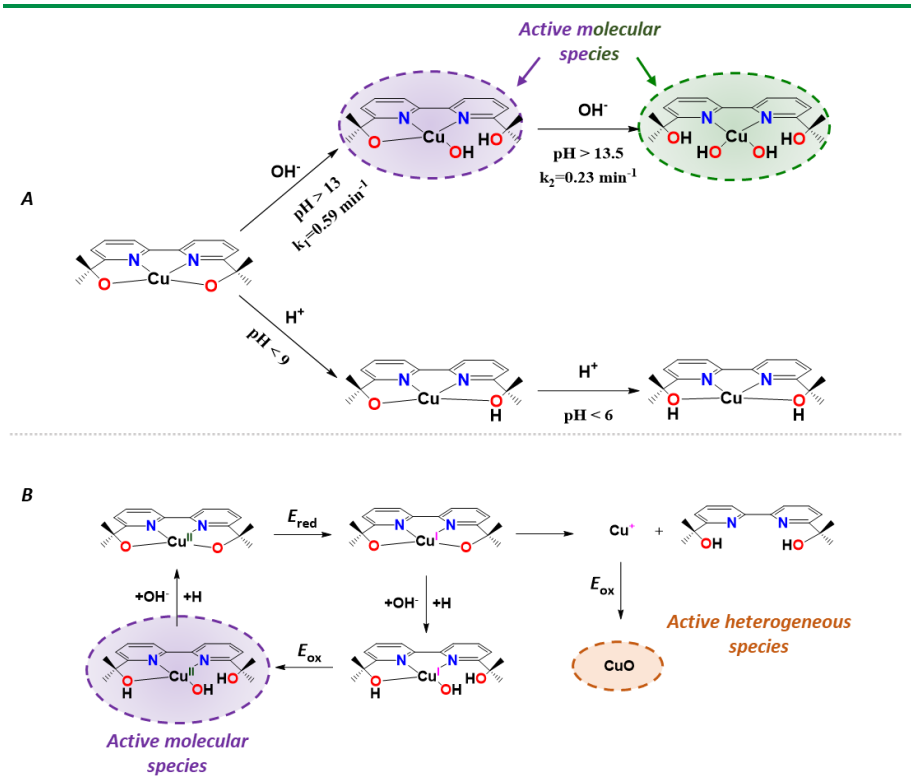

IV

Due to the fast substitutions processes, we analyze their kinetic by stopped-flow UV-vis experiment at pH 14 by mixing a pH 12 solution containing 1 mM of **[(bpk)Cu^{II}]** with a 1 M NaOH solution and we record the UV-vis spectra during the first seconds of reaction (Figure 5, left). We then fitted the experimental data to a model where two consecutive irreversible reactions take place as shown in the Figure 5, right.

$$[(bpk)Cu] \xrightarrow[k_{H,1}]{+H_2O} [(Hbpk)(OH)Cu]^{+} \xrightarrow[k_{H,2}]{+H_2O} [(H_2bpk)(OH)_2Cu]^{2+} \qquad (1)$$

Both experimental and fitting data were in good agreement with calculated kinetic constants of 0.59 min^{-1} and 0.23 min^{-1} (Scheme 1, top). Figure S20 also shows the calculated UV-Vis spectra for the formed species and the distribution diagram vs. time where the initial decrease of complex

[(bpk)Cu^{II}] give rise first to a fast increase of complex **[(Hbpk)(OH)Cu^{II}]** which in turn runs out to produce the di-substituted species **[(H$_2$bpk)(OH)$_2$Cu^{II}]**.

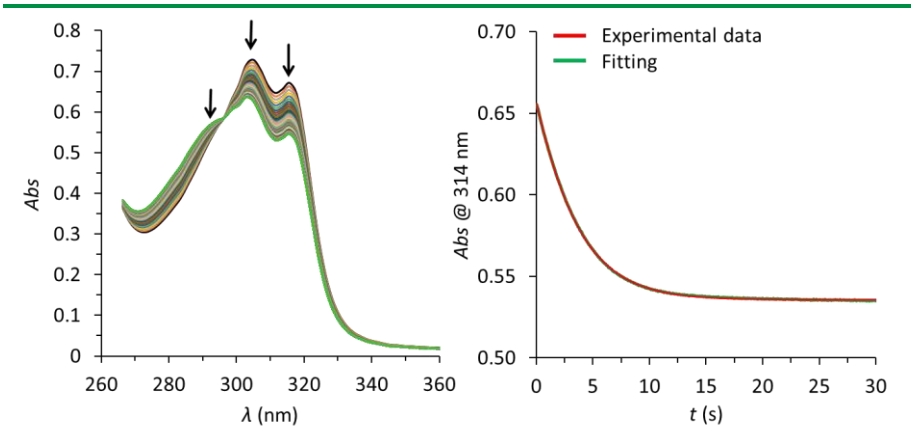

Figure 5. (A) Evolution of the UV-Vis spectra of complex **[(H$_2$bpk)Cu]$^{2+}$** upon sudden basification from 12 to 13.9 by addition of conc. NaOH (1M) solution by stopped-flow experiment. The mixing time was set to 10 ms. (B) Experimental (red line) and fitted (green line) data of the evolution of the absorbance at 314 nm with the time.

Formation of substituted complexes was also studied by paramagnetic ^{1}H-NMR in D_2O at different pD values, since the Cu(II) species is paramagnetic (Figure S21). Spectrum of complex **[(bpk)Cu^{II}]** at pD 12 features a wide band around 9 ppm corresponding to the bipyridinic protons that are highly influenced by the presence of the paramagnetic Cu^{II} center. At higher field a single singlet signal from the methyl groups appears as expected for a complex with symmetric geometry. However, when the pD was increased up to 13.6, the singlet corresponding to the methyl groups was split into three different signal indicating the break of the symmetry due to the introduction of one or two hydroxo groups. We also observe the speciation of complex **[(bpk)Cu^{II}]** upon basification by EPR spectroscopy and results are shown in Figures 6 and S23. In all the cases, the observed clear $g_{||} > g_{\perp}$ suggests the presence of distorted

square-planar geometries with the $d_{x^2-y^2}$ ground state. However, the appearing differences in the g values together with the differences in hyperfine splitting clearly indicate different coordination environment of the copper center at the studied pH values. This fact is consistent with the structural distortion exerted by the coordination of the hydroxo molecules and the resulting steric hindrance with the H_2bpk ligand.

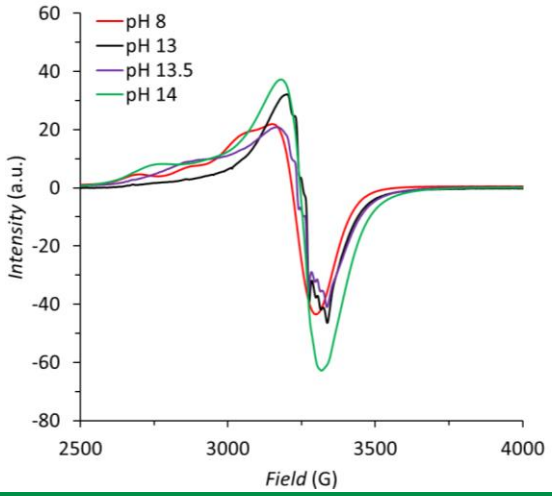

Figure 6. EPR spectra of **[(H$_2$bpk)Cu]$^{2+}$** showing changes in the nature of the copper species in solution at different pH values (8-14). Conditions: **[(H$_2$bpk)Cu]$^{2+}$** = 10 mM in distilled water basify by addition of conc. NaOH (10 M).

We also explore the generation of the substituted species **[(Hbpk)(OH)Cu^{II}]** and **[(H$_2$bpk)(OH)$_2$Cu^{II}]** by reduction of the initial complex. As already discussed at pH 7, generation of Cu^I implies a strong structural reorganization from square-planar to tetrahedral geometries that eventually ends up with the release of Cu^+ ions to the solution. We then investigated the same reduction process in presence of basic media (pH 12) with the aim of facilitating the alkoxo decoordination and hydroxo introduction due to the structural stress exerted by the rigid ligand in the frustrated tetrahedral structure. Figure S16 displays successive CV cycles in pH 12 using complex **[(bpk)Cu^{II}]** in the potential range from -0.8 V, where the complex is reduced to **[(bpk)Cu^{I}]$^-$**, up to 1.6 V. Those

data reveal the existence of an activation process since there is consecutive increase in the current corresponding to the Cu^{III}/Cu^{II} couple that becomes irreversible featuring two differentiable wave peaks. Similar results were obtained when we subject the solution to controlled potential electrolysis (CPE) at -0.6 V during 120 seconds and we subsequently scan through anodic potentials (Figure 7, left).

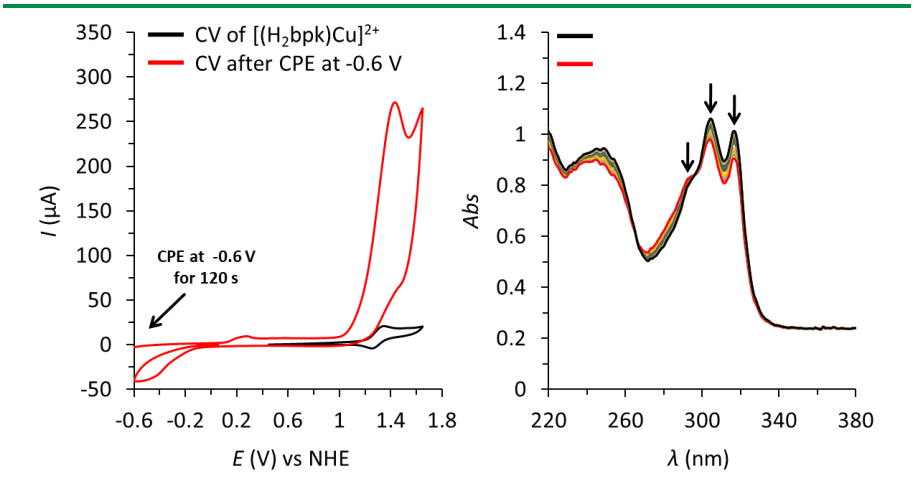

Figure 7. (Left) CVs of a 0.1 M phosphate aqueous solution containing 1 mM of the complex **$[(H_2bpk)Cu]^{2+}$** at pH 12 before (black line) and after (red line) a CPE at -0.6 V for 120 seconds. (Right) Evolution of the UV-Vis spectra of complex **$[(H_2bpk)Cu]^{2+}$** during a CPE at -0.6 V for 120 seconds in a spectroelectrochemical cell.

The used glassy carbon electrode (GC) was rinsed with water and analyzed in a fresh buffer solution at pH 12 showing some electrocatalytic activity respect to a bare glassy carbon electrode as indicative of deposition of an active material (Figure S17, left). Moreover, successive CVs performed using a Cu^{II} salt also showed electrodeposition as the current at around 1.25 V increases. Comparison of those deposited materials with the last CV of the activated solution indicates that part of the electrocatalytic activity comes from electrodeposited copper based-material corresponding to the second catalytic peak observed at 1.40 V (Figure S17, right). This material was confirmed to be a mixture CuO and Cu^0 by means of scanning electron microscopy (SEM), energy.dispersive x-ray

spectroscopy (EDX) and x-ray photoelectron spectroscopy (XPS) analysis (Figures S28, S31 and S32 and Table S3).

However, there is a contribution to the catalytic activity at lower potentials around 1.2 V that we associated with molecular species. In order to confirm the nature of those molecular species, we performed a spectroelectrochemical analysis of the solution by recording UV-vis spectra during a Controlled Potential Electrolysis (CPE) at -0.6 V (Figure 7, right). Interestingly, the spectrum of complex **[(bpk)Cu^{II}]** slowly turned in to the one similar to the corresponding spectrum of monoprotonated species **[(Hbpk)(OH)Cu^{II}]** (Figure S24). Since the π-π* transition bands are expected to be quite independent of the oxidation state of the metal center, those results demonstrate the generation of the active species **[(Hbpk)(OH)Cu^{I}]$^{-}$** upon reduction to Cu^{I} and consecutive anodic scan that is responsible for part of the catalytic activity observed in previous experiments. However, that species is not stable at long term in pH 12 solution as we recover the initial UV-vis spectrum some minutes after stopping the CPE experiment (Figure S25). This was also checked by electrochemistry by performing a CPE at -0.6 and analyzing the initial and the resulting species by CV (Figure S22). After different lengths of CPE (0.5 to 2 h) upon stirring, the CV of the solution did not show any catalytic activity but just similar behavior to the initial complex. That supports the instability of the hydroxo species at pH 12 that can be only generated on the double layer in contact with the electrode during the timescale of a CV.

IV

D.2.3. Catalytic performance of Cu-hydroxo species and proposed mechanism

Following the identification of the species responsible for the observed activity, we pursued the characterization of the catalytic performance by electrochemical methods. First we performed a CPE at 1.4 V in a two-compartment cell using a GC sponge working electrode and a 1.5 mM solution of **[(bpk)Cu^{II}]** at pH 13, conditions that favors the formation

of the mono protonated species **[(Hbpk)(OH)Cu^{II}].** Analysis of the oxygen evolved using a Clark electrode revealed the production of around 0.16 μmols during 35 mins with a Faradaic efficiency of 85%, very close to the ideal value of 100% (Figure S26, left). Subsequent analysis of the used GC sponge electrode and a GC plate submitted to the same oxidative conditions (CPE at 1.4 V for 1 h) did not show any indication of deposited copper-based materials on SEM, EDX and XPS measurements (Figures S29, S31, S33 and Table S3), demonstrating that species **[(Hbpk)(OH)Cu^{II}]** can act as homogeneous molecular catalyst for water oxidation. When the CPE was performed in absence of the catalysts, no oxygen was detected.

Similar experiment was performed at pH 14 to promote the formation of the disubstituted species **[(H2bpk)(OH)$_2$Cu^{II}]**, whose activity was found to be just slightly higher than the GC background based on the CV (Figure 3) and previous results.[17] This might be due to the strong degradative oxidation of the glassy carbon electrode in strong basic pH which would hinder the electrocatalytic activity of the complex. Simultaneous analysis of the oxygen evolved also resulted in a generation of 0.14 μmols in 60 min, approximately half of the generation reached by **[(Hbpk)(OH)Cu^{II}]**. This lower activity at pH 14 is in agreement with the lower electrocatalytic wave found in CV. The Faradaic efficiency in this case is around 80 % due to the mentioned degradative oxidation of the glassy carbon electrode.(Figure S26, right).[20] Similarly to the previous experiment, analysis of the used electrode and GC plate prepared under the same oxidative stress did not reveal the formation of any deposited copper based material on the surface confirming the homogeneous nature of this catalyst (Figures S30, S31, S33 and Table S3). Once again, experiment in the absence of the catalysts did not show any indication of water oxidation and the high current obtained is assigned to the oxidation of the carbonaceous electrode surface.

Foot of the wave analysis (FOWA) was also performed according to the procedure described in the literature and that is summarized in equation 2.[21] We considered again the CVs in pH 13 and pH 14 where the major catalytic species in solution are **[(Hbpk)(OH)Cu^{II}]** and **[(H2bpk)(OH)$_2$Cu^{II}]** respectively (Figure S27).

$$\frac{i}{i_p} = \frac{8.96\sqrt{\frac{RT}{F\upsilon}k_{obs}}}{1+\exp\left[\frac{F}{RT}\left(E^0_{PQ}-E\right)\right]} \qquad (2)$$

In equation 1, i_{cat} is the catalytic current, i_d the one-electron oxidation current of the complex, F is the Faraday constant, R is the ideal gases constant, υ is the scan rate, T is the temperature and k_{obs} is defined as "$k_{cat}\cdot C^0_A$" where C^0_A is the concentration of the substrate (55.56 M for water). Since the one-electron Cu^{III}/Cu^{II} redox wave lies behind the catalytic wave, we estimate i_p CV at pH 12 in absence of catalytic activity. This will be a conservative value since the conversion to substituted species can be as high as 100%. We obtained k_{obs} values of 2.28 s^{-1} and 0.44 s^{-1} for **[(Hbpk)(OH)Cu]** and **[(H$_2$bpk)(OH)$_2$Cu]** respectively, revealing the faster catalytic process in the case of the former, with both values in the range of the reported copper-based molecular catalyst.

We finally studied the water oxidation mechanism for both catalytic species by DFT using the B3LYP-D3 functional and the SMD implicit method of solvation (SI for full computational details). In aqueous solution, complex **[(H$_2$bpk)Cu^{II}]$^{2+}$** features an expected square-planar geometry with an empty apical position: water molecules end up forming hydrogen bonds with the amide groups and coordination of an OH^- group requires an energy consumption of 6.8 kcal·mol^{-1}. The calculated pK_a values of the coordinated alkoxo groups is around 10.5 and 6.9, which are in good agreement with the experimental values obtained from the Pourbaix diagram, 9.5 and 7. Regarding the one-electron oxidized complex **[(H$_2$bpk)Cu^{III}]$^+$**, the most stable electronic structure consist of

singlet species with an oxidized copper(III) center. In this case, the pKa values are 1.8 and -8.5 due to the coordination to the more acidic Cu(III) metal center, indicating that **[(H$_2$bpk)Cu^{II}]$^+$** is deprotonated upon oxidation in the whole working pH range. The calculated redox potential for the proton coupled electron transfer from **[(Hbpk)Cu^{II}]** to [(bpk)Cu^{III}] is 1.31 V that compares well with the experimentally observed one (1.36 V). The second one-electron oxidation involves a potential of around 1.92 V and lead to the formation of a quartet species **[(bpk··)Cu^{II}]**. In this species the electron is taken from the ligand, whose coordinating capability to the metal center diminishes and promotes an internal electron transfer to reduce the copper oxidizing the other alkoxo group. However, this oxidation requires an extremely high potential for the experimental conditions in the CVs so that the background signal hinder the observation of this process and the possible appearance of catalytic activity.

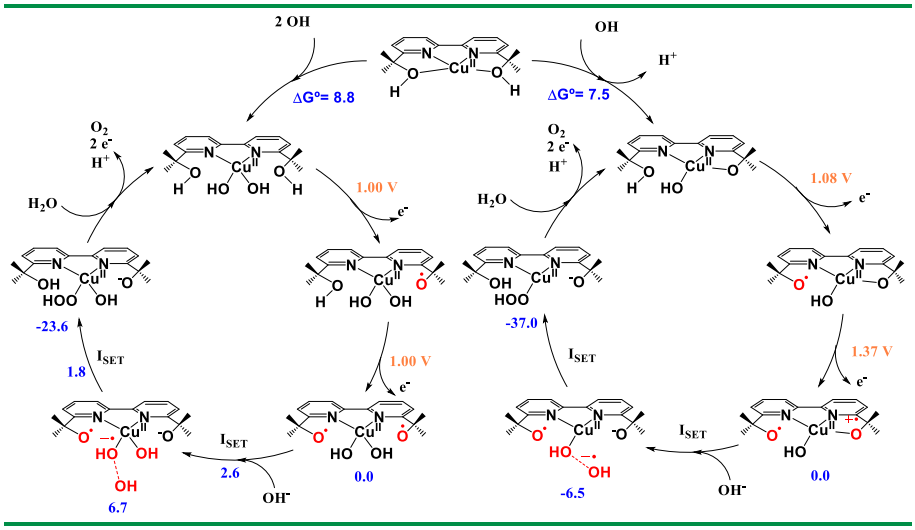

Figure 8. Catalytic cycle for the hydroxo derivatives from complex **[(H$_2$bpk)Cu]$^{2+}$**. Cycles include the electrochemical activation of both catalysts and the SET-WNA mechanism for the O-O bond formation step. Free energy changes are indicated as blue number in kcal·mol-1 and calculated redox potential as orange number in volts.

In the presence of OH-, corresponding to the more basic conditions, the coordination of a hydroxo molecule in the equatorial position of the

deprotonated complex **[(bpk)Cu^{II}]** by exchange with an alkoxo group is thermodynamically demanding. However, coordination of one or two OH^- molecules to the mono- and di- protonated complexes respectively is exergonic. Formation of the species **[(Hbpk)(OH)Cu^{II}]** and **[(H$_2$bpk)(OH)$_2$Cu^{II}]** is thermodynamically favored by 7.5 and 8.8 kcal·mol^{-1} indicating that the pendant alkoxo groups protonate after coordination of the hydroxo molecules as experimentally evidenced. The pka values of the dangling alcohol groups are 20.4 for **[(Hbpk)(OH)Cu^{II}]** and for **[(H$_2$bpk)(OH)$_2$Cu^{II}]** they are 20.7 and 19.6, supporting all the previous experimental observations.

Those two new hydroxo species are responsible for the catalytic activity toward water oxidations so we have studied the oxidation and formation of the O-O bond for each one (Figure 8). Regarding the complex **[(Hbpk)(OH)Cu^{II}]**, the oxidation to the deprotonated triplet species **[(bpk·)(OH)Cu^{II}]** takes place through a proton coupled electron transfer (PCET) at a potential of 1.08 V, close to the experimental value for the catalytic onset potential 1.1 V. This oxidation generates a radical with an unpaired electron mainly located in the uncoordinated alkoxo group. Upon subsequent oxidation, the quartet species **[(bpk··)(OH)Cu^{II}]** is formed at 1.37 V, where both alkoxo groups are oxidized and each one accommodate an unpaired electron with a spin density of 0.8 and 0.84.

We have further investigate the interaction of this doubly oxidized species with an external OH^- molecule by relaxed potential energy scan aiming to study the O-O bond formation step (Figure S37 and S38). As previously found for a copper complex bearing a redox active ligand,[14] an external OH^- molecule transfer one electron to reduce the ligand at distances longer than 4 Å and supporting a mechanism based on the reported Single Electron Transfer-Water Nuclephilic Attack (SET-WNA). We were not able to characterize the electronic structure of the adduct before the first single electron transfer as we directly obtained the highly favored electronic structure where the electron has been already transferred from the

external OH^- to the ligand, **[(bpk·)(HO···OH·)Cu^{II}]** (Figure S37). As the two oxygen get closer, there is the second single electron transfer from the external OH^- to reduce again the ligand through a minimum energy crossing point (MECP) connecting the previous quartet species with the doublet product **[(bpk)(H_2O_2)Cu^{II}]**. Interestingly in this case, the second single electron transfer takes place before the formation of any stable intermediate as obtained for other catalysts[16] and thus there is not any barrier.

Complex **[(H_2bpk)(OH)$_2$Cu^{II}]** follows a similar reaction mechanism as previously explained. A first PCET process affords the radical triplet species **[(Hbpk·)(OH)$_2$Cu^{II}]** at 1.00 V where one electron is mainly released from the dangling alkoxo group. A second oxidation process takes place at the same potential of 1.00 V releasing a second electron from the other alkoxo unit and formally forming the quartet species **[(bpk··)(OH)$_2$Cu^{II}]** with an spin density of around 0.7 on each oxygen. At this point, interaction of the coordinated hydroxo with an external hydroxo molecule at long distances do not promote the electron transfer until the distance between both oxygens is around 2.39 Å (Figure S38). At this distance, the electronic structure of the system reorganize so that an electron is transferred from the external hydroxo to reduce one alkoxo group, althought the overall multiplicity remain as quartet. This first electron transfer can be detected as a crossing point between the two potential energy surfaces in red color from Figure S38. Upon further oxygen approximation, the new formed electronic structure evolves to an intermediate at a O-O distance of 2.29 Å in which both oxygen accommodate one unpaired electron forming the two centres-three electrons (2c-3e) species **[(Hbpk)(OH)(HO···OH·)Cu^{II}]**. Similar species have been already characterized as intermediates for the SET-WNA using many other copper-based systems and all share similar electronic features and O-O bond distances. At shorter O-O bond distances, the second single electron transfer takes place through a MECP in which the electronic

structure goes from quartet to doublet, leading to the formation of the hydroperoxo species **[(Hbpk)(OH)(H_2O_2)Cu^{II}]**. The barrier for both single electron transfers is estimated from the potential energy surface to be as low as 2.8 and 1.8 kcal·mol^{-1} respectively. The intramolecular pathway using **[(H_2bpk)$(OH)_2Cu^{II}$]** has been also investigated but lead to energy barrier higher than 25 kcal·mol^{-1} as obtained from Figure S39.

It is interesting to highlight that the coordinated ligand bpk^{2-} does not features redox activity in the studied potential range (from 0.2 to 1.4 V) and therefore requires an extremely high energy to accumulate two oxidative charges necessary to promote the O-O bond formation. However, upon exchange by coordinating hydroxo molecules, the resulting dangling alcohol/alkoxo groups confer the ligand redox activity. This is in good agreement with the electrochemistry of the free ligand in solution that shows a redox wave at around 1.3 V (Figure S19). Therefore a doubly oxidized species can be obtained at affordable potential values and that lead to the formation of O-O bond and eventually the release of oxygen. This is an important example that rigid square planar copper complexes cannot afford high oxidation states in the metal center but instead, they need the redox activity of ligands (or coordinated hydroxo molecules) to promote the electron transfers needed for the catalytic water oxidation. The role of the metal among other is to serve as a scaffold to hold alkoxyl radicals in close proximity ready to be transferred to the O-O bond formation process ending up in the peroxide intermediate.

D.3. Conclusions

In conclusion, we have found that the use of redox inactive tetradentate ligands with a rigid planar geometry prevent the presence of catalytic activity in the apical position of copper complexes, in agreement with previous results by Batista and coworkers. However, the presence of controlled basic conditions promotes a partial ligand decoordination and the

introduction of OH^- molecules that substitutes the previously coordinated alkoxo groups in the equatorial position. Once decoordinated, the alkoxo groups get protonated forming alcohols and that provide the ligand with a redox non-innocent character as those alcohol groups can be oxidized. Those changes in the structure and redox features of the complex enable the catalytic activity toward water oxidation.

D.4. Acknowledgments

We thank MINECO and FEDER (Grants CTQ2014-57761-R, CTQ-2016-80058-R, Severo Ochoa Excellence Accreditation 2014-2018 SEV-2013-0319, CTQ-2014-52974-REDC) and CERCA Programme/Generalitat de Catalunya for financial support. I.F.-A. thanks the Severo Ochoa predoctoral training fellowship (ref: SVP-2014-0686662). P.G.-B. thanks "La Caixa" foundation for a Ph.D. grant.

D.5. References

1 Berardi, S.; Drouet, S.; Francàs, L.; Gimbert-Suriñach, C.; Guttentag, M.; Richmond, C.; Stoll, T.; Llobet, A. *Chem. Soc. Rev.* **2014**, *43* (22), 7501–7519

2 Melis, A. *Energy Environ. Sci.* **2012**, *5* (2), 5531–5539

3 Nocera, D.G. *Acc. Chem. Res.* **2017**, *50*, 616-619

4 J. D. Blakemore, R. H. Crabtree and G. W. Brudvig, *Chem. Rev.* 2015, **115**, 12974-13005

5 M. D. Kärkäs, O. Verho, E. V. Johnston, B. Åkermark, *Chem. Rev.*, 2014, **114**, 11863-12001

6 Kärkäs, M. D.; Åkermark, B. *Dalton Trans.* **2016**, *45* (37), 14421–14461

7 Wang, N.; Zheng, H.; Zhang, W.; Cao, R. *Chin. J. Catal.* **2018**, *39*, 228-244

8 Singh, A.; Spiccia, L. *Coord. Chem. Rev.* **2013**, *257*, 2607-2622

9 Barnett, S. M.; Goldberg, K. I.; Mayer, J. M. *Nat. Chem.* **2012**, *4*, 498−502.

10 M.-T. Zhang, Z. Chen, P. Kang and T. Meyer, *J. Am. Chem. Soc.* 2013, **135**, 2048.

11 J. S. Pap, L. Szyrwiel, D. Srankó, Z. Kerner, B. Setner, Z. Szewczuk and W. Malinka, *Chem. Commun.*, 2015, **51**, 6322.

12 Zhang, T.; Wang, C.; Liu, S.; Wang, J.-L.; Lin, W. *J. Am. Chem. Soc.* **2014**, *136*, 273−281.

13 Gerlach, D. L.; Bhagan, S.; Cruce, A. A.; Burks, D. B.; Nieto, I.; Truong, H. T.; Kelley, S. P.; Herbst-Gervasoni, C. J.; Jernigan, K. L.; Bowman, M. K.; Pan, S.; Zeller, M.; Papish, E. T. *Inorg. Chem.* **2014**, *53*, 12689−12698.

14 P. Garrido-Barros, I. Funes-Ardoiz, S. Drouet, J. Benet-Buchholz, F. Maseras and A. Llobet, *J. Am. Chem. Soc.*, 2015, **137**, 6758.

15 Fisher, K. J.; Materna, K. L.; Mercado, B. Q.; Crabtree, R. H.; Brudvig, G. W. *ACS Catal.* **2017**, *7*, 3384-3387.

16 Funes-Ardoiz, I.; Garrido-Barros, P.; Llobet, A.; Maseras, F. *ACS Cat.* **2017**, *7*, 1712-1719.

17 Rudshteyn, B.; Fisher, K. J.; Lant, H. M. C.; Yang, K. R.; Mercado, B. Q.; Brudvig, G. W.; Crabtree, R. H.; Batista, V. S. *ACS Catal.* **2018**, *8*, 7952-7960.

18 Qi, H.; Teesdale, J. J.; Pupillo, R. C.; Rosenthal, J.; Bard, A. J. *J. Am. Chem. Soc.* **2013**, *135*, 13558-13566.

19 Ganesan, V.; Sivanesan, D.; Yoon, S. I*norg. Chem*, **2017**, 56, 1366-1374.

20 Hyde, J. T.; Hanson, K.; Vannucci, A. K.; Lapides, A. M.; Alibabaei, L.; Norris, M. R.; Meyer, T. J.; Harrison, D. P. *ACS Appl. Mater. Interfaces* **2015**, *7*, 9554-9562.

21 Costentin, C.; Drouet, S.; Robert, M.; Savéant, J.-M. *J. Am. Chem. Soc.* **2012**, *134*, 11235-112342.

D.6. Supporting information

Experimental Section

Materials

All general reagents and chemicals were used as purchased from Sigma-Aldrich, Fluka and Merck chemical companies without further purification unless otherwise stated. The ligand precursor ([2,2'-bipyridine]-6,6'-dicarboxylic acid) was prepared according to the experimental procedure reported in the literature.[1] Air and moisture sensitive reactions were carried out under N_2 or Ar in oven-dried (120°C) glassware. Evaporation of solvents *in vacuo* was done with a *Büchi Rotevapor R-200* at 40°C.

Instrumentation and measurements

NMR spectra were measured on a *Bruker AV-500* and *Bruker 300 MHz* spectrometers. All NMR experiments were performed at room temperature in corresponding deuterated solvents and using internal protons as reference.

UV-Vis spectra were measured on a *Cary 50 UV-vis* spectrometer by *Varian Inc.*

Electrospray ionization mass spectra (ESI-MS) were performed on an *Agilent Technologies 6130-Quadrupole LC/MS* connected to an *Agilent Technologies HPLC-1200 series*. Samples were dissolved in MeOH and injected directly with an auto-sampler.

Exact mass analyses were performed with a micrOTOF mass spectrometer (from Bruker company) using Electrospray ionization technique in methanol by direct injection and detecting with positive polarity.

Elemental Analysis of the samples was carried out in a Thermo Finnigan elemental analyzer Flash 1112 model.

Electrochemical measurements

Differential pulse voltammetry (DPV) and cyclic voltammetry (CV) were measured on a IJ-Cambria CHI660D potentiostat using a three-electrode cell. Glassy carbon - d = 3 mm - (GC) working electrode were employed while a Pt disk/mesh was used as counter electrode and a $Hg/HgSO_4$ (K_2SO_4 sat.) or Ag/AgCl (KCl sat.) electrode was used as a reference electrode. Working electrodes were polished with 1 and 0.05 micron alumina paste, washed with distilled water and acetone and sonicated in acetone for 5 minutes before each measurement. CVs were typically recorded at a scan rate of 100 mV/s. DPVs were recorded with the following parameters: amplitude= 50 mV, step height=4 mV, pulse width= 0.05 s. All redox potentials in the present work are reported versus NHE by adding 0.648 V to the measured potential.

O_2 evolution experiments

Controlled Potential Electrolysis (CPE) experiments were performed at different potentials and different pH values to catalyze the water oxidation reaction by the complexes by using a two-compartment cell closed with a septum. As working electrode large surface glassy carbon sponge electrodes were used together with a silver/silver chloride (KCl sat.) as a reference electrode. These ones were placed in one of the compartments that was filled with a 1.5 mM solution of the complex in the correspondin pH solution. In the other compartment, containing only the clean electrolyte solution, a mesh platinum counter electrode was used (Figure S1).

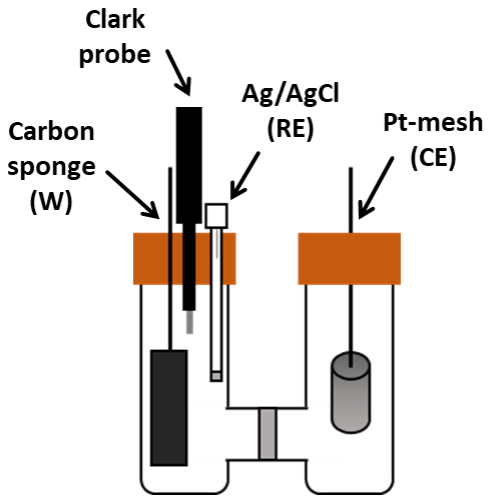

Figure S1. Schematic representation of the set up used for O2 detection experiments.

The oxygen evolution was monitored with an OXNP type Clark electrode in gas phase (from Unisense Company). The CPE was carried out using an IJ-Cambria CHI-660 potentiostat and was started as soon as the oxygen sensor signal was stable under air atmosphere. During the experiment, solutions of both compartments were vigorously stirred. Calibration of the oxygen sensor was performed after each experiment by adding known amounts of pure oxygen into the cell using a Hamilton syringe. The results of the water oxidation catalysis with the complexes were compared with blank experiments under the same conditions but in the absence of the complex. The Faradaic efficiency was determined according to the total charge passed during the CPE and the total amount of generated oxygen by taking into account that water oxidation is a $4e^-$ oxidation process.

Synthesis of H_2bpk

Dimethyl [2,2'-bipyridine]-6,6'-dicarboxylate: 850 mg (3.5 mmol) of [2,2'-bipyridine]-6,6'-dicarboxylic acid were suspended in 85 mL of anhydrous MeOH containing a catalytic amount of H_2SO_4 (10%) and the mixture was refluxed at 85 ºC under a nitrogen atmosphere during 24 hours. Afterwards the methanol was evaporated in vacuum and the remaining solution was dissolved in 20 mL of water, which was neutralized by adding $NaHCO_3$ and extracted with 3 x 100 mL of DCM. The organic phase was evaporated yielding the desired product without further purification. Yield: 767 mg, 2.8 mmol, 80%. ^{1}H-NMR (CD_2Cl_2-d_2): δ [ppm] = 8.77 (H_1, dd, J= 7.9, 1.2 Hz, 2H), 8.23(H_3, dd, J= 7.7, 1.2 Hz, 2H), 8.14 (H_2, t, J= 7.8 Hz, 2H), 4.06 (H_4, s, 6H).

2,2'-([2,2'-bipyridine]-6,6'-diyl)bis(propan-2-ol) (**H_2bpk**): To a solution of Dimethyl [2,2'-bipyridine]-6,6'-dicarboxylate (700 mg, 2.6 mmol) in dry THF (60 mL) at 0 ºC, 4.5 equivalents of Methylmagnesium bromide in Et_2O was added dropwise, and the mixture was stirred at room temperature and under a nitrogen atmosphere during 16 hours. Then, the reaction was quenched by adding a saturated solution of NH_4Cl (20 mL) and 60 mL of Et_2O were added, the organic layer was separated and the aqueous layer was extracted with Et_2O (3 x 60 mL). The organic layers were combined, dried with $MgSO_4$ and concentrated in vacuum to obtain a yellow oil. The desired product was obtained after purification by chromatographic column (5:1 Hexane/Ethyl acetate) as a white powder. Yield: 305 mg, 1.1 mmol, 43%. ^{1}H-NMR ($CDCl_3$-d_1): δ [ppm] = 8.37 (H_1, dd, J= 7.8, 0.9 Hz, 2H), 7.90 (H_2, t, J= 7.8, 2H), 7.44 (H_3, dd, J= 7.8, 0.9 Hz, 2H), 1.63 (H_4, s, 12H). ^{13}C-NMR ($CDCl_3$-d_1): 165.45 (C_5), 153.28 (C_1), 138.1 (C_3), 119.18 (C_4), 119.0 (C_2), 71.8 (C_6), 30.7 (C_7). ESI-MS (MeOH) m/z positive mode: 273.16 $[M-H^+]^-$; m/z = 274.16 $[M-2H^+]^{2-}$. Elemental analysis (% found): C, 70.39; H, 7.40; N, 10.29. Calcd for $C_{16}H_{20}N_2O_2$: C, 70.56; H, 7.40; N, 10.29.

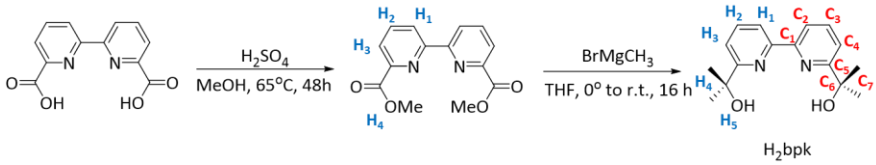

Figure S2. Schematic drawing of synthetic route employed for the preparation of H_2bpk and their ^{1}H-NMR and ^{13}C-NMR assignments.

Synthesis of $[(H_2bpk)Cu]^{2+}$

A solution of $Cu(OTf)_2$ (133 mg, 0.37 mmol) of $Cu(OTf)_2$ in 50 mL of MeCN was slowly added to a solution of H_2bpk (100 mg, 0.37 mmol) in MeCN and the mixture was stirred overnight at 60 °C (Figure S3). Afterwards, the remaining blue solution was distributed in several vials and diffused with Et_2O favoring the crystallization of $[(H_2bpk)Cu^{II}](OTf)_2$ as blue needles. Yield: 185 mg, 0.29 mmol, 79%. ESI-MS (MeOH) m/z positive mode: m/z = 334.0 $[M - 2H^+ - 2OTf]^-$. Elemental analysis (% found): C, 31.86; H, 2.99; N, 4.15. Calcd for $C_{16}H_{20}CuN_2O_2$ + 2.4 OTf^-: C, 31.86; H, 2.91; N, 4.04.

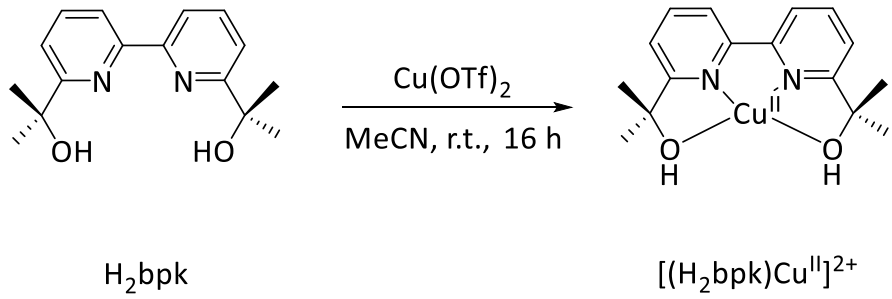

Figure S3. Schematic drawing of the preparation of **$[(H_2bpk)Cu^{II}]^{2+}$**.

Spectroscopic Characterization

NMR and Mass Spectroscopy

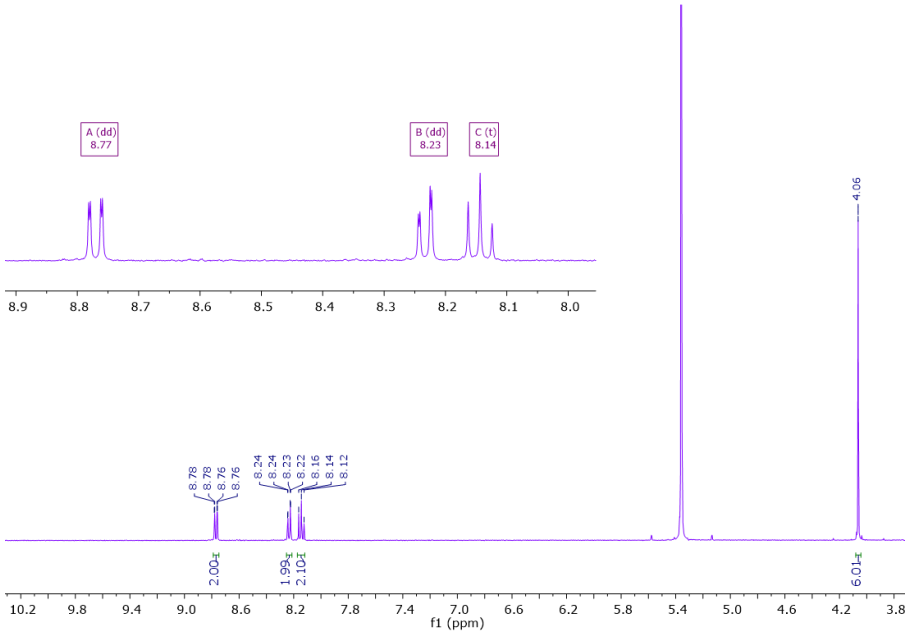

Figure S4. ^{1}H-NMR spectrum of Dimethyl [2,2'-bipyridine]-6,6'-dicarboxylate (CD_2Cl_2-d_2, 400 MHz, 25 °C).

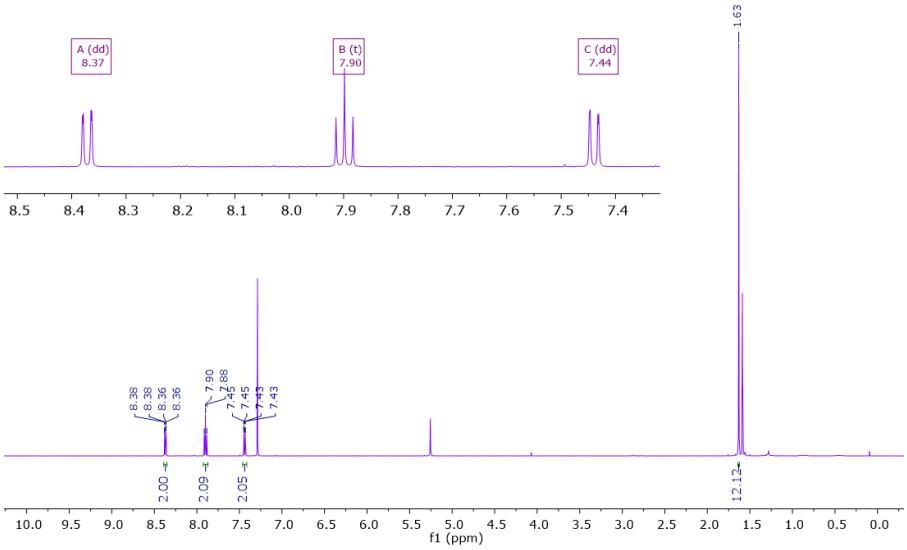

Figure S5. ^{13}C-NMR spectrum of H_2bpk ($CDCl_3$, 500 MHz, 25 °C).

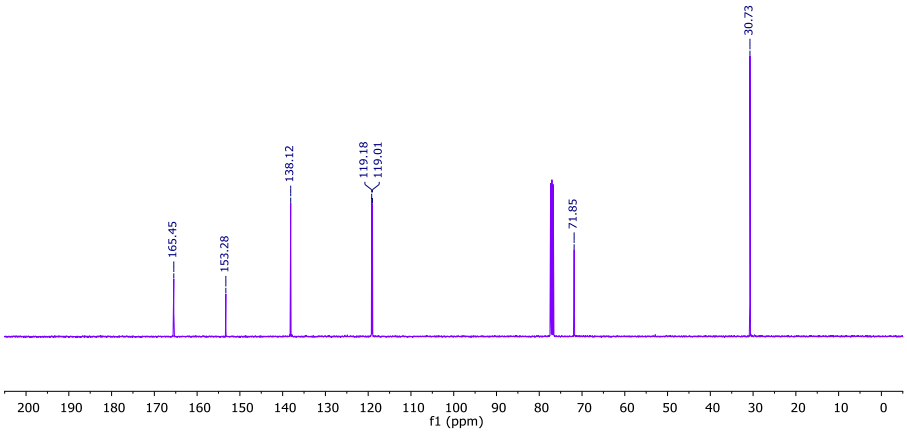

Figure S6. ^{13}C-NMR spectrum of H_2bpk ($CDCl_3$, 500 MHz, 25 °C).

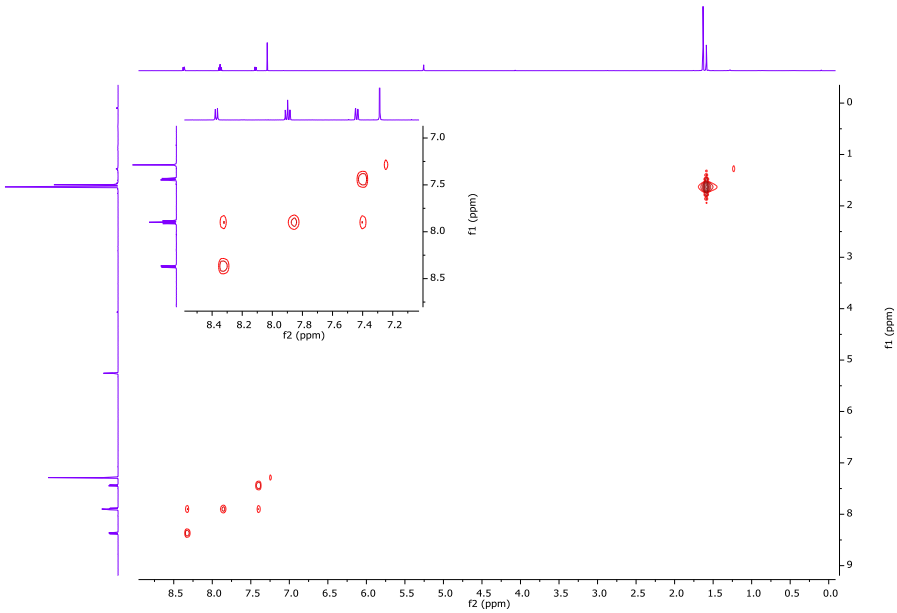

Figure S7. COSY spectrum of H_2bpk ($CDCl_3$, 500 MHz, 25 °C).

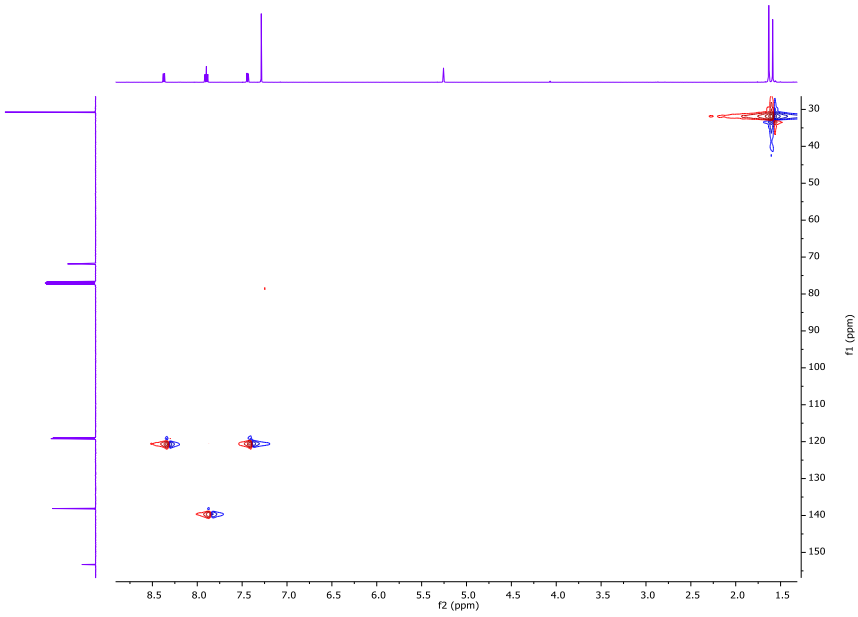

Figure S8. HSQC spectrum of H_2bpk ($CDCl_3$, 500 MHz, 25 °C).

From ligand-based to metal-based electron transfer in water oxidation catalysis

Mass-spectrometry

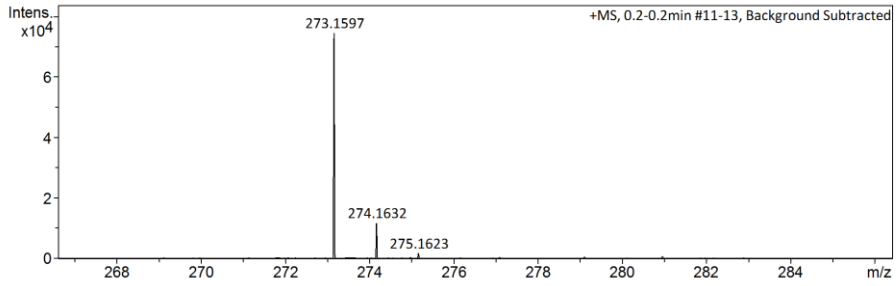

Figure S9. (+)-ESI-MS spectrum of H_2bpk. m/z = 273.16 $[M\text{-}H^+]^-$; m/z = 274.16 $[M\text{-}2H^+]^{2-}$.

IV

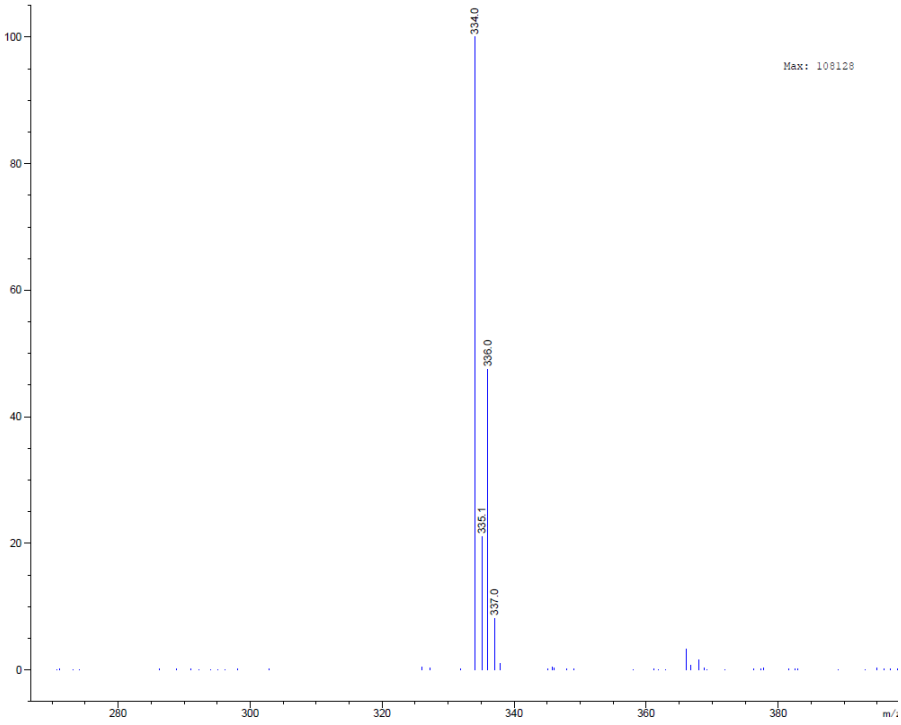

Figure S10. (+)-ESI-MS spectrum of **$[(H_2bpk)Cu^{II}]^{2+}$.** m/z = 334.0 [M-2H+-2OTf]-.

IR-Spectroscopy

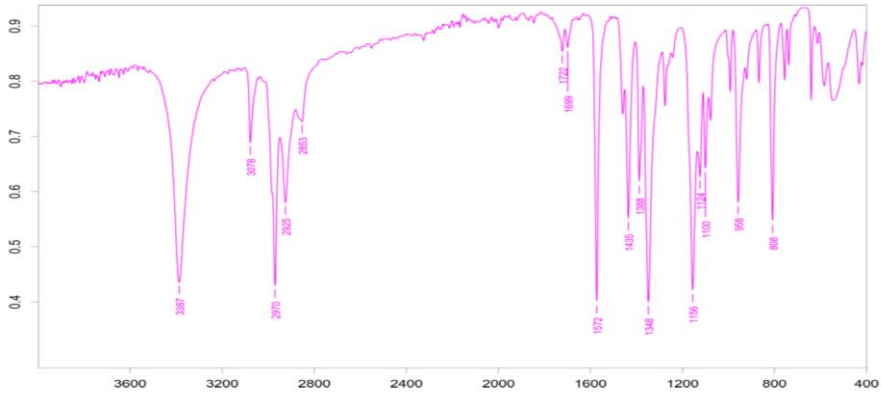

Figure S11. FT-IR spectrum of H_2bpk. Wavenumber (cm^{-1}): 3387 (O-H, Stretch), 3078 (Aromatic, Stretch), 2970-2925 (-CH_3, Stretch).

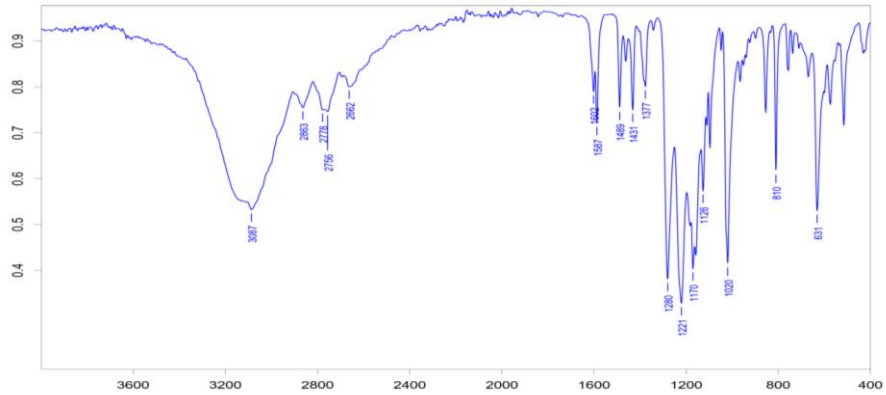

Figure S12. FT-IR spectrum of **$[(H_2bpk)Cu^{II}]^{2+}$**. Wavenumber (cm^{-1}): 3387 (O-H, Stretch), 3078 (Aromatic, Stretch), 2970-2925 (-CH_3, Stretch).

From ligand-based to metal-based electron transfer in water oxidation catalysis

UV-Vis Spectroscopy

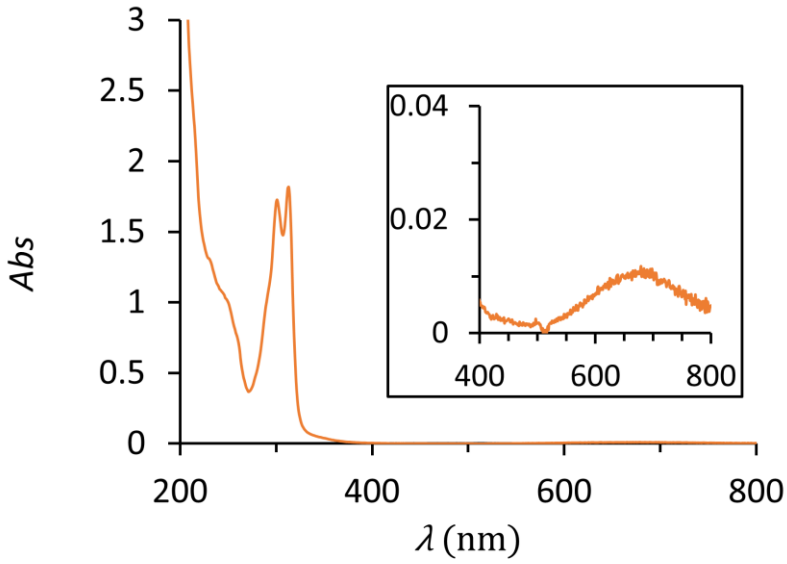

Figure S13. UV-Vis spectra of **[(H$_2$bpk)Cu^{II}]$^{2+}$** showing intense absorption bands between 250-400 nm, corresponding to π-π* transitions of the ligand. (*Inset*) enlargement of the visible region showing less intense absorption bans, with a maximum at 680 nm, corresponding to MLCT transition and the d-d transition bands. Conditions: **[Complex]** = 0.1 mM in MeCN.

X-Ray Crystallography

Crystal preparation: Crystals of **$[(H_2bpk)Cu^{II}]^{2+}$** were grown in MeCN (by slow diffusion of Et_2O). The crystals were selected using a Zeiss stereomicroscope using polarized light and prepared under inert conditions immersed in perfluoropolyether as protecting oil for manipulation.

Data collection: Crystal structure determination for sample **$[(H_2bpk)Cu^{II}]^{2+}$** was carried out using a Apex DUO Kappa 4-axis goniometer equipped with an APPEX 2 4K CCD area detector, a Microfocus Source E025 IuS using MoK_α radiation, Quazar MX multilayer Optics as monochromator and an Oxford Cryosystems low temperature device Cryostream 700 plus (T = -173 ˚C). Full-sphere data collection was used with ω and φ scans. *Programs used:* Bruker Device: Data collection APEX-2[4], data reduction Bruker Saint[5] V/.60A and absorption correction SADABS[6].

Structure Solution and Refinement: Crystal structure solution was achieved using the computer program SHELXT[7]. Visualization was performed with the program SHELXle[8]. Missing atoms were subsequently located from difference Fourier synthesis and added to the atom list. Least-squares refinement on F^2 using all measured intensities was carried out using the program SHELXL 2015[9]. All non-hydrogen atoms were refined including anisotropic displacement parameters.

From ligand-based to metal-based electron transfer in water oxidation catalysis

Table S1. Crystal data and structure refinement for **[(H$_2$bpk)Cu^{II}]$^{2+}$**.

Identification code **[(H$_2$bpk)Cu^{II}]$^{2+}$**

Empirical formula C18 H20 Cu F6 N2 O8 S2

Formula weight 634.02

Temperature 100(2) K

Wavelength 0.71073 Å

Crystal system Monoclinic

Space group P2(1)/n

IV

Unit cell dimensions a = 10.0210(5)Å α= 90°.

b = 9.7375(5)Å β = 91.6693(11)°.

c = 24.2843(11)Åγ = 90°.

Volume 2368.6(2) Å3

Z 4

Density (calculated) 1.778 Mg/m3

Absorption coefficient 1.194 mm-1

F(000) 1284

Crystal size 0.40 x 0.10 x 0.05 mm3

Theta range for data collection 1.678 to 34.982°.

Index ranges -15<=h<=16,-14<=k<=15,-38<=l<=28

Reflections collected 34869

Independent reflections 9679[R(int) = 0.0354]

Completeness to theta =34.982° 92.9%

Absorption correction Multi-scan

Max. and min. transmission 0.943 and 0.764

Refinement method Full-matrix least-squares on F2

Data / restraints / parameters 9679/ 0/ 346

Goodness-of-fit on F2 1.052

Final R indices [I>2sigma(I)] R1 = 0.0308, wR2 = 0.0775

R indices (all data) R1 = 0.0389, wR2 = 0.0813

Largest diff. peak and hole 0.823 and -0.685 e.Å-3

From ligand-based to metal-based electron transfer in water oxidation catalysis

Electrochemical behaviour

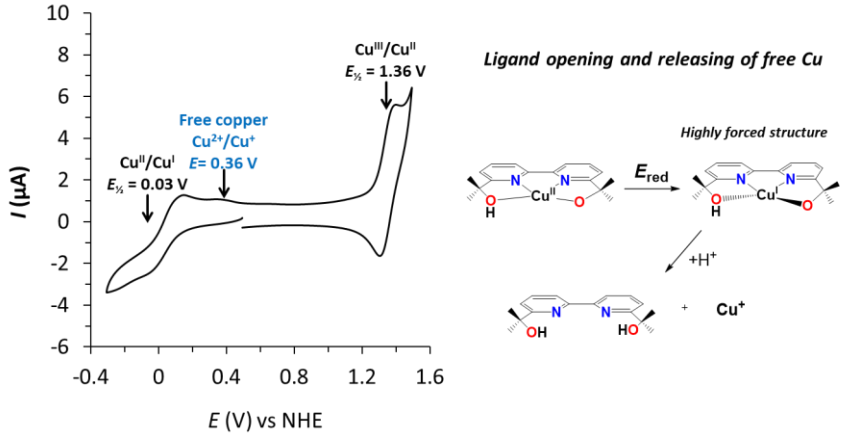

Figure S14. (**Left**) Cyclic Voltammograms of 1 mM solution of **[(Hbpk)Cu^{II}]$^{+}$** in 0.1 M phosphate buffer (pH 7) with a scan rate of 100 mVs^{-1}. (**Right**) Schematic representation of the ligand partial decoordination process, which end with the releasing of free Cu^{+} to the solution.

IV

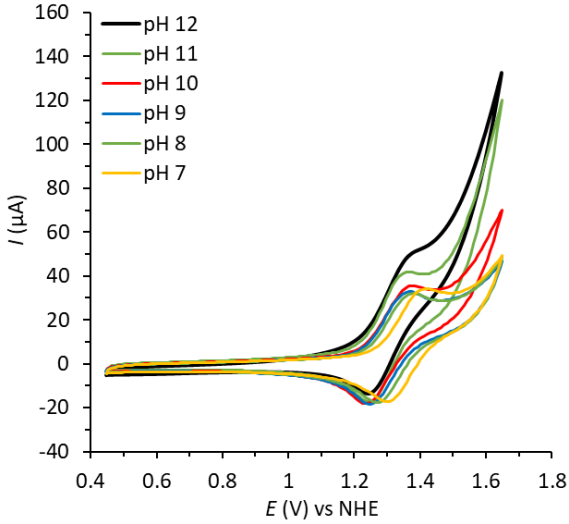

Figure S15. Cyclic Voltammograms of **[(H$_2$bpk)Cu^{II}]$^{2+}$** at different pH values (7-12) with a scan rate of 100 mVs^{-1}. Conditions: **[(H$_2$bpk)Cu^{II}]$^{2+}$** = 1 Mm in 0.1 M phosphate buffer solutions (I = 0.1) acidify by addition of conc. H_2SO_4 (1 M).

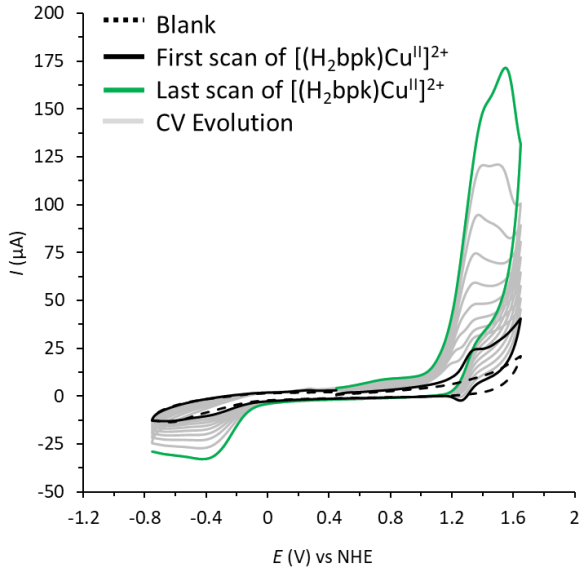

Figure S16. Evolution of cyclic voltammograms of 1 mM solution of **[(H2bpk)CuII]2+** in 0.1 M phosphate buffer (pH 7) during 10 cycles, with a scan rate of 100 mVs^{-1}. First scan (black line), CV Evolution (grey line), last scan (green line), blank (dashed line).

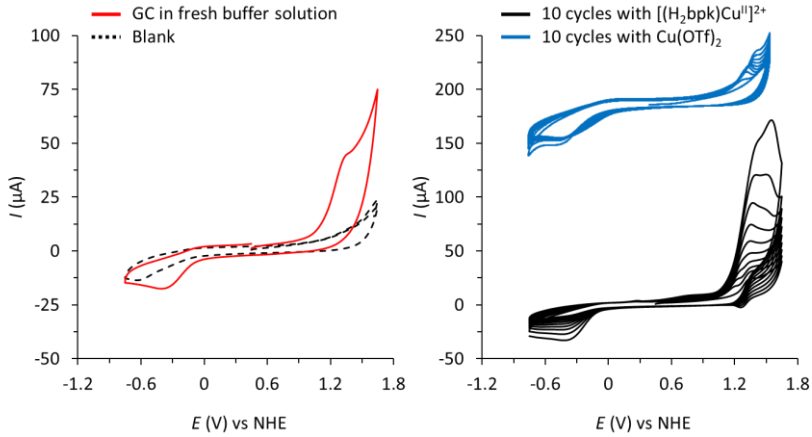

Figure S17. (**Left**) CV measurement with a GC electrode that has performed the previous 10 cycles of the complex (red line) or of a blank solution (blue line) immersed in a freshly-prepared catalyst-free 0.1 M phosphate buffer pH 11.84, showing catalytic response due to the presence of heterogeneous materials deposited onto the surface of the electrode. (**Right**) Comparison of CV evolution during 10 cycles of 1 mM solution of **[(H2bpk)CuII]2+** in 0.1 M phosphate buffer pH 11.84 (black line) and 1 Mm of $Cu(OTf)_2$ (blue line), with a scan rate of 100 mVs^{-1}.

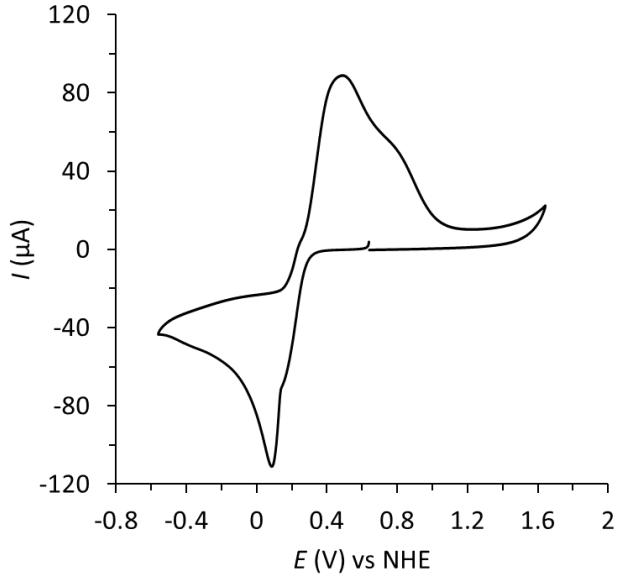

Figure S18. Cyclic Voltammograms of 0.1 M solution of $Cu(ClO_4)_2$ in 0.1 M phosphate buffer (pH 7) with a scan rate of 100 mVs^{-1}.

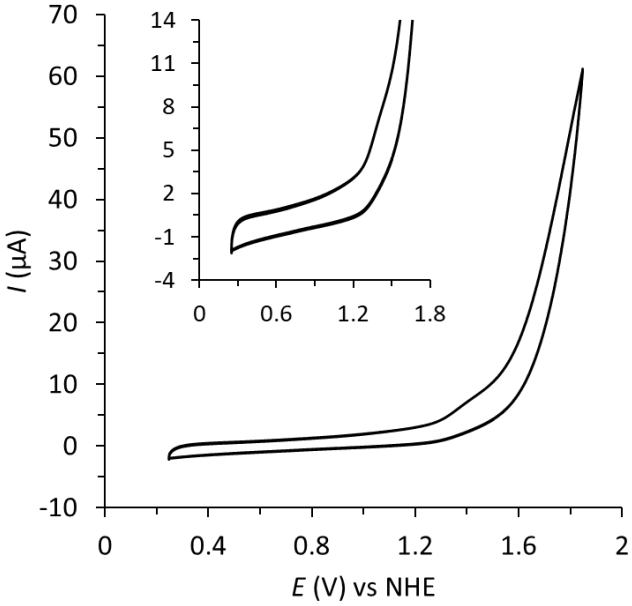

Figure S19. Cyclic Voltammograms of 0.1 mM solution of H_2bpk in 0.1 M phosphate buffer (pH 12) with a scan rate of 100 mVs^{-1}.

Spectroscopic Characterization of Cu-Hydroxo Species

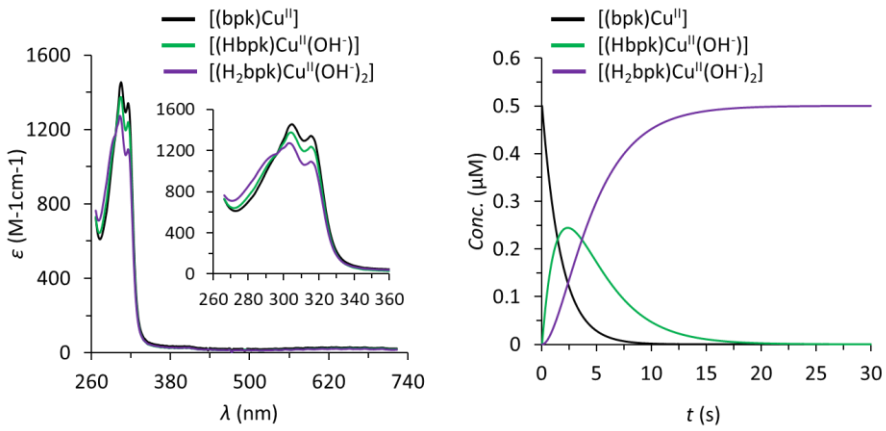

Figure S20. (**Left**) Calculated UV-Vis spectra for the proposed species in solution upon sudden basification from pH 12 to 13.9 using conc. NaOH (1M) by stopped-flow experiment. (**Right**) Calculated distribution diagram vs. time for the different species.

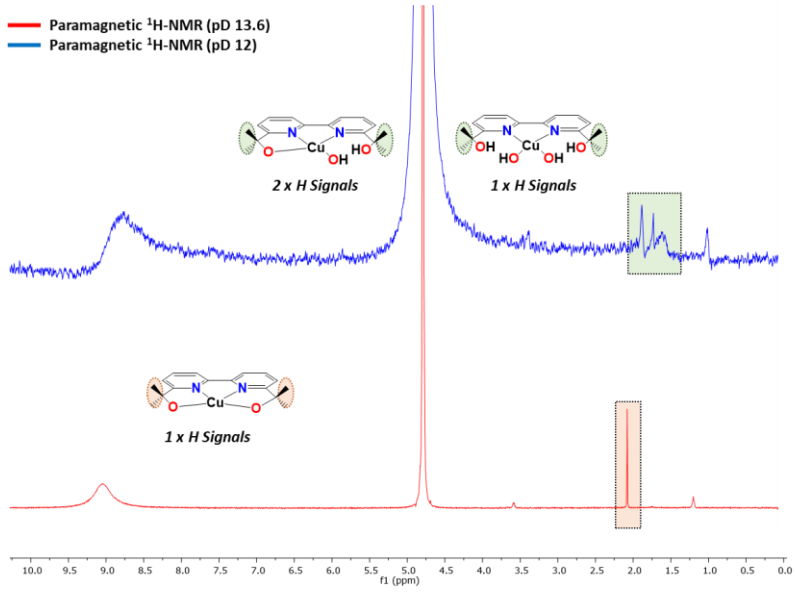

Figure S21. Paramagnetic ^{1}H-NMR of **[(bpk)Cu^{II}]** in D_2O basify by addition of conc. NaOD (40%) until pH 13.6 (top) and 12 (bottom). The comparison of the spectra shows a change in the splitting of aliphatic signals assigned to the methyl groups at pH 13.6, which indicate the presence of a mixture of two species assigned to **[(Hbpk)(OH)Cu^{II}]** and **[(H$_2$bpk)(OH)$_2$Cu^{II}]**.

From ligand-based to metal-based electron transfer in water oxidation catalysis

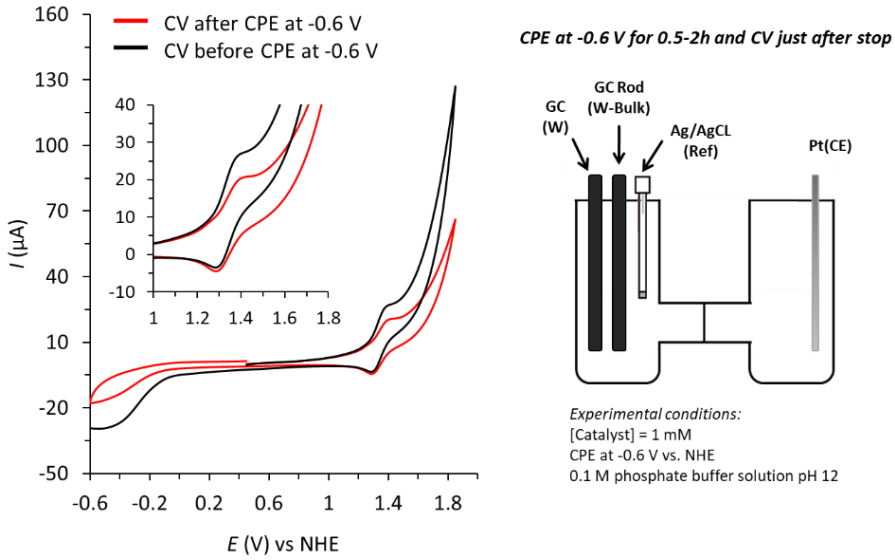

IV

Figure S22. (**Left**) Cyclic Voltammograms of 1 mM solution of **$[(H_2bpk)Cu^{II}]^{2+}$** in 0.1 M phosphate buffer (pH 12) with a scan rate of 100 mVs^{-1} before (black line) and after (red line) CPE at -0.6 V vs. NHE. (**Right**) Schematic representation of the two-compartment cell used for this experiment. Both compartments were closed with a septum for avoiding the introduction of O_2 during the experiment and were vigorously stirred. The CPE was carried out using an IJ-Cambria CHI-730 bipotentiostat appling a potential of-0.6 V at different times (0.5-2h) and CVs were performed just after stopping the CPE experiment.As working electrode for CPE, large surface glassy carbon rod electrode (GC Rod) was used together with a glassy carbon disk electrode (d = 3 mm) used for recording the CVs and a silver/silver chloride (KCl sat.) as a reference electrode. These ones were placed in one of the compartments that was filled with a 1.0 mM solution of the complex in 0.1 M phosphate buffer solution pH 12. In the other compartment, containing only the clean electrolyte solution, a mesh platinum counter electrode was used.

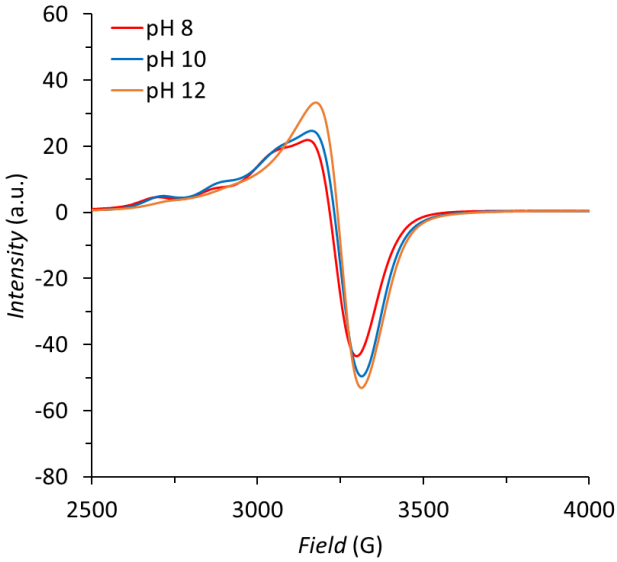

Figure S23. EPR spectra of **[(H₂bpk)Cu^{II}]$^{2+}$** showing changes in the nature of the copper species in solution at different pH values (8-12). Conditions: **[(H₂bpk)Cu^{II}]$^{2+}$** = 10 mM in distilled water basify by addition of conc. NaOH (10 M).

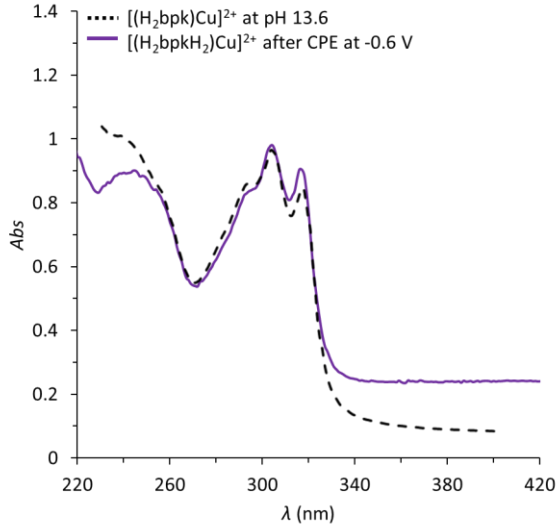

Figure S24. Comparison of UV-Vis spectra of complex **[(H₂bpk)Cu^{II}]$^{2+}$** obtained after a CPE at -0.6 V for 120 seconds in a spectroelectrochemical cell (purple line) and in a 0.1 M phosphate aqueous solution basify with conc. NaOH (10 M) until pH 13.6, without applying any electrolysis time.

From ligand-based to metal-based electron transfer in water oxidation catalysis

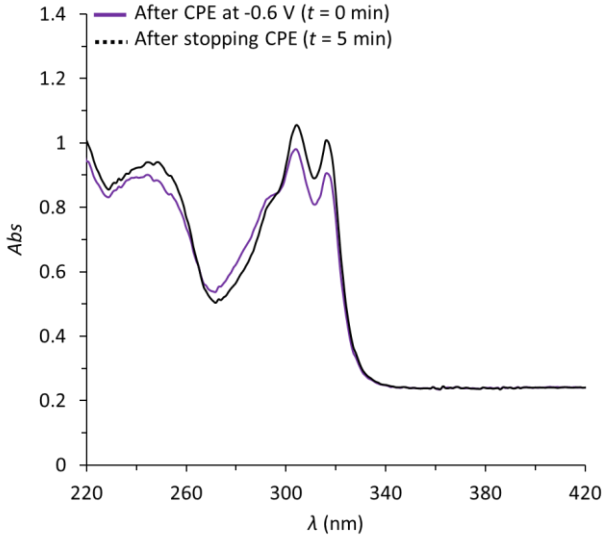

IV

Figure S25. UV-Vis spectra of complex **$[(H_2bpk)Cu^{II}]^{2+}$** obtained after a CPE at -0.6 V for 120 seconds in a spectroelectrochemical cell (purple line) and the same sample measured 5 minutes after stopping the CPE at -0.6 V (black line). The comparison shows that Cu-Hydroxo formed species after applying -0.6 V are not stable at pH 12, the ligand coordinate again forming the initial complex **$[(H_2bpk)Cu^{II}]^{2+}$**.

O_2 detection experiments

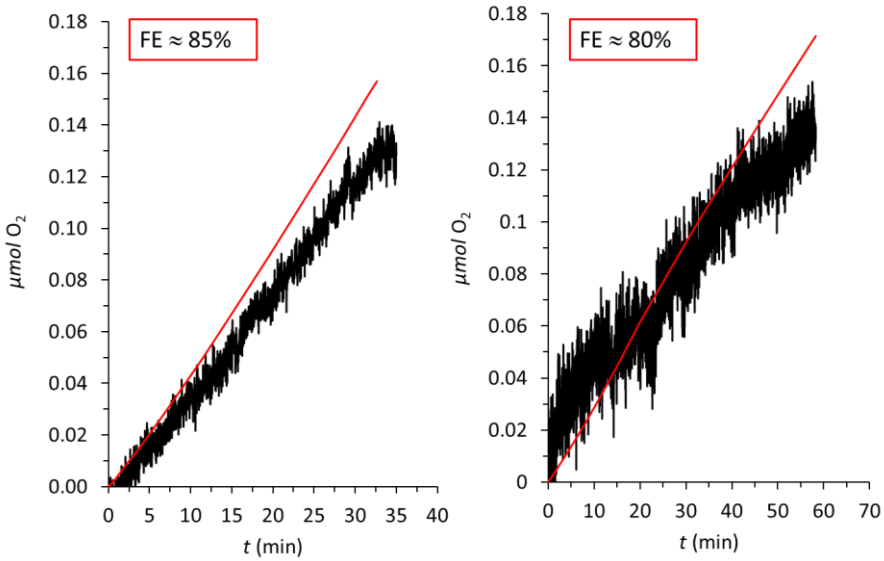

Figure S26. Comparison between current, expressed as µmol of O_2 (red line) and the number of mmol of O_2 detected by the Clark electrode (black line), obtained during the CPE experiment of **$[(H_2bpk)Cu^{II}]^{2+}$** at 1.4 V vs. NHE in 0.1 M phosphate buffer basify by addition of conc. NaOH (10 M) until pH 13 (left) and **$[(H_2bpk)Cu^{II}]^{2+}$** in a 1 M NaOH pH 14 (right). Baseline and blank were subtracted before calculation of Faradaic Efficiency.

Determination of Kinetic constants, Foot of the Wave Analysis (FOWA).

Under catalytic conditions:

$$\frac{i}{i_p} = \frac{8{,}96\sqrt{\frac{RT}{Fv}k_{obs}}}{1 + exp\left[\frac{F}{RT}\left(E^0_{PQ} - E\right)\right]}$$

Where E^0_{PQ} is the standard potential for the catalysis-initiating redox couple, i is the CV current intensity in the presence of the substrate, i_p is the peak current intensity of a one-electron redox process of the catalyst (extracted from Cu^{III}/Cu^{II} couple observed in CV experiment performed at pH 12), F is the Faradaic constant, v is the scan rate and R is 8.314 J mol^{-1} K^{-1}.

Table S2. Summary of the electrochemical parameters used for the calculations of k_{obs}.

	CuO/[(bpyalkH)(OH)Cu]$^{2+}$	[(bpyalkH)(OH)Cu]$^{2+}$	[(bpyalkH)$(OH)_2$Cu]$^{2+}$
i_p (A)	6.7 x 10^{-6}	6.7 x 10^{-6}	6.7 x 10^{-6}
v (mVs^{-1})	100	100	100
E^0_{PQ} (V)	1.23	1.25	1.24
k_{obs} (s^{-1})	1287	2.28	0.44

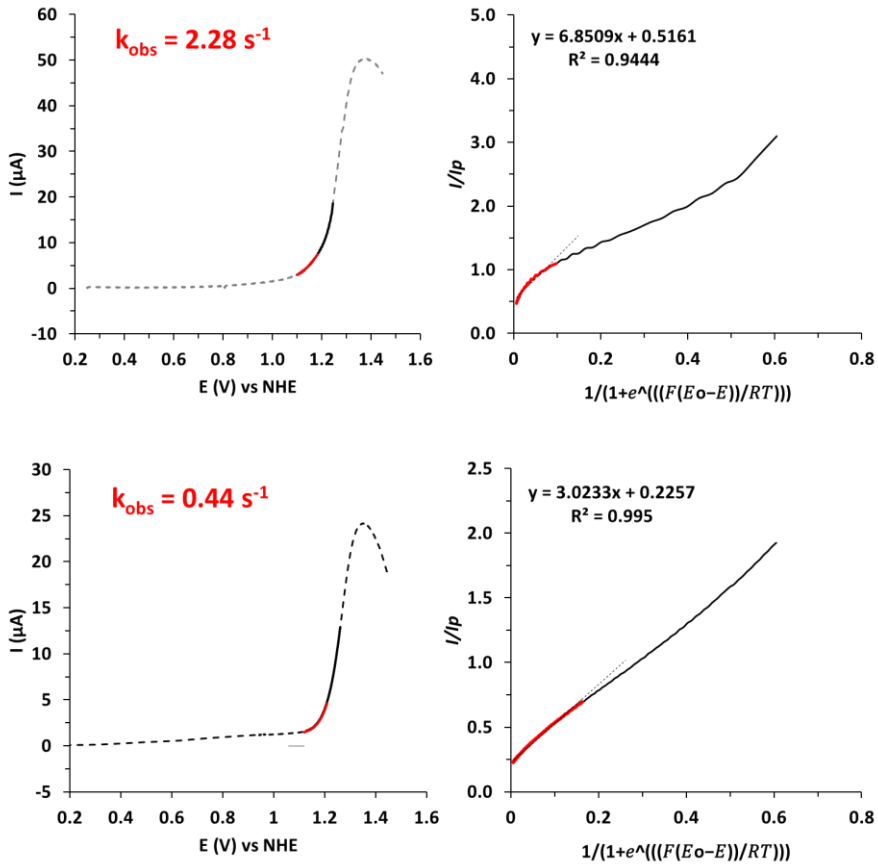

Figure S27. Linear Sweep Voltammetry (LSV) and FOWA region (obtained by plotting i/i_p^0 vs. $1/\{1+\exp[(F/RT)(E^0_{PQ}-E)]\}$) of 1 mM solutions of **[(H₂bpk)Cu^{II}]$^{2+}$** after CPE at -0.6 V for 120 seconds in 0.1 M phosphate buffer pH 12 (top), **[(H₂bpk)Cu^{II}]$^{2+}$** in 0.1 M phosphate buffer basify by addition of conc. NaOH (10 M) until pH 13 (middle) and **[(H₂bpk)Cu^{II}]$^{2+}$** in 1 M NaOH pH 14 (bottom). Solid black line corresponds to the experimental data used for FOWA analysis and Solid red line shows the region used for the determination of k_{obs}.

Scanning Electron Microscopy, EDX and XPS

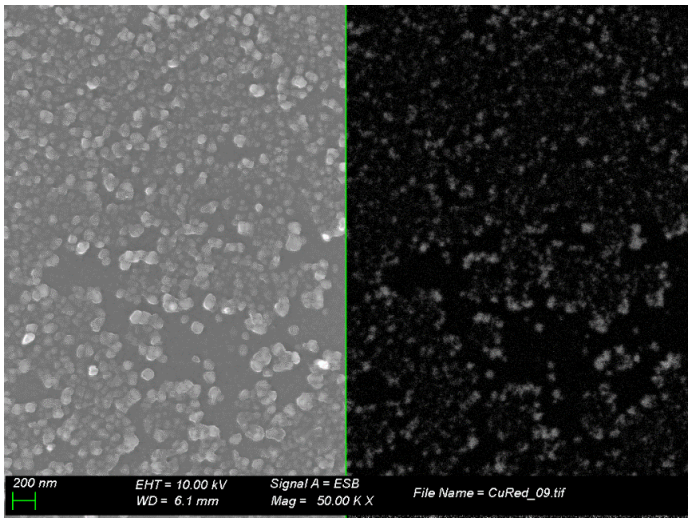

Figure S28. SEM micrographs (left) and corresponding back-scattered electron micrographs (right) of a glassy carbon electrode after CPE of **$[(H_2bpk)Cu^{II}]^{2+}$** (1.5 mM) at -0.6 V vs. NHE during 1 hour in 0.1 M phosphate buffer pH 11.84. The image shows presence of copper-based aggregated nanomaterials deposited materials on the electrode.

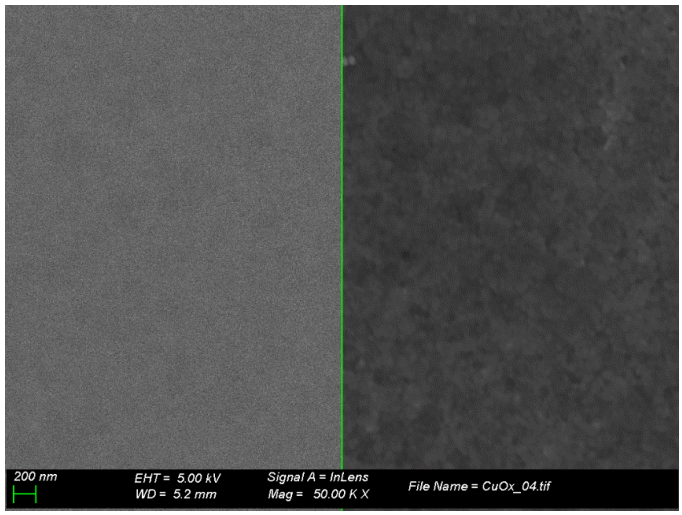

Figure S29. SEM micrographs (left) and corresponding back-scattered electron micrographs (right) of a glassy carbon electrode after CPE of **$[(H_2bpk)Cu^{II}]^{2+}$** (1.5 mM) at 1.4 V vs. NHE during 1 hour in 0.1 M phosphate buffer basify by addition of conc. NaOH (10 M) until pH 13. There is no appreciable presence of copper oxide nanoparticles or deposited materials on the electrode.

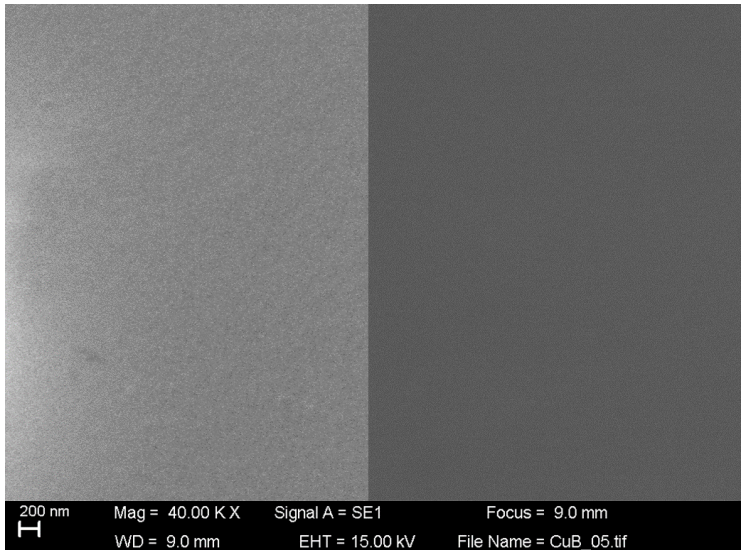

Figure S30. SEM micrographs (left) and corresponding back-scattered electron micrographs (right) of a glassy carbon electrode after CPE of **$[(H_2bpk)Cu^{II}]^{2+}$** (1.5 mM) at 1.4 V vs. NHE during 1 hour in 1 M NaOH (pH 14). There is no appreciable presence of copper oxide nanoparticles or deposited materials on the electrode.

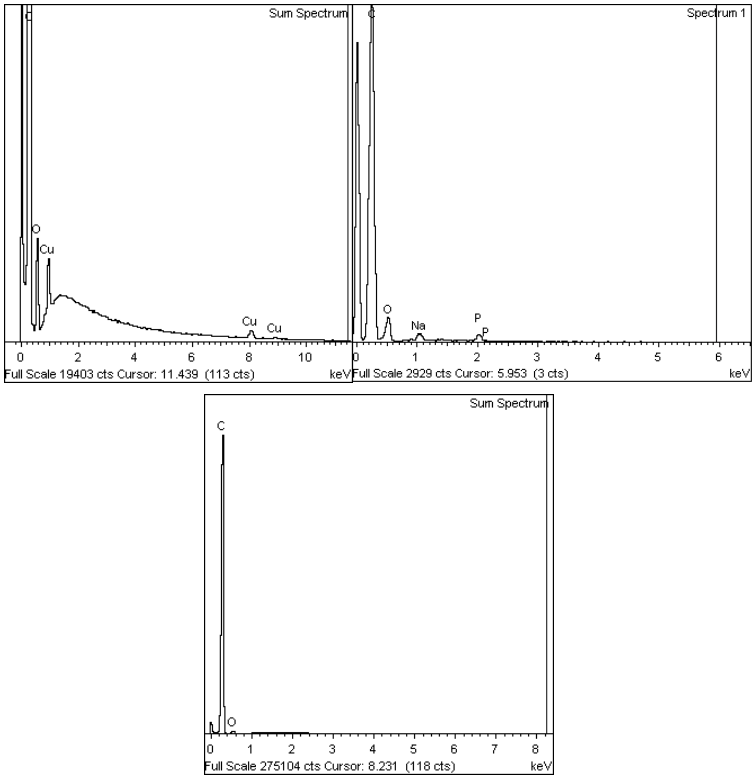

IV

Figure S31. EDX analysis of glassy carbon electrodes obtained after 1h-CPE of 1.5 mM solution of **$[(H_2bpk)Cu^{II}]^{2+}$** at -0.6 V in 0.1 M phosphate buffer pH 11.84 (left), 1.4 V in 0.1 M phosphate buffer basify by addition of conc. NaOH (10 M) until pH 13 (middle) and 1.4 V in 1 M NaOH pH 14 (right).

Table S3. Elemental composition found by EDX analysis of glassy carbon electrodes obtained after 1h-CPE of 1.5 mM solution of **$[(H_2bpk)Cu^{II}]^{2+}$** at -0.6 or 1.4 V in different pHs solutions.

Entry	E_{app} (V)	*pH*	*Cu* (%)	*C* (%)	*O* (%)
1	-0.6	11.8	0.45	95.55	4.0
2	1.4	13.0	-	83.52	15.41
3	1.4	14.0	-	96.5	3.5

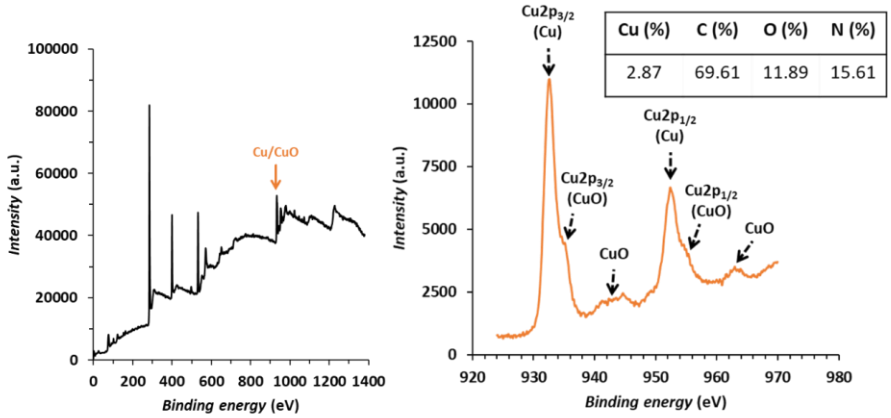

Figure S32. **(Left)** XPS spectra for the glassy carbon electrode obtained after 1h-CPE of 1.5 mM solution of **$[(H_2bpk)Cu^{II}]^{2+}$** at -0.6 V in 0.1 M phosphate buffer pH 11.84. **(Right)** Cu 2P spectra showing the presence of Cu^0 and CuO deposited on the electrode. (*Inset*) Elemental composition found by XPS analysis. **Note:** Energies have been calibrated according to the C 1s band of graphite at 284.2 eV.

IV

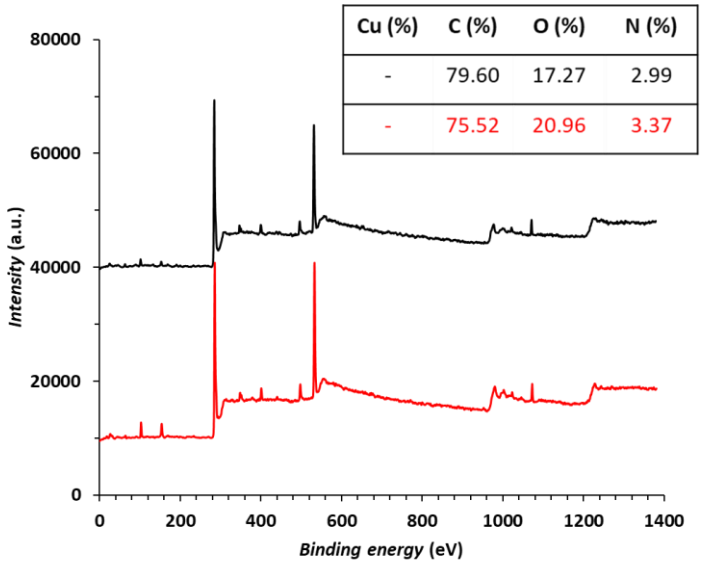

Figure S33. (**Left**) XPS spectra for glassy carbon sponges after 1h-CPE of 1.5 mM solution of **$[(H_2bpk)Cu^{II}]^{2+}$** at 1.4 V in 0.1 M phosphate buffer basify by addition of conc. NaOH (10 M) until pH 13 (red line) and 1 M NaOH (pH 14) (black line). (*Inset*) Elemental composition found by XPS analysis showing no appreciable presence of copper-based deposited materials on the electrode. **Note:** Energies have been calibrated according to the C 1s band of graphite at 284.2 eV.

Computational Study

Computational Details

We perform all the calculations with the Gaussian09 program package[11] using the DFT methodology. We employed B3LYP functional including empirical dispersion correction proposed by Grimme (B3LYP-D3).[12,13] We split the basis set into 6-31+G(d) for C, N, S, O and H,[14] and LANL2TZ(f) for Cu.[15,16] Implicit solvation was introduced through the SMD model,[17] with water as the solvent. All geometry optimizations were computed in solution without symmetry restrictions. We confirmed the nature of all computed stationary points as minima or transition states through vibrational frequency calculations. Free energy corrections were calculated at 298.15 K and 105 Pa pressure, including zero point energy corrections (ZPE). In addition, a correction term of 1.9 kcal/mol (at 298 K) was added when necessary to account for the standard state concentration of 1 M, except for water whose considered concentration was 55.6 M and the correction term 4.3 kcal/mol. Unless otherwise mentioned, all reported energy values are free energies in solution.

We estimate the reaction energy barriers from potential energy relaxes scan when the transition states cannot be found (or do not exist), applying entropic corrections from the minima to compute an estimated free energy change.

In the transformation from free energies to electrochemical magnitudes we took from the literature the values of 4.28 V for the absolute potential of the standard hydrogen electrode[18] and-11.72 eV for the free energy of the proton in aqueous solution at pH=1.[19] The value for the free energy of the proton was translated to the experimental pH value by adding a correction term of -0.059*pH, following the same procedure as other authors.[20]

The functional for the DFT calculations was B3LYP-D3 based on the calibration carried out in a previous work on related systems,[3,21] where its performance was compared with that of M06, M06-D3, M06L, M06-2X, ωB97xD and B97D. In order to validate this DFT methodology, we compared the calculated optimized structures with the X-Ray ones. The following table summarize all the main metrics of the coordination environment for the copper metal center:

Table S4. Comparison of the main metrics for the X-Ray structure and the DFT optimized structure.

METRIC	X-RAY (SOLID)	DFT OPTIMIZED (WATER)
CU-N	1.918 Å, 1.915 Å	1.977 Å, 1.970 Å
CU-O	1.966 Å, 1.976 Å	2.058 Å, 2.069 Å
N-CU-N	81.67°	80.63°
O-CU-O	116.71°	122.62°

Moreover, we also validate our methodology with respect to the experimental value for the redox ppotential of the Cu(III)/Cu(II) redox couple for both catalysts in water solutions:

Table S5. Comparison of the experimental and calculated redox potential for the Cu(III)/Cu(II) couples at pH 7-.

$E_{1/2}^{o}$ (EXP)	$E_{1/2}^{o}$ (CALC)
1.38 V	1.31 V

Chapter 4

Redox behavior of [(H₂bpk)Cu^II]²⁺

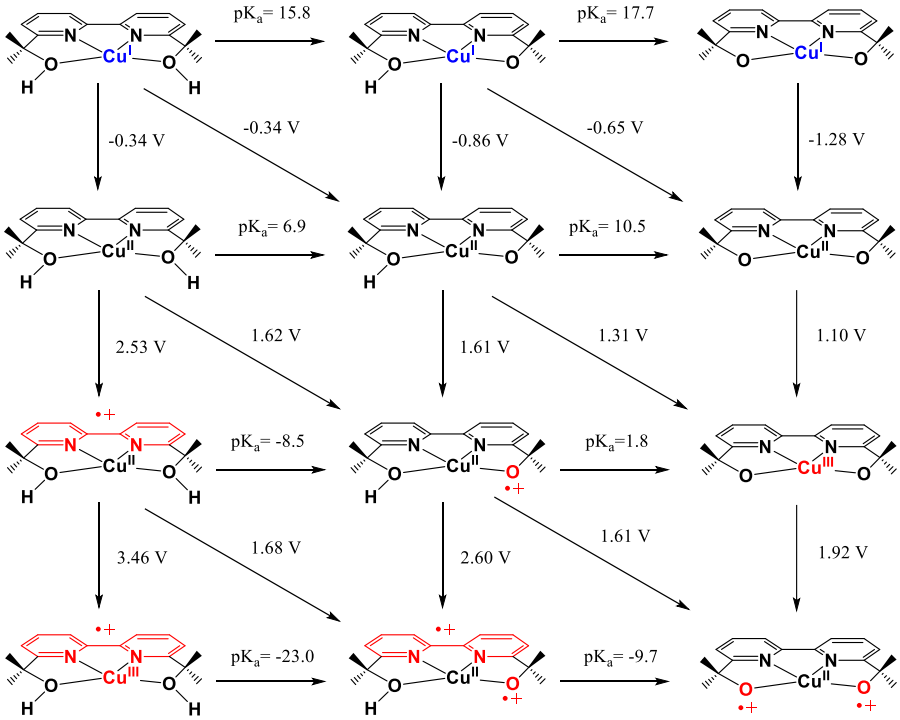

Figure S34. Pathways for the redox processes of complex **[(H₂bpk)Cu^II]²⁺** .

IV

From ligand-based to metal-based electron transfer in water oxidation catalysis

Activation of [(Hbpk)(OH)Cu^{II}]$^{2+}$ catalyst

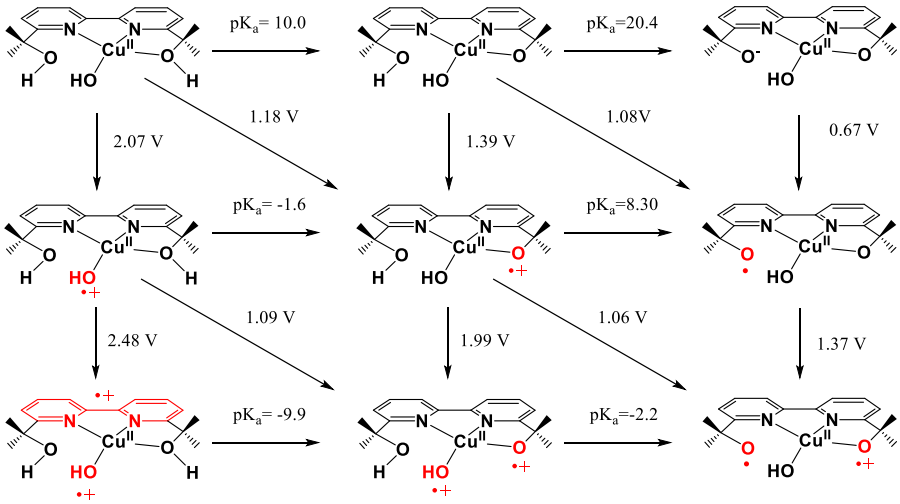

Figure S35. Possible pathways for the oxidative activation of catalyst **[(Hbpk)(OH)Cu^{II}]$^{2+}$** to generate an active species for the O-O bond formation step.

IV

Activation of $[(H_2bpk)(OH)_2Cu^{II}]^{2+}$ catalyst

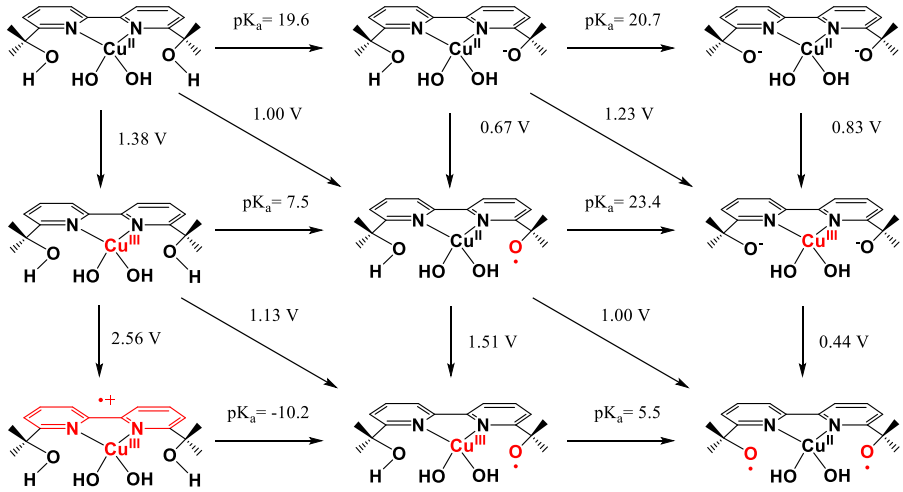

Figure S36. Possible pathways for the oxidative activation of catalyst **$[(H_2bpk)(OH)_2Cu^{II}]^{2+}$** to generate an active species for the O-O bond formation step.

From ligand-based to metal-based electron transfer in water oxidation catalysis

O-O bond formation with [(Hbpk)(OH)Cu^{II}]$^{2+}$ catalyst

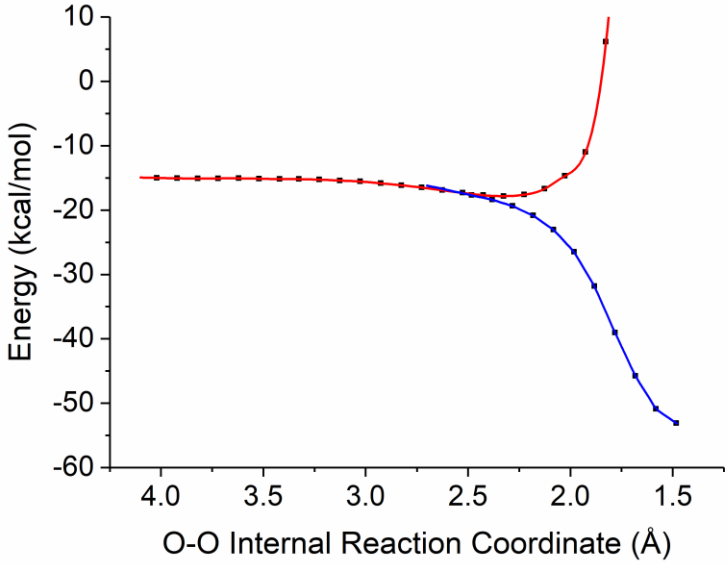

Figure S37. Potential energy relaxed scan for catalyst **[(Hbpk)(OH)Cu^{II}]$^{2+}$** of the O-O reaction coordinate. Red color represents the quartet state while blue color indicates the doublet state.

O-O bond formation with [(H₂bpk)(OH)₂Cu^{II}]$^{2+}$ catalyst

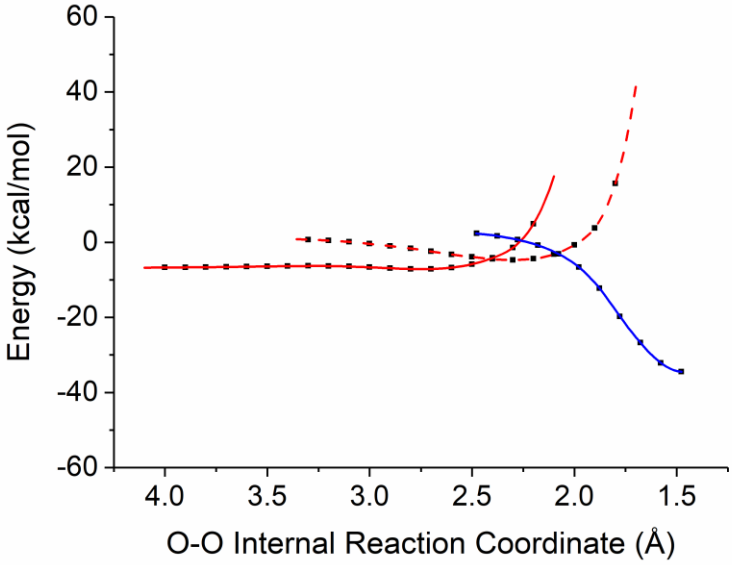

Figure S38. Potential energy relaxed scan for catalyst **[(H₂bpk)(OH)₂Cu^{II}]$^{2+}$** of the O-O reaction coordinate. Red color represents the quartet state of the (solid) initial electronic structure and (dashed) after the first SET, while blue color indicates the doublet state.

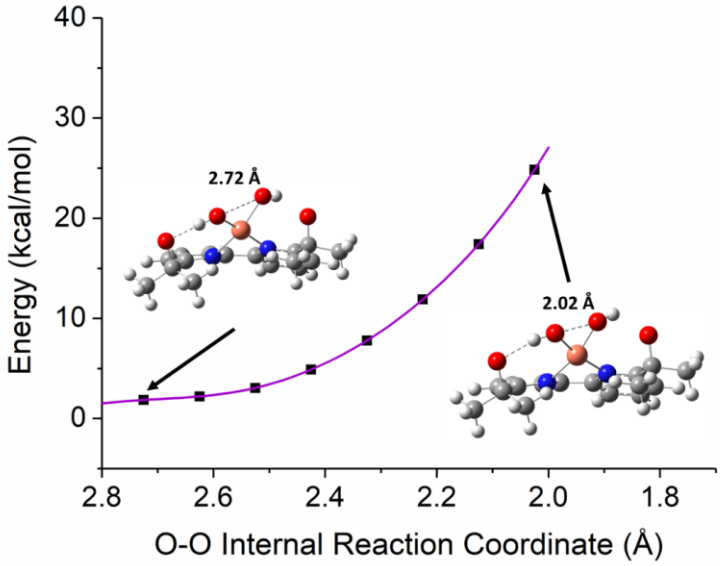

Figure S39. Potential energy relaxed scan of the intramolecular HO---OH coupling using catalyst **$[(H_2bpk)(OH)_2Cu^{II}]^{2+}$** .

Structure and spin density distribution of 2c-3e intemediate

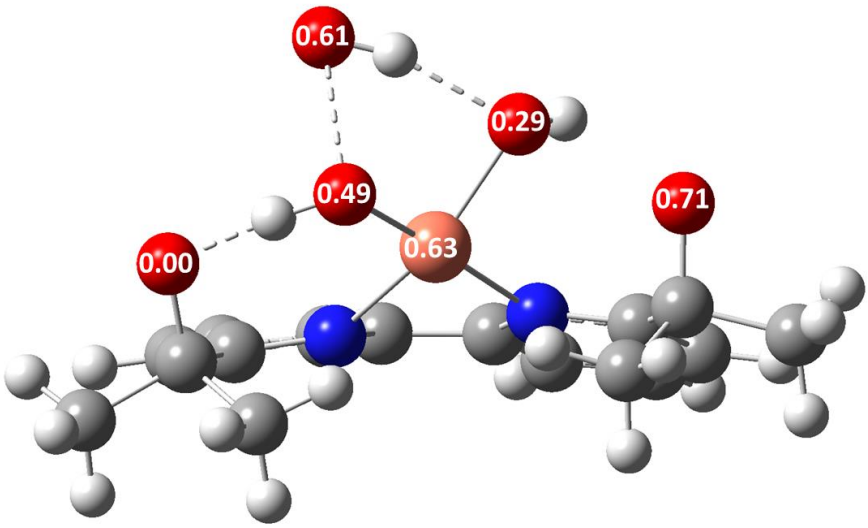

Figure S40. Optimized structure of the 2c-3e intermediate derived from catalyst **$[(H_2bpk)(OH)_2Cu^{II}]^{2+}$** with the spin distribution as white numbers.

References

1 Bozoklu, G.; Marchal, C.; Gateau, C.; Pécaut, J.; Imbert, D.; Mazzanti, M.; *Chem. Eur. J.* **2010**, *16*, 6159-6163.

2 Shao, j.; Qiao, Y.-H.; Lin, H.; Lin, H.-K. *J. Lumin.* **2008**, *128*, 1985-1988.

3 Garrido-Barros, P.; Funes-Ardoiz, I.; Drouet, S.; Benet-Buchholz J.; Maseras F.; Llobet, A. *J. Am. Chem. Soc.* **2015**, *137*, 6758-6761.

4 Data collection with APEX II version v2013.4-1. Bruker (2007). Bruker AXS Inc., Madison, Wisconsin, USA.

5 Data reduction with Bruker SAINT version V8.30c. Bruker (2007). Bruker AXS Inc., Madison, Wisconsin, USA.

6 SADABS: V2012/1 Bruker (2001). Bruker AXS Inc., Madison, Wisconsin, USA. Blessing, Acta Cryst. **1995**, A51, 33-38.

7 SHELXT; V2014/4 (Sheldrick 2014). Sheldrick, G.M. *Acta Cryst.* **2015**, A71, 3-8.

8 SHELXle; C.B. Huebschle, G.M. Sheldrick & B. Dittrich; J. Appl. Cryst. **2011**, 44, 1281-1284.

9 SHELXL; SHELXL-2014/7 (Sheldrick 2014). Sheldrick, G.M. *Acta Cryst.* **2015**, C71, 3-8.

11 Gaussian 09, Revision **D.01**, M. J. Frisch, G. W. Trucks, H. B. Schlegel, G. E. Scuseria, M. A. Robb, J. R. Cheeseman, G. Scalmani, V. Barone, B. Mennucci, G. A. Petersson, H. Nakatsuji, M. Caricato, X. Li, H. P. Hratchian, A. F. Izmaylov, J. Bloino, G. Zheng, J. L. Sonnenberg, M. Hada, M. Ehara, K. Toyota, R. Fukuda, J. Hasegawa, M. Ishida, T. Nakajima, Y. Honda, O. Kitao, H. Nakai, T. Vreven, J. A. Montgomery, Jr., J. E. Peralta, F. Ogliaro, M. Bearpark, J. J. Heyd, E. Brothers, K. N. Kudin, V. N. Staroverov, R. Kobayashi, J. Normand, K. Raghavachari, A. Rendell, J. C. Burant, S. S. Iyengar, J. Tomasi, M. Cossi, N. Rega, J. M. Millam, M. Klene, J. E. Knox, J. B. Cross, V. Bakken, C. Adamo, J. Jaramillo, R. Gomperts, R. E. Stratmann, O. Yazyev, A. J. Austin, R. Cammi, C. Pomelli, J. W. Ochterski, R. L. Martin, K. Morokuma, V. G. Zakrzewski, G. A.

Voth, P. Salvador, J. J. Dannenberg, S. Dapprich, A. D. Daniels, Ö. Farkas, J. B. Foresman, J. V. Ortiz, J. Cioslowski, and D. J. Fox, Gaussian, Inc., Wallingford CT, 2009.

12 A.D. Becke, *J. Chem. Phys.*, 1993, **98**, 5648-5652.

13 S. Grimme, J. Antony, S. Ehrlich and H. Krieg, *J. Chem. Phys.*, 2010, **132**, 154104.

14 a) W.J. Hehre, R. Ditchfield, J.A. Pople, *J. Chem. Phys.*, 1972, **56**, 2257. b) P.C. Hariharan, J.A. Pople, *Theor. Chim. Acta.*, 1973, **28**, 213-222. c) M.M. Francl, W.J. Petro, W.J. Hehre, J.S. Binkley, M.S. Gordon, D.J. DeFrees and J.A. Pople, *J. Chem. Phys.*, 1982, **77**, 3654-3665.

15 a) P. J. Hay and W. R. Wadt, *J. Chem. Phys.*, 1985, **82**, 270-283. b) P. J. Hay and W. R. Wadt, *J. Chem. Phys.*, 1985, **82**, 284-298. c) P. J. Hay and W. R. Wadt, *J. Chem. Phys.*, 1985, **82**, 299-310.

16 Taken from EMSL Basis set Library: a) D. Felier, *J. Comp. Chem.,* 1996, **17**, 1571-1586. b) K.L. Schuchardt, B.T. Didier, T. Elsethagen, L. Sun, V. Gurumoorthi, J. Chase, J. Li and T.L. Windus, *J. Chem. Inf. Model.,* 2007, **47**, 1045-1052.

17 S. A. V. Marenich, C. J. Cramer and D. G. Truhlar, *J. Phys. Chem. B.*, 2009, **113**, 6378-6396.

18 a) A. Lewis, J. A. Bumpus, D. G. Truhlar and C. J. Cramer, *J. Chem. Ed.*, 2004, **81**, 596-603. b) A. Lewis, J. A. Bumpus, D. G. Truhlar and C. J. Cramer, *J. Chem. Ed.*, 2007, **84**, 934 [Erratum].

19 A. V. Marenich, A. Majunmdar, M. Lenz, C. J. Cramer and D. G. Truhlar, *Angew. Chem. Int. Ed.,* 2012, **51**, 12810-12814.

20 S.G. Winikoff and C.J. Cramer, *Catal. Sci. Technol.*, 2014, **4**, 2484-2489.

21 I. Funes-Ardoiz, P. Garrido-Barros, A. Llobet and F. Maseras, *ACS Cat.*, 2017, **7**, 1712-1719.

Chapter 5

From molecules to solid state: Copper-Based Molecular Anodes

The copper complex $[Cu^{II}\text{-mox}]^{2-}$ has been modified to include a pyrene functionality resulting in an improvement of the catalytic features compared to the unmodified homologue. Moreover, both complexes have been used to build molecular anodes by anchoring on graphene-based electrodes through π-π stacking. The extended π-interations exerted by the graphene enhance the catalytic performance of both catalysts, reaching one the highest kinetic constants in copper WOC.

Paper E: Electronic π-Delocalization Boots Catalytic Water Oxidation by Cu(II) Molecular Catalysts Heterogenized on Graphene Sheets

Garrido-Barros, P.; Gimbert-Suriñach, C.; Moonshiram, D.; Picón, A.; Monge, P.; Batista, V. S.; Llobet, A. *J. Am. Chem. Soc.* **2017**, *139*, 12907-12910.

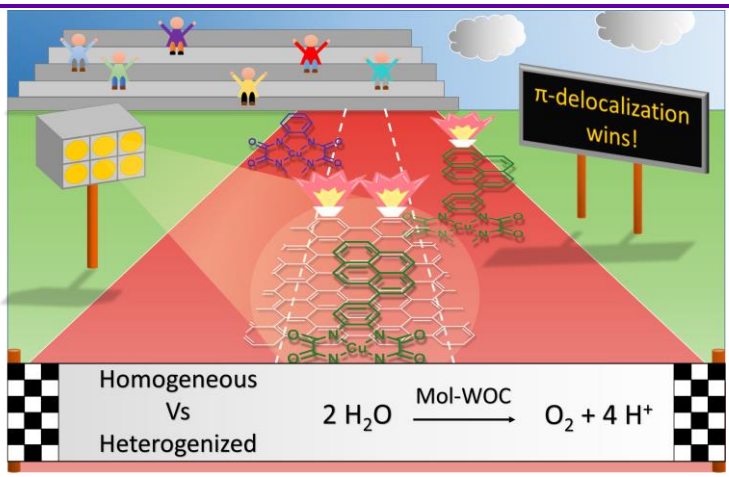

V

Abstract

A molecular water oxidation catalyst based on the copper complex of general formula $[(L_{py})Cu^{II}]^{2-}$, $\mathbf{2}^{2-}$, (L_{py} is 4-pyrenyl-1,2-phenylenebis(oxamidate) ligand) has been rationally designed and prepared to support a more extended π-conjugation through its structure in contrast with its homologue, the $[(L)Cu^{II}]^{2-}$ water oxidation catalyst, $\mathbf{1}^{2-}$ (L is o-phenylenebis(oxamidate)). The catalytic performance of both catalysts has been comparatively studied in homogeneous phase and in heterogeneous phase by π-stacking anchorage to graphene based electrodes. In the homogeneous system, the electronic perturbation provided by the pyrene functionality translates into a 150 mV lower overpotential for $\mathbf{2}^{2-}$ with respect to $\mathbf{1}^{2-}$ and an impressive increase in the kcat from 6 to 128 s^{-1}.

Upon anchorage, π-stacking interactions with the graphene sheets provide further π-delocalization that improves the catalytic performance of both catalysts. In this sense, **2**$^{2-}$ turned out to be the most active catalyst due to the double influence of both the pyrene and the graphene, displaying an overpotential of 538 mV, a kcat of 540 s^{-1} and producing more than 5300 TONs..

Contributions:

Pablo Garrido Barros synthetized and characterized all the compounds and electrodes, carried out the electrochemical and spectroscopic analysis, performed the computational calculations and prepared the manuscript.

E.1. Introduction

Heterogenized water-oxidation catalysis based on earth abundant transition metals, such as Mn, Fe, Co, Ni and Cu, are highly desired for sustainable energy technologies that exploit direct solar water-splitting.[1] An advantage of Heterogenized homogeneous catalysts, when compared to heterogeneous catalysts,[2] is that they can be improved by ligand design. Yet, first-row transition metal complexes pose several challenges. They usually get deactivated when immobilized on electrode surfaces and they suffer from instability due to hydrolytic behavior and decomposition into metal-oxides upon oxidation of the organic ligands.[3] However, from an engineering perspective, solid-state electroanodes are desired due to the simplicity of assembly for potential devices. Therefore, it is imperative to understand the influence of the anchoring functionality on the performance of the immobilized catalysts to learn how to anchor and stabilize functional molecular catalysts on electrode surfaces.[4,5] Here, we focus on water oxidation by Cu(II) molecular catalysts heterogenized on graphene surfaces.

A family of copper complexes based on tetraamide ligands, such as $[(L)Cu^{II}]^{2-}$, **1**$^{2-}$, (L = o-phenylenebis(oxamidate)) shown in Figure 1, have

been recently reported to be effective at catalyzing oxygen evolution by water oxidation at basic pH.[6] Remarkably, the rate-determining step (rds) was found to involve reversible oxidation of the phenyl ring. Here, we explore whether the catalytic properties of these complexes can be manipulated by electronic perturbation of the tetraamide π- system, either by modification of the ligand or by π-stacking to graphitic electrode surfaces.

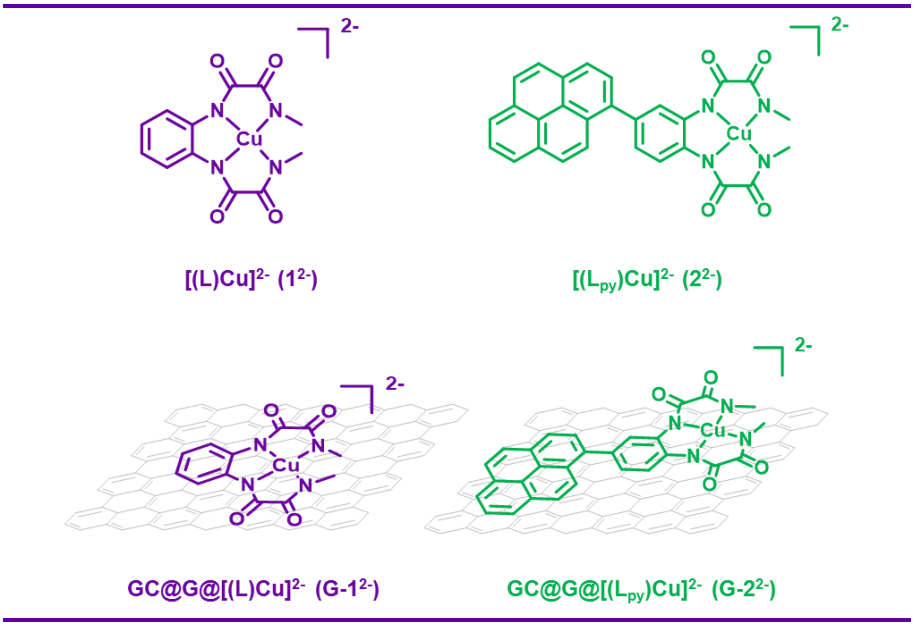

Figure 1. Structural representation and labeling code of the complexes and the hybrid materials used in this work.

E.2. Results and discussion

We focus on complex $\mathbf{1}^{2-}$ as well as on the analogous catalyst $[(L_{py})Cu^{II}]^{2-}$, $\mathbf{2}^{2-}$ with the 4-pyrenyl-1,2-phenylenebis- (oxamidate) ligand $(L_{py})^{4-}$ that has extended π-conjugation via a pyrene moiety covalently connected to the phenyl ring (see SI for a detailed synthetic description) (see Figure 1). We analyze the water oxidation catalytic performance both in the homogeneous phase and heterogenized on graphene sheets. The pyrene anchoring functionality is ideally suited for the comparative analysis because it allows for strong attachment to graphitic surfaces with molecular-

surface interactions that are not as much affected by the supporting electrolyte as in the case of oxo-acid type of functionalities.[7]

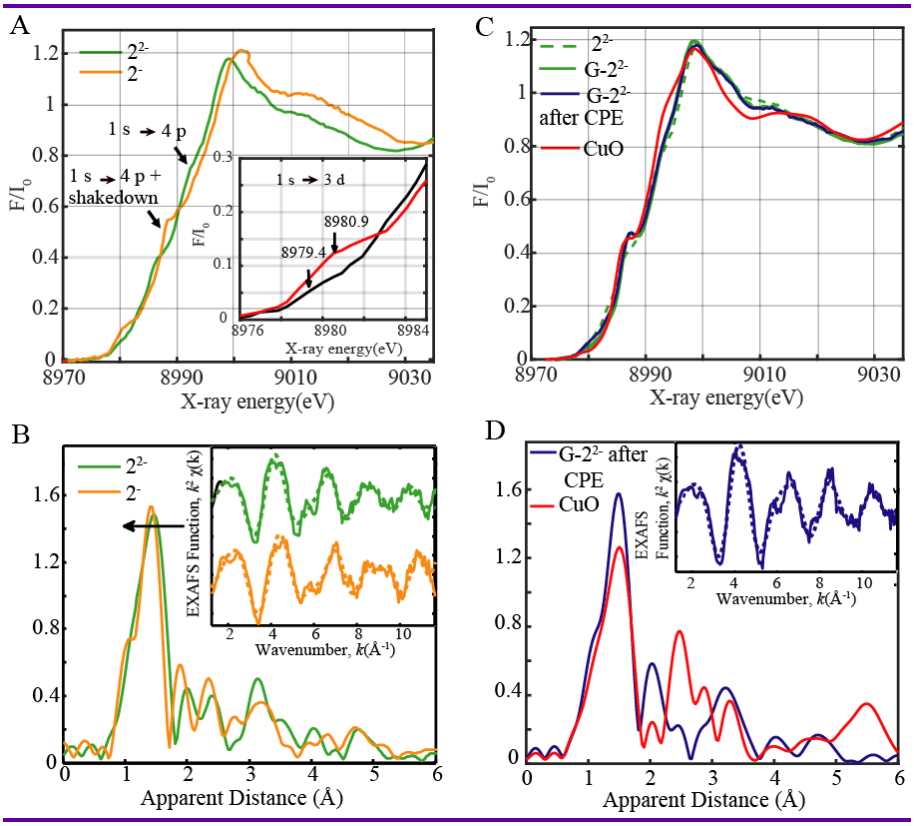

Figure 2. (A) Normalized Cu K-edge XANES of $\mathbf{2}^{2-}$ and $\mathbf{2}^{-}$ in MeCN. Inset: zoom-in of the pre-edge regions. (B) Experimental Fourier transforms of k^2-weighted Cu EXAFS of $\mathbf{2}^{2-}$ and $\mathbf{2}^{-}$ in MeCN. Inset. Back Fourier transforms, experimental results (solid lines) and fitting (dashed lines) $k^2\,\chi(k)$ for $\mathbf{2}^{2-}$ and $\mathbf{2}^{-}$ – in MeCN. Experimental spectra were calculated for k values of 1.212 to 11.6 Å^{-1}. (C) Normalized Cu K-edge XANES of $\mathbf{2}^{2-}$, G-$\mathbf{2}^{2-}$, G-$\mathbf{2}^{-}$ after controlled potential electrolysis (CPE) at 1.25 V and CuO. (D) Experimental Fourier transforms of k^2-weighted Cu EXAFS of G-$\mathbf{2}^{2-}$after CPE and CuO. Inset: Back Fourier transforms, experimental results (solid lines) and fitting (dashed lines) $k^2\,\chi(k)$ for G-22– after CPE. Experimental spectra were calculated for k values of 1.212 to 11.6 Å^{-1}.

The synthesis of complex $[(L_{py})Cu^{II}]^{2-}$, $\mathbf{2}^{2-}$, is straightforward (as described in the SI). We characterized complex $\mathbf{2}^{2-}$ and its one electron oxidized homologue $[(L_{py})Cu^{III}]^{-}$, $\mathbf{2}^{-}$, by using analytic, spectroscopic and electrochemical techniques as well as DFT calculations. Furthermore,

MeCN frozen solutions of $\mathbf{2}^{2-}$ and $\mathbf{2}^{-}$ (potentiometrically prepared) were studied by X-ray absorption near edge structure (XANES) (Figure 2A) and extended X-ray absorption fine structure (EXAFS) spectroscopy (Figure 2B).

Cu K-edge XANES are generally characterized by two peaks along the rising maximum edge, namely the 1s→4p main transition along with a 1s→(4p+shakedown) transition, assigned as the 1s→4p transition with concurrent ligand to metal charge transfer (LMCT), as illustrated in Figure 2A and S16.[8] The XANES spectrum of $\mathbf{2}^{-}$ relative to $\mathbf{2}^{2-}$ shows a clear edge energy shift of 1.5 eV at around half height and 0.65 normalized absorption, reflecting the higher ionization energy required for ejecting a core 1s electron from a more positively charged ion. The distinct metal-centered oxidation state of $\mathbf{2}^{-}$ vs $\mathbf{2}^{2-}$ is shown by the 1.5 eV energy shift in the pre-edge energy range from 8979.4 to 8980.9 eV, corresponding to the 1s→3d electronic transition (Figure 2A, S16, Table S1). Moreover, the 1s→(4p+shakedown) transition is strikingly more intense than the 1s→4p main transition in $\mathbf{2}^{-}$ than in $\mathbf{2}^{2-}$ as illustrated by XANES K-edge fits (Figure S16), providing another indication for the oxidation of Cu(II) to Cu(III) as previously demonstrated by Solomon and co-workers and X-ray photoelectron studies carried out on Cu(II) and Cu(III) oxides.[9,10] The EXAFS spectra (Figure 2B) further revealed a prominent peak in the first coordination sphere corresponding to the Cu−N bond distances. Analysis of the first peak resolves the Cu−N distances for $\mathbf{2}^{2-}$ and $\mathbf{2}^{-}$ to be 1.93 and 1.86 Å respectively, in agreement with the calculated relaxed structures from DFT geometry optimization and typical shortened Cu−N/O bond lengths expected for oxidized Cu(III) species (Table S2, S3, Figure S17). Cu K-edge EXAFS for $\mathbf{1}^{2-}$ and $\mathbf{1}^{-}$ in MeCN solutions were also carried out under identical experimental conditions and yielded similar Cu−N bond distances and similar 1.54 eV edge energy shift at half height in the XANES spectra as $\mathbf{2}^{2-}$ and $\mathbf{2}^{-}$, respectively (Table S2, S3, Figure S18). Interestingly, however, a decreased intensity in the pre-edge

features of both $\mathbf{1}^{2-}$ and $\mathbf{1}^{-}$ compared to $\mathbf{2}^{2-}$ and $\mathbf{2}^{-}$ was observed, most likely due to the more rigorous centrosymmetric environment displayed by $\mathbf{1}^{2-}$ and $\mathbf{1}^{-}$ (Figure S18A).[11]

The UV−vis spectra for $\mathbf{2}^{2-}$ and $\mathbf{2}^{-}$ both in MeCN and in aqueous solution at pH = 12 are depicted in Figure 3A. The corresponding spectra of $\mathbf{1}^{2-}$ and $\mathbf{1}^{-}$ are provided in the SI. The Cu(III) spectrum of $\mathbf{2}^{-}$ in MeCN is characterized by a small hypsochromic shift with regard to that of Cu(II) in $\mathbf{2}^{2-}$. In sharp contrast, the spectrum of $\mathbf{2}^{-}$ in aqueous solution is characterized by a drastic decrease of the intensity of the bands at 340 nm. This is consistent with the fact that the first oxidation process occurs at the pyrene moiety[12] rather than at the Cu center in aqueous solution. This striking difference is associated with the increase in π-delocalization due to the pyrene functionalized ligand, L_{py}, that significantly lowers the oxidation potential at the ligand site[13] together with the large stabilization to the putatively charged oxidized species in the aqueous environment.

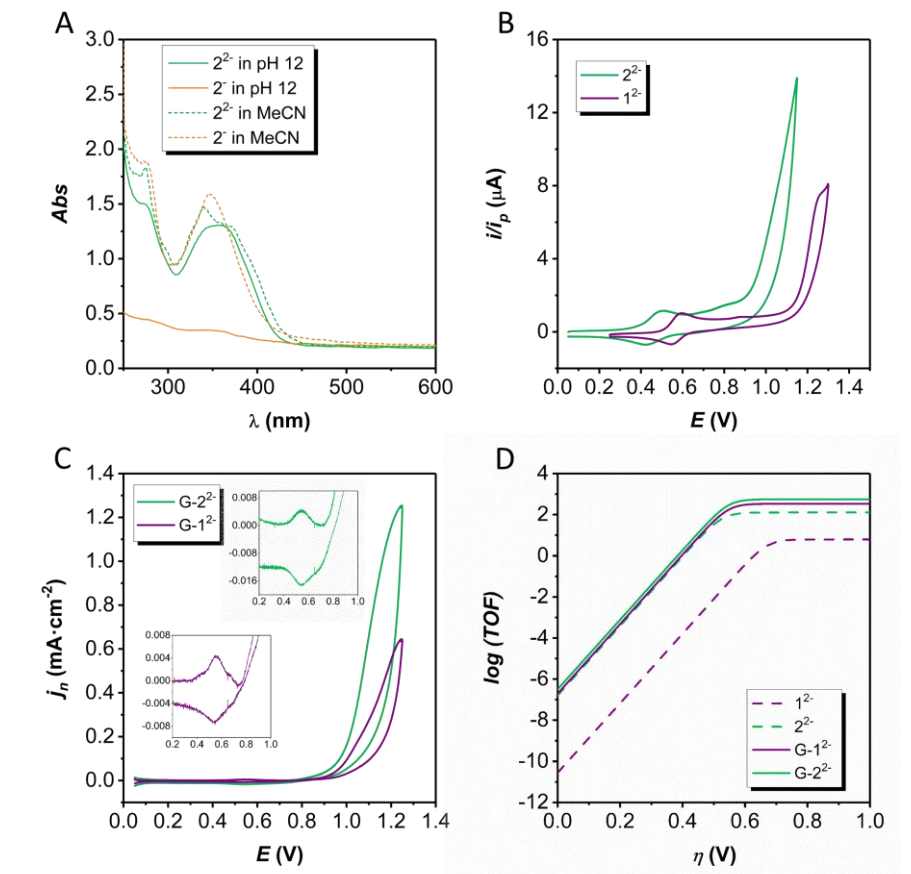

Figure 3. (A) UV−vis spectra for $\mathbf{2}^{2-}$ and $\mathbf{2}^{-}$ in MeCN and in aqueous solution at pH = 12. (B) CV of $\mathbf{1}^{2-}$ and $\mathbf{2}^{2-}$. (C) Background corrected CV of $\mathbf{G\text{-}1}^{2-}$ and $\mathbf{G\text{-}2}^{2-}$. Inset shows an enlargement of the 0.2−1.0 V potential range. (D) Tafel plots for $\mathbf{1}^{2-}$, $\mathbf{2}^{2-}$, $\mathbf{G\text{-}1}^{2-}$ and $\mathbf{G\text{-}2}^{2-}$.

Figure 3B−D provides further support for π-delocalization as manifested by the redox properties of the complexes. Figure 3B shows the CVs of $\mathbf{1}^{2-}$ and $\mathbf{2}^{2-}$ at pH = 12. The anodic scanning of $\mathbf{1}^{2-}$ exhibits a first wave at 0.56 V vs NHE, assigned to the Cu(III)/Cu(II) couple.[14] A sharp increase in current density at around 1.2 V is associated with the electrocatalytic oxidation of water to dioxygen, after formation of the radical cation $[(L^{+})Cu^{III}(OH)]^{-}$. The first oxidation wave of $\mathbf{2}^{2-}$ is cathodically shifted by 130 mV due to the pyrene oxidation. This ligand-based oxidation was further confirmed by electrochemical means on a homologue $[(L_{py})Zn]^{2-}$

complex, because Zn is a redox nonactive metal (see SI Figure S22). The electrocatalytic wave is also cathodically shifted by approximately 150 mV. In this case, the oxidation occurs first at the ligand and subsequently at the metal center, concomitant with OH^- coordination, as supported by DFT calculations of the complete catalytic cycle (Scheme 1). Analogous to the mechanism of $\mathbf{1}^{2-}$, the rate-determining step involves ET transfer to generate $[(L_{py}^{+})Cu^{III}(OH)]^-$.

Scheme 1. Computed Catalytic Cycle for the Catalyst $\mathbf{2}^{2-}$.[a]

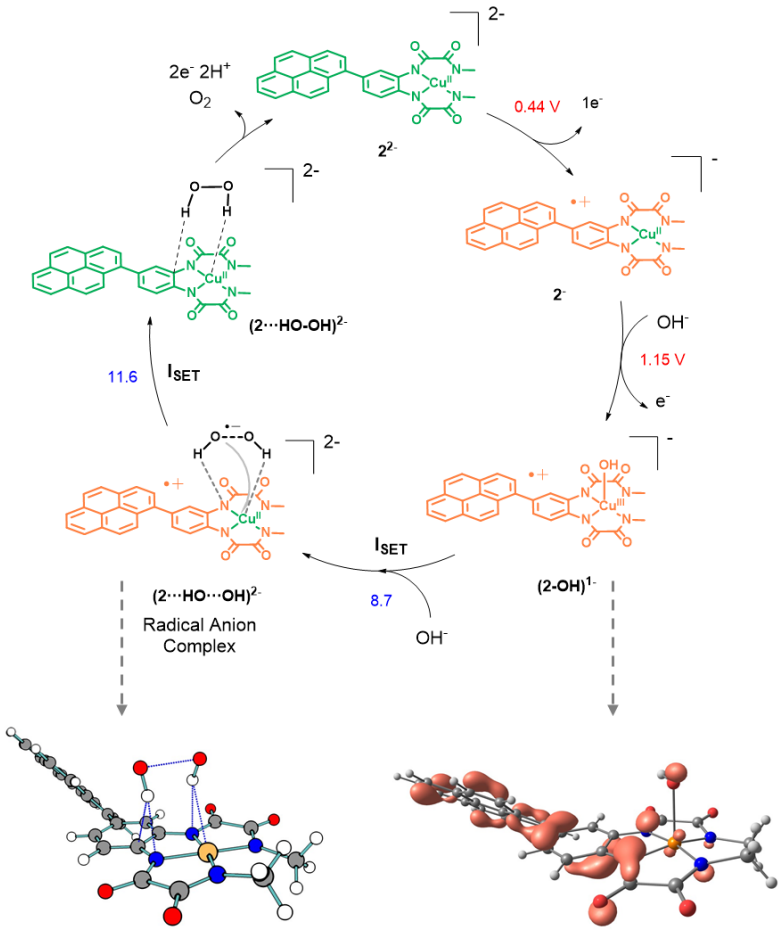

[a]Green color represents the reduced form of the metal center and the ligand whereas orange color represents their oxidized forms. The values in red refers to calculated oxidation potentials in V and the blue values are free energy in kcal·mol^{-1}.

The foot of the wave analysis (FOWA) was carried out to further characterize the electrocatalytic phenomenon,[15,16] giving a maximum turn over frequency (TOF_{max}) of 6.2 s^{-1} for $\mathbf{1}^{2-}$. In sharp contrast, the TOF_{max} of $\mathbf{2}^{2-}$ increases up to 128 s^{-1} under the same conditions, manifesting the strong influence of π-delocalization over catalysis.

Complexes $\mathbf{1}^{2-}$ and $\mathbf{2}^{2-}$ were anchored to graphene by preparing a dispersion of 1 mg of graphene (G) per mL of a methanol solution containing 1 mM $\mathbf{1}^{2-}$ or $\mathbf{2}^{2-}$. The dispersion was stirred overnight at RT to afford a modified graphene material which was subsequently dropcasted into glassy carbon (GC) electrodes. The resulting preparative procedure generated hybrid materials **GC@G@**$\mathbf{1}^{2-}$ (**G-**$\mathbf{1}^{2-}$) and **GC@G@**$\mathbf{2}^{2-}$ (**G-**$\mathbf{2}^{2-}$) with surface coverages of 0.052 and 0.050 nmol/cm^2 respectively, as measured from CV experiments (see SI). The anchored species were characterized by XANES and EXAFS and were found to have similar bond distances and XANES features as those obtained in MeCN frozen solutions of the individual molecules (Figures 2C, S19, Tables S2,S3). It is interesting to note that the 1s→4p (+shakedown) transition at 8987 eV and 0.5 normalized fluorescence of the immobilized **G-**$\mathbf{2}^{2-}$complex is found at a slightly higher energy and intensity than the corresponding transition for homogeneous $\mathbf{2}^{2-}$. Further, the CVs of the anchored catalysts displayed in Figure 3C show a first oxidation wave at 0.52 V and a huge catalytic wave associated with the oxidation of water to dioxygen basically at nearly the same overpotential (η) as in the case of $\mathbf{2}^{2-}$ in the homogeneous phase. The 100 mV anodic shift of the first oxidation couple in heterogeneous phase with respect to $\mathbf{2}^{2-}$ (0.53 vs 0.43 V) is due to the lower degree of solvent stabilization of the anion radical cation in contact with the hydrophobic surface of graphene. A FOWA analysis was again carried out to quantify the electrocatalytic rates obtaining TOF_{max} of 320 and 540 s^{-1} for **G-**$\mathbf{1}^{2-}$ and **G-**$\mathbf{2}^{2-}$, respectively.

These are the highest TOF_{max} values ever reported for molecular first row transition metals (Table S4 in SI),[17] demonstrating the importance of electronic delocalization for fast catalysis even in heterogenized complexes.

The stability of the anchored molecular catalysts on graphene, **G-1**$^{2-}$ and **G-2**$^{2-}$, was analyzed under catalytic turnover by comparing the anodic charge under the first oxidation wave with the charge in the corresponding reduction wave after the electrocatalytic process as shown in the inset of Figure 3C. The comparative analysis showed basically no difference, revealing the high stability of the molecular species in the graphene support. Further evidence for high stability was also obtained by X-ray absorption spectroscopy (XAS), as discussed below and further illustrated in Figure 2C,D, and by Raman spectroscopy (Figure S35). Both techniques unambiguously show the absence of CuO after catalysis. A rotating ring disk electrode experiment (RDDE) was carried out for **G-1**$^{2-}$ and **G-2**$^{2-}$ (see Figure S37) to characterize the electrocatalytic generation of oxygen. A linear sweep voltammetry (LSV) was applied in the disk electrode reaching the threshold potential for electrocatalytic water oxidation whereas the ring electrode was set at E_{app} = −0.35 V, for the reduction of the generated dioxygen. The setup yielded Faradaic efficiencies of 23% and 26% for **G-1**$^{2-}$ and **G-2**$^{2-}$, respectively. In addition, a bulk electrolysis experiment was also carried for **G-2**$^{2-}$ deposited on a 1 cm^2 glassy carbon plate as a working electrode and with a Clark electrode placed at the headspace of the electrochemical cell for measurement of the generated dioxygen in situ (Figure S33). An applied potential E_{app} = 1.25 V for 20 min yielded 0.34 Coulombs and 0.21 μmols of O_2, corresponding to a Faradaic efficiency of 24.5%, similar to the calculated value based on RDDE experiments. The TONs are >5300 and are the largest ever reported for first row transition metal-based molecular catalysts (see Table S4 in the SI).[17] The low Faradaic efficiency is then likely due to graphene oxidation in parallel to water oxidation reaction in basic solutions.[7] Nevertheless, the molecular catalyst remains intact after catalysis

as evidenced by CV and XAS spectroscopy. Indeed, Figure 2C shows that the species after bulk electrolysis are identical to those obtained before catalysis. More important, Figure 2C,D shows that no traces of CuO are revealed by XANES or EXAFS spectra, suggesting that the molecular **G-2**$^{2-}$ active catalyst is robust. This observation is extremely important because most of the molecular catalysts reported so far degrade during the catalytic process yielding the corresponding oxides. This is particularly acute with WOCs based on first row transition metals.[3] Figure 3D shows the catalytic Tafel plots for **1**$^{2-}$, **2**$^{2-}$, **G-1**$^{2-}$ and **G-2**$^{2-}$. It is interesting to observe that the pyrene functionalization of the tetraamide ligand and anchoring to the graphene support has two beneficial effects: decrease of the overpotential (η) for catalytic water oxidation by about 200 mV and increase the TOF_{max} by about 2 orders of magnitude.

In the homogeneous phase, the role of the pyrene group is to stabilize the aromatic ring of the tetraamide moiety via π- delocalization leading to a drastic reduction of the overpotential (η) necessary for catalysis. In the heterogenized **G-1**$^{2-}$, a complex without a pyrene functionality, π-delocalization is provided by graphene. Interestingly, **G-2**$^{2-}$exploits the benefit of having both the pyrene moiety and stacking interactions with graphene and ends up being the best catalyst. The larger TOF_{max} of **G-2**$^{2-}$ when compared to **G-1**$^{2-}$ suggests that the resulting extended π-delocalization due to pyrene−graphene interactions enhances the ET from the catalyst to the graphene electrode, supporting ET as the rds of the catalytic process.

E.3. Conclusions

In conclusion, we have found an extremely rugged and efficient molecular WOC based on Cu, a first-row transition metal complex that is efficient both in the homogeneous phase and heterogenized on graphene electrodes. Importantly, we demonstrated that the molecular catalyst remains intact under catalytic turnover when immobilized on graphene exhibiting

no sign of decomposition or formation of CuO during or after catalysis. Furthermore, we found that the pyrene functionality not only acts as a very robust anchoring unit but also facilitates the electrocatalytic oxidation of water to dioxygen both from a thermodynamic and a kinetic perspective. Finally, **G-1**$^{2-}$ and **G-2**$^{2-}$ are oxidatively robust hybrid materials with exceptional catalytic performance for water oxidation, rendering them as excellent electroanode candidates for direct solar water-splitting devices.

E.4. Acknowledgments

MINECO and FEDER are gratefully acknowledged (CTQ2016-80058-R, CTQ2015-73028-EXP, SEV 2013-0319, ENE2016-82025-REDT (FOTOFUEL), CTQ2016-81923-REDC (INTECAT). P. G.-B. acknowledges "La Caixa" foundation for the PhD grant. A.P. acknowledges funding from the European Union's Horizon 2020 research and innovation program under the Marie Sklodowska-Curie Grant Agreement No. 702565. XAS experiments were performed at the CLAESS beamline at ALBA Synchrotron with the collaboration of ALBA staff under proposal No. 2015091457 and additionally used resources of sector 20 beamline at the Advanced Photon Source (APS) at Argonne Na-tional Laboratory. Sector 20 beamline at APS is operated by the U.S DOE and the Canadian Light Source. V.S.B. acknowledges supercomputer time from NERSC and financial support from as part of the Argonne-Northwestern Solar Energy Research (ANSER) Center, an Energy Frontier Research Center funded by the U.S. Department of Energy, Office of Science, Office of Basic Energy Sciences under Award Number DE-SC0001059.

E.5. References

1 Berardi, S.; Drouet, S.; Francas, L.; Gimbert-Surinach, C.; Guttentag, M.; Richmond, C.; Stoll, T.; Llobet, A. *Chem. Soc. Rev.* **2014**, *43*, 7501–7519.

2 Liu, Y.; Nocera, D. G. *J. Phys. Chem. C* **2014**, *118*, 17060–17066.

3 Wang, J.-W.; Sahoo, P.; Lu, T.-B. *ACS Catal.* **2016**, *6*, 5062–5068.

4 Karousis, N.; Tagmatarchis, N.; Tasis, D. *Chem. Rev.* **2010**, *110*, 5366–5397.

5 Alibabaei, L.; Sherman, B. D.; Norris, M. R.; Brennaman, M. K.; Meyer, T. J. *Proc. Natl. Acad. Sci. U. S. A.* **2015**, *112*, 5899–5902.

6 Garrido-Barros, P.; Funes-Ardoiz, I.; Drouet, S.; Benet-Buchholz, J.; Maseras, F.; Llobet, A. *J. Am. Chem. Soc.* **2015**, *137*, 6758–6761.

7 Hyde, J. T.; Hanson, K.; Vannucci, A. K.; Lapides, A. M.; Alibabaei, L.; Norris, M. R.; Meyer, T. J.; Harrison, D. P. *ACS Appl. Mater. Interfaces* **2015**, 7, 9554–9562.

8 DuBois, J. L.; Mukherjee, P.; Collier, A. M.; Mayer, J. M.; Solomon, E. I.; Hedman, B.; Stack, T. D. P.; Hodgson, K. O. *J. Am. Chem. Soc.* **1997**, *119*, 8578–8579.

9 DuBois, J. L.; Mukherjee, P.; Stack, T. D. P.; Hedman, B.; Solomon, E. I.; Hodgson, K. O. *J. Am. Chem. Soc.* **2000**, *122*, 5775–5787.

10 Solomon, E. I.; Heppner, D. E.; Johnston, E. M.; Ginsbach, J. W.; Cirera, J.; Qayyum, M.; Kieber-Emmons, M. T.; Kjaergaard, C. H.; Hadt, R. G.; Tian, L. *Chem. Rev.* **2014**, *114*, 3659–3853.

11 Westre, T. E.; Kennepohl, P.; DeWitt, J. G.; Hedman, B.; Hodgson, K. O.; Solomon, E. I. *J. Am. Chem. Soc.* **1997**, *119*, 6297–6314

12 Naqvi, K. R.; Melø, T. B. *Chem. Phys. Lett.* **2006**, *428*, 83–87. Related examples in the literature also show that for the pyrene radical cation the absorption at 420 nm either disappear or suffer a very severe loss of intensity.

13 Pysh, E. S.; Yang, N. C. *J. Am. Chem. Soc.* **1963**, *85*, 2124–2130. It is important to realize here that the oxidation potential of naphthalene is 700 mV lower than that of benzene. Thus even if the π-delocalization of the pyrene moiety over the phenyl ring of the tetraamdie ligand is small, it will have a very strong impact into the ligand based redox potential.

14 All redox potentials described in this paper are referred to the NHE reference electrode.

15 Costentin, C.; Drouet, S.; Robert, M.; Savéant, J.-M. *J. Am. Chem. Soc.* **2012**, *134*, 11235–112342.

16 Matheu, R.; Neudeck, S.; Meyer, F.; Sala, X.; Llobet, A. *ChemSusChem* **2016**, *9*, 3361–3369.

17 Blakemore, J. D.; Crabtree, R. H.; Brudvig, G. W. *Chem. Rev.* **2015**, *115*, 12974–13005.

E.6. Supporting information

Experimental details

Materials

All the chemicals used in this work were provided by Sigma Aldrich Chemical Co and they have been used without further purification. The solvents were selected to be HPLC grade and the deionized water was obtained with high purity by passing through a nanopore Milli-Q water purification system. Aqueous basic buffer solutions at pH 12 were prepared using the necessary amount of dibasic and tribasic sodium phosphate salts and adjusting the pH to the desired value so that the final ionic strength was 0.1 M.

Graphene was purchased from Nanostructured & Amorphous Materials, Inc. (NanoAmor) with a purity > 98%, 1-3 layers (1-3 nm of thickness), 2-10 μm of diameter and a specific surface area of about 500-700 $m^2 \cdot g^{-1}$.

GC plate electrodes (GCp) were purchased from HTW, Germany, and are made of glassy carbon SIGRADUR® with the dimensions 20x10x0.18 mm.

Elemental Analysis and Mass Spectrometry

Elemental Analysis of the samples was carried out in a Thermo Finnigan elemental analyzer Flash 1112 model.

Exact mass analyses were performed with a micrOTOF mass spectrometer (from Bruker company) using Electrospray ionization technique in methanol by direct injection and detecting with positive polarity.

Spectroscopic Techniques

NMR spectroscopy was carried out in a 400 MHz Bruker Advance II spectrometer and a Bruker Advance 500 MHz. All the measurements were done at room temperature in deuterated DMSO using residual protons as internal references.

IR spectrometry was performed using a FTIR-ATR TR0 equipment using the pure synthetized compounds as solids.

UV-vis spectrometry was done using a Cary 50 (Varian) UV-vis spectrophotometer.

Resonance Raman Spectroscopy was performed in a Renishaw inVia Confocal Reflex RAMAN microscope instrument (Gloucestershire, UK), equipped with an Ar ion laser, operating at 514 nm. The spectrometer was equipped with a Peltier-cooled CCD detector (-70°C) coupled to a Leica DM-2500 microscope. Calibration was carried out with respect to Si standard.

General electrochemistry

Cyclic Voltammetry (CV), Linear Sweep Voltammetry (LSV), Differential Pulse Voltammetry (DPV) and Controlled Potential Electrolysis (CPE) experiments were carried out on an IJ-Cambria CHI-660 potentiostat. We used a one-compartment three-electrode cell for these measurements. Glassy Carbon (GC) disk electrodes (3 mm of diameter) were used as working electrodes, Pt wire (unless indicated) as counter electrode, Mercury/Mercurous sulfate (K_2SO_4 sat.), MSE, as reference electrode for CV, LSV and DPV. For CPE, Silver/Silver Chloride (KCl sat.) was used as reference and either GC disk or GC plate (as indicated) as working electrode. All redox potentials in the present work are reported versus NHE by adding 0.65 V or 0.2 V to the measured potential, depending on

whether MSE or Silver/Silver Chloride electrodes were employed respectively.

GC disk working electrode pretreatment for homogeneous phase analysis consisted in polishing with 0.05 μm alumina paste, rinsing after with water and acetone and blow-dried finally. GC disk used for catalyst deposition were polished with 1, 0.3 and 0.05 μm alumina paste, then rinsed with water and sonicated for 15 min in acetonitrile. Finally, they were washed with acetone and blow-dried.

CVs and LSVs were collected at 50 $mV \cdot s^{-1}$ except other specification. DPV were obtained with the following parameters: amplitude= 50 mV, step height=4 mV, pulse width= 0.05 s, pulse period= 0.5 s and sampling width= 0.0167 s. $E_{1/2}$ values for the reversible waves were obtained from the half potential between the oxidative and reductive peaks, and the one for irreversible processes are estimated according to the potential at the I_{max} in DPV measurements. All the measurements were done applying IR compensation.

When acetonitrile was used as organic solvent, tetrabutylammonium hexafluorophosphate ($[NBu_4]PF_6$) was added in a concentration of 0.1M as supporting electrolyte.

Surface coverage (Γ) calculation

The surface coverage (Γ) was calculated based on electrochemical measurements according to the following formula:

$$\Gamma\ (mol \cdot cm^{-2}) = \frac{Q}{n \cdot S \cdot F} \qquad \text{(S1)}$$

Q is the charge under the oxidative peak of the reversible, one-electron wave obtained by integration in the CV; n is the number of electrons involved in that oxidation process, which is 1; S is the geometrical surface of the electrode that is 0.07 cm^{-2} or 1 cm^{-2} for GCd and GCp respectively;

finally F is the Faradaic constant. In this work, the average surface coverage for each hybrid catalyst was calculated from 5 independent electrodes that were subjected to CV under same conditions. The error of the measurements was expressed as the standard deviation among the different values obtained. Moreover, the surface coverage of each electrode used for different analyses was calculated.

Rotating Ring Disk Electrode

Rotating Ring Disk Electrode (RRDE) was used to evaluate the catalytic performance of the immobilized catalysts. For this purpose, a RRDE-3A Rotating Ring Disk Electrode from IJ-Cambria was employed with an electrode composed of a GC disk and a Pt ring electrodes and the following diameters: 7 mm outer, 5 mm middle and 4 mm inner. The solution is placed in a one-compartment cell with a Teflon top that closes hermetically. The top has a big hole for the RRDE, two smaller holes for reference and counter electrodes and finally two more thin holes for nitrogen flow tubes, all of them fitting tightly. The electrodes were connected to a IJ-Cambria CHI-660 potentiostat for electrochemical measurements. Before each experiment, the solution was purged with nitrogen during 10 minutes, and then a nitrogen atmosphere was maintained during the measurement.

O_2 detection by Clark electrode

Controlled Potential Electrolysis (CPE) experiments were performed to assess the catalytic performance by the immobilized catalyst using a one-compartment three-electrode cell closed with septum. A GC plate electrode (1 cm^2) supporting the graphene loaded with the catalyst was employed as large surface working electrode. The Ag/AgCl (KCl sat) electrode was used as reference electrode and a Pt mesh as the counter electrode. The cell was filled with phosphate buffer solution at pH 12 with 0.1 M of ionic strength. The CPE was carried out using an IJ-Cambria CHI-660 potentiostat.

During the CPE experiment, the oxygen evolution was monitored with an OXNP type Clark electrode in gas phase (from Unisense Company). This electrode was placed in the cell through the septum without immersion in the solution (gas phase detection from headspace). Once the set up was ready, we remove the oxygen by bubbling nitrogen during 30 min. Once the Clark signal reached values close to 0 mV, the nitrogen flow was stopped and we left the base line to stabilize during 15 min under nitrogen atmosphere. The CPE was started as soon as the Oxygen sensor signal was stable. The experiment was performed under vigorous stirring. Calibration of the oxygen sensor was performed after each experiment by adding known amount of pure oxygen into the cell using a gas tight Hamilton syringe. The blank experiment was performed following the same procedure with bare graphene on the GC plate. The Faraday efficiency was determined according to the total charge passed during the CPE and the total amount of generated oxygen by taking into account that water oxidation is a 4-e^- oxidation process.

Spectroelectrochemistry

Spectroelectrochemical study was carried out in an optically transparent thin-layer electrochemical (OTTLE) cell (OMNI-CELL SPECAC, by Prof. Frantisek Hartl's group, University of Reading). The optical path length of the cell is 0.2 mm. This cell contains two Pt grid electrodes (working and counter) and a silver wire pseudo reference electrode (-0.2 V respect to NHE). To perform the experiment, the cell is filled with less than 0.3 ml of a 5 mM catalyst solution in phosphate buffer at pH 12 that has a 0.1 M of ionic strength. Special care was taken to avoid gas bubbles formation within the cell.

The OTTLE cell was placed in a Cary 50 (Varian) UV-vis spectrophotometer and the electrodes were connected to an IJ-Cambria CHI-660 potentiostat. Cyclic voltammetry was performed at 2 $mV \cdot s^{-1}$ to ensure full conversion of species during the redox processes. UV-vis spectra were

recorded continuously to monitor the changes in the electronic structure upon oxidation and successive reduction.

X-ray Absorption Spectroscopy (XAS) Methods

X-ray absorption spectra were collected at the Advanced Photon Source(APS) at Argonne National Laboratory on bending magnet beamline 20 at electron energy 9.0 KeV and average current of 100 mA and at the CLAESS beamline at ALBA synchrotron light source The radiation at APS was monochromatized by a Si(110) crystal monochromator. The intensity of the X-rays were monitored by three ion chambers (I_0, I_1 and I_2) filled with 80% nitrogen and 20% helium and placed before the sample (I_0) and after the sample (I_1 and I_2).Cu metal was placed between ion chambers I_1 and I_2 and its absorption was recorded with each scan for energy calibration. The samples were kept at 20 K in a He atmosphere at ambient pressure. Hybrid materials on glassy carbon surfaces were recorded as fluorescence excitation spectra using a 13-element energy-resolving detector. All samples were measured in a continuous helium flow cryostat in fluorescence mode with a 13-element Germanium detector. Around 15-20 XAS spectra were collected for each solution sample. No more than 5 scans were taken at each sample position at any condition. Two glassy carbon sheets with sub-monolayer coverage of the hybrid materials were on the other hand stacked on top on each other and wrapped in kapton tape. Around 30 XAS spectra of each hybrid sample were collected. Care was again taken to measure at several sample positions on each sample and no more than 5 scans were taken at each sample position. In order to reduce the risk of sample damage by x-ray radiation, 80% flux was used in the defocused mode (beam size 5500 μm(Horizontal) x 600 μm(Vertical)) and no damage was observed scan after scan to any samples. All samples were also protected from the x-ray beam during spectrometer movements by a shutter synchronized with the scan program. Cu XAS energy was calibrated by the first maxima in the second derivative of the copper metal X-ray Absorption Near Edge

Structure (XANES) spectrum. The CuO reference compound diluted with Boron Nitride (BN) and some Cu hybrid complexes were additionally measured on the CLAESS wiggler beamline at the ALBA synchrotron light source whereby the radiation was monochromatized using a pair Si(111) crystals. Similarly, two glassy carbon sheets wrapped in kapton tape were mounted between PEEK sample holders and measured with a circular beam spot size of around 15 μm using a liquid nitrogen cryostat cooled down to 77 K. Fluorescence absorption measurements were carried out on hybrid materials at ALBA with an Amptek silicon drift solid state detector (XR-100 SDD)[1] placed at 90 degrees to the incoming beam. The silicon drift detector was placed on a motorized stage allowing the sample-detector distance to be easily changed between 30-110 mm[1]. Solid CuO diluted with BN powder was pressed between polypropylene and mylar tape, and measured in the cryostat in transmission mode. Around 3 scans were collected on CuO and around 20-25 scans were collected on hybrid materials. Care was once again taken to measure at several positions on each sample to minimize radiation damage

Extended X-ray Absorption Fine Structure (EXAFS) Analysis

Athena software[1] was used for data processing. The energy scale for each scan was normalized using copper metal standard. Data in energy space were pre-edge corrected, normalized, deglitched (if necessary), and background corrected. The processed data were next converted to the photoelectron wave vector (k) space and weighted by k^3. The electron wave number is defined as $k = [2m(E - E_0)/\hbar^2]^{1/2}$, E_0 is the energy origin or the threshold energy. K-space data were truncated near the zero crossings k = 1.212 to 11.6 $Å^{-1}$ for the solution and the hybrid materials, in Cu EXAFS before Fourier transformation. The k-space data were transferred into the Artemis Software for curve fitting. In order to fit the data, the Fourier peaks were isolated separately, grouped together, or the entire

(unfiltered) spectrum was used. The individual Fourier peaks were isolated by applying a Hanning window to the first and last 15% of the chosen range, leaving the middle 70% untouched. Curve fitting was performed using *ab initio*-calculated phases and amplitudes from the FEFF8[2] program from the University of Washington. *Ab initio*-calculated phases and amplitudes were used in the EXAFS equation

$$\chi(k) = S_0^2 \sum_j \frac{N_j}{kR_j^2} f_{eff_j}(\pi, k, R_j) e^{-2\sigma_j^2 k^2} e^{\frac{-2R_j}{\lambda_j(k)}} \sin(2kR_j + \phi_{ij}(k)) \qquad \text{(S2)}$$

where N_j is the number of atoms in the j^{th} shell; R_j the mean distance between the absorbing atom and the atoms in the j^{th} shell; $f_{eff_j}(\pi, k, R_j)$ is the *ab initio* amplitude function for shell *j*, and the Debye-Waller term $e^{-2\sigma_j^2 k^2}$ accounts for damping due to static and thermal disorder in absorber-backscatterer distances. The mean free path term $e^{\frac{-2R_j}{\lambda_j(k)}}$ reflects losses due to inelastic scattering, where $\lambda_j(k)$, is the electron mean free path. The oscillations in the EXAFS spectrum are reflected in the sinusoidal term $\sin(2kR_j + \phi_{ij}(k))$, where $\phi_{ij}(k)$ is the *ab initio* phase function for shell *j*. This sinusoidal term shows the direct relation between the frequency of the EXAFS oscillations in k-space and the absorber-backscatterer distance. S_0^2 is an amplitude reduction factor.

The EXAFS equation[3] (Eq. S2) was used to fit the experimental Fourier isolated data (q-space) as well as unfiltered data (k-space) and Fourier transformed data (R-space) using *N*, S_0^2, E_0, *R*, and σ^2 as variable parameters (Table S4, S5). *N* refers to the number of coordination atoms surrounding Cu for each shell. The quality of fit was evaluated by R-factor and the reduced Chi^2 value. The deviation in E_0 ought to be less than or equal to 10 eV. R-factor less than 2% denotes that the fit is good enough3 whereas R-factor between 2 and 5% denotes that the fit is correct within a consistently broad model. The reduced Chi^2 value is used to compare

fits as more absorber-backscatter shells are included to fit the data. A smaller reduced Chi^2 value implies a better fit. Similar results were obtained from fits done in k, q, and R-spaces.

Synthetic details and electrode preparation

H_4L and $[(L)Cu](NMe_4)_2$

The H_4L ligands and the corresponding copper complex $[(L)Cu](NMe_4)_2$ were synthetized according to the procedures described in literature.[4,5,6]

H_4L_{py} and $[(L_{py})Cu](NMe_4)_2$

General scheme

Scheme 1. Reaction scheme for the synthesis of $[(L_{py})Cu]^{2-}$.

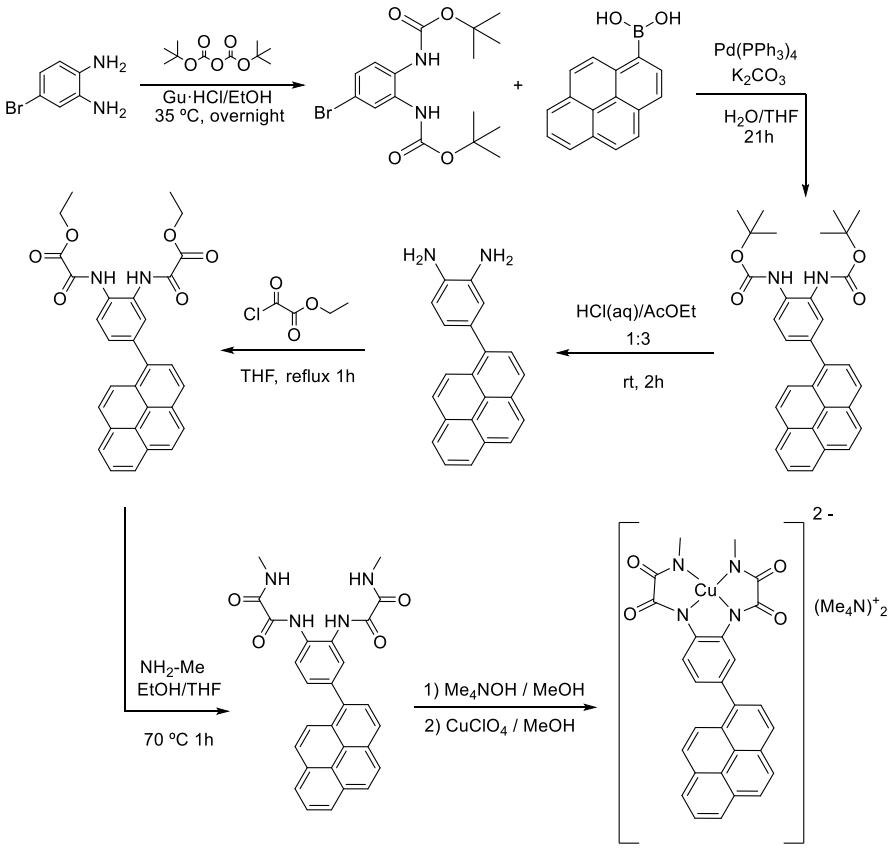

Synthesis of di-tert-butyl (4-bromo-1,2-phenylene)dicarbamate

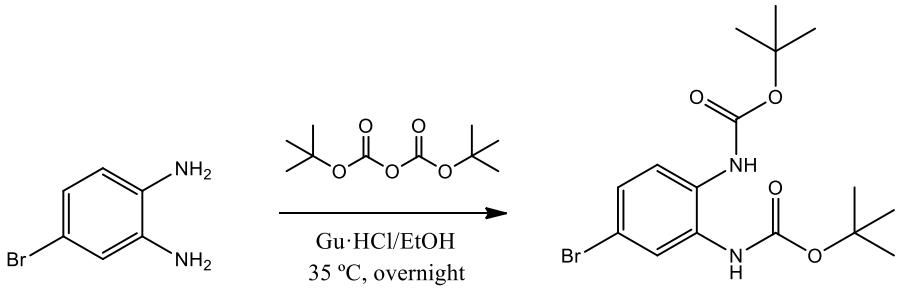

The product was prepared following a procedure similar to a previously reported one[7]: 2.0 mmols of the starting product (4-bromo-1,2-diamino-benzene), 5.0 mmols of di-tert-butyl dicarbonate and 1.25 mmols of guanidine hydrochloride were mixed and dissolved in 20 mL of ethanol (96% v/v). The mixture was set to 35 ºC and left over-night under stirring. Then the ethanol was evaporated and the resulting solid was extracted with dichloromethane and filtered. Upon evaporation of dichloromethane, a brown solid appears which was washed with hexane until filtrate was colorless.

Yield: 657 mg (1.69 mmols), 77%. ^{1}H-NMR (DMSO-d6): δ [ppm] = 8.57 (H-NPh, s, 1H) 8.55 (H-N'Ph, s, 1H), 7.69 (H-1, s, 1H), 7.39 (H-2, d, J = 8.6 Hz), 7.23 (H-3, dd, J_1 = 8.6 Hz, J_2 = 2.3 Hz), 1.45 ([-O-(C(CH$_3$)$_3$)], s, 9H), 1.44 ([-O'-(C(CH$_3$)$_3$)], s, 9H).

Synthesis of di-tert-butyl (4-(pyren-1-yl)-1,2-phenylene)dicarbamate

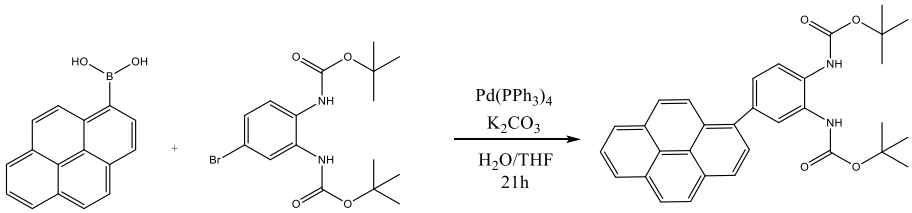

The synthesis of the pyrene adduct was performed using a Suzuki coupling in similar conditions to reported existing reactions with pyrene-1-

boronic acid[8]. 2.5 mmol of di-tert-butyl (4-bromo-1,2-phenylene)dicarbamate, 2.5 mmol of pyrene-1-boronic acid and 7.5 mmol of potassium carbonate are mixed. After degasing and placing the solids under nitrogen atmosphere, 0.25 mmols tetrakis(triphenylphosphine)palladium(0) were added also under nitrogen atmosphere. Then 8 mL of distilled water and 40 mL of THF that had been previously degassed by bubbling nitrogen under stirring were added. The reaction mixture was left for 21h at reflux. Afterwards, ice cool distilled water was added and the mixture was extracted with 4x20 mL of DCM. After evaporation of the solvent, the solid is purified by liquid chromatography. Silica was used as stationary phased and a mixture of hexane/ethylacetate 9:1 was used as mobile phase.

Yield: 924 mg (1.81 mmols), 72%. IR: υ_{max} [cm^{-1}] = 3319 (N-H tension); 3038 (=C-H tension, aromatic); 2976, 2930 (C-H tension); 1696 (C=O tension), 1149 (C-H bending). ^{1}H-NMR (DMSO-d6): δ [ppm] = 8.66 (H-NPh, s, 1H), 8.63 (H-N'Ph, s, 1H), 8.33 (H-4 or H-5, d, J= 7.9 Hz), 8.30 (H-8 or H-10, dd, J_1 = 7.6 Hz J_2 = 1.0 Hz, 1 H), 8.26 (H-8 or H-10, dd, J_1 = 7.7 Hz J_2 = 0.9 Hz, 1 H),) 8.19 - 8.11 (group H-12, H-11, H-7, H-6, multiple signals, 4H), 8.07 (H-9, dd, J_1 = 7.6 Hz, J_2 = 7.6 Hz), 7.97 (H-4 or H-5, d, J = 7.9 Hz, 1H), 7.70 (H-1, broad signal, 1H), 7.66 (H-2, d, J = 8.2 Hz, 1H), 7.33 (H-3, dd, J1 = 8.2, J2 = 2.08, 1H), 1.49 (-O'-(C(CH_3)$_3$), s, 9H), 1.42 (-O'-(C(CH_3)$_3$), s, 9H). ^{13}C-NMR (DMSO-d6): δ [ppm] = 153.97 (-NH-COO-, 1C), 153.90 (-NH-C'OO-, 1C), 136.79 (1C), 136.70 (1C), 131.36 (1C), 130.77 (1C), 130.65 (1C), 130.53 (1C), 129.79 (1C) 128.28 (1C), 128.00 (1C), 127.93 (1C), 127.82 (1C), 126.99 (1C), 126.56 (1C), 125.90 (1C), 125.52 (1C), 125.45 (1C), 124.90 (1C), 124.54 (1C), 124.41 (1C), 80.40 (-C-(CH_3)$_3$, 1C), 80.37 (-C'-(CH_3)$_3$, 1C), 28.45 (-C-(C'H_3)$_3$, 3C), 28.41 (-C-(C'H_3)$_3$, 3C).

Synthesis of 4-(pyren-1-yl)benzene-1,2-diamine

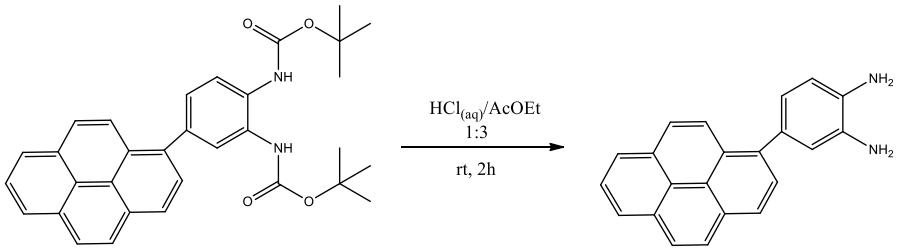

The product was prepared by following an acid hydrolysis similar to what had been described in similar reactions.[9] 1.77 mmols of di-tert-butyl (4-(pyren-1-yl)-1,2-phenylene)dicarbamate were dissolved in 8 mL mixture of HCl (37%, aq) and AcOEt in a 1:3 proportion. The mixture is left under stirring at room temperature for 2h. Then distilled water is added and the solution is brought to basic pH by adding excess solid K_2CO_3. Then the mixture is extracted with 5x20 mL of AcOEt. The organic phase is recovered and solvent is evaporated.

Yield: 543 mg (1.76 mmols) 99%. HR-MS (ESI positive mode, CH_2Cl_2): m/z $[M+H]^+$ = 309.1398 (Expected: 309.1391). IR: υ_{max} [cm^{-1}]= 3394, 3355, 3308, 3184 (N-H, tension) 3040 (=C-H, tension), 1500 (-C=C- aromatic, tension), 1280 (C-N, tension). ^{1}H-NMR (DMSO-d6): δ [ppm] = 8.30-8.23 (pyrene, multiple signals, 4H), 8.18 (pyrene, d, J = 9.0 Hz, 1H), 8.15 (pyrene, d, J = 8.9 Hz, 1H), 8.12 (pyrene, d, J = 9.3 Hz, 1H), 8.05 (H-4, dd, J_1 = 7.6 Hz, J_2 = 7.6 Hz), 7.94 (pyrene, d, J = 7.9 Hz, 1H), 6.83 (H-1, d, J = 1.9 Hz, 1H), 6.73 (H-2, d, J = 7.8 Hz, 1H), 6.67 (H-3, dd, J_1 = 7.8 J_2 = 1.9 Hz, 1H), 4.71 (H_2-HPh, broad signal, 2H) 4.67 (H_2-N'Ph, broad signal, 2H). ^{13}C-NMR (DMSO-d6): δ [ppm] = 139.42 (1C), 135.99 (1C), 135.20 (1C), 131.55 (1C), 131.03 (1C), 129.62 (1C), 129.53 (1C), 128.85 (1C), 128.02 (1C), 127.91 (1C), 127.17 (1C), 126.67 (C-4, 1C), 126.00 (1C), 125.33 (1C), 125.28 (1C), 124.98 (1C), 124.80 (1C), 124.73 (1C) 120.04 (C-3, 1C), 116.94 (C-1, 1C) 114.89 (C-2, 1C).

From molecules to solid state: Copper-based molecular anodes

Synthesis of N1,N1'-(4-(pyren-1-yl)-1,2-phenylene)bis(N2-methyloxalamide) (H_4L)

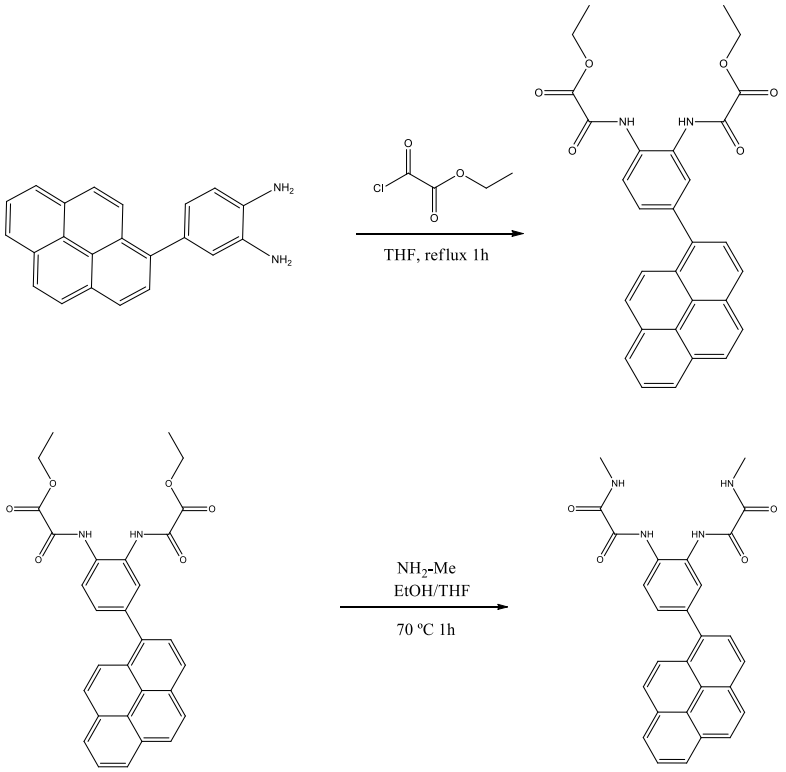

The product was synthesized following a similar two steps procedure to the synthesis of ligand H_4L that has been previously cited.[4-6] Firstly, 0.17 mmol of the 4-(pyren-1-yl)benzene-1,2-diamine were dissolved in 3 mL of THF. Then 0.4 mmol (66 μL) of the ethyl clorooxoacetate were added drop wise. The mixture was refluxed for 1h and the appearing solid waste was removed by filtration. The resulting solution was evaporated and an oil product was formed. Upon addition of distilled water, a white solid formed, which was collected by centrifugation. After washing with water it was left to dry, to then solubilize it with 6 mL of THF. Afterward, 130 μL of a 33% wt methylamine solution in MeOH were added and the mixture was left at 70 ºC for 1 h. The appearing solid corresponds to the target ligand and is filtrated and washed with THF and ether.

Yield: 28 mg (0.05 mmol) 32%. Elemental Analysis calc.(%) for $C_{28}H_{22}N_4O_4 \cdot 3.5\ H_2O$: C 62.10, H 5.40, N 10.35, found (%): C 61.83, H 4.23, N 11.33. HR-MS (ESI positive mode, CH_2Cl_2): m/z $[M+H]^+$ = 501.1526 (Expected: 501.1539). IR: υ_{max} [cm^{-1}]= 3350, 3297, 3241 (N-H, tension), 3040 (=C-H aromatic, tension), 2940 (C-H, tension), 1656, 1681 (C=O, tension), 1530, 1506, 1409, (C-N, tension). ^{1}H-NMR (DMSO-d6): δ [ppm] = 10.73 (H-N-C=O & H-N'-C=O, broad signal, 2H), 9.06-8.99 (H-N-CH_3 & H-N'-CH_3, m, 2H) 8.39 (H-4/H-5, d, J = 7.9 Hz, 1H), 8.36-8.31 (H-8 & H-10, m, 2H), 8.27-8.18 (group H-6, H-7, H-11 and H-12, m, 4H), 8.11 (H-9, dd, J_1 = 7.6 Hz, J_2 = 7.6 Hz), 8.06 (H-4/H-5, d, J = 7.9 Hz, 1H), 7.91 (H-1, d, J = 2.1 Hz, 1H), 7.87 (H-2, d, J = 8.3 Hz, 1H), 7.59 (H-3, dd, J_1 = 8.3 J_2 = 2.1 Hz, 1H), 2.79 (H_3-C-NH-, d, J = 4.8 Hz, 3H), 2.75 (H_3-C'-NH-, d, J = 4.8 Hz, 3H). ^{13}C-NMR (DMSO-d6): δ [ppm] = 160.61 (C-10/C-11, 1C), 160.56 (C-10/C-11, 1C), 159.37 (C-12/C-13, 1C), 159.28 (C-12/C-13, 1C), 138.31 (1C), 136.33 (1C), 131.45 (1C), 130.85 (1C), 130.80 (1C), 130.34 (1C), 129.78 (1C), 129.76 (1C), 128.39 (C-2, 1C) 128.11 (C-4/C-5, 1C), 128.05 (1C), 127.84 (1C), 127.66 (C-1, 1C), 126.97 (C-6, 1C), 125.95 (C-3, 1C) 125.58 (C-4/C-5, 1C), 125.52 (1C), 124.90 (1C), 26.61 (C-8/C-9, 1C), 26.56 (C-8/C-9, 1C).

From molecules to solid state: Copper-based molecular anodes

Synthesis of $[(L_{py})Cu](NMe_4)_2$

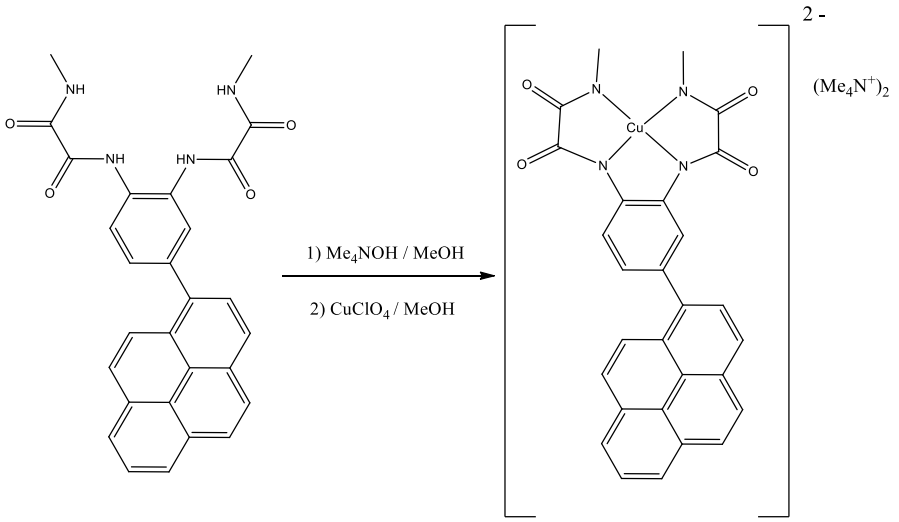

The complex was synthesized by an adaptation of the procedure presented in the previously mentioned works.[4-6] 0.05 mmols of the precursor ligand were weighted and dispersed in 1 mL of MeOH using a sonicator for 15 minutes. The mixture was brought to 70 ºC and a tetramethylamoniumhydroxide solution was added until a clear solution was formed. At that moment, a copper perchlorate hexahydrate solution of 0.05 mmols in 2 mL of MeOH is prepared and added to the mixture drop wise and slowly. After 1 hour, solid formed is removed by filtration and the solvent is evaporated until about 1 mL solution. After addition of 1 mL of MeCN more solid was removed by filtration. Finally, the remaining solution is treated with acetone and abundant ether which causes a brown solid to precipitate. This solid quickly became an oil through absorption of atmospheric water. Water was removed at the pump in a heating bath at 40 ºC and the solid was kept under nitrogen atmosphere.

Yield 28 mg (0.04 mmols) 80%. Elemental Analysis calc.(%) for $C_{36}H_{42}CuN_6O_4 \cdot 5\ H_2O$: C 55.69, H 6.75, N 10.82, found (%): C 55.47, H 7.44, N 10.59. HR-MS (ESI negative mode, CH_2Cl_2): m/z $[M+H]^+$ = 538.0702 (Expected: 538.0708).

Chapter 5

Synthesis of [(L_{py})Zn]Na_2

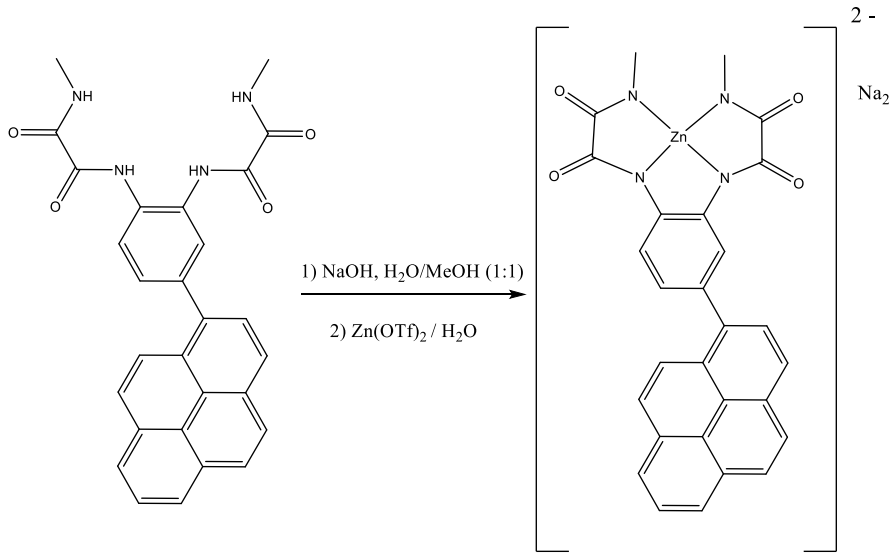

This complex was synthesized by a different procedure than in the case of Cu complex, adapted from a related reported complex.[5] 0.02 mmols of the precursor ligand were weighted and dispersed in 1 mL of water/MeOH mixture (1:1) using a sonicator for 15 minutes. The mixture was brought to 80 ºC and 0.1 ml of a solution containing 1mmol/ml of NaOH in water was added. The mixture was stirred at 80ºC for 30 minutes. Then, a $Zn(OTf)_2$ solution of 0.02 mmols in 0.2 mL of water is added to the mixture drop wise and slowly. After 1 day at the same temperature, suspended solid is removed by filtration and the solvent is totally evaporated. The obtained solid was dissolved in MeOH to remove unreacted ligand by filtration and solvent is again evaporated. Finally, the remaining solid was washed with ether and vacuum dried.

Yield 4.5 mg (0.008 mmols) 40%.

From molecules to solid state: Copper-based molecular anodes

Preparation of hybrid materials G-1^{2-} and G-2^{2-}

As supporting material, graphene (1-3 layers) deposited onto glassy carbon electrodes was used due to its high electroactive surface area and conductivity. Graphene is also produced extremely pure, without containing any catalytically active transition metal that would make the analysis harder. The immobilization procedure consists in preparing a 1mM solution of either **1**$^{2-}$ or **2**$^{2-}$ in methanol; then graphene (1-3 layers) in a ratio of 1mg/ml solution was added forming a suspension that was sonicated for 15 minutes and stirred overnight, allowing enough time for the π-π interaction to cover the maximum surface. This new modified material was separated from the solution, washed three times with fresh methanol and finally dispersed again in the same solvent. The electrode was prepared by dropcasting and evaporating 5 consecutive times 5 μL of that suspension on the surface of two kind of glassy carbon electrodes: glassy carbon disks (GCd, 0.07 cm^2) for most of electrochemical measurements and glassy carbon plates (GCp, 1 cm^2) for oxygen measurement and XAS experiments. The electrodes were finally dried under vacuum for 1 h and then were ready for use. They were named GC@G@[(L)Cu]$^{2-}$ and GC@G@[(L$_{py}$)Cu]$^{2-}$ (**G-1**$^{2-}$ and **G-2**$^{2-}$ respectively).

Scheme S2. Schematic representation of the electrode preparation procedure.

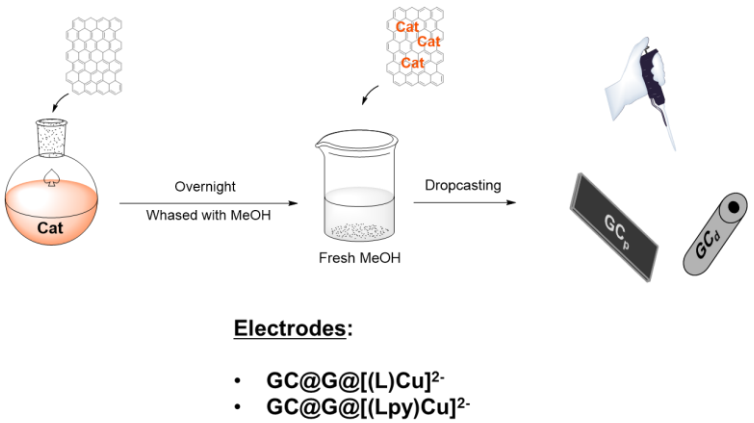

Chapter 5

Spectroscopic characterization

NMR Spectroscopy

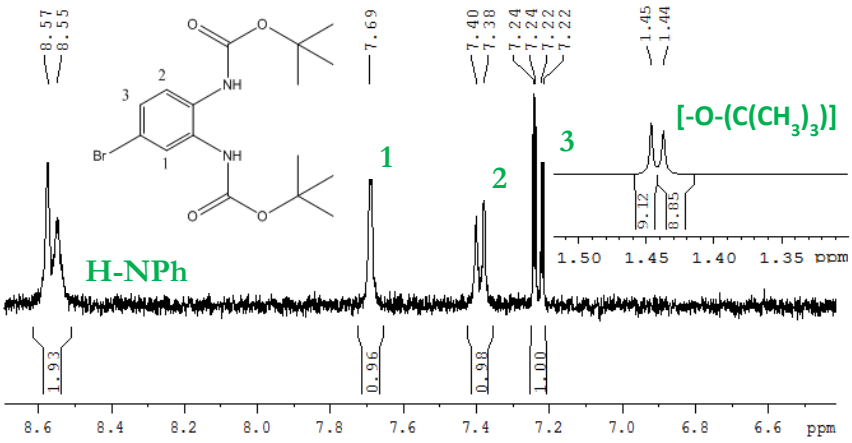

Figure S1. ^{1}H-NMR spectrum of di-tert-butyl (4-bromo-1,2-phenylene)dicarbamate in DMSO-d_6.

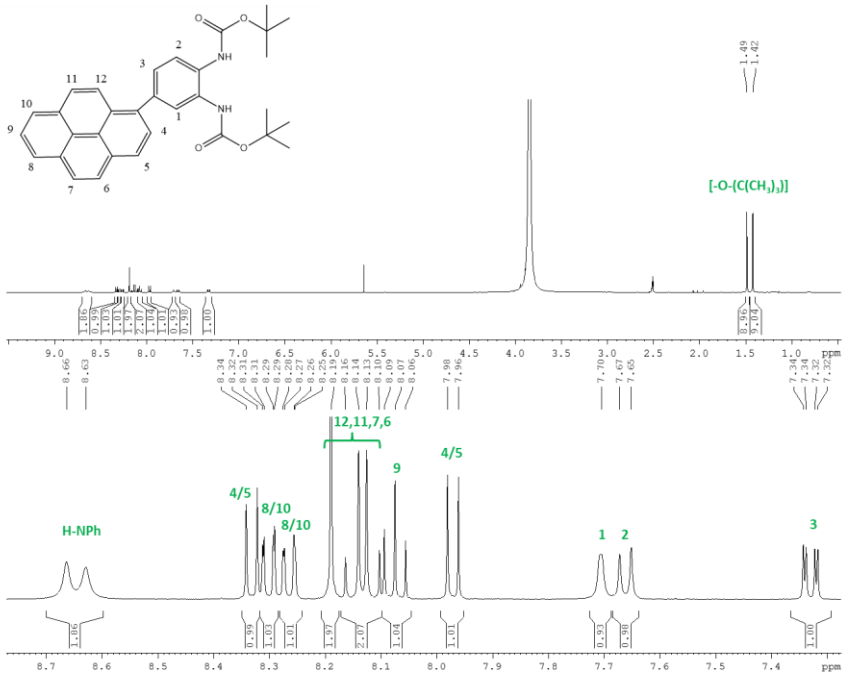

Figure S2. ^{1}H-NMR spectrum of di-tert-butyl (4-(pyren-1-yl)-1,2-phenylene)di-carbamate in DMSO-d_6.

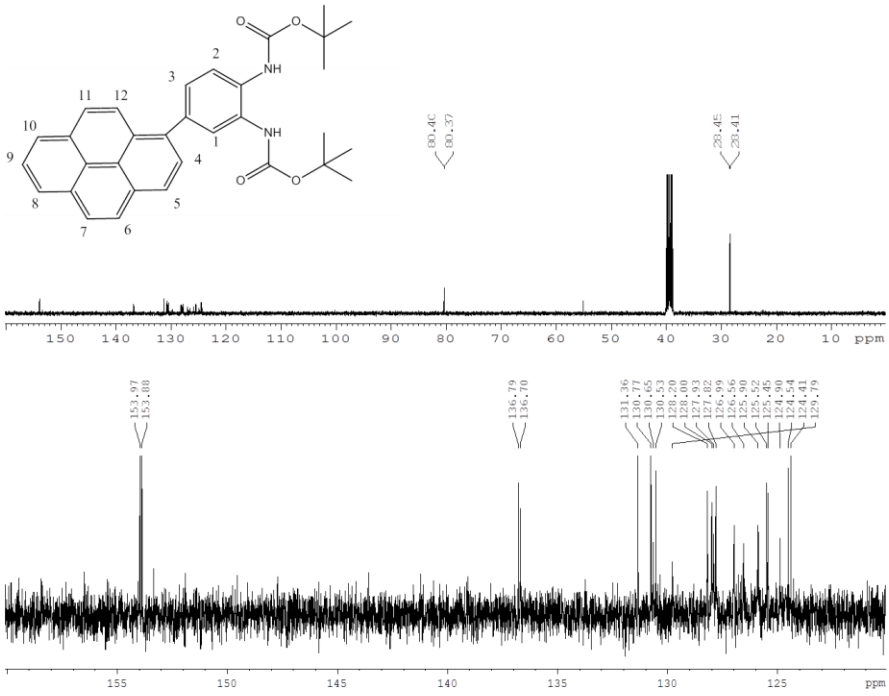

Figure S3. ^{13}C-NMR spectrum of di-tert-butyl (4-(pyren-1-yl)-1,2-phenylene)dicarbamate in DMSO-d_6.

From molecules to solid state: Copper-based molecular anodes

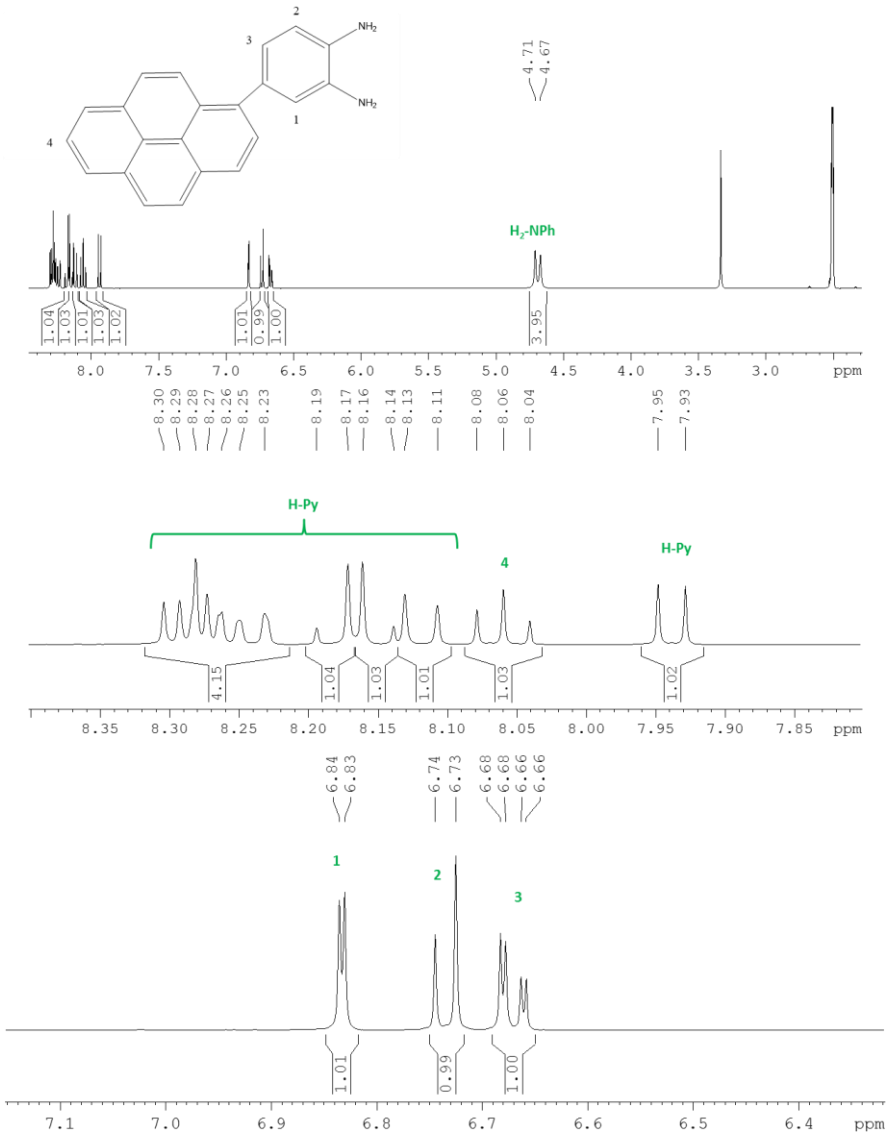

Figure S4. ^{1}H-NMR spectrum of 4-(pyren-1-yl)benzene-1,2-diamine in DMSO-d_6.

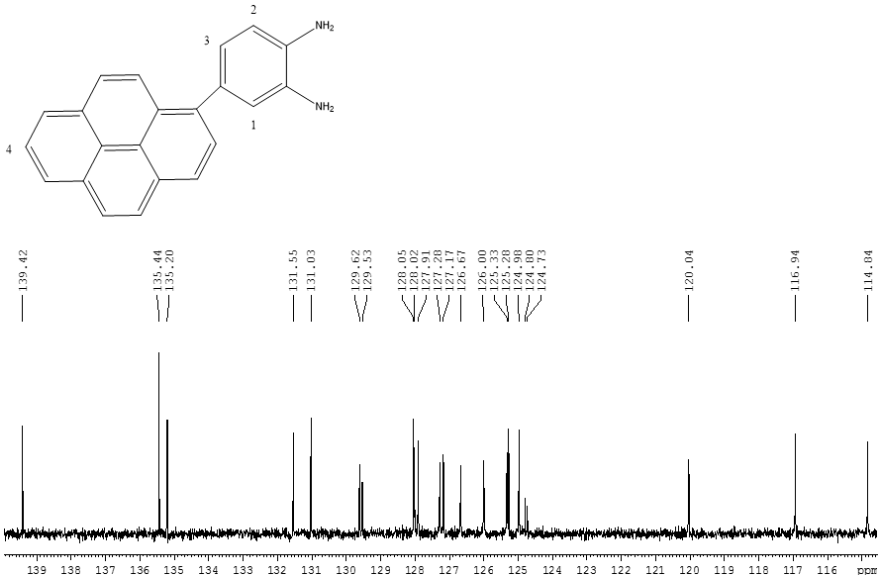

Figure S5. ^{13}C-NMR spectrum of 4-(pyren-1-yl)benzene-1,2-diamine in DMSO-d_6.

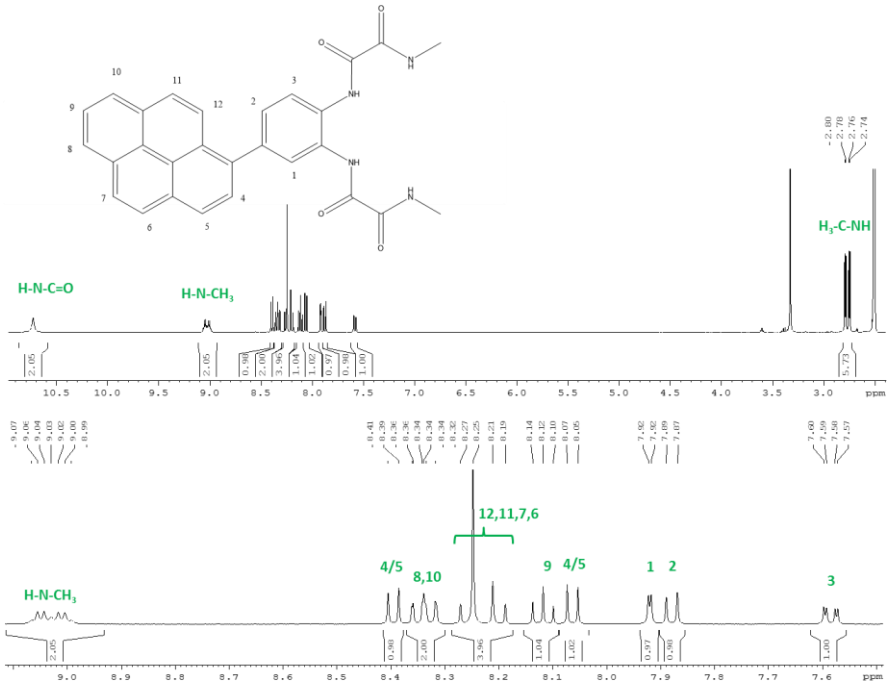

Figure S6. ^{1}H-NMR spectrum of N1,N1'-(4-(pyren-1-yl)-1,2-phenylene)bis(N2-methyloxalamide) (H_4L) in DMSO-d_6.

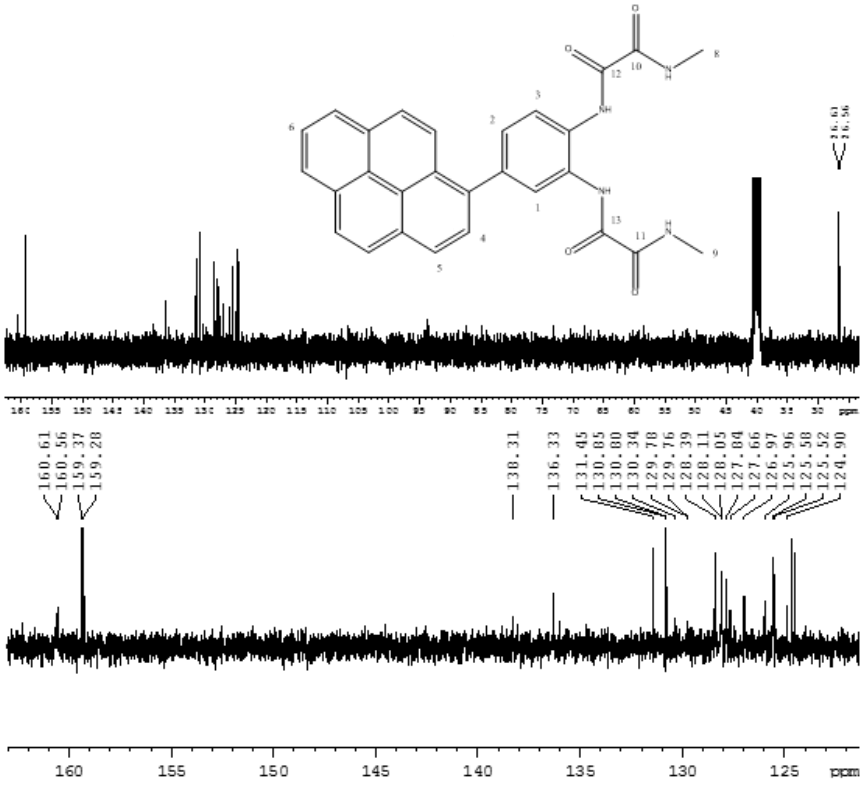

Figure S7. ^{13}C-NMR spectrum of N1,N1'-(4-(pyren-1-yl)-1,2-phenylene)bis(N2-methyloxalamide) (H_4L) in DMSO-d_6.

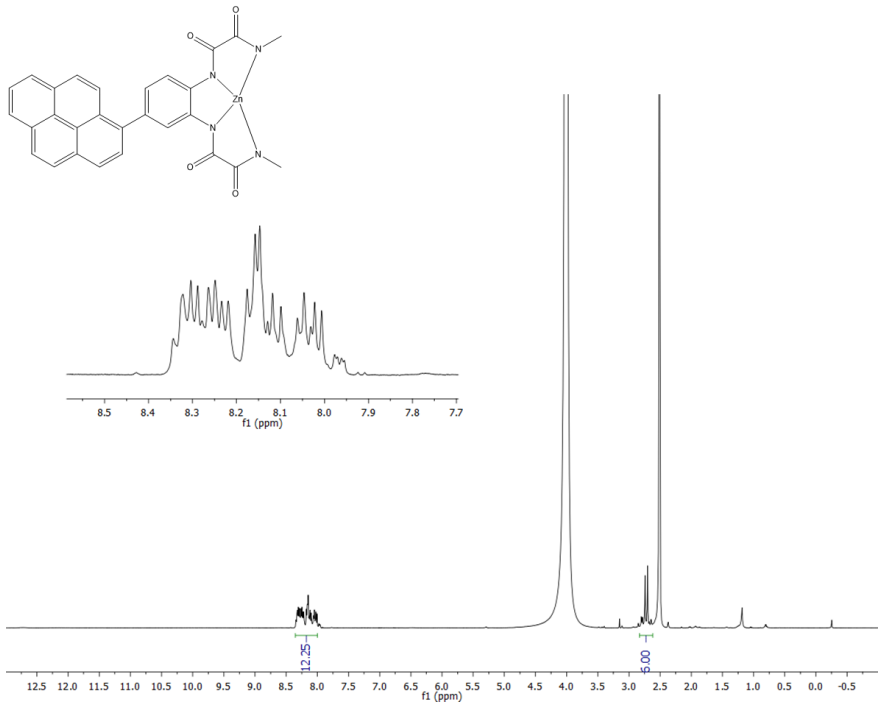

Figure S8. ^{1}H-NMR spectrum of complex $[(Lpy)Zn]^{2-}$ in DMSO-d_6 with 1% v/v of a solution 1M NaOD in D_2O.

IR Spectroscopy

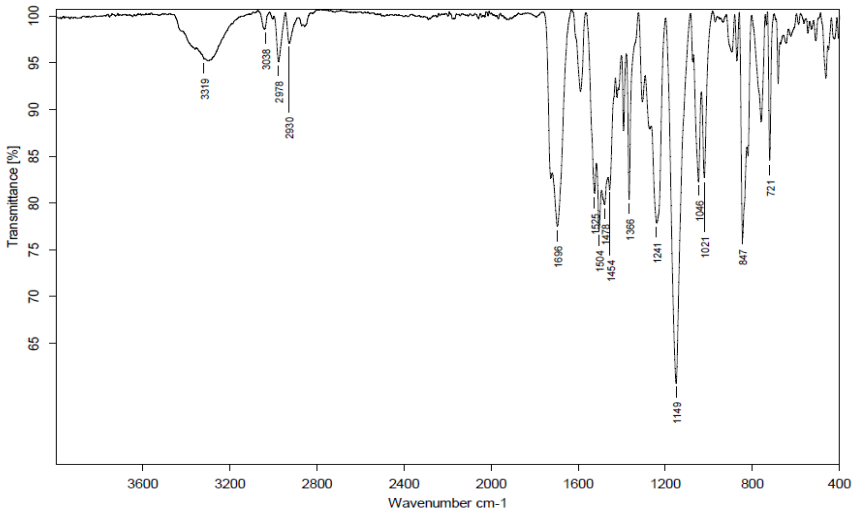

Figure S9. IR spectrum of di-tert-butyl (4-(pyren-1-yl)-1,2-phenylene)dicarbamate.

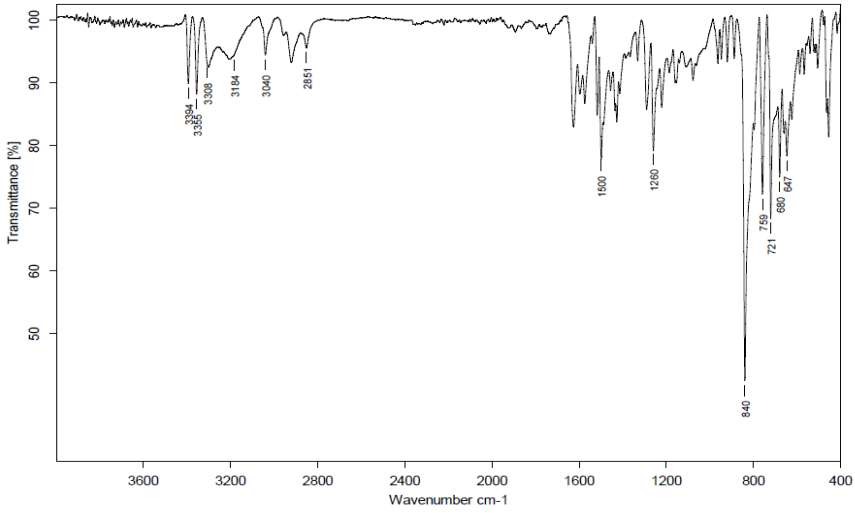

Figure S10. IR spectrum of 4-(pyren-1-yl)benzene-1,2-diamine.

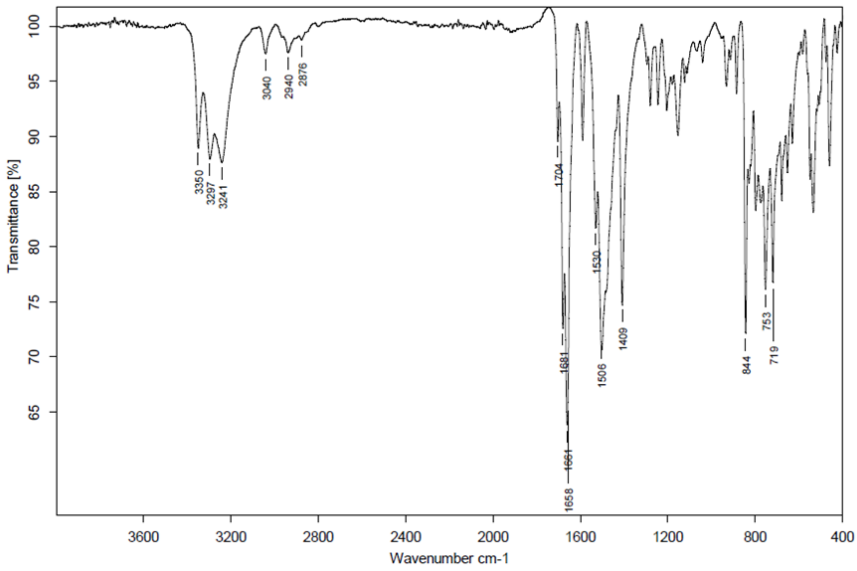

Figure S11. IR spectrum of N1,N1'-(4-(pyren-1-yl)-1,2-phenylene)bis(N2-methyloxalamide) (H_4L).

V

Uv-vis Spectroscopy

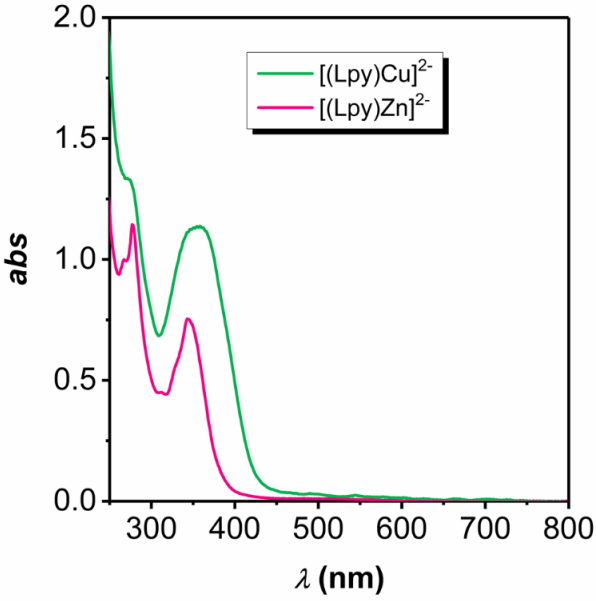

Figure S12. UV-vis spectra for $[(L_{py})Cu]^{2-}$ and $[(L_{py})Zn]^{2-}$ in pH 12 phosphate buffer solution (0.1 M of ionic strenght).

From molecules to solid state: Copper-based molecular anodes

Spectroelectrochemistry

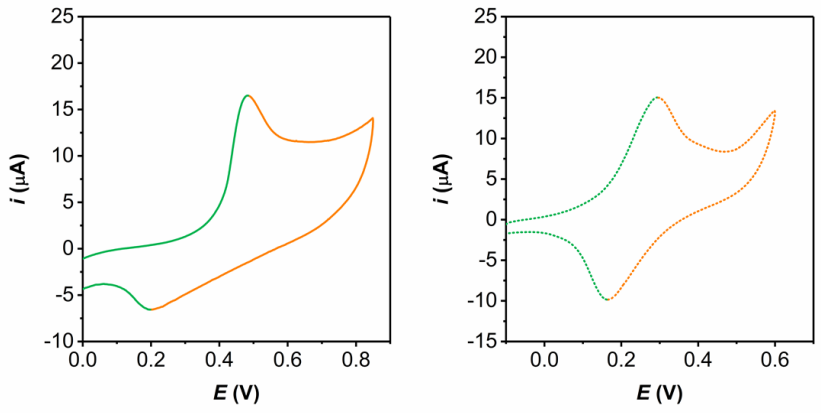

Figure S13. CVs performed in an OTTLE type spectroelectrochemical cell in pH 12 aqueous (left) and acetonitrile (right) solution of $\mathbf{2}^{2-}$ (4mM) at 2 mV/s with Pt mesh working and counter electrode and a silver wire pseudo reference electrode (-0.2 V respect to NHE).

V

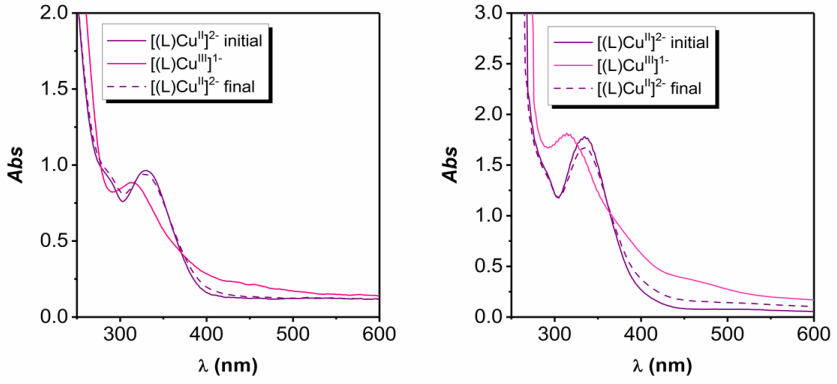

Figure S14. UV-vis spectra for $\mathbf{1}^{2-}$ recorded during spectroelectrochemistry experiment in an OTTLE type spectroelectrochemical cell in pH 12 aqueous (left) and acetonitrile (right) solution containing 4mM of the catalyst.

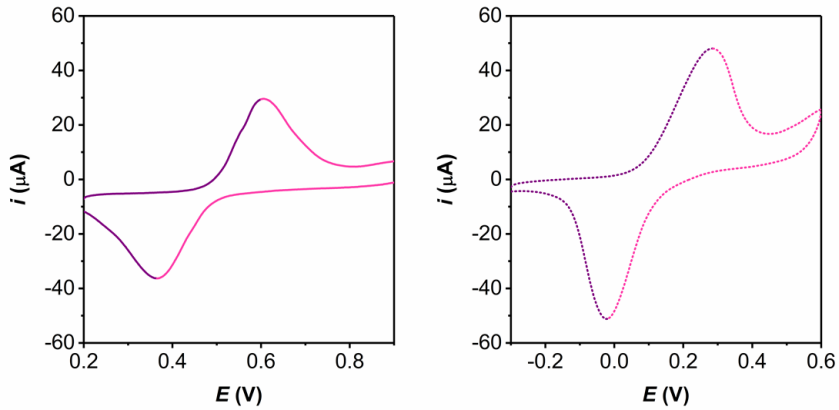

Figure S15. CVs performed in an OTTLE type spectroelectrochemical cell in pH 12 aqueous (left) and acetonitrile (right) solution of $\mathbf{1}^{2-}$ (4mM) at 2 mV/s with Pt mesh working and counter electrode and a silver wire pseudo reference electrode (-0.2 V respect to NHE).

X-Ray Absorption Spectroscopy

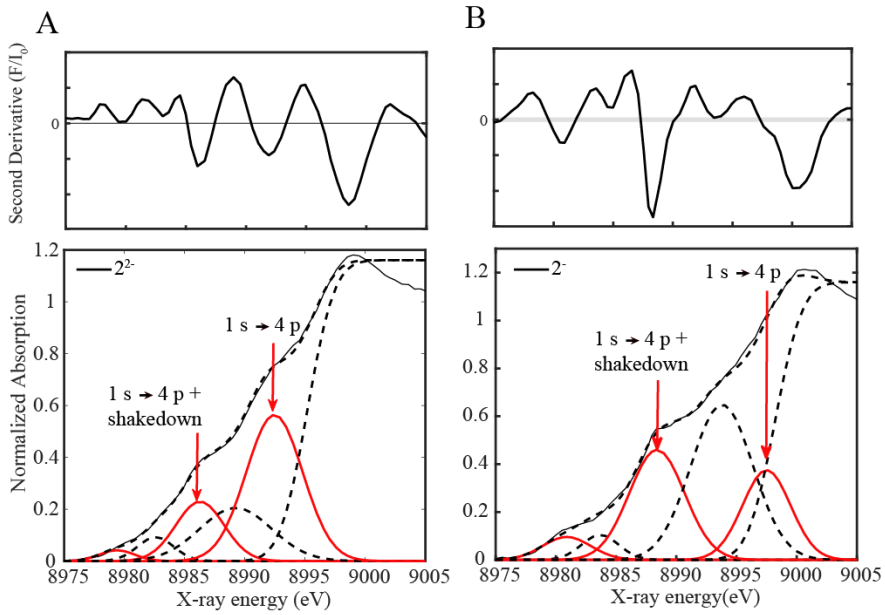

Figure S16. Results of fits to K-edge data for: A. $\mathbf{2}^{2-}$ and B. $\mathbf{2}^{-}$. Data are shown as solid black lines and fits as black dashed lines. Each fit is the sum of the five Gaussian peaks and one error function curve (dashed black line) shown. Peak assignments are as shown on the plots. Second derivatives of the data are plotted over each spectrum. Peak positions are clearly visible in the second derivative spectra. The curve fittings for the edge spectra of $\mathbf{2}^{2-}$ and $\mathbf{2}^{-}$ are shown below.

XANES fitting procedure as shown in Figure S16:

The near edge fit and pre-edge peak fits were carried out with an error function and 5 Gaussian functions respectively. The formulas for the error (erf) and Gaussian functions(gauss) are as follows:

Error function: $$A\left[erf\left(\frac{e-E_0}{w}\right)+1\right] \quad \text{(S3)}$$

Gaussian function: $$\left(\frac{A}{w\sqrt{2\pi}}\right)\exp\left[\frac{-(e-E_0)^2}{(2w^2)}\right] \quad \text{(S4)}$$

Where A corresponds to the amplitude; w, the width; E_0, the centroid of the pre-edge and near edge peaks and e, the x-ray energy. The parameters E_0, A and w used for each sets of functions for the experimental fits are tabulated below (Table S1).

Table S1. Sets of functions with parameters used for the experimental XANES fits of $\mathbf{2}^{2-}$ and $\mathbf{2}^{-}$.

2^{2-} Expt			
Function	**Centroid**	**Amplitude**	**Width**
Gauss (Pre-edge)	8979.40	0.150	1.44
Gauss	8982.60	0.346	1.50
Gauss (shakedown)	8986.29	1.15	2.00
Gauss	8989.26	1.53	2.99
Gauss (main peak)	8992.47	3.32	2.35
Erf	8995.20	0.580	2.52
2^{-} Expt.			
Function	Centroid	Amplitude	Width
Gauss (Pre-edge)	8980.90	0.480	2.00
Gauss	8983.67	0.403	1.55
Gauss (shakedown)	8988.39	2.65	2.30
Gauss	8993.79	4.20	2.58
Gauss (main peak)	8997.49	1.88	2.00
Erf	8998.20	0.580	2.52

From molecules to solid state: Copper-based molecular anodes

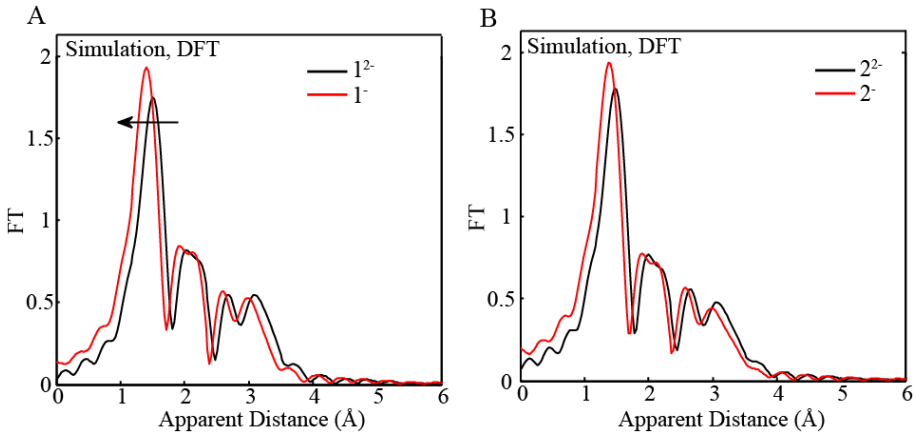

Figure S17. Simulated Fourier transforms using DFT optimized coordinates as input of k^2-weighted Cu EXAFS of: A. $\mathbf{1}^{2-}$ (black) and $\mathbf{1}^{-}$ (red) in acetonitrile, B. $\mathbf{2}^{2-}$ (black) and $\mathbf{2}^{-}$ (red) in acetonitrile.

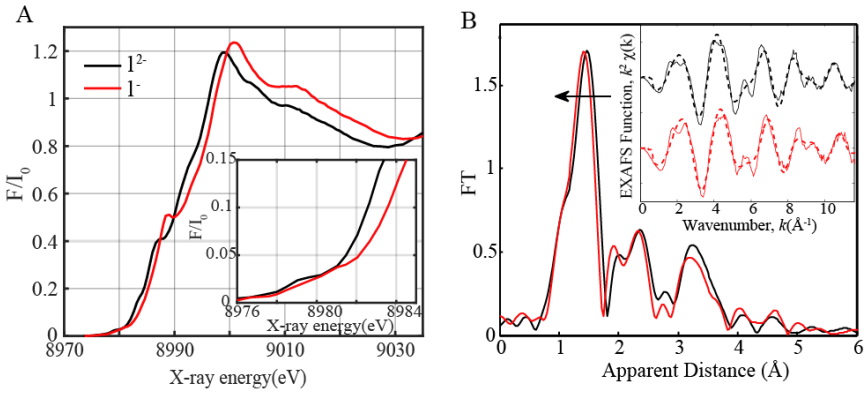

Figure S18. A, Normalized Cu K-edge XANES of $\mathbf{1}^{2-}$ (black) and $\mathbf{1}^{-}$ (red) in MeCN. Inset: Zoom-in of the pre-edge regions. B, Experimental Fourier transforms of k^2-weighted Cu EXAFS of $\mathbf{2}^{2-}$ (black) and $\mathbf{2}^{-}$ (red) in MeCN.

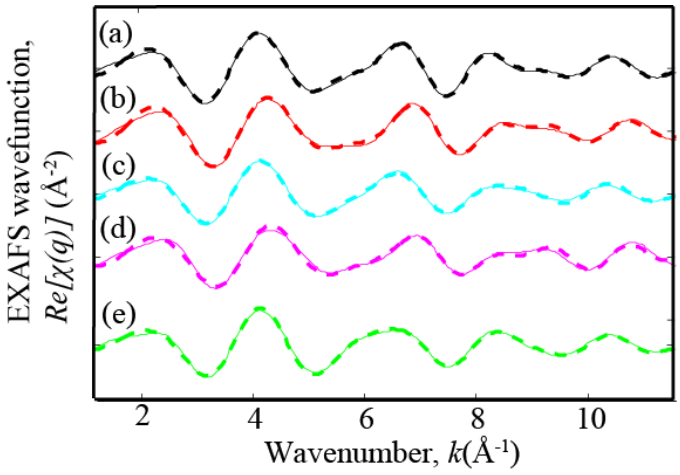

Figure S19. Back Fourier transformed experimental (solid lines) and fitted (dashed lines) Re[χ(q)](Å^{-2}) for **1**$^{2-}$ (a), **1**$^{-}$ (b), **2**$^{2-}$ (c), **2**$^{-}$ (d), **G-2**$^{2-}$ (e).

Table S2. EXAFS summary of fits.

Sample	Fit	Peak	Shell,N	R, Å	E^0	ss.^{2} (10-3)	R-factor	Reduced Chi-square
1^{2-} in CH_3CN	1	I	Cu-N,4	1.94	0.87	2.8	0.0026	104
	2	I,II	Cu-N,4 Cu-C,5 Cu-C,12	1.94 2.75 3.01	0.83	3.0 2.4 3.7	0.0046	87
1^{-} in CH_3CN	3	I	Cu-N,4	1.88	1.1	3.7	0.0015	35
	4	I,II	Cu-N,4 Cu-C,6 Cu-C,12	1.88 2.69 2.94	0.75	4.0 6.1 3.5	0.0055	60

2^{2-} in CH_3CN	5	I	Cu-N,4	1.94	0.24	3.9	0.0027	26
	6	I,II	Cu-N,4 Cu-C,5 Cu-C,12	1.93 2.74 3.02	-0.33	4.0 12.1 1.7	0.0031	14
2^{-} in CH_3CN	7	I	Cu-N,4	1.87	0.33	5.2	0.0079	43
	8	I,II	Cu-N,4 Cu-C,6 Cu-C,12	1.86 2.66 2.92	-0.73	5.5 11.5 5.8	0.0097	24
G-2^{2-}	9	I	Cu-N,4	1.96	0.10	3.2	0.0043	52
	10	I,II	Cu-N,4 Cu-C,6 Cu-C,12	1.95 2.67 2.98	-1.9	3.5 10.5 0.1	0.0038	21
G-2^{2-} after controlled potential electrolysis (CPE)	11	I	Cu-N,4	1.95	-0.5	3.5	0.0034	30
	12	I,II	Cu-N,4 Cu-C,6 Cu-C,12	1.94 2.65 3.00	-3.0	3.6 13.0 1.5	0.0041	17

Table S3. Metric parameters obtained for complexes $\mathbf{1}^{2-}$, $\mathbf{1}^{-}$ in MeCN, $\mathbf{2}^{-}$, $\mathbf{2}^{2-}$ in MeCN, **G-2**$^{2-}$, **G-2**$^{2-}$ after CPE.

Species, Fit number in Table S2	**EXAFS Shell: N x distance in Å**	**DFT optimized coordinates for the Cu-N atoms within the 1st coordination shell, (Å)**
$\mathbf{1}^{2-}$ in CH_3CN, **fit 2**	Cu-N: 4 x 1.94 Cu-C: 5 x 2.75 Cu-C: 12 x 3.01	Cu-N: 1.98, 1.98, 2.01, 2.01
$\mathbf{1}^{-}$ in CH_3CN, **fit 4**	Cu-N: 4 x 1.88 Cu-C: 6 x 2.69 Cu-C: 12 x 2.94	Cu-N: 1.87, 1.88, 1.91, 1.91
$\mathbf{2}^{2-}$ in CH_3CN, **fit 6**	Cu-N: 4 x 1.93 Cu-C: 5 x 2.74 Cu-C: 12 x 3.02	Cu-N: 1.96, 1.96, 1.98, 1.98
$\mathbf{2}^{-}$ in CH_3CN, **fit 8**	Cu-N: 4 x 1.86 Cu-C: 6 x 2.66 Cu-C: 12 x 2.92	Cu-N: 1.86, 1.86, 1.90, 1.90
G-2^{2-}, **fit 10**	Cu-N: 4 x 1.95 Cu-C: 6 x 2.67 Cu-C: 12 x 2.98	Cu-N: 1.96, 1.96, 1.97, 1.98
G-2 $^{2-}$ after CPE, **fit 12**	Cu-N: 4 x 1.94 Cu-C: 6 x 2.65 Cu-C: 12 x 3.00	

Electrochemistry

Homogeneous phase

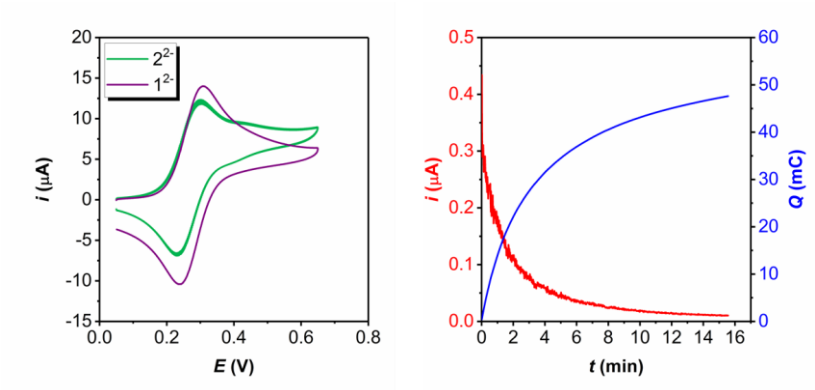

Figure S20. (Left) CVs of an acetonitrile solution containing 1 mM of $\mathbf{1}^{2-}$ (purple) and $\mathbf{2}^{2-}$ (green) with 0.1 M of tetrabutylammonium hexafluorophosphate. GC working electrode was employed and the scan rate was set to 100 mV/s. (Right) Controlled Potential Electrolysis (CPE) at 0.55 V in 1mM $\mathbf{2}^{2-}$ acetonitrile solution containing 0.1 M of tetrabutylammonium hexafluorophosphate. Large surface Pt mesh was used as both working and counter electrode. A two-compartment cell was employed with one compartment containing the complex solution and the other a blank solution. Total charged passed and the end of the bulk corresponds to a 1 e^- oxidation process.

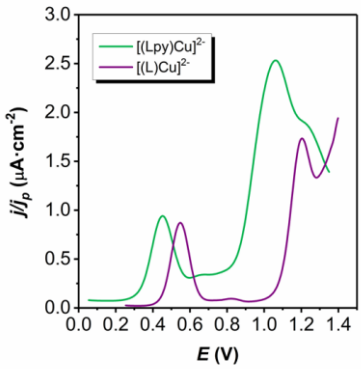

Figure S21. DPVs of 1mM $\mathbf{1}^{2-}$ (purple) and $\mathbf{2}^{2-}$ (green) in phosphate buffer at pH 12 (0.1 M of ionic strength), using GC working electrode and 100 mV/s of scan rate.

Homologue systems in homogeneous phase

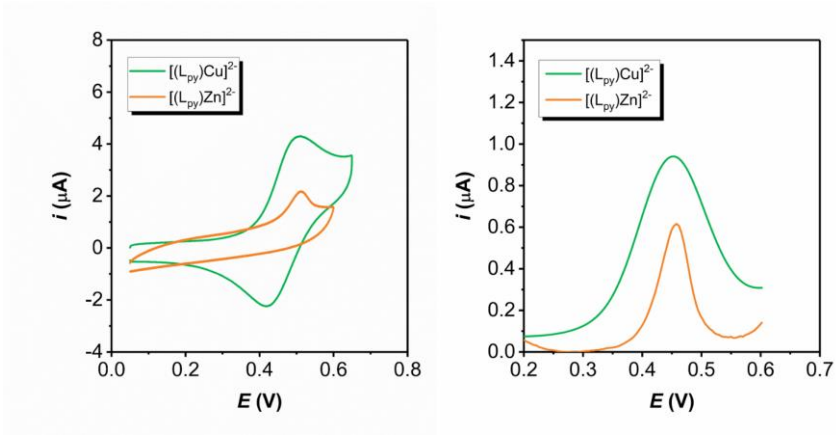

Figure S22. (Left) Background corrected CVs at 100 mV·s^{-1} and (Right) DPVs of [(L$_{py}$)Cu]$^{2-}$ (1mM) and its homologue [(L$_{py}$)Zn]$^{2-}$ (0.5mM) in phosphate buffer at pH 12 with 0.1 M of ionic strength.

The coincidence of the redox potentials at 0.45 V for the Cu and Zn complexes indicates that it is a ligand based transformation since Zn is redox inactive transition metal.

Heterogeneous phase

Normalization procedure:

We found that for similarly prepared electrodes, the charging current (i_c) of the double-layer was different when doing CVs under the same conditions (Figure S23, left). This means that the nonfaradaic processes were different and therefore, they affect in a different way to the intensity of the faradaic processes. The i_c depends on the scan rate and the capacitance of the double-layer according to equation S5. The capacitance of the double-layer in turns depends on the specific capacitance of the material, C_s, and the electroactive surface area, ECSA, as shown in equation S6. Since the scan rate was equal for all the CVs performed it can be considered constant, likewise the specific capacitance because we are using same materials for all the electrodes. Then, the different ECSA of the electrodes is the only responsible for the different charging current observed. This is mainly due to the relative hydrophobicity of the graphene material, since some little air bubbles remained in the electrode-solution interphase and lead to different ECSA, *i.e.* different current densities for homologue electrodes.

$$i_c = \nu \cdot C_{DL} \tag{S5}$$

$$C_{DL} = ECSA \cdot C_s \tag{S6}$$

$$i_c \propto ECSA \tag{S7}$$

Due to the difficulties to control the ECSA as aforementioned, all the CVs were normalized in order to counter the differences in the resulting charging intensity. For electrodes with equal ECSA, the i_c should be similar according to equation S7. Then dividing the intensity from the CV of each electrode by the value of its charging intensity i_c, we can obtain CVs with equivalent i_c and thus equivalent ECSA, removing the influence of

the nonfaradaic processes. The value of the i_c was obtained from a non-faradaic region of the CV, such as the intensity at 0.3 V, far enough from the faradaic processes. This normalization procedure finally allows us to compare fairly the CVs of different electrodes (Figure S23).

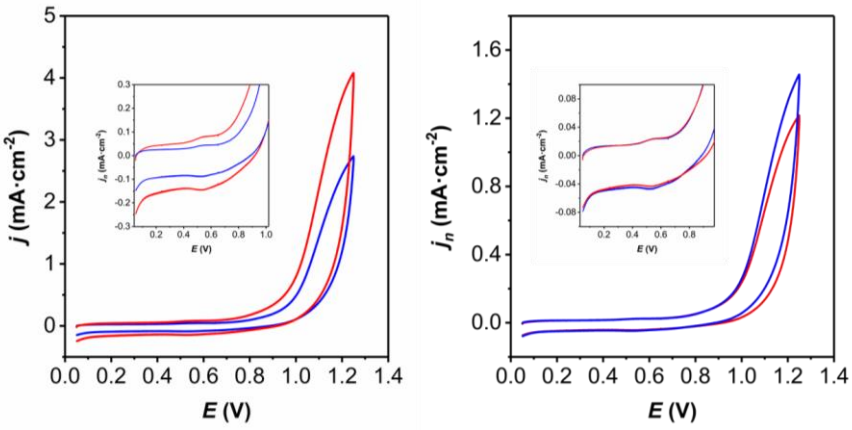

Figure S23. (Left) CVs and (Right) normalized CVs at 50mV·s^{-1} of two different **G-2**$^{2-}$ in phosphate buffer at pH 12 with 0.1 M of ionic strength. In the non-normalized CVs, the charging current and thus the catalytic current are very different when comparing both electrodes. After normalization, both electrodes present equal charging current and thus very close catalytic activity.

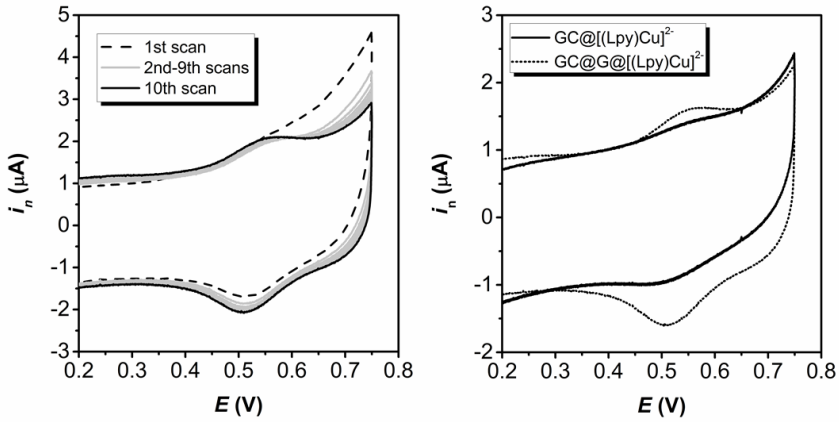

Figure S24. (Left) Consecutive CVs of **G-2**$^{2-}$ hybrid electrodes in phosphate buffer at pH 12 (0.1 M of ionic strength), at 50 mV·s^{-1} of scan rate. In the 10th scan, a stable peak current is obtained. (Right) CVs of **2**$^{2-}$ anchored on bare GC disk electrode (solid line) and on graphene over GC disk electrode (dotted line) in phosphate buffer at pH12 at 50 mV·s^{1}.

V

After repeated CVs (10th scans), the anodic and cathodic intensities increase up to a stationary value, indicating that more active material is being exposed (Figure S24, left). The reason could come from some reorganization promoted by the hydrophobic character of the graphene. Therefore, before every electrochemical measurement, the electrodes were subjected to 10 previous scans.

Bare glassy carbon electrodes were also used (Figure S24, right) as supporting material by soaking them overnight into a 1mM catalyst solution in methanol followed by washing with fresh methanol. The so-prepared electrodes showed much less catalyst concentration in comparison with the graphene modified electrodes due to its lower surface and thus were discarded for further analysis.

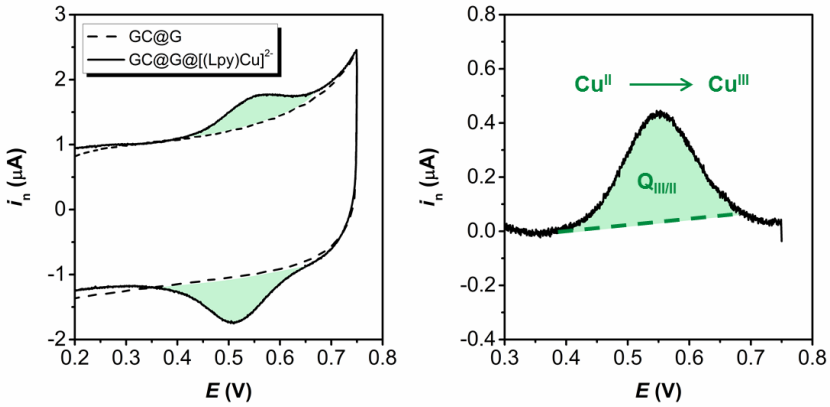

Figure S25. (Left) CVs of **G-2**$^{2-}$ hybrid electrodes (solid line) and unmodified graphene (dashed line) in phosphate buffer at pH 12 (0.1 M of ionic strength), at 50 mV/s of scan rate. The green regions represent the charge passed due to the oxidation and reduction of the complex on the electrode. (Right) Background corrected LSV of the hybrid electrode **G-2**$^{2-}$ in the same conditions as before.

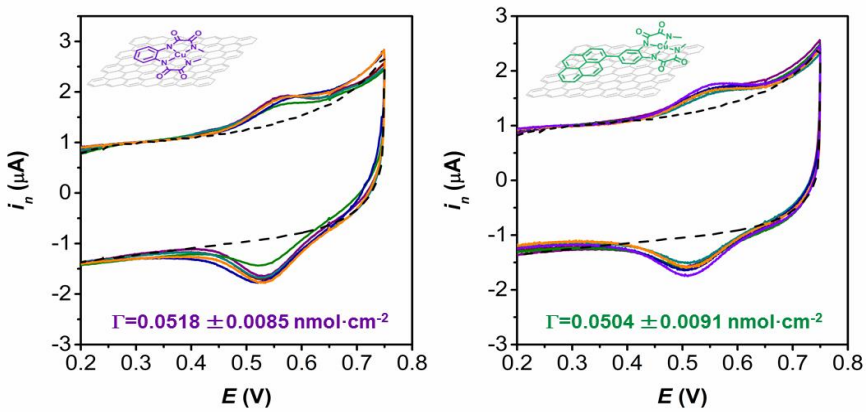

Figure S26. CVs of **G-1**$^{2-}$ (left) and **G-2**$^{2-}$ (right) hybrid electrodes (solid lines) and unmodified graphene (dashed line) in phosphate buffer at pH 12 (0.1 M of ionic strength), at 50 mV/s of scan rate. The surface coverage, Γ, was calculated from the charge integrated under the background corrected oxidation peak, averaged over five replicates.

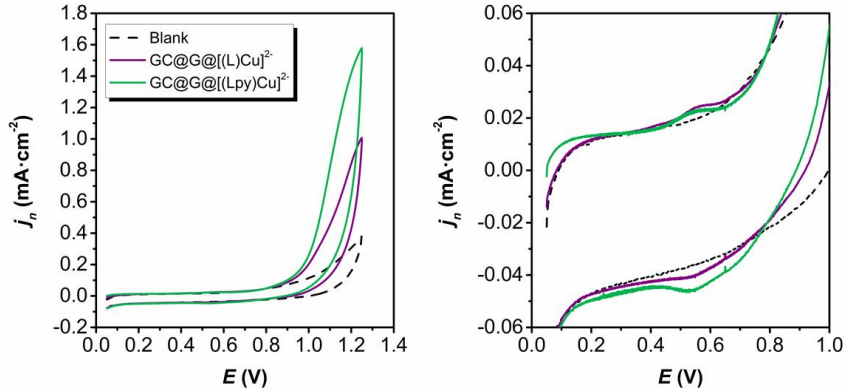

Figure S27. (Left) CV at 50mV·s^{-1} of **G-1**$^{2-}$, **G-2**$^{2-}$ and bare graphene over GC in phosphate buffer at pH 12 with 0.1 M of ionic strength. The coverage was calculated to be 0.043 and 0.044 nmol·cm^{-2} for. **G-1**$^{2-}$ and **G-2**$^{2-}$ respectively. (Right) Zoom of the reversible wave region from the previous CVs.

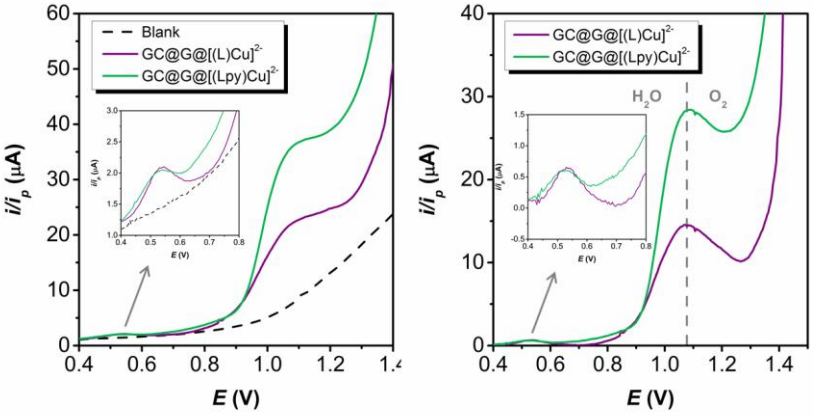

Figure S28. DPVs (left) and background subtracted DPVs (right) of **G-1**$^{2-}$, **G-2**$^{2-}$ and bare graphene over GC in phosphate buffer at pH 12 with 0.1 M of ionic strength. The coverage was calculated to be 0.043 and 0.044 nmol·cm^{-2} for. **G-1**$^{2-}$ and **G-2**$^{2-}$ respectively. The insets show a zoom of the one-electron wave region.

Kinetic analysis by FOWA

Foot of the wave analysis (FOWA) was applied according to the procedures described in the literature.[6,10,11,12] For homogeneous water oxidation catalysis, the following expression is deducted for a mechanism where just one catalyst molecule is involved and assuming that the rds is the last electron-transfer step coupled to a chemical reaction:

$$\frac{i}{i_d} = \frac{n \cdot 2.24 \cdot \sqrt{\frac{R \cdot T}{F \cdot V} \cdot k_{obs}}}{1 + \exp\left[\frac{F}{R \cdot T}(E^0_{cat} - E)\right]} \qquad \text{(S8)}$$

In the case of heterogeneous water oxidation with equivalent mechanism, the equation changes:

$$\frac{i}{q_d} = \frac{k_{obs}}{1 + \exp\left[\frac{F}{R \cdot T}(E^0_{cat} - E)\right]} \qquad \text{(S9)}$$

where E^0_{cat} is the standard potential for the catalysis-initiating redox couple (calculated from DPV), i is the current intensity, i_d is the current intensity associated with the Cu^{III}/Cu^{II} couple, q_d is the charge under the oxidative peak of the reversible wave Cu^{III}/Cu^{II}, n is the number of electrons involved in the catalytic cycle (4 e^- in water oxidation), F is the faraday constant, v is the scan rate, k_{obs} is defined as "$k_{cat} \cdot C^o_A$" where C^o_A is the concentration of substrate (55.56 M for water), and R is 8.314 $J \cdot mol^{-1}K^{-1}$. Background corrected LSVs of the catalysts are shown in Figure S29-S32. Now, k_{obs} can be extracted from the plot of i_{cat}/i_d *vs.* $1/(1+\exp[(F/RT)(E^o_{cat}-E)])$.

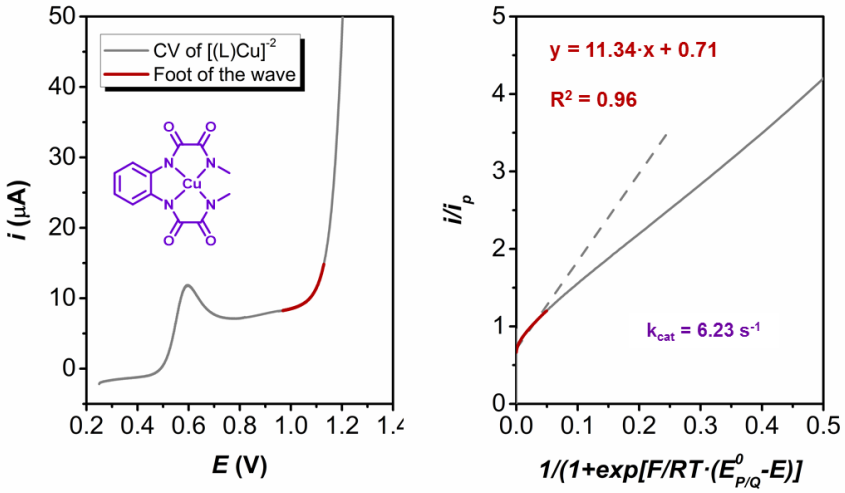

Figure S29. Background corrected LSV of 1mM $\mathbf{1}^{2-}$ in phosphate buffer at pH 12 (0.1 M of ionic strength), using GC working electrode and 100 mV/s of scan rate. Foot of the wave region is highlighted in red color. (Right) Foot of the wave analysis (FOWA) by plotting i_{cat}/i_d *vs.* $1/(1+\exp[(F/RT)(E^o_{cat}-E)])$.

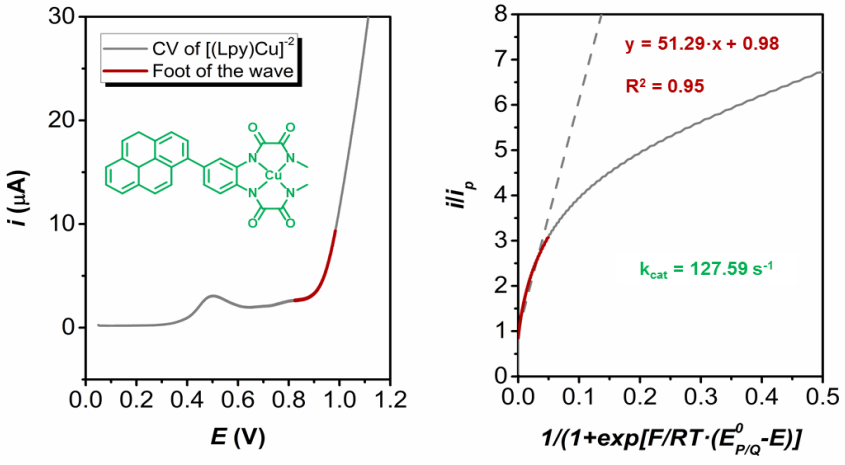

Figure S30. Background corrected LSV of 1mM $\mathbf{2}^{2-}$ in phosphate buffer at pH 12 (0.1 M of ionic strength), using GC working electrode and 100 mV/s of scan rate. Foot of the wave region is highlighted in red color. (Right) Foot of the wave analysis (FOWA) by plotting i_{cat}/i_d *vs.* $1/(1+\exp[(F/RT)(E^o_{cat}-E)])$.

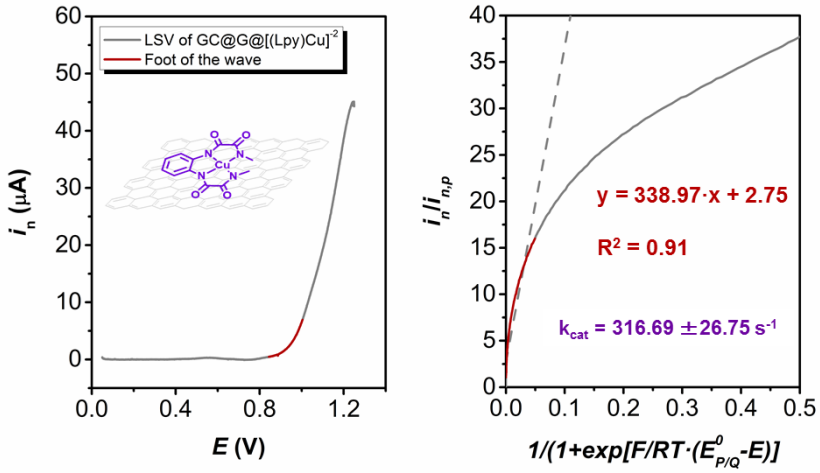

Figure S31. Background corrected LSV of a hybrid electrode **G-1**$^{2-}$ in phosphate buffer at pH 12 (0.1 M of ionic strength), at 50 mV/s of scan rate. Foot of the wave region is highlighted in red color. (Right) Foot of the wave analysis (FOWA) by plotting i_{cat}/i_d *vs.* $1/(1+\exp[(F/RT)(E^o_{cat}-E)])$. The kinetic constant, k_{cat}, was obtained as the average from analysis to 5 different electrodes.

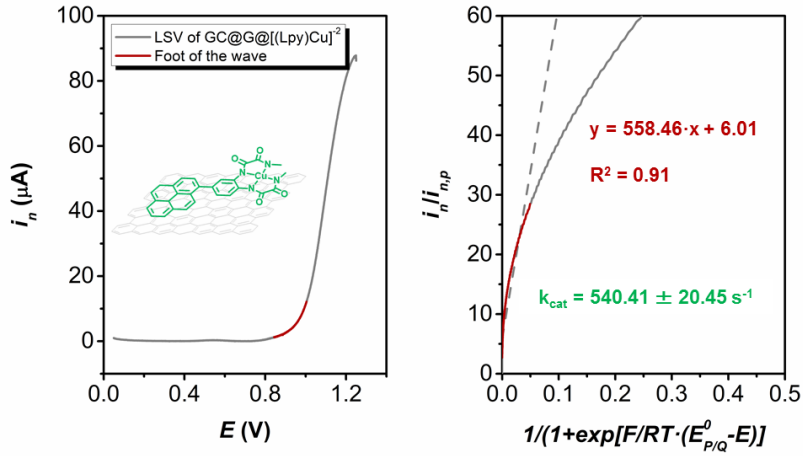

Figure S32. Background corrected LSV of a hybrid electrode **G-2**$^{2-}$ in phosphate buffer at pH 12 (0.1 M of ionic strength), at 50 mV/s of scan rate. Foot of the wave region is highlighted in red color. (Right) Foot of the wave analysis (FOWA) by plotting i_{cat}/i_d *vs.* $1/(1+\exp[(F/RT)(E^o_{cat}-E)])$. The kinetic constant, k_{cat}, was obtained as the average from analysis to 5 different electrodes.

From molecules to solid state: Copper-based molecular anodes

Bulk electrolysis, O2 evolution and stability

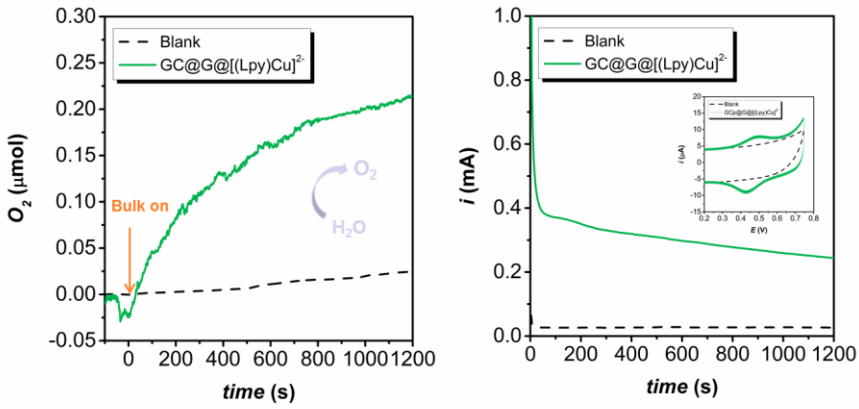

Figure S33. (Left) Oxygen evolution detected by Clark electrode during a CPE experiment using a **G-2**$^{2-}$ hybrid electrode (green solid line) and a bare graphene GC electrode (dashed black line). A GC plate was used in this case as supporting electrode to increase the total amount of catalyst. (Right) CPE at 1.25 V performed during the oxygen evolution experiment in a pH 12 solution using the same electrodes, with a Pt mesh counter electrode and an Ag/AgCl reference electrode.

*The inset show a CV of both electrodes in the reversible wave region, and the charge under the oxidative peak was used to determine the catalyst loading that turned out to be 0.0394 nmol·cm^{-2}. The resulting TON from the measured O_2 was 5388.

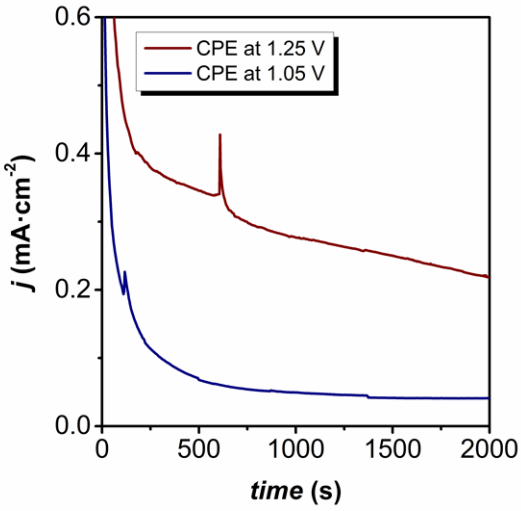

Figure S34. CPE at 1.25 V (red) and 1.05 V (blue) performed with different **G-2**$^{2-}$ hybrid electrodes in a pH 12 solution, with a Pt mesh counter electrode and a MSE reference electrode. GC disk (3mm) supporting electrode was used for the hybrid electrode. At higher potentials, degradation of the electrode appears to be faster although higher intensities are reached.

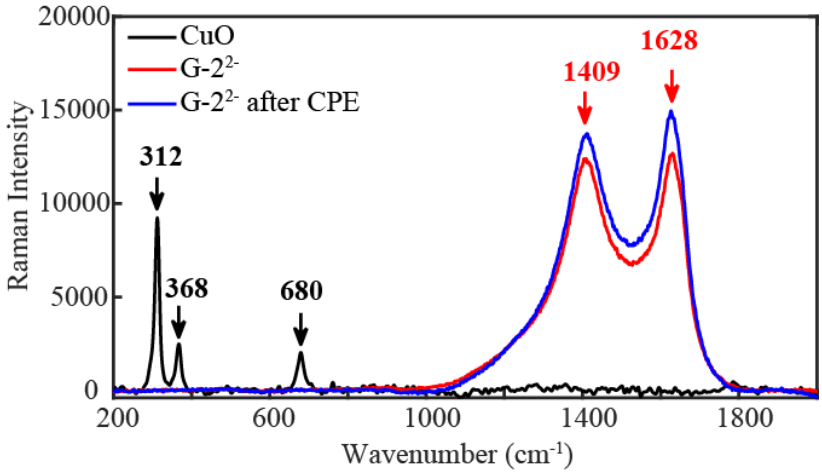

Figure S35. Resonance Raman with excitation at 532 nm of CuO solid, **G-2**$^{2-}$ and **G-2**$^{2-}$ after CPE recorded at room temperature.

V

Raman measurements of CuO, hybrid materials **G-2**$^{2-}$ and **G-2**$^{2-}$ after controlled potential electrolysis (at 1.25 V) were carried out and are shown in Figure S35. As shown from Raman measurements, the characteristic Raman features of CuO at 312 cm^{-1}, 368 cm^{-1} and 680 cm^{-1} were absent in the hybrid materials confirming lack of any traces of CuO. Only the Raman peaks at 1409 cm^{-1} and 1628 cm^{-1} corresponding to that of graphene were observed in **G-2**$^{2-}$ and **G-2**$^{2-}$ after CPE.[13]

RRDE for O_2 and H_2O_2 generation assessment

The collection efficiency of the RRDE, N, was previously determined by using the redox couple $Fe(CN)_6^{4-}$ / $Fe(CN)_6^{3-}$ as well defined one-electron transfer process. We prepared a 1 mM solution of the reduced ferrocyanide $K_4Fe(CN)_6$ in pH 12 solution of phosphate buffer, and it was oxidized during a LSV at 10 $mV \cdot s^{-1}$ in the disk electrode to ferricyanide $Fe(CN)_6^{3-}$. This last was detected at the Pt ring by performing a CPE at 0.05 V vs NHE to yield the reduction to the initial ferrocyanide. The collection efficiency was determined by the rate between the intensity in the ring and the intensity in the disk electrodes when they reach stable values at the plateau, i_{ring}/i_{disk}. The efficiency was found to be 0.4. Results are shown in Figure S36 for 1600 rpm.

The oxygen reduction reaction was also studied at the Pt ring electrode under same experimental conditions to analyze the number of electrons involved, according to procedure described in the literature.[14] For that, three different solutions were prepared at pH 12 with phosphate buffer: N_2 saturated, air saturated and O_2 saturated. Then a LSV at 10 $mV \cdot s^{-1}$ was performed through negative potentials to reduce the dissolved oxygen, that was detected by an increase in the ring current. In N_2, no current was detected as expected, while in air and O_2 current increased when the potential was negative enough to reduce the oxygen. In those last cases, the current reached an approximately stable signal at -0.6 V vs NHE. With these stable current values, the apparent number of electrons (n_{app}) involved in the reduction of oxygen can be calculated from the Levich equation for the rotating ring:

$$\left|i_{ring}\right| = 0.62 \cdot n_{app} \cdot F \cdot \pi \cdot (r_o^3 - r_m^3)^{2/3} \cdot D^{2/3} \cdot \omega^{1/2} \cdot \nu^{-1/6} \cdot [O_2] \quad \text{(S10)}$$

F is the Faraday constant, r_o and r_m are the outer and middle radio that define the Pt geometry, D is the Difussion coefficient for oxygen in water

calculated to be $2.52 \cdot 10^{-5}$ $cm^2 \cdot s^{-1}$ with Wilke's correlation,[15] ω is the rotation rate in $rad \cdot s^{-1}$, ν is the kinematic viscosity of the solution that is $0.0085 cm^2 \cdot s^{-1}$ and $[O_2]$ is the concentration of oxygen in the solution calculated to be $1.28 \cdot 10^{-6}$ $mol \cdot cm^{-3}$ for O_2 saturated solution and $2.67 \cdot 10^{-7}$ $mol \cdot cm^{-3}$ for air saturated solution.[16] With all these values, the apparent number of electrons involved in the oxygen reduction turned out to be *ca.* 2 at 1600 rpm for both air and oxygen saturated solutions, which means reduction of O_2 to H_2O_2 in pH 12 at -0.6 V vs NHE. Those results are shown in Figure S36.

Collection efficiency and n_{app} calculation for O_2 evolution

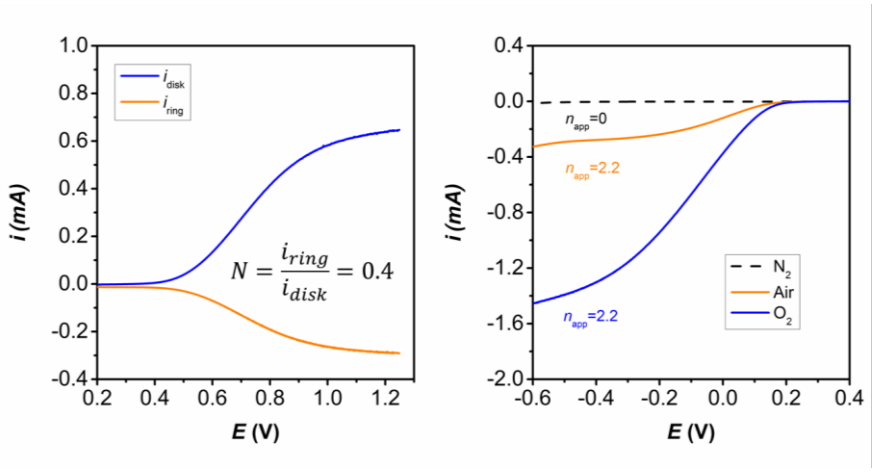

Figure S36. (Left) RRDE experiment using 1 mM of ferrocyanide $K_4Fe(CN)_6$ in pH 12 solution of phosphate buffer (0.1 M ionic strength). In the disk electrode, a LSV was performed at 10 $mV \cdot s^{-1}$ (blue) to oxidize to ferricyanide $Fe(CN)_6^{3-}$. In the ring electrode, a CPE was performed at 0.05 V to yield the reduction to the initial ferrocyanide $Fe(CN)_6^{4-}$ (orange line). The rotation speed was 1600 rpm. (Right) LSVs performed at 10 $mV \cdot s^{-1}$ with the Pt ring electrode in three different pH 12 solutions with phosphate buffer: N_2 saturated (black dashed line), air saturated (orange solid line) and O_2 saturated (blue solid line).

*Catalytic O_2 evolution by hybrid catalysts **G-1**$^{2-}$ and **G-2**$^{2-}$*

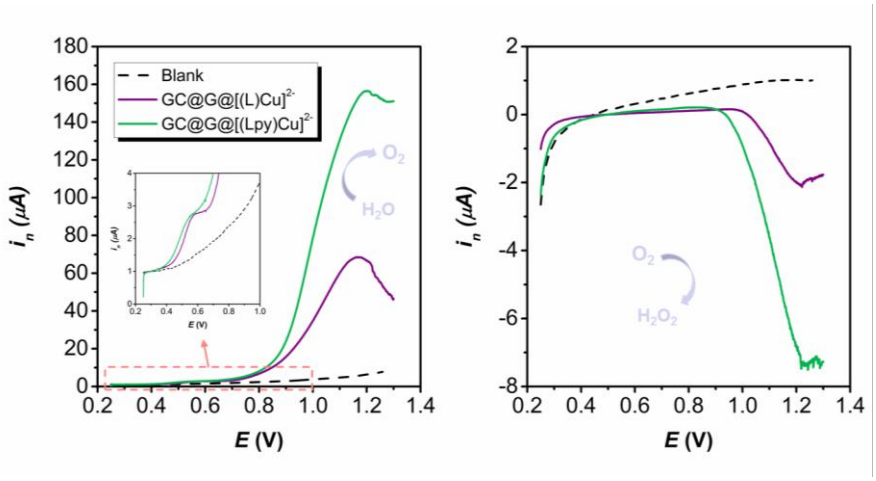

Figure S37. (Left) LSV of bare graphene (blank), **G-1**$^{2-}$ and **G-2**$^{2-}$ electrodes using RRDE in phosphate buffer at pH 12 (0.1 M of ionic strength) under nitrogen atmosphere and at 1600 rpm. (Right) Simultaneous oxygen reduction at Pt ring of the RRDE by CPE at -0.35 V.

In order to further characterize the catalytic activity toward water oxidation, a Rotating Ring Disk Electrode (RRDE) was used in a similar way as described by Jaramillo et al. for heterogeneous catalysts.[14] The graphene loaded with the catalyst was deposited on the surface of the glassy carbon disk electrode, which was used as the working electrode to perform the water oxidation. To evaluate the catalytic activity, the disk electrode was subjected to a CV experiment in pH 12 at a slow scan rate (10 mV/s) in the potential range from 0.25 V to 1.3 V while the whole RRDE was rotating at a constant rate of 1600 rpm under nitrogen atmosphere. The oxygen produced in this electrode moves to the surrounding Pt ring electrode due to the centrifugal force generated by the rotation. In this ring electrode, the oxygen is electrochemically detected by its reduction applying a constant potential of -0.35 V. The resulting data for both

G-1^{2-} and **G-2**$^{2-}$ (GC@G@[(L)Cu]$^{2-}$ and GC@G@[(L_{py})Cu]$^{2-}$ respectively) compare to the blank (GC@G electrode) are represented in Figure S37, which shows the normalized intensity passed through the disk (left) and ring (right) electrode at every potential. As expected, when the disk reaches potentials 0.9-1.0 V, a huge catalytic current is observed leading to the formation of molecular oxygen that is then reduced in the ring electrode with the subsequent increase in the ring intensity. In the case of the blank, no oxygen was detected despite of the increase in the intensity, meaning that this current is due to electrode oxidation and degradation. From these experiments we can also obtain the Faradaic efficiency of the catalysts for water oxidation based on the relation between both disk and ring intensities, as shown in the equation below for a 2-e$^-$ reduction of oxygen to hydrogen peroxide:

$$\varepsilon = \frac{2 \cdot i_r}{i_d \cdot N} \qquad \text{(S11)}$$

In this equation, N is the collection efficiency previously calculated, and i_d and i_r are the values taken from the top of the peaks, where the intensity reaches a pseudo-stationary value before it starts to decrease due to electrode oxidative degradation. The Faradaic efficiency ε was calculated as the average of three independent samples and for both systems was practically equal: 23.36% for **G-1**$^{2-}$ and 25.56% for **G-2**$^{2-}$. Those values are relatively low due to the extensive graphene oxidation in these conditions, as has also been observed previously in literature when carbon based electrodes are used.[14] This oxidation process could be complete releasing CO2 or partial, generating some oxygenated group in the surface of the electrode. In both cases, the morphological changes occurring in the surface would lead to catalyst leaching and thus the loose of the activity. The similarity in the efficiencies also supports this idea since both values, and thus the main degradation pathway, do not seem to depend on the catalyst architecture.

RDDE calibration for H_2O_2 detection

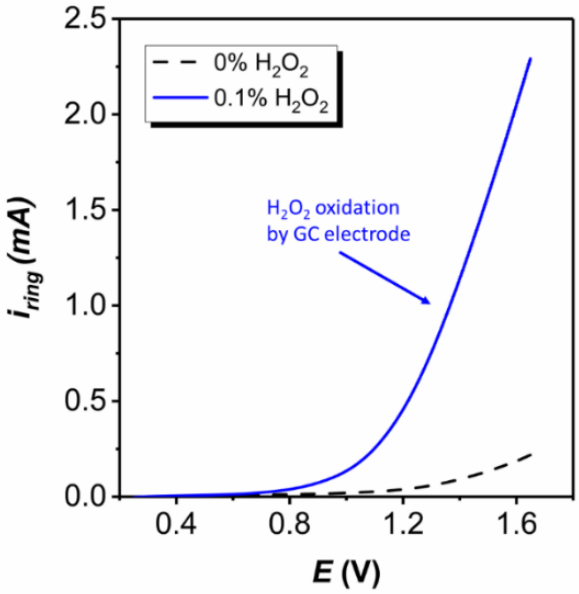

Figure S38. LSV of GC ring electrode in phosphate buffer at pH 12 (0.1 M of ionic strength) under nitrogen atmosphere and at 1600 r.p.m. in presence (solid blue line) and absence (dashed black line) of 0.1% H_2O_2. This shows that above 1.0 V the ring potential can already detect HOOH.

From molecules to solid state: Copper-based molecular anodes

H_2O_2 detection during catalytic water oxidation

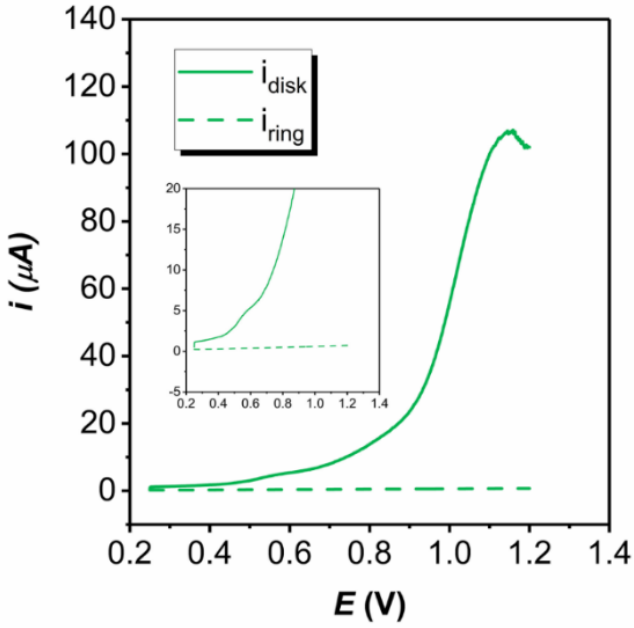

V

Figure S39. LSV of G-22- electrodes using RRDE in phosphate buffer at pH 12 (0.1 M of ionic strength) under nitrogen atmosphere and at 1600 r.p.m. The applied potential at the Ring is 1.45V. Intensity at the disk electrode is represented as a solid line while the intensity measured at the ring electrode is shown with dashed line. Inset shows a zoom at the 0-20 □ A range. No significant current density is observed over the whole potential scan indicating the absence of HOOH. This methodology has also been applied to the study of O_2 reduction reaction.[17]

Comparison of relevant water oxidation catalysts

Table S4. Summary of the catalytic performance of some relevant water oxidation catalysts based on first row transition metals.

Entry	Catalyst	Overpotential, V	TOF_{max}, s^{-1}	TONs (based on)
1[tw]	G-2^{2-}	558	540	5300
2[6]	1^{2-}	708	6.2	1947
3[18]	[(bpy)Cu$(OH)_2$]	750	100	>30
4[19]	[(6,6'-bobp)Cu$(OH_2)_2$]	510	0.4	400
5[20]	[Cu$(pyalk)_2$]	520-580	0.7	>30
6[21]	[(dbzbpen)Cu(OH2)]$^{2-}$	570	13.1	-
7[22]	[(2GH2−)Cu(H_2O)]	620	53	-
8[23]	[(Py3P)Cu(OH)]$^{-}$	500	38	19
9[24]	Fe$(ClO_4)_3$	-	9.6	436
10[25]	[Co^{II}(qpy)$(OH_2)_2$]$^{2+}$	-	4	335

*tw: this work.

Computational Study

Computational Details

All calculations were carried out with the Gaussian09 (v. D.01) program package[26]. In the present work, we study two different systems, homogeneous and heterogeneous, which drastically differ in the number of atoms. Therefore, for practical reasons, we need to use two different methodologies to calculate them, with a full-QM methodology in the case of homogeneous one and a multiscale QM/MM method to study the heterogeneous system.

For the homogeneous system models, we employed Density Functional Theory (DFT) methodology. All the calculations were computed using B3LYP as functional including Grimme's empirical dispersion correction (B3LYP-D3).[27,28] The basis set was split, using 6-31+G(d) for C, N, O and H,[29] and LANL2TZ(f) for Cu (including the associated pseudopotential).[30,31] The solvation was considered implicitly using the SMD model[32], with either water (ε = 78.3553) or acetonitrile (ε = 35.688) as solvent as specified in the text. All geometry optimizations were computed in solution without symmetry restrictions. The nature of all computed stationary points was confirmed by vibrational frequency calculations. Free energy corrections were calculated at 298.15 K and 105 Pa pressure, including zero point energy corrections (ZPE). In addition, a correction term of 1.9 kcal/mol (at 298 K) was added when necessary to account for the standard state concentration of 1 M. Unless otherwise mentioned, all reported energy values are free energies in solution. The stability of the electronic states corresponding to the intermediates was confirmed by stability analysis of the wavefunction. This methodology was already benchmarked in previous works providing satisfactory results for this type of systems. [6,36] Once again, in the new system reported here the agreement with the experimental potentials is very good, confirming the validity of this methodology for copper water oxidation catalysis.

For the heterogeneous system, QuantumMechanics/MolecularMechanics (QM/MM) was applied using 2-layer ONIOM to model the anchoring architectures of both homogeneous catalysts on the graphene surface. For this model, a graphene layer was selected with a size big enough to avoid edge interactions with the catalyst (14x14 phenyl groups). The low-level layer was modeled with molecular mechanics, using the Universal Force Field (UFF), while high-level layer was computed using DFT methodology with M06 as functional, which has the dispersion correction intrinsically parameterized and was shown to reproduce as well as B3LYP-D3 this family of catalysts.[6,36] We changed the functional to avoid introducing empirical dispersion corrections, which can lead to errors in combination with MM calculation. For this layer, we selected as basis sets 6-31G(d) for C, N, O and H, and LANL2DZ(f) for Cu. We reduced the size of the basis set for technical reasons, since the computational cost when we introduced diffuse functions was too large for our system. The nature of stationary points was also confirmed by frequency analysis, with zero imaginary frequencies for all the points computed for heterogeneous system.

The electrochemical magnitudes were calculated from the free energies using the values of 4.28 V found in literature for the absolute potential of the standard hydrogen electrode[33] and-11.72 eV for the free energy of the proton in aqueous solution at pH=1.[34] The value for the free energy of the proton was translated to the experimental pH value of 12 by adding a correction term of -0.059*pH, following the same procedure as other authors.[35]

Cu(II) speciation in aqueous solutions at pH=12

Before calculations of the catalytic cycle intermediates, we analyzed first which is the species that is formed in aqueous solution after addition of $[(L_{py})Cu]^{2-}$.

Through rotation of the C-C bond between phenyl ring and pyrene group we can obtain several conformers that may be stable. Then we first scan the dihedral angle between those two groups in order to find the most stable conformer. We defined that dihedral angle with the atoms high-lighted in blue shown in Figure S40. The most stable conformer turn out to be the one having a dihedral angle of about -130.

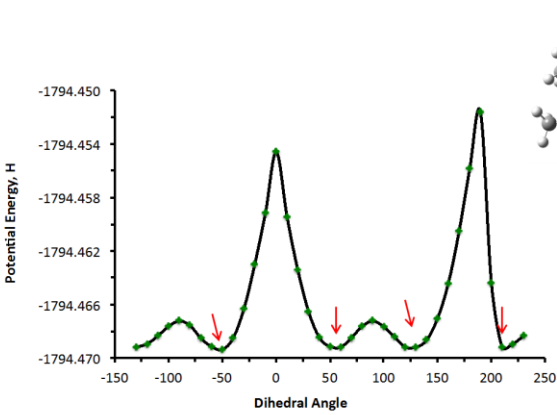

Dihedral Angle	Free Energy, H
-129.854	-1794.1277
52.42	-1794.1276
-53.447	-1794.1272
126.099	-1794.1263

Figure S40. Potential energy relaxed scan of the dihedral angle defined by the atoms in blue from the catalyst picture. The energies of each species are calculated in H. The table in the right part show the free energy in H of the four minima obtained from the scan.

Secondly, we analyzed the possibility of water or hydroxo coordination in the free apical positions. In all cases, the external molecules ended up forming hydrogen bonds with the nitrogen atoms of the ligand, what is consistent with the pH independency found for the Cu(II)/Cu(III) redox couple as well as with previous results using $[(L)Cu^{II}]^{2-}$ catalyst.[6,36]

Electrochemical activation of $[(L_{py})Cu]^{2-}$ catalyst

As can be deducted from the electrochemistry, water oxidation catalysis starts after two consecutive one-electron oxidations, first in the ligand and second in the metal center together with a hydroxo group coordination. These two redox processes have been computed and the resulting calculated potentials are in good agreement with the observed experimental ones: 0.44 V and 1.15 V vs 0.43 V and 1.06 V respectively (less than ±0.1 V deviation). The found sequence of oxidation was the same with a first oxidation in the ligand and a second oxidation in the metal center. The final formed species is a radical-Cu(III) complex with an unpaired electron highly delocalized mainly through the phenyl, pyrene and hydroxo groups and that is active toward O-O bond formation reaction. Probably due to the stabilization of the radical species through the delocalized π-orbitals, the redox potential for the ligand oxidation is much lower than in the unsubstituted catalyst $\mathbf{1}^{2-}$.

Scheme S3. Calculated mechanism for the electrochemical activation of the $[(L_{py})Cu]^{2-}$ catalyst. The values for the potentials correspond to the calculated ones.

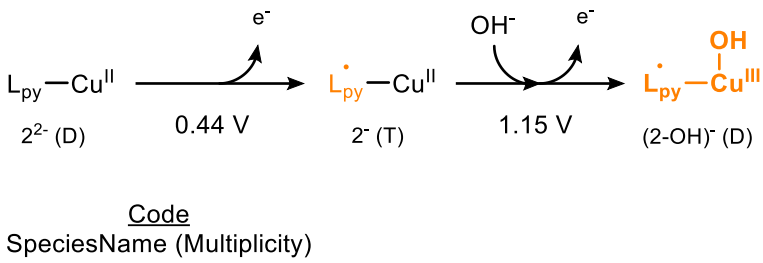

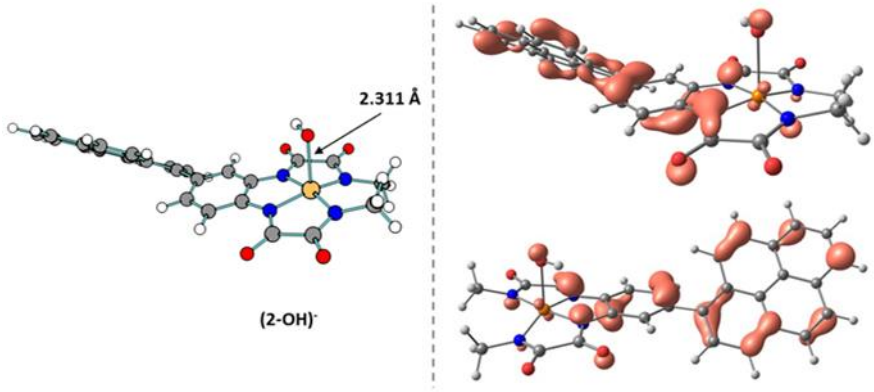

Figure S41. (Left) DFT optimized structure for the active species $[(L_{py})*Cu^{III}(OH)]^-$, **(2-OH)**$^-$. (Right) Two different views of the SOMO representation for the active species.

O-O bond formation step

As found for **1**$^{2-}$ catalyst in previous work,[6,36] the mechanism for the O-O bond formation in **2**$^{2-}$ has been found to follow a Single Electron Transfer-Water Nucleophilic Attack (SET-WNA).[42] After the generation of $[(L_{py})*Cu^{III}(OH)]^-$, **(2-OH)**$^-$, this species is highly oxidizing and susceptible to be attacked by an OH^- coming from the solution to the coordinated hydroxo group, yielding the O-O bond formation. In order to analyze this mechanism, we perform a relaxed scan studying the O-O distance as reaction coordinate, as shown in Figure S42.

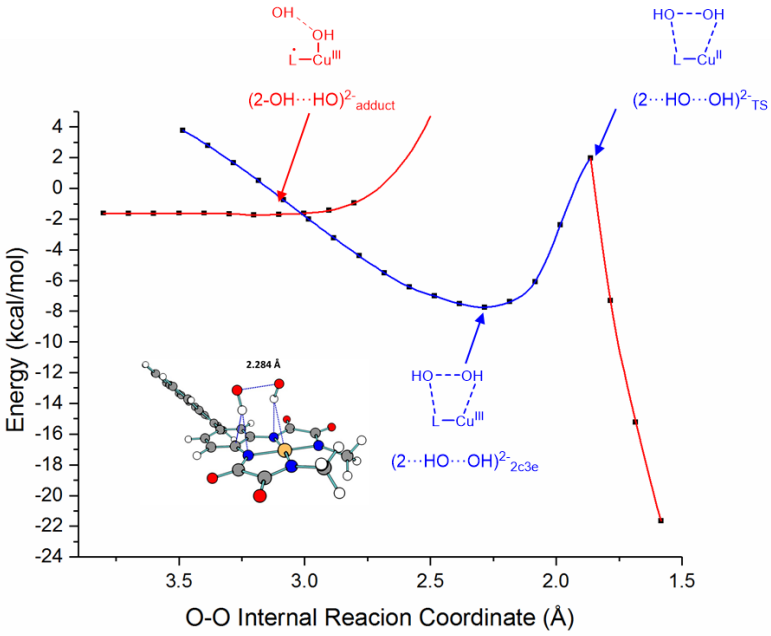

Figure S42. Potential energy relaxed scan of the O-O reaction coordinate, where energy is expressed in kcal·mol^{-1}. Color code is based on the electronic structure of both oxygen centers where red is for closed shell and blue for radical species.

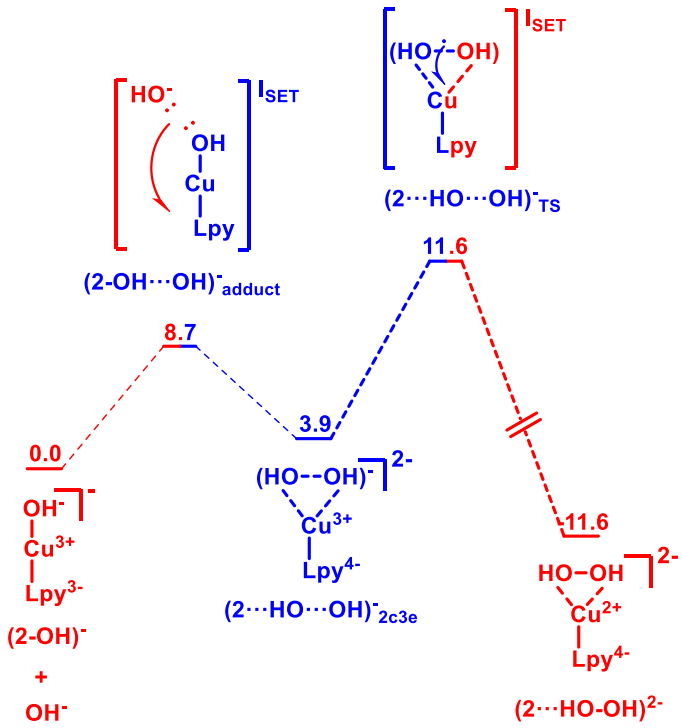

V

Figure S43. Free energy profile of the O-O bond formation reaction, where energy is expressed in kcal·mol^{-1}. Color code is the same as in previous Figure S42, based on the electronic structure of both oxygen centers where red is for closed shell and blue for radical species.

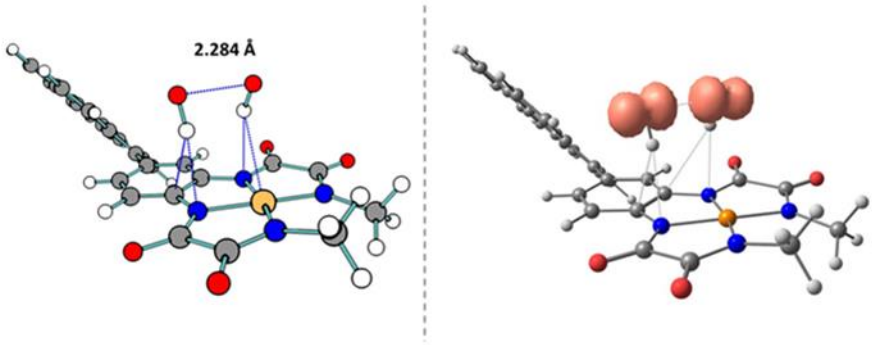

Figure S44. (Left) DFT optimized structure for the 2c-3e$^-$ intermediate **(2-OH···OH)**$^{2-}$. (Right) Calculated spin density for the same species.

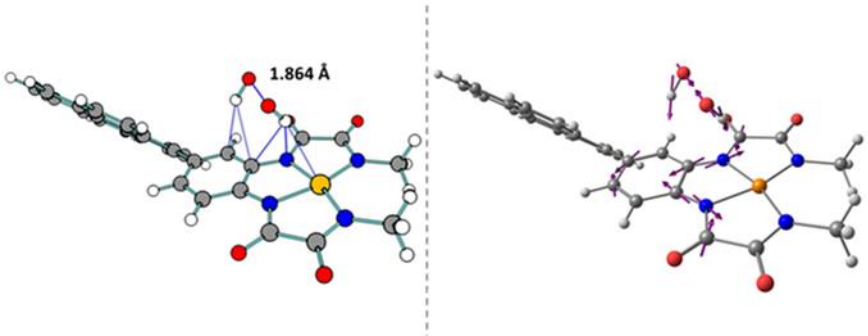

Figure S45. (Left) Computed transition state for the second single electron transfer connecting **(2-OH···OH)**$^{2-}$ and **(2···HO-OH)**$^{2-}$. (Right) Displacement vectors of the normal mode associated with the imaginary frequency in the same transition state.

From molecules to solid state: Copper-based molecular anodes

O_2 release and catalyst regeneration

After the O-O bond step formation, hydrogen peroxide remains hydrogen bonded to the catalyst in its initial species form, i.e. with the ligand reduced and the metal center in oxidation state II. Then, the release of one electron has a potential of 0.51 V so it will takes place at the applied potential for water oxidation catalysis (1.08 V). Once again, the ligand is the first being oxidized generation a triplet species with the peroxide still hydrogen bonded. Last oxidation occurs as a proton coupled electron transfer (PCET) at very low potential (0.38 V) which means that is highly favored to generate a quartet species. In this case, the electron is released from the peroxide species with the concerted loss of a proton. Finally, the last proton is highly acidic and its release leads to the initial molecular catalyst along with the evolution of oxygen.

Scheme S4. Calculated mechanism for the third and fourth oxidations that lead to the oxygen evolution and catalyst regeneration. The values for the potentials and pKa correspond to the calculated ones and are in good agreement with the experimental observations.

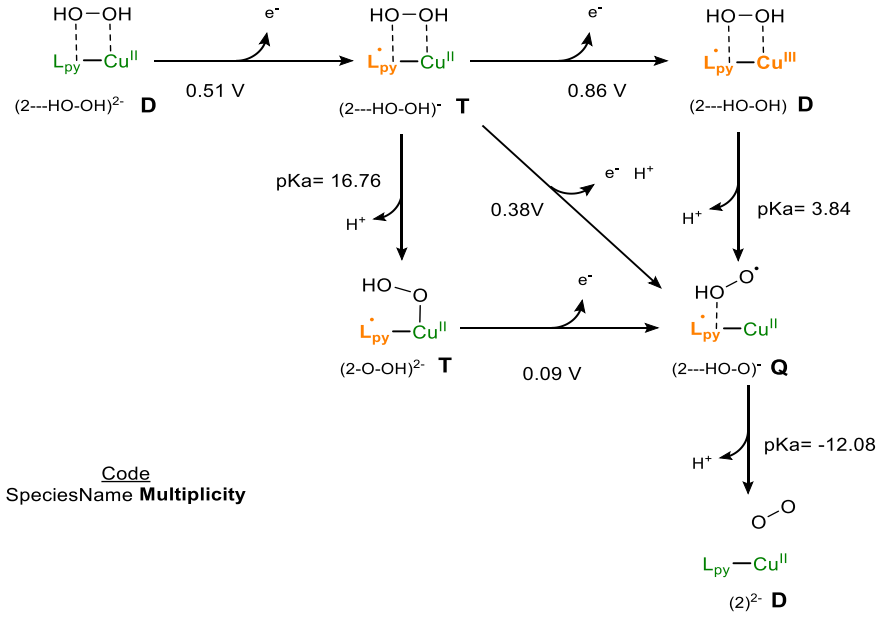

Hybrid catalyst structure

In order to analyse the anchoring structure of both catalysts on the graphene layers, QMMM calculations were performed (see computational details section). Thanks to the square-planar geometry of $\mathbf{1}^{2-}$ it is able to interact strongly with the graphene layer through π-π interactions, which is reflected in the short Cu-Graphene distance of about 3.522 Å. Regarding the coordination environment, changes respect to the structure in solution are negligible, with similar Cu-N distances. On the other hand, complex $\mathbf{2}^{2-}$ undergoes a significant rearrangement upon interaction with the graphene layer. Due to the capability of both moieties (the pyrene group and the phenyloxamidate) to interact through π-π interactions with the graphene layer, there is a bond rotation and the dihedral angle changes from -130º in solution to around 0º when deposited on the graphene. This allows for higher delocalization of electrons through the whole ligand as well as more π orbitals interacting with the graphene. Current computational studies are being peformed to further characterize the different oxidation states of the hybrid catalysts and the catalytic properties of both.

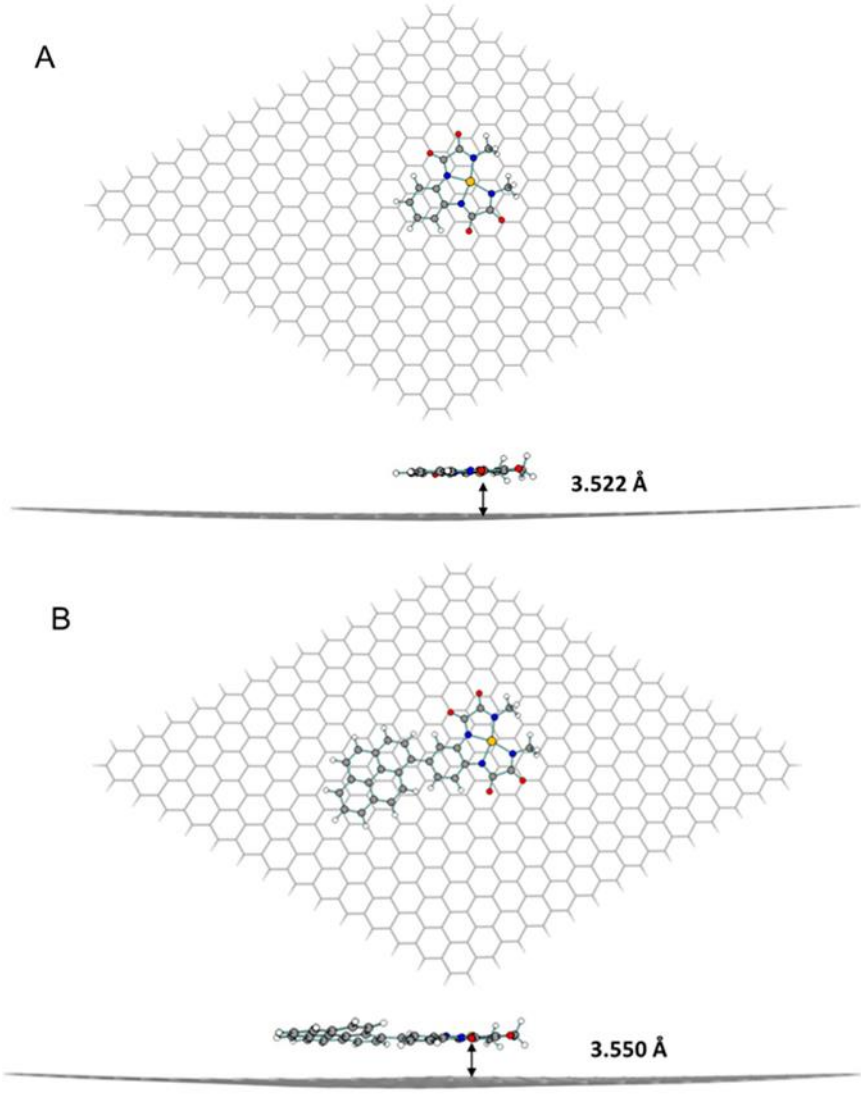

Figure S46. DFT optimized structure of the QMMM model for both hybrid catalysts **G-1**$^{2-}$ (A) and **G-2**$^{2-}$ (B).

References

1 Ravel, B.; Newville, M. *J. Synchrotron Rad.* **2005**, *12*, 537-541.

2 Rehr, J. J.; Albers, R. C. *Rev. Mod. Phys.* **2000**, *72*, 621-654.

3 Koningsberger, D. C.; Prins, R. *X Ray Absorption: Principles, Applications, Techniques of EXAFS, SEXAFS and XANES*; John Wiley & Sons: New York, 1988.

4Stumpf, H. O.; Pei, Y.; Kahn, O.; Sletten, J.; Renard, J. P. *J. Am. Chem. Soc.* **1993**, *115*, 6738.

5Ruiz, R.; Surville-Barland, C.; Aukauloo, A.; Anxolabehere-Mallart, E.; Journaux, Y.; Cano, J.; Carmen Munoz, M. *J. Chem. Soc., Dalton Trans.* **1997**, 745-752.

6 Garrido-Barros, P.; Funes-Ardoiz, I.; Drouet, S.; Benet-Buchholz, J.; Maseras, F.; Llobet, A. *J. Am. Chem. Soc.* **2015**, *137*, 6758-6761.

7 Jahani, F.; Tajbakhsh, M.; Golchoubian, H.; Khaksar, S. *Tetrahedron Lett.* **2011,** *52*, 1260-1264.

8 Kwon, J.; Hong, J.-P.; Lee, S.; Hong, J.-I. *New J. Chem.* **2013**, *37*, 2881–2887.

9 Lebedeva, M. A.; Chamberlain, T. W.; Davies, E. S.; Mancel, D.; Thomas, B. E.; Suyetin, M.; Bichoutskaia, E.; Schröder, M.; Khlobystov, A. N. *Chem.Eur. J.* **2013**, *19*, 11999–12008

10 Costentin, C.; Savéant, J.-M. *ChemElectroChem* **2014**, *1*, 1226-1236.

11 Rountree, E. S.; McCarthy, B. D.; Eisenhart, T. T.; Dempsey, J. L. *Inorg. Chem.* **2014**, *53*, 9983-10002.

12 Matheu, R.; Neudeck, S.; Meyer, F.; Sala, X.; Llobet, A. *ChemSusChem* **2016**, *9*, 3361−3369

13 Kaniyoor, A.; Ramaprabhu, S., *AIP Adv.*, **2012**, 2, 032183.

14 McCrory, C. C. L.; Jung, S. H.; Peters, J. C.; Jaramillo, T. F. *J. Am. Chem. Soc.* **2013**, *135*, 16977−16987.

15 Wilke, C. R.; Chang, P., *AIChE J,* **1955**, *63*, 264-270.

16 Tromans, D., Hydrometallurgy, **1998**, *50,* 279–296.

17 Rigsby, M. L., Wasylenko, D. J., Pegis, M. L., Mayer, J. M., *J. Am. Chem. Soc.,* **2015**, *137*, 4296–4299.

18 Barnett, S. M.; Goldberg, K. I.; Mayer, J. M. *Nat. Chem*. **2012**, *4*, 498-502.

19 Zhang, T.; Wang, C.; Liu, S.; Wang, J.-L.; Lin, W. *J. Am. Chem. Soc*. **2014**, *136*, 273-281.

20 Fisher, K. J.; Materna, K. L.; Mercado, B. Q.; Crabtree, R. H.; Brudvig, G. W. *ACS Catal.* **2017**, *7*, 3384-3387.

21 Shen, J.; Zhang, P.; Jiang, J.; Sun, L. *Chem. Commun.* **2017**, *53*, 4374-4377.

22 Pap, J. S.; Szyrwiel, L.; Sranko, D.; Kerner, Z.; Setner, B.; Szewczuk, Z.; Malinka, W. *Chem. Commun*. **2015**, *51*, 6322-6324.

23 Coggins, M. K.; Zhang, M.-T.; Chen, Z.; Song, N.; Meyer, T. J. *Angew. Chem. Int. Ed.* **2014**, *53*, 12226-12230.

24 Chen, G.; Chen, L.; Ng, S.-M.; Man, W.-L.; Lau, T.-C. *Angew. Chem. Int. Ed.* **2013**, *52*, 1789-1791.

25 Leung, C.-F.; Ng, S.-M.; Ko, C.-C,; Man, W.-L.; Wu, J.; Chen, L.; Lau, T.-C. *Energy Environ. Sci*. **2012**, *5*, 7903-7907.

26 Gaussian 09, Revision **D.01**, Frisch, M. J.; Trucks, G. W.; Schlegel, H. B.; Scuseria, G. E.; Robb, M. A.; Cheeseman, J. R.; Scalmani, G.; Barone, V.; Mennucci, B.; Petersson, G. A.; Nakatsuji, H.; Caricato, M.; Li, X.; Hratchian, H. P.;

Izmaylov, A. F.; Bloino, J.; Zheng, G.; Sonnenberg, J. L.; Hada, M.; Ehara, M.; Toyota, K.; Fukuda, R.; Hasegawa, J.; Ishida, M.; Nakajima, T.; Honda, Y.; Kitao, O.; Nakai, H.; Vreven, T.; Montgomery, J. A., Jr.; Peralta, J. E.; Ogliaro, F.; Bearpark, M.; Heyd, J. J.; Brothers, E.; Kudin, K. N.; Staroverov, V. N.; Kobayashi, R.; Normand, J.; Raghavachari, K.; Rendell, A.; Burant, J. C.; Iyengar, S. S.; Tomasi, J.; Cossi, M.; Rega, N.; Millam, J. M.; Klene, M.; Knox, J. E.; Cross, J. B.; Bakken, V.; Adamo, C.; Jaramillo, J.; Gomperts, R.; Stratmann, R. E.; Yazyev, O.; Austin, A. J.; Cammi, R.; Pomelli, C.; Ochterski, J. W.; Martin, R. L.; Morokuma, K.; Zakrzewski, V. G.; Voth, G. A.; Salvador, P.; Dannenberg, J. J.; Dapprich, S.; Daniels, A. D.; Farkas, Ö.; Foresman, J. B.; Ortiz, J. V.; Cioslowski, J.; Fox, D. J. Gaussian, Inc., Wallingford CT, 2009.

27 Becke, A.D., *J. Chem. Phys.***1993**, *98*, 5648-5652.

28 Grimme, S.; Antony, J.; Ehrlich, S.; Krieg, H., *J. Chem. Phys.***2010**, *132*, 154104.

29 a) Hehre, W.J.; Ditchfield, R.; Pople, J.A., *J. Chem. Phys.* **1972**, 56, 2257. b) Hariharan, P.C.; Pople, J.A., *Theoret. ChimicaActa* **1973**, *28*, 213-222. c) Francl, M.M.; Petro, W.J.; Hehre, W.J.; Binkley, J.S.; Gordon, M.S.; DeFrees, D.J.; Pople, J.A., *J. Chem. Phys.* **1982**, *77*, 3654.

30 a) Hay, P. J.; Wadt, W. R., *J. Chem. Phys.***1985**, *82*, 270. b) Hay, P. J.; Wadt, W. R., *J. Chem. Phys.***1985**, *82*, 284. c) Hay, P. J.; Wadt, W. R., *J. Chem. Phys.***1985**, *82*, 299.

31Taken from EMSL Basis set Library: a) Felier, D., *J. Comp. Chem.***1996**, *17*, 1571-1586. b) Schuchardt, K.L.; Didier, B.T.; Elsethagen, T.; Sun, L.; Gurumoorthi, V.; Chase, J.; Li, J.; Windus, T.L., *J. Chem. Inf. Model.*, **2007**, *47*, 1045-1052.

32 Marenich, S. A. V.; Cramer, C. J.; Truhlar, D. G., *J. Phys. Chem. B*, **2009**, *113,* 6378-6396.

33a) Lewis, A.; Bumpus, J. A.; Truhlar, D. G.; Cramer, C. J., *J. Chem. Ed.* **2004**, *81*, 596-604. b) Lewis, A.; Bumpus, J. A.; Truhlar, D. G.; Cramer, C. J., *J. Chem. Ed.* **2007**, *84*, 934.

34 Marenich, A. V.; Majunmdar, A.; Lenz, M.; Cramer, C. J.; Truhlar, D. G., *Angew. Chem. Int. Ed.* **2012**, *51*, 12810-12814.

35 Winikoff, S.G.; Cramer, C.J.; *Catal. Sci. Technol.* **2014**, *4*, 2484-2489.

36 Funes-Ardoiz, I.; Garrido-Barros, P.; Llobet, A.; Maseras, F. *ACS Catal.* **2017**, *7*, 1712−1719.

Chapter 6

An extension to Nickel

Motivated by the lack of information in nickel-based mol-WOC, the previous strategies using copper complexes are applied to the development of nickel catalysts. The complex $[Ni^{II}\text{-mox}]^{2-}$ is synthetized and its catlytic performance toward water oxidation is evaluated. This system allows to study the factors determining the low stability of molecular nickel complexes in aqueous solutions under oxidative conditions and thus, their opportunities as molecular catalysts or precursor of active nickel oxides

An extension to Nickel

6.1. Paper F: Can Ni complexes behave as molecular water oxidation catalysts?

Garrido-Barros, P.; Grau, S.; Drouet, S.; Benet- Buchholz, J; Gimbert-Suriñach, C.; Llobet, A. **2018**, *submitted.*

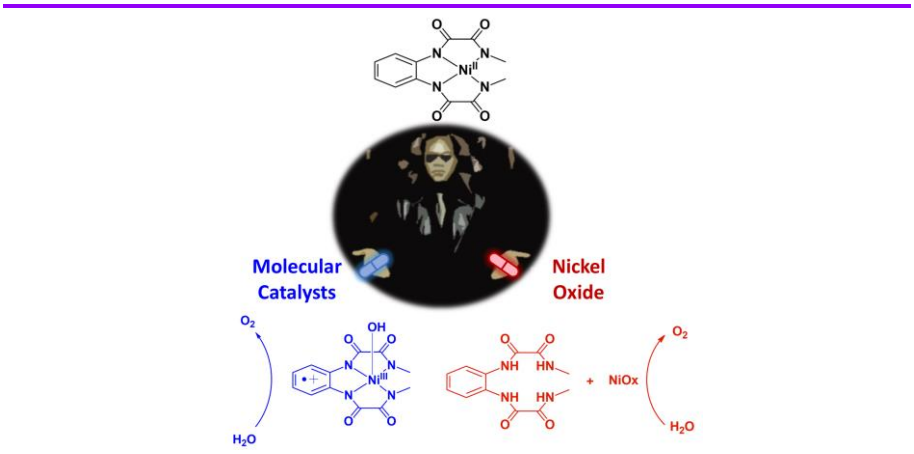

Abstract

The present report uncovers the borderline between homogeneous and heterogeneous water oxidation catalysis using a family of Ni complexes containing oxamidate anionic type of ligands. In particular, the Ni complex $[(L^1)Ni^{II}]^{2-}$ (**1**$^{2-}$; L^1 = o-phenylenebis(oxamidate)) and its modified analogues $[(L^2)Ni^{II}]^{2-}$ (**2**$^{2-}$;L^2 = 4,5-dimethyl-1,2-phenylenebis(oxamidate)) and $[(L^3)Ni^{II}]^{2-}$ (**3**$^{2-}$;L^2 = 4-methoxy-1,2-phenylenebis(oxamidate)) have been prepared and evaluated as molecular water oxidation catalysts at basic pH. Their redox features have been analyzed by mean of electrochemical measurements revealing a crucial involvement of the ligand in the electron transfer processes. Moreover, the stability of those complexes has been assessed both in solution and immobilized on graphene-based electrodes at different potentials and pHs. The degradation of the molecular species generates a NiOx layer, whose stability and activity as water oxidation catalyst has also been stablished. Electrochemical methods, together with surface characterization techniques, have shown the

VI

complex mechanistic scenario in water oxidation catalyzed by this family of Ni complexes, which consists of the coexistence of two catalytic mechanism: a homogeneous pathway driven by the molecular complex and a heterogeneous pathway based on NiOx. The electronic perturbations exerted through the ligand framework has manifested a strong influence over the stability of the molecular species under turnover conditions. Finally, $\mathbf{1}^{2-}$ has been used as a molecular precursor for the formation of NiFeOx anodes that behave as extremely powerful water oxidation anodes.

Contributions:

Pablo Garrido Barros synthetized and characterized all the compounds and electrodes, carried out the electrochemical and spectroscopic analysis, performed the computational calculations and prepared the manuscript.

F.1. Introduction

Water oxidation to molecular dioxygen is not only an essential reaction in biology, due to its implications in the natural photosynthesis,[1] but also a key step in the development of new sustainable energy schemes based on artificial photosynthesis.[2,3,4] In this context, molecular complexes based on first row transition metals (FR-TM) are attracting increasing attention as inexpensive homogeneous water oxiation catalysts (WOCs) that can potentially operate close to the thermodynamic limit.[5,6,7]

One of the attracting features of molecular WOCs is the existence of a synthetic versatility that thanks to the ligand variation allows to prepare a large variety of complexes where electronic, steric and supramplecular effects can be finely tuned. In addition there is a wide range of spectroscopic techniques that allows a deep characterization of molecular species including reactive intermediates. Thus molecular science is an ideal platform to study the reaction mechanism that operate in the water

An extension to Nickel

oxidation reaction as well as the factors that determine their activity and robustness.[8]

On the other hand, water oxidation requires a thermodynamic potential of 1.23 V vs NHE at pH 0, plus an additional overpotential to overcome the kinetic barriers. This high potential value can promote total or partial ligand oxidation as a parallel undesired deactivation reactions.[9,10,11,12] Besides, the relatively high metal-ligand bond lability of FR-TM complexes can lead to partial or total ligand substitution reactions by solvent molecules. The latter is favored at extreme pH values.[13,14,15,16,17] This can foster the subsequent formation of metal oxides that can be responsible for the observed water oxidation catalysis. Therefore, deeper understanding of all these processes is essential to establish the real catalytic species that operate in a particular system and thus to obtain meaningful information for the design of more stable and active molecular catalyst.

Stability considerations are of special importance in Ni based molecular complexes due to its high affinity to form Ni oxide in aqueous solution upon oxidation.[18,19,20,21] True homogeneous catalysis based on Ni complexes are rare and thus is a relatively unexplored field.[22,23,24]

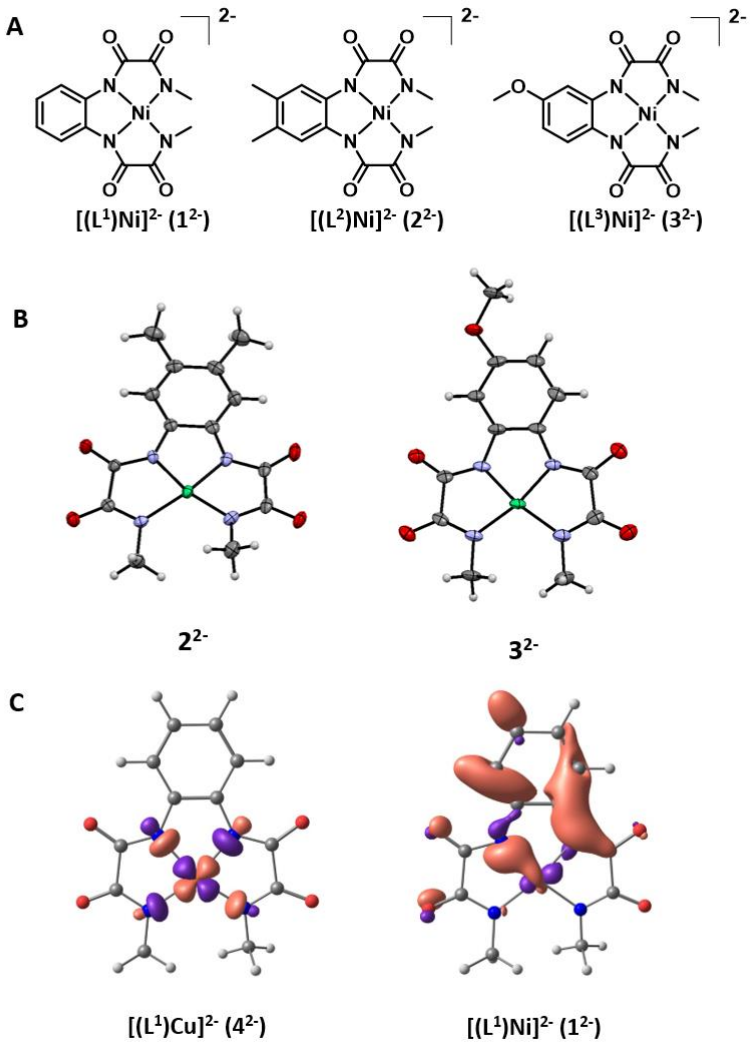

Figure 1. (A) Schematic representation and labeling of the homogeneous catalysts used in this work. (B) ORTEP figure of complexes $\mathbf{2}^{2-}$ and $\mathbf{3}^{2-}$. (C) HOMO orbital of the copper and nickel complexes $\mathbf{4}^{2-}$ and $\mathbf{1}^{2-}$ calculated by Natural Orbital (NO) analysis.

In order to decipher the narrow line between homogeneous and heterogeneous catalysis using molecular Ni complexes, we have chosen the recently reported $[(L^1)Ni^{II}]^{2-}$ (L^1 = o-phenylenebis(oxamidate)) complex, $\mathbf{1}^{2-}$,[19] and its aryl substituted analogues $[(L^2)Ni^{II}]^{2-}$ (L^2 = 4,5-

An extension to Nickel

dimethyl-1,2-phenylenebis(oxamidate)), $\mathbf{2}^{2-}$, and $[(L^3)Ni^{II}]^{2-}$ (L^2 = 4-methoxy-1,2-phenylenebis(oxamidate)), $\mathbf{3}^{2-}$ reported here for the first time (See Figure 1 for a drawn structure and crystal structure). We study in depth the catalytic pathways available to this family of complexes together with the deactivation paths that can lead to the formation of NiOx.

F.2. Results and discussion

F.2.1 Synthesis, structure and redox properties of $\mathbf{1}^{2-}$-$\mathbf{3}^{2-}$

We have prepared and characterized complexes $\mathbf{1}^{2-}$, $\mathbf{2}^{2-}$ and $\mathbf{3}^{2-}$ in Figure 1A following similar procedures described in the literature (See SI).[23,25] As already reported for $\mathbf{1}^{2-}$, complexes $\mathbf{2}^{2-}$ and $\mathbf{3}^{2-}$ with Me and MeO substitution at the aromatic ring respectively, also feature a pseudo square-planar geometry typical of a low spin d^8 Ni(II) complex as shown in their crystal structure presented in Figure 1B. The Ni-N distances range from 1.852 to 1.918 Å and are slightly shorter than those of the analogous copper complexes,[25] reflecting the strength and stability of the Nickel-amidate bonds.

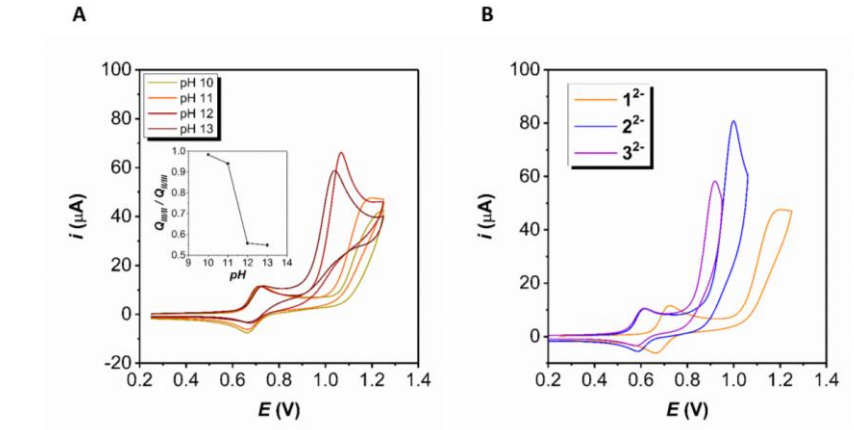

Figure 2. (A) CVs of 1 mM $\mathbf{1}^{2-}$ in aqueous solutions at different pH values. The inset figure shows the ratio between the reductive and oxidative charge ($Q_{III/II}$ and $Q_{II/III}$ respectively) under the Ni^{II}/Ni^{III} redox wave as function of the pH. (B) CVs of a solution containing 1mM of $\mathbf{1}^{2-}$, $\mathbf{2}^{2-}$ and $\mathbf{3}^{2-}$ at pH 11.

Figure 2A shows the electrochemical behavior of $\mathbf{1}^{2-}$ in basic aqueous solutions from pH 10 to 13. In this pH range, this complex is stable in solution over time as demonstrated by the lack of changes in its electrochemical performance (Figure S4), but it undergoes demetallation due to the protonation of the amidate groups at pHs lower than 10. The cyclic voltammetry (CV) and differential pulse voltammetry (DPV) (Figure 2 and S3) reveal a first electrochemically quasi-reversible, chemically reversible metal based wave at 0.67 V due to the pH-independent Ni(III)/Ni(II) redox couple, to form $[(L^{1})Ni^{III}]^{-}$. A UV-vis spectrum of the oxidized complex (Figure S5) confirms the metal based assignment and generation of the Ni(III) species at this pH based on the similarity with that obtained for the same complex in dry acetonitrile reported in the literature.[26]

At pH 10-13 a second oxidation process due to the electrocatytic oxidation of H_2O to O_2 is observed. The second oxidation takes place mainly at the aromatic ring generating a phenyl radical cation with concomitant coordination of a hydroxo group to form $[(L^{1})^{\cdot}Ni^{III}(OH)]^{-}$ (see Scheme 1, bottom). The latter species is responsible for the O-O bond formation and final oxygen release as shown in Scheme 1. A Foot-of-the-wave analysis (FOWA) of the catalytic current[27] allows us to calculate the observed kinetic constant for water oxidation resulting in a value around 0.20 s^{-1} (Figure S7). This is slightly lower than the 3.56 s^{-1} obtained for the analogous copper complex, manifesting the lower reactivity of the Ni catalyst that could be partly associated to the lower driving force due to the decrease in overpotential of the latter (500 mV for Ni vs 700 mV for Cu at pH = 12).

An extension to Nickel

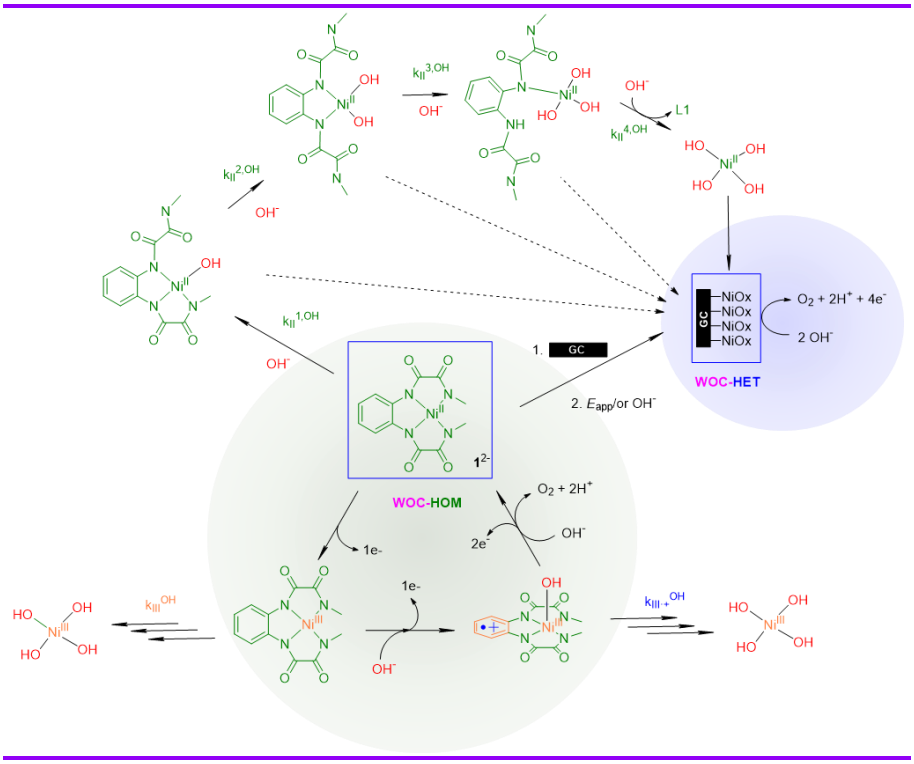

Scheme 1. Catalytic cycle for water oxidation by complex $\mathbf{1}^{2-}$ and mechanism for deactivation of complex $\mathbf{1}^{2-}$ and formation of NiOx.

VI

Similarly to $\mathbf{1}^{2-}$, complexes $\mathbf{2}^{2-}$ and $\mathbf{3}^{2-}$ feature two oxidation processes as shown in Figure 2. In both cases, the electronic perturbations induced by the electron-donor substituents in the phenyl ring lead to a decrease in the overpotential for water oxidation of around 170 and 220 mV respectively, supporting the assignment of a second ligand-based oxidation. In contrast to the analogous copper complexes, these modifications have also an influence on the first reversible wave that are cathodically shifted by approximately 100 mV. Since the metal coordination environment is practically identical in the 3 complexes, the change in the III/II potential can be attributed to a significant ligand contribution at their HOMO orbitals as shown by DFT calculations as opposed to the copper analogue $[(L^1)Cu]^{2-}$, $\mathbf{4}^{2-}$ (Figure 1 and S30).[28]

One of the most interesting features of catalyst $\mathbf{1}^{2-}$ arises from the reversibility observed in the first redox wave after going through the catalytic process, which is very unusual in Ni-based complexes proposed as water oxidation catalysts.[22,24,29,30,31,32] Reversibility of precatalytic waves is an important indicator of robustness since it implies that the coordination environment in the metal center remains intact after catalytic turnovers. Regarding the substituted analogous, complex $\mathbf{2}^{2-}$ also features similar reversible behavior while $\mathbf{3}^{2-}$ experiences a significant decrease in the reduction wave during the cathodic scan after the catalytic process. Similar results were obtained in the related family of copper complexes and point out to the presence of competing deactivation reaction possibly involving the reactive phenyl radical cation.[25]

F.2.2. Molecular Catalyst stability in Homogeneous Phase

F.2.2.1. Stability of the one electron oxidized derivative $[(L^1)Ni^{III}]^-$, $\mathbf{1}^-$

The stability of the oxidized species generated from the Ni(II) complex $\mathbf{1}^{2-}$, was monitored electrochemically at the pH range 10-13. From pH 10 to 12, the Ni(III)/Ni(II) redox wave for $\mathbf{1}^{2-}$, shows a reversible behavior at 25-200 $mV \cdot s^{-1}$ scan rates within the 0.25-0.85 V range where the corresponding Ni(III) complex is generated. Further, the intensity of the oxidative peak depends linearly with the square root of the scan rate, as expected for a diffusion controlled process from the Randles–Sevcik equation. However, at pH 13 the reversibility decreases with the scan rate and the oxidative current shows an important deviation of the Randles–Sevcik equation (see Figures S8-S9).

This result reveals that while the Ni(III) species $\mathbf{1}^-$, is fully stable within the pH 10-12 within the CV timescales, at pH = 13, it likely undergoes progressive hydroxo substitution as proposed in equations 1-4 and graphically depicted in Scheme 1.

An extension to Nickel

$$[Ni^{III}(L^1\text{-}\kappa\text{-}N^4)]^- + OH^- \leftrightarrow [Ni^{III}(L^1\text{-}\kappa\text{-}N^3)(OH)]^{2-} \quad (1)$$

$$[Ni^{III}(L^1\text{-}\kappa\text{-}N^3)(OH)]^{2-} + OH^- \leftrightarrow [Ni^{III}(L^1\text{-}\kappa\text{-}N^2)(OH)_2]^{3-} \quad (2)$$

$$[Ni^{III}(L^1\text{-}\kappa\text{-}N^2)(OH)_2]^{3-} + OH^- \leftrightarrow [Ni^{III}(L^1\text{-}\kappa\text{-}N^1)(OH)_3]^{4-} \quad (3)$$

$$[Ni^{III}(L^1\text{-}\kappa\text{-}N^1)(OH)_3]^{4-} + OH^- \leftrightarrow [Ni^{III}(OH)_4]^- + L^{14-} \quad (4)$$

F.2.2.2. Formation of ligand radical cation $[(L^1)^{\cdot}Ni^{III}(OH)]^-$ and catalysis at different pHs

The stability of complex $\mathbf{1^{2-}}$ was also evaluated during electrocatalytic process at pH 10-13 by monitoring the ratio between the charge under the reductive and oxidative waves ($Q_{III/II}/Q_{II/III}$) calculated by integration of the Ni^{II}/Ni^{III} redox wave of the CVs (See inset in Figure 2). This ratio is very close to 1 when working at pH 10 but drastically drops at higher pH, suggesting an important decrease in the stability of the complex during catalysis turnover at higher pH.

Here besides the potential substitution processes described in equations 1-4 that can also occur in this doubly oxidized species, there is an additional pathway for degradation that involves the phenyl radical cation species present in $[(L^1)^{\cdot}Ni^{III}(OH)]^-$, $\mathbf{1(OH)^-}$. Indeed, this species will be highly reactive towards the hydroxylation of the aromatic ring with the OH^- present in the medium that in turn is competing with the O-O bond formation that drives the desired catalytic process (Scheme 1, bottom right). The relative ratios of these two reactions will dictate the stability of the initial complex and thus its ruggedness as a water oxidation catalyst.

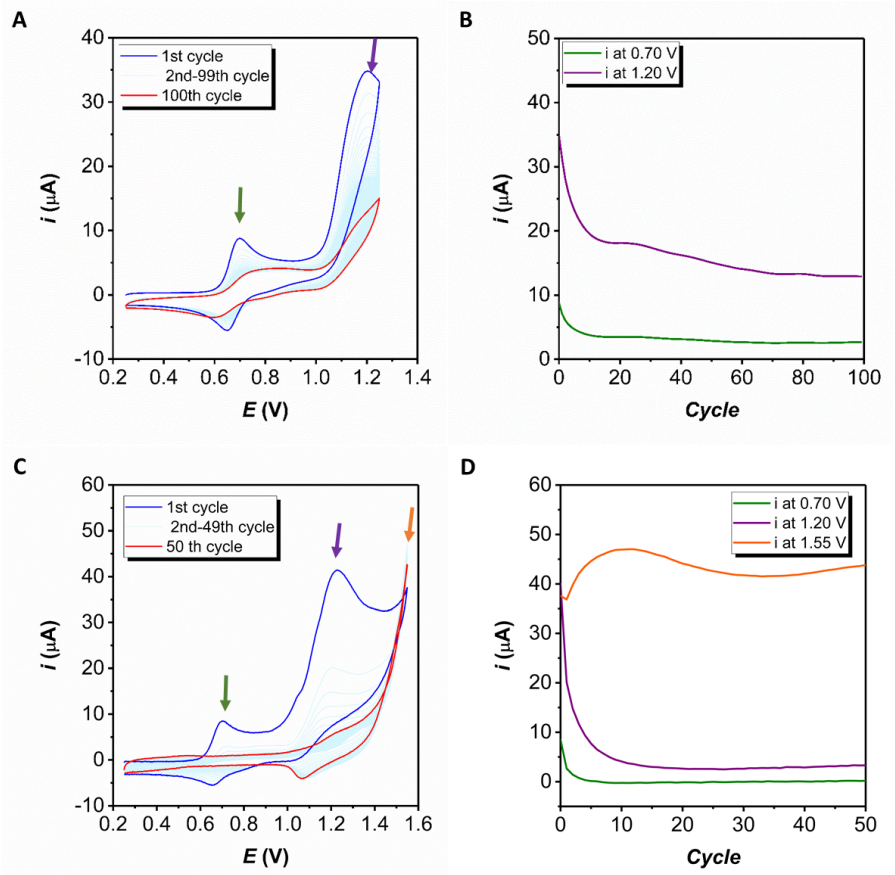

Figure 3. (A) 100 consecutive CVs in an aqueous solution containing 1 mM of $\mathbf{1}^{2-}$ at pH 10 from 0.25 V to 1.25 V. (B) Evolution of the intensity at 0.70 V and 1.20 V with the consecutive cycles. (C) 100 consecutive CVs in an aqueous solution containing 1 mM of $\mathbf{1}^{2-}$ at pH 10 from 0.25 V to 1.55 V. (D) Evolution of the intensity at 0.70 V, 1.20 V and 1.55 V with the consecutive cycles

The stability of $\mathbf{1}^{2-}$ as catalyst at longer time scales was monitored via repetitive CVs at a scan rate of 100 mV/s in the potential range from 0.25 to 1.25 V for 100 consecutive scans in the pH range 10-14. Figure 3A shows that at pH =10 for the first cycle the degree of degradation is practically non-existent as judged by the reversibility of the III/II couple. However, upon repetitive cycles, Figure 3B shows that the intensity of the anodic peak decreases by half after 10 cycles as is also the case of the catalytic current (see green and purple lines, respectively). This decrease

An extension to Nickel

continues in the following cycles suggesting the presence of a deactivation pathway that generates inactive species. Figure 3C illustrates the effect of increasing the anodic potential up to 1.50 V. In this potential range, even after the first cycle the returning cathodic wave of the III/II couple reduces its intensity by half with regards to its anodic counterpart. Further cycling shows the typical waves associated with the formation of NiOx/NiOOHx that remain attached at the surface of the electrode: the Ni(II)/Ni(III) at $E_a \approx$ 1.2 V and the catalytic wave starting at $E_{cat} \approx$1.45 V.

Thus under these conditions it seems that the homogeneous catalysts is competing with two other reactions: one that deactivates the catalyst towards the formation of aromatic hydroxylated species that have no water oxidation activity and a second one that triggers the formation of NiOx/NiOOHx that absorb at the surface of the electrode and that is the active catalyst towards the water oxidation reaction at higher potential than the molecular catalyst.

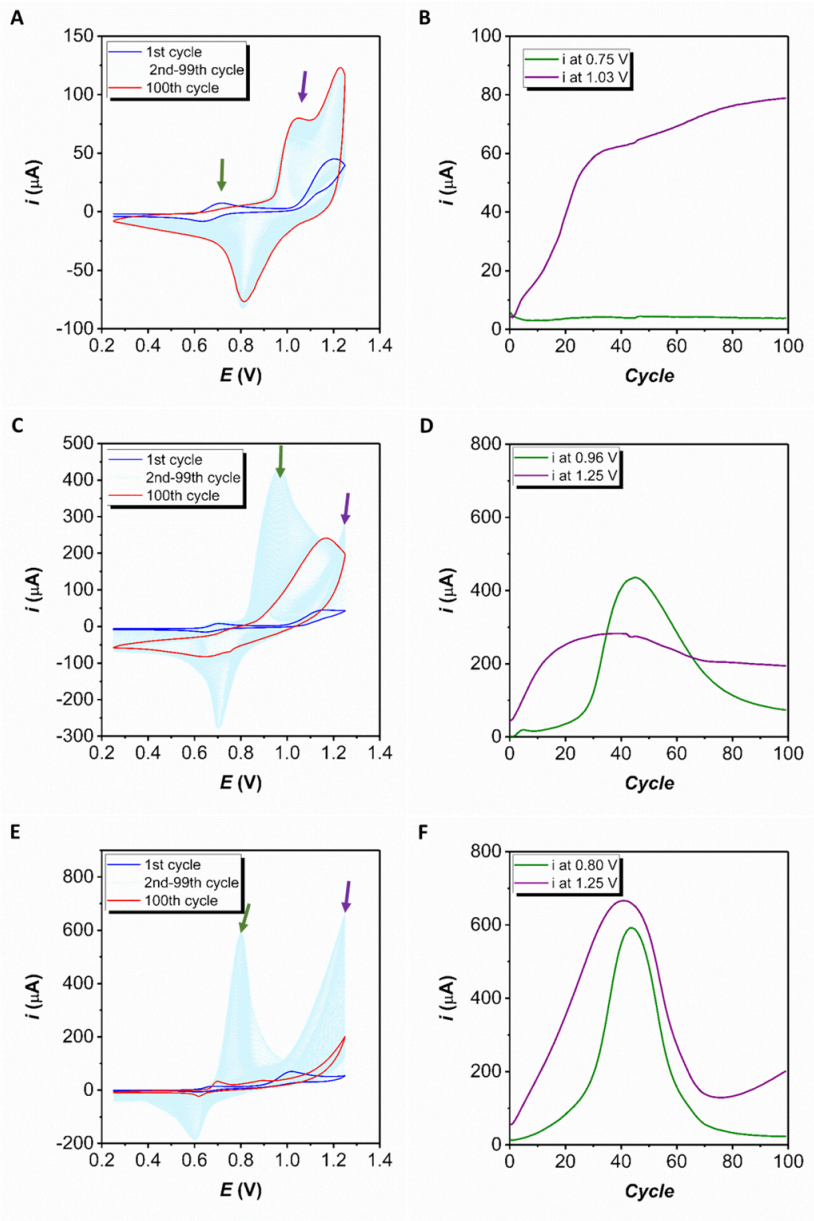

Figure 4. (A) 100 consecutive CVs in an aqueous solution containing 1 mM of $\mathbf{1}^{2-}$ at pH 11. (B) Evolution of the intensity at 0.75 V and 1.03 V with the consecutive cycles. (C) 100 consecutive CVs in an aqueous solution containing 1 mM of $\mathbf{1}^{2-}$ at pH 12. (D) Evolution of the intensity at 0.96 V and 1.25 V with the consecutive cycles. (E) 100 consecutive CVs in an aqueous solution containing 1 mM of $\mathbf{1}^{2-}$ at pH 13. (B) Evolution of the intensity at 0.80 V and 1.25 V with the consecutive cycles.

An extension to Nickel

At pH = 11 the repetitive CVs displayed in Figure 4A and analyzed in Figure 4B, show that the wave associated with NiOx/NiOOHx (intensity at 1.03 V represented as the purple line) increases as the III/II wave of the complex (intensity at 0.75 V, green line) decreases suggesting that the dominant pathway here is the formation of the NiOx/NiOOHx. Interestingly the amount of deposited oxide increases mainly linearly up to 25 cycles and then slightly levels off suggesting a saturation at the surface of the electrode. The catalytic activity of this NiOx/NiOOHx lies at higher potentials that are not represented in the CV scale.

At pH = 12, the formation of the NiOx/NiOOx takes place readily reflecting the high impact of increasing the pH (Figure 4C). At the initial cycles the activity of the formed NiOx, represented by the intensity at 1.25 V (orange line), lies at similar potential as the catalytic wave of the molecular complex and grows linearly while the amount of deposited NiOx remain low as can be inferred from the current intensity at 0.96 V (purple line). After an induction period of around 20 cycles, the deposition of NiOx increases exponentially while the activity reaches a plateau. After 40 cycles the deposited NiOx starts to redisolve as reflected by the strong decay in the intensity whereas the activity keeps approximately constant. Finally, at pH 13, Figures 3 E,F, a similar behavior is found except for the activity of the NiOx that after reaching 40 cycles, decreases together with the amount of deposited NiOx. These last results at pH > 12 indicate that, beside the NiOx/NiOOHx formation, there is a second process that dissolves that material in the solution taking place at longer timescale.

F.2.2.3. The impact of the applied potential (E_{app})

The stability of $\mathbf{1}^{2-}$ was also analyzed as a function of the applied potential using potentiostatic methodologies. Controlled potential electrolysis (CPE) experiments were first conducted at a lower potential of 0.85 V

(Figure S11) where just the one electron oxidized Ni(III) species $\mathbf{1}^{-}$ is generated. At pH < 12 the molecular complex was stable against degradation and formation of NiOx/NiOOHx. On the other hand, NiOx/NiOOHx was confirmed after CPE at pH 12-13 by a continuous increase in the electrochemical activity of the used electrode when analyzed in a fresh buffer solution (Figure S11C, D). EDX and XPS confirmed the presence of NiOx species at higher pHs but only for the electrodes with high loading (Figure S26). This fact reflects the high sensitivity of the electrochemical techniques to detect even low amounts of deposited materials with characteristic redox features. When the same experiment of generating $\mathbf{1}^{-}$ potentiostatically is performed in pH 12 solutions and at lower potential (E_{app} =0.7 V), formation of NiOx is avoided as depicted in Figure 5A,B. This is in sharp contrast to the results obtained with a similar experiment at E_{app} = 0.7 V in the presence of free metal ions, which showed a clear formation of NiOx on the electrode (Figure S12). All these results confirm that NiOx deposited from $\mathbf{1}^{-}$ comes from Ni ions in solutions, which are generated by the substitution reactions in equations 1-4 under certain E_{app} and pH conditions.

An extension to Nickel

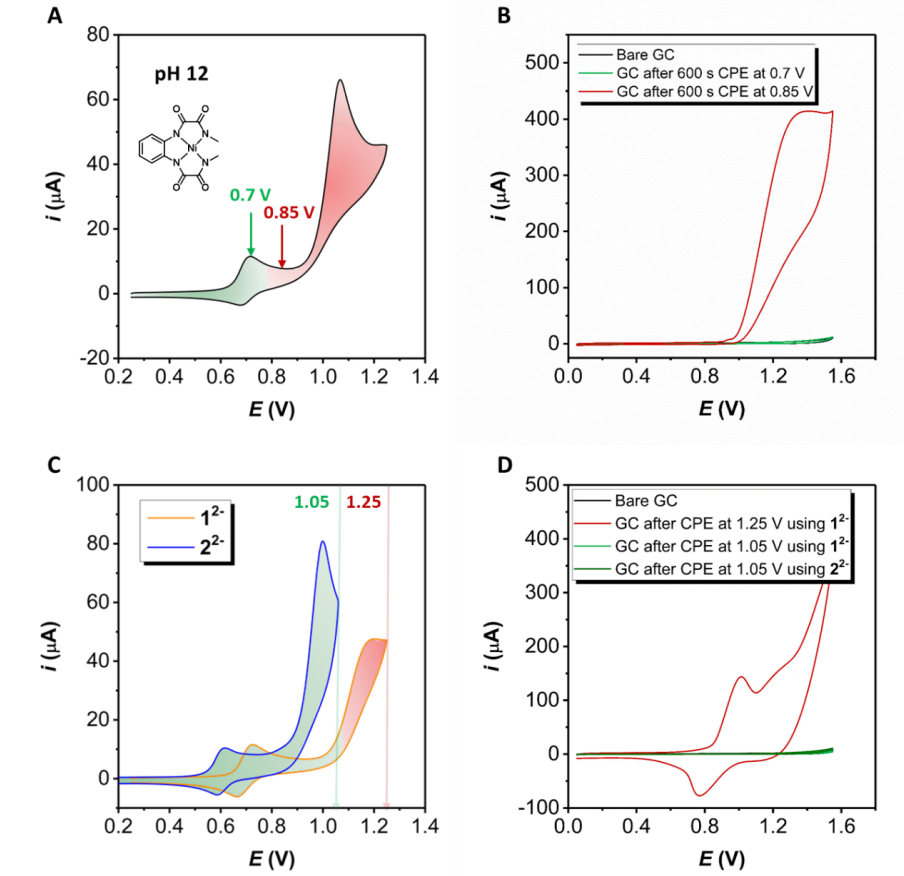

VI

Figure 5. (A) CVs of 1mM solution of complex $\mathbf{1}^{2-}$ in aqueous phosphate buffer at pH 12. (B) CVs in a fresh buffer solution at pH 12 of a bare GC electrode (black line) and GC electrodes after CPE in a 1mM solution of $\mathbf{1}^{2-}$ at different potentials (red and green lines). (C) CVs of 1mM solution of complex $\mathbf{1}^{2-}$ and $\mathbf{2}^{2-}$ in aqueous phosphate buffer at pH 11. (D) CVs in a fresh buffer solution at pH 11 of a bare GC electrode (black line) and GC electrodes after 3600 s CPE at 1.25 V (red line) and 1.05 V (green line) in a 1mM solution of $\mathbf{1}^{2-}$ and $\mathbf{2}^{2-}$ respectively. Green and red zones represent the conditions under which NiOx was present and absent respectively after CPE. GC disk was used as working electrode and the scan rate was set to 100 mV/s.

CPE experiments were also conducted at higher potentials to assess the stability under catalysis. Figure 5C,D shows the response of the electrode in a clean electrolyte solution after applying higher potentials of 1.05 and 1.25 V for 1h at pH 11. At the E_{app} = 1.05 V no NiOx can be observed and thus manifests the high stability of the Ni(III) species in $\mathbf{1}^{-}$ (green line,

Figure 5D) indicating that the substitution processes shown in equations 1-4 are negligible under these conditions. However, when the E_{app} = 1.25 V, the formation of the NiOx is evident (red line, Figure 5D)and thus points out towards the degradation of the initial molecular complex as was described for the previous section using voltammetric techniques.

At pH 10, similar behavior is observed with formation of NiOx only at the highest potential of 1.25 V (Figure S14 and S15). At pH values of 12 and 13, NiOx is also formed under catalytic conditions, although the speed of formation and the final NiOx amount is much higher than at lower pH values, which is in agreement with previous voltammetric measurements (Figure S14 and S15). Moreover, similar saturation process and final decay of the NiOx activity are present at pH 12 and 13, since the catalytic activity of the NiOx increases during the first 120 s but then it significantly decreases until 600 s.

F.2.2.4. The unique case of stabilization by Me groups in $\mathbf{2}^{2-}$

Similar experiments were carried out for $\mathbf{2}^{2-}$, where the benzene ring is substituted with two methyl groups with regard to $\mathbf{1}^{2-}$. As already mentioned, at an E_{app} = 1.05 V for 1h at pH 11, catalyst $\mathbf{1}^{2-}$ does not degrade to form NiOx, even though at this potential the catalytic current is rather low. In contrast, catalyst $\mathbf{2}^{2-}$ shows high current intensity values in the same experimental conditions due to the cathodic shift of the waves induced by the electron-donating methyl groups. Thus, at E_{app} = 1.05 V the reaction takes place well beyond the electrocatalytic current for $\mathbf{2}^{2-}$ (Figure 5C). Interestingly, this complex shows a spectacular stability as demonstrated by the absence of any NiOx absorbed at the electrode (Figure 5D). These results reveal that neither equations 1-4 nor the deactivation process proposed for the cation radical $[(L^{1\cdot})Ni^{III}(OH)]^{-}$ operate at any significant length. On the other hand, as in the previous case, increasing the pH increases the OH^- concentration that in turn habilitate the deactivation pathways. Thus, similar experiments carried out for $\mathbf{2}^{2-}$ at pH 12

An extension to Nickel

and 13 generate NiOx at the surface of the electrode as can be seen in Figure S17.

The high stability of complex $\mathbf{2}^{2-}$ under catalytic conditions in pH 11 shown in Figure 5C,D is not only very remarkable but actually unprecedented in molecular Ni complexes. The extra stability of the $\mathbf{2}^{2-}$ as compared to $\mathbf{1}^{2-}$ is due to the electronic effects exerted by the two methyl groups at the aromatic moiety of the ligand over the stability of singly and doubly oxidized Ni(III) and Ni(III)-OH-radical cation species. This electronic effect can be appreciated in the CV of Figure 5C for $\mathbf{2}^{2-}$ where the redox potentials decrease by approximately 200 mV for each redox couple with respect to that of $\mathbf{1}^{2-}$.

F.2.3. Molecular catalyst stability in heterogeneous phase

To test the stability of the molecular catalyst in heterogeneous phase, complex $\mathbf{1}^{2-}$ was anchored on Graphene sheets via pi-pi stacking interactions in a similar manner as it had previously been done for related Cu complexes with the same ligand.[33] The procedure consists of suspending the Graphene sheets in a 1 mM of the complex and stirring the mixture overnight. After separation and washing of the functionalized graphenic material, it was dropcasted on a glassy carbon (GC) electrode generating the $\mathbf{G@1}^{2-}$ hybrid materials (see experimental section in the SI for additional details).

The performance of $\mathbf{G@1}^{2-}$ was assessed by electrochemical techniques including CV, DPV and rotating ring disk electrode (RRDE). The CVs at pH 10-14 are displayed in Figure 6A, which shows a relatively similar behavior as in homogeneous phase except that the onset of the catalytic waves are shifted by 100 mV toward the cathodic region. This is a result of the pi-interaction of the graphene with the pi- system of complex $\mathbf{1}^{2-}$, in a similar manner as had been previously observed for the Cu analogue $[(L^1)Cu]^{2-}$, $\mathbf{4}^{2-}$.[33]

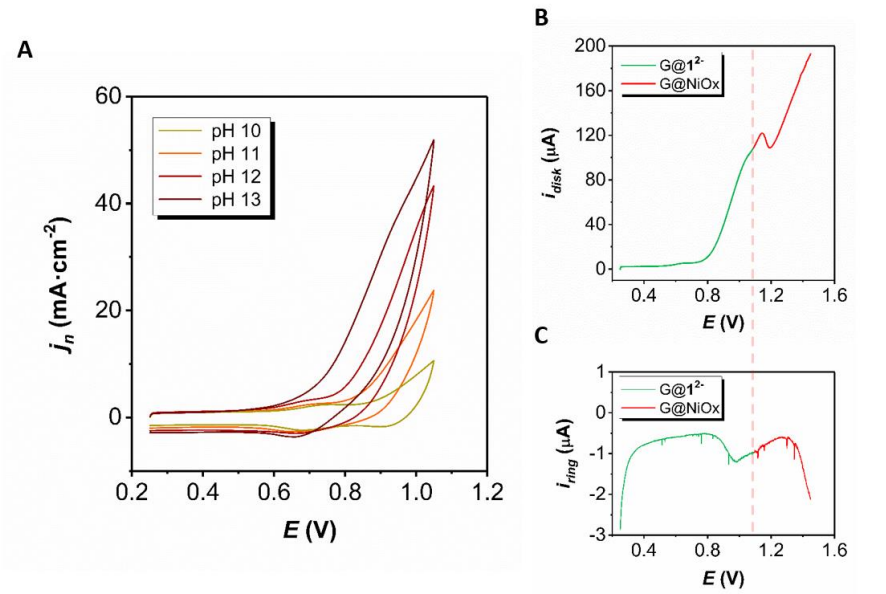

Figure 6. (A) CVs of **G@1^{2-}** electrodes in aqueous solutions at different pH values (B) LSV of **G@1^{2-}**/NiOx generated after cycling a **G@1^{2-}** electrode for four times in the range from 0.3 to 1.05 V. The hybrid material was supported on the disk of a RRDE in phosphate buffer at pH 11. Experiment was performed under nitrogen atmosphere and at 1600 rpm. (C) Simultaneous CPE at -0.35 V performed in the Pt ring of the RRDE for the reduction of the generated oxygen. Green color represents the molecular domain while red color refers to the electrochemical response of the NiOx.

Repetitive cyclic voltammetric experiments (Figure S18) similar to the ones performed in homogeneous phase display a relatively similar behavior and thus show that the anchoring process do not stabilize the molecular catalyst against the formation of NiOx.

To further characterize these hybrid materials the graphene sheets functionalized with **1^{2-}** were deposited at the surface of the graphitic working electrode of a RRDE and the results are displayed in Figure 6B,C and S19. A linear sweep voltammetry (LSV) at 2 mV/s from 0.3 to 1.5 V for **G@(1^{2-}/NiOx)** is shown in Figure 6B at pH 11.0 after depositing a mixture of the molecular catalyst and NiOx at the surface of the working electrode, following the protocol described in the SI, while the ring disk

An extension to Nickel

potential was fixed at -0.35 V where the reduction of oxygen to superoxide occurs (Figure 6C).[33]The Figures show that the first release of oxygen is detected under the catalytic wave of the molecular species, at potential values between 0.65 and 0.80 V. Further, there is a second increase in the oxygen detected due to the NiOx at higher potentials (with onset at ca. 1.3 V). The two phenomena can be clearly distinguished since the rate at which oxygen is formed is different and this is translated into a change in curvature that is clearly appreciated in Figure 6B and C. Similar phenomena can be observed at other pHs as shown in Figure S19.

F.2.4 Preparation and water oxidation performance of NiFeOOH from NiL

As already demonstrated, NiOx owes its high activity for water oxidation partly due to the incorporation of Fe impurities from the solution forming $Ni_{1-x}Fe_x(OH)_2$ films. [34,35] It has been found that an iron composition between 5-25% provide the electrodes with the maximum activity at the lowest overpotential. Therefore, using the optimal conditions that we found for NiOx deposition from the homogeneous catalyst **1^{2-}** (CPE at 0.85 V and pH 13, Figure S20) we prepared new $Ni_{1-x}Fe_x(OH)_2$ electrodes in the presence of 0.05 mM of $Fe^{II}(ClO_4)_2$, based on reported methodologies for cathodic codeposition (SI for details).[36] As expected, this procedure led to electrodes with largely improved catalytic performance in comparison with the previous ones due to the greater incorporation of Fe atoms in the oxide structure (Figure 7). XPS and EDX analysis of the material deposited on GC plates electrodes confirm the presence of $Ni_{1-x}Fe_x(OH)_2$ species on the surface, with around 7-10% of Fe (Figure S27 and S28). SEM images of the same electrodes revealed the formation of a film of material extended over the whole surface of the electrode (Figure S29).

Control of the total charge passed in the CPE during deposition resulted in different loadings of this material, as calculated by integration of the oxidative Ni^{II}/Ni^{III} wave (Figure S21 and S22).[37] The calculated surface

coverage ranged from 1 to a maximum of 50 nmol·cm^{-2}, which are in general low loading values compare to most of the reported $Ni_{1-x}Fe_x(OH)_2$ materials prepared with different methods.[36] This fact can be explained as there is only a partial degradation of the molecular complex induced by the electrode within the time scale of the CPE (0-600s).

We also analyzed the Electrochemically Active Surface Area (ECSA) measuring the non-Faradaic capacitive current as a function of the scan rate[38] (Figure S23) resulting in an average value of 0.17 ± 0.06 cm^2. The ECSA was calculated for the different electrodes but in all the cases the value ranged from 0.075 to 0.218 cm^2 without apparent dependence on the loading. This suggests that the increase in the metal loading increases the number of internal layers, keeping the electroactive surface and thus the exposed catalytic sites approximately constant. These values for the ECSA are relatively low compared to other reported NiFeOx, as expected from the low loading.

We further assessed the performance of these active electrodes following standard methodologies previously described to compare metal oxides.[37,38] Firstly, using a RRDE we evaluated the Faradaic efficiency for water oxidation, resulting essentially in 100% as reported for many other oxides in alkaline conditions (Figure S24). As metrics to compare the catalytic activity of heterogeneous metal oxides, many parameters have been described, referred to the amount of deposited material. The most popular ones are the specific current density and the Turnover Frequency (TOF) at certain overpotential (normally 300-350 mV), as defined in the literature.[37,38] These two standard parameters allow for fair comparison among the catalyst reported, so we have calculated them as a function of the loading of our active electrodes. As deducted from the results summarized in Figure S25, the current density at η=300 mV decreases as the loading of the electrode increases, featuring the maximum values between 1 and 6 nmol·cm^{-2}. Figure 7A shows the CV for an electrode featuring one of the maximum current densities of around 3.57 and 11.77 mA·cm^{-}

An extension to Nickel

^{2} at 300 and 350 mV respectively, or 1.42 and 4.86 mA·cm^{-2} considering the ECSA instead of geometric area. Those maximum values are among the highest reported for NiFeOx electrodes, despite the low loading and ECSA values of our electrodes.[18,37,38,39,40,41,42] Similar observation were made when analyzing the TOF at η=300 and 350 using the integration of the Ni(II)/Ni(III) oxidation peak as measurement for the estimation of the total metal sites. There is a significant increase in the TOF as the deposited material decreases, reaching maximum values around 2 and 11 s^{-1} at overpotential values of 300 and 350 mV respectively (Figure 7B). Those TOF values exceed other high performance NiFeOx catalysts as well as other metal oxides electrodes, although comparison should be made carefully according to the employed TOF calculation method.[37]

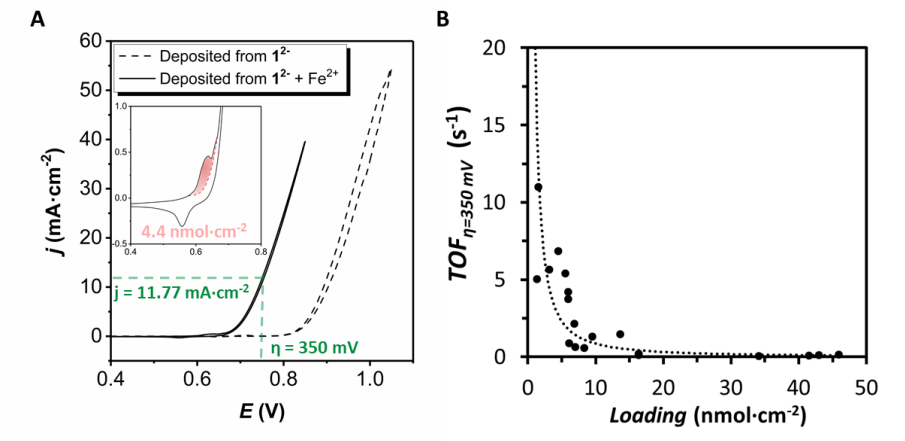

Figure 8. (A) CV of one NiFeOx on GC electrode in a 1 M KOH aqueous solutions at 10 mV/s. Inset shows a zoom of the redox wave corresponding to the Ni^{II}/Ni^{III} couple with a loading of 4.4 nmol·cm^{-2} calculated from integration of the red area. (B) Representation of the TOF values calculated at η=350 mV for electrodes with different loading values.

These results demonstrate that there is a clear benefit when codepositing $Ni_{1-x}Fe_x(OH)_2$ from the molecular Ni complex **1**$^{2-}$ by degradation due to molecule-electrode interactions, compared to traditional methods.

F.3. Conclusions

The present work shows how slight modification of different experimental conditions namely, pH, E_{app}, time of exposure (scan rate) can determine the robustness of molecular Ni complexes influencing both the amount and nature (electrocatalytic activity) of the derived NiOx/NiOOx species (particle size and morphology) and the stability of the oxide attached at the surface of the electrode. Further, it also discloses the complex reaction system involved during the catalyst activity in homogeneous phase and its progressive anchoring and water oxidation activity in solid supports. It thus brings light to this very thin border between the homogeneous and heterogeneous activity summarized in Scheme 1 and Figure 8. Moreover, it is striking to see the spectacular increase of stability of the molecular **2**$^{2-}$ complex, with Me-substituted ligand L^2, as compared to L^1 under exactly the same conditions and thus manifest how small variations on the organic ligands can strongly influence the combination of reactions involved in the catalyst behavior.

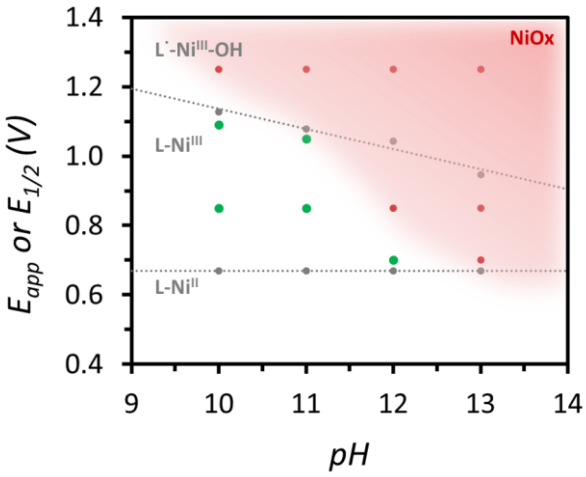

Figure 8. Pourbaix diagram of complex **1**$^{2-}$ with experimental redox potential as grey points. Points in green represent the CPE performed in those pH and E_{app} conditions that did not form NiOx whereas points in red represent the CPE where NiOx was detected on the electrode.

An extension to Nickel

Overall the work described here indicates how thorough, cautious and careful analysis and interpretations should be done to fully understand the complicated behavior of Ni complexes as water oxidation catalysts.

F.4. Acknowledgments

MINECO and FEDER are gratefully acknowledged (CTQ2016-80058-R, CTQ2015-73028-EXP, SEV 2013-0319, ENE2016-82025-REDT (FOTOFUEL), CTQ2016-81923-REDC (INTECAT). P. G.-B. acknowledges "La Caixa" foundation for the PhD grant.

F.4. References

1 McEvoy, J. P.; Brudvig, G. W. *Chem. Rev.* **2006**, *106*, 4455-4483.

2 Melis, A. *Energy Environ. Sci.* **2012**, *5* (2), 5531–5539.

3 Berardi, S.; Drouet, S.; Francàs, L.; Gimbert-Suriñach, C.; Guttentag, M.; Richmond, C.; Stoll, T.; Llobet, A. *Chem. Soc. Rev.* **2014**, *43* (22), 7501–7519.

4 Nocera, D.G. *Acc. Chem. Res.* **2017**, *50*, 616-619.

5 Kärkäs, M. D.; Åkermark, B. *Dalton Trans.* **2016**, *45* (37), 14421–14461.

6 Wang, N.; Zheng, H.; Zhang, W.; Cao, R. *Chin. J. Catal.* **2018**, *39*, 228-244.

7 Singh, A.; Spiccia, L. *Coord. Chem. Rev.* **2013**, *257*, 2607-2622.

8 Garrido-Barros, P.; Gimbert-Suriñach, C.; Matheu, R.; Sala, X.; Llobet, A. *Chem. Soc. Rev.* **2017**, *46* (20).

9 Sheelan, S. W.; Thomsen, J. M.; Hintermair, U.; Crabtree, R. H.; Brudvig, G.W.; Schmuttenmaer, C. A. *Nat. Commun.* **2015**, *6*, 6469-6477.

10 Francàs, L.; Sala, X.; Benet-Buchholz, J.; Escriche, L.; Llobet, A. *ChemSusChem*, **2009**, *2*, 321–329.

11 Sander, A. C.; Schober, A.; Dechert, S.; Meyer, F. *Eur. J. Inorg. Chem.* **2015**, 4348–4353.

12 Radaram, B.; Ivie, J. A.; Singh, W. M.; Grudzient, R. M.; Reibenspies, J. H.; Webster C. E.; Zhao, X. *Inorg. Chem.* **2011**, *50*, 10564–10571.

13 Ellis, W. C.; McDaniel, N. D.; Bernhard, S.; Collins, T. J. *J. Am. Chem. Soc.* **2010**, *132*, 10990–10991.

14 Wang, J.-W.; Sahoo, P.; Lu, T.-B. *ACS Catal.* **2016**, *6*, 5062-5068

15 Hong, D.; Mandal, S.; Yamada, Y.; Lee, Y.-M.; Nam, W.; Llobet, A.; Fukuzumi, S. *Inorg. Chem.* **2013**, *52*, 9522-9531.

16 Daniel, Q.; Ambre, R. B.; Zhang, B.; Philippe, B.; Chen, H.; Li, F.; Fan, K.; Ahmadi, S.; Rensmo, H.; Sun, L. *ACS Catal.* **2017**, *7*, 1143–1149

17 Najafpour, M. M.; Feizi, H. *Catal. Sci. Technol.* **2018**, *8*, 1840-1848.

18 Singh, A.; Chang, S. L. Y.; Hocking, R. K.; Bach, U.; Spiccia, L. *Energy Environ. Sci.* **2013**, *6*, 579-586.

19 Singh, A.; Chang, S. L. Y.; Hocking, R. K.; Bach, U.; Spiccia, L. *Catal. Sci. Technol.* **2013**, *3*, 1725-1732.

20 Wang, D.; Ghiirlanda, G.; Allen, J. P. *J. Am. Chem. Soc.* **2014**, *136*, 10198-10201.

21 Najafpour, M. M.; Feizi, H. *Dalton Trans.* **2018**, *47*, 6519-6527

22 Han, Y.; Wu, Y.; Lai, W.; Cao, R. *Inorg. Chem.* **2015**, *54*, 5604-5613.

23 Lin, J.; Kang, P.; Liang, X.; Ma, B.; Ding, Y. *Electrochimica Acta*, **2017**, *258*, 353-359.

24 Wang, D.; Bruner, C. O. *Inorg. Chem.* **2017**, *56*, 13638-13641.

25 Garrido-Barros, P.; Funes-Ardoiz, I.; Drouet, S.; Benet-Buchholz, J.; Maseras, F.; Llobet, A. *J. Am. Chem. Soc.* **2015**, *137*, 6758-6761.

26 Ottenwaelder, X.; Aukauloo, A.; Journaux, Y.; Carrasco, R.; Cano, J.; Cervera, B.; Castro, I.; Curreli, S.; Muñoz, M. C.; Roselló, A. L.; Soto, B.; Ruiz-García, R. *Dalton Trans.* **2005**, *0*, 2516-2526.

27 Costentin, C.; Drouet, S.; Robert, M.; Savéant, J.-M. *J. Am. Chem. Soc.* **2012**, *134*, 11235.

28 Ottenwaelder, X.; Ruiz-García, R.; Blodin, G.; Carrasco, R.; Cano, J.; Lexa, D.; Journaux, Y.; Aukauloo, A. *Chem. Commun.,* **2004**, *0*, 504-505.

29 Wang, J.-W.; Hou, C.; Huang, H.-H.; Liu, W.-J.; Ke, Z.-F.; Lu, T.-B. *Catal. Sci. Technol.* **2017**, *7*, 5585-5593.

30 Luo, G.-Y.; Huang, H.-H.; Wang, J.-W.; Lu, T.-B. *ChemSusChem* **2016**, *9*, 485-491.

31 Zhang, M.; Zhang, M.-T.; Hou, C.; Ke, Z.-F.; Lu, T.-B. *Angew. Chem. Int. Ed.* **2014**, *53*, 13042-13048.

32 Wang, L.; Duan, L.; Ambre, R. B.; Daniel, Q.; Chen, H.; Sun, J.; Das, B.; Thapper, A.; Uhlig, J.; Dinér, P.; Sun, L. *J. Catal.* **2016**, *335*, 72-78.

33 Garrido-Barros, P.; Gimbert-Suriñach, C.; Moonshiram, D.; Picón, A.; Monge, P.; Batista, V. S.; Llobet, A. *J. Am. Chem. Soc.* **2017**, *139*, 12907-12910.

34 Trotochaud, L.; Young, S. L.; Ranney, J. K.; Boettcher, S. W. *J. Am. Chem. Soc.* **2014**, *136*, 6744-6753.

35 Stevens, M. B.; Trang, C. D. M.; Enman, L. J.; Deng, J.; Boettcher, S. W. *J. Am. Chem. Soc.* **2017**, *139*, 11361-11364.

36 Dionigi, F.; Strassser, P. *Adv. Energy Mater.* **2016**, *6*, 1600621.

37 Stevens, M. B.; Enman, L. J.; Batchellor, A. S.; Cosby, M. R.; Vise, A. E.; Trang, C. D. M.; Boettcher, S. W. *Chem. Mater.* **2017**, *29*, 120-140.

38 McCrory, C. C. L.; Jung, S.; Peters, J. C.; Jaramillo, T. F. *J. Am. Chem. Soc.* **2013**, *135*, 16977-16987.

39 Chakthranont, P.; Kibsgaard, J.; Gallo, A.; Park, J.; Mitani, M.; Sokaras, D.; Kroll, T.; Sinclair, R.; Mogensen, M. B.; Jaramillo, T. F. *ACS Catal.* **2017**, *7*, 5399-5409.

40 Guo, D.; Qi, J.; Zhang, Q.; Cao, R. *ChemSusChem* **2017**, *10*, 394-400.

41 Görlin, M.; De Araújo, J. F.; Schmies, H.; Bernsmeier, D.; Dresp, S.; Gliech, M.; Jusys, Z.; Chernev, P.; Kraehnert, R.; Dau, H.; Strasser, P. *J. Am. Chem. Soc.* **2017**, *139*, 2070-2082.

42 Qi, J.; Zhang, W.; Xiang, R.; Liu, K.; Wang, H.-Y.; Chen, M.; Han, Y.; Cao, R. *Adv. Sci.* **2015**, *2*, 1500199.

An extension to Nickel

F.6. Supporting information

Experimental Section

Materials

All the chemicals used in this work were provided by Sigma Aldrich Chemical Co and they have been used wihtout further purification. The solvents were selected to be HPLC grade and the deionized water was obtained with high purity by passing through a nanopore Milli-Q water purification system. Aqueous basic buffer solutions at pH 12 were prepared using the necessary amount of dibasic and tribasic sodium phosphate salts and adjusting the pH to the desired value so that the final ionic strength was 0.1 M.

Graphene was purchased from Nanostructured & Amorphous Materials, Inc. (NanoAmor) with a purity > 98%, 1-3 layers (1-3 nm of thickness), 2-10 μm of diameter and a specific surface area of about 500-700 $m^2 \cdot g^{-1}$.

GC plate electrodes were purchased from HTW, Germany, and are made of glassy carbon SIGRADUR® with the dimensions 20x10x0.18 mm.

Elemental Analysis and Mass Spectrometry

Elemental Analysis of the samples was carried out in a Thermo Finnigan elemental analyzer Flash 1112 model.

Exact mass analyses were performed with a micrOTOF mass spectrometer (from Bruker company) using Electrospray ionization technique in methanol by direct injection and detecting with positive polarity.

Spectroscopic Techniques

NMR spectroscopy was carried out in a 400 MHz Bruker Advance II spectrometer and a Bruker Advance 500 MHz. All the measurements

were done at room temperature in deuterated DMSO using residual protons as internal references.

UV-vis spectrometry was done using a Cary 50 (Varian) UV-vis spectrophotometer.

General electrochemistry

Cyclic Voltammetry (CV), Linear Sweep Voltammetry (LSV), Differential Pulse Voltammetry (DPV) and Controlled Potential Electrolysis (CPE) experiments were carried out on an IJ-Cambria CHI-660 potentiostat. We used a one-compartment three-electrode cell for these measurements. Glassy Carbon (GC) disk electrodes (3 mm of diameter) were used as working electrodes, Pt wire (unless indicated) as counter electrode, Mercury/Mercurous sulfate (K_2SO_4 sat.), MSE, as reference electrode for CV, LSV and DPV. For CPE, Silver/Silver Chloride (KCl sat.) was used as reference and either GC disk or GC plate (as indicated) as working electrode. All redox potentials in the present work are reported versus NHE by adding 0.65 V or 0.2 V to the measured potential, depending on whether MSE or Silver/Silver Chloride electrodes were employed respectively.

GC disk working electrode pretreatment for homogeneous phase analysis consisted first in two consecutive washes with HNO_3/HCl mixture (1:3) and KOH in propanol in order to remove the rest of metallic impurities deposited on the surface. Then, we continue by polishing with 0.05 μm alumina paste, rinsing after with water and acetone and blow-dried finally. GC disk used for catalyst deposition were polished with 1, 0.3 and 0.05 μm alumina paste, then rinsed with water and sonicated for 15 min in acetonitrile. Finally they were washed with acetone and blow-dried.

CVs and LSVs were collected at 100 $mV \cdot s^{-1}$ except other specification. DPV were obtained with the following parameters: amplitude= 50 mV, step height=4 mV, pulse width= 0.05 s, pulse period= 0.5 s and sampling

An extension to Nickel

width= 0.0167 s. $E_{1/2}$ values for the reversible waves were obtained from the half potential between the oxidative and reductive peaks, and the one for irreversible processes are estimated according to the potential at the I_{max} in DPV measurements. All the measurement were done applying IR compensation.

When acetonitrile was used as organic solvent, tetrabutylammonium hexafluorophosphate ($[NBu_4]PF_6$) was added in a concentration of 0.1M as supporting electrolyte.

Surface coverage (Γ) calculation

The surface coverage (Γ) was calculated based on electrochemical measurements according to the following formula:

$$\Gamma\ (mol \cdot cm^{-2}) = \frac{Q}{n \cdot S \cdot F}$$

Q is the charge under the oxidative peak of the reversible, one-electron wave obtained by integration in the CV; n is the number of electrons involved in that oxidation process, which is 1; S is the geometrical surface of the electrode that is 0.07 cm^{-2} or 1 cm^{-2} for GCd and GCp respectively; finally F is the Faradaic constant.

Calibration of the Rotating Ring Disk Electrode

The collection efficiency of the RRDE, N, was previously determined by using the redox couple $Fe(CN)_6^{4-}$ / $Fe(CN)_6^{3-}$ as well defined one-electron transfer process. We prepared a 1 mM solution of the reduced ferrocyanide $K_4Fe(CN)_6$ in pH 12 solution of phosphate buffer, and it was oxidized during a LSV at 10 $mV \cdot s^{-1}$ in the disk electrode to ferricyanide $Fe(CN)_6^{3-}$. This last was detected at the Pt ring by performing a CPE at 0.05 V vs NHE to yield the reduction to the initial ferrocyanide. The collection efficiency was determined by the rate between the intensity in the

ring and the intensity in the disk electrodes when they reach stable values at the plateau, i_{ring}/i_{disk}. The efficiency was found to be 0.4.

The oxygen reduction reaction was also studied at the Pt ring electrode under same experimental conditions to analyze the number of electrons involved, according to procedure described in the literature. For that, three different solutions were prepared at pH 12 with phosphate buffer: N_2 saturated, air saturated and O_2 saturated. Then a LSV at 10 $mV \cdot s^{-1}$ was performed through negative potentials to reduce the dissolved oxygen, that was detected by an increase in the ring current. In N_2, no current was detected as expected, while in air and O_2 current increased when the potential was negative enough to reduce the oxygen. In those last cases, the current reached an approximately stable signal at -0.6 V vs NHE. With these stable current values, the apparent number of electrons (n_{app}) involved in the reduction of oxygen can be calculated from the Levich equation for the rotating ring:

$$|i_{ring}| = 0.62 \cdot n_{app} \cdot F \cdot \pi \cdot (r_o^3 - r_m^3)^{2/3} \cdot D^{2/3} \cdot \omega^{1/2} \cdot \nu^{-1/6} \cdot [O_2]$$

F is the Faraday constant, r_o and r_m are the outer and middle radio that define the Pt geometry, D is the Difussion coefficient for oxygen in water calculated to be $2.52 \cdot 10^{-5}$ $cm^2 \cdot s^{-1}$ with Wilke's correlation,[1] ω is the rotation rate in $rad \cdot s^{-1}$, ν is the kinematic viscosity of the solution that is $0.0085 cm^2 \cdot s^{-1}$ and $[O_2]$ is the concentration of oxygen in the solution calculated to be $1.28 \cdot 10^{-6}$ $mol \cdot cm^{-3}$ for O_2 saturated solution and $2.67 \cdot 10^{-7}$ $mol \cdot cm^{-3}$ for air saturated solution.2 With all these values, the apparent number of electrons involved in the oxygen reduction turned out to be *ca.* 2 at 1600 r.p.m. for both air and oxygen saturated solutions, which means reduction of O_2 to H_2O_2 in pH 12 at -0.6 V vs NHE.

An extension to Nickel

Synthetic details and characterization

H_4L^1, H_4L^2 and $[(L^1)Ni](NMe_4)_2$

These compounds were prepared and characterized following the procedures already described in the literature.[3,4,5]

$[(L^2)Ni](NMe_4)_2$

To a suspension of ligand L2 (0.653 mmol, 0.200 g) in methanol (10 mL) was added (1.37 mL) a 25% wt. methanol solu-tion of NMe_4NOH. Afterwards a methanol solution of $Ni(ClO_4)_2.6H2O$ (0.653 mmol, 0.238 g) was added dropwise under stirring. A white solid of Me4NClO4 was formed that was filtered off and the solution was concentrated under vacuum using a rotatory evaporator. The Ni complex was then precipitated by adding ether and acetone, filtered off, washed with ether and dried under vacuum giving rise to a yellow to orange solid (0.309, 93%). ESI-MS (MeOH) m/z (negative mode): 361.0448 [(L2Ni+H]-. ^{1}H-NMR (500 MHz, DMSO-d6): δ [ppm]= 7.74 (s, 2H, H2), 2.36 (s, 6H, N-CH3), 1.98 (s, 6H, CH3). ^{13}C-NMR (DMSO-d6): δ [ppm] = 170.14 (C5, 2C), 163.82 (C4, 2C), 141.93 (C1, 2C), 126.13 (C5, 2C), 119.23 (C2, 2C), 32.93 (C6, 2C), 19.45 (C7, 2C).

$[(L^3)Ni](NMe_4)_2$

To a suspension of the corresponding ligand L3 (0.325 mmol, 0.100 g) in methanol (6 mL) was added (680 μL) a 25% wt. methanol solution of NMe_4NOH. Afterwards a methanol solution (3 cm^3) of $Ni(ClO_4)_2.6H2O$ (0.325 mmol, 0.121 g) was added dropwise under stirring. A white solid of Me_4NClO_4 was formed that was filtered off and the solution was concentrated under vacuum using a rotatory evaporator. The Ni complex was then precipitated by adding ether and acetone, filtered off, washed with ether and dried under vacuum leading to a yellow to orange solid (0.148 mg, 89%). ESI-MS (MeOH) m/z (negative mode): 363.0239 [(L3Ni+H]-

. ^{1}H-NMR (500 MHz, DMSO-d6): δ [ppm] = 7.82 (d, 3J = 8.6 Hz, 1H, H2'), 7.65 (d, 4J = 2.8 Hz, 1H, H2), 6.05 (dd, 3J = 8.5 Hz, 4J = 2.8 Hz, 1H, H1'), 3.57 (s, 3H, OCH3), 2.38 (s, 3H, N-CH3), 2.38 (s, 3H, N-CH3) . ^{13}C-NMR (500 MHz, DMSO-d6): δ [ppm] = 170.17 (C5, 1C), 169.80 (C5', 1C), 164.51 (C4, 1C), 163.44 (C4', 1C), 153.29 (C1, 1C), 144.81 (C3', 1C), 138.11 (C3, 1C), 117.07 (C2', 1C) 104.76 (C2, 1C), 104.09 (C1', 1C), 54.94 (Me-O-Ph), 1C), 32.95 (Me-N, 1C), 32.90 (Me-N, 1C)..

An extension to Nickel

NMR Spectroscopy

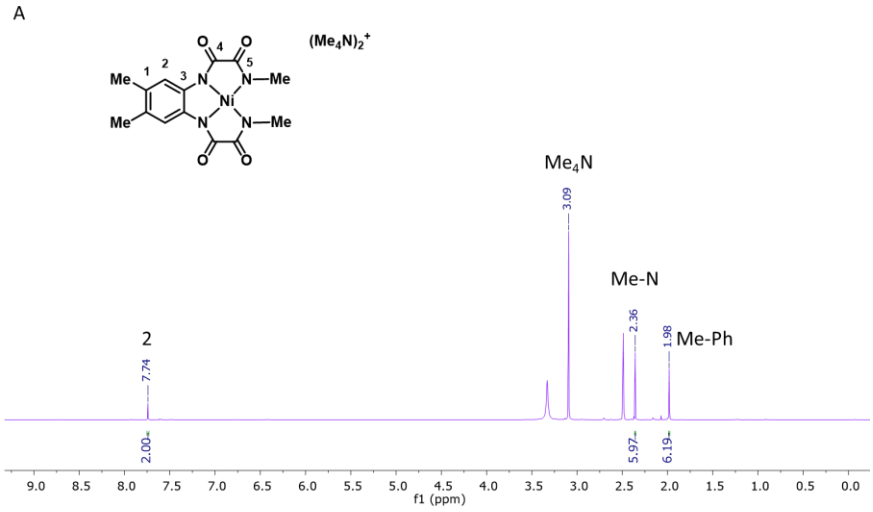

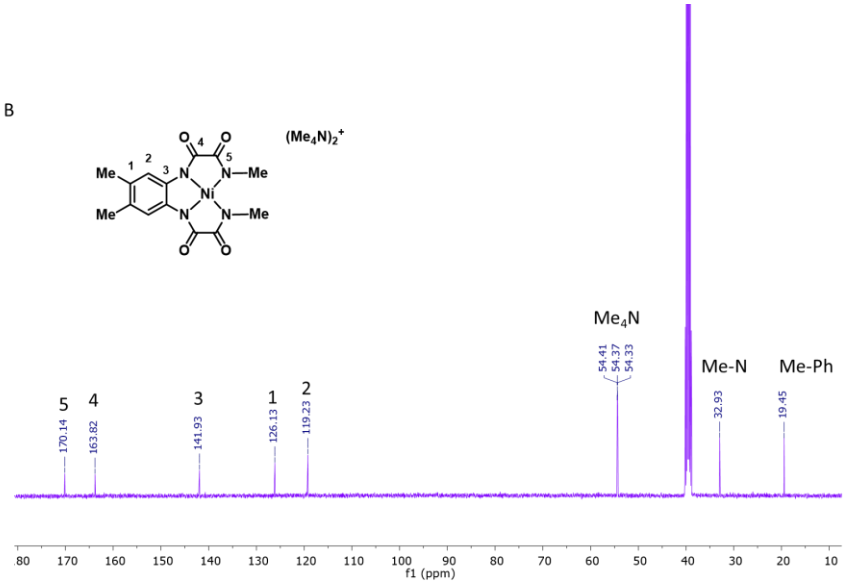

VI

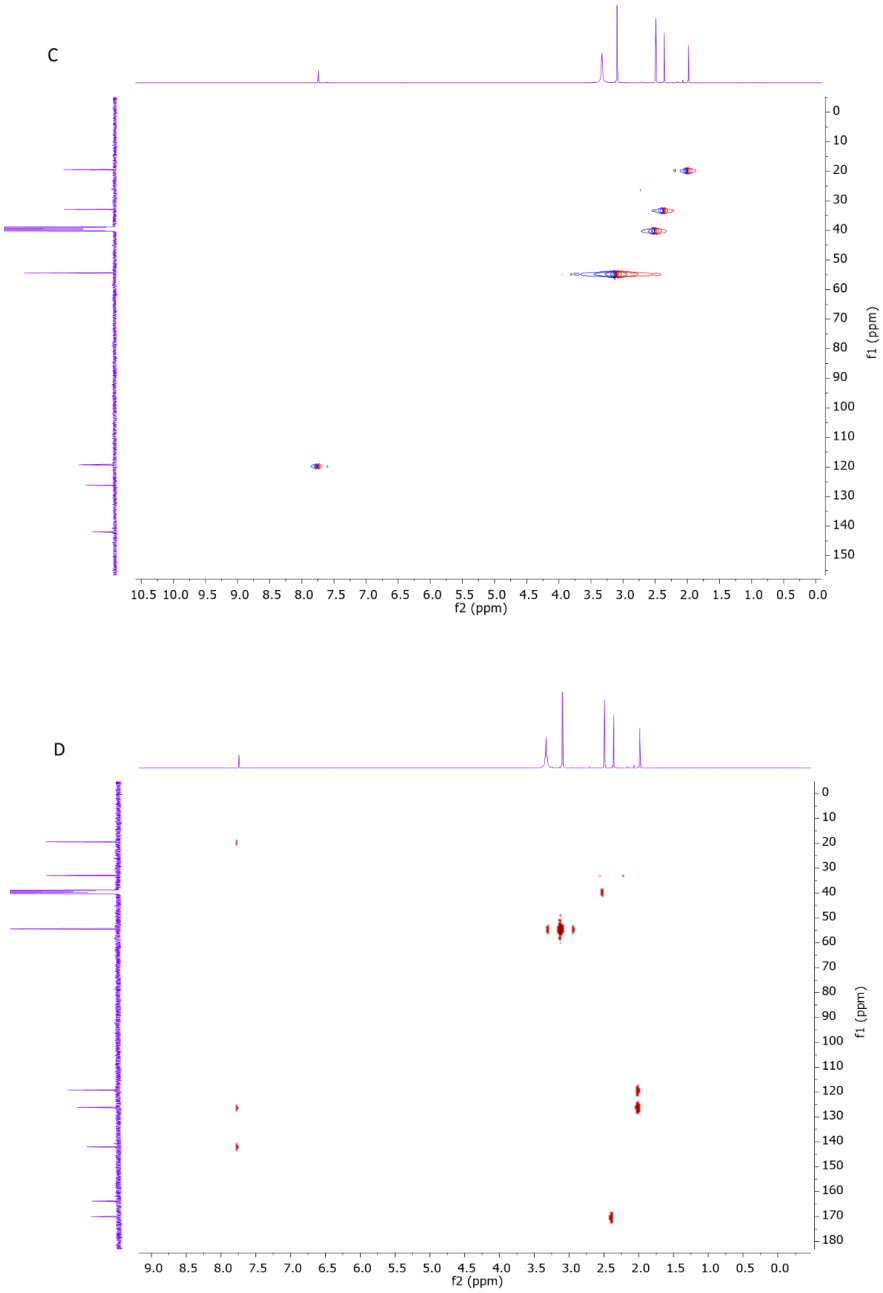

Figure S1. (A)^{1}H-NMR (B)^{13}C-NMR (C)HSQC (D)HMBC spectra of complex $[(L^{2})Ni^{II}]^{-2}$ in DMSO-d6.

An extension to Nickel

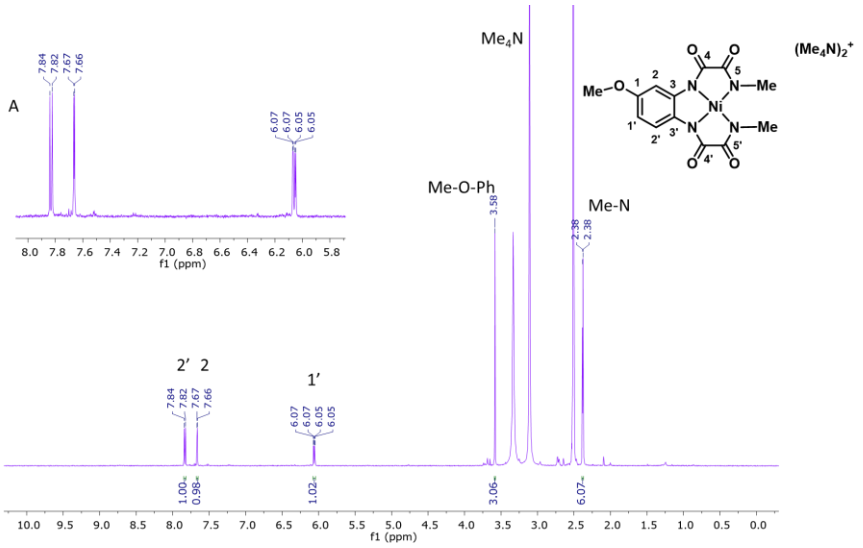

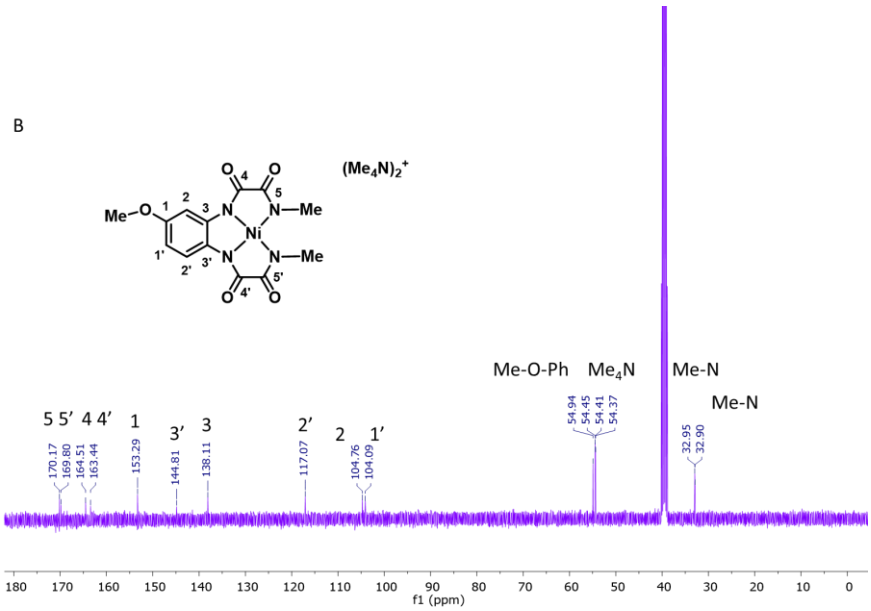

VI

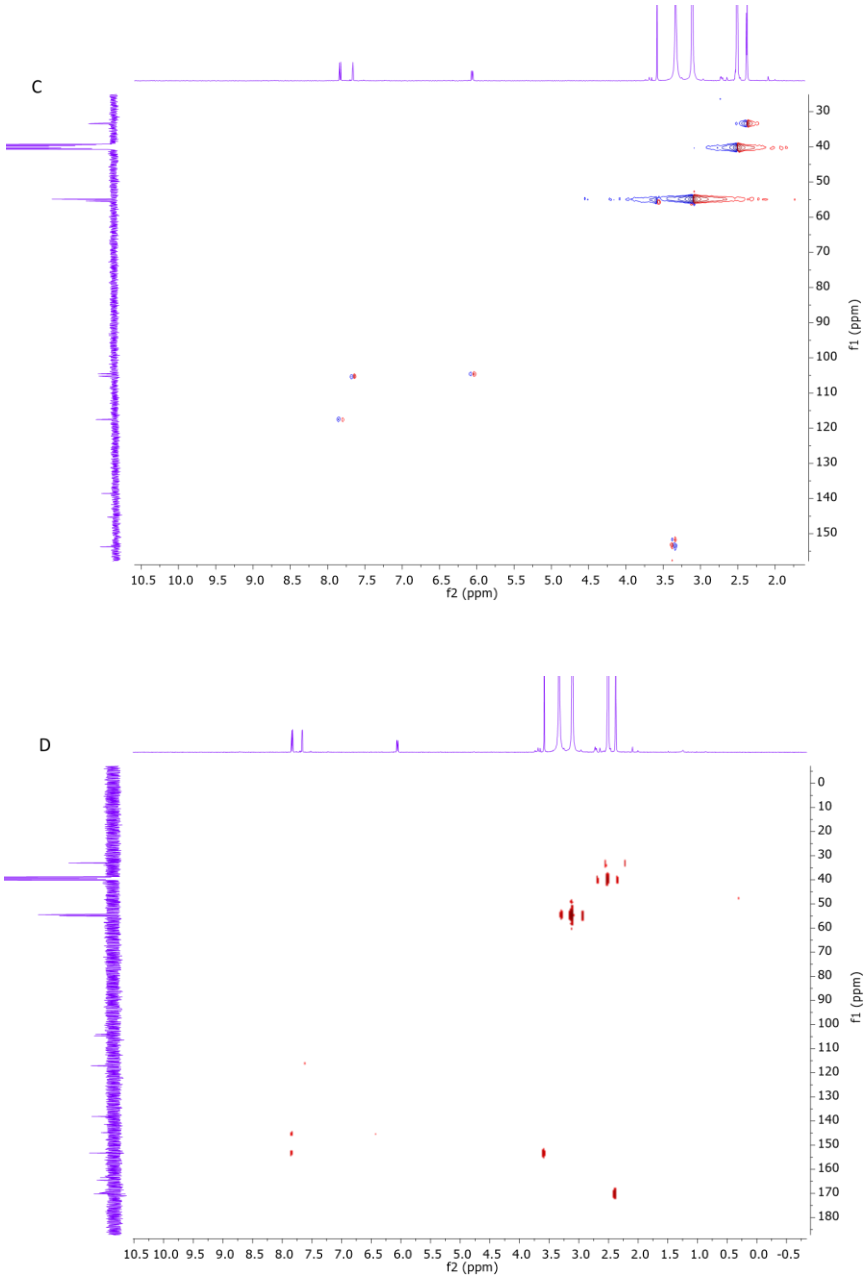

Figure S2. (A)^{1}H-NMR (B)^{13}C-NMR (C)HSQC (D)HMBC spectra of complex $[(L^{3})Ni^{II}]^{-2}$ in DMSO-d6.

An extension to Nickel

Electrode preparation

Preparation of G@1^{2-} electrodes

As supporting material, graphene (1-3 layers) deposited onto glassy carbon electrodes was used due to its high electroactive surface area and conductivity. Graphene is also produced extremely pure, without containing any catalytically active transition metal that would make the analysis harder due to their general high activity in basic solutions. The immobilization procedure consists in preparing a 1mM solution of either $\mathbf{1}^{2-}$ or $\mathbf{2}^{2-}$ in methanol; then graphene (1-3 layers) in a ratio of 1mg/ml solution was added forming a suspension that was sonicated for 15 minutes and stirred overnight, allowing enough time for the π-π interaction to cover the surface. This new modified material was separated from the solution, washed three times with fresh methanol and finally dispersed again in the same solvent. The electrode was prepared by dropcasting and evaporating 5 consecutive times 5 μL of that suspension on the surface of two kind of glassy carbon electrodes: glassy carbon disks (GCd, 0.07 cm^2) for most of electrochemical measurements and glassy carbon plates (GCp, 1 cm^2) for oxygen measurement and XAS experiments. The electrodes were finally dried under vacuum for 1 h and then were ready for use. They were named GC@G@$[(L1)Ni]^{2-}$ (**G-$\mathbf{1}^{2-}$**).

Preparation of G@1^{2-}/NiOx electrodes

The G@$\mathbf{1}^{2-}$ electrodes generated with the previous procedure were subjected to ten consecutive cycle voltammetries from 0.3 to 1.05 so that the molecular species partially degrades to NiOx diving rise to a certain mixture of both catalytic species attached to the same electrode. They were named G@$\mathbf{1}^{2-}$/NiOx.

Preparation of NiFeOx electrodes

A basic solution at pH 13 (0.1 M NaOH) containing 1 ml of catalyst $\mathbf{1}^{2-}$ and 0.05 mM of $Fe^{II}(ClO_4)_2$ was freshly prepared before each electrode preparation. Then a clean GC electrode were immersed and a CPE at 0.85 vs NHE was performed during different time in order to deposit diferent amount of material. Then the electrode was rinsed with abundant water and immersed in a 1 M KOH aqueous solution (pH 14) to perform a CPE at 0.15 V vs NHE during 300 s so that all the nickel species were reduced to Ni^{II} oxidation state. Therefore, quantification by integration of the Ni^{II}/Ni^{III} oxidation peak is accurate.

An extension to Nickel

Electrochemical analysis of molecular catalysts

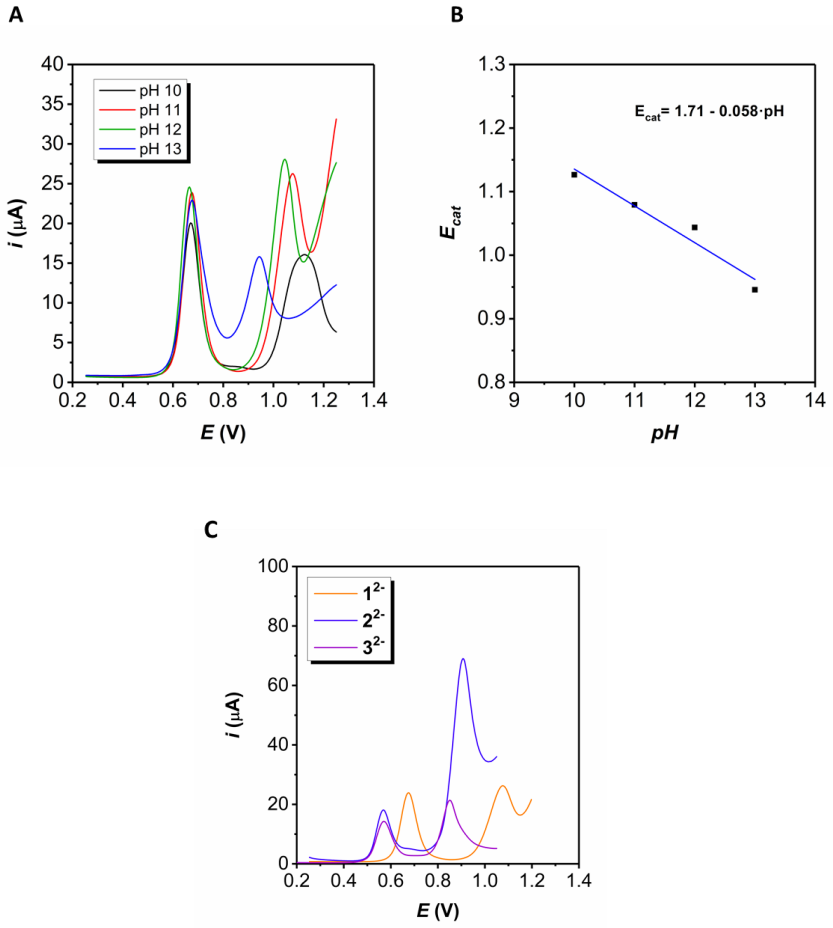

Figure S3. (A) DPVs of 1 mM $\mathbf{1}^{2-}$ in aqueous solutions at different pH values. GC disk was used as working electrode. (B) Dependence of the potential for second oxidation process on the pH and linear fit, showing that the slope is close to the predicted value for proton coupled electron transfer from the Nernst equation. (C) DPVs of an aqueous solutions containing 1 mM of $\mathbf{1}^{2-}$, $\mathbf{2}^{2-}$ and $\mathbf{3}^{2-}$ at pH 11. GC disk was used as working electrode.

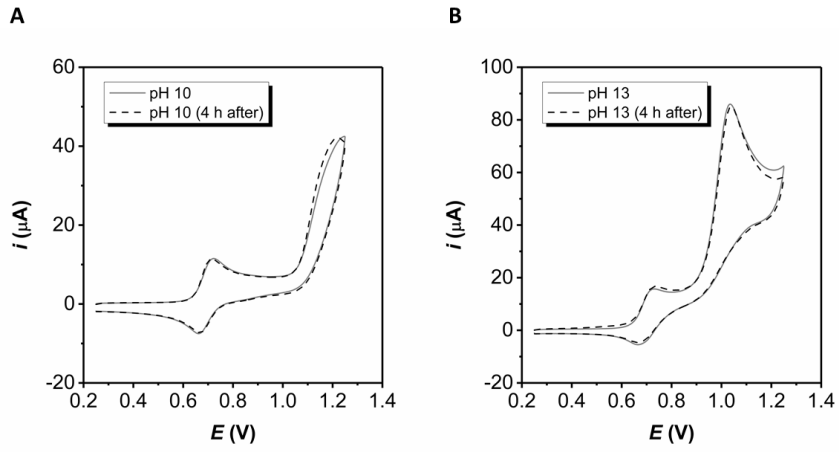

Figure S4. CVs of 1 mM $\mathbf{1}^{2-}$ in aqueous solution at pH 10 (A) and 13 (B) just dissolved (grey solid line) and after 4 hours of solution (dashed black line). GC disk was used as working electrode and the scan rate was set to 100 mV/s.

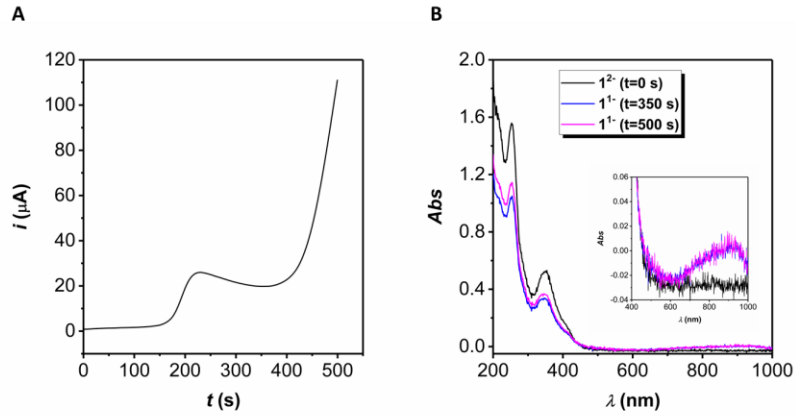

Figure S5. (A) LSVs of 1 mM $\mathbf{1}^{2-}$ in aqueous solution at pH 11 using a spectro-electrochemical cell with a Pt mesh working electrode, a Pt wire counter electrode and a mercurous sulfate reference electrode. The scan rate was 2 mV·s^{-1} and the path length of the cell was 1 mm. (B) UV-vis spectra recorded at different times during the previous LSV experiment.

An extension to Nickel

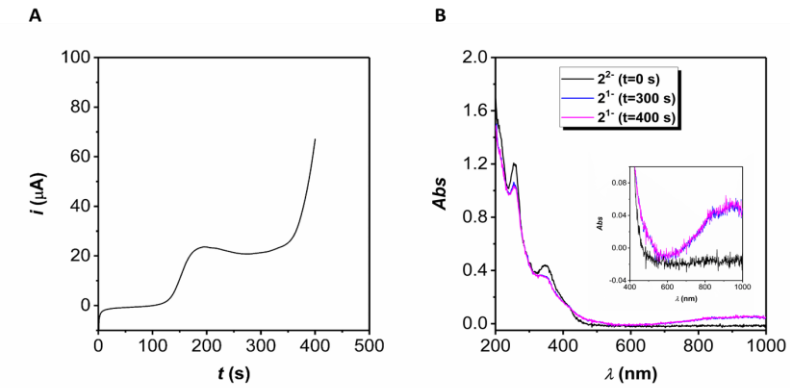

Figure S6. (A) LSVs of 1 mM **2²⁻** in aqueous solution at pH 11 using a spectroelectrochemical cell with a Pt mesh working electrode, a Pt wire counter electrode and a mercurous sulfate reference electrode. The scan rate was 2 $mV \cdot s^{-1}$ and the path length of the cell was 1 mm. (B) UV-vis spectra recorded at different times during the previous LSV experiment

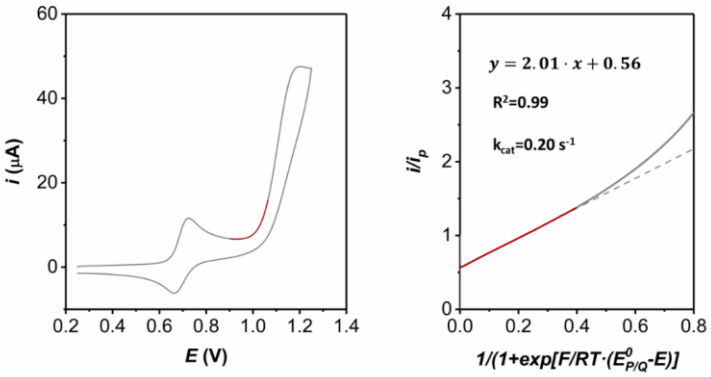

Figure S7. (A) CV of 1 mM **1²⁻** in aqueous solution at pH 11 using a GC disk as working electrode and the scan rate was set to 100 mV/s. The red line represents the data range corresponding to the the foot of the wave. (B) Foot of the wave analysis (FOWA) by plotting i_{cat}/i_d vs. $1/(1+\exp[(F/RT)(E^o_{cat}-E)])$.

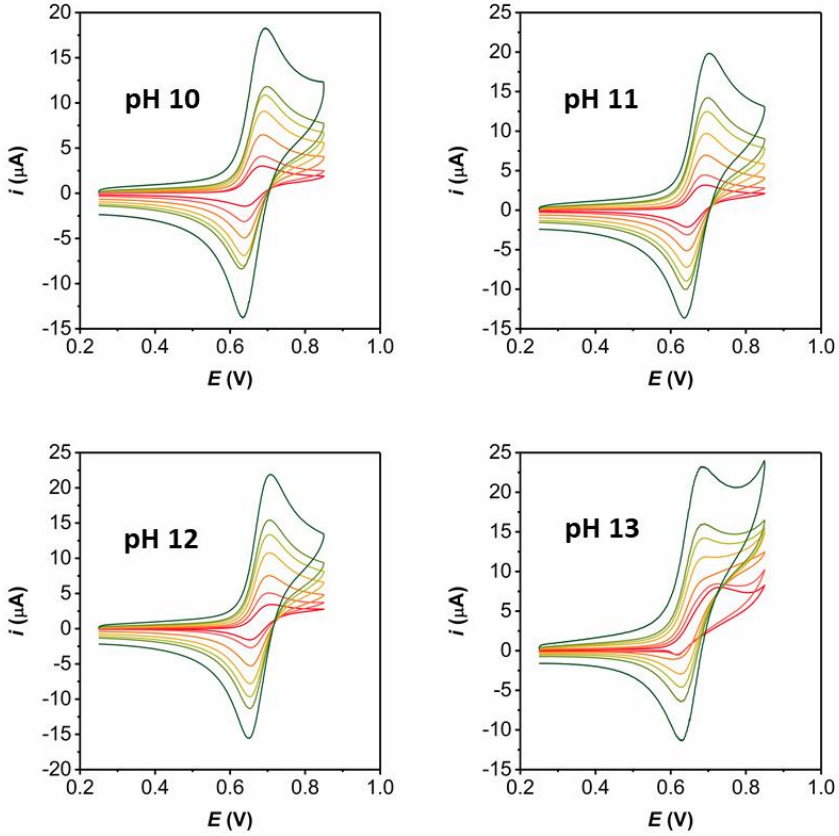

Figure S8. CVs in 1 mM aqueous solution of $\mathbf{1}^{2-}$ at different pH values and different scan rates.

An extension to Nickel

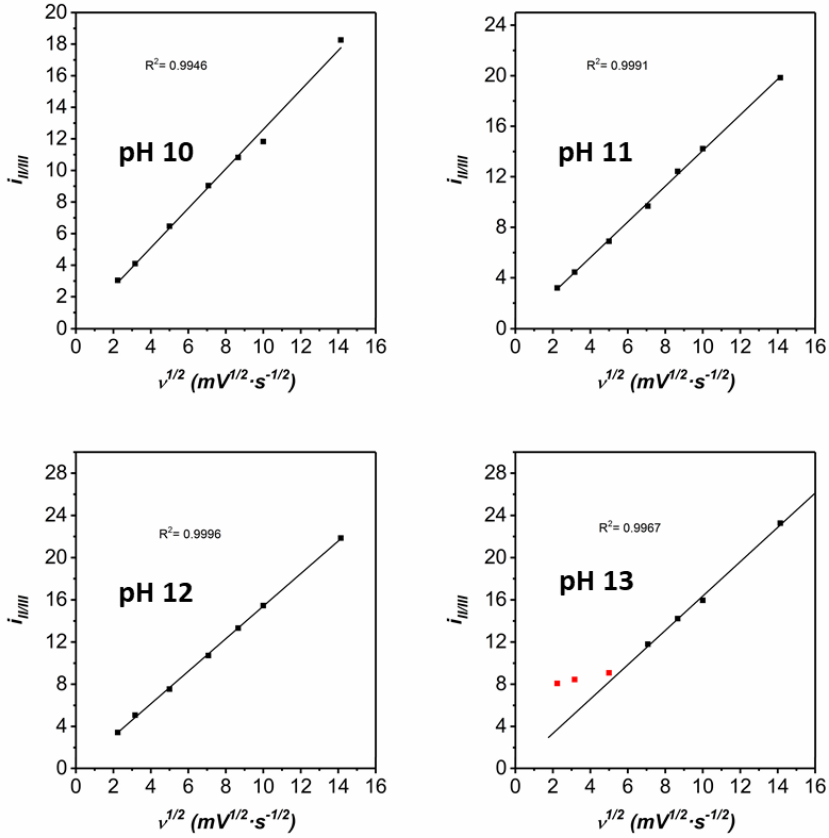

VI

Figure S9. Plot of the current corresponding to the oxidative peak Ni(II)/Ni(III) in different pH solutions versus the square root of the scan rate and the linear fit according to the Randles–Sevcik equation.

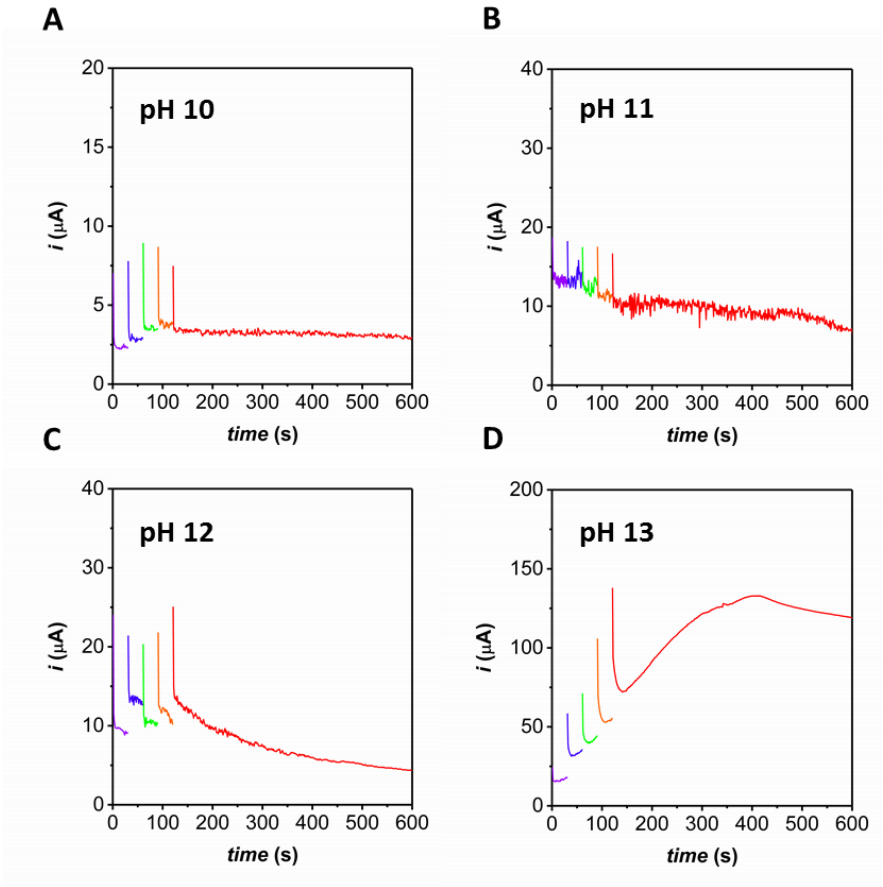

Figure S10. Consecutive CPE experiments at 0.85 V during different times (30, 30, 30, 30 and 480 s) using solutions containing 1 mM $\mathbf{1}^{2-}$ at different pH values: (A) 10, (B) 11, (C) 12 and (D) 13. GC disk was used as working electrode for the CPE. After each bulk, the working electrode was rinsed with water and analyzed in a fresh buffer solution.

An extension to Nickel

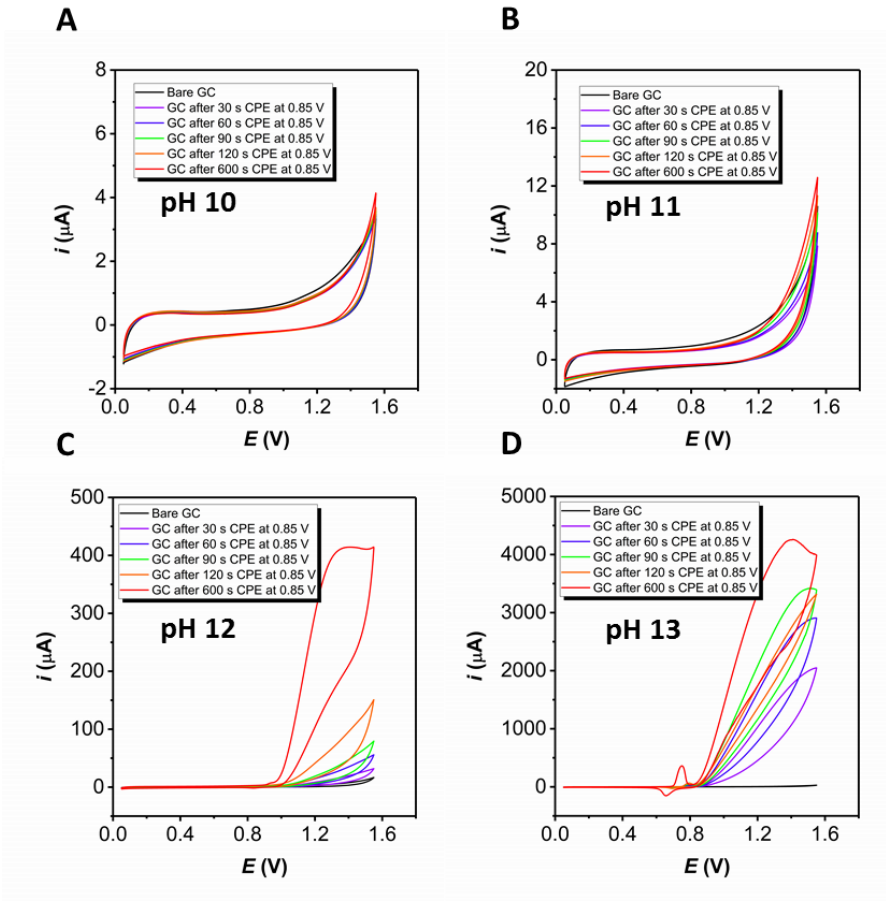

Figure S11. CVs in a fresh buffer solution at (A) pH 10, (B) pH 11, (C) pH 12 and (D) pH 13 of a bare GC electrode (black line) and GC electrodes after CPE in a 1mM solution of $\mathbf{1}^{2-}$ at 0.85 V during increasing times (from purple to red lines).

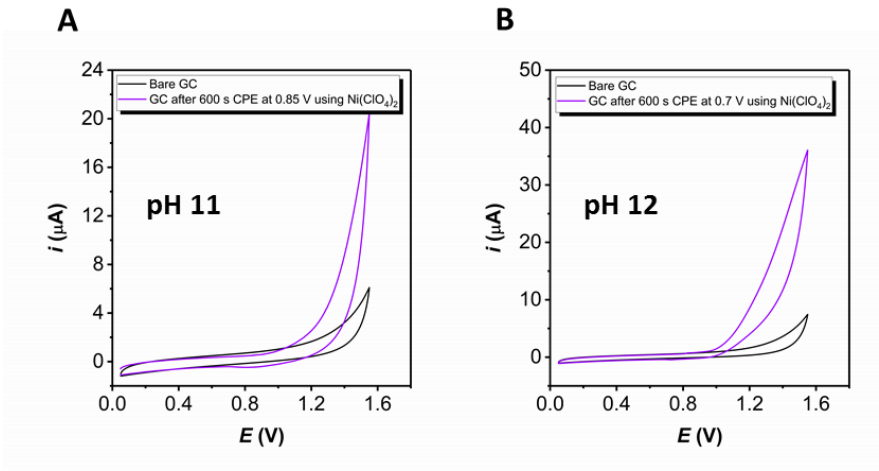

Figure S12. CVs in a fresh buffer solution at (A) pH 11 and (B) pH 12 of a bare GC electrode (black lines) and GC electrodes after CPE in a 1mM solution of $Ni(ClO_4)_2$ (purple lines). That indicates that free metal ions in the solutions readily form NiOx upon CPE under same conditions where complex $\mathbf{1}^{2-}$ did not form.

An extension to Nickel

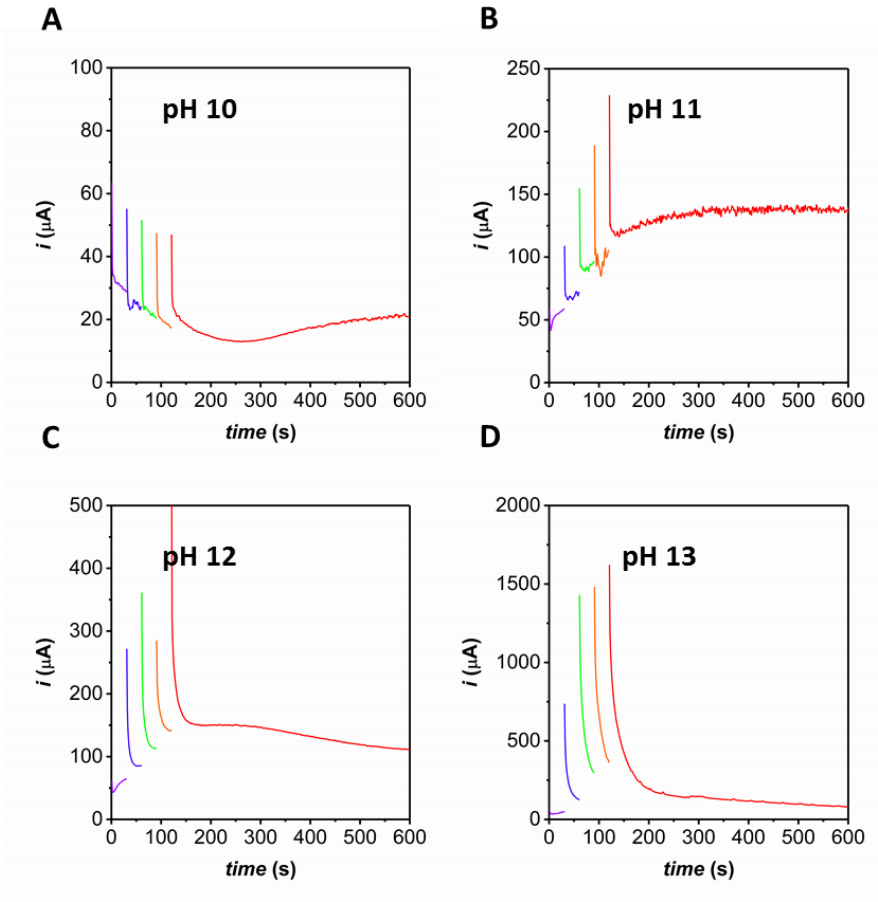

Figure S13. Consecutive CPE experiments at 1.25 V during different times using solutions containing 1 mM $\mathbf{1}^{2-}$ at different pH values: (A) 10, (B) 11, (C) 12 and (D) 13. GC disk was used as working electrode and the scan rate was set to 100 mV/s. After each bulk, the working electrode was rinsed with water and analyzed in a fresh buffer solution.

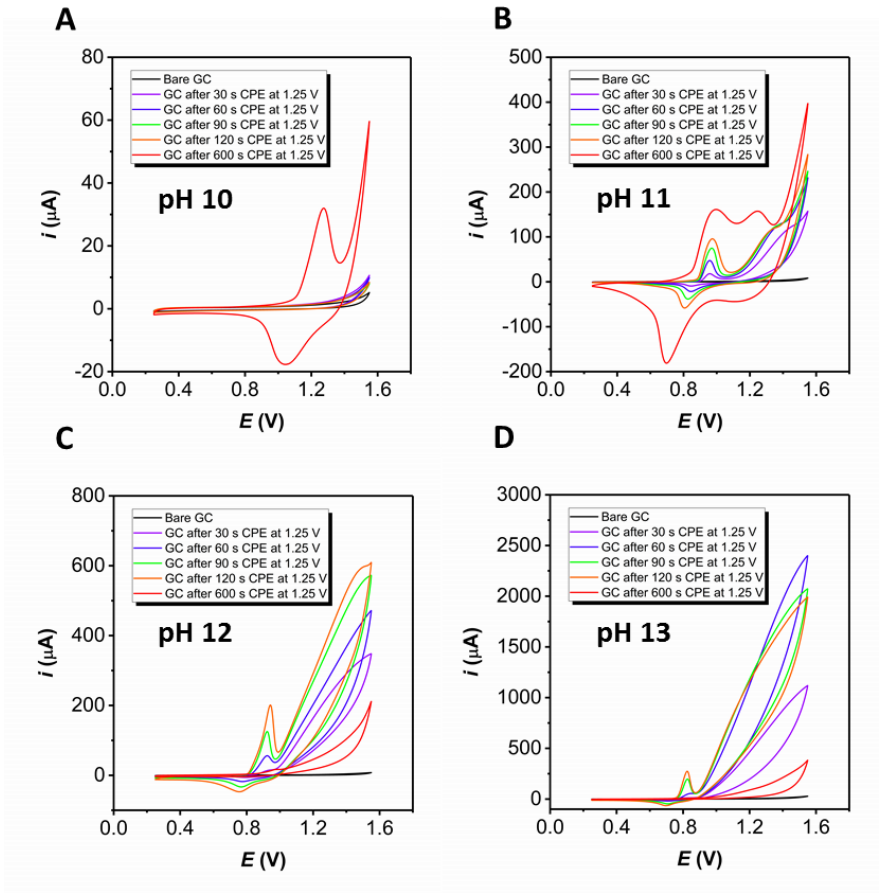

Figure S14. CVs in a fresh buffer solution at (A) pH 10, (B) pH 11, (C) pH 12 and (D) pH 13 of a bare GC electrode (black line) and GC electrodes after CPE in a 1mM solution of $\mathbf{1}^{2-}$ at 1.25 V during increasing times (from purple to red lines).

An extension to Nickel

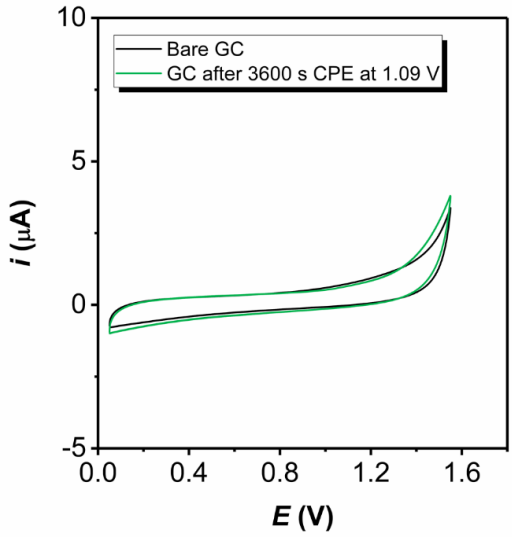

Figure S15. CVs in a fresh buffer solution at pH 10 of a bare GC electrode (black line) and GC electrode after 3600 s CPE in a 1mM solution of $\mathbf{1}^{2-}$ at 1.09 V.

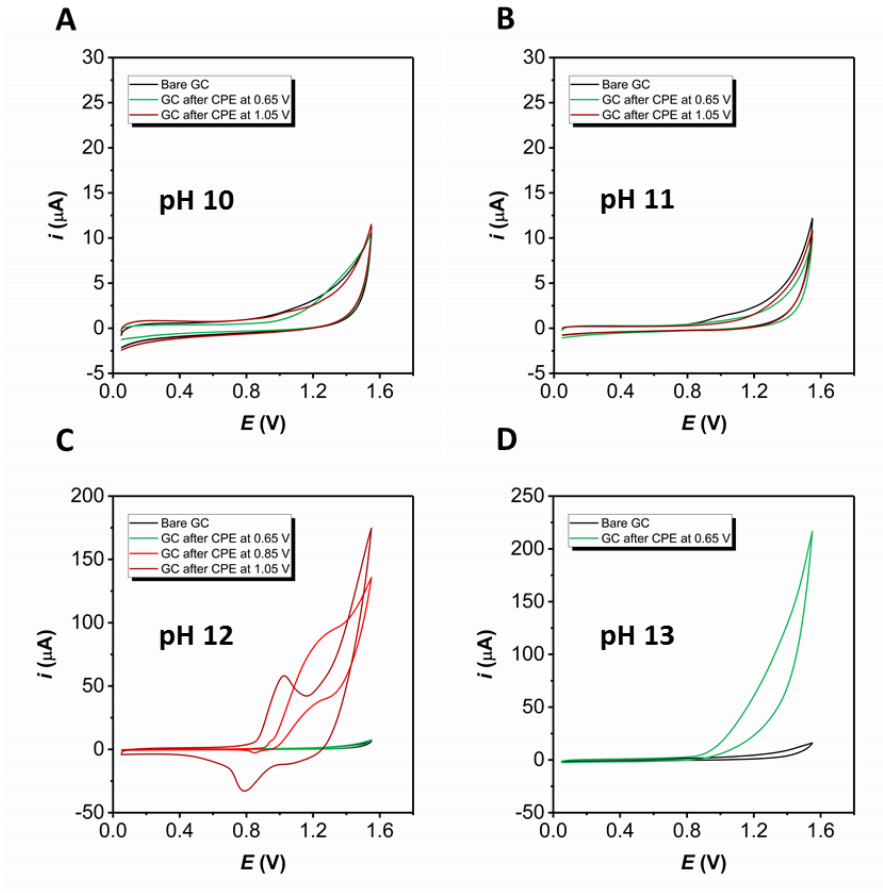

Figure S16. CVs in a fresh buffer solution at (A) pH 10, (B) pH 11, (C) pH 12 and (D) pH 13 of a bare GC electrode (black line) and GC electrodes after 600 s of CPE in a 1mM solution of $\mathbf{2}^{2-}$ at different potentials (from red, brown and green lines).

An extension to Nickel

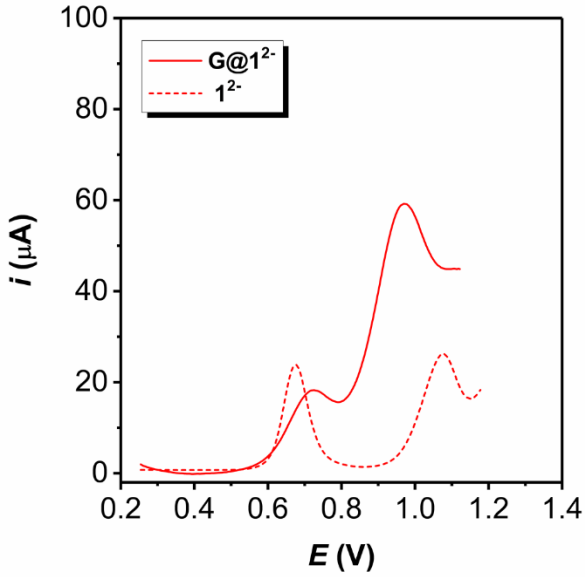

Figure S17. DPV of **G@1²⁻** compared with a 1 mM solution of **1²⁻** both at pH 11, showing a decrease of around 100 mV in the potential of the catalytic wave.

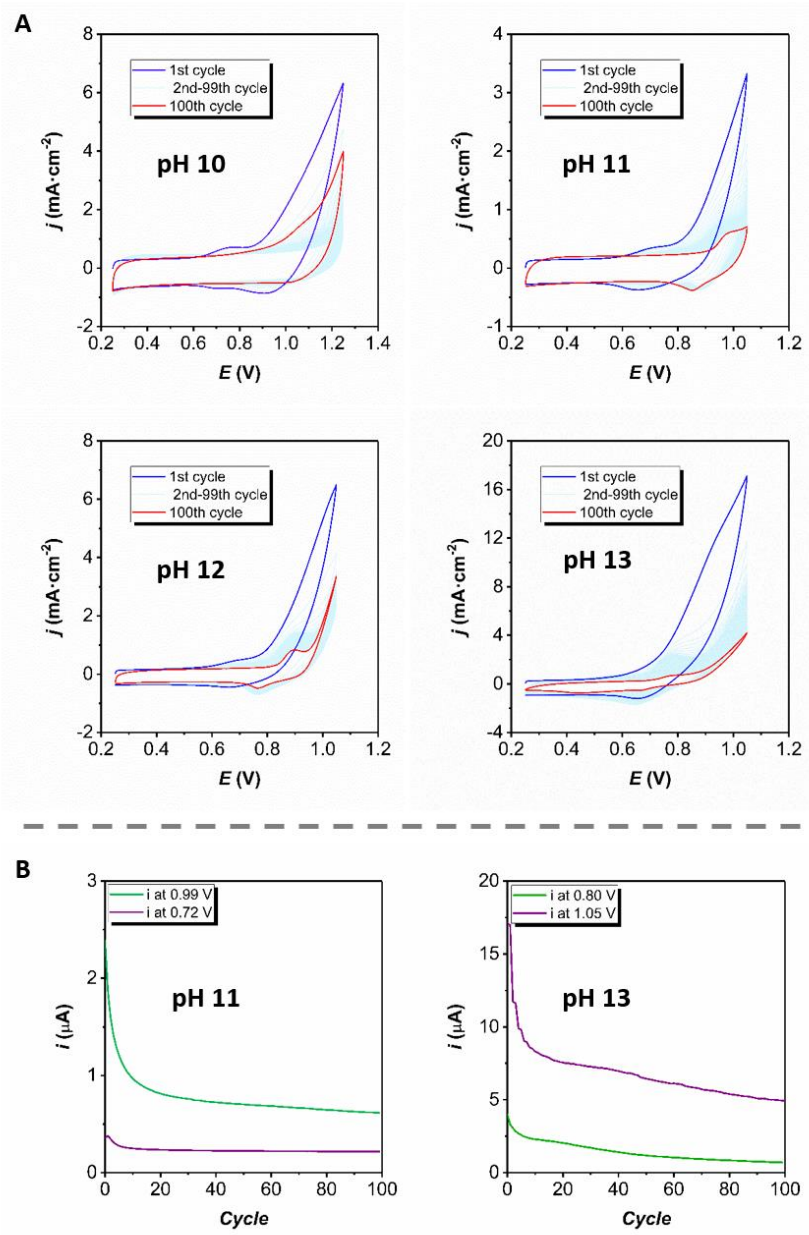

Figure S18. (A) 100 consecutive CVs of electrodes **G@1**$^{2-}$ at different pH values at a scan rate of 100 mV/s. (B) Evolution of the intensity at different potentials with the consecutive cycles in solutions at (left) pH 11 and (right) 13.

An extension to Nickel

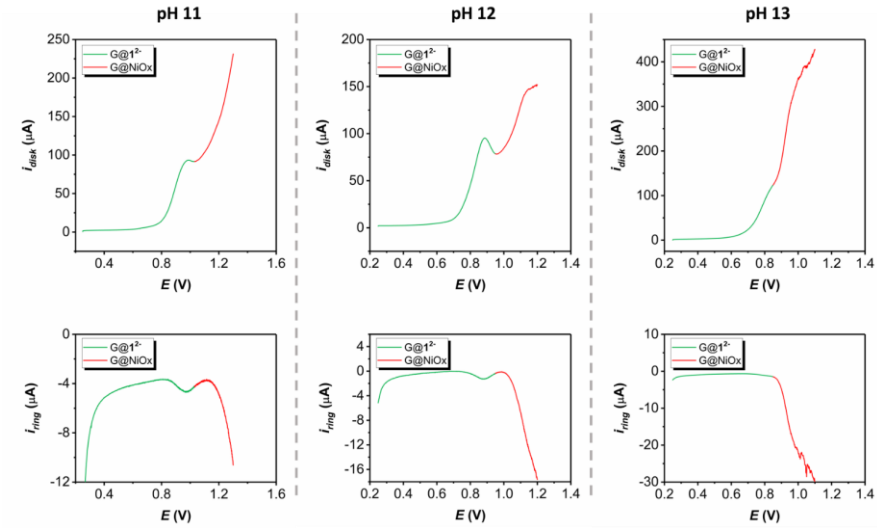

Figure S19. Top figures represents the LSVs of G@(**1²⁻**/NiOx) electrodes generated after cycling G@**1²⁻** electrodes four times supported on the disk of a RRDE in phosphate buffer at different pH values. Experiments were performed under nitrogen atmosphere and at 1600 rpm. Bottom figures show simultaneous CPE at -0.35 V performed in the Pt ring of the RRDE for the reduction of the generated oxygen. Green color represent the molecular domain while red color refers to the electrochemical response of the NiOx.

Electrochemical analysis $Ni_{1-x}Fe_x(OH)_2$ electrodes

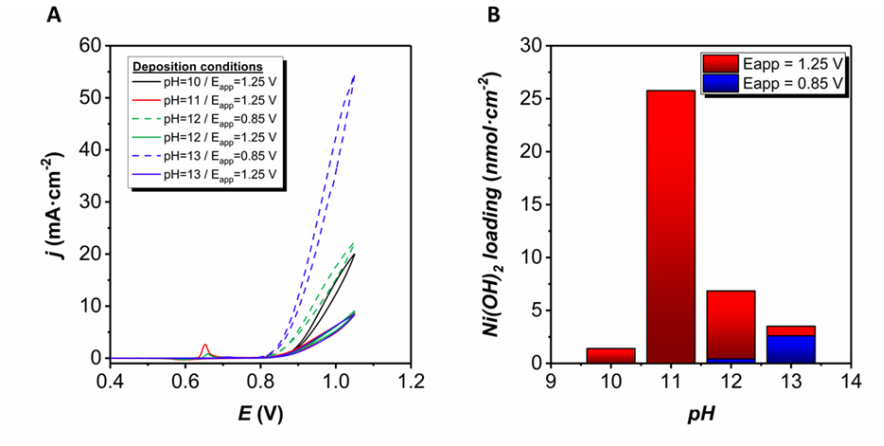

Figure S20. . (A) CVs of NiOx, deposited in a GC electrode from 1mM $\mathbf{1}^{2-}$ under different conditions of pH and E_{app}, obtained in a 1 M KOH aqueous solutions at 10 mV/s. (B) $Ni(OH)_2$ loading obtained by integration of the redox Ni^{II}/Ni^{III} wave for the different electrodes.

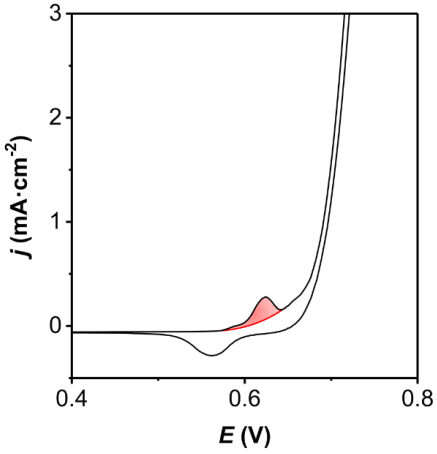

Figure S21. CVs of a NiFeOx in a 1 M KOH aqueous solutions at 10 mV/s. The area of integration is colored in red and obtained using an exponential function as baseline.

An extension to Nickel

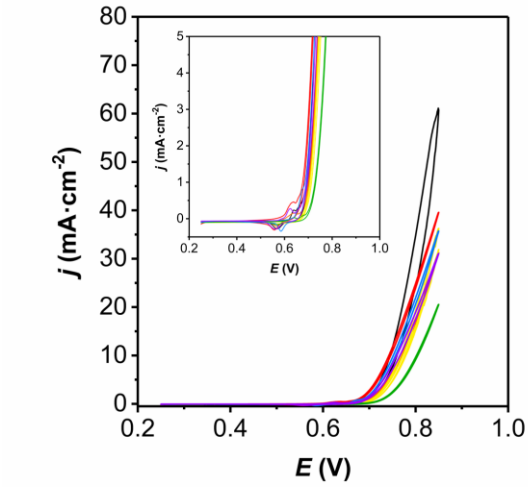

Figure S22. CVs of different NiFeOx electrodes prepared with different loadings obtained in a 1 M KOH solution at 10 mV/s.

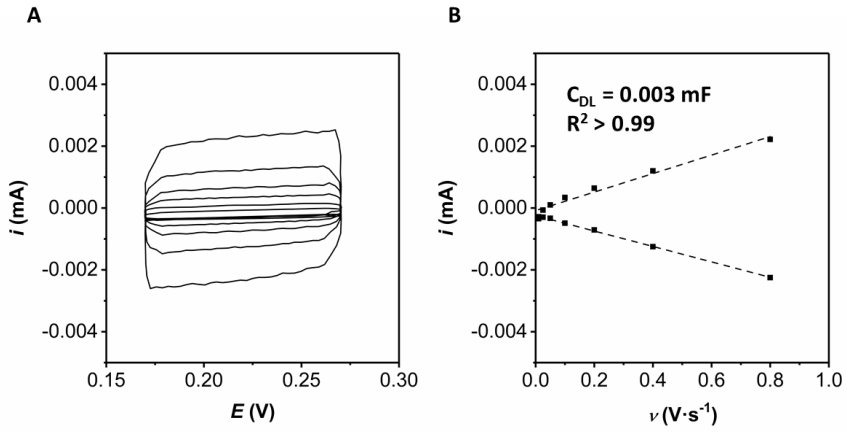

Figure S23. (A) CVs taken at different scan rates in a non-Faradaic region using a NiFeOx electrode. Before every sweep pf potential, the working electrode was held at the limit potential values during 10 s. (B) Representation of the cathodic and anodic charging current in function of the scan rate. Linear fitting of those data allows to calculate the double-layer capacitance from the slope.

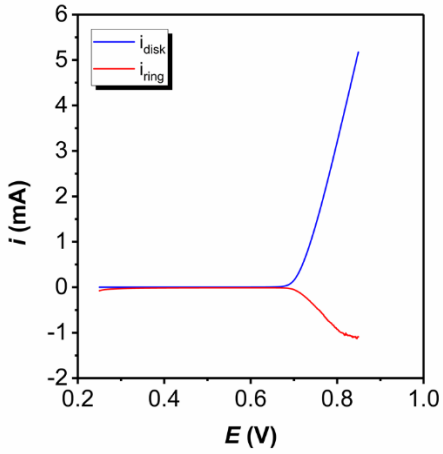

Figure S24. RRDE voltammetry for determination of the Faradaic efficiency. Blue line represents the current in the disk electrode obtained by doing a linear sweep voltammetry of NiFeOx deposited on the GC disk electrode at 10 mV/s (blank). Red line represents the current in the Pt ring electrode obtained by doing a CPE at -1 V to reduce the oxygen produced in the disk. The rotation speed was set to 1600 rpm and the experiment was performed in a 1 M KOH aqueous solution.

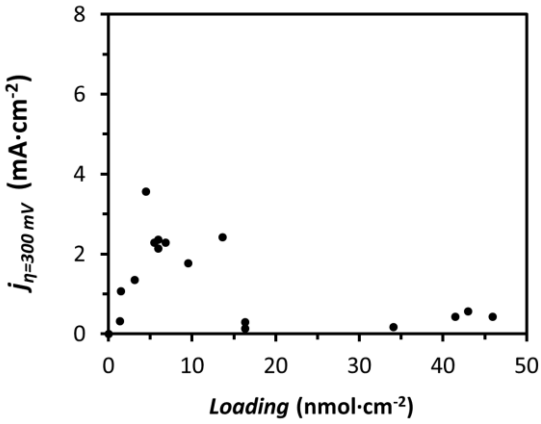

Figure S25. Current densities obtained at 300 mV overpotential taken from CVs of the NiFeOx electrodes prepared with different loadings.

An extension to Nickel

Physical and chemical characterization of electrode surface

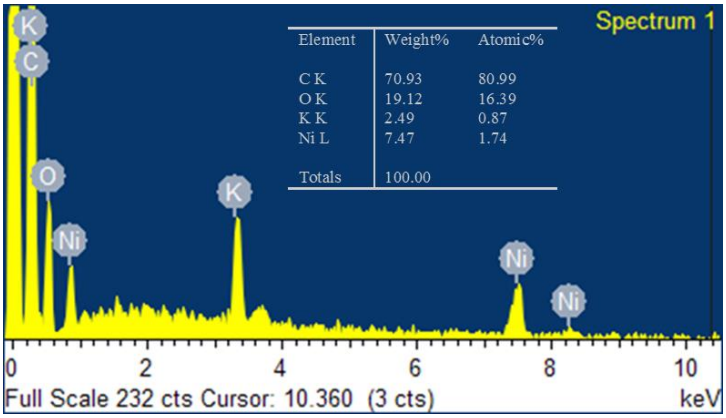

Figure S26. EDX analysis of deposited NiOx on GC plates from molecular complex $\mathbf{1}^{2-}$ by CPE at 1.25 V in pH 13 solution.

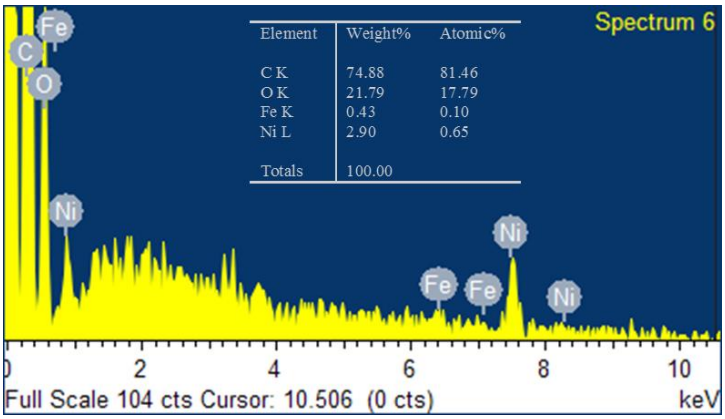

Figure S27. EDX analysis of codeposited on GC plates NiFeOx from a solution containing molecular complex $\mathbf{1}^{2-}$ and $Fe(ClO_4)_2$ by CPE at 0.85 V in pH 13 solution.

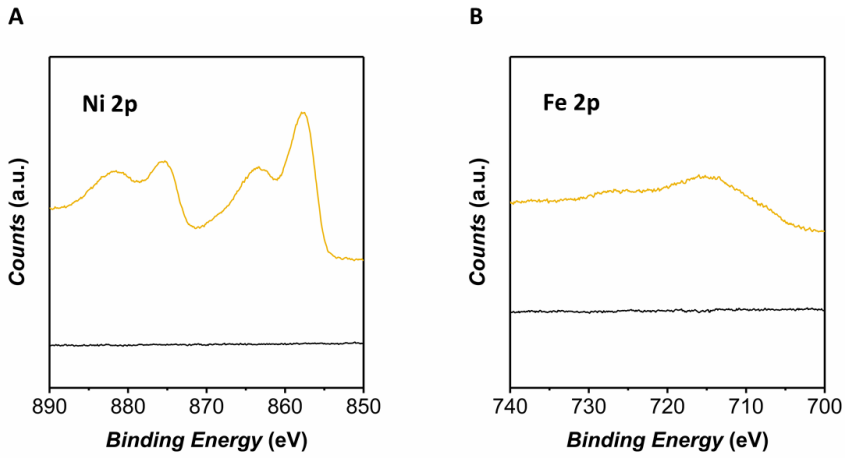

Figure S28. XPS analysis of codeposited NiFeOx on GC plates from a solution containing molecular complex $\mathbf{1}^{2-}$ and $Fe(ClO_4)_2$ by CPE at 0.85 V in pH 13 solution.

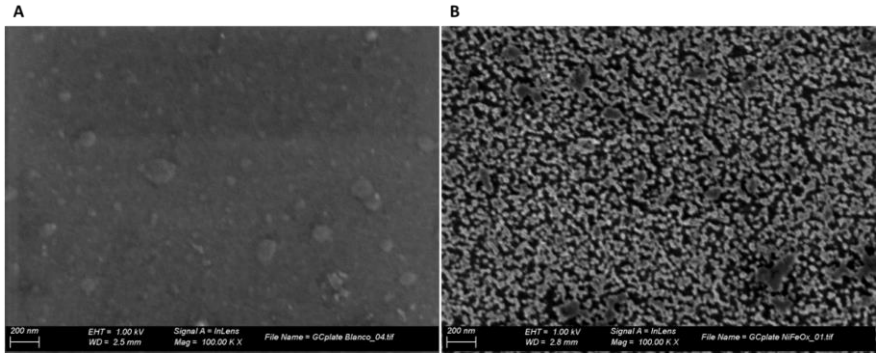

Figure S29. SEM images of (A) bare GC plate electrode and (B) codeposited NiFeOx on GC plates from a solution containing molecular complex $\mathbf{1}^{2-}$ and $Fe(ClO_4)_2$ by CPE at 0.85 V in pH 13 solution.

An extension to Nickel

Computational details

All calculations were carried out with the Gaussian09 (v. D.01) program package[6]. We employed Density Functional Theory (DFT) methodology using the long-range corrected wB97xD as functional.[7] The basis set was split, using 6-31+G(d) for C, N, O and H,[8] and LANL2TZ(f) for Ni and Cu (including the associated pseudopotential).[9,10] The solvation was considered implicitly using the SMD model[11], with water (ε = 78.3553) as solvent. All geometry optimizations were computed in solution without symmetry restrictions. The nature of all computed stationary points was confirmed by vibrational frequency calculations. Free energy corrections were calculated at 298.15 K and 105 Pa pressure, including zero point energy corrections (ZPE). In addition, a correction term of 1.9 kcal/mol (at 298 K) was added when necessary to account for the standard state concentration of 1 M. Unless otherwise mentioned, all reported energy values are free energies in solution. The stability of the electronic states corresponding to the intermediates was confirmed by stability analysis of the wavefunction. The electrochemical magnitudes were calculated from the free energies using the values of 4.28 V found in literature for the absolute potential of the standard hydrogen electrode[12] and-11.72 eV for the free energy of the proton in aqueous solution at pH=1.[13] The value for the free energy of the proton was translated to the experimental pH value of 12 by adding a correction term of -0.059*pH, following the same procedure as other authors.[14] In the systems reported here the agreement of the calculated redox potential with the experimental ones is very good, confirming the validity of this methodology.

Table S1. Comparison between the experimental and the calculated redox potential of the first wave corresponding formally to the Ni^{II}/Ni^{III} transition for the three Nickel complexes studied in this work.

Complex	Redox potential Ni^{II}/Ni^{III} in V	
	E^0_{exp}	E^0_{calc}
$[(L^1)Ni^{II}]^{2-}$	0.67	0.65
$[(L^2)Ni^{II}]^{2-}$	0.57	0.50
$[(L^3)Ni^{II}]^{2-}$	0.57	0.52

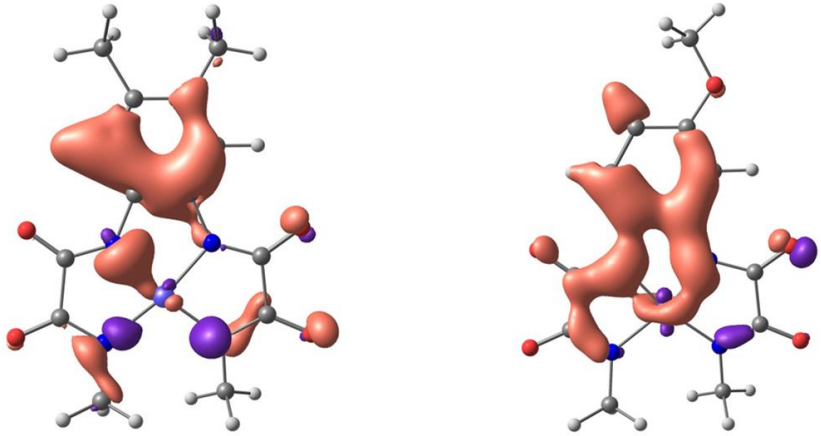

Figure S30. HOMO orbital of the different copper and nickel species calculated by Natural Orbital (NO) analysis. In the case of the copper complex, the HOMOI is mainly located in a d orbital of the metal center, supporting the first metal center oxidation. In the case of the Nickel complexes, the HOMO is shared between the metal center and the ligand, supporting the involvement of the ligad into the first oxidation.

An extension to Nickel

References

1 Wilke, C. R.; Chang, P., *AIChE J,* **1955**, *63*, 264-270.

2 Tromans, D., Hydrometallurgy, **1998**, *50,* 279–296.

3 Stumpf, H. O.; Pei, Y.; Kahn, O.; Sletten, J.; Renard, J. P. *J. Am. Chem. Soc.***1993**, *115*, 6738.

4 Ruiz, R.; Surville-Barland, C.; Aukauloo, A.; Anxolabehere-Mallart, E.; Journaux, Y.; Cano, J.; Carmen Munoz, M. *J. Chem. Soc., Dalton Trans.***1997**, 745.

5 Garrido-Barros, P.; Funes-Ardoiz, I.; Drouet, S.; Benet-Buchholz, J.; Maseras, F.; Llobet, A. *J. Am. Chem. Soc.* **2015**, *137*, 6758.

6 Gaussian 09, Revision **D.01**, Frisch, M. J.; Trucks, G. W.; Schlegel, H. B.; Scuseria, G. E.; Robb, M. A.; Cheeseman, J. R.; Scalmani, G.; Barone, V.; Mennucci, B.; Petersson, G. A.; Nakatsuji, H.; Caricato, M.; Li, X.; Hratchian, H. P.; Izmaylov, A. F.; Bloino, J.; Zheng, G.; Sonnenberg, J. L.; Hada, M.; Ehara, M.; Toyota, K.; Fukuda, R.; Hasegawa, J.; Ishida, M.; Nakajima, T.; Honda, Y.; Kitao, O.; Nakai, H.; Vreven, T.; Montgomery, J. A., Jr.; Peralta, J. E.; Ogliaro, F.; Bearpark, M.; Heyd, J. J.; Brothers, E.; Kudin, K. N.; Staroverov, V. N.; Kobayashi, R.; Normand, J.; Raghavachari, K.; Rendell, A.; Burant, J. C.; Iyengar, S. S.; Tomasi, J.; Cossi, M.; Rega, N.; Millam, J. M.; Klene, M.; Knox, J. E.; Cross, J. B.; Bakken, V.; Adamo, C.; Jaramillo, J.; Gomperts, R.; Stratmann, R. E.; Yazyev, O.; Austin, A. J.; Cammi, R.; Pomelli, C.; Ochterski, J. W.; Martin, R. L.; Morokuma, K.; Zakrzewski, V. G.; Voth, G. A.; Salvador, P.; Dannenberg, J. J.; Dapprich, S.; Daniels, A. D.; Farkas, Ö.; Foresman, J. B.; Ortiz, J. V.; Cioslowski, J.; Fox, D. J. Gaussian, Inc., Wallingford CT, 2009.

7 Chai, J.-D.; Head-Gordon, M. *Phys. Chem. Chem. Phys.* **2008**, *10*, 6615-6620.

8 a) Hehre, W.J.; Ditchfield, R.; Pople, J.A., *J. Chem. Phys.* **1972**, 56, 2257. b) Hariharan, P.C.; Pople, J.A., *Theoret. ChimicaActa* **1973**, *28*, 213-222. c) Francl, M.M.; Petro, W.J.; Hehre, W.J.; Binkley, J.S.; Gordon, M.S.; DeFrees, D.J.; Pople, J.A., *J. Chem. Phys.* **1982**, *77*, 3654.

9 a) Hay, P. J.; Wadt, W. R., *J. Chem. Phys.***1985**, *82*, 270. b) Hay, P. J.; Wadt, W. R., *J. Chem. Phys.***1985**, *82*, 284. c) Hay, P. J.; Wadt, W. R., *J. Chem. Phys.***1985**, *82*, 299.

10 Taken from EMSL Basis set Library: a) Felier, D., *J. Comp. Chem.***1996**, *17*, 1571-1586. b) Schuchardt, K.L.; Didier, B.T.; Elsethagen, T.; Sun, L.; Gurumoorthi, V.; Chase, J.; Li, J.; Windus, T.L., *J. Chem. Inf. Model.*, **2007**, *47*, 1045-1052.

11 Marenich, S. A. V.; Cramer, C. J.; Truhlar, D. G., *J. Phys. Chem. B*, **2009**, *113,* 6378-6396.

12a) Lewis, A.; Bumpus, J. A.; Truhlar, D. G.; Cramer, C. J., *J. Chem. Ed.* **2004**, *81*, 596-604. b) Lewis, A.; Bumpus, J. A.; Truhlar, D. G.; Cramer, C. J., *J. Chem. Ed.* **2007**, *84*, 934.

13 Marenich, A. V.; Majunmdar, A.; Lenz, M.; Cramer, C. J.; Truhlar, D. G., *Angew. Chem. Int. Ed.* **2012**, *51*, 12810-12814.

14 Winikoff, S.G.; Cramer, C.J.; *Catal. Sci. Technol.* **2014**, *4*, 2484-2489.

Chapter 7

General Conclusions

According to the general objectives proposed in the present thesis, this chapter gather the general conclusions obtained. Specific and more detailed conclusions are presented at the end of each chapter from 3 to 7.

General Conclusions

A new family of copper complexes based on the redox non-innocent ligand H_4mox (H_4mox is N^1,$N^{1'}$-(1,2-phenylene)bis(N^2-methyloxalamide))) generated efficient and robust catalyst toward water oxidation to molecular oxygen.

Firstly, this tetra-anionic ligand has a strong σ-donating character and, once coordinated to the metal center, it imposes a rigid square planar geometry. Both factors are essentials in order to stabilize high oxidation states of copper complexes (such as Cu(III)), which are potentially involved in the catalytic cycle as intermediates. Secondly, as already mentioned, this ligand has also a redox non-innocent character and its one-electron oxidation enables the generation of a radical species $[(mox^{\cdot})(OH)Cu(III)]^-$ that can promote the O-O bond formation and eventually release oxygen regenerating the initial catalyst. As this ligand oxidation is tied to the rate determining step of the catalytic cycle, simple modifications ligand's electronic features can translate into an excellent control of the catalytic propierties such as overpotential or kinetic constant. Therefore, introduction of more electron-donating substituent in the phenyl ring allowed to gradually decrease the overpotential for water oxidation to a record value of 150 mV.

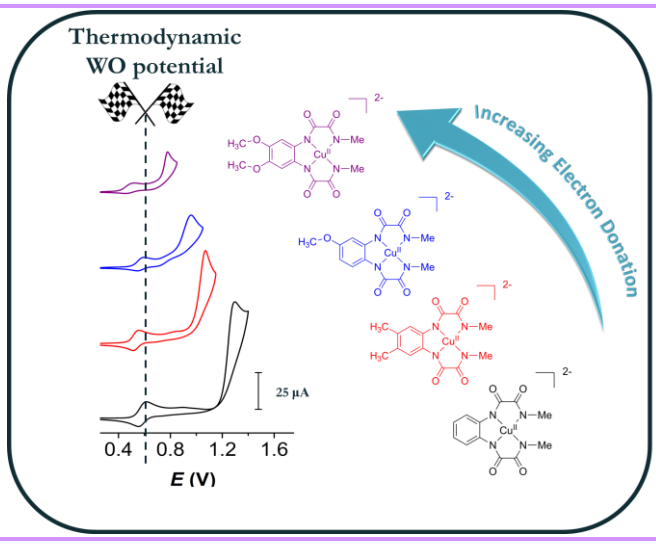

Figure 1. Cyclic voltammetry of the different copper complexes from the $[(mox)Cu]^{2-}$ family showing the relationship between overpotential and electron-donation character of the phenyl substituents.

Chapter 7

New unprecedented mechanism for the O-O bond formation is found for molecular water oxidation using copper complexes: Single Electro Transfer-Water Nucleophilic Attack (SET-WNA).

Ruthenium complexes have been long studied as water oxidation catalysts giving rise to valuable mechanistic knowledge. However, the redox flexibility of those complexes allows them to reach high oxidation states such as Ru(V) or Ru(VI) that are able to activate coordinated oxo groups toward the water nucleophilic attack. Therfore the O-O bond is formed through a single, concerted two-electron transfer. However, first row transition metal complexes are more reluctant to reach those high oxidation states and as a consequence one-electron transfer steps are favoured. Considering this new outlook, three different catalytic system based on copper complexes have been computationally studied. Beside the structural and electronic differences, the O-O bond formation mechanism was found to be equivalent in the three cases. After two consecutive oxidations, an active species is formed featuring a Cu(III) center and a radical in the ligand or bonded hydroxo/oxo group. This species promotes a first single electron transfer with an external OH^- molecule giving rise to a two centres-three eleectrons intermediate. The latter undergoes a second single electron transfer making the O-O bond and forming a hydroperoxo intermediate. This new mechanism has been named as Single Electron Transfer-Water Nucleophilic Attack and enabled to complete the mechanistic scenario of water oxidation by molecular complexes catalysts.

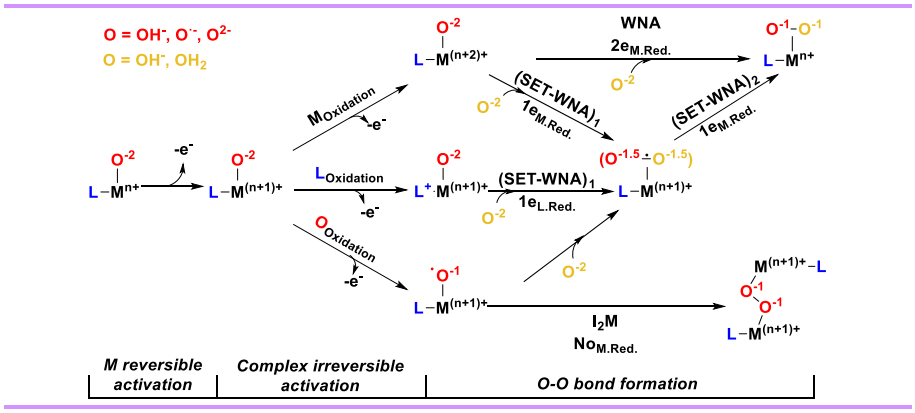

Figure 2. Overview of the water oxidation mechanisms. The oxygen initially attached to the metal is marked in red; the incoming oxygen is marked in yellow.

General Conclusions

The redox activity of the ligand or coordinated hydroxo/oxo groups is essential to promote the O-O bond formation since copper metal center is reluctant to accumulate two oxidative equivalents.

The work performed with $[(mox)Cu(II)]^{2-}$ has shown that Cu(IV) species are reluctant to be formed during the water oxidation mechanism even when higly σ-donating ligand are used (such as tetra-amide ligands). Instead, either the ligand or a coordinated hydroxo/oxo group is oxidized generating the key species that are active toward water oxidation. In this context, two new systeems with different redox features have been analyzed as water oxidation catalyst. First, the copper complex [(*p*-bdam)Cu] (where *p*-bdam is 4,4'-(([2,2'-bipyridine]-6,6'-dicarbonyl)bis(azanediyl)) dibenzenesulfonic acid) has demonstrated to catalytically oxidized water to dioxygen at basic pH. Interistingly, during the water oxidation mechanism, the metal center does not change the oxidation state and, instead, two oxidations taking place in the ligand promote the generation of the active species toward the O-O bond formation. Although the copper center remain as a spectator from a redox point of view, it is essential for the coordination of the hydroxo molecules in the equatorial position that are required during the catalytic cycle. The lack of catalytic activity in the analogous complex [(*p*-bdam)Cu] (where *o*-bdam is 2,2'-(([2,2'-bipyridine]-6,6' dicarbonyl)bis(azanediyl)) is attributed to the sterical difficulties in coordinating hydroxo molecules due to the ortho position of the sulfonate groups.

On the other hand, the copper complex [(bpk)Cu] (where bpk is 6,6'-diisopropanoate-2,2'-bipyridine) has also been studied for water oxidation. In the pH range of 7-12, the ligand remained deprotonated with both alkoxo unit coordinating the metal center. In these conditions, the ligand is redox innocent and the complex can only be oxidize once to a Cu(III) species that is not able to promote water oxidation. However, between pH 13 and 14, there is a partial ligand decoordination and either one or two hydroxo molecules are coordinated in the equatorial position. The dangling alkoxo moieties are thus protonated forming alcohol groups that confer redox activity to the ligand. This change in the electronic features enables to accumulate more than one oxidative equivalent in the complex and then becomes active for catalytic water oxidation.

Chapter 7

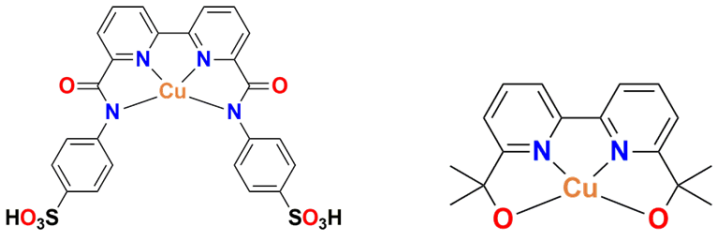

[(*p*-bdam)Cu] [(bpk)Cu]

Figure 3. Structural representation of the water oxidation catalysts [(*p*-bdam)Cu] and [(bpk)Cu].

Anchoring of molecular copper catalysts bearing non-innocent ligands to π-delocalized surface by π-π stacking forces boosts the reaction rate of water oxidation catalysis.

The water oxidation catalyst $[(mox)Cu^{II}]^{2-}$ and its modified analogue including a pyrene functional group in the phenyl ring have been studied in order to analyzed the influence that a π-delocalized functionality exerts on the catalytic performance. Results show that both the overpotential for water oxidation and the observed kinetic constant improved respect to the unfunctionalized catalysts: the overpotential decreases around 150 mV and the k_{cat} increases two order of magnitude. Moreover, both catalysts have been used to generate anodes upon immobilization on the surface of graphenic electrodes by π-π stacking forces. Therefore, the effect of the π-delocalization exerted by the graphene layers is added leading to an increase in the k_{cat} in both cases respect to the homogeneous systems. The new immobilized system containing the pyrene functionality is one of the fastest and most robust catalysts based on first row transition metals complexes with TON values of 5300 and with a k_{cat} of 540 s^{-1}.

General Conclusions

Nickel complexes features more labile metal-ligand bonds than the copper analogous complexes. Then, substitution of those bonds by hydroxo molecules coming from the solvents takes place more easily leading to degradation under oxidative potential and basic pH values.

Considering the results and mechanistic information obtained with the copper catalyst $[(mox)Cu(II)]^{2-}$, the same ligand framework has been used to generate nickel complexes that have been studied for water oxidation catalysis. Interestingly, beside the similar structural features of both Cu and Ni complexes revealing strong metal-ligand bonds, Ni complexes are susceptible to substitution reactions under the water oxidation condition that eventually release free ligand and result in the formation of Ni oxide on the surface of the electrode. Therefore, two catalytic cycles can operate simultaneously: one based on the molecular complex acting as homogeneous catalyst and the other based on the Ni oxide acting as heterogeneous catalyst. The degradation of the molecular species and formation of Ni oxide is highly determined by the experimental conditions and modification of the ligand can strongly influence the relationship between both systems increasing the stability of the molecular catalysts.

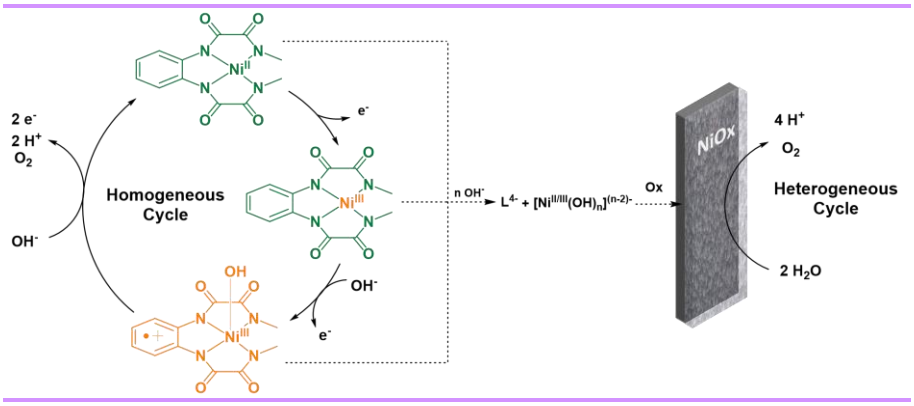

Figure 4. Simplified proposed catalytic cycle for water oxidation by complex 12- and mechanism for deactivation of complex 12- and formation of NiOx.

Annexes

Glossary of terms and abbreviations

bpp^-	3,5-bis(2-pyridyl)pyrazolate
bpy	2,2'-bipyridine
C_{DL}	Double Layer Capacitance
COSY	Correlation Spectroscopy
CPE	Controlled Potential Electrol-
C_S	ysis
	Specific Capacitance
CV	Cyclic Voltammetry
BDD	Boron Doped Diamond
d	doublet
δ	Chemical shift
DCM	Dichloromethane
DFT	Density Functional Theory
dmso	Dimethyl sulfoxide
DPV	Differential Pulse Voltamme-
	try
E	Potential
ECSA	Electrochemically Active Sur-
	face Area
ε	Extintion Coefficient
E½	Half wave potential
ESI-MS	Electrospray Ionization Mass
	Spectrometry
FE	Faradaic Efficiency
FOWA	Foot of the Wave Analysis
GC	Glassy Carbon
H2bda	[2,2'-bipyridine]-6,6'-dicarbox-
HER	ylic acid
HEC	Hydrogen Evolution Reaction
hν	Hydrogen Evolution Catalyst
	Light
J	Coupling constant
λ	Wavelenght
M	Molar
I	Ionic force
I2M	Bimolecular Interaction
i	Mechanism
j	Current
	Current density

m/z	Mass-to-Charge ratio
MLCT	Metal to Ligand Charge Transfer
MS	Mass Spectrometry
η	Overpotential
NHE	Normal Hydrogen Electrode
NMR	Nuclear Magnetic Resonance
NOESY	Nuclear Overhauser Spectroscopy
NPs	Nanoparticles
OEC	Oxygen Evolving Center
PCET	Proton Coupled Electron Transfer
PEC	Photoelectrochemical cell
PEM	Proton Exchange Membrane
Ph	Phenyl
ppm	Parts per million
PSI	Photosystem I
PSII	Photosystem II
PT	Proton Transfer
PV	Photovoltaic
py	Pyridine
RDV	Rotating Disk Voltammetry
RF	Roughness Factor
RT	Room Temperature
S	Surface of the electrode
s	Singlet
SCE	Saturated Calomel Electrode
t	Triplet
$TBAPF_6$	Tetra(N-butyl)ammonium hexafluorophosphate
TEA	Trimethylamine
TOF	Turnover Frequency
TON	Turnover Number
trpy	2,2':6',2"-terpyridine
UV-vis	Ultraviolet-visible Spectroscopy
v	Scan rate
vs.	versus
WNA	Water Nucleophilic attack
WO	Water Oxidation
WOC	Water Oxidation Catalyst

UNIVERSITAT ROVIRA I VIRGILI
MOLECULAR WATER OXIDATION CATALYSTS BASED ON COPPER AND NICKEL COMPLEXES
Pablo Garrido Barros

UNIVERSITAT ROVIRA I VIRGILI
MOLECULAR WATER OXIDATION CATALYSTS BASED ON COPPER AND NICKEL COMPLEXES
Pablo Garrido Barros

UNIVERSITAT ROVIRA I VIRGILI
MOLECULAR WATER OXIDATION CATALYSTS BASED ON COPPER AND NICKEL COMPLEXES
Pablo Garrido Barros

UNIVERSITAT
ROVIRA i VIRGILI